

NATIONAL AERONAUTICS AND SPACE ADMINISTRATION

*Technical Report 32-1586*

*Mariner 9 Navigation*

*W. J. O'Neil, J. F. Jordan, J. W. Zielenbach, S. K. Wong,  
R. T. Mitchell, W. A. Webb, P. E. Koskela, et al.*

(NASA-CR-139521) ...  
(Jet Propulsion Lab.) ...

87-20120  
T.M.U.  
87-20120  
60415  
5-11+



**JET PROPULSION LABORATORY  
CALIFORNIA INSTITUTE OF TECHNOLOGY  
PASADENA, CALIFORNIA**

November 13, 1973

NATIONAL AERONAUTICS AND SPACE ADMINISTRATION

*Technical Report 32-1586*

*Mariner 9 Navigation*

*W. J. O'Neil, J. F. Jordan, J. W. Zielenbach, S. K. Wong,  
R. T. Mitchell, W. A. Webb, P. E. Koskela, et al.*

**JET PROPULSION LABORATORY  
CALIFORNIA INSTITUTE OF TECHNOLOGY  
PASADENA, CALIFORNIA**

November 13, 1973

Prepared Under Contract No. NAS 7-100  
National Aeronautics and Space Administration

## **Preface**

The work described in this report was performed by the Mission Analysis Division of the Jet Propulsion Laboratory.

# Contents

<b>Introduction</b>	1	✓
W. J. O'Neil		
<b>Figures</b>		
1. Mariner Mars 1971 Mission Operations Organization	18	
2. Mariner Mars 1971 Navigation Team	19	
<b>Interplanetary Orbit Determination</b>		
J. W. Zielenbach, C. H. Acton, G. H. Born, W. G. Breckenridge, C. C. Chao, T. C. Duxbury, D. W. Green, N. Jerath, J. F. Jordan, N. A. Mottinger, S. J. Reinhold, K. H. Rourke, G. L. Sievers, and S. K. Wong		
I. Interplanetary Operations	20	✓
A. Introduction	20	
B. The Interplanetary OD Group	20	
C. Interfaces With Outside Groups	21	
D. Data Used in the Orbit Determination Process	22	
E. Software Used by the Orbit Determination Groups	23	
II. Pre-flight Analysis	25	
A. Introduction	25	
B. Major Error Sources for Radio Navigation	26	
C. Assumed Magnitudes of the Radio Navigation Error Sources	28	
D. Error Sources for Onboard Optical Navigation	28	
E. Assumed Magnitudes of the Optical Navigation Error Sources	29	
F. Development of OD Strategies	29	
III. Orbit Determination	30	
A. Introduction	30	
B. Pre-midcourse Results	30	
C. Midcourse Maneuver Analysis	31	
D. Post-midcourse Results	32	
E. Pre-MOI Support	35	
F. The Current Best Estimate	36	
G. An Evaluation of Mars Orbit Insertion With Radiometric Data	36	
H. Determination of Astrodynamics Constants From Interplanetary Data	37	
I. Determination of DSS Locations From Interplanetary Data	38	

IV. Station Locations and the Orbit Determination Process	39
A. Introduction	39
B. How DSS Locations Are Involved in OD	39
C. Obtaining "True" Station Locations	39
D. Locations Recommended for Real-Time Use	42
E. Sensitivity to Station Locations or ESLEs as a Function of Data Arc	42
F. Estimating Station Locations in Flight	43
V. Attitude Control Leaks	43
A. Introduction	43
B. Determination of Accelerations Induced by Gas Leaks From Attitude Control Telemetry	44
C. Use of Advanced Filtering Techniques	46
D. Differenced Radiometric Data as a Countermeasure for the Process Noise Problem	50
VI. Radiometric/Optical Navigation	54
A. Introduction	54
B. The Optical Data Instrument	54
C. Optical Data Errors	54
D. Optical Data Types and Their Information Content	54
E. Advantages of Combined Radiometric and Optical Data Sets	55
F. Selection of Approach Pictures	56
G. Operational Techniques and Results	57
H. Post-flight Sensitivity Studies	58
I. Conclusions	60
References	60
Appendix A. Definition of B-Plane Parameters	110
Appendix B. Mars Mission Lockfile	112
<b>Tables</b>	
1. Standard deviations of residuals based on a state-only solution from Run 000967	62
2. Transfer trajectory navigation accuracy requirements, $3\sigma$	62
3. A priori uncertainties in radio tracking parameters	62

4. <i>A priori</i> uncertainties in elements of the Martian natural satellites . . . . .	62
5. Some typical parameter sets . . . . .	63
6. Comparison of nongravitational parameter solutions using pre-midcourse data . . . . .	63
7. Pre-midcourse (post-unlatch) results . . . . .	64
8. Pre-sporadic gas leak results . . . . .	65
9. Pre-unlatch results . . . . .	66
10. Comparison of <b>B</b> -plane parameters for pre-unlatch orbits, adjusted for unlatch and maneuver $\Delta$ 's . . . . .	67
11. Orbit changes caused by scan platform unlatch and engine gas line venting (Run UPBM16) . . . . .	67
12. Comparison of <b>B</b> -plane parameters for pre-midcourse orbits, adjusted for maneuver $\Delta$ 's . . . . .	67
13. Differences between current best estimate of encounter orbit and final aiming point for the maneuver . . . . .	67
14. Commanded midcourse maneuver and current best estimate of achieved maneuver . . . . .	68
15. Comparison of <b>B</b> -plane estimate.. using different ephemerides . . . . .	68
16. Comparison of AC coefficients using post-midcourse data . . . . .	68
17. Predicted <b>B</b> -plane parameters at MOI - 12 h . . . . .	68
18. Predicted <b>B</b> -plane parameters at MOI - 2 h . . . . .	68
19. Predicted <b>B</b> -plane parameters for selected radio-only solutions . . . . .	69
20. Solutions supporting current best estimate of <b>B</b> -plane parameters . . . . .	72
21. Comparison of estimated maneuver parameters . . . . .	72
22. Determination of GM Earth from Mariner 9 data . . . . .	73
23. Influence of consider parameters on GM Earth determination . . . . .	73
24. DSS locations determined from interplanetary data . . . . .	74
25. Torque directions around spacecraft axes caused by roll-jet thrusts . . . . .	75
26. Current best estimate of accelerations during interplanetary phase induced by roll-jet leak . . . . .	75
27. Formation of certain radiometric data types . . . . .	76
28. Summary of data used in dual-station experiment . . . . .	76
29. Estimated frequency offsets in mHz from F3, F2, and MU solutions . . . . .	77
30. Deimos coverage . . . . .	77

## Figures

1. Tracking coverage provided by the DSN for MM'71 interplanetary operations	78
2. Standard deviations of MARK 1A passes from the state-only solution of Run 000967	85
3. Average residuals of all TAU and MU ranging passes from the state-only solution of Run 000967	86
4. Residuals of post-1969 planetary ranging data from DE69	87
5. Residuals of 1971 planetary ranging data from DE78	88
6. Differences (DE79 - DE78) in geocentric spherical coordinates of Mars	88
7. Interaction of radiometric data processing programs	88
8. Optical navigation demonstration software	89
9. Data arc effects	89
10. Data type effects	89
11. B-plane behavior of state-only solutions during the interplanetary phase	90
12. Secular behavior of solutions for solar pressure coefficients	91
13. Summary of inflight and post-flight B-plane predictions	92
14. Spacecraft and station coordinate system	93
15. Range rate observables	93
16. Spacecraft AC roll jets and forces	93
17. Typical AC telemetry data represented by polynomials fit to them	94
18. Angular accelerations computed for a typical period of small ("constant") gas leaks	95
19. Angular accelerations computed for a typical period of large roll-jet leaks	96
20. Current best estimate of translational acceleration magnitudes caused by AC jet leaks during the interplanetary phase	96
21. Evolution of state estimates in the B-plane for the batch filter (set 1)	96
22. Comparison of November approach solution with current best estimate	97
23. Time history of B · R solutions from the batch filter (set 1)	97
24. Time history of B · R solutions from the batch filter (set 2)	97
25. Time history of perturbations in B · R caused by +7-m $\lambda$ and +3-m $r$ , errors in all station locations using a batch filter	97

26. Time history of <b>B · R</b> solutions for the $10^{-12}$ km/s <sup>2</sup> process noise sequential filter (set 1)	97
27. Time history of <b>B · R</b> solutions for the $10^{-12}$ km/s <sup>2</sup> process noise sequential filter (set 2)	98
28. Time history of <b>B · R</b> solutions for the $10^{-11}$ km/s <sup>2</sup> process noise sequential filter (set 1)	98
29. Time history of <b>B · R</b> solutions for the $10^{-11}$ km/s <sup>2</sup> process noise sequential filter (set 2)	98
30. Time history of perturbations in <b>B · R</b> due to +7-m $\lambda$ and +3-m $r_e$ errors in all stations located for the $10^{-11}$ km/s <sup>2</sup> process noise sequential filter	98
31. Summary of November 6 solutions in the <b>B</b> -plane	98
32. Transmitting and receiving configuration for two-way and three-way data	98
33. Interpolation of near-simultaneous range points	99
34. Interrelationship of station location and baseline parameters	99
35. Selection of two-way data for the dual-station experiment	99
36. Distribution of differenced data	100
37. <b>B</b> -plane results for the dual-station experiment	101
38. Typical residuals showing removal of process noise by differencing	102
39. <b>B</b> -plane solutions for various combinations of weights on $\Gamma_3$ , F2, F2, and MU data	103
40. Approach Deimos picture	104
41. Predicted approach Deimos picture	104
42. Approach trajectory geometry	104
43. Approach picture sequence	105
44. Approach Deimos/star geometry	105
45. Deimos observation residuals	106
46. Near-real-time trajectory estimates	107
47. Expected trajectory estimation accuracy	107
48. Trajectory estimate using no stars	108
49. Trajectory estimate using one star per picture	108
50. Trajectory estimate using many stars per picture	108
51. Optical data solution (coordinates)	108
52. Optical data solution (time of flight)	109
53. Estimate of time of flight using optical data	109

54. Sensitivity to Mars ephemeris error	109
A-1. Definition of <b>B</b> -plane parameters	111

**Satellite Orbit Determination**

J. F. Jordan, D. H. Boggs, G. H. Born, E. J. Christensen, A. J. Ferrari  
D. W. Green, R. K. Hylkema, S. N. Mohan, S. J. Reinbold, and G. L. Sievers

I. Introduction	119
II. Satellite Orbit Determination Pre-flight Studies	120
A. Scope and Methodology of Pre-flight Studies	120
B. Orbit Convergence Problem and Partial-Step Algorithm	121
C. Major Error Sources Affecting Converged Solution Accuracy	122
D. Qualitative Description of Satellite OD Accuracy Properties	125
E. Simulation Studies	126
F. Orbit Determination Solution Strategy for the Satellite Phase of the Mission and Expected Accuracy	126
III. Mariner 9 Data and <i>A Priori</i> Astrodynamical Constants	127
A. DSN Data	127
B. Spacecraft Data	128
C. Observer Location and Transmission Media Calibrations	130
D. Martian Astrodynamical Constants	130
E. Planetary Ephemerides	131
IV. Pre-trim 1 Orbit Determination History and Support of Trims 1 and 2	131
A. Initial Orbit Convergence	131
B. Single-Revolution State Solutions	133
C. Multi-Revolution Solutions	133
D. Conclusions of the Pre-trim Solutions	133
E. OD Support for the Second Orbit Trim Maneuver	133
V. Martian Gravity Analysis	134
A. Gravity Solution Description	134
B. Physical Description of the Gravity Field of Mars	135
C. Consistency of Gravity Solutions	135
D. Error Sources for Gravity Field Solutions	136

VI. Science Support Orbit Determination History	136
A. Solution Procedures	136
B. Solution Summaries and Accuracies	137
VII. Perturbed Orbital Motion of Mariner 9	
A. Theoretical Considerations	139
B. Analysis of Orbit Evolution	139
VIII. Confirmation of Doppler-Determined Orbits With TV Imaging Data	142
A. Data-Processing Method	142
B. <i>A Priori</i> Parameter Values	143
C. Corrections to the Mariner 9 Orbit	144
D. Estimated Landmark Locations in Areographic Coordinates	144
E. Mars Spin-Axis Direction Solutions	145
IX. Determination of Normal Points for the Relativity Experiment	146
A. Definition of Normal Points	146
B. Computation of the Normal Points	146
C. Normal Point Accuracy	147
D. Normal Point Residuals	147
References	149

#### Tables

1. Approximate areocentric orbital elements of Mariner 9	151
2. Satellite OD Group staffing levels	151
3. Error source standard deviations for encounter OD results	151
4. Standard deviations for Mars harmonics based on dimensional analysis	151
5. Comparison of unmodeled acceleration magnitudes at periapsis	151
6. Local position and extrapolated period error caused by low-order gravity coefficient errors	152
7. Pre-flight required and predicted OD accuracy summary (pre-gravity sensing/post-sensing)	152
8. Approximate station location values for MM'71 satellite mission	152
9. Values of the AU and GM used with Earth-Mariner planetary ephemeris	152

10. SATODP first orbit convergence history	153
11. Mariner 9 harmonic solutions	153
12. Coefficients for the tenth-degree harmonic gravity model (C/S)	154
13. Short-arc solution summary	156
14. Long-arc solution summary	157
15. Characteristics of periodic variations	157
16. Secular rates	157
17. One-sigma measurement uncertainties for observed landmarks	158
18. Variation of $\Omega$ relative to a mean continuous node evolution	158
19. Elevation results from landmark data processing	159
20. One-sigma uncertainties in Mariner 9 position when ranging is taken	159
21. Effect of position uncertainties on Earth-Mars measurement	159

#### Figures

1. Encounter OD position error at periapsis as a function of data termination time	160
2. Range-rate time history for two different values of orbital period	160
3. Worst-direction diagram in phase space	160
4. Worst-direction convergence profile as a function of data termination time	161
5. Geometric shape of low-order $U$ -functions	161
6. Earth-station/Mars-spacecraft configuration	162
7. Projection of true and estimated orbit in Earth's plane of sky	162
8. Time histories of pre-flight state estimate uncertainty over a single revolution (November 14, 1971)	162
9. Effect of period error on mapped position error at periapsis	162
10. Pre-gravitation sensing solution history (pre-flight simulated data)	163
11. Antenna elevation angle vs time: (a) November 15, 1971, (b) May 5, 1972	163
12. Evolution of doppler data accuracy	165
13. Differenced range minus integrated doppler time histories: (a) August 20 (order fit 8), (b) August 23 (order fit 3), (c) August 25 (order fit 3)	166

14. Distribution of observation times relative to time of periapsis passage of spacecraft for pictures used in optical OD	166
15. Landmark locations: (a) South polar region, (b) Pavonis Lacus, (c) Nodus Gordii	167
16. Engineering telemetry data	168
17. Typical roll-axis leak	169
18. Gas leak acceleration and $\Delta V$ history for mid-December 1971	171
19. Celestial coordinates (1950.0) of Martian north pole	171
20. TRKED initial orbit convergence	172
21. First orbit convergence history (position)	173
22. First orbit convergence history (period)	174
23. Near-real-time pre-gravity sensing solution history	175
24. Effects of $C_{22}$ and $S_{22}$ on orbit of Mariner 9 (view along Martian spin axis): (a) Unstable equilibrium, (b) Energy of probe decreases, (c) Stable equilibrium, (d) Energy of probe increases	175
25. Variation in Mariner 9 post-trim 1 orbit period	176
26. Estimated differences of single-revolution state at periapsis for first 10 revolutions	176
27. Variation in estimates of harmonic coefficients	176
28. Effect of gas leak modeling on estimate of harmonics	177
29. Effect of ephemeris errors on estimate of harmonics	177
30. Time history of $r_p$ and $z_p'$	178
31. Time history of ratios of in-track and out-of-plane position deviations to $r_p \Delta \Omega$	179
32. Time history of $r_p \Delta \Omega$ from mean for short-arc fits	180
33. Prediction error in $T_p$ for tenth-degree harmonic model	181
34. Typical fit and predicted doppler residuals	181
35. Time history of predicted revolutions below 2-s time error	182
36. High-frequency orbital element variations	183
37. Long-period osculating orbit elements: (a) In-plane elements, (b) Orientation angles relative to Mars true equator	184
38. Error in predicted mean anomaly and $T_p$ using various gravity models	185
39. Error in predicted mean anomaly at periapsis	185
40. $\Omega$ correction time history	185
41. TV image residuals: (a) Pavonis Lacus, (b) Nodus Gordii, (c) Nix Olympica, (d) South polar region	186

42. Time history of landmark image residuals	187
43. Topography of Mars (from radar-ranging data) relative to center of mass	188
44. Topography of Mars (from UVS and occultation data) relative to an equipotential surface	188
45. Altitude profile of Middle Spot	189
46. IRR view of South Spot	190
47. North pole of Mars in Laplacian plane of Deimos	191
48. Mars spin-axis direction solutions from Mariner 9 data	191
49. Normal-point residuals referenced to fit to data through July 31, 1972	192
<b>Maneuver Analysis</b>	
R. T. Mitchell, G. R. Hintz, and G. Preston	
I. Strategy Evolution	193
II. Maneuver Mechanization	194
III. Maneuver Constraints	195
IV. Maneuver Software	196
A. Design and Analysis Midcourse	196
B. Design and Analysis Insert	196
C. Design and Analysis Trim	196
D. Command Midcourse	196
E. Command Insert	196
F. Command Trim	197
V. Injection	197
VI. Interplanetary Maneuvers	198
VII. Orbit Insertion Maneuver	200
VIII. Trim Maneuvers	201
A. First Trim Maneuver	201
B. Second Trim Maneuver	203
IX. Contingency Insertion Planning	204
Reference	205

## Tables

1. Maneuver-execution error statistics, $3\sigma$	206
2. Ideal and commandable turns	206
3. Interplanetary delivery results	206
4. First midcourse maneuver performance	206
5. Second midcourse maneuver tradeoffs	206
6. Pre-insertion OD results and predicted errors	206
7. Insertion results	207
8. Insertion performance	207
9. First trim performance	207
10. First trim results	207
11. Second trim performance	208
12. Second trim results	208
13. Contingency insertion maneuver data	208

## Figures

1. Maneuver constraints on Mariner 9 orbit trim 2, December 30, 1971	209
2. Targeting data at injection	210
3. Targeting data for launch	210
4. Mars orbit insertion	210
5. Second midcourse maneuver accuracy improvement	210
6. Execution errors vs $\Delta V$	211
7. Arrival time target	211
8. Turn quantization	211
9. Mars orbit insertion target criteria	212
10. $\Delta V$ trim	212
11. Orbit trim strategy	213
12. Encounter conditions	213
13. MOI geometry	213
14. MOI statistical relationships	213
15. Predicted trim situation pre-MOI	214
16. Number of required orbital trims as a function of post-insertion period and $h_p$	214
17. Period sensitivity to ignition time	214

18. Trim situation	214
19. Node and inclination gradients	214
20. Argument of periapsis	215
21. Period and time of periapsis passage gradients	215
22. Periapsis altitude gradient	215
23. Flight plane velocity space	215
24. Orbit trim 2 geometry	216
25. Pointing directions resulting in planetary impact	216
26. Fraction of all possible pointing directions leading to planetary impact	217
<b>Trajectory Description</b>	<b>218</b>
W. A. Webb	
I. Launch Phase	218
II. Interplanetary Cruise Phase	219
A. Aiming Point	219
B. Midcourse Maneuver	219
III. Encounter Phase	220
<b>Tables</b>	
1. Mariner 9 launch sequence of events	221
2. Geocentric orbital elements at injection	221
3. Post-engine-vent geocentric orbital elements	221
4. Post-midcourse heliocentric orbital elements	221
5. Areocentric orbital elements at encounter	221
<b>Figures</b>	
1. Mariner 9 injection and midcourse aiming points	222
2. Projection of heliocentric trajectory in the ecliptic plane (launch, May 5, 1971; arrival, November 14, 1971)	222
3. Transfer trajectory as a function of calendar date: (a) Heliocentric latitude, (b) Heliocentric longitude	223
4. Mariner 9 distance as a function of calendar date: (a) Earth-spacecraft, (b) Sun-spacecraft	223

5. Mars-spacecraft distance as a function of calendar date	224
6. Near-encounter geometry	224
<b>Science Sequence Design</b>	225
P. E. Koskela, W. E. Bollman, J. E. Freeman, M. R. Helton, R. J. Reichert, E. S. Travers, and S. J. Zawacki	
I. Introduction	225
II. Software	225
A. POGASIS	225
B. POGASIS Plot	226
C. LIBPOG	226
D. SCOUT	226
E. In-flight Enhancements	226
III. Procedures	227
A. Advance Planning	227
B. Daily Operations	228
C. Evolution of a Zenith/Nadir Orbital Sequence	229
IV. Science Sequences	230
A. Pre-insertion Planning	230
B. Post-insertion Planning	231
C. Science Sequence Summaries	232
V. Accuracy of TV Camera Targeting	233
References	235
<b>Table</b>	
1. Data for narrow-angle frame targeting	236
<b>Figures</b>	
1. Mission sequence plan (profile) for mapping cycle III	237
2. Science sequence design process	238
3. Sample taken from orbital sequence plan	239
4. Typical Goldstone zenith science sequence	240
5. Typical Goldstone nadir science sequence	240

6. Key to sequence summaries	241
7. Post-orbital insertion mapping, calibration, and phase function sequences, revolutions 1 to 15	242
8. Interim sequences, revolutions 16 to 23	242
9. Zenith revolutions 24 to 62, reconnaissance I	243
10. Nadir revolutions 25 to 63, reconnaissance I	244
11. Zenith revolutions 64 to 98, reconnaissance II	245
12. Nadir revolutions 65 to 99, reconnaissance II	246
13. Zenith revolutions 100 to 138, mapping cycle I	247
14. Nadir revolutions 101 to 137, mapping cycle I	248
15. Zenith revolutions 140 to 176, mapping cycle II	249
16. Nadir revolutions 139 to 177, mapping cycle II	250
17. Zenith revolutions 178 to 216, mapping cycle III	251
18. Nadir revolutions 179 to 217, mapping cycle III	252
19. Zenith revolutions 218 to 262, extended mission phase I	253
20. Nadir revolutions 219 to 261, extended mission phase I	254
21. Post-orbital insertion mapping sequences, revolution I	255
22. Interim sequences, zenith revolution 16	256
23. Interim sequences, nadir revolution 17	257
24. Reconnaissance I, zenith revolution 26	258
25. Reconnaissance I, nadir revolution 27	259
26. Reconnaissance II, zenith revolution 74	260
27. Reconnaissance II, nadir revolution 75	261
28. Mapping cycle I, nadir revolution 119	262
29. Mapping cycle I, zenith revolution 120	263
30. Mapping cycle II, zenith revolution 174	264
31. Mapping cycle II, nadir revolution 175	265
32. Mapping cycle III, zenith revolution 188	266
33. Mapping cycle III, nadir revolution 189	267
34. Extended mission phase I, zenith revolution 220	268
35. Extended mission phase I, nadir revolution 221	269
36. TV narrow-angle frame targeting	270

## **Abstract**

This report provides a final, comprehensive description of the navigation of Mariner 9 — the first U.S. spacecraft to orbit another planet. The Mariner 9 navigation function included not only precision flight path control but also pointing of the spacecraft's scientific instruments mounted on a two-degree of freedom scan platform. To the extent appropriate, each section describes the pre-flight analyses on which the operational strategies and performance predictions were based. The in-flight results are then discussed and compared with the pre-flight predictions. Post-flight analyses, which were primarily concerned with developing a thorough understanding of unexpected in-flight results, are also presented.

174-29121

## Introduction

W. J. O'Neil

Mariner 9 is the first U.S. spacecraft in orbit about another planet. Launched from Cape Kennedy, Florida, on May 30, 1971, Mariner 9 achieved orbit about Mars on November 14, 1971, after a near-nominal interplanetary flight. The spacecraft transmitted approximately 54 billion bits of scientific data representing observations of Mars while in orbit, including over 7,000 television pictures. The mission ended on October 27, 1972, when depletion of attitude control gas resulted in loss of attitude stabilization and consequent loss of solar power and telecommunications.

This report describes the navigation of Mariner 9, which included not only precision flight path control but also pointing of the scientific instruments mounted on a two-degree of freedom scan platform. Flight path control involved the determination of the spacecraft trajectory (classically referred to as orbit determination) and the design and execution of the propulsive maneuvers required to effect the necessary changes in the trajectory. Radiometric tracking data provided by the JPL Deep Space Network (DSN) were the principal data type used in the orbit determination process. During the Mars approach phase, optical tracking data were also used, but only on an

experimental basis. The optical data were obtained by imaging the Martian natural satellites (Phobos and Deimos) against the star background with the spacecraft television system. The JPL Orbit Determination Program (ODP) operating in a Univac 1108 computer was the primary tool used in the orbit determination process.

The required propulsive maneuvers were computed with the JPL Maneuver Operations Program System (MOPS), which also operated in the 1108 computer. Each maneuver was defined by four "commandable" quantities, namely, the spacecraft roll and yaw turns required to achieve the proper thrusting attitude, the engine ignition time, and the velocity increment to be achieved. After translation of these parameters into command words, they were transmitted to the spacecraft by the DSN. A single, 1300-N (300-lb) thrust, bipropellant, liquid rocket engine was used for all propulsive maneuvers.

Pointing of Mariner 9's scientific instruments involved the design of the sequence of scan platform movements which would cause the instruments to observe targets specified by the science investigators. Generally, a sequence was designed for a single orbital revolution begin-

ning at apoapsis and ending at the following apoapsis, with the majority of observations made near periapsis, where the greatest resolution was achieved. The sequence design further involved the precise specification of the time at which each television picture was to be shuttered. The JPL Planetary Observation Geometry and Science Instrument Sequence (POGASIS) Program operating in the 1108 computer was the principal tool used for sequence design. The observation requests made by the science investigators and a precise prediction of the spacecraft trajectory based on the aforementioned orbit determination process were the principal inputs to the sequence design process. The outputs were instrument shutter times and the required positions of the scan platform.

Mariner 9 navigation was the responsibility of the Navigation Team within the Mission Operations System (MOS). The Navigation Team was functionally organized into seven groups. This report is similarly organized and represents the final report of the in-flight and post-flight activities of the Team. There is a direct correspondence between the Trajectory, Science Sequence Design, Manuever, Interplanetary and Satellite Orbit Determination Groups and major sections of the report. The activities of the Advanced Sequence Planning Group are included in the *Science Sequence Design* Section and those of the Optical Navigation Measurements Group in the *Interplanetary Orbit Determination* Section. With few exceptions, the contributing authors were members of the Mariner 9 Navigation Team.

To the extent appropriate, each section describes the pre-flight analyses on which the operational strategies and performance predictions were based. The in-flight results are then discussed and compared with the pre-flight predictions. Post-flight analyses, which were primarily concerned with developing a thorough understanding of unexpected in-flight results, are also presented. Each major section is essentially self-contained, so that the reader can easily focus his attention in the area of his interest. The remainder of this introductory section provides a description of the Navigation Team operations and a synopsis of the most significant navigation events. The synopsis chronologically summarizes the mission from a navigation standpoint and indicates where in the report additional details can be obtained.

## 1. Navigation Team Operations

The Mariner 9 flight operations were conducted by the Mission Operations System organization (depicted in Fig.

1), under the direction of the Chief of Mission Operations (CMO). The CMO was the final authority for most decisions, although conduct of extremely critical operations such as the propulsive maneuvers required authorization from the Mission Director. As illustrated in Fig. 1, the MOS organization was functionally divided into two tiers: the Navigation, Science Recommendation, Spacecraft, and DSN Project Engineering Teams comprised the upper tier; the Command, Science Data, Data Processing, and DSN Mission Operations Teams the lower tier. During orbital operations, the upper tier performed the day-to-day, adaptive, mission planning, analysis, and sequencing functions. The longer-range (i.e., more than 3 weeks ahead) planning was performed by the Mission Analysis and Engineering Manager and his staff, with extensive support from the upper tier teams. These long-range plans were finalized in 20-day segments known as cycles, which established the framework within which the daily sequences were developed. The development of the daily sequences by the upper tier was coordinated by the Mission Sequence Working Group (MSWG). The MSWG, which was chaired by a member of the CMO's staff and included representatives from most organizational elements, successfully adjudicated nearly all sequencing conflicts and, thereby, largely determined the course of events within each 20-day cycle.

At prescribed times each day, the upper tier delivered to the lower tier the detailed spacecraft sequence of events (S/C-SOE) and the command file to be executed by Mariner 9 on its zenith/nadir revolution pair 3 days and 1 day hence, respectively. In other words, delivery of the S/C-SOE preceded delivery of the corresponding command file by 2 days. In fact, the preparation for a given revolution pair was a serial process of 6 days' duration; consequently, every stage of preparation was under way for different revolution pairs each day in assembly-line fashion. The upper tier worked 7 days a week, and both the Navigation and Spacecraft Teams worked two shifts a day, but different functions were performed on each shift.

The upper tier performed its functions essentially "off-line" but was "on-line" to effect final updates and monitor propulsive maneuvers. In contrast, the lower tier was on-line continuously (i.e., 24 h a day, 7 days a week) under the direction of the Assistant CMO — a position rotated among five individuals. The Sequence Group on staff to the ACMO generated the detailed operational sequence of events based on the S/C-SOE and other inputs. The lower tier was responsible for transmitting the command files to the spacecraft, continuously monitoring the telem-

etry and tracking data and effecting the delivery of these data to the upper tier, preparing the science data records, and providing the necessary computer support to all the elements of the organization.

The key interfaces of the Navigation Team with the other elements of the organization are described in the following paragraphs. The principal functions of the Navigation Team were (1) precise trajectory determination and prediction, (2) design of the propulsive maneuvers, and (3) design of the science sequences. The trajectory estimates and predictions were used internally in the design of the maneuvers and science sequences, and they were also exported in the form of Probe Ephemeris Tapes (PETs) to the DSN Mission Operations Team and the Science Data Team (SDT). The DSN NATTRK (Network Analysis Team-Tracking) element used the PETs to generate the tracking station observable predictions. NATTRK was also responsible for delivering the DSN tracking data to the Navigation Team. The SDT used the PETs for generation of the *post facto* estimates of the coverage and geometrical observation conditions actually obtained by the science instruments. This information which was an essential element of the Supplementary Experimenter Data Records (SEDRs), was mechanically generated by the SDT using the LIBPOG Program (a special version of POGASIS developed and maintained by the Navigation Team — see Section II of *Science Sequence Design*) inputting the appropriate PET and estimates of the actual scan platform pointing directions derived from spacecraft telemetry. As discussed in *Satellite Orbit Determination*, very stringent accuracy requirements were placed on these "smoothed" PETs required for the SEDRs.

In essence, the science sequence design involved integrating the experimenters' observation desires into viable scan platform observation sequences. The observation desires, as formulated by the Science Recommendation Team (SRT), were grossly compatible with the geometrical constraints as a result of continuing interaction between the Navigation Team and the SRT. Through this interaction, the Navigation Team kept the SRT apprised of what areas would be viewable on future revolutions and gained an early understanding of the SRT desires. Because the Navigation Team's interface with the SRT was the most demanding, a staff position to the Navigation Team Chief — that of SRT Representative — was dedicated to coordinating this interface and representing the Navigation Team in the MSWG. Six days before execution, the observation targets for a given revolution pair were finalized and delivered to the Navigation Team.

Based on prescribed observation times relative to periapsis, the POGASIS Program was then used to target the required scan platform pointing directions. Constraint violations uncovered in the targeting process, such as insufficient time to slew the platform between observations, were resolved by timing and/or target adjustments negotiated through the MSWG. The final sequence for a revolution pair was defined in terms of observation times and platform cone and clock angles, and was delivered by the Navigation Team to the Spacecraft Team for implementation 4 days before execution. The sequence evolution process is described in considerable detail in *Science Sequence Design*.

The Navigation Team controlled the Mariner 9 flight path through specification of the propulsive maneuver parameters to the Spacecraft Team. These parameters, which uniquely defined each propulsive maneuver, were the spacecraft roll and yaw turns, the  $\Delta V$  to be imparted, and the engine ignition time. Throughout the mission, the Navigation Team adjusted the overall maneuver strategy in accordance with the evolution of the mission objectives and constraints, as discussed later in the Synopsis. The maneuver strategy determined when a maneuver was to be performed and the targeting criteria for the maneuver (e.g., the desired post-maneuver orbital period, periapsis altitude, etc.). The precision targeting was performed with the Maneuver Operations Program System described in Section IV of *Maneuver Analysis*. The required inputs were the latest precise trajectory prediction, the prescribed ignition time, the targeting criteria, and pertinent spacecraft characteristics. The spacecraft characteristics, which were supplied by the Spacecraft Team, included the mass and the thrust components in spacecraft coordinates as a function of time from ignition and predictions of thrust pointing and shutoff accuracy. The MOPS output the required  $\Delta V$  and eight roll-yaw turn pairs, any one of which would achieve the required thrusting direction. Plots of the traces of the Earth, Sun, and Mars in spacecraft cone/clock angle were also output for each turn pair. The Navigation and Spacecraft Teams jointly analyzed these plots with constraint overlays to select the best turn pair. This process is further discussed in *Maneuver Analysis*. All significant elements of the maneuver design were presented to the CMO and Mission Director for approval prior to implementation. It is noteworthy that the monumental effort of the Navigation Team required for precision flight path control (i.e., the processing of literally thousands of tracking observations to solve for tens of trajectory and model parameters and the development of the maneuver strategy requiring exhaustive statistical analysis) distilled into four crucial

numbers (i.e., the roll/yaw turn pair, ignition time, and  $\Delta V$ ) delivered to the Spacecraft Team for execution of a given maneuver.

The functions of the seven groups and three staff positions within the Navigation Team are summarized in Fig. 2. During the orbital mission, the functions of the Trajectory Group were absorbed into the Advanced Sequence Planning Group when the latter group was formed. The number of engineers that staffed each element is indicated. The computer programs used by each group are described in the respective sections of this report.

All the Navigation Team computer programs were operated in the Univac 1108 computers, whereas the pre-processing of the tracking data and the generation of station observable predictions by the DSN were performed in the IBM 360/75 computers. The deliveries of tracking data to the Navigation Team and of PETs to the DSN were accomplished by hand-carrying magnetic tapes between the computers, which were located on adjacent floors of the Space Flight Operations Facility (SFOF). The Data Processing Team coordinated these data transfers; however, any technical problems with the data were handled directly between the Navigation Team and NATTRK. Although considerable problems were experienced in this tracking interface during pre-launch testing, the interface worked quite well throughout the flight. The Navigation Team and NATTRK closely monitored the incoming tracking data on closed-circuit TV displays of the raw data being received over teletype and the pseudo-residuals of the data, which were computed based on the tracking predictions in the 360/75 computer. The pseudo-residual displays were also used for realtime monitoring of the propulsive maneuver through the doppler signature.

The POGASIS program runs for science sequence design were run from remote 1108 demand terminals located in the Navigation (Nav) Area. The graphical display capability of these Tektronix CRT terminals was essential to rapid sequence design. It provided an immediate display of the predicted coverage, which the POGASIS engineer would inspect to judge what changes should be made in the sequence parameter inputs. He would enter these changes at the keyboard and obtain a new coverage display. This procedure would be repeated until a satisfactory sequence was obtained. The Tektronix terminal also provided hard copies when desired; these were particularly useful when it was necessary to discuss a coverage problem with people in a different location.

In general, and with the exception described above, all Navigation programs were loaded at the Univac 9300 remote bulk terminals by the Data Processing Team (DPT) in an area adjacent to the Navigation Area. The DPT was responsible for picking up the run decks from the engineers in the Nav Area and delivering the output to them. The DPT controlled Tektronix access to the 1108 also. They cooperated to the fullest possible extent in serving the computing needs of the Navigation Team, and in fact, the 1108 computing priorities were essentially established by the Navigation Team Chief or his representative. It was found that the runs to be loaded into the 1108 had to be very judiciously selected in order to maintain a run mix in the 1108 core and backlog compatible with the automatic job swapping of the 1108 Executive. The difference in the ratio of throughput time to central processor unit (CPU) time between judicious and indiscriminate loading could easily be as high as a factor of ten — that is, the ratio would increase from 3 to 30.

The most serious 1108 problem for the Navigation user was created when the 1108 Executive system was enlarged to the point that 130K words of core were no longer available. The Navigation programs were tailored to require no more than 65K words, so that two of them could co-reside in core based on the original allocation of 130K words to the user programs. Consequently, few of the Navigation programs could co-reside, and the judicious loading became even more important. Another problem was the lack of a roll-out/roll-in capability whereby the load on the 1108 could have been immediately reduced by entirely removing selected jobs, completing a very high priority job(s), and then returning the removed jobs to continue computation at the point of interruption. In critical situations, it was necessary to "kill" jobs in order to expedite those of higher priority, and those "killed" had to be restarted later from the beginning. However, in spite of these problems, the overall performance of the 1108 was truly excellent from a Navigation standpoint throughout the mission.

## II. Synopsis of Navigation Activity

A chronological summary of the most significant navigation events is presented in this section. The loss of Mariner 8 due to a launch vehicle failure resulted not only in the redesign of the desired orbit about Mars to accommodate the objectives of both Missions A and B into the single mission remaining but also in an increased emphasis on reliability. Virtually all the ground-based

resources (i.e., manpower and equipment) planned for the two missions were retained and concentrated on the single spacecraft. This resulted in essentially continuous tracking coverage of Mariner 9 from launch through the end of the primary orbital mission. A slight relaxation of the tolerances on the desired Mars orbit was negotiated with the Scientific Investigators in order to utilize a maneuver strategy which would achieve the final orbit with a single in-orbit trim maneuver rather than the two trims previously planned. The elimination of the second in-orbit trim prior to the execution of the primary scientific mission was considered a very significant reduction in risk, since any propulsive maneuver could result in a catastrophic failure.

Mariner 9 was launched by Atlas/Centaur AC-23 from Complex 36B at the Air Force Eastern Test Range (AFETR) on May 30, 1971, at 2223 GMT, about 6 min into a 1-h launch window. Details of the launch trajectory, which was very near nominal, are given in the *Trajectory Description*. Estimates of the Centaur trajectory transmitted to the Navigation Team by voice and teletype from the Real Time Computer Complex at AFETR during the first hour after launch indicated that the trajectory was sufficiently near nominal for the already generated nominal DSN predicts to be adequate. (The estimates were based on tracking the Centaur C-band beacon from Antigua and Ascension Islands.) This was later confirmed by the first precision orbit determination by the Navigation Team based on DSS 51 doppler and angle data from the spacecraft. At this point, it was clear that the first midcourse planned for 6 days after launch would easily remove the launch guidance errors and bias.

During the near-Earth mission phase, a member of the DSN Network Analysis Team (NAT) resided in the Navigation Team to expedite the production and transmission of the DSN tracking predicts and the receipt of tracking data. Also, because of problems experienced by the DSN during pre-launch testing in preprocessing the tracking data in the 360/75 computers, tracking data tapes were generated in parallel on the 7094 system for the first few hours of the flight. Fortunately, the 360/75 performed satisfactorily in producing the tracking tapes during this phase, and the 7094-produced tapes were not required.

Since the scan platform unlatch and engine venting would perturb the spacecraft trajectory, these events were commanded 1 day after launch to (1) provide an unperturbed, 1-day, near-Earth tracking arc to obtain a reasonably good orbit solution, (2) provide a 5-day arc for the orbit re-determination upon which the midcourse would

be based, and (3) preclude the perturbation on the post-midcourse trajectory.

Following the unlatch and venting, the Chief of Mission Operations requested for logistical reasons that the midcourse be advanced to launch plus 5 days. Because the orbit determination was going exceptionally well — the quality of the data fits was significantly better than obtained on previous planetary missions — and the expected maneuver execution error would dominate the expected OD error, the Navigation Team concurred. At midcourse minus 12 h, the orbit solution for the final first midcourse design was selected. This solution estimated solar pressure components and station locations in addition to state. The excellence of the data fit, coupled with the reasonableness of the solution parameters, gave high confidence in the solution. The pre-midcourse orbit determination activity experienced no significant difficulty. Early ranging data again proved their value in that the differences between the doppler-only and doppler-plus-range solutions facilitated the identification of data biases. (See Sections C1 and C2 of *Interplanetary Orbit Determination* for details.)

The first midcourse design was an integral part of the overall maneuver strategy. The predicted orbit insertion errors were much too large to permit inserting directly into the final desired Mars orbit within the tolerances specified. Consequently, the strategy was to insert into an initial orbit that would facilitate achieving the final orbit with a single orbit trim maneuver in most cases. The final desired orbit orientation and periapsis altitude could be satisfactorily achieved at insertion, thus requiring the single trim only for orbital period adjustment. The target value of the initial orbital period was to be 12.5 h, and the arrival time at Mars was to be such that the first periapsis passage would occur 2.5 h before the middle (i.e., zenith) of the Goldstone view period. This would ensure that even in the presence of dispersions as high as  $3\sigma$ , the time of periapsis passage on subsequent revolutions would migrate quickly into the 1-h window following Goldstone zenith. At the periapsis occurring within this window, the single trim would adjust the orbital period such that every other subsequent periapsis would occur within the window throughout the primary mission.

The orbit insertion was to be a coplanar maneuver of 1610 m/s targeted to the 12.5-h period and a periapsis altitude of 1300 km, with the B-magnitude of the approach trajectory targeted to maximize the resulting apsidal rotation of the orbit in the presence of dispersions. To ensure rotation greater than 138 deg with high

probability, the target value of **B**-magnitude was selected as 8200 km, with the understanding that the periapsis altitude target would be allowed to float upward (and would not be corrected after insertion) for actual approaches above 8250 km.<sup>1</sup> This strategy is illustrated in Fig. 4 of *Maneuver Analysis*.

The foregoing dictated the aim point for the midcourse, namely, a **B**-magnitude of 8200 km and an inclination to the Mars equator of 65 deg. The predicted accuracy was such that a planetary quarantine bias was not required. The arrival time target of November 14, 0029 GMT, was intentionally biased 25 min late so that the likely second midcourse 20 days before encounter would be a 2-m/s maneuver along the approach direction. Small adjustments in the maneuver direction would produce the required correction of the **B**-magnitude error from the first midcourse. This technique would minimize the second midcourse execution errors by orienting the dominant error source (i.e., the fixed shutoff error is dominant for small maneuvers) nearly perpendicular to the **B**-magnitude gradient. The **B**-magnitude was by far the most critical delivery parameter, and the stress on this parameter will be evident throughout the interplanetary phase of this synopsis. The probability that a second midcourse would be necessary to achieve the required **B**-magnitude accuracy of 350 km was estimated to be 40% at the time of the first midcourse.

The launch injection aim point had been selected to satisfy two constraints: (1) a propulsion system constraint that the first maneuver exceed 5.6 m/s, and (2) the constraint to utilize a maneuver direction such that the low-gain spacecraft antenna would point to Earth, providing engineering telemetry during the motor burn. These constraints required biasing the injection aim point over 40,000 km and the arrival time about 1 day late. The aim point bias easily satisfied the planetary quarantine constraint and corresponded to a nominal midcourse of about 8 m/s.

On the third day after launch, the Navigation Team Chief presented a review of the overall maneuver strategy and the preliminary first midcourse design to the Mission Director for his approval. Following approval, the maneuver parameters were transmitted to the spacecraft and stored in the central computer and sequencer (CC&S). The orbit solution selected for the final design on the day of the maneuver indicated **B**·**T** = 26,312 km, **B**·**R** =

19,839 km, and arrival time = November 14, 1935 GMT, corresponding to a Centaur injection error of slightly more than 1  $\sigma$ . The OD uncertainty (1  $\sigma$ ) was 119 km – well within the Project-specified accuracy requirement of 250 km. A 6.731-m/s maneuver was designed to achieve **B**·**T** = 5473 km, **B**·**R** = 6106 km, corresponding to the **B**-magnitude of 8200 km and inclination of 65 deg, and the arrival time of November 14, 0029 GMT. The spacecraft CC&S was updated accordingly, following the final command approval conference. The maneuver was executed as planned. During the motor burn, realtime monitoring of the doppler shift indicated that a near-nominal maneuver was executed.

For a few days following the midcourse, orbit determinations were performed daily to gain confidence that the maneuver had, in fact, been normal and, therefore, no corrective maneuver would be required until the scheduled second midcourse. Full confidence was achieved when fitting post-midcourse data with an extremely loose *a priori* estimate produced satisfactory results. It was then known on the basis of radio tracking alone (i.e., no reliance on telemetry) that the midcourse execution errors were less than  $\frac{1}{2} \sigma$ . The execution errors could be fairly well determined at this point by differencing the pre- and post-midcourse orbit solutions since the major errors in the orbit determination process would be common to the pre- and post-solutions. Thereafter, the Navigation Team updated its estimate of the trajectory weekly during the interplanetary cruise.

Shortly after the first midcourse and periodically thereafter, the Navigation Team designed an orbit insertion maneuver which would place the spacecraft in a 12-h Mars orbit based on the current prediction of the encounter conditions. The maneuver was then loaded into the spacecraft CC&S along with a repetitive orbital science instrument sequence which would provide the best chance of obtaining some orbital science data in the event command capability was lost before encounter. See Section IX of *Maneuver Analysis* for details regarding the design of this "automatic" insertion maneuver.

Because the actual first midcourse execution errors were known to be small and the orbit determination uncertainty in **B**-magnitude was only 119 km (1  $\sigma$ ) at the time of the maneuver, the probability of needing the second midcourse dropped considerably based on the formal statistics. However, the necessity of fully preparing for the second midcourse was unchanged. The Mars approach trajectory was to be controlled to 350 km (3  $\sigma$ ) in **B**-magnitude, corresponding to a periapsis altitude error

<sup>1</sup>See Section II of *Trajectory Description* for definition of **B**-plane parameters.

of 300 km. The pre-flight allocation of this tolerance was "equally" divided between orbit determination and second midcourse execution - 250 km ( $3\sigma$ ) each. Because of the special biasing of the first midcourse to minimize the errors of the second as described earlier, the execution errors would now be negligible relative to 350 km. Consequently, the entire 350-km tolerance could have been reallocated to orbit determination. However, the emphasis during the interplanetary cruise would be placed on gaining a thorough understanding of the potentially serious orbit determination error sources both in the tracking data and the model parameters in contrast to "beating down" the formal statistics.

Because of the potential second midcourse, the Navigation Team had to be prepared to accurately redetermine the approach trajectory using *only* the medium arc of radio data obtained during the last 18 days of approach. This would ensure detection of any maneuver execution anomalies and would also provide a solution insensitive to unmodeled nongravitational forces on the spacecraft. At 6 h before encounter, an orbit solution was required to effect the final adjustment of the orbit insertion maneuver commands. In fact, the requirement that the B-magnitude uncertainty was not to exceed 50 km (at 1000 km range) was the most stringent interplanetary orbit determination accuracy requirement.

The medium-arc orbit solutions would be particularly susceptible to DSN station location errors. Although the approach Optical Navigation Demonstration was expected to obtain very accurate estimates which would be fully independent of radio error sources, these estimates were experimental and could not be relied upon to navigate the spacecraft. Consequently, the DSN Inherent Accuracy Group, supported by Navigation Team personnel mounted an intensive effort during cruise to obtain the best possible station locations for use with the planetary ephemeris being developed for encounter activities. Station locations are intimately tied to the planetary ephemeris. JPL planetary ephemeris DE69, which was developed for Mariner Mars 1969 encounter operations, was used in the design of the first midcourse. Because secular drifts were observed in the DE69 Mars ephemeris based on radar ranging to Mars since its release, a new ephemeris was to be developed by the JPL Ephemeris Group for Mariner 9 encounter based on the DE69 data set plus pertinent optical and radar data obtained since 1969, including Mars radar data to be obtained during cruise. Station location estimates would be obtained by reprocessing the encounter tracking data from all previous Mariner missions for each interim ephemeris produced

by the Ephemeris Group in order to evolve the best possible locations and ephemeris for encounter.

Throughout interplanetary cruise, orbit solutions for a variety of data sets and solution vectors were analyzed, and the effects of mismodeling certain key parameters were studied. This approach would ensure obtaining the best orbit estimate for the second midcourse by identifying the optimum data set and the most reliable model parameter values. Orbit solutions were released weekly for generation of DSN tracking predicts and to keep other elements of the Project apprised of the current best estimate of the encounter conditions. Trajectory geometry data were supplied to the Spacecraft Team regularly for their telecommunications and celestial reference system performance analysis and prediction.

Cruise activities went smoothly until September 15, when one of the spacecraft attitude control system (ACS) roll jets failed to close properly after firing. The resulting gas leak produced a continuous torque large enough to prevent the spacecraft from returning to that side of the limit cycle which would cause another firing of the leaking jet. Consequently, ground commands were sent to switch the spacecraft ACS from celestial to inertial mode, which would result in the firing of all jets once again. As hoped for, this resulted in the leaking jet reseating properly after firing, indicating that some particle had been caught between the valve and its seat during the previous closing movement. While leaking, being unbalanced by its companion jet in the couple, the jet produced a serious translational acceleration on the spacecraft. The acceleration was serious not in terms of its perturbation of the actual trajectory but rather because of its potential effect on the estimation process. Such accelerations, if not very accurately modeled, can cause substantial errors in the estimate of the encounter conditions. Since these accelerations could not be very well determined from the tracking data, accurate modeling was unlikely. The corrective action described above was, therefore, required not only to arrest depletion of the limited supply of ACS gas but also to avoid serious errors in the estimation of the encounter conditions.

The jet leaked sporadically throughout the remainder of the flight, as illustrated in Fig. 20 of *Interplanetary Orbit Determination*. Whenever it did not clear itself shortly, the corrective commanding was used, and, consequently, the encounter conditions were not significantly affected nor did any serious loss of gas occur. For the remainder of the mission, the Spacecraft Team provided the Navigation Team with estimates of the unbalanced force pro-

duced by ACS leaks based on their telemetry analysis. As a result of the collaboration of the Navigation and Spacecraft Teams in analyzing the "leaky" jet, it was also confirmed that another jet had a very small, constant leak within spec since launch. This had been suspected earlier because of the secular behavior of the solutions for solar pressure coefficients, as seen in Fig. 12 of *Interplanetary Orbit Determination*. A discussion of the handling of the accelerations induced by the gas leaks in the in-flight orbit determination process is presented in *Interplanetary Orbit Determination*. Post-flight studies of this problem, including the use of advanced filtering techniques and dual station tracking, are also described there.

The estimates of the encounter conditions were quite stable throughout the cruise phase. As the scheduled date for the second midcourse approached, October 19 was set as the date to decide whether or not the maneuver should be performed. The orbit estimate was, of course, critically important to this decision. Fortunately, a long, unperturbed data arc up to September 15 was available. When station locations were included in the solution vector, the longitudes moved about 7 m from the pre-flight value — considerably more than the *a priori* uncertainty. This was not of immediate concern, since encounter estimates obtained with long data arcs would be insensitive to station location errors. It was also known that the gas leaks could not have changed the actual encounter conditions a large amount. The main concern was the selection of an orbit determination strategy which would take full advantage of all the data available, including those obtained after the large sporadic leak started, without allowing the leak accelerations to corrupt the estimation process. After considering several alternatives, it was decided that the best strategy would be to (1) solve for the small constant leak acceleration since launch and the solar pressure coefficients using the long arc prior to the sporadic leaks, (2) input the values obtained in (1) and the Spacecraft Team estimates of the sporadic leak accelerations obtained from telemetry to the trajectory model, and (3) then obtain a state-only solution for the entire data arc to date. Based on (1) the resulting solution, (2) indications that the yet-to-be-delivered new ephemeris would reduce the B-magnitude estimate by about 50 km, (3) the possibility of additional sporadic gas leaks, and (4) lesser factors, the B-magnitude estimate was set at  $8235 \pm 100$  km. The 100-km tolerance was not a statistical quantity but rather a conservative judgment of the maximum amount the estimate could reasonably change between then and near-encounter (i.e., before significant trajectory bending due to Mars gravity) based on all known error mechanisms and the additional information (e.g., tracking data) to be

gained. The  $1-\sigma$  uncertainty in the estimate was considered to be 95 km. See *Interplanetary Orbit Determination* for additional details.

During cruise, the Scientific Investigators became more concerned over the lack of an upper bound on periapsis altitude and negotiated a requirement that periapsis altitude be controlled to lie between 1200 and 1500 km. They further specified a preference for an apsidal rotation of 140 deg instead of the maximum possible. The maneuver strategy was modified accordingly. To maximize the probability that one in-orbit trim would suffice, the probability of requiring a periapsis altitude correction had to be minimized. This was accomplished by setting the altitude target at 1350 km — in the middle of the acceptable range — since the dispersions in altitude were essentially symmetrical. There was now a small but significant chance that an altitude trim would be required. In this event, a three-trim sequence would be performed; the first and second trims would correct the orbital timing and the third the periapsis altitude. The correlation between post-insertion period and periapsis altitude was such that if altitude was out of tolerance, it was very likely that the period error would be so large as to require two timing trims. For B-magnitudes between 8150 and 8250 km, the apsidal rotation of 140 deg could be targeted by varying the insertion  $\Delta V$  as illustrated in Fig. 9 of *Maneuver Analysis*. Fortunately, the new requirements and maneuver strategy preserved the optimum B-magnitude close to 8200 km — the first midcourse target.

In support of the second midcourse decision, the trade-off data presented in Table 5 of *Maneuver Analysis* were generated based on the orbit solution described earlier (i.e., B = 8235 km). It is seen in the table that very little would be gained by performing the maneuver. The 25-min arrival time bias, introduced with the first midcourse, could be compensated for by simply targeting to a slightly smaller orbital period. On October 19, the Navigation Team recommended that the second midcourse be cancelled, and the Mission Director approved.

Because the second midcourse was not required, the long-arc orbit determination techniques could now be utilized to obtain the encounter estimates to be used in computing the Mars orbit insertion maneuver commands. It was no longer necessary to rely on the medium, 18-day tracking data arc as originally planned. Anticipation of this circumstance had not, however, influenced the second midcourse decision. All elements of the flight operations,

including the Navigation Team, were fully prepared to support the second midcourse if necessary.

Attention was now focused on preparing for the orbit insertion. A series of well understood, stable, long-arc solutions existed. It was anticipated that there would be recurrences of the large, sporadic gas leak; however, these would not significantly perturb the actual trajectory. Only a near-catastrophic event on board the spacecraft (e.g., rupture of a pressure vessel) or a large ephemeris error could invalidate the fidelity of the present estimate.

According to plan, the DSN Inherent Accuracy Group had been processing encounter tracking data from previous Mariner missions to obtain the best set of station locations to use with the new planetary ephemeris, DE78. Development Ephemeris DE78 was now available; however, the Navigation Team was awaiting the corresponding new station locations before incorporating DE78 in the navigation operations. In spite of very substantial efforts, the DSN was unable to obtain a Location Set (LS) that agreed satisfactorily with each previous mission. Furthermore, the intense scrutiny revealed that this problem existed for all ephemerides under consideration, including the current standard, DE69. This was the most distressing problem experienced in the interplanetary navigation operations. However, since it was no longer necessary to rely on the medium arc for the orbit insertion command generation, the station location problem was not of immediate concern. Medium arcs would now be of prime importance only in the event of a spacecraft failure capable of significantly perturbing the actual trajectory. It was decided that station location set LS35, which was based on uncalibrated Mariner 6 encounter tracking data and DE78, would be the best set for the Mariner 9 short arcs. The station location problem is discussed in detail in Section D of *Interplanetary Orbit Determination*.

On November 1, 1971, DE78 and LS35 were incorporated in navigation operations. As anticipated, DE78 caused the B-magnitude estimate to drop about 50 km into the 8200-8220 km range, as illustrated in Fig. 11 of *Interplanetary Orbit Determination*. Medium-arc solutions were obtained in addition to the long-arc solutions throughout the approach phase (i.e., the last 18 days before encounter). This gave maximum possible assurance that if any further problems developed, they would be detected because the difference in arc length would make the solutions sensitive to different error sources. Although statistically consistent with the long-arc solutions, the medium-arc solutions were unstable, exhibiting changes in B-magnitude of over 200 km. Nevertheless, an orbit in-

sertion maneuver based on any of the credible medium-arc solutions would have been satisfactory.

At 5 days before encounter, the contingency "automatic" insertion maneuver in the CC&S was replaced with the insertion commands for the standard orbit insertion and trim sequence. The insertion commands had been computed using the maneuver strategy described earlier and an orbit solution having a B-magnitude estimate of 8203 km. This solution (POSTMC-42-A) was obtained with the long arc of doppler and range data to encounter minus 7 (E-7) days employing the same technique used to obtain the second midcourse decision orbit, as described earlier. POSTMC-42-A was selected because the long-arc solutions were well behaved, and it was clear that the sporadic gas leak could not have altered the trajectory significantly. The maneuver strategy had been well established and approved earlier, and the commandable quantities for the insertion maneuver were computed routinely. Details are provided in *Maneuver Analysis*.

The next update of the orbit insertion commands was scheduled for the day before encounter at about E-24 h. In addition, there was to have been an opportunity to update all four maneuver parameters (i.e., turns, ignition time, and  $\Delta V$ ) based on tracking data to E-12 h and an opportunity to update  $\Delta V$  only based on data to E-6 h; the commands would be prepared, approved, and transmitted by E-6 h and E-3 h, respectively. The final  $\Delta V$  update incorporating tracking data to E-6 h would allow the orbit determination process to begin to "see" the Mars gravity bending the trajectory and, thereby, significantly reduce the B-magnitude uncertainty. The navigation design for the Mariner 1971 mission was, in fact, based on reducing the B-magnitude uncertainty to 150 km (3  $\sigma$ ) by tracking to E-6 h and then updating the  $\Delta V$  command to achieve an accurate orbit insertion. However, following the E-5 day update, the Mission Director declared for reliability reasons that the E-24 h update would be the last. The later updates would be used only if mandatory to save the orbital mission.

After the E-5 day update, short-arc orbit solutions were obtained in addition to the medium- and long-arc solutions. The short-arc solutions would best "see" the gravity bending near encounter and, therefore, detect any serious Mars ephemeris error. The optical-based solutions would detect an ephemeris error much earlier, but, as mentioned before, they could not be depended upon.

A few days before encounter, it was learned that the Mars radar data taken during the summer, which were

included in the DE78 data set, had a 1-s timing error. The Ephemeris Group immediately launched a crash effort to generate a new ephemeris with the data error corrected. The new ephemeris, DE79, was produced in 1 day and was found to increase the estimate of B-magnitude by about 30 km. Since it was clear that DE79 was very little different from, and probably slightly better than, DE78, the Navigation Team incorporated it into operations on November 12. This "last-minute" ephemeris change was made in order to obtain the best possible estimate of the encounter conditions for the E-24 h orbit insertion command update. The differences between the three ephemerides (DE69, DE78, and DE79) were sufficiently small that the use of one rather than another would not in any way jeopardize the mission. Therefore, the decision to use DE79 was known to be of little consequence.

The long-arc orbit determinations were still clearly superior to the medium arcs. The orbit solution selected for computation of the "final" insertion command update at E-24 h indicated a B-magnitude of 8231 km. The changes in the other encounter parameters (i.e., inclination and time of arrival) were so slight that the significant advantage of the update could be achieved by simply updating the  $\Delta V$  magnitude command by 3.7 m/s to 1604.2 m/s. The maneuver commands presently on board the spacecraft (i.e., those loaded at E-5 days) would result in a nominal post-insertion period of 12 h 32 min based on the current B-estimate, rather than the preferred value of 12 h 24 min. Consequently, without the update, the nominal situation would require the orbit trim maneuver near the fourth periapsis, whereas the update would delay it to the sixth periapsis.

Performing the trim at the sixth periapsis was preferred because there would then be an additional day to prepare for the trim following insertion. The nominal placement of the trim was, in fact, the only significant factor relating to the update. The Mission Director considered that the advantage of the update did not warrant the risk involved in commanding the spacecraft at this point and canceled the update.

Now, 1 day before insertion, the stage was completely set for the execution of the orbit insertion maneuver. Only a truly extraordinary event could warrant updating the insertion commands during these last 24 h. Attention turned to the Optical Navigation Demonstration (OND), which would shortly provide a completely independent estimate of the encounter conditions. In fact, processing of the first set of optical navigation pictures was already under way.

The OND was based on imaging Mars' natural satellites, Deimos and Phobos, against the star background to obtain measures of the direction from the spacecraft to the mass center of Mars with respect to the stellar references. The demonstration was funded by NASA's Office of Aeronautics and Space Technology (OAST) to demonstrate the feasibility of using optical approach data to navigate outer planet missions.

During the last 3 days before encounter, three pre-orbital science picture sequences (POS I, II, and III) were to be taken. Each POS sequence covered a 24-h period during which 31 pictures would be recorded on board the spacecraft and then transmitted to Earth at the end of the sequence during the Goldstone view. The OND was allocated six, seven, and eight pictures in POS I, II, and III, respectively. Because orbit insertion would occur early in the Goldstone view period, the POS III pictures would not be played back until after insertion. Consequently, only the POS I and II data would be available for Mariner 9 navigation purposes.

The entire 13-picture allocation in POS I and II was targeted for Deimos observations because it was superior to Phobos for the OND purposes. The first of the six POS I Deimos pictures was lost in transmission. The OND estimate of B-magnitude was about 8290 km based on the POS I data, which compared favorably with the then current radio estimate of about 8235 km. This was conclusive proof that there was no large error in the Mars ephemeris and the insertion commands on board the spacecraft were satisfactory. By E-8 h, when the POS II data had been processed and combined with the POS I data, an optical only estimate of 8260 km was available. Statistical combination of the radio and optical solutions also yielded a B estimate of about 8260 but indicated an inclination several tenths of a degree larger than either the radio or the optical solutions. The change in the inclination estimate was consistent with the covariances of the independent estimates and, therefore, not disturbing. The Optical Navigation Demonstration plans and results are discussed in more detail in Section F of *Interplanetary Orbit Determination*. A post-flight sensitivity study is also described there.

During the remaining 12 h to encounter, the orbit determination effort concentrated on the short-arc radio solutions. The rapid increase in the Mars gravitational acceleration of the spacecraft during these last hours of approach would be clearly visible in the doppler data, which would provide a continuing reduction in the encounter parameter uncertainties. The encounter plan pro-

vided for updating the orbit insertion velocity increment command at E-3 h based on tracking data taken to E-6 h. However, as mentioned earlier, this update would now be used only if the encounter estimate based on the stronger doppler data changed so drastically that the primary mission could not be achieved without the update. Following the excellent agreement between the long-arc radio and the optical solutions, the update was virtually out of the question. Nonetheless, continuing the short-arc solutions all the way to initiation of the insertion maneuver was important for two reasons. It could provide evidence of a spacecraft anomaly, and it would provide for increasingly accurate predictions of the post-insertion orbit. Accurate prediction of the post-insertion orbit was particularly important to facilitate rapid post-insertion orbit determination convergence.

Because of a 360/75 computer failure, no tracking data were delivered to the Navigation Team from E-8 h to E-4 h. At E-4 h, the missing data were delivered. The short-arc solution obtained with the addition of these data indicated a B-magnitude of 8261 km (within 1 km of the best post-flight estimate!). The Navigation Team now predicted with virtual certainty 2 h before encounter that the orbit trim maneuver would be required at the fourth periapsis after insertion, providing the spacecraft executed the insertion maneuver within specification (i.e., execution errors less than  $3\sigma$ ). Operations continued without further incident, and the spacecraft accurately executed the orbit insertion maneuver, as shown in Table 8 of *Maneuver Analysis*. The 15-min engine burn, which imparted a 1600-m/s velocity increment, began at E-13 min, following a roll-yaw turn sequence of 42 deg and 125 deg, respectively. Realtime monitoring of the doppler residuals during the burn and for 15 min following burnout prior to Earth occultation confirmed that Mariner 9 was indeed in a satisfactory orbit about Mars.

Accurate determination of Mariner 9's orbit about Mars was known from pre-flight studies to be quite a different problem than interplanetary orbit determination. Station location errors, planetary ephemeris errors, and non-gravitational accelerations would not be of major importance. Rather, nonlinearities in the estimation process and lack of knowledge of the Mars gravity field were the major potential problem areas. Nonlinearity problems arise when the perturbations in the observables (e.g., doppler data) are not linearly related to perturbations in the spacecraft state at the solution epoch. Because of the very dynamic nature of the observables during a Mars orbit and the possibility of a large post-insertion state knowledge error, this situation might prevail for the initial

post-insertion orbit determinations. To avoid estimator divergence due to the nonlinearities (which could easily occur using the standard, full-step correction algorithm existing in the ODP) an optional, partial-step algorithm (PSA) was implemented in the ODP. As described in Section B of *Satellite Orbit Determination*, pre-flight performance analysis of the PSA demonstrated that it would achieve convergence in the worst imaginable situations.

The values of the harmonic coefficients of the Mars gravity field were unknown except for the oblateness coefficient ( $J_2$ ), which had been determined from observations of Deimos and Phobos and from Mariner 4 encounter tracking data. The *a priori* values of all the other coefficients were zero. In order to develop the orbit determination strategy to be used in flight to cope with the unknown field, it was necessary to establish realistic bounds on the coefficients. This was done by extrapolation of the Earth gravity model to a body the size and mass of Mars, assuming similar material and equal stresses, as discussed in Section C of *Satellite Orbit Determination*. Table 5 in that section shows that the uncertainty in acceleration near periapsis due to the unknown coefficients would be much greater than that due to all other effects combined.

Inclusion of near-periapsis tracking data in the presence of these unknown accelerations could severely degrade a state-only orbit solution. Processing a nearly complete single revolution of data - deleting only the data taken within 1 h of periapsis - would yield a locally accurate state-only solution, since the unknown gravity accelerations would not significantly influence the motion away from periapsis, and their perturbation of the actual state in the periapsis region would be *locally* insignificant. There would be no point in attempting to solve for the gravity coefficients with a single full revolution of tracking data, since this would (1) provide no global information on the field, (2) complicate the estimation process, and (3) probably degrade the local solution.

It was clear that the longitude of node in the Earth's plane-of-sky would be the most locally uncertain of the estimated orbital elements. Because of the lack of significant parallax at Earth-Mars distance, a pure rotation of the orbit about the Earth-Mars line would produce no significant change in the Earth-based tracking data. Time of periapsis passage would be the least accurately *predicted* element, since it would be in error by the cumulative effect of the orbital period error for each revolution mapped forward. The position error at a given future epoch near periapsis would be the combination of the initial node error component ( $\sim r_p \Delta\Omega$ , where  $r_p$  is

the projection of the periapsis radius on the Earth's plane of sky) and the time of periapsis passage error ( $\Delta T_p$ ) component ( $V_p \Delta T_p$ , where  $V_p$  is the speed at periapsis), as illustrated in Fig. 9 of *Satellite Orbit Determination*. In order to have adequate time to generate and validate the commands required to accurately point the scientific instruments mounted on the spacecraft scan platform, it would be necessary to predict the spacecraft position in the periapsis region to 10-km accuracy 14 revolutions (7 days) ahead. This was the most stringent satellite orbit determination requirement. Extensive covariance analyses and simulation studies demonstrated that this requirement could not be met until at least the low-order gravity coefficients were determined. Consequently, the following strategy was established:

- (1) *Pre-gravity sensing mode*. Using a batch-weighted, least-squares estimator, solve for the state (position and velocity) of the spacecraft from a single revolution of tracking data, omitting the data within an hour of periapsis which are most sensitive to the gravity errors. Use the partial-step algorithm for convergence if necessary. If severe convergence problems arise, shorten the data span, and work up to a full revolution of data.
- (2) *Gravity sensing mode*. Accumulate several successive revolutions of data. Then, using the conditions arrived at in step (1) as initial conditions, solve for the state plus low-order gravity coefficients.
- (3) *Post-sensing mode*. As more data become available, resolve for the state from a single revolution of tracking data, with the gravity terms obtained from step (2) placed in the spacecraft trajectory integration model.

The pre-flight predicted position uncertainty for mapping 14 revolutions ahead was 400 km and 7 km for pre-gravity sensing and post-gravity sensing, respectively. Clearly, gravity sensing would be essential to meet the instrument pointing requirements.

Gravity sensing would not be necessary to meet the orbit control requirements. The most stringent control requirement was that the error in time of periapsis passage was not to exceed 78 min 120 revolutions (60 days) after the synchronizing trim maneuver. The preflight results indicated that a single revolution, state-only pre-gravity sensing solution would contribute no more than 15 min to this error.

To expedite the initial post-insertion orbit solutions, the partial step algorithm was added to a state-only orbit determination program called TRKED, which was then certified for use in flight operations. TRKED, with its simplified trajectory model and interactive 1108 computer interface, would vastly reduce the wall clock time required to obtain a preliminary orbit solution. The first satellite orbit solution was obtained with TRKED using about 2 h of two-way, 1-min count doppler, which began at earth occultation exit, about 66 min from periapsis. This solution was within 26 km and 3 m/s of the *a priori* based on the final approach orbit determination, and a nominal insertion maneuver. The orbital period estimate was 12h35m24s - within 2 min that predicted immediately before insertion. Although it was used, the PISA was not actually required since the correction to the *a priori* state was well within the linear region of convergence. This first solution, which was obtained within minutes after receipt of the tracking data, was then input to the SATODP, and it converged to a state-only solution within 10 km of the TRKED solution. SATODP state-only solutions were later obtained with 4, 8, and 10.5 h of data as the data became available. The movement of the estimate between these solutions was almost entirely in the earth's plane of sky, confirming pre-flight expectations. The solution based on 10.5 h was the first of the pre-gravity sensing, single-revolution, state-only solutions. According to the established plan, the design of the first orbit trim maneuver was based on this solution except for the exact ignition time, which was to be updated shortly before execution.

The trim maneuver was to reduce the orbital period to 11h58m48s, which would properly synchronize the orbit with the Goldstone view period, causing every subsequent even-numbered periapsis to occur near Goldstone zenith, as explained in the earlier discussions of the maneuver strategy. The target period was to be achieved within an accuracy of  $\pm 0.65$  min. Performing the trim in the direction opposite the local velocity would require the least  $\Delta V$  and would not change any of the other orbit parameters. However, designing the maneuver for execution at 20 min before periapsis in the direction opposite the local velocity at that point would not significantly increase the  $\Delta V$  required or disturb the other orbit parameters, but it would be extremely advantageous operationally. As shown in Fig. 17 of *Maneuver Analysis*, the change in orbital period for such a design would be quite sensitive to the ignition time. Consequently, vernier control of the period change could be effected by simply changing the ignition time. Ignition would occur a fixed time interval after receipt by the spacecraft of a direct command

(DC-52) from Earth initiating the maneuver sequence. The Earth transmit time of DC-52 would then determine the nominal period change the maneuver would produce. The operational advantage would be as follows. The maneuver  $\Delta V$  and roll-yaw turn sequence would be calculated based on the first single-revolution orbit solution mapped forward to 20 min before the fourth periapsis. These parameters would be more than adequate even for the worst imaginable orbit determination errors (e.g.,  $10 \sigma$ ). These calculations, the subsequent generation and validation of the spacecraft commands, and the loading of the spacecraft CC&S could then be accomplished at a leisurely pace well in advance ( $\sim 1$  day) of the maneuver execution. The orbit determination activity could continue, independently and in parallel, processing data up to a few hours before the maneuver. The DC-52 transmit time could then be based on an orbit solution obtained just hours before ignition.

Based on the first single-revolution, the  $\Delta V$  and roll-yaw sequence was 15.25 m/s and 34.4 deg and 128.7 deg, respectively. These parameters were loaded in the CC&S about 1 day before the maneuver, as planned. Meanwhile, the second single-revolution orbit solution was obtained and, subsequently, the third. Comparison of the results from the three single-revolution solutions was disconcerting. The dispersions of the periapsis position estimate in the Earth's plane of sky and the orbital period estimate were three to four times greater than predicted on the basis of the pre-flight gravity uncertainties. Consequently, gravity sensing was begun immediately. A state plus second- and third-degree gravity coefficients solution was obtained using the first 2.5 revolutions of data. This solution agreed well with the three single revolution, state-only solutions but estimated the gravity coefficients to be four times larger than expected. Since this solution was based on data from only about 6% of the planet, there was no way of knowing whether the global field effects were actually four times greater than anticipated or whether Mariner 9 was simply experiencing a localized gravity anomaly. The former was considered more likely, which would mean that the orbital period would oscillate much more than anticipated. The locally determined period was clearly decreasing from revolution to revolution; however, there was no way of knowing at this point whether the local value was above or below the mean. There was no point in delaying the orbit trim maneuver in order to attempt to determine the true orbital period signature by fitting several more revolutions of data. If the trim was not performed as scheduled near the fourth periapsis, two trims would then be required in any case --

the first to get back into the Goldstone window and the second to synchronize when back in it.

Because the 2.5-revolution, gravity sensing solution agreed well with each of the single-revolution, state-only solutions, it was used to compute the desired ignition time. It predicted an orbital period in the fifth revolution 15 s less than the first single-revolution solution indicated. Consequently, the DC-52 was transmitted 1 min earlier than had been tentatively planned in order to reduce the period correction by 15 s and nominally give the desired period of 11h58m48s in the fifth revolution. Exactly the same period correction could have been obtained by sending the DC-52 15m40s late (see Fig. 17 of *Maneuver Analysis*), and this would have been done if the first transmission had not been successful. In fact, if the first and second transmissions failed, the DC-52 would have been sent repeatedly in hopes of reducing the periapsis migration away from Goldstone zenith.

Monitoring the real-time doppler residuals during the maneuver gave immediate confirmation that the maneuver was near-nominal. The first single-revolution orbit solution after the maneuver indicated that a fifth-revolution orbital period of 11h58m49s had been achieved -- an error of only 1 s. The maneuver performance is summarized in Tables 9 and 10 of *Maneuver Analysis*.

On the day following the maneuver, a fourth-order gravity harmonic solution was obtained by fitting the tracking data over the four pre-trim revolutions. This model was used for the single-revolution, state-only solutions through revolution 10. The marked improvement in the stability of these solutions, which is illustrated in Fig. 26 of *Satellite Orbit Determination*, gave increased confidence in the model. Integrating the trajectory forward with this model indicated that the orbital period would oscillate in a quasi-sinusoidal manner with an amplitude of  $\pm 35$  s and a wavelength of 32 revolutions. Most importantly, it indicated that the mean period would be about 31 s less than the local value had been in revolution 5. About a week after the trim, sixth-order harmonic solutions had been obtained for both the four-revolution pre-trim data arc and a six-revolution post-trim data arc. The estimated parameters for the latter solution included the Mars pole direction, which moved about 1 deg from the *a priori* value. The various gravity model solutions were fairly consistent and gave further evidence that the orbital period would oscillate. The latest model indicated an amplitude of  $\pm 43$  s and a wavelength of 40 revolutions. The predicted oscillation was due to the solved-for values of the tesserial harmonic coefficients  $C_{11}$ .

and  $S_{22}$ , which were much larger than anticipated. These values suggested that the cross section of Mars normal to its spin axis is rather elliptical. The Navigation Team explained how such a mass asymmetry could physically produce the period oscillation. This explanation, which was subsequently fully confirmed, is given in Section IVF of *Satellite Orbit Determination*.

Periodically, new sixth-order gravity models were obtained using the most recent four-to-eight-revolution data arcs. These models were used in the single-revolution fits as they became available. For the first week after the maneuver, the observed orbital period decreased at a nearly constant rate of about 5 s per revolution, exactly as the new gravity models predicted. There was considerable anxiety, however, to observe the period actually "bottom out" and begin increasing, as the model predicted would occur after about revolution 20. It was most gratifying when this also occurred exactly as predicted. By revolution 42 on December 5, the actual observed period had completed a full cycle. The observed signature is illustrated in Fig. 25 of *Satellite Orbit Determination*. The observed amplitude of  $\pm 40$  s and wavelength of 37 revolutions clearly confirmed the recent harmonic coefficient solutions. The orbital period could now be accurately and confidently predicted. The mean period was, in fact, 11h58m13s - 35 s less than the orbit trim target value. Although this 35-s error was within the  $\pm 39$ -s (i.e.,  $\pm 0.65$ -min) accuracy requirement, it was causing operational difficulties, which would grow as the mission progressed.

Mariner 9's primary objective - mapping the surface of Mars between 65 deg south and 25 deg north latitude - was to be accomplished by taking a full tape recorder load of pictures at each periapsis. All recorded data were to be played back to DSS-14 at Goldstone because the Goldstone station could receive the data at 8 times the rate of the overseas stations. Controlling the orbital period such that every other periapsis passage would occur near the middle of the Goldstone view period was essential to this mapping plan. Pictures recorded at the preceding (i.e., nadir) periapsis would be played back during the first  $\sim 3$  h of a Goldstone view. A new load of pictures would then be recorded at the "zenith" periapsis and immediately played back during the last  $\sim 3$  h of the view. In this way, two full tape recorder loads of periapsis data would be obtained each day. The mapping would be accomplished in four complete longitudinal circuits. Because of the growth in the Goldstone view period with orbital mission time, a periapsis passage time error of  $\pm 78$  min would be tolerable on the 60th day. This was

the basis of the  $\pm 0.65$ -min period accuracy spec. The anticipated data rate reduction from 16 to 8 kbits/s after the 60th day removed the importance of accurate period control. Unfortunately, the mapping mission, which was to have commenced immediately after the orbit trim maneuver, had to be postponed because of a planet-wide dust storm on Mars. In its place, a reconnaissance mission was performed. As discussed in *Science Sequence Design*, the reconnaissance mission involved entirely different science sequences than the mapping mission. The new sequences required taking TV observations farther from periapsis; consequently, playback of the data acquired at the nadir periapsis had to begin over DSS-62 at Madrid, Spain, in order to be completed early enough in the Goldstone view for the early TV data to be recorded. Since DSS 62 could receive data at only 1/8 the rate of DSS-14 at Goldstone, this was very inefficient, in addition to being logistically complicated. The advisability of a second orbit trim maneuver to alleviate this problem was now considered.

By mid-December, Mariner 9's observations of the planet indicated that the dust storm was clearing and that the mapping of the Mars surface could begin at the end of the month. A new 60-day mapping mission was designed which would complete the three-longitudinal circuits of Mars between the 50th and the 110th day in orbit. This mission design *required* a second orbit trim maneuver which would adjust the orbital period such that a signal transmitted from the spacecraft 15 min after the 220th periapsis passage (on day 110) would reach DSS-14 within 72 min of its zenith with 95% probability. The trim was to be performed in the 94th revolution. Consequently, the post-trim target value of the *mean* period would be 11h59m32s, and the 72-min timing tolerance implied a mean period control accuracy requirement of 17 s ( $1\sigma$ ). Since the current mean period was now known to be 11h58m13s, a 79-s increase in the period would be required. The spacecraft trajectory was integrated forward beyond one full orbital period wavelength using the latest sixth-order harmonic gravity model with a 79-s period increase applied in revolution 94. As expected, the orbital period signature amplitude and wavelength changed only slightly - from  $\pm 40$  s and 37 revolutions to  $\pm 37$  s and 39 revolutions, respectively - as a result of the period adjustment. Therefore, it would be satisfactory to simply increase the local orbital period in revolution 94 by 79 s. In addition to correcting the period, it was also desired to raise the periapsis altitude about 300 km in order to reduce the gores (i.e., underlap) in the planned mapping coverage.

Because of the excellent condition of the spacecraft, the Project was not apprehensive about performing another propulsive maneuver. Normally, in order to conserve propellant when period and periapsis altitude are to be changed, a trim is performed at apoapsis to adjust the periapsis altitude, followed by a trim at periapsis to adjust the period. In this particular case the period and altitude could be corrected with a single trim, as illustrated in Fig. 24 of *Maneuver Analysis*. The velocity increment required would be about 42 m/s in contrast to 22 m/s for the two-trim sequence, but this was inconsequential because ample propellant was available as a result of the near-nominal navigation performance to date. The operational advantages of performing one rather than two maneuvers were overwhelming. Of the two possible single maneuver points shown in Fig. 24, the inbound one was the clear choice because the other required a spacecraft attitude which would preclude a communication link during the burn. As shown, the velocity increment would be applied essentially perpendicular to the local velocity in order to raise the periapsis altitude without producing a large period change. The small required period increase of the 79 s would be produced by "tilting" the velocity increment just enough to increase the *magnitude* of the local velocity the required amount. Consequently, the orbital period control error would be dominated by the spacecraft *pointing* error and the *nominal* velocity increment magnitude. This resulted in the interesting circumstance that the allowable altitude increase was limited by the maximum velocity increment, which would yield a period error of 17 s ( $1\sigma$ ). Accordingly, the periapsis altitude target was set at 1650 km. As in the first maneuver, the DC-52 maneuver-initiate command would provide for vernier adjustment of period correction based on tracking to a few hours before execution. However, there would not be a second opportunity to send the DC-52 — it would be necessary to wait until the following day. Because period control accuracy was critically dependent on precise alignment of the velocity increment relative to the local velocity and nearly all the tolerance was already allocated to the spacecraft pointing error, the DC-52 transmit time tolerance was only  $\pm 14$  s, compared with several minutes for the first trim.

Several days before the maneuver, the desired  $\Delta V$  and roll-yaw sequence was computed to be 41.8 m/s and 33 deg and 118 deg, respectively, based on the latest orbit solution. These were subsequently loaded in the CC&S. On the day of the maneuver, a single-revolution, state-only solution from revolution 93 tracking and based on the latest sixth-order harmonic model was used to calculate the exact DC-52 transmit time. The maneuver was

executed without incident and monitored as before. The maneuver performance is summarized in Tables 11 and 12 of *Maneuver Analysis*. Notice that the local period error was only 6 s, well within the specified tolerance and, this time, the *mean* period was controlled with equivalent accuracy. This concluded the Mariner 9 flight path *control* activities, no further propulsive maneuvers were required.

Conclusion of the flight path control function did not result in a significant reduction in the Navigation Team's workload but rather, in a change in emphasis. From now on, the Team would be involved almost exclusively in science sequence design and implementation and the very accurate prediction of Mariner 9's trajectory for that purpose. The Navigation Team had been performing this function ever since Mariner 9 began its final approach to Mars. Calculating the scan platform cone and clock angles required to accurately capture Mars in the instrument fields-of-view during the approach was completely routine from a navigation standpoint because of the large distances involved. In contrast, imaging the natural satellites (Deimos and Phobos) for optical navigation was quite difficult because of the large uncertainties in their ephemerides, as discussed in Section F of *Interplanetary Orbit Determination*. Originally, it was planned to take very simple TV mapping sequences near each periapsis after orbit insertion only until the orbit was synchronized by the trim maneuver. In anticipation of the existence of a relatively large orbital period uncertainty for a few hours after insertion, special provisions were made to effect a late update of the start time of the mapping sequence at the first periapsis. This update was successfully achieved based on the 4-h post-insertion data arc fit mentioned earlier. The primary contiguous mapping was to begin soon after the trim.

The TV pictures from the simple pre-trim mapping sequences showed that the dust storm was almost totally obscuring the surface of Mars, and it would have been pointless to begin the contiguous mapping before the storm cleared. Therefore, the simple mapping sequences were continued after the trim maneuver. This activity, known as cycle 1, was terminated on revolution 15. Cycle 2, which provided for more global reconnaissance than cycle 1, was conducted on revolutions 16 through 23, while a new reconnaissance-oriented science plan was being developed. It was cycle 2 global observations at about 2 h before periapsis that necessitated playback of part of the nadir periapsis data over DSS-62 at Madrid. In essence, cycle 2 invalidated the orbital period control accuracy spec of  $\pm 0.65$  min and first prompted consideration of a second trim maneuver, as discussed earlier.

The new reconnaissance mission plan was implemented on revolution 24. It consisted of two cycles, Reconnaissance I (revolutions 24 through 63) and Reconnaissance II (revolutions 64 through 99), which were quite similar. Global observations with the wide-angle A-camera and observations of specific targets with the narrow-angle, high-resolution B-camera were obtained on each revolution. The primary feature of the plan was that the pictures from A-camera global observations were inspected to identify specific targets in relatively dust-free areas for observation by the B-camera several revolutions later. This activity required far more strenuous scan platform targeting operations by the Navigation Team than the original mission plan. Although occasionally a target was missed as a result of an orbit prediction error, the overall performance of these targeting operations was excellent.

Mariner 9's primary mission of contiguously mapping 70% of the Mars surface began on revolution 100, shortly after the second orbit trim maneuver. Mapping cycles, 1, 2, and 3 were executed on revolutions 100 to 138, 139 to 177, and 178 to 217, respectively. These cycles mapped the latitude band from 65 deg south to 25 deg north over the full 360 deg of longitude. Each cycle included several discretionary TV frames which were allocated to targets of opportunity as the mission progressed. Toward the end of mapping cycle 3, the increasing Earth-Mars distance and the movement of Earth away from the high-gain antenna boresight necessitated cutting the playback rate to DSS-14 from 16 to 8 kbits/s. Consequently, two full tape recorder loads (i.e., ~30 pictures each revolution) could no longer be returned to Goldstone daily, and the number of observations had to be reduced to about 20 pictures on each revolution by the end of the cycle. This situation was well anticipated when the target criteria for the second orbit trim maneuver were established. The trim was, in fact, targeted to maximize the probability that the zenith periapsis time would be near the middle of the Goldstone view at the end of this cycle, so that an equal number of nadir and zenith pictures could be obtained each day. The picture balance was required in order to obtain uniform coverage from one side of the planet to the other.

Completion of mapping cycle 3 marked the complete achievement of the major mission objectives. However, because of the excellent condition of the spacecraft, an extended mission was authorized which, in fact, lasted until October 27, 1972, when Mariner 9 ceased functioning. During the extended mission, alternate roll reference stars (other than Canopus) were used to overcome the

scan platform clock angle limits, and spacecraft attitude maneuvers were performed to point the high-gain antenna to Earth for playback of the TV pictures and other science data. The involvement of the Navigation Team in these activities is described at the end of the *Maneuver Analysis* and *Science Sequence Design* sections. During the extended mission, Mariner 9 finished mapping the entire planet.

Each of the science cycles is described in considerable detail in *Science Sequence Design*. Sequence summary tables presented there define every TV sequence and picture taken during the first 262 revolutions. Sample orthographic and mercator plots of the coverage obtained are also included.

The bulk of the satellite phase orbit solutions was generated in support of science sequence design, implementation, and *post facto* science data reduction. As mentioned earlier, the requirement to predict near-periapsis position within 10 km accuracy 14 revolutions ahead was the most stringent of the satellite orbit determination accuracy requirements. The 14-revolution lead time (i.e., 7 days) was necessary to allow ample time for the final design and implementation of the science sequences (i.e., the scan platform cone and clock angles and instrument shutter times). The 10-km requirement was consistent with the scan platform pointing control accuracy of 0.5 deg ( $3\sigma$ ).

It was known from the pre-flight studies that gravity sensing would be necessary for accurate 14-revolution prediction; however, the unexpected "roughness" of the field, as discussed earlier, made the sensing even more important than had been anticipated. Table 11 of *Satellite Orbit Determination* lists the 23 different gravity models generated. Note that the eighth-degree model (#21), which was generated by the Celestial Mechanics Experimenters, and the Navigation Team's tenth-degree model (#23) were based on 38 revolutions of data — the number required for periapsis to cover 360 deg of longitude. Consequently, these models were valid for all subsequent navigation operations, including sequence design. The coefficients of the tenth-degree model are given in Table 12 of *Satellite Orbit Determination*. Table 13 of that section summarizes the short-arc orbit solutions generated in support of the science sequence design. The number of revolutions over which the periapsis time was predicted to 2-s accuracy — corresponding roughly to the 10-km requirement — is indicated for each solution. Note that the 10-km, 14-revolution prediction accuracy requirement was not met until the eighth-degree gravity

model (#21) was introduced. Thereafter, the requirement was generally met. The long-arc solutions used for the *post facto* science analysis are summarized in Table 14. Section V of *Science Sequence Design* discusses all the observation targeting error sources. Table 1 of that section presents the targeting error for three cases, which represent the entire spectrum of error experienced. The

worst case (revolution 157) is very atypical. The periapsis time error of nearly 25 s was the result of a procedural problem wherein the targeting had to commence just before the next orbit solution was available; and it was this next solution that would have met the accuracy requirement. In other words, the problem was of a nontechnical nature.

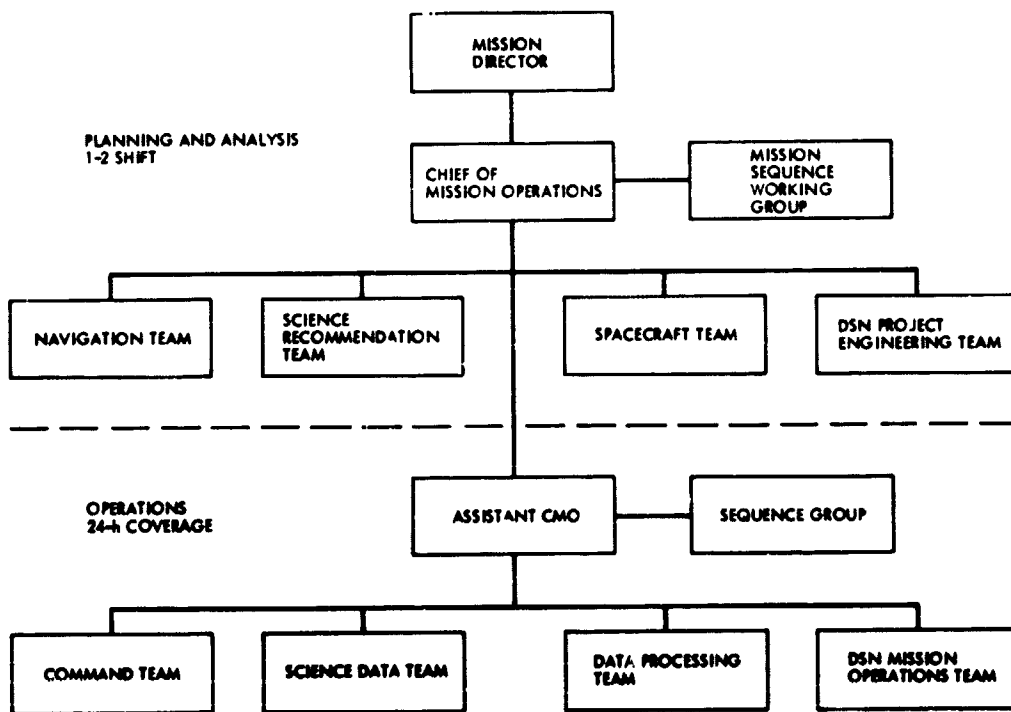
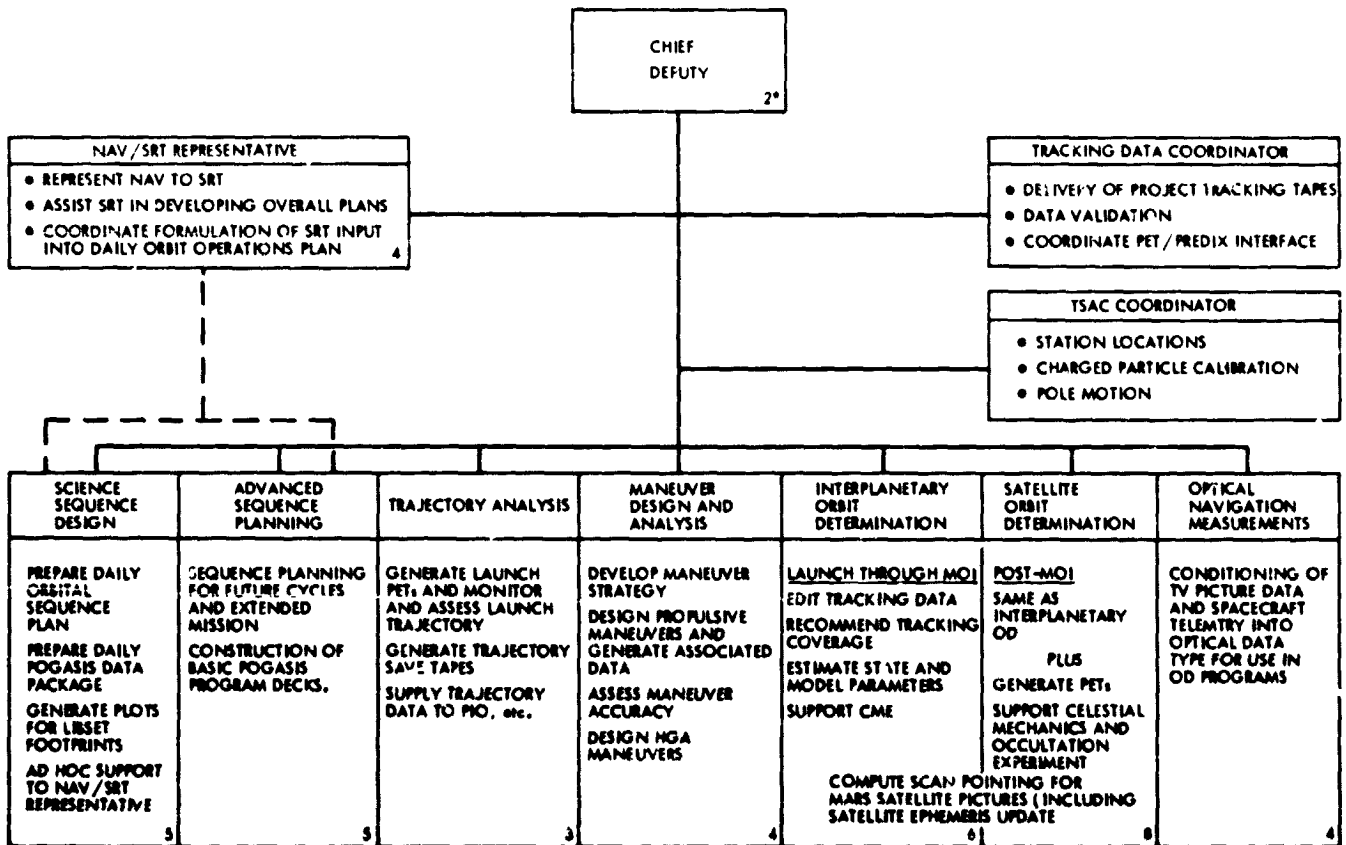


Fig. 1. Mariner Mars 1971 Mission Operations Organization



\*NUMBER INDICATES PEAK STAFFING LEVEL.

Fig. 2. Mariner Mars 1971 Navigation Team

# Interplanetary Orbit Determination

J. W. Zielenbach, C. H. Acton, G. H. Born, W. G. Breckenridge, C. C. Chao, T. C. Duxbury, D. W. Green, N. Jerath, J. F. Jordan, N. A. Mottinger, S. J. Reinbold, K. H. Rourke, G. L. Sievers, and S. K. Wong

## I. Interplanetary Operations

### A. Introduction

This section describes the logistical aspects of orbit determination (OD) in the interplanetary phase of the Mariner Mars 1971 mission and discusses the working arrangements for the OD personnel, both within the Navigation Team and with outside groups. The section also briefly describes the various types of data used in the OD process and indicates the sources of the data. It further provides functional descriptions of the individual elements of the OD software and brief sketches of their modes of operation.

### B. The Interplanetary OD Group

During the interplanetary phase, four OD engineers were dedicated full time to operations. They obtained the tracking data tapes from the Deep Space Network (DSN) personnel and pre-processed them for use in the OD programs, validating the data by iterative analysis of preliminary residuals on the UNIVAC 1108. In performing the basic OD, the group analyzed solutions based on differing solution sets, data sets, and arc lengths, and recorded, compared, and contrasted solutions. The results were then confirmed or rejected after consultation with spacecraft or tracking system hardware analysts.

The group also was responsible for inclusion of new ephemerides and station locations, and the day-to-day tracking system analytic calibrations (TSAC), which will be discussed later. This task involved cooperating with various suppliers in producing the information and directing the validation and analysis of the results, when they were included in the process. Additional personnel (at least five) participated at one time or another on a consulting basis as requested by the group.

The work schedules in effect during routine cruise differed from those immediately before or after spacecraft maneuvers. The normal operations called for single (prime) shift support 5 days a week. The DSN accumulated the tracking data and transferred them twice weekly to the Navigation Team. On these days the tracking data validator had the data available for the OD engineers at the start of the work day. The OD engineers then processed the new data, performing the analysis and comparisons mentioned previously, and provided an updated estimate of the orbit weekly.

During critical periods, the same four group members provided the OD support, but on a much more rigid timetable. Prior to any maneuver, the sequence of events defined a series of times at which the maneuver param-

eters stored in the spacecraft could be updated. At each of these times, the Navigation Team Chief required a set of maneuver parameters based on the best available orbit solution. This often necessitated numerous full OD sequences each day, from initial data transfer through validation, orbit determination, and covariance analysis. The task often required working a double shift at hours dictated by the maneuver execution time. Immediately following launch or a maneuver, a definition of the new orbit was usually required to ensure that it was as anticipated. This definition was based on a minimum of 1 h of tracking data.

**C. Interfaces With Outside Groups**

The OD engineers obtained their basic data from groups outside the Navigation Team, and the final orbits produced eventually went to other elements of the Mariner Mars 1971 Project. The interfaces were well defined before the mission; each group knew its obligations and had agreed upon a single point of contact through which the data would flow. These interfaces were tested by pre-flight simulations.

All problems and results were communicated to the Navigation Team Chief, who was responsible for distributing information and requesting any necessary additional support.

**1. Radiometric data.** The bulk of the information came from the DSN, which was responsible for raw radiometric data and the TSAC. The tracking data were collected by the Network Analysis Team for Tracking (NATTRACK) in the Space Flight Operations Facility (SFOF) at the Jet Propulsion Laboratory (JPL). This group operates 24 h a day monitoring data for data outages and system performance, manually adjusting certain quantities on the master tracking data file, and answering requests from the various projects for selected data from that file. During critical periods, a member of NATTRACK was assigned to the Navigation Team area to trouble-shoot and to ensure optimum communication between supplier and user. If for any reason the NATTRACK system data record (SDR) is lost, the data can be recalled from temporary storage at the station or at a switching computer at JPL. During the Mariner Mars 1971 mission, SDRs were produced and stored on an IBM 360/75. All OD runs were performed on a UNIVAC 1108 in the SFOF, and the data were transferred between computers on magnetic tape.

**2. Tracking system analytic calibrations.** The TSAC data include timing, polar motion, troposphere, and charged-particle calibrations, all of which were produced on the UNIVAC 1108 under control of the DSN-funded Navigation Accuracy Group. This group was responsible for collecting raw data from the available sources, converting the data to a convenient form (usually polynomials), assessing the errors in the raw data and their polynomial representation, and collaborating with the OD engineers in analyzing the effect of these data on the solutions. The calibrations were made available in card form, according to an established schedule. Both the data and the schedules for their delivery are discussed in Ref. 1.

The tracking station locations are also under the aegis of the TSAC activity. They are produced with the OD program using radiometric data from the previous missions and calibrations like those mentioned above. Theoretically, the data are constant and are made available once for the entire mission. In practice, ongoing technological advances have often meant that improved sets become available before the mission was over.

**3. Planetary ephemerides.** Because new planetary radar bounce data were to be taken at Mars opposition in the summer of 1971, the Project agreed to accept an improved planetary ephemeris between launch and encounter. It was the responsibility of the Project-supported Ephemeris Development Group to produce and certify this new ephemeris, to specify how it differed from the old ephemeris and how it would affect the B-plane (see Appendix A) coordinates of the probe, and to provide a covariance on the Earth and Mars positions for use during the mission. In addition, this group informed those involved in the station location effort whenever the new ephemeris changed the planetary positions from their positions at previous mission encounters.

**4. Spacecraft data.** Another important OD interface was with the Project's spacecraft analysts, who provided information on such quantities as spacecraft mass, solar reflectivity, attitude and propulsion system performance, etc. This information was most helpful when gas leaks occurred (see Section V).

**5. Computer operations.** The closest OD interface was with the Flight Support Group, whose functions included program deck setup and UNIVAC 1108 computer operations. This group handled transfer of tapes between computers, as well as the monitoring and scheduling of program executions.

#### D. Data Used in the Orbit Determination Process

1. **DSN radiometric data.** The DSN supported the Mariner Mars 1971 mission with Deep Space Station (DSS) 12 and DSS 14 at Goldstone, California; DSS 41 near Woomera, Australia; DSS 51 near Johannesburg, South Africa; and DSS 62 near Madrid, Spain.<sup>1</sup> The first four sites tracked the spacecraft from launch (L) through Mars orbit insertion (MOI), whereas DSS 62 began tracking at L + 26 days. Because of the desire for continuous telemetry coverage, the DSN provided nearly continuous tracking from launch through encounter for the first time on an interplanetary mission.

Figure 1 shows the tracking coverage provided by the DSN by data type, station, and timespan. The data types available were hour angle (HA), declination (DEC), and one-, two-, and three-way S-band doppler (F1, F2, and F3, respectively), MARK 1A, TAU, and MU ranging.<sup>2</sup> DSS 14 was the only station with TAU ranging. MU ranging was available only at DSS 12, and only after July 11. The MARK 1A equipment, available at all but DSS 14, was originally designed for ranging at lunar distances, and, although the hardware had been improved, in the past it could only be used during the first few weeks of interplanetary missions before its useful range was exceeded. Because of the most recent hardware changes at the stations, MARK 1A ranging was taken at DSSs 41 and 51 through the middle of July, almost 7 weeks after launch.

To indicate the quality of the tracking data, Table 1 gives the standard deviation of the residuals for the individual data types from each station. The deviation is based on a post-flight solution which fit doppler and range data over the period from the midcourse maneuver (June 5) to 45 min before MOI (November 14). This solution included only the state vector for the probe, so that such quantities as the  $GM^2$  of the Moon, attitude control leakages, and station locations still contributed their signatures to the statistics. Figure 2, derived from Run 000967, indicates the pass-by-pass standard deviations of the MARK 1A data, whose quality degrades noticeably with increasing distance. Figure 3, also from the same run, indicates that the rather large standard deviations for the TAU and MU data types are due not so much to the hardware as to errors in the  $GM$  of the Moon and to attitude control system leakages. Because these phenomena have also affected the doppler and the MARK 1A data, Table 1 gives

<sup>1</sup>DSS 14 has a 64-m antenna. The others have 38-m antennas.

<sup>2</sup>Mathematical descriptions of these data types appear in Sections VII through X of Ref. 2.

an upper bound to the hardware errors. In general, the northern hemisphere stations (DSSs 12, 14, and 62) show slightly noisier residuals because of the increased troposphere and charged-particle effects at the lower elevation view angles.

2. **DSN station locations.** During the period from January 1 to October 20, 1971, three different sets of station locations were recommended to the Mariner Mars 1971 Project. The characteristics of each of these sets and a detailed history of their development are presented in the second section of Ref. 1.

3. **Planetary ephemerides.** Three different planetary ephemerides were used during the interplanetary phase of the mission. All were numerical integrations fit to optical and radar bounce data with JPL's solar system data processing system (SSDPS). These ephemerides were made available on tapes by the Ephemeris Development Group in the usual development ephemeris (DE) format (Ref. 3).

The ephemeris available in early 1971 was DE69 (Ref. 3), which had been created for the Mariner Mars 1969 mission. This ephemeris was based on 34,000 United States Naval Observatory (USNO) meridian circle observations covering the period from 1912 to 1968, about 800 planetary radar bounce points from 1964 to 1968, and 200 Mariner 5 range points taken during the 10-day encounter interval with Venus. The radar data for Mars consisted of 39 measurements from Arecibo Observatory (1964/1965) and 10 high-precision compressed points taken at the Massachusetts Institute of Technology's Haystack facility in 1967. In the 18 months following the release of DE69, additional Mars ranging was obtained, which indicated a secular drift in the Mars ephemeris, as shown in Fig. 4. Because of this, the Project agreed to fund development of a new ephemeris for encounter support, which would include the latest ranging data available. Although interim ephemerides were available at the time of launch, the first midcourse maneuver was based on the well tested and understood DE69.

The ephemeris planned for encounter support DE78, was delivered to the Navigation Team on September 30, 1971. In addition to the data used for DE69, it included USNO optical data from June 30, 1968, to July 17, 1969; the JPL Mars range data taken from May 7, 1969, to September 10, 1971; and the JPL Venus range measure-

<sup>3</sup>In the OD process, the quantity  $G \times M$  is used, where  $G$  is the universal gravitational constant and  $M$  is the mass of the body.

ments taken between July 22 and December 31, 1970. After initial consistency checks, this ephemeris replaced DE69 for all Navigation Team functions and was used to derive new station locations.

Shortly before the Mariner 9 arrival at Mars, it was discovered that a co'cer error in the Goldstone equipment had caused all of the 1971 Mars ranging data to be wrong by the equivalent of one second in epoch time. The Ephemeris Development Group found they could correct the observations in the reduction software, and thus produced DE79. The residuals (corrected data minus DE78 predictions) in Fig. 5 show the error resulting from using the faulty data. Figure 6 displays the difference in the geocentric range ( $\rho$ ), right ascension ( $\alpha$ ), and declination ( $\delta$ ) of Mars for the period of interest. At encounter, the differences are  $-9$  km,  $-0''05$ , and  $+0''04$  in  $\rho$ ,  $\cos \delta \Delta \alpha$ , and  $\Delta \delta$ , respectively.

The use of DE79 instead of DE78 induced a change of 30 km in the B plane encounter predictions, as discussed in Section III.

**4. TSAC.** The sources, characteristics, and reduction techniques of the timing, polar motion, troposphere, and charged-particle data are discussed in detail in Ref. 1.

**5. Spacecraft attitude information.** These data were required for support of the onboard optical navigation demonstration (OND) described at length in Section VI. The data were helpful in the analysis of the attitude control system leakages during the later portions of cruise (Section V).

The information was made available to the optical navigation engineers on tapes produced by the UNIVAC 1219 mission test computer (MTC) from raw telemetry data. The spacecraft transmitted quantized values of the positions of celestial reference bodies in the spacecraft sensors at 4.2-s intervals of time throughout the mission. These values were used in the optical programs to establish the camera pointing angles in inertial space.

These data were regularly monitored by personnel in the Guidance and Control Division at JPL to analyze attitude control system performance. Section V describes how these data can be used to identify gas leaks. Such leaks were in fact noticed by those monitoring the data. They identified the leaking valves and computed thrust profiles and communicated their findings in written form to the Navigation Team. The OD engineers then con-

verted the thrust profiles to acceleration profiles along the appropriate program reference axes.

**6. Optical data base.** The optical navigation observables are the locations of objects in TV picture coordinates, defined as the picture element (pixel) and scan line (line) numbers. The objects include natural satellites, planets, landmarks, stars, and reseaux. These observables are obtained in either of two ways: visually, by measurements of hard copies of the TV pictures, or by computer location of object images on a tape of telemetered video information.

During the 3-day approach period prior to MOI, three pre-orbital science picture sequences (POS I, II, and III) were taken. Section VI-F indicates how the OND influenced the content of these pictures and what use was made of them.

## E. Software Used by the Orbit Determination Groups

**1. Radiometric tracking.** Obtaining an estimate of the B-plane coordinates and associated statistics of the probe trajectory from DSN tracking data involves operation of two sets of software, known collectively as the data editing program (DEP) and the orbit determination program (ODP). The ODP is also known as the satellite orbit determination program (SATODP) and the double-precision orbit determination program (DPODP).

The first step in the data processing is conversion of the raw radiometric tracking data file produced by the tracking data processor (TDP) on the IBM 360/75 to UNIVAC 1108 format. Next, the orbit data editor (ODE) is used to select the data types and time spans to be processed. The ODE then reformats the range and angle information and computes the doppler frequencies used by the ODP. The raw doppler data are readouts, sampled at regular intervals, of the cumulative number of cycles of a signal that have passed through the receiver. By differencing the number of cycles read out at two successive times and dividing by the elapsed time, an average frequency over that interval is obtained. If nonconsecutive samples are used for this purpose, the doppler is compressed to a count time given by the interval between the two readouts used. Data noise caused by readout quantization will decrease as the count time increases. Compression, if done properly, will not destroy any information inherent in the data, and it will decrease the number of points to be processed.

Once a file of data is available, it is passed through a high speed, limited capability program (for Mariner Mars 1971, it was TRKED), which computes residuals based on the most recent trajectory. If blunder points are detected, the ODE is rerun to ignore the bad points and possibly to compress the remaining doppler. The result is a file of clean observables for use in OD.

The ODP is a collection of programs to perform high-precision differential correction of a variety of parameters that are used to compute observables. The "solve-for" variables include quantities like the space, aft position and velocity at some specified epoch, solar pressure and attitude control leakage coefficients, maneuver velocity increments, tracking station locations, aerodynamic constants, station and spacecraft ranging delays, planetary ephemeris parameters, gravitational harmonic coefficients, etc. The mathematical formulation of the ODP is given in Ref. 2.

The differential correction process requires residuals, partial derivatives, and some solution algorithm. To evaluate the results, it is necessary to have statistics on the solution, and it is often desirable to transform the results into a more easily comprehensible coordinate system. For these applications, the ODP includes the following programs:

- (1) DPTRAJ. DPTRAJ uses the Cowell method to numerically integrate the spacecraft cartesian coordinates. It displays various trajectory information and produces a probe ephemeris tape (PET).
- (2) VARY. VARY numerically integrates the partial derivatives of the spacecraft cartesian coordinates with respect to those parameters which affect them and writes a file containing sum and difference arrays for the probe ephemeris and variational equations.
- (3) REGRES. REGRES computes predicted observables and their partial derivatives with respect to the prescribed model parameters and writes them and certain auxiliary information for each data point on a file.
- (4) ACCUME. ACCUME uses the Householder algorithm to compress all the observation equations (conditional equations) into a set of  $N$  simultaneous equations in  $N$  unknowns. ACCUME also adds certain TSACs to the data, generates data weights, and tests deletion criteria.

- (5) SOLVE1. SOLVE1 solves the system of linear equations for any specified subset of unknowns, treating *a priori* uncertainties in the variables as additional information. It forms the classical covariance on the solution, as well as an augmented ("consider") covariance, which includes the effect of uncertainties in other parameters that affect the observables but are not solved for.
- (6) SOLVE2. SOLVE2 obtains a solution, when the simultaneous equations are nonlinear, by means of an algorithm (Ref. 4) which chooses some fraction of the correction indicated by SOLVE1.
- (7) MAPGEN. MAPGEN generates matrices of partial derivatives of the "more understandable" coordinates with respect to those parameters which affect the motion of the spacecraft on its trajectory.
- (8) MAPSEM. MAPSEM uses the matrices generated by MAPGEN to convert corrections and statistics for the "more understandable" parameters.
- (9) OUTPUT. OUTPUT plots and prints data residuals, as well as linearized residuals obtained by substituting solutions back into the observation equations. It then computes statistical information on these data.

Certain of these programs are usually concatenated to accomplish a specific function. For example, during cruise, when various solution strategies are under investigation, the OD engineer produces a file of residuals and partial derivatives of data for all parameters that might reasonably be solved for, which involves DPTRAJ, VARY, and REGRES. Once the necessary mapping matrices are obtained using MAPGEN, the effect of changing solution parameter sets on a given data set is studied using ACCUME, SOLVE1, MAPSEM, and OUTPUT. This latter type of run constituted the majority of inflight OD analyses for Mariner 9. As new data accumulated, they were added to the file, and usually two different data sets were examined: (1) that using doppler alone, and (2) that which included range and doppler. At times, these were processed both with and without charged-particle TSACs. For each data-batch/calibration combination, at least seven different parameter set solutions were obtained, which will be described later. Previous experience has proven this to be an invaluable OD procedure (see Section II), and the programs have consequently been designed to optimize this sort of operation. The interaction of all these programs is displayed in Fig. 7.

2. **Optical data.** Another software system (Fig. 8) was developed to gather and process onboard optical navigation data. This system was used for navigation studies, mission planning, and training before encounter, as well as for real-time OD. Although the OND was not critical to the success of the mission, this system was documented, verified, and tested to the Mariner Mars 1971 standards and placed within the mission-controlled software system.

The optical software processes data from Mariner spacecraft, which have three-axis-stabilized attitude, a two-degree-of-freedom scan platform, and vidicon television cameras. Raw data consist of telemetered TV pictures in digital and hard-copy form and telemetered spacecraft engineering data. The system processes the data and generates a file of optical-data residuals and partial derivatives for use in ACCUME of the ODP. The specific functions of the component programs in this software system are described below:

- (1) **STRFIL.** The reduced star catalogue program (STRFIL) scans a tape containing the 250,000 entries from the Smithsonian Astrophysical Observatory (SAO) star catalogue and creates a subset catalogue of stars within user-specified right ascension, declination, and visual magnitude limits.
- (2) **XTR.** Extractor (XTR) computes the celestial pointing direction of the scan platform at the time a TV picture is taken, using telemetered spacecraft engineering data (pitch, yaw, roll, and scan platform gimbal angles).
- (3) **CGG.** The celestial geometry generator (CGG) combines spacecraft trajectory, satellite ephemeris, star catalogue, and camera pointing data to compute *a priori* star- and satellite-image locations. Plotted output for each picture is scaled to match near-real-time hard copy to assist in locating and identifying observed images.
- (4) **IMP.** The image processing program (IMP) is used to search for and graphically display star, satellite, planet, and resseau images contained in the telemetered TV video data. IMP will automatically scan an entire TV picture, producing a line printer "plot" of video intensity in a 20 line by 20 pixel portion of a picture, centered about each detected bright spot.
- (5) **ODCR.** The optical data calibration and rectification program (ODCR) estimates measurement errors and computes expected image locations cor-

rected for known errors associated with the TV camera and spacecraft. Observed image locations, expected image locations, partial derivatives of image locations with respect to measurement errors, and observation statistics are passed on to the optical observable and partial generator (see 7).

- (6) **TGP.** The trajectory geometry program (TGP) is used to generate geometric quantities necessary to plan TV picture sequences and to process data from these sequences. TGP can operate in an interactive mode to expedite input/output during mission operations.
- (7) **OOPG.** The optical observable and partial generator program (OOPG) uses data from ODCR to generate observables and partial derivatives. These are then written on a file that is passed to ACCUME.
- (8) **ODAP.** The optical data analysis program (ODAP) is an estimation program specifically developed to meet the needs of optical navigation. ODAP uses a sequential formulation of the minimum variance filter with a generalized consider option. The sequential formulation allows the evaluation of optical data errors, which are modeled as exponentially time-correlated processes. The generalized consider option allows the evaluation of filter performance in the presence of unmodeled or mis-modeled parameters. Errors in *a priori* parameters and data noise can be accommodated. B-plane and plane-of-sky mapping is available.
- (9) **CERPLP.** The celestial and residual plot program (CERPLP) plots optical data (pixel and line) residuals from OOPG and ODAP data files and for B-plane estimates obtained from ODAP. CERPLP also plots spacecraft-centered and target-centered celestial geometries of spacecraft, planets, natural satellites, stars, and landmarks from TGP data files.

## II. Pre-flight Analysis

### A. Introduction

This section discusses the analysis which served as a basis for spacecraft delivery accuracy predictions. It enumerates the major error sources that affect the data used and presents the best pre-flight estimates of the uncertainties in these parameters. Whenever appropriate, the means by which these estimates were modified or confirmed by actual flight experience are indicated. The discussion includes a description of the strategies devel-

oped for conducting the OD and their rationale. References 5, 6, and 7 contain additional information on error sources and strategies.

The Project accuracy requirements for interplanetary OD (Table 2) were specified in terms of three separate phases: (1) pre-midcourse, from spacecraft injection to the first midcourse maneuver, (2) post-midcourse, from the first midcourse maneuver to approximately MOI - 30 days, and (3) pre-MOI, from MOI - 30 days to MOI.

Although strategies were developed to handle all three phases, this section will concentrate on those designed for the third phase, and will indicate wherever possible how these would be modified for the other phases.

## B. Major Error Sources for Radio Navigation

These sources consist of (1) observer-related, (2) spacecraft related, and (3) ephemeris-related errors. The first errors result from the use of models not accurate enough to locate the observer in inertial space and to calibrate out the effects of the transmission media. The second type of errors arise from inadequate modeling of all of the accelerating forces on a spacecraft. The last errors involve incorrectly specified positions of the planets.

**1. Observer-related errors.** These fall into two main categories:

- (1) Those that corrupt or distort the actual information content of the observation, e.g., charged-particle effects in the space plasma and Earth's ionosphere.
- (2) Those that influence the position of the observer (tracking station) in inertial space, such as polar motion and variation in the Earth's rotation rate (time variations).

All produce diurnal signatures, and at any instant their combined effect can be represented by an equivalent set of station locations which would produce the same observable. Hence, they are often referred to as equivalent station location errors (ESLEs).

Errors, real or equivalent, in the coordinates of a tracking station have different effects for different data types, geometries, and station combinations. Range rate data, from which the right ascension and declination of the probe are primarily obtained, depend heavily on the absolute longitude  $\lambda$  and the spin axis distance  $r_s$  of the station. Ranging data, when more than one station is tracking, are extremely sensitive to errors in relative longitudes, spin axis distances, and  $z$  heights (off the equator).

These facts must be considered when strategies are developed. The error sources are:

- (1) *Charged-particle effects.* The radio signals traveling between a station and a spacecraft pass through the ionosphere of the Earth, the interplanetary space plasma, and, infrequently, the ionospheres of other planets. The interaction between the radio signal and the charged particles in the medium causes, among other things, a change in the propagation velocity. The group velocity decreases, whereas phase velocity increases in the presence of charged particles. As the density of charged particles varies, the resultant time rate of change of the phase velocity corrupts doppler measurements made from the radio signal.

The Earth's ionosphere results from solar ultraviolet radiation ionizing the upper atmosphere. Consequently, the ionosphere above a tracking station increases and decreases with, roughly, a diurnal period. If the ionospheric effect is not measured or modeled, it can not be distinguished from errors in tracking station location and may cause significant errors in the real-time OD.

The uncertainty in the magnitude of these effects results more from the absence of continuous raw calibration data during the mission than from the quality of the measurements themselves. The quality depends on the measurement noise and bias, the proximity of the measurements to the spacecraft line-of-sight, etc.

- (2) *Tropospheric effects.* Refraction in the troposphere slows the phase and group velocities equally. The retardation is minimal at the zenith, where the least atmosphere is traversed, but the amount varies because of daily and seasonal weather changes. The refractive index of the troposphere depends on pressure, temperature, and relative humidity, and it is the unpredictable variations in these that causes the uncertainty in the troposphere model.
- (3) *Polar motion.* Although the DSS locations may be relatively well fixed on the Earth's crust, it is the station coordinates with respect to the Earth's instantaneous spin axis, and with respect to the equatorial plane defined by that axis, which are important for navigational accuracy considerations. The Earth's crust is not fixed with respect to the spin axis, and it is this so-called polar motion (the motion of the Earth's crust with respect to the spin

axis) which causes the DSS locations to be a function of time relative to the spin axis.

Polar motion data are available from a number of institutions, whose results often disagree by as much as 2 m. The uncertainty in polar motion is due to the noise on the raw data used for determination of the pole location and disagreement about which sources produce the "true" pole position.

- (4) *Timing errors.* Accurate specification of the inertial position and velocity of the tracking station requires knowledge of the instantaneous rotational position of the Earth on its axis. Because of tidal friction, etc., the Earth's rotation rate is decreasing as time goes on so that the time (Universal Time [UT1]) derived from the rotational position of the Earth differs from the uniformly flowing (Newtonian) ephemeris time (ET).

The variations in rotation rate are measured from Earth by (a) using photographic zenith tubes to observe the International Atomic Time (IAT) of transits of selected stars over the meridian or (b) using astrolabes to observe the IAT of selected star transits over specific circles of elevation angle. The errors in measuring the star positions, the errors in the star catalogues, and the discordance among results from the various suppliers of UT1 all contribute to the remaining uncertainties in time.

- (5) *Actual DSS locations* Except for geologic effects such as earthquakes and continental drift, the tracking stations do not move with respect to the Earth's crust. However, because the locations are best determined by analysis of existing tracking data, there are location uncertainties because of ESLEs discussed above and from other lesser sources.

**2. Spacecraft-related errors.** These errors include any unmodeled or mismodeled forces that affect the motion of the spacecraft on its trajectory. Some of these forces are gravitational, resulting from attractions by massive bodies; if the masses are not known accurately, the computed trajectory will be in error. Other forces arise from engineering particulars of the spacecraft. These non-gravitational forces include those involving the spacecraft's interaction with its environment, such as solar pressure and drag, and others involving spacecraft operation, like propellant leaks and attitude control thruster imbalances.

Accelerations from these sources are very small ( $\sim 10^{-11}$  km/s<sup>2</sup>) and are dangerous not for the amount by which they perturb the actual motion of the spacecraft, but rather for the way they can resemble other forces being solved for in the data filter. This ability to be "soaked up" by other parameters can sometimes decrease with increasing data are if the changing geometry helps the other forces (usually gravitational) to distinguish themselves.

- (1) *Solar pressure.* The most obvious solar pressure acceleration is in a radial direction away from the Sun. There are also two smaller forces orthogonal to this because of asymmetry of the spacecraft configuration (e.g., the high-gain antenna, which is canted off the spacecraft roll axis). The magnitudes of these three forces depend on the projected cross-sectional areas and reflection coefficients in those directions, which are very difficult to measure in a laboratory. Moreover, experience with previous Mariners indicates a slow but perceptible secular decrease in solar pressure (3% over the mission). This decrease is commonly attributed to degradation of exposed surfaces, which results in decreased reflectivity.
- (2) *Propulsion system.* Gas leaks can arise from imperfect seat tolerances on the valves of the main propulsion system. Because the amount of propellant carried to Mars for the orbit insertion far exceeded the amount required for any past or present midcourse requirements, the Mariner 9 spacecraft had a significant potential for leaks after its midcourse correction. The tolerable magnitude of such leaks was included in the design specifications.
- (3) *Attitude control system.* The attitude control thruster imbalances which arise from imperfect matching of the jets on opposite sides of the spacecraft, and the leaks from incomplete seating of the associated valves, are much more difficult to model because so little is known about their temporal characteristics. The effect of imbalances would presumably vary as the number of gas firings, but the valve seating problems could improve or degrade with time. Here, again, the design specifications included the tolerable leak magnitudes.

**3. Planetary ephemeris errors.** The accuracy with which the Mars-centered position of a probe near encounter can be predicted using Earth-based tracking depends on the accuracy of the prediction of the geocentric position of the probe and of Mars at that time. Determination of the geocentric position of the probe from radio tracking is

corrupted by the errors mentioned above. The geocentric position of Mars is obtained directly from the planetary ephemeris, so its errors are simply the vector difference between the absolute position errors for Earth and Mars on that ephemeris. Admittedly, the trajectory of the probe depends on the absolute position of Mars, which is an attracting body, and the position of the observer depends on the absolute position of the Earth; but the displacement of Mars from where it is expected to be when the spacecraft arrives is the most easily understood effect. The least obvious, but nevertheless important, effect is in the determination of station locations, which are "observer-related" errors (Sections III and IV).

### C. Assumed Magnitudes of the Radio Navigation Error Sources

Before every mission, OD analysts assess the state-of-the-art accomplishments in each of the above areas and establish the uncertainty of their knowledge about them. In subsequent studies, they use this information, along with assumptions about the measurement errors in the real observables, to compute uncertainties in the deliverable B-plane results.<sup>4</sup> The same procedure is used in operations, when the final selection of data is available. The delivery uncertainties quoted later in this section are based on such consider covariances. The accuracies predicted by pre-flight analysis can be achieved in operations if the estimate of error magnitudes is realistic. The magnitudes assumed for considering and estimating these parameters are listed in Table 3. The consider values, which will be discussed first, are the best estimate of the true uncertainties.

The solar pressure values reflect the laboratory measurement uncertainty mentioned earlier. The attitude control estimates were based on propulsion and attitude control leakage specifications. The station location errors are the combined equivalent of all the observer-related errors (DSS location, timing, polar motion, charged particles, and troposphere). The ephemeris values give a geocentric Martian position uncertainty of 10 km in the plane of motion and 50 km perpendicular to it.

As the mission progressed, some of these quantities, like solar pressure and constant attitude control accelerations, became better defined. However, it was very seldom that

<sup>4</sup>The ODP obtains a covariance on the solved-for quantities based on data noise alone, and modifies it to account for the effect on the computed observables of errors in the other not-solved-for (consider) parameters. (For a mathematical description, see Sections XV and XVI of Ref. 2.)

these or the above consider values were used as *a priori* information in a solution for such quantities because, in general, to do so restricted the capability to determine them independently with observational data. This may be a result of ignoring correlations in the uncertainties or of inappropriate data weights, both of which need to be investigated further.

The data errors assumed for the accuracy studies were 3 mm/s for a 60-s count time doppler point, and 100 m for range data. During the mission, these errors were changed to 1 mm/s and 30 m, respectively, in light of the results shown in Table 1.

### D. Error Sources for Onboard Optical Navigation

The onboard optical data determine the distance and direction to Mars by observing how the apparent orbits of Phobos and Deimos change against the background stars as the spacecraft approaches Mars. The two main classes of errors that corrupt optical navigation results are those which affect the measuring instrument (TV camera), and those which affect the computed apparent celestial coordinates of the observed objects.

**1. Instrument errors.** The measured line and pixel locations of images are used to determine the directions of objects. Electromagnetic distortion in the electron beam scanning circuitry, optical distortion in the telescope of the instrument, and errors in instrument parameters (e.g. focal length) can corrupt the measured direction.

Electromagnetic distortion can be caused by (1) a non-uniform magnetic deflection field, (2) a fringe field outside the deflection region of a vidicon tube, (3) interaction between the focusing and deflection fields, (4) a nonuniform electric deceleration field, (5) electromagnetic bias shifts, (6) a common rotation of the scan deflection fields with respect to the target raster, and (7) nonorthogonality of the scan line and pixel deflection fields.

Optical distortion results from: (1) imperfect design and/or construction of the telescope lens, (2) misalignment (nonorthogonality) of the lens optical axis with the target raster, and (3) decentering of the lens optical axis in relation to the center of the target raster.

An error in the value of focal length used to describe the instrument transfer function causes a symmetric radial distortion about the principal point. Errors in the values of the pointing direction used to describe the instrument transfer function have an effect similar to errors in the

values used for the location of the principal point on the target raster.

**2. Celestial direction finding errors.** Here, the primary contributions to errors are satellite ephemeris errors. Since the size and shape of the apparent orbit determine the probe's position, errors in the satellite ephemeris have an important effect.

#### **E. Assumed Magnitudes of the Optical Navigation Error Sources**

Because of the TV and scan platform calibration sequence performed about 30 days before MOI, there was an opportunity to assess the magnitude of the errors in the optical navigation instrument in its flight configuration. The TV geometric distortion was calibrated to better than 0.5 picture elements, (3"0)  $1\sigma$ , using the reseau grid. The residual distortion after calibration was random and did not change in character through MOI. Since the ability to image a number of stars was proven during this sequence, it was obvious that the TV pointing direction could be determined to the limiting accuracy of the residual TV distortion because the positions of the stars were assumed to be perfectly known. With this as background, it was decided to weight the Phobos and Deimos data from star-satellite pictures at 3"0 in the ODP.

The *a priori* uncertainties in the satellite ephemeris elements are given in Table 4.

#### **F. Development of OD Strategies**

Pre-flight analysis and past mission experience show that the best way to detect the presence of errors is to compare and contrast a variety of solutions based on differing data arcs, data types, and solved-for parameters. Then, after identification of the errors present, strategies can be applied to obtain a good solution in spite of them.

One effective means of ferreting out problems is to compare solutions using different length data arcs or arcs located at different places along the orbit. Often a short arc will erroneously absorb phenomena into the state which would not be interpreted as the state in a long arc because of the distinguishing effects of changing geometry (Fig. 9). For example, the deleterious effects of ignoring certain TSACs seem to decrease as the data arc is lengthened. A similar situation occurs when stochastic gas leaks on both Mariners 4 and 9 are ignored.

A second approach is to play different data types against each other. Doppler and range have different

sensitivities to many phenomena. For example, doppler can easily mistake nongravitational for gravitational forces because it determines the position of the probe from its observed geocentric acceleration (time rate of change of doppler). Using the planetary ephemeris to determine the relative acceleration between the Earth and the body whose gravitational acceleration is currently dominating the probe's motion, an OD program would deduce the probe-body acceleration by vector subtraction. It then simply infers the probe-body relative position using the law of universal gravitation. Nongravitational spacecraft accelerations can obviously degrade the determination of the distance of the probe from such a body unless another means is found to constrain the solution for position. Ranging data often fill this gap because, in conjunction with a planetary ephemeris, they can independently set limits on the probe-planet distance (Fig. 10). However, this situation makes ranging particularly susceptible to ephemeris errors. Onboard optical data are insensitive to either of these errors but are dependent on satellite ephemeris errors, and so on. If solutions using one data set differ noticeably from those using another, or from those using a combined data set, then probably something is mis-modeled.

Another technique is comparison of solutions obtained using different parameter sets, with an accompanying evaluation of the new solved-for values. If these values are unreasonable in light of what is known *a priori* (e.g., a changed sign on the transverse solar pressure), then it may be that these parameters are absorbing some other error. Another indication is poor consistency between solutions using different parameter sets. This entire concept, of course, assumes that sufficient data are being used to make a meaningful solution possible.

After detection of mismodeled phenomena, it is not always easy to correct the model. It may be that the detection scheme showed the difference in effects on two runs and did not indicate the absolute effect. It may be that the phenomena can not be parameterized in the software. It is often more important from the engineering point of view to find an approach which minimizes the effect or avoids the problem than to obtain a questionable solution. The runs that constitute the detection scheme usually indicate the course to be taken.

The strategy for this mission was to compare results using long, medium, and short data arcs starting at the first midcourse maneuver, the second midcourse maneuver (planned for MOI - 20 days), and MOI - 5 days,

respectively. In each case, the comparison would be extended to MOI - 8 h (before gravitational bending).

For each arc, doppler and range data were to be processed separately and in combination. Because optical measurements would be available only after MOI - 3 days, the short arc would afford the only opportunity to use these data by themselves. However, they were to be used in combination with radio observables on both the intermediate and short arcs. It was also desirable to investigate results obtained with and without charged-particle calibrations on the radiometric data. For each of these data type/arc sets, results were to be compared based on two or more of the vectors shown in Table 5.

There was no commitment beforehand to base the final recommendations on any particular data type/arc/parameter set combination. Section III will indicate how the strategies were actually applied in flight and what combinations were used to produce the OD results.

### III. Orbit Determination

#### A. Introduction

This section summarizes the results obtained by the OD group of the Navigation Team using interplanetary data. It describes the major problems encountered and indicates how the strategies discussed in Section II were applied to obtain the final recommendations. It compares the answers derived in flight with those produced by post-flight analysis and examines the performance in light of the pre-flight predictions. Finally, it discusses new determinations of various constants using this data span. References 8 and 9 contain additional information about the inflight and post-flight results.

As indicated previously, the mission plan allowed for two midcourse maneuvers. The first would correct the launch bias required by planetary quarantine constraints, as well as any launch vehicle errors. If necessary, the second would be designed to remove OD and maneuver execution errors associated with the first, and to allow any late change of planned insertion altitude or inclination. In practice, the second midcourse maneuver was not necessary and was never performed.

The continuity of the pre-midcourse phase was broken by squib firings to unlatch the spacecraft scan platform from the stowed position. Previous experience with Mariners 6 and 7 showed that the squib firings could noticeably affect the trajectory, and thus they should

occur before the first midcourse to preclude perturbations of the post-midcourse trajectory. Because of the velocity change which results from the firings, the pre-midcourse phase is divided into two data blocks, the pre-unlatch and the post-unlatch.

The post midcourse phase was near optimum from the spacecraft trajectory standpoint. There were small gas leaks from the attitude control system throughout the mission that affected OD, but these small leaks were within design specifications. However, a series of much larger, intermittent leaks, occurring after September 15, 1971, had a major effect on the OD strategies employed.

Run identifications are included with the tabular results below to enable access to the microfilmed listings. All times are given in Universal Time Coordinated (UTC), and all cartesian coordinates are referred to the Earth mean equator and equinox of 1950.0 unless otherwise noted. Appendix B contains a listing of the basic constants input to the ODP.

#### B. Pre-midcourse Results

Injection into the Earth-Mars transfer trajectory occurred at 22<sup>h</sup>34<sup>m</sup>59<sup>s</sup>.70 on May 30, 1971. Within 2 h after injection, the angle data recorded by the DSN became insignificant compared with range and doppler in the OD process. Only one solution was computed using the angle data, and it indicated that the injection was sufficiently accurate to make the pre-computed DSN predicts usable.

As more and more stations began to track the spacecraft, a series of data/station consistency checks were made to ensure that performance and calibration within both the DSN and the tracking system software were as anticipated. This procedure, standard during any mission, uncovered an incorrect ranging transponder delay input to the ODE. This phase of the mission is the only one in which it is possible to calibrate the basic delays in the ranging machines using spacecraft dynamics instead of ground equipment because the deceleration on the probe caused by the Earth is so large that the law of universal gravitation allows determination of the spacecraft range by doppler alone to ~100 m. The fact that ranging data agreed with doppler-only orbits to that accuracy indicated the basic delays were reasonable. Other checks at this time and later during the mission ensured that the biases between ranging passes from different stations (caused either by miscalibrated station delays or incorrect values for the distance of the stations from the equator) never exceeded 20 m.

Pre-flight analysis indicated that the prime error sources during this phase would be mismodeled solar pressure (SP) forces and/or attitude control (AC) system leaks. Errors from these sources could not be particularly well determined because of the shortness of the data arc, and, if errors occurred in either of these sources, they would map to a large dispersion at encounter because of the length of the trajectory. It would be impossible to obtain a real separation of the two because of the restricted geometry and range of Sun-probe distances; thus, they were combined as SP. All available ranging data were used because they gave the most information about these non-gravitational forces.

Table 6 compares the pre-flight SP and AC parameter values with those obtained during the pre-midcourse phase of operations, those derived by post-flight processing of pre-midcourse data, and their current best estimates (CBEs). The uncertainties in the estimated values can be found in Tables 7 and 8. When comparing these values, it is worth remembering that the uncertainty quoted in the pre-flight values was  $\pm 0.03$ .

The scan platform unlatch was scheduled for L + 1 day to allow sufficient time to redetermine the orbit before the first midcourse maneuver at L + 5 days. Although there was no critical requirement for an orbit prior to that for the midcourse maneuver, a solution based on data to L + 1 day was provided to support preliminary maneuver planning.

Although station location errors were known to have little effect on the B-plane results at this stage, they were included in a solution set to serve as a indicator of abnormalities. Solution sets A, B, and C (Table 5) were examined using doppler alone and doppler and range in combination.

The pre-unlatch orbit solution quoted in flight and the final post-flight orbit based on the same data appear in Table 9. When the solutions are adjusted by the final estimated  $\Delta$ 's caused by the scan platform unlatch and the midcourse maneuver, they give the B-plane parameters displayed in Table 10. The remarkable performance of the inflight pre-unlatch orbit should be qualified by pointing out that there were a number of canceling error sources. The timing polynomials, station locations, SP, AC, and planetary ephemeris used in flight would have caused much larger errors than are indicated in column D. Column F illustrates this because it is due almost entirely

to the combined SP and AC errors. The pre-unlatch data are not strong enough to correct the *a priori* values for these quantities, which are given in column F of Table 6.

The velocity increment to the spacecraft was obtained by combining data on either side of a 3-h period during which the small nongravitational unlatch and line venting accelerations occurred, and estimating an equivalent  $\Delta V$  using the instantaneous maneuver model of the ODP. The results given in Table 11 include the effect of the unlatch itself, which occurred at 22<sup>h</sup>32<sup>m</sup> on May 31, 1971, as well as of a gas venting from lines upstream of the engine values at 01<sup>h</sup>28<sup>m</sup> on June 1, 1971. The two events were modeled with a single burn at 0<sup>h</sup>0<sup>m</sup>0<sup>s</sup> on June 1, and all the data between them were ignored. The B-plane effects were obtained by differencing the B-plane estimates of the pre- and post-unlatch orbits computed using the same model.

Because there was insufficient experience and confidence in fitting maneuvers in flight, most of the effort to obtain a reliable orbit for the midcourse maneuver calculations was spent processing the post-unlatch data. The solution recommended at midcourse - 12 h was PREM/C-10-C, chosen over the A and B solutions based on the same data set because of superior fit to the data and because the solved-for parameters had undergone reasonable changes from the anticipated standard. (There were other solutions with unreasonable changes.) The inflight and post-flight estimates appear in Table 7. When these solutions are adjusted by the final  $\Delta$ 's caused by the midcourse maneuver, they produce the results seen in Table 12. The same qualifications apply here as for pre-unlatch. In both cases, the rather large  $T_{CA}$  errors in flight are due primarily to the incorrect *a priori* value of  $SP_x$  seen in column C of Table 6.

Table 12 shows that the error in B-magnitude was well within the 250-km ( $1-\sigma$ ) accuracy requirement at L + 5 days. Pre-flight analysis indicated that an uncertainty of 223 km in  $|B|$  should be expected at this time; the inflight uncertainty was 119 km.

### C. Midcourse Maneuver Analysis

The midcourse maneuver was a 5.11-s burn that started at 00<sup>h</sup>22<sup>m</sup>05<sup>s</sup> on June 5, 1971. The differences between the final aiming point for the maneuver and the current best estimate of the achieved B-plane parameters are

given in column A of Table 13. These differences are due to a number of factors, chief among which are:

- (1) Errors in the geocentric orbit determined from the pre-midcourse tracking data, which include errors in the geocentric state, as well as errors in the SP and AC forces mentioned previously.
- (2) Errors in the Mars ephemeris used for designing the maneuver. Even if the geocentric orbit were correct, a Mars ephemeris error would cause the achieved orbit to miss the aiming point.
- (3) Omission in flight of the effects of the sporadic gas leaks which perturbed the post-midcourse trajectory.
- (4) Spacecraft maneuver execution errors.

Column B of Table 13 shows the effect of changing ephemerides from DE69, which was used in flight for computing the midcourse, to DE80, which was used for the post-flight analysis (DE80-DE69). Column C is an attempt to determine the errors described in (1) by adjusting the differences of Table 7 for the change from DE69 to DE80 (post-flight - inflight is shown). Column D gives the best available estimate of the sporadic gas leak effects of item (3).

Table 14 compares the commanded maneuver with the best post-flight estimate of its components. This post-flight analysis was based on data through August 1, 1971, and is subject to the uncertainties indicated. The effect of using the different maneuver values in integrating a trajectory to encounter is seen in column E of Table 13. The residual error in column F (Table 13) is the combined effect of the errors in all the above items. Additional study is needed to explain why column F does not equal column A.

#### D. Post-midcourse Results

The planning and execution of the first midcourse maneuver are described in the *Maneuver Analysis* section of this report. Following the maneuver, an estimate of the orbit had to be reestablished. Once this was done, the somewhat stable routine of cruise allowed time to prepare for the next major orbit delivery deadline, at MOI - 18 days (October 26, 1971), when the recommendations for the second midcourse maneuver were due. Most of the solutions studied during this period had their epoch on June 5, 1971, immediately after the first midcourse maneuver.

Cruise was the period chosen for phasing in the new ephemeris and the enhanced versions of the SATODP which were to be used for encounter support. As each was incorporated, extensive comparisons were made between old and new to facilitate understanding of the resulting B-plane changes. In all, four different versions of the SATODP were used:

- (1) Phase A, pre-flight through August 13, 1971.
- (2) Phase B, August 5, 1971, through September 28, 1971.
- (3) Phase C0.0, September 29, 1971, through October 22, 1971.
- (4) Phase C1.0, October 23, 1971, on.

The three different ephemerides were employed as follows:

- (1) DE69, pre-flight through October 31, 1971.
- (2) DE78, November 1, 1971, through November 11, 1971.
- (3) DE79, November 12, 1971, on.

Some post-flight analyses used DE80, which was available in early December of 1971.

As more data accumulated and the newer ephemerides and software came into use, the B-plane parameters from the long arc solutions (set A, Table 5) displayed the behavior seen in Fig. 11. The discontinuities correspond to software or ephemeris changes, whereas the gradual drifts indicate the effect of increased amounts of data in the presence of modeling errors.

The gradual degradation of solutions up to August 4, 1971, and the noticeable discontinuity at that time were fully expected. They indicate the effects of outdated timing and polar motion, which were replaced when the change was made from SATODP-A to SATODP-B. Up to that time, the timing and polar motion data available at launch were used. The accuracy of these data decreased the further they were extrapolated into the future. However, the data were used until August 4 because SATODP-A required the data in a format that had not been produced at JPL since January 1, 1971. The launch deck was produced by hand and was believed to be adequate for launch and midcourse support. With the advent of SATODP-B, the new format decks could be used. These decks were updated weekly throughout cruise and daily near encounter.

The other noticeable breaks occurred on October 31, when DE78 replaced DE69, and on November 11, when DE79 replaced DE78. As Table 15 indicates, the size of the breaks in the solutions correlated very well with the differences seen in trajectories integrated using the different ephemerides, and in that sense were well understood.

Although the drifting before August 4 is partially explained by the outdated timing and polar motion, other results indicated that additional problems might be present. As was mentioned in Section II, throughout the long arc, estimates obtained were based on a number of the solutions sets listed in Table 5. By comparing values of the solved-for parameters from run to run with their *a priori* values, it could be seen that certain parameters changed to new values and stayed there, whereas others showed secular trends. Among the first type were DSS station locations and the GM of the Moon. Solar pressure coefficients are an example of the other class.

GM of the Moon was the least controversial. The values that kept recurring were in fine agreement with those obtained from Mariners 6 and 7 and were believed to be quite reasonable. The DSS absolute longitude changes, however, were significantly larger than the *a priori* uncertainties were estimated to be and were outside the spread of solutions used to form the recommended set, LS 35. These results were not particularly damaging to the long arc B-plane predictions because the sensitivity of the solved-for state (and thus the miss parameters) to station locations is very small (e.g., less than 5 km for a 10-m longitude error). The implications, however, were much more important. If, for some reason, a short arc of data, whose sensitivity to station locations is high, had to be relied on, then a longitude error of the size indicated in the long arcs (-7 m) could have a 50- to 100-km effect on the miss parameters. In view of this, every attempt was made to reinvestigate the data that went into LS 35 and to study the possibility of obtaining credible DSS locations from a long arc. This is discussed further in Section IV.

As for solar pressure, these coefficients, or anything that resembles them, have a significant effect on long trajectories because their accelerations can integrate to a substantial position displacement. They were, therefore, the dominant error source for the pre-midcourse OD and also for all solutions whose epochs were early in the mission (e.g., the long arcs).

The SP/AC model in the ODP computes spacecraft accelerations in three directions according to the expression

$$\begin{aligned} \ddot{\mathbf{r}} = & (AC_R + \Delta AC_R + \frac{k}{r^2} SP_R) \mathbf{R} \\ & + (AC_X + \Delta AC_X + \frac{k}{r^2} SP_X) \mathbf{X} \\ & + (AC_Y + \Delta AC_Y + \frac{k}{r^2} SP_Y) \mathbf{Y} \end{aligned}$$

where

$r$  = Sun-probe distance, km

$k$  = a factor depending on spacecraft mass and area and solar flux constant

$\mathbf{R}$  = unit vector directed out from Sun to spacecraft

$\mathbf{X}$  = unit vector along spacecraft + X direction (pitch axis)

$\mathbf{Y}$  = unit vector along spacecraft + Y direction (yaw axis)

$SP_{R,X,Y}$  = solved-for reflectivity coefficients along  $\mathbf{R}$ ,  $\mathbf{X}$ , and  $\mathbf{Y}$ .

$AC_{R,X,Y}$  = solved-for constant leak components

$\Delta AC_{R,X,Y}$  = additional nonsolved-for, time-varying leak components

Over a small range of Sun-probe distances, any gas leaks,  $AC_{R,X,Y}$ , could be absorbed in  $SP_{R,X,Y}$  and, as long as they were small enough, would give SP values within reasonable dispersions from the *a priori* mentioned in Section II. However, as the Sun-probe distance increases so that the  $1/r^2$  factor comes into play, the continued absorption of constant AC leaks into SP would mean a secularly changing set of SP coefficients. Because the behavior shown in Fig. 12 occurred, it was deduced that the probe must have had a small AC leak.

Meanwhile, the AC subsystem engineers were making estimates of the magnitudes of the leaks, which they had discovered independently through analysis of the engineering telemetry. Their estimates were the first confirmation that the OD deductions were well founded and showed that the leaks were well within the subsystem design specifications. What prompted them to bring

these leaks to the Navigation Team's attention at all was the concern the OD engineers showed over the much larger sporadic leaks that began on September 15.

The character of these leaks is discussed at greater length in Section V. Briefly, one of the roll-axis valves would aperiodically fail to close entirely, possibly because of small particles caught in the valve seat. The valve would leak until such time as it was required to fire again, when the particle would be blown away. The new firing would come either as a response to normal torques on the spacecraft or, in the case of large leaks, after specific corrective commands from the ground.

The appearance of these sporadic leaks, and the confirmation of a long-standing constant leak prompted renewed analysis of OD strategies. The strategies would depend on the expected magnitude of the B-plane changes caused by these leaks as well as the ODP's ability to handle such phenomena. In general, the long-arc solutions, which included nonstate parameters, gave results significantly different from the state-only cases, when sporadic gas leaks were present in the data. Some very disturbing correlations were observed between station locations and AC coefficients, which will be discussed further in Sections IV and V. When it was found that the constant leak would move the trajectory only 50 km in the B-plane and that the sporadic leaks would probably mean less than 10 km, it was easier to put these problems in perspective. It was important to choose an approach that would not allow these accelerations to corrupt the estimation process. The choices were:

- (1) To recommend the results based on long-arc solutions up to the beginning of sporadic leaks.
- (2) To solve for AC and SP using the data prior to the sporadic leaks, and inputting these data to the trajectory along with the sporadic leak magnitudes provided by the AC subsystem personnel, fit the entire long arc of data, and use the state-only solution.
- (3) To rely on the approach of (2) applied to a short arc starting a few weeks before the planned second midcourse maneuver to minimize the errors caused by integration over a long trajectory.

Other options were discarded as the number of sporadic leaks began exceeding the maximum number of solved-for leaks in the ODP. Item (3) involved fitting data from October 4 to October 25, during which time there were no

sporadic leaks, but the information content of these data was insufficient to meet the Project's required delivery accuracy. A decision was made to pursue options (1) and (2) simultaneously and to postpone the final decision for as long as possible.

Option (1) used a long arc of data up to 0 h on September 15. Until the OD engineers were officially notified of the gas leaks, they had been fitting the data with trajectories that had zero values for  $AC_{R,X,Y}$ . According to plan, they had generated partial derivatives for those parameters. They found they could obtain nonzero values for them in the solutions, but that their effect could alternatively be absorbed in the solar pressure to give an equivalent B-plane result to within 10 km.

Table 16 shows that the solved-for  $AC_{R,X,Y}$  results were noticeably different from those suggested by the AC subsystem engineers. However, after consultation, the engineers indicated that the uncertainties in their estimates would not exclude the OD values, and that the greater magnitude in the Y direction could be caused by leaks from two opposing roll jets on the +Y solar panel, which, in turn, would explain some additional anomalous behavior they had observed. Therefore, the values in column E were adopted for option (2) and all subsequent OD. The current best estimate of these parameters, determined from post-flight analysis of the same data arc, is also included in Table 16. The solution based on approach (1) in flight is compared with post-flight solution in Table 8. The covariances here did not include the effect of "consider" parameters and so are somewhat optimistic. Pre-flight studies suggest a  $\sigma |B|$  of 95 km.

On October 26, when the orbit estimates were due for designing the second midcourse maneuver, only long-arc solutions were available, based on DE69 and the AC information in Table 16. Initial indications from the Ephemeris Development Group were that the still-to-be-delivered new ephemeris (DE78) would change  $|B|$  downward by 50 km. From analysis of the first three sporadic leaks, the OD engineers concluded that, if such leaks continued, they would serve to increase  $|B|$ , but by no more than 10 km. (The first three leaks amounted to +2.69 km in  $|B|$ .) In addition, if the station locations were in fact in error by the -7 m indicated, the long-arc solutions would be affected by no more than 5 km. After factoring all this information in with the solutions seen in Table 8, the Navigation Team Chief was advised that  $|B|$  would be  $8235 \pm 100$  km.

### E. Pre-MOI Support

When the second midcourse maneuver was canceled, the continuity and integrity of the long arc could be preserved. Nonetheless, according to the planned strategy, a series of intermediate-arc solutions was initiated. If these results agreed with the long arcs, it would indicate that there was no problem; if not, the varying sensitivities of the two data spans might help to pinpoint the problem. The results obtained are shown in Fig. 11.

The epoch was chosen at October 4 because, at the time the decks were set up for these runs, there had been no gas leaks since October 4. The dispersion in the solutions, although within the considered covariance, was nonetheless disquieting. Attempts were made using simulated data to determine whether ephemeris errors could possibly cause such behavior before MOI - 5 days, but they were inconclusive. A more readily accepted explanation was the corruptive effects of the possibly poorly modeled sporadic leaks. Once the *a priori* state was constrained to 100 km and 0.1 m/s, state-only solutions matched their long-arc counterparts to within a few kilometers.

Eventually, the awareness that these arcs were really being processed as a backup for the long arcs lessened the concern about their instability. There was not enough time during the actual operations to explain their behavior adequately, and, because there already were a series of understandable stable solutions, no crash effort was made to resolve the problems. Nevertheless, intermediate-arc solutions were made up to MOI. Some post-flight analyses of the intermediate arc are discussed in Section V.

In addition, according to the pre-flight strategy, short-arc results were studied. The epoch for the short arc was November 9 (MOI - 5 days). Since there were still sporadic leaks at this time, in addition to the long standing constant leak, all short-arc trajectories included the solved-for values of Table 8 and the latest estimates of the sporadic leak magnitudes by AC subsystem engineers.

The experience of past missions was that the short arc would not provide solutions of comparable accuracy to those of the long arc until the spacecraft was within a day of encounter. After this time, short-arc results should provide a good check on the long-arc solutions, and, perhaps, a better estimate of the parameter  $T_{CA}$ . The strategy was to rely on the solutions for the state-only and the state and station locations. The station locations are important if a short arc is to absorb any possible timing or ephemeris

errors. The GM of Mars was not as important as the station locations because three flyby determinations had already been made of it. The effects of SP and AC errors on the trajectory would be almost insignificant because of the short integration time, which, in combination with the unpredictable sensitivity of their partial derivatives to the intermittent gas leaks, would make them bad candidates for inclusion in the solution.

At MOI - 5 days, there was an opportunity to update the spacecraft central computer and sequencer (CC&S) with a new set of maneuver commands. To support this update, the OD team had to provide a recommended orbit and associated uncertainty. Of the long- and intermediate-arc solutions available at the time, POSTMC-42-A was chosen. The B-plane parameters were:

- (1)  $|B| = 8203.41$  km.
- (2)  $B \cdot \hat{R} = 6004.71$  km.
- (3)  $B \cdot \hat{T} = 5589.22$  km.
- (4)  $T_{CA} = 0^{\circ}31^m46^s.64$ , November 14, 1971.

This selection was based on the comparative stability of the long-arc solutions which had been obtained throughout the mission and the assumption that there would be enough inertia provided by the data up to September 15 to maintain an even keel through the period of intermittent gas leaks.

The results of the radio short-arc solutions, whose epoch was MOI - 5 days, are plotted in Fig. 11. This was the span during which optical data became available. The results based on POS I and POS II data, alone and in combination with radio data, also appear in Fig. 11.

At MOI - 12 h, another orbit was required to prepare for the final possible full CC&S load. By this time, all orbits had been recomputed using DE79, all the POS I and POS II optical data were available, and the short-arc solutions were improving. The individual results considered are shown in Table 17, in which the long-arc solution was supplied for the MOI computations. The very good agreement between the optical-only and radio-only results renewed confidence in the long-arc solution. There had to be no significant Mars ephemeris error because the optical solution, which was ephemeris-independent, and the radio solution, which was highly ephemeris-dependent, were nearly identical.

At the time of the final possible update, the solutions only had data up to MOI - 8 h because of a failure on the

NATTRACK computer. The short-arc solutions drifted upwards in  $|B|$  and were holding at the values shown in Table 18. The long-arc solutions, also shown in that table, did not move as they experienced more and more gravitational bending.

There were four possible choices for the final update recommendation:

- (1) Use the long-arc solution up to September 15, corrected for the new ephemeris and the trajectory effect of the subsequent gas leaks.
- (2) Use the long-arc, state-only solution, fit to all the data up to MOI-8 h.
- (3) Use the short-arc solution with data up to MOI-8 h.
- (4) Use the combined optical and radio solution.

The large movement in  $B \cdot R$  on the short arc was unexpected but was somewhat confirmed by the optical data. However, the short arcs were susceptible to unmodeled leaks. Thus, the final recommendation, based on (2) was POSTMC-56-A, which was bolstered by its reasonable similarity to the pre-September 15 data result.

As can be seen from any of the above tables, the inflight recommendations were quite accurate. Pre-flight analysis had predicted a 93-km uncertainty in  $|B|$  at MOI-5 days, and 120 km and 50 km for the short and long arcs, respectively, at MOI-12 h.

Figure 13 gives an indication of the overall OD performance from launch to encounter. The 50-km bands around the current best estimate represent the allowable  $1-\sigma$   $|B|$  delivery error at MOI-6 h. The insertion maneuver was actually based on an orbit whose  $|B|$  error was 58 km, even though there were improved orbits available in time to reload the CC&S (e.g., at MOI-12 h).

Table 19 contains information about the radio solutions plotted in Fig. 11.

The available charged-particle calibrations were used in flight on an experimental basis. Although the results were not in particularly good agreement with the current best estimate, they showed no more dispersion than the intermediate-arc solutions. The studies, which are described in detail in the sixth article of Ref. 1, were inconclusive and did not influence the final orbit recommendations.

## F. The Current Best Estimate

The current best estimate (CBE) was obtained by comparison of post-flight results using three strategies: (a) a long arc from midcourse maneuver to MOI, (b) a short arc from MOI-5 days to MOI, and (c) a short arc covering MOI-5 days to MOI+10 h that included an MOI burn model. The results shown in Columns B, D, and E of Table 20 apply to strategies a, b, and c, respectively. The individual values were the conclusions drawn from a study of a variety of data sets and solution parameters for each arc of data. Strategy c was believed to be the best solution for orbital inclination and the one that would be least dependent on ephemeris and station location errors.

The differences between inflight and post-flight results are due primarily to the use of updated timing, AC coefficients, and ephemerides. The improved AC coefficients came from post-flight analysis of the arc from midcourse maneuver to September 15, using tighter doppler data weights. Although DE80 was used for all but the long-arc post-flight analysis, comparison of column B of Table 20 (which solves for the ephemeris) with column C (which estimates only the state) shows that the long-arc cases seemed to compensate adequately for the change in the relative position of Mars with respect to the Earth.

A still unresolved problem is the apparent inertia of the long-arc solutions during the last day. It is believed that the problem lay with a particular operational procedure for adding new data to an existing data set. All the inflight long-arc results from MOI-1 day on relied on this procedure because of time constraints. When post-flight analysis used a supposedly equivalent but more time-consuming technique, the problem disappeared. The questionable procedure will be revised for future missions.

## G. An Evaluation of Mars Orbit Insertion With Radiometric Data

The acceleration of the spacecraft caused by a motor burn is represented in the ODP by

$$\ddot{r} = aU[u(t - T_s) - u(t - T_f)] \quad (2)$$

where

$a$  = magnitude of  $r$

$U$  = unit vector in direction of  $i$

$T_s$  = effective start time of motor

$T_f$  = effective stop time of motor

$t$  = current time

$$u(t-T_0) = \begin{cases} 1, & \text{for } t \geq T \\ 0, & \text{for } t < T \end{cases}$$

The effective stop time  $T_f$  is given by

$$T_f = T_0 + T$$

where  $T$  is the input burn duration. The quantity  $T_f$  can alternatively be computed within the program as the instant at which the accumulated  $|\Delta V|$  of the burn reaches an input value.

The acceleration magnitude  $a$  is given by

$$a = \frac{F(\tau)}{m(\tau)} C = \frac{F_0 + F_1\tau + F_2\tau^2 + F_3\tau^3 + F_4\tau^4}{m_0 - M_0\tau - \frac{M_1\tau^2}{2} - \frac{M_2\tau^3}{3} - \frac{M_3\tau^4}{4}} C \quad (3)$$

where

$F(\tau)$  = magnitude of thrust at time  $t$

$F_0, F_1, F_2, F_3, F_4$  = polynomial coefficients of  $F(\tau)$

$\tau = t - T_0$ , seconds

$m(\tau)$  = spacecraft mass at time  $t$

$m_0$  = spacecraft mass at  $T_0$

$M_0, M_1, M_2, M_3$  = polynomial coefficient of propellant mass flow rate (positive)

$C = 0.001$  for  $F$  in newtons and  $m$  in kilograms

The unit vector  $U$  in the direction of thrust is given by

$$U = \begin{bmatrix} U_x \\ U_y \\ U_z \end{bmatrix} = \begin{bmatrix} \cos \delta \cos \alpha \\ \cos \delta \sin \alpha \\ \sin \delta \end{bmatrix} \quad (4)$$

where  $\alpha, \delta$  = right ascension and declination, respectively, of  $U$ , referred to the mean Earth equator and equinox of 1950.0.

The finite burn model was estimated using doppler data only over the period from MOI-5 days to MOI + 11 h. The data were broken into three spans:

- (1) November 09, 00:00:00 to November 13, 23:00:00, weighted at 0.015 Hz.

- (2) November 13, 23:00:00 to November 14, 01:49:00, weighted at 0.120 Hz.

- (3) November 14, 01:49:00 to November 14, 11:00:00, weighted at 0.010 Hz.

The second data span was weighted loosely because the spacecraft turns and maneuver occurred during this period.

Three basic strategies were examined in solving for the maneuver parameters. The first restricted the  $|\Delta V|$  to 1600.6854 m/s (which was a preliminary result obtained from the Navigation Team's maneuver group) and solved for the  $F_i$ 's,  $\alpha$ , and  $\delta$ . The *a priori* values were obtained by telemetry analysis and are given in Column C of Table 21. The iterated solution appears in Column D. The rather large change in  $F_0$ , as well as the considerable difficulty in fitting the data, suggested that the  $|\Delta V|$  might be wrong. The second and third approaches both allow the ODP to obtain its own best estimate of  $|\Delta V|$  by patching the pre- and post-burn data together.

The second scheme estimates the  $F_i$ 's,  $\alpha$ ,  $\delta$ , and the duration  $T$  without using radiometric data taken during the burn. The results appear in Column E of Table 21.

From the estimated model, the  $|\Delta V|$  imparted to the spacecraft was computed using

$$|\Delta V| = C \int_{T_0}^{T_f} \frac{F_0\tau + T_1\tau + F_2\tau^2 + F_3\tau^3 + F_4\tau^4}{m_0 - M_0\tau - \frac{M_1\tau^2}{2} - \frac{M_2\tau^3}{3} - \frac{M_3\tau^4}{4}} dt \quad (5)$$

giving 1601.852 m/s. The derived  $|\Delta V|$  is remarkably stable regardless of whether the basic trajectory includes or excludes gas leaks. The rather large correction to  $T$  is disconcerting because the propulsion engineers feel they know the instants of motor start and stop to within 60 ms. However, since including the data taken during the burn improves the value of  $T$  while maintaining the same  $|\Delta V|$ , this solution, given in column F, was chosen as the best maneuver estimate. The commanded  $|\Delta V|$  and roll and yaw turns are given in Column B for comparison.

#### H. Determination of Astrodynamics Constants From Interplanetary Data

Inflight and post-flight analyses have yielded new determinations for the GMs of the Earth, Mars, and the Moon.

The solutions for Earth, using four different data spans, appear in Table 22. Data span 1 gives the most reliable solution because it contains unadulterated data closest to Earth, from injection to scan platform unlatch at  $L + 1$  day. Data span 2 (injection to midcourse maneuver), data span 3 (injection to  $L + 25$  days), and data span 4 (unlatch to midcourse maneuver) give results consistent with those from span 1, which further increases confidence in span 1. The new value is compared with determinations from other missions in Ref. 10. Table 23 shows the sensitivity of the solution to various error sources.

New determinations of *GM* Mars came from two data arcs: the first extends from  $MOI - 5$  days to  $MOI - 45$  min and includes both doppler and ranging, whereas the second continues on to  $MOI + 11$  h but contains only doppler. The values obtained (in  $\text{km}^3/\text{s}^2$ ) are  $42828.60 \pm 0.60$  (E001WL) and  $42828.25 \pm 0.55$  (MOI08A), respectively. As was the case with *GM* Earth, a variety of different solution sets and input models were investigated which gave results varying from 42827.98 to 42828.65. The results quoted use the AC subsystem engineers' sporadic leak model with the current best estimate of the continuous leak from Table 12, and the tenth-order Mars harmonic model referred to the updated pole given in Table 4 of the *Satellite Orbit Determination* section. The burn model for the second arc is that of strategy 2 in Table 21.

The *GM* Moon solutions are derived from processing the long data arcs of interplanetary cruise because the monthly revolution of the Earth around the Earth-Moon barycenter impresses a periodic signature on the cruise doppler and ranging data, whose amplitude is a function of the ratio of the Earth and Moon masses.

A number of solutions were examined with different combinations of weights for each data type and different sets of estimated parameters. The standard set of estimated parameters includes the probe state, SP, AC, station locations, and the Earth-Moon mass ratio. An *a priori* uncertainty of 0.0166 was assumed for the mass ratio parameter. The solutions were:

**Case 1.** Doppler only ( $1-\sigma$  doppler noise assumed to be 0.015 Hz) with standard estimated parameter set, giving 81.30068.

**Case 2.** Range only ( $1-\sigma$  range noise assumed to be 100 m) with standard estimated parameter set, giving 81.30067.

**Case 3.** Doppler and range ( $1-\sigma$  doppler and range noise assumed to be 0.015 Hz and 100 m, respectively) with standard estimated parameter set, giving 81.30067.

**Case 4.** Doppler and range weighted the same as Case 3, with standard estimated parameter set plus Mars and Earth-Moon barycenter ephemeris parameters, giving 81.30067.

**Case 5.** Doppler and range ( $1-\sigma$  doppler and range noise assumed to be 0.015 Hz and 50 m, respectively) with the estimated parameter set the same as in Case 4.

All solutions yielded nearly the same mass ratio. Cases 1 and 2 indicate a remarkable agreement on the mass ratio between the two data types. With such good agreement, the relative weight of the two data types becomes less significant. Cases 3 and 4 show that the lunar ephemeris error is probably too small to have an effect on the mass ratio estimate. A possible error source is the periodic variations in the interplanetary medium. Melbourne (Ref. 11) has shown that a 28-day sinusoidal variation of solar flux of 0.1% could produce an error of about 0.001 in the mass ratio, but he also pointed out that it is not likely to be the case. The agreement of the mass ratios computed from the data gathered from several interplanetary spacecraft also does not include this sort of systematic error unless the phase of the flux variation is the same for each mission, which does not seem likely.

## I. Determination of DSS Locations From Interplanetary Data

Four different data arcs have provided station location estimates: (1) Pre-midcourse, from unlatch to midcourse maneuver; (2) post-midcourse, from midcourse maneuver to September 15; (3) pre-encounter, from  $MOI - 5$  days to  $MOI - 45$  min; (4) pre- and post-encounter, from  $MOI - 5$  days to  $MOI + 11$  h. Except for the post-midcourse, which was processed using DE79, all arcs have been fit using DE80. Final Bureau Internationale de l'Heure (BIH) timing and polar motion were used, although no charged-particle calibrations have been applied.

The results of the estimates are shown in Table 24. Both DSS 14 and DSS 62 show 2- to 3-m changes in spin axis near  $MOI$ . Changes of this size are not disconcerting in view of the absence of charged-particle calibrations and the well-known seasonal character of these effects. What is noteworthy is the 7- to 9-m decrease in absolute longi-

tudes throughout the DSN. This effect was seen in flight as well as in post-flight studies of the intermediate arc (October 4 to MOI-45 min). There is currently no explanation for this phenomenon.

#### IV. Station Locations and the Orbit Determination Process

##### A. Introduction

This section is an investigation of the use of deep space station locations (DSSL) by the OD groups of the Navigation Team. The discussion indicates why DSSL are so important for OD by providing a simplified analysis of the diurnal data signature. It then establishes the concept of "true" DSSL determined by post-flight analysis of previous missions and discusses the extent to which these can be employed for inflight OD support. The discussion also shows that the effect of DSSL errors on real-time OD results is a function of tracking data arc length, with short arcs being most error-prone. Finally, it explores the benefits and hazards of estimating these parameters in flight.

##### B. How DSS Locations Are Involved in OD

The current Deep Space Instrumentation Facility (DSIF) radiometric hardware measures range and range rate to better than 15 m and 1 mm/s, respectively. Even with this accuracy, it is remarkable how well the three-dimensional motion of a distant spacecraft can be determined with only a few days' data. The explanation lies with the daily rotation of the Earth and the movement of the tracking station with it. For range rate data, Hamilton and Melbourne have presented a simplified analysis in Ref. 12, which will be briefly described below. Reference 13 and Section II-A-3 of Ref. 14 explain the role of station  $z$  heights in processing ranging data.

The basic parameters involved in the range rate effect are illustrated in Fig. 14, which shows a distant spacecraft being tracked by a station on Earth. The spacecraft position is expressed in terms of geocentric range ( $r$ ), right ascension ( $\alpha$ ), and declination ( $\delta$ ). The Earth-fixed location of the tracking station is given by its distance off the spin axis ( $r_s$ ), longitude ( $\lambda$ ), and distance from the equator ( $z$ ). The range rate measured at the tracking station (Fig. 15) results from the combined motion of the spacecraft and the tracking station, with the station imposing a sinusoidal signature on the observed range rate. Excluding the effect caused by geocentric motion of the probe, the

diurnal signature on range rate data can be approximated by

$$\omega r_s \cos \delta \sin (\omega \text{UTI} + \alpha_0 + \lambda - \alpha) \quad (6)$$

where

$\alpha_0$  = instantaneous right ascension of mean Sun

$\omega$  = mean rotation rate of Earth of date

$\alpha$  and  $\delta$  = instantaneous coordinates of probe

Here, the amplitude and phase of the sinusoid depends not only on the tracking station location but on the spacecraft angles as well. Indeed, uncertainties in  $\delta$  (through  $\cos \delta$ ) are indistinguishable from uncertainties in  $r_s$ . Similarly, uncertainties in  $\lambda$  are indistinguishable from uncertainties in  $\alpha$ . For this reason, uncertainties in the locations of the tracking stations are the principal limitation to determination of spacecraft geocentric angles from single passes of tracking data. Accordingly, when short data arcs are used, station location uncertainties usually prove to be the major error source in determining the orbit of an interplanetary spacecraft. Station location errors of 3 to 7 m can produce orbit estimate errors on the order of 100 to 200 km at typical Earth-Mars encounter distances of  $10^6$  km.

In addition to the major effect of the station location errors, there are other secondary effects in the radiometric measurements which, when unaccounted for, introduce error signatures essentially equivalent to those of station location errors (viz., the ESLEs mentioned in Section II-B-1). In addition to the actual location errors, ESLEs include Earth polar motion and rotation rate variations, as well as tropospheric and ionospheric modeling errors. These errors not only additionally corrupt spacecraft orbit estimates, but they also degrade attempts to recover the actual station location errors from spacecraft tracking data.

##### C. Obtaining "True" Station Locations

There is a set of numbers which indicates the position of each physical DSS with respect to imaginary axes fixed somehow in the Earth. Except for such geophysical processes as earthquakes and continental drift, these DSS locations are absolutely immutable and, at least theoretically, determinable.

Station coordinates can be "absolute," i.e., giving positions with respect to the 1903.0 pole and prime meridian, or "relative," giving positions of one station relative to

another. The latter type of information is most easily obtained because the diurnal rotation of the Earth brings the stations successively into view of the same spacecraft. When the spacecraft is on a reasonably smooth ballistic trajectory, its short-term behavior is quite predictable and provides a very strong common link between the participating stations.

Determination of absolute DSS locations at any given time, even post-flight, when all the available calibrations are in, is a task made difficult by:

- (1) The questionable existence of an "absolute," well defined reference frame against which to measure DSS locations.
- (2) The nature of the attempted tie between the DSS and the reference frame of (1).
- (3) The influence of ESLEs mentioned above. (The media effects also have a strong bearing on relative locations.)

**1. The reference frame.** The question of a well defined reference frame is philosophically the most interesting and perhaps the most difficult to solve. Because of the oceans, it is impossible to determine relative distances between stations on different continents by rod and chain methods. Surveyors have long since resorted to astronomical techniques, hoping that observation of the stars would help them. For their purposes, the frame of reference provided by a star catalog was sufficiently close to inertial to provide the accuracies they hoped to obtain. Even through the early years of the space program, when the star catalogs were replaced by numerically integrated planetary ephemerides, such techniques were feasible; however, as technology progressed, the ability to determine the topocentric range of the probe and the instant of its meridian crossing has improved far beyond the precision and accuracy of any astronomical techniques for measuring the same quantities for celestial objects. For example, in the absence of transmission media effects, a full pass of typical DSN two-way doppler data during cruise or flyby can determine the instant of meridian crossing to  $\pm 2.5$  ms. Obviously, errors exceeding this amount in the star catalogs or in planetary ephemerides would have some influence on the derived station locations. It remains to be seen how such errors would manifest themselves.

During a flyby, because of the very high planetocentric acceleration on the probe, the law of universal gravitation allows determination of the distance of closest approach to within 1 or 2 km, irrespective of ephemeris errors, and

hence observation of the instant of the planet's meridian crossing to effectively the same precision ( $\pm 2.5$  ms or  $0''04$ ). The hour angle  $H$  of the probe is exactly zero at transit. Further, it depends on the true sidereal time  $\theta$ , the east longitude of the station  $\lambda$  relative to the true pole (corrected for polar motion), and the true right ascension of the probe  $\alpha$  (which is tied to the planet's  $\alpha$  to within  $0''04$ ), according to

$$H = (\theta + \lambda) - \alpha \quad (7)$$

Thus, errors in either  $\theta$  or  $\alpha$  could affect the determination of  $\lambda$ . If these errors were constant biases over the years, then, except for media effects, the longitudes obtained, although in error, would be the same for different flybys. If the errors were not constant, the derived longitudes would change from mission to mission.

There is mounting evidence that the star catalogs do not represent a truly inertial system. When the fundamental catalogs now in use were created, the designers adjusted the observed centennial variations for the drift between the equinoxes determined at different epochs. This adjustment was intended to remove the effects of precession from the centennial variations, but, in the process, an error given by the algebraic difference of the errors in the individual equinox determinations, divided by the time between them, was introduced. This fictitious rate has no basis in reality but nevertheless affects all the derived star coordinates. The fourth Fundamental Katalog (FK4), for example, to which both UT1 and the planetary ephemerides are referred, is believed to be drifting with respect to a truly inertial system by about  $1''$  century.

Because the ODP computes the sidereal time  $\theta$ , using the UT1 provided by BIH, it is obvious that the angular position of the Earth's prime meridian in space is not represented with respect to an inertial frame of reference.

This would not be a concern if the planetary ephemerides could somehow be adjusted to absorb the fictitious rotation. However, the advent of precision planetary ranging, better planetary masses from spacecraft flybys, and numerically integrated planetary ephemerides, based strictly on relativistic gravitational theories and fit to both optical and radio data, is making such distortions ever less possible. Whether the current best JPL ephemerides themselves define an inertial reference frame is open to question, but it is also a moot point because, until the FK4 equinox drift can be rectified, the derived station longitudes will still be drifting at approximately 0.3 m/year.

2. **Tying the probe to the reference frame.** Assuming there were a well defined inertial coordinate system to which time and the planetary ephemeris could be referred, there is still the problem of determining the spacecraft location in this system. Planetary encounters, as mentioned earlier, can give the probe's position with respect to the target planet very accurately. The strength depends on the gravitational bending of the trajectory, which, of course, continues after the instant of closest approach. Unadulterated data of this sort are available for the Mariner 4 spacecraft, which encountered Mars on July 15, 1965, and for Mariner 5, which flew by Venus on October 19, 1967. Mariner 2, which flew past Venus on December 14, 1962, had serious gas leaks and was tracked using L-band, which is more susceptible to charged-particle effects. Mariners 6 and 7, which encountered Mars on July 31 and August 5, 1969, respectively, both had gas venting at encounter minus 45 min (E-45 min) to cool an experiment. In addition, Mariner 7 had an unexplained "happening" at E-5 days, which caused perceptible nongravitational accelerations until E-1 day. Mariner 9 started the MOI burn shortly before encounter. Obviously, for all but Mariners 4 and 5, there are limitations to the strength of the tie to the target planet, but there are continuing efforts underway to better model the various disturbances and thereby increase the samples.

The other customary geometry for determining station locations depends on the low sensitivity of Eq. (6) to declination, when the declination is near 0 deg. Various spacecraft have passed through the 0-deg declination region (some more than once) and have provided data used extensively for the determination of  $r_s$ . Efforts have centered on the Mariner 5 0-deg declination crossings in August and November of 1967, but the appropriate arcs from the various Pioneer missions will eventually be added to the selection.

The classical approach for both of these situations is the use of a short arc of data (5-10 days for a flyby, 6-8 weeks for a 0-deg crossing) centered around, or leading up to, in the case of Mariners 2, 6, 7, and 9, the critical event. The short arc of data limits the accumulated effect of unmodeled forces in the trajectory and minimizes the number of unmodeled random effects one must contend with. More recently there has been some interest in the use of longer arcs of data, linking Earth and the target planet for example, in the hope that this might diminish the effects of certain ESLEs for  $r_s$ , and allow gravitational bending by the Sun, in conjunction with the ephemeris of the Earth, to help establish the probe's right ascension and thus the longitudes of the stations.

3. **The influence of ESLEs.** Usually after a mission is over, time is available to carefully reexamine the calibrations and support information produced in near-real time. Additional data are often taken after the mission, which puts earlier results in a different light. This happens with the timing and polar motion data, the planetary ephemeris, and the media calibrations. In fact, as often as there are improvements in the reduction procedures, revised estimates of these will be obtained for long defunct spacecraft, providing the raw data are still available. The frequency of the updates is a sufficient disclaimer about the "absolute" accuracy of any of the calibrations.

The BIH "final" timing and polar motion data are published approximately 6 months after the fact. The data represent the smoothed results from many observations, but they are known to be biased from the results of other agencies producing timing and polar motion. Because these other agencies differ among themselves, there is currently no way of telling which is correct.

The planetary ephemeris is subject to change as more data are added. Better topography for the planets will mean improved radii and, possibly, different orbits, when radar data are employed. Incorporation of Mariner 9 orbital phase data will provide geocentric ranging to the Mars center of gravity good to approximately 50 m, independent of topography, over nearly a one-year period.

The media calibration data are also nondefinitive. The models used in analysis of the raw data are state of the art and are under continuing investigation. The final results must be represented by a smoothed curve fit to noisy data because the specification of all the possible causative effects is too complex.

For the above reasons, it will always be impossible to obtain the final "definitive, absolute locations," although the uncertainties may reasonably be expected to decrease in time.

4. **Definition of the current best set of deep space station locations.** The locations published as "current best" are obtained by combinations of results from the various missions processed. The amount of data included the ephemeris and TSACs used, and the combination procedure employed, change from time to time. The production of LS35, the set recommended for Mariner 9, is described in the second section of Ref. 1.

By modifying the combination procedure, including corrected charged-particle calibrations, and incorporating all the results in a mathematically simpler way, with no attempt at applying engineering judgment, a new set, LS37, also described in the above article, has been derived from post-flight analysis. This set uses the same ephemeris, timing, and neutral particles at LS35, and therefore suffers from their shortcomings. Otherwise, it represents the best software, calibration, and combination techniques.

#### D. Locations Recommended for Real-Time Use

The current best estimate described above is the kind of information produced in advance of a mission requiring critical station location support. However, in practice, these locations could not be used directly in the OD process because some of the calibrations used for post-flight analysis are not available for all the stations in near real time. Charged-particle information, especially when obtained from Faraday rotation devices, has been routinely mailed to the SFOF. (From Australia, this can take 2-4 weeks.) If "absolute" station locations, which were determined using charged-particle calibrations, were used when processing data for which no such calibrations were available, significant signatures would develop that might have a deleterious effect on the OD. In such a situation, there is the choice of (1) providing calibrations based on a model for the charged-particle behavior, or (2) applying appropriate ESLEs to the absolute locations to account for the predicted effect. The selection is usually made on the basis of availability.

For Mariner 9 encounter support, it was decided to use the Mariner 6 uncalibrated locations for real-time encounter support because of

- (1) The absence of charged-particle calibrations for the overseas data and the rather spotty coverage at Goldstone.
- (2) The absence of appropriate ESLEs to account for these effects for Mariner 9.
- (3) The excellent prediction (post-flight) of Mariner 6 encounter afforded by the uncalibrated Mariner 6 station locations used for LS35.

#### E. Sensitivity to Station Locations or ESLEs as a Function of Data Arc

1. **Sensitivity of long arcs to ESLEs.** It has been determined from covariance studies and actual data processing that the probe state becomes ever less sensitive to ESLEs

as the data arc lengthens. For example, Ref. 15 shows that, on a representative Mariner Mars 1971 trajectory, with two-way doppler data from two stations (DSSs 12 and 41) over the period MOI-5 days to MOI-6 h, a 3-m error in  $r$ , and a 5-m error in  $\lambda$  would cause an 85-km error in the predicted  $B \cdot T$  and 133 km in  $B \cdot R$ . When the data arc starts at  $T + 5$  days (and the arc is 160 days long), the same errors cause less than a 2-km error in either  $B \cdot R$  or  $B \cdot T$ .

There has long been the feeling that the longer arcs somehow "average" the ESLE effects, and allow decent solutions despite them. This phenomenon was studied (Ref. 1, Section 6) for tropospheric refraction calibrations by comparing the solved-for spacecraft state using slightly different refraction models. The results clearly indicate the decreasing error with increasing data arc. Similar investigations are currently underway for charged-particle and timing effects. What is really needed, however, is a technique to show why this should happen.

The so-called "C function" approach currently being applied to this and a number of other data-selection-effect problems at JPL may provide new insight into the reason. The concept is basically quite simple. The classical least-squares estimation formula is

$$dx = (A^T W A)^{-1} A^T W (o - c) = C (o - c) \quad (8)$$

where

$x$  = the vector of  $n$  solved-for parameters

$c$  = an  $m$  vector of computed values of the actual data, whose observed values are  $o$

$W$  = an  $m \times m$  weighting matrix

$A$  = the  $m \times n$  matrix of partial derivatives  $\partial c / \partial x$

The various rows of  $C$  are called the C functions, each of which indicates the sensitivity of that particular parameter to the individual data points. The functions obviously depend on the number, distribution, and weighting of the data, as well as on the particular parameter set being estimated. Because the total adjustment to a given parameter value is given by the dot product of its C function with the residual vector,  $o - c$ , the more the residual signatures resemble the function, the larger the parameter change.

Although the technique has not yet been applied to Mariner 9 data, there are plans to do so. Hopefully, it will then be possible to better understand the sensitivity of

solutions to data arc length, parameter sets, and data weighting, and thereby to develop better OD strategies for future missions.

**2. Status of short arcs.** In view of the decreased sensitivity of long arcs to ESLEs, it is reasonable to ask why ESLEs are of so much concern, and why not simply process long arcs of data and reduce the TSAC effort. From the mission operations and OD standpoint, there are two reasons:

- (1) More tracking support is required if a long arc is carefully monitored than if a short arc is intensely covered.
- (2) Projects often require spacecraft events close to encounter which militate against long-arc fits. The Viking Project, for example, wishes to make a final midcourse maneuver as late as MOI - 10 days.

#### **F. Estimating Station Locations in Flight**

Total dependence on pre-computed "absolute" station locations to fly a mission may justifiably create an uneasy feeling. As mentioned before, the "absolute" locations were obtained with the full benefit of the most and best media calibrations available. Such plentiful data are seldom available in real time so that, even if the "absolute" station locations were the true ones, they would not be compatible with the data because there would be no way to remove the media effects.

The timing and polar motion calibrations are obtained by fitting polynomials to raw (and usually noisy) data. As each new day's data are introduced, the computed polynomials change, with reverberations that may extend as far back as three to four weeks in the previous tracking data. The end of the data span (i.e., today, when daily updates are received) has more than likely the least well-known calibrations of any time up to the present. With a short arc, near encounter but not close enough to sense the planet, bad timing maps directly into the derived right ascension of the probe.

The planetary ephemeris in use at the time was probably the basis for the "absolute" station locations, which makes the station location errors highly correlated with the ephemeris errors. In particular, station locations are dependent upon the characteristics of the given ephemeris for Venus, the barycenter, and Mars at earlier epochs than the one now in question. Whether the possible earlier errors will map similarly to the present time is unknown.

In the presence of all these uncertainties, only one thing is sure: if, in fact, the true station locations were available but one of these other errors were present, a signature would arise in the data which, if the choice of data arc and solution parameter set were unlucky, would at a critical time be disastrously absorbed in the state. It would be better, then, to use the incorrect station location that compensated for this effect. This is the rationale for estimating station locations in flight. Such reasoning was used during the 1969 and Mars missions, not so much as the approved strategy but as a means to detect the other errors. Other means were sought to avoid the problems caused by such errors, if they were present, and solutions that included station locations were to be used only as a last resort. The hesitation comes because moving station locations to compensate for other errors can possibly create more problems than it solves. Station locations will pick up timing, polar motion, ephemeris, and neutral and charged-particle effects; but they also can behave in a most peculiar manner when unmodeled gas leaks are present. For a single spacecraft, moving station locations may be justifiable, but for a dual-spacecraft mission like Mariner Mars 1969, it gives absolutely no indication of what the true errors actually were, and there is no recourse but to do the same for the second spacecraft.

It might be believed that the types of ESLEs acting during a mission could be understood by solving for station locations in an academic fashion during cruise, when no harm can result. A study of this belief was made during the 1971 mission, both on the Mariner 9 data and on data from previous missions. For Mariner 9, it was necessary to wait until after encounter to grade the experiment, but with Mariners 4, 5, and 6, the long-arc cruise results were compared directly with the short-arc encounter solutions used in the generation of LS35. Only Mariner 9 gave cruise solutions comparable to those from post-flight encounter analysis. Continued research on this problem is needed.

#### **V. Attitude Control Leaks**

##### **A. Introduction**

This section discusses the gas-leak problem which occurred during the interplanetary portion of the flight operations. The gas leaks occasioned the use of special pre-flight strategies and the design of new ones on-line. They also warranted considerable post-flight analysis. Three separate approaches were used in the post-flight analysis. The first involves the determination of leak mag-

nitudes from engineering telemetry to include this information in the trajectory acceleration model. The second approach attempts to use sequential filtering techniques to overcome the deleterious effects of the leaks. The third approach differences two- from three-way doppler taken simultaneously at different stations, thereby eliminating the unmodeled accelerations common to both data types. Continued development of all of these approaches will hopefully give independent and, therefore, redundant means to deal with this problem on future missions. Because the real-time response to this problem was discussed in Sections III-D and III-E, the discussion here concentrates on the post-flight developments in these three areas.

## B. Determination of Accelerations Induced by Gas Leaks From Attitude Control Telemetry

1. Background. The Mariner 9 spacecraft was attitude-stabilized by a system which consists of Sun and Canopus sensors and coupled pitch, roll, and yaw gas jets. The pitch and yaw jets were aligned perpendicular to the plane of the solar panels, but the roll jets were in the plane and canted by 21 deg to keep the jet plumes from impinging on the panels (see Fig. 16).

In September 1971, the roll jet on the  $-x$ -axis began to develop occasional leaks. These leaks are believed to have been caused by particles from an eroding valve stem which were caught in the valve during the closing of a normal firing. The valve remained ajar until the spacecraft fired that jet again, and the particles were then presumably blown away. The jet would fire when the acceleration from the leak diminished sufficiently (because of crushing of the particle) for the spacecraft to swing to that side of the deadband, or when ground action was taken to switch the spacecraft from celestial to inertial reference. The leaks produced spacecraft accelerations with magnitudes above  $10^{-11}$  km/s<sup>2</sup>.

The leak magnitudes and duration times were calculated from telemetered data of the time history of the limit cycle position error signals from the Sun and Canopus sensors. Given the moments of inertia of the spacecraft, the sensor data can be translated into the rotational time history. The fact that the center of mass of the spacecraft did not lie in the plane of the solar panels meant that gas leaks from one roll jet would produce torques about all three axes. Hence, when the roll jet leaked, slight rotations also occurred in pitch and yaw, thus eliminating the ambiguity in the determination of the leaking jet and enabling computation of the resulting acceleration direc-

tions. Because the roll jets were canted 21 deg, components of acceleration occurred in both the pitch and yaw directions.

2. Derivation of thrust magnitudes. Figure 16 will facilitate understanding how leak thrust magnitudes are derived from the telemetry data. The parts labeled a, b, c, and d are the four roll-axis attitude control thrusters. The arrows at the center of mass indicate the torques resulting from leaks in the jet labeled a. The arrows at the jet indicate the components of the translative force. The distance  $O$  is the offset of the center of mass from the center of the roll-axis jet couple. The distance  $m$  is the moment arm for the torque around the roll axis. Table 25 shows what torques would be caused about each axis by a leak in any of the jets. A right-hand coordinate system is assumed, and torques which cause a counterclockwise (CCW) rotation of the spacecraft as viewed by an observer at the "end" of a positive axis are defined to be positive.

Attitude control was maintained by a negative feedback system whose inputs were voltage signals derived from sensors directed at the Sun and at the star Canopus. The output of these sensors was proportional to the angular separation between the null point of the sensor and the reference celestial object. The output was sampled at approximately 4.2-s intervals, digitally encoded, and returned to Earth as part of the engineering telemetry.

Figure 17 is a plot of the sensor telemetry data for each of the three axes over a typical time span of 3 h. The ordinate is raw telemetry units or data numbers (DN), which are equivalent to approximately 0.27 mrad/unit for the pitch and yaw axes and 0.52 mrad/unit for roll. The scales cover about 0.5 deg for each axis.

To facilitate the analysis, so that preliminary reductions could be performed and the results evaluated, the following assumptions were made about the spacecraft motion:

- (1) The spacecraft acceleration around any axis of rotation could be treated as a constant between two successive jet firings. (This does not necessarily mean two successive firings from the same jet.) Thus, the motion between firings could be represented by a quadratic of the form:

$$\Omega = \Omega_0 + \omega t + \frac{\dot{\omega} t^2}{2} \quad (9)$$

where

$\Omega$  = angular position of spacecraft at time  $T$

$\Omega_0$  = angular position of spacecraft at earlier firing  $T_0$

$\omega$  = angular velocity of spacecraft

$t = T - T_0$

$\dot{\omega}$  = angular acceleration of spacecraft

Figure 17 shows the quadratic fit to each of the data arcs as a solid line.

This assumption appears to be reasonable inasmuch as the leaks typically lasted for several hours, whereas the duration between firings was on the order of a few minutes.

- (2) Initially, the torques for any roll axis leak were approximated by the expression

$$\tau_i = \dot{\omega}_i I_{ii} \quad (10)$$

where

$\tau_i$  = torque about  $i$ th axis

$\dot{\omega}$  = angular acceleration about  $i$ th axis

$I_{ii}$  = diagonal term of inertia matrix corresponding to  $i$ th axis

This led to the equations

$$\left. \begin{aligned} \dot{\omega}_x I_{xx} &= \pm T m \cos 21 \text{ deg} \\ \dot{\omega}_y I_{yy} &= \pm T O \sin 21 \text{ deg} \\ \dot{\omega}_z I_{zz} &= \pm T O \cos 21 \text{ deg} \end{aligned} \right\} \quad (11)$$

where

$T$  = thrust due to leak

$\dot{\omega}_x, \dot{\omega}_y, \dot{\omega}_z$  = angular accelerations in roll, yaw, and pitch, respectively

$m$  = moment arm of roll jet couple

$O$  = offset of center of mass from center of roll jet couple

Inversion of the roll-axis equation gave

$$T = \frac{\dot{\omega}_z I_{zz}}{m \cos 21 \text{ deg}} \quad (12)$$

for the thrust magnitude. Examination of the sigma of  $\omega_y$  and  $\omega_x$  in conjunction with Table 25 would indicate which jet was leaking and hence give the thrust direction.

The rigorous equations for the rotational dynamics are

$$\left. \begin{aligned} \tau_x &= I_{xx} \dot{\omega}_x - \omega_y \omega_z (I_{yy} - I_{zz}) \\ \tau_y &= I_{yy} \dot{\omega}_y - \omega_z \omega_x (I_{zz} - I_{xx}) \\ \tau_z &= I_{zz} \dot{\omega}_z - \omega_x \omega_y (I_{xx} - I_{yy}) \end{aligned} \right\} \quad (13)$$

which, because of the nonequality of the diagonal terms of the inertia matrix, will not agree with Eq. (10) for each arc. The values of  $\tau$  from Eq. (10) would be expected to fluctuate by some  $\pm \Delta\tau$  around the true value. Fortunately, the average  $\tau$  appears to be generally quite close to the true  $\tau$ , so that the results to date are credible.

**3. Fitting the telemetry data.** The process used to break the telemetry data into discrete arcs and to compute the angular acceleration over each arc was as follows: An arbitrary time span of 63 s (15 data points) was least-squares fit with a quadratic polynomial. This polynomial was then extrapolated forward until an arbitrary number of data points, 15, differed by more than a specified tolerance from the extrapolated curve. Any new points were then added, and the curve refit until a stage was reached where 15 consecutive points lay outside of tolerance. The arc was terminated at this point, and the process restarted.

Figure 18 is a plot of the resulting angular accelerations from a sample period. The center bar in each box is the computed acceleration. The top and bottom of the box are the computed acceleration  $\pm 1 \sigma$ , where the sigmas are computed from the least-squares fit. The units of the plots are DN/s<sup>2</sup>, and the plots are on a folded log scale showing the values from  $+10^{-6}$  to  $+10^{-4}$  and  $-10^{-6}$  to  $-10^{-4}$ , with values from  $-10^{-6}$  to  $+10^{-6}$  being shown as zero.

As may be seen, the scatter between consecutive acceleration values tends to be larger than the formal  $1-\sigma$  statistics. This is believed to be caused by cross-coupling between axes of the torque from attitude control jet firings. For example, in the fourth arc of pitch axis data

in Fig. 17, there is an apparent discontinuity at a time which is coincident with a jet firing in the roll axis. Here, the change in angular velocity in the pitch axis is large enough that the filter used was able to separate it. For slightly smaller changes, the filter is unable to discriminate the angular velocity change as a separate delta and averages it into the acceleration. A more sophisticated algorithm is being developed, which causes a firing on any axis to terminate the data arcs on both other axes.

**4. Locating and quantifying leaks.** Figure 19 shows a plot similar to Fig. 18 but covering the period shown in Fig. 17. The acceleration in the roll axis and the coupling into the other two axes can be seen. The leak model presented in Table 26 was prepared by scanning plots like these for the two months prior to MOI and recording the start and stop times and acceleration magnitudes of periods exhibiting a similar signature. Table 26 is represented graphically in Fig. 20.

The spacecraft accelerations  $\Delta AC_x$  and  $\Delta AC_y$  of Section III-D were obtained by

$$\begin{aligned}\Delta AC_x &= \frac{T \sin 21 \text{ deg} \times 10^3}{M} \\ \Delta AC_y &= \frac{T \cos 21 \text{ deg} \times 10^3}{M}\end{aligned}\quad (14)$$

where

$M$  = spacecraft mass, 995 kg

$T$  = thrust from leaking jet, given by Eq. (12)

Here

$m = 3.05 \text{ m}$ ,  $I_{zz} = 553 \text{ kg}\cdot\text{m}^2$ , and  $\dot{\omega}_z = 2ac$

where

$a$  = quadratic term from data fits

$c = (0.0298 \text{ deg/DN}) (0.017 \text{ rad/deg})$

**5. Discussion.** The basic analytical concepts described above are not particularly new. They are discussed in Section IV-D of Part 1 of Ref. 16 and have received additional study in Ref. 17. The Mariner 9 analysis, however, has developed some basic software which can be used on future missions to provide near-real-time determinations of thrust magnitudes. Such programs will relieve the drudgery of visual inspection and manual computation of

these accelerations, which required a significant use of manpower for Mariner Mars 1971. Coordination of these efforts with the attitude control personnel will enable routine determinations of spacecraft moments of inertia from flight data.

Continued study is necessary to determine the uncertainties associated with these estimates and to obtain reliable values for the long-term "constant" leak mentioned earlier.

### C. Use of Advanced Filtering Techniques

**1. Background.** The OD filters that have been used in navigating past interplanetary missions are fundamentally equivalent to the well-known least-squares methods developed by Gauss more than 100 years ago. These traditional methods have been retained despite the considerable theoretical and practical filter developments of the past decade. Theoretically antiquated, the least-squares filter has nevertheless proven to be a simple yet accurate means for providing interplanetary orbit estimates, largely because of the accuracy of the dynamic models of interplanetary ballistic spacecraft motion. However, the increased accuracy requirements for radio OD and the availability of progressively more accurate radio measurements are making even the current models inadequate. The principal errors arise from unmodeled small forces caused by spacecraft attitude control and propulsion system leaks, and mismodeled solar radiation pressure. The direct effect of these unaccounted-for forces on the computed trajectory is usually small, but they can severely limit the capability to solve for the orbit using Earth-based radio measurements. Fortunately, the advanced filtering methods developed by Kalman and others are well suited for these dynamic systems influenced by dynamic model errors.

As stated in Section IV-B, accurate OD estimates rely on the stability of the range rate and/or range measurements over a 12-h period. For example, a 3-m error in a tracking station coordinate produces a daily oscillating range change as large as 6 m. Similar range changes can arise over 12 h because of the accumulated effect of unmodeled spacecraft accelerations as small as  $6 \times 10^{-12} \text{ km/s}^2$ .

Because of the random nature of the spacecraft acceleration errors, the advanced filtering techniques can, to some degree, distinguish their effect from the station location errors which so strongly affect the orbit estimates.

2. **OD filter algorithms (Ref. 18).** Consider a spacecraft with cartesian position and velocity vectors  $\mathbf{X}$ ,  $\mathbf{V}$ , respectively. The spacecraft motion is represented in terms of a system of differential equations:

$$\left. \begin{aligned} \dot{\mathbf{X}} &= \mathbf{V} \\ \dot{\mathbf{V}} &= \mathbf{G}(\mathbf{X}) + \mathbf{u}(t) \quad t > t_0 \\ \mathbf{X}(t_0) &= \mathbf{X}_0 \\ \mathbf{V}(t_0) &= \mathbf{V}_0 \end{aligned} \right\} \quad (15)$$

where  $\mathbf{G}(\mathbf{X})$  represents gravitational accelerations and  $\mathbf{u}(t)$  represents spacecraft acceleration errors. The spacecraft motion is observed via data equations:

$$\mathbf{Z}(t_i) = \mathbf{F}(\mathbf{X}, \mathbf{V}, t_i) + \boldsymbol{\epsilon}(t_i) \quad \text{for } i = 1, \dots, N \quad (16)$$

where  $\mathbf{F}(\mathbf{X}, \mathbf{V}, t)$  expresses observables like doppler and range in terms of the spacecraft state. The  $\boldsymbol{\epsilon}(t)$  represents data errors.

Analytical procedures for data filtering (i.e., estimating  $\mathbf{X}$  and  $\mathbf{V}$  from the data sequence in Eq. 16) usually rely on linearized forms of Eqs. (15) and (16). These involve the linearized state  $\mathbf{x}(t)$  given by

$$\mathbf{x}(t) = \begin{pmatrix} \mathbf{X}(t) - \mathbf{X}^*(t) \\ \mathbf{V}(t) - \mathbf{V}^*(t) \end{pmatrix} \quad (17)$$

and the observables  $\mathbf{z} = (\mathbf{Z} - \mathbf{Z}^*)$ . Here  $\mathbf{X}^*$  and  $\mathbf{V}^*$  are nominal spacecraft position and velocity functions, chosen (by iteration procedures) to ensure that the following relationships are approximated to a sufficient degree:

$$\mathbf{x}(t) = \boldsymbol{\Phi}(t, t_0)\mathbf{x}_0 + \int_{t_0}^t \boldsymbol{\Phi}(t, s)\mathbf{u}(s) ds \quad (18)$$

$$\mathbf{z}(t_i) = \mathbf{A}(t_i, t_0)\mathbf{x}_0 + \int_{t_0}^{t_i} \mathbf{A}(t_i, s)\mathbf{u}(s) ds + \boldsymbol{\epsilon}(t_i) \quad (19)$$

Here

$$\mathbf{A}(t, s) = \frac{\partial \mathbf{F}(t)}{\partial (\mathbf{X}, \mathbf{V})} \boldsymbol{\Phi}(t, s) \quad (20)$$

where  $\boldsymbol{\Phi}(t, s)$  is the state transition matrix for  $\mathbf{x}$  obtained from a variational analysis of Eq. (15) for the nominal trajectory  $\mathbf{X}^*$  and  $\mathbf{V}^*$ .

The problem in orbit determination is to estimate  $\mathbf{x}(t)$ , given  $\mathbf{z}(t_i)$ , for  $t_i < t$ . If  $\mathbf{u}(t) = 0$ , or can be represented in terms of a limited number of parameters, then estimating  $\mathbf{x}(t)$  reduces to estimating  $\mathbf{x}_0$  and the  $\mathbf{u}$ -parameters, i.e., a set of fixed quantities. The problem can be solved with conventional least-squares or "batch" filtering algorithms. However, if  $\mathbf{u}(t)$  is too complex in structure to permit representation by a limited set of parameters, an alternate approach is required.

It is assumed, then, that  $\mathbf{u}(t)$  can be represented as a piecewise constant function; i.e. for a sequence of break times  $T_1, \dots, T_m$ ,  $\mathbf{u}(t)$  satisfies

$$\mathbf{u}(t) = \mathbf{u}_k \quad \text{if } T_k < t \leq T_{k+1}, \quad k = 1, \dots, M \quad (21)$$

where  $\mathbf{u}_k$  ( $k = 1, \dots, M$ ) is a sequence of constant vectors. The linearized system can then be recast into a sequential form as follows:

$$\mathbf{x}_k = \mathbf{x}(T_k) \quad (22)$$

and

$$\begin{pmatrix} \mathbf{z}(t_{k_1}) \\ \mathbf{z}(t_{k_2}) \\ \vdots \end{pmatrix} \quad (23)$$

where

$$T_k < t_{k_1} < t_{k_2} \dots T_{k+1}$$

Then

$$\mathbf{x}_{k+1} = \boldsymbol{\Phi}(T_{k+1}, T_k)\mathbf{x}_k + \boldsymbol{\Gamma}(T_{k+1}, T_k)\mathbf{u}_k \quad (24)$$

where

$$\boldsymbol{\Gamma}(T_{k+1}, T_k) = \int_{T_k}^{T_{k+1}} \boldsymbol{\Phi}(T_{k+1}, s) ds \quad (25)$$

In addition

$$\mathbf{z}_k = \mathbf{A}_k\mathbf{x}_k + \mathbf{B}_k\mathbf{u}_k + \boldsymbol{\epsilon}_k \quad (26)$$

where

$$\begin{pmatrix} A_k = \\ A(t_{k_1}, T_k) \\ A(t_{k_2}, T_k) \\ \vdots \end{pmatrix} \quad (27)$$

and

$$\begin{pmatrix} B_k = \\ \int_{T_k}^{t_{k_1}} A(t_{k_1}, s) ds \\ \int_{T_k}^{t_{k_2}} A(t_{k_2}, s) ds \\ \vdots \end{pmatrix} \quad (28)$$

and

$$\begin{pmatrix} \epsilon_k = \\ \epsilon(t_{k_1}) \\ \epsilon(t_{k_2}) \\ \vdots \end{pmatrix} \quad (29)$$

The above system of equations is referred to as the batch sequential filter model. The dynamical systems associated with OD are, typically, slowly varying with respect to data rate, which means that the batches can contain many data points. This is the prime motivation for the batch sequential form: allowing improved filter models without sustaining the decrease in data-processing efficiency associated with a "point sequential" model, for which each batch break time is an observation time.

Algorithms for constructing an estimate of  $x_k$ , given  $z_j$  for  $j = 1, \dots, k$ , usually require specification of *a priori* quantities:

- (1) Initial state *a priori*:  
 $E[x_1, x_1^T]$
- (2) Data noise *a priori*:  
 $E[\epsilon_k \epsilon_k^T], k = 1, \dots, M$
- (3) Acceleration error (process noise) *a priori*:  
 $E[u_k u_k^T], k = 1, \dots, M$

These quantities, along with the batch structure  $T_1, \dots, T_M$ , can be considered as the design parameters for the sequential filter. Additionally, there exist several options

for treating the acceleration error sequence  $u_k$ . In the following application, the  $u_k$ 's are not directly estimated but are accounted for in the mapping equation (Eq. 24).

**3. Data used in the filter evaluation.** The data span used in the filter evaluation was the intermediate arc mentioned in Section III-E, which began at 06 h UTC on October 4, 1971, and continued to MOI-6 h.

Two sets of station locations were used. Set 1 was LS36 (see Section IV-D). Set 2 was obtained by post-flight processing of the last seven days of the Mariner 9 cruise data. The primary difference between the values of the two sets is the 7-m longitude difference mentioned in Section III-I.

Solutions were obtained by both including and excluding the leak acceleration model of Table 26 in the spacecraft equations of motion.

**4. Batch filter results.** Figure 21 illustrates the history of batch processed estimates of  $B \cdot \hat{T}$  and  $B \cdot \hat{R}$  as a function of the time of the last data point processed (in days past October 4). The last solution, for day 41, includes data to November 13, 18 h. Because station location Set 1 was used in the observable model and no acceleration model was included in the equations of motion, this figure represents a conservative, realistic solution history.

Most of the movement of the solution, as more data are included in the processing, is in the  $B \cdot \hat{R}$  direction. The lack of orbit bending perpendicular to the ecliptic plane makes the solution for  $B \cdot \hat{R}$  prone to station location and acceleration errors, with sensitivities that fluctuate in magnitude as data are added to the span. This large sensitivity is also illustrated by Fig. 22, in which the B-plane parameters of the batch solution at November 6, 06 h, are compared to the current best estimate. A 1- $\sigma$  dispersion ellipse for each value is also presented. The size of the dispersion ellipse at November 6 is due primarily to the ephemeris-error-associated station location uncertainties of 7 m in  $\lambda$  and 3 m in  $r$ . The encounter solution ellipse (data to MOI-45 min) is due primarily to Mars ephemeris uncertainties.

Because the salient solution behavior obviously lies in the  $B \cdot \hat{R}$  direction, the remaining solution time histories presented will illustrate that coordinate only. Figure 23 gives the  $B \cdot \hat{R}$  solutions as a function of the time of the last processed data point using station location Set 1, with and

without the acceleration model ( $\Delta AC$ ) of Table 26. When the first leak of this data set occurs on October 25, the solutions separate, the solution without the  $\Delta AC$  model tends toward a larger  $B \cdot \hat{R}$  error, while the solution containing the  $\Delta AC$  model improves and remains more accurate for the duration of the approach.

Figure 24 illustrates a similar solution history for station location Set 2. The solutions are shifted from the Set 1 solutions in the  $-B \cdot \hat{R}$  direction by approximately 200 km, which decreases the total error, and supports the conclusion that the values of the station locations determined for Mariner 9 (Set 2) are naturally more consistent with the Mars ephemeris in 1971 than the Mariner 6 (Set 1) values. Again with Set 2, as with Set 1, inclusion of the  $\Delta AC$  model determined by the engineering data results in a more accurate solution after the start of the gas leaks.

The batch solutions all have a characteristic sensitivity to the values of the station locations and of the random accelerations. Station location differences between Set 1 and Set 2 (7 m in  $\lambda$ , and 3 m in  $r_s$ ) map to a 200-km difference in  $B \cdot \hat{R}$  for data taken to November 6. The  $\Delta AC$ -in,  $\Delta AC$ -out difference in the equations of motion results in a  $B \cdot \hat{R}$  change of more than 150 km with either station location set. A batch solution with the  $\Delta AC$  included and using Set 2 naturally is more accurate than the other solutions. However, the rapid solution improvement shortly after inclusion of the data in the vicinity of the first gas leak (October 25) is not predictable from the sensitivity analysis performed to date. The time history of perturbations in the solution of  $B \cdot \hat{R}$  because of  $+7\text{-m } \lambda$  and  $+3\text{-m } r_s$  errors in all of the tracking stations is given in Fig. 25. Although the drop in sensitivity to spin axis on October 16 can explain the rapid solution change in Fig. 21 on or around October 16, no such sensitivity change is evident in Fig. 25 near October 25. Thus, either the estimate is strongly sensitive to some model parameter other than the station location, or the value for the leak magnitude is strongly overmodeled. This problem has not yet been resolved and is currently under study.

**5. Sequential filter results.** The sequential filter used for comparison processes successive batches 18 h in duration. While processing each batch of data, the constraints imposed on the state solution by the data in previous batches are loosened by the addition of instantaneous "process noise" on the velocities at the beginning of the batch (Section V-B). The magnitude of this degrading  $\Delta V$  is determined by integrating the values of an assumed

constant acceleration over the 18-h duration of the previous batch. Three magnitudes of assumed accelerations were considered in this study:  $10^{-12}$  km/s<sup>2</sup>,  $10^{-11}$  km/s<sup>2</sup>, and  $10^{-10}$  km/s<sup>2</sup>. The values of instantaneous process noise are computed on the basis of these acceleration levels.

Figure 26 presents the  $B \cdot \hat{R}$  solution time history for the sequential filter constructed with  $\Delta V$  process noise corresponding to an acceleration error of  $10^{-12}$  km/s<sup>2</sup>. Station location Set 1 is employed in the observable model, and curves for  $\Delta AC$ -in and  $\Delta AC$ -out are shown. Figure 27 illustrates the same sequential filter results for station location Set 2.

The differences between the  $\Delta AC$ -in and  $\Delta AC$ -out solutions appear much smaller for the sequential processor than for the batch. The final difference in  $B \cdot \hat{R}$  for both station location sets is only a few kilometers. Thus, the  $10^{-12}$  km/s<sup>2</sup> process noise appears to decrease markedly the sensitivities of the solutions to the presence or absence of the gas leak model. In addition, the solutions are brought closer to the current best estimate by the addition of process noise into the filter, and they are within 50 km for the Set 2 station locations. The trend continues as the process noise is increased to correspond to accelerations of  $10^{-11}$  km/s<sup>2</sup>, as shown in Figs. 28 and 29. The  $\Delta AC$  model has little effect on the solution behavior, and solutions are more accurate than those with the smaller values of process noise.

The sensitivities of the sequential filter solutions to correlated station location errors are presented in Fig. 30 and are seen by comparison with Fig. 25 to have been decreased by the addition of  $10^{-11}$ -km/s<sup>2</sup> process noise. These smaller sensitivities are consistent with the smaller absolute  $B \cdot \hat{R}$  errors occurring with the sequential processors.

**6. Conclusions.** The results presented in Sections V-B-4 and V-B-5 are summarized in Fig. 31 wherein the B-plane solutions with data up to November 6 are shown for the batch (B) and sequential filters ( $S_1$ ,  $S_2$ ,  $S_3$ ), with process noise values representing acceleration errors of  $10^{-12}$ ,  $10^{-11}$ , and  $10^{-10}$  km/s<sup>2</sup>, respectively. Both Set 1 and Set 2 results are shown, with the  $\Delta AC$ -in and  $\Delta AC$ -out solutions represented by the heads and tails of the arrows, respectively.

The following conclusions can be drawn:

- (1) The solutions from the sequential filter are markedly improved over the batch solutions. The sensitivity to the  $\Delta AC$  model is significantly diminished, and

cating that the sequential filter does "filter out" the effects of random gas leaks.

- (2) The sequential filter alleviates the effects of station location errors during the approach phase of the mission. A comparison of the sensitivity analysis plots in Figs. 25 and 30 bears this out. The phenomenon may very possibly be peculiar to the Mariner 9 geometry and tracking pattern and may not occur generally.
- (3) The sequential filters appear to perform better than the batch filter over a wide spread of process noise magnitude assumptions ( $10^{-10}$  to  $10^{-12}$  km/s<sup>2</sup>); hence, performance does not seem to be very sensitive to the user's choice of process noise. Also, the times of the chosen batch separation points do not coincide with the times of gas leaks. Thus, the filter behavior is probably not significantly degraded by the choice of any reasonable batch-break structure.

#### D. Differenced Radiometric Data as a Countermeasure for the Process Noise Problem

1. Background. The process noise problem may be addressed with the use of newly envisioned Earth-based radiometric data types that involve simultaneous or near-simultaneous tracking from widely separated stations. Simultaneous data by themselves will not help, but when they are used in a new data type formed by simply differencing the data taken at one station from simultaneous data taken at another station, the geocentric information, which has been corrupted by the process noise, can effectively be eliminated. The basic concepts are elaborated further in Ref. 13.

Table 27 gives a brief description of how the basic doppler and range data types are formed.

As illustrated in Fig. 32, the transmitting and receiving stations may or may not be the same. If they are, the data are called "two-way"; otherwise they are referred to as "three-way." The two-way data are inherently superior to the three-way because, with two-way, the frequency standard (or clock) used to generate (or time) the transmitted signal is the same one used to analyze the received signal. Three-way doppler data have never been relied upon in interplanetary navigation because the differing stabilities of the rubidium oscillators can produce biases in three-way data as large as 1-2 mm/s. The use of hydrogen masers will alleviate the oscillator instability problems and make it possible to use three-way doppler.

Although range data are also sensitive to oscillator frequency instability, the primary error source for three-way range is asynchronization of the clocks at the transmitting and receiving stations. An epoch offset  $\Delta t$  between the clocks will cause a three-way range error equal to  $c\Delta t$ , where  $c$  is the speed of light. For example, to reduce this range error to less than 1 m, it is necessary to ensure that the bias between the transmitter and receiver clocks be less than 3 ns, which is extremely difficult, even with very long baseline interferometry (VLBI) techniques. This difficulty may be circumvented, however, because most of the information contained in simultaneous two-way and three-way range data may also be extracted from near-simultaneous two-way range, taken from the same stations. The primary difficulty associated with this technique is the modeling of the spacecraft motion so that range data taken at different times may be interpolated to a common time, as shown in Fig. 33. If  $\Delta\dot{r}$  is the error in the computed topocentric range rate and  $T$  is the interval between near-simultaneous data points, the error in the difference between the interpolated range points will be  $\Delta\dot{r}T$ . For example, if the topocentric range rate is known to  $10^{-6}$  km/s, it is necessary to take two-way points every 15 min to keep the range error under 1 m.

2. Theoretical development. For a distant spacecraft, the two-way and three-way down links can be represented by the same plane wave propagating toward the two receiving stations, which gives the differenced doppler observable the same form as the fringe rate of classical VLBI, viz.:

$$F_2 - F_3 = v = -\frac{\omega}{\lambda} r_b \cos \delta \cos(\lambda_b - \alpha) + \Delta v_M + \Delta f \quad (30)$$

where

$r_b$  = baseline projection on equatorial plane

$\lambda_b$  = baseline longitude (defined below)

$\omega$  = Earth rotation rate

$\lambda$  = wavelength of received radio wave

$\alpha, \delta$  = right ascension and declination of spacecraft

$\Delta v_M$  = error caused by transmission media

$\Delta f$  = frequency offset between two frequency standards at two stations

These quasi-very-long-baseline interferometry (QVLBI) data give the right ascension and declination of the spacecraft, provided that the frequency offset  $\Delta f$  and media noise  $\Delta v_M$  can be well calibrated and the baseline parameters  $r_b$  and  $\lambda_b$  are well-determined. One should note that the differenced data are sensitive directly to the baseline parameters, and only through them to the individual station coordinates.

The relations between baseline parameters  $r_b$ ,  $\lambda_b$  and the station location parameters for stations 1 and 2 are as follows (see Fig. 34):

$$r_b = \sqrt{r_{s_1}^2 + r_{s_2}^2 - 2r_{s_1}r_{s_2}\cos\Delta\lambda} \quad (31)$$

$$\lambda_b = \lambda_1 + \theta \quad (32)$$

where

$$\Delta\lambda = \lambda_2 - \lambda_1 \quad (33)$$

and

$$\sin\theta = \frac{r_{s_1} - r_{s_2}\cos\Delta\lambda}{r_b} \quad (34)$$

$$\cos\theta = \frac{r_{s_2}\sin\Delta\lambda}{r_b}$$

For the case when  $r_{s_1} = r_{s_2}$ ,

$$\theta = \frac{\Delta\lambda}{2} \quad (35)$$

The z component of the baseline vector, which does not appear in the equation for  $v$ , is related to the z components of the two stations by

$$z_b = z_1 - z_2 \quad (36)$$

Equation (30) can also be derived by directly differencing the Hamilton-Melbourne (Ref. 7) expressions for the simultaneous two-way and three-way doppler

$$\dot{\rho}_2 = \dot{r} + \omega r_{s_1} \cos\delta \sin\omega(t - t_1) + \omega r_{s_1} \Delta\alpha \cos\delta \cos\omega(t - t_1) + \Delta N_1 \quad (37)$$

$$\dot{\rho}_2 = \dot{r} + \omega r_{s_2} \cos\delta \sin\omega(t - t_2) + \omega r_{s_2} \Delta\alpha \cos\delta \cos\omega(t - t_2) + \Delta N_2 \quad (38)$$

and expressing the station location quantities in terms of baseline vector parameters to give

$$\dot{\rho}_2 - \dot{\rho}_1 = a - \omega r_b \Delta\alpha \cos\delta \sin\omega(t - t_b) - \omega r_b \cos\delta \cos\omega(t - t_b) \quad (39)$$

where  $a = \Delta N_1 - \Delta N_2$ , the errors caused by frequency offsets, transmission media, etc.

**3. Description of the experiment.** The latter part of the cruise phase of Mariner 9 provided an opportunity for experimental verification of the differenced doppler tracking technique. Hydrogen masers provided by Goddard Space Flight Center had been installed at DSSs 12 and 41, which had a 4-h overlap of their view periods. The spacecraft had been experiencing gas leaks, which would make the results an excellent test of the scheme. Consequently, permission was obtained to extend the coverage by DSSs 12 and 41 to track throughout their mutual view period on 16 days during the period October 4 to November 14, 1971.

The DSN was requested to perform the handover (re-assignment of transmitters) at the center of the overlap, so that equal amounts of three-way data could be obtained from both stations. This request could not always be met because it was often necessary to have command capability from Goldstone until DSS 12 set. As a result, only four handovers were executed in the center of the overlap.

The F2 and F3 data obtained at DSS 12 and DSS 41 during the experiment were specially compressed to synchronize their timetags while maximizing the number of usable points. This gave count times which varied from 2 to 10 min. All F2 data were deleted except for those in the common view period (called the overlap set) and those within  $\frac{1}{2}$  h of the adjacent meridian passages (Fig. 35). The distribution of the differenced data is shown in Fig. 36, while the total count appears in Table 28.

The ODP was not designed for differenced data types, so auxiliary programs were written to difference the data and compute partial derivatives for the baseline parameters and frequency biases.

In the initial stages of data analysis, the ODP was used with a trajectory which had been corrected for gas leaks. The F2-only solutions were so close to the current best estimate that there was little hope of improvement when

<sup>5</sup>A more detailed discussion of the experiment and its findings appears in Ref. 19.

three-way data were added. Consequently, a trajectory which ignored the gas leaks was used, so that improvements obtained by employing two-station doppler could show the advantages of this technique if the occurrence of gas leaks could not be well-determined or their magnitudes were highly uncertain.

All of the analysis was performed after the flight. The method used was to process the data as though any gas leaks were unknown and to compare results using various combinations of four data types (F2, F3, F3-F2, and MU). It was assumed that some F2, F3, or MU data were needed to establish the geocentric orbit, but a way had to be found to weight the data to give only as much geocentric information as necessary to avoid the process noise problems. Some criteria had to be developed for judging the quality of the results, because they showed the typical intermediate-arc dispersions of 100-200 km in  $\mathbf{B} \cdot \hat{\mathbf{R}}$ .

Some difficulties were expected in the analysis because the area was new. The majority of these were software or operational problems, for which remedies have been or are being found. The greatest difficulty occurred in attempts to eliminate the frequency biases.

Even though the expected frequency biases using the hydrogen masers were about 0.003 Hz, they still could be seen in the data and had to be removed one way or another. Analysis of the instrument calibration data showed that the uncertainty in the determination of the clock drifts (which cause the biases) was much larger than the magnitude of the drifts themselves, which seemed to indicate that those measurements could not be used to model the biases. The only recourse was to estimate the biases in the ODP. There were some constraints that could be applied, however. The exceptional stability of the masers would suggest slowly varying biases, if any, although short period (8-h) changes might be induced from other portions of the tracking system, like the synthesizer. For analysis purposes, the biases were assumed to be constant over any pass from a given station. When there was a handover from one station to the other, the biases for the two stations were assumed to be equal in magnitude but opposite in sign. Highly correlated *a priori* covariances were also used to constrain biases in consecutive passes from the same station not to change by more than 0.003 Hz.

The following criteria were established for judging the credibility of the solved-for bias values:

- (1) They should be invariant with data weight and parameter set.

- (2) They should be less than 0.01 Hz and be fairly constant over the 40-day span.
- (3) They should be consistent with the residuals when the differenced doppler was not included in the solution.

#### 4. Discussion of results.

*a. F2 data only.* Two different nominal trajectories, with and without gas leak corrections, were used to process the F2 data described earlier, giving the results shown in Fig. 37. The solutions based on the trajectory with gas leak correction (case A-J) agreed better with the current best estimate than the other set (case A'-J') without the corrections, and they were not particularly sensitive to any parameters except solar pressure. The way solutions without gas leak calibrations spread out in the direction perpendicular to  $\mathbf{B}$  bears out the predicted sensitivity of station location and solar pressure solutions to gas leaks when only F2 data are present.

When all F2 data from DSSs 12 and 41 between October 4 and November 13 (2600 points) were included, the results based on the trajectory without leaks improved somewhat, but the solutions involving station locations, solar pressure, and GM of the Moon were still quite volatile. For example, when the GM of the Moon was not included in the solution, the longitude corrections became as large as 18 m. Thus, it was concluded that the observed sensitivity was not just a data selection effect but involved an inherent difficulty with the F2 data.

The sigma used for weighting all the F2 data was 0.045 Hz for a 60-s count time. All data with elevation angles lower than 10 deg were deleted. The results of the overlap set of F2 data processed without gas leak correction were chosen as reference for later comparisons because

- (1) The set involved the same number of passes as were available for the F3 and F3-F2 data.
- (2) The set gave reasonable solutions for the various estimated parameters.
- (3) The absence of gas leak corrections provided an opportunity to prove the effectiveness of the differenced data.

*b. F2 and MU data.* When 14 MU ranging points ( $\sigma_{MU} = 150$  m) were included with the truncated F2 data, the  $\mathbf{B} \cdot \hat{\mathbf{T}}$  components of the errors were all decreased by 50 km, into closer agreement with the current best estimate. Although the longitude at each station changed 2 m

from the F2-only solution, no other parameters changed significantly. The spread of these results in the **B**-plane indicates that solutions involving station locations and *GM* of the Moon are still affected by the gas leaks, but that the solar pressure parameters no longer are as important because certain components of the position of the spacecraft are well determined by range data.

*c. F2, F3, MU.* Once F3 points were included, the frequency offset between the two station clocks from the data had to be estimated. A total of 28 bias parameters representing the frequency offset at each station on each day were added to the "solve-for" sets A through J. The results for the biases were discouraging because they varied with changes in data weight and solve-for parameters and were not slowly varying as anticipated. The bias parameters were absorbing not only the frequency offset, but also all the constant biases over the pass because of process noise such as gas leaks, uncalibrated medium effects, etc. Unfortunately, there was no way to separate these phenomena.

Table 29 serves to illustrate the variation seen by showing results for typical days. For example, on October 23, when the data (F2 and F3) were abnormally noisy because of the sporadic gas leaks, the estimated value of the bias reached  $-9.2$  mHz at DSS 41. The values changed drastically from case J to case C, wherever station location parameters were estimated.

The station locations remained essentially unchanged for DSS 12 but, when the F3 data were tightly weighted, moved 2 m in  $r_s$  and 1.5 m in  $\lambda$  at DSS 41, where most of the F3 data were taken. The inconsistency is probably related to the questionable results for the solved-for biases. The **B**-plane results were not noticeably different from those in the F2 and MU data set.

*d. F3 - F2.* Differencing F2 from F3 data gave significantly cleaner residuals than either data type taken separately. Figure 38 shows the residuals of F2, F3, and F3-F2 during two relatively noisy passes on October 28 and 29 and clearly indicates that the process noise which is common to both F2 and F3 data has been removed during the differencing.

Solutions which contained only F3-F2 data were studied, but the six state parameters were highly corre-

lated because of the poor geometry covered by this particular arc. As mentioned earlier, the differencing destroys geocentric range-rate information, leaving only the right ascension and declination of the spacecraft. As with classical astronomical observations, the restriction to angular measurements demands longer arcs or a better geometry to determine the orbit. Thus, two-way doppler and ranging data were introduced to resolve this problem.

*e. F3-F2, F2, and MU.* Once the geocentric information (F2 and MU) is included, the indeterminacy of the orbit decreases. Although about half the correlations among the state parameter are still above 0.9 when F2 and MU data are included, the improved **B**-plane behavior suggested that the problem was disappearing. There were other encouraging results as well. Because of the comments made in Section V-D, the partial derivatives with respect to baseline parameters  $r_b$  and  $\lambda_b$  were inserted in place of those for station location parameters for the F3-F2 data. The estimated corrections to station locations provided by the F2 and MU data are about  $-4$  m in  $\lambda$  and  $< 2$  m in  $r_s$ . The correction to  $\lambda_b$  is also  $-4$  m, but  $\Delta r_b$ , at 12 m, is larger than expected from the  $r_s$  and  $\lambda$  changes. This could be caused by the large *a priori* value used for  $r_b$  ( $\sigma_{r_b} = 1$  km) and the relatively high correlations with the bias parameters ( $\rho \approx 0.7$ ).

There also was good repeatability of the estimated bias values for solutions with different data weights and estimated parameters. The average magnitude of the estimated biases was about 4 mHz, and they were slowly varying most of the time, which means that the earlier variations were, in fact, caused by absorption of process noise on a pass-by-pass basis. The **B**-plane solutions show significant improvement when the differenced data are tightly weighted (Fig. 39). Among the solutions, cases A, B, and J coincide with one another, as do cases E, G, and H. This fact indicates that solutions based primarily upon differenced data with some F2 and MU are not sensitive to solar pressure, attitude control, *GM* Moon, *GM* Mars, and ephemerides, which is to be expected since they all affect the geocentric motion. They are sensitive only to station locations and baseline parameters.

*f. F3 - F2, F2.* Solutions ( $\sigma_{F3-F2} = 0.002$  Hz,  $\sigma_{F2} = 0.011$  Hz) without MU data were attempted, but they moved the **B**-plane results further away from the current best estimate. The residuals induced in F2 were far too large, and the station location changes were unreasonable.

## VI. Radiometric/Optical Navigation

### A. Introduction

Although there was an unofficial optical navigation demonstration (OND) group during the Mariner Mars 1969 mission that provided near real-time OD estimates to the Navigation Team Chief during the 1971 mission, the OND personnel were actually made a bona fide part of the Navigation Team, contributing to the pre-flight studies, participating in all the training and testing exercises, and providing OD estimates that were considered in the strategies finally adopted.

This section discusses the use of optical data in combination with radiometric data to determine the Mariner 9 approach orbit. The discussion includes the basic TV instrument and the information content and error sources in the various optical data. After a brief analysis of how the optical and radio data complement each other, it shows how pictures were chosen and processed in real time to achieve the combined radio/optical estimate. The discussion includes the sensitivity of the optical data to the number of stars per picture, the amount of TV distortion, the availability of *a priori* trajectory information, and the quality of the Mars ephemeris.

### B. The Optical Data Instrument

The narrow-angle science television camera provided the optical navigation observations for Mariner 9. This device had a 500-mm focal length with  $f/2.5$  Schmidt-Cassegrain optics and a selenium-sulfur vidicon tube with a  $7 \times 9$  reseau grid. The electronics scanned a  $9.6 \times 12.5$ -mm area on the vidicon target with 700 lines and 832 pixels per line. The video intensity of each pixel was digitized to 9 bits. Each pixel, therefore, was defined by its pixel number (1 to 832), its line number (1 to 700), and its intensity (0 to 511). The active area of the vidicon target gave a  $1.1 \times 1.4$ -deg field of view with a pixel angular size of 6 arc sec.

To allow sufficient time to read out and record a picture, the camera could not be shuttered more often than once every 84 s. Exposure times could be changed by ground command from 0.006 to 6.144 s, enabling detection of stars as dim as ninth magnitude.

### C. Optical Data Errors

Optical data errors are classified as instrument and model errors. Instrument errors include TV distortions, TV pointing errors, image center-finding errors, and random measurement errors.

TV distortion errors corrupt the relative geometry of images within a picture. They are caused by nonuniform deflection fields which sweep the electron readout beam across the vidicon target nonuniformly. TV distortion causes image location errors in raw data of a few pixels near the center of the vidicon to tens of pixels near the edges of the vidicon. This distortion can be accurately modeled as a sixth-order polynomial of the radial distance from the center of the vidicon, as discussed in Ref. 20. Either reseau or star images may be used to calibrate TV distortion. Distortion from the optics is negligible.

TV pointing errors (i.e., imperfect knowledge of TV pointing directions at shutter times) cause a global shift of all images in a picture and also corrupt the relative image geometry within a picture because of the non-linearity of the TV distortion. These errors can be eliminated if stars with known directions are included in the picture. Preliminary estimates of the TV pointing direction can be obtained from either reduced telemetry data or the desired (planned) TV pointing. Using the desired pointing direction gives errors of hundreds of pixels. Processing telemetry reduces errors by an order of magnitude and makes them random in nature from picture to picture. Star data further decrease them to the pixel level.

Image center-finding errors result when finite-size images, such as those of Deimos and Phobos, are dealt with. Also, limit-cycle motion during exposure, diffraction in the optics, and blooming of saturated images combine to yield finite-size images. These random center-finding errors are of pixel or subpixel magnitude for Phobos and Deimos. Random measurement errors result from random center-finding errors and TV resolution.

Model errors include satellite ephemeris errors as well as planet gravity and spin-axis errors. Deimos and Phobos ephemerides were modeled by a first-order analytic theory (Ref. 21). For Mariner 9, the effects of these model errors were minimized by including Deimos and Phobos orbital elements and the GM and spin-axis direction of Mars as estimated parameters.

### D. Optical Data Types and Their Information Content

The optical navigation observables were the image locations (pixel and line numbers) of Deimos, Phobos, stars, and reseaux. Figure 40 shows an approach picture containing the images of Deimos, ten stars of magnitude 3.9 to 9.2, and the  $7 \times 9$  reseau grid. Stray light from Mars is seen in the lower left portion of the picture. The picture

was enhanced to bring out the dim images. Figure 41 is a computer-drawn version of the predicted picture, which is used to distinguish the star pattern from noise or vidicon blemishes.

Reseau images were used during the mission to compute the coefficients of the sixth-order TV distortion polynomial to subpixel accuracy. During post-flight analysis, star images were used instead of reseaux to yield equally accurate calibrations. The reseau data used for real-time operations and a majority of post-flight evaluation were obtained from pictures taken about a month before orbit insertion. With the TV distortion being stable to pixel level, no additional reseau data were processed during Mars approach. The star and reseau data were independent of the spacecraft trajectory for this application and could be processed either separately or as the satellite data were being reduced.

Star images were used to compute the TV pointing direction to an accuracy commensurate with the TV angular resolution of  $3''0$ ,  $1 \sigma$ . Star directions, accurate to  $1''0$ , were assumed to be perfectly known.

The satellite images contained information on satellite ephemerides, the spacecraft trajectory, and the Mars GM and spin-axis direction.

### E. Advantages of Combined Radiometric and Optical Data Sets

Solutions which use a combination of radiometric and optical data are of particular value during planetary approach because these data types complement one another. The primary error sources prior to encounter in solutions using only radiometric data are target planet ephemeris errors, station location errors, and nongravitational accelerations. Optical data are insensitive to these errors because the data directly relate the planet and spacecraft positions. On the other hand, optical data suffer from the inability to determine accurately the time of flight and velocity ( $V_\infty$ ) of the spacecraft, quantities which are well determined by radiometric data. Hence, the combination of radiometric and optical data yields extremely accurate solutions. In particular, they may be combined to give a good estimate of encounter conditions much earlier than either data type taken separately. This is of primary importance if an additional corrective maneuver is contemplated. This subsection presents a simple analysis illustrating why combined solutions are so powerful.

Regardless of whether the optical observation is of the planet's limb or its natural satellites, basically, an attempt is made to measure the angle between the planet center of mass and a reference direction, e.g., a star direction. For the purpose of this analysis, the error in this angular measurement represents the total from all sources, such as center-finding errors, satellite ephemeris errors, biases, and camera pointing errors, all of which effectively degrade the observed angle.

Assume that the spacecraft is moving on trajectory 1 (Fig. 42). Let  $\theta_1$  and  $\theta_2$  represent two angular measurements of the direction between the reference star and the center of mass of the planet. For simplicity, the reference star is assumed to lie along the  $V_\infty$  vector. In general, the observable equation is

$$\tan \theta_i = \frac{|B|}{V_\infty T_i} \quad (40)$$

where

$$T_i = T - t_i \quad (41)$$

and

$|B|$  = magnitude of B vector

$V_\infty$  = velocity on approach asymptote

$T$  = time of flight

$t_i$  = time of its observation

From Eq. (40), it is seen that the time of flight  $T$  can be determined from two perfect observations of  $\theta$ . However, only the ratio  $|B|/V_\infty$  can be determined from observations of  $\theta$ . This is because the observation history for any parallel trajectory with the same value of  $|B|/V_\infty$  (for example, trajectory 2 in Fig. 40) will be identical to that for the true trajectory. These parallel trajectories also will have the same time of flight as the true trajectory. Two perfect direction observations determine the plane of motion.

From Eq. (40),

$$\frac{\delta \theta}{\sin \theta \cos \theta} = \frac{\delta |B|}{|B|} - \frac{\delta V_\infty}{V_\infty} - \frac{\delta T}{T} \quad (42)$$

or for small values of  $\theta$ ,

$$\frac{\delta|\mathbf{B}|}{|\mathbf{B}|} = \frac{\delta V_\infty}{V_\infty} + \frac{\delta T}{T} + \frac{\delta\theta}{\theta} \quad (43)$$

Consequently, even with perfect observations, the limiting accuracy for  $|\mathbf{B}|$  is determined by  $\delta V_\infty$ , i.e.,

$$\delta|\mathbf{B}| = \frac{|\mathbf{B}|}{V_\infty} \delta V_\infty \quad (44)$$

Even though in theory two perfect observations of  $\theta$  uniquely determine time of flight, in practice this quantity is rather poorly determined by optical data because it is extremely sensitive to errors in  $\theta$ . This can be illustrated by examining an expression for the time-of-flight uncertainty.

Assume that two observations of  $\theta$  are taken. Then solving Eq. (40) for  $T$  yields

$$T = \frac{t_2 \tan \theta_2 - t_1 \tan \theta_1}{\tan \theta_2 - \tan \theta_1} \quad (45)$$

Assuming that  $\theta_1$  and  $\theta_2$  are small,

$$T = \frac{t_2 \theta_2 - t_1 \theta_1}{\theta_2 - \theta_1} \quad (46)$$

and

$$\delta T = \frac{(t_2 - t_1)(\theta_2 \delta \theta_1 - \theta_1 \delta \theta_2)}{(\theta_2 - \theta_1)} \quad (47)$$

Assuming independent observations, the standard deviation of  $T$  becomes

$$\sigma_T = \left[ \frac{V_\infty T_1 T_2 (T_1^2 + T_2^2)^{1/2}}{|\mathbf{B}|(T_1 - T_2)} \right] \sigma_\theta \quad (48)$$

From Eq. (48), it is seen that the uncertainty in time of flight is very sensitive to the uncertainty in pointing angle when the spacecraft is far from the target planet, and decreases as the spacecraft approaches the planet. Equation (48) emphasizes the importance of stars in the data because they minimize the contribution of pointing errors to  $\sigma_\theta$ . Obviously, a larger  $|\mathbf{B}|$ , which increases parallax, minimizes the error. A smaller  $V_\infty$  also gives more parallax by decreasing the range at which the observations are taken. Finally, for a fixed measurement time  $T_1$ , Eq. (48) is minimized as  $T_2$  is taken closer to encounter.

Equations (44) and (48) indicate why the quantities  $V_\infty$  and  $T$  are weakly determined by optical data. Because these same quantities are determined very well by Earth-based radiometric data, the combination of the two data types can yield good solutions much sooner than either type used separately.

The above analysis shows how the individual weaknesses of optical and radiometric data a few days out from encounter are offset by each other's strengths. Just as with radiometric data, the closer the spacecraft gets to the planet with the optical measurements, the better the solution that results. As the spacecraft approaches the planet, parallax effects in the case of natural satellite observations allow solving for  $V_\infty$ . Also, the time-of-flight solution becomes less sensitive to pointing errors. Furthermore, by then, sufficient data will have been taken to estimate the natural satellite ephemeris relative to the target planet, thus reducing effects of this error source. In the case of planet limb observations,  $V_\infty$  can not be accurately determined until planetary bending of the approach trajectory occurs.

For Deimos, parallax effects are discernible long before planetary bending occurs. In addition, its small size makes image center-finding errors negligible. These two factors make satellite observations significantly more accurate than Mars observations for approach navigation.

## F. Selection of Approach Pictures

During the 3-day approach prior to MOI, three pre-orbital science picture sequences (POS I, II, and III) were taken (Fig. 43). Each POS sequence covered a 24-h period in which 31 pictures were recorded aboard the spacecraft and then transmitted to Earth during a 3-h period near the DSS 14 meridian. Since MOI occurred early in the Goldstone view period, the POS III pictures were played back after orbit insertion.

Not all of these pictures were available for OND. The Project required that a minimum of 24 of the 31 pictures in both POS I and II be used to obtain two full revolutions of Mars surface coverage at 15-deg surface longitude intervals. Also, a minimum of 23 of the 31 pictures in POS III were required for additional Mars surface coverage and for photometric calibration of the wide-angle camera. Despite the fact that the OND was on a non-interference and noncommittal basis with the mission, it was allocated all but one of the remaining pictures.

OND personnel were given complete freedom in selecting the targets and exposures of their pictures, and the

only timing constraint was noninterference with either the Mars pictures (1-h centers) or the 3-h playback periods. Because only POS I and II pictures were to be played back prior to insertion, the optical OD engineers targeted Deimos in all 13 pictures in these two sequences to reduce its ephemeris uncertainty to a level which would not seriously degrade the approach spacecraft trajectory estimates produced during real-time operations. The small angular separation of Phobos and Mars during this period made Phobos an undesirable target because of possible Mars stray-light interference. Three of the eight satellite pictures in POS III were of Phobos.

The positions of Deimos as viewed from Mariner 9 against the star background are shown in Fig. 44. The orbital coverage of Deimos is listed in Table 30. Because the first Deimos picture was lost during transmission to JPL, real-time and post-flight data processing had only five POS I pictures. Also, one of the three Phobos pictures in POS III was missed because of improper pointing of the TV camera. With only two Phobos approach pictures and large *a priori* Phobos ephemeris uncertainties, the Phobos data did not improve the navigation accuracy beyond that achieved with the Deimos data.

### G. Operational Techniques and Results

Optical measurements and radiometric data are completely independent data types, which have some common information content but are subject to many error sources not common to both. Because of this, procedures were established to eliminate, as much as possible, the error sources peculiar to each data type before they were combined in a single solution. This served to reduce the number of iterations required on the whole data set. The processing of radiometric data toward this end was described in Sections II and III. Analogous preliminary reductions were performed on the optical data.

The first stage of the optical data reduction processed only star images to estimate TV pointing errors, which were usually large enough to be outside the linear region because of the nonlinearities in the TV distortion. A second iteration, required to ensure that the pointing parameters were within the linear region, was performed in the second stage of processing.

As an additional goal, the second stage was to make preliminary corrections to the satellite ephemeris, which was expected to be in error by as much as 500 km. This error was large enough to require another iteration, which was left for the third stage. The data included both star

and satellite images. The solution list contained the spacecraft state, and four elements of the Deimos orbit. Because Deimos is in a near-circular, near-equatorial orbit, only two orientation angles, inclination and mean anomaly, were included in the solution along with semimajor axis and eccentricity. A trajectory based on radio data only was used with a loose *a priori* uncertainty (thousands of kilometers). The spacecraft trajectory parameters were included to allow a more accurate satellite ephemeris improvement, but the new probe conditions were not used for the trajectory employed in the third-stage processing. Instead, the same orbit input to the second stage was used.

The third stage involved the actual combination of radiometric and optical data to solve for the spacecraft trajectory and the Deimos ephemeris. Once the Deimos ephemeris had been updated by use of POS I data, the second and third stages were combined by adding the pointing parameters to the solution list.

The optical residuals before the first-stage fit for Deimos (D) and stars (O) are shown in Fig. 45. The residuals in Fig. 45a were obtained using *a priori* Deimos ephemerides, a short arc trajectory based on radiometric data to MOI-19 h, and TV pointing based on reduced spacecraft telemetry data. The clusters of star residuals reflect the global offset of the images caused by TV pointing errors. The TV pointing errors became large at the end of POS II and throughout POS III in the pixel direction but were smaller and more random in the line direction.

The residuals in Fig. 45b are before the second-stage solution and were generated using the same conditions as those in Fig. 45a, with the exception that TV pointing errors were removed by using the star images. The star residuals, which are only sensitive to pointing errors, now have a zero mean. With these errors removed, the Deimos residuals reflect Deimos ephemeris errors and spacecraft trajectory errors. The Deimos ephemeris errors are evident in the 30-h periodic cycle seen in POS II and POS III residuals. The spacecraft trajectory error is seen as a slope in the periodic line residuals.

Figure 45c shows the residuals after solving for the spacecraft trajectory and Deimos ephemeris in the third stage. Here, the residuals are random with zero mean and a standard deviation of less than 0.5 pixels (3 $\sigma$ ). The combined solution of optical and radiometric data indicated a 400-km correction to the Deimos orbit and an 80-km spacecraft trajectory error.

Figure 46 shows the B-plane trajectory estimates, which were generated in near-real time. The radiometric-only solution and its  $1-\sigma$  error ellipse were based on data to MOI-13 h. The radiometric plus optical iterated solution and  $1-\sigma$  error ellipse were based on radiometric data to MOI-19 h and optical data from POS I and II. Solutions denoted as optical were generated, using a trajectory based on radiometric data but processing optical data only. These optical solutions were obtained from the second iteration of optical data to remove nonlinearities.

Post-flight studies have given greater insight into the data and have confirmed the accuracy of the real-time trajectory estimates.

#### H. Post-flight Sensitivity Studies

1. **Number of stars per picture.** In analyzing the dependence of OD accuracy on the number of stars per picture, the following three cases were studied:

- (1) No stars per picture.
- (2) One star per picture.
- (3) An average of five stars per picture.

All three cases had *a priori* TV pointing information from reduced spacecraft telemetry data. Also, the nominal trajectory was based on radiometric data only from MOI-30 days to MOI-16 h. OD accuracies for the three cases are shown in Fig. 47, and the associated trajectory estimates are presented in Figs. 48 through 50. In these last three figures, the numbers on the broken lines indicate the number of sequential pictures (starting from No. 2 of Table 30) used to produce that result.

Figures 49 and 50 show that the first picture in POS I for cases 2 and 3 drives the trajectory estimate to within 15 km of the current best estimate. The time behavior of cases 2 and 3 is very similar, with the trajectory estimates agreeing to within 10 km at the end of the POS I and POS II data and to within 2 km at the end of the POS III data. The expected accuracies of cases 2 and 3 (Fig. 47) are the same. It is seen, therefore, that the full accuracy potential of the optical data can be obtained with only one star per picture. This would also be true if the desired TV pointing were used as *a priori* instead of reduced spacecraft telemetry data.

TV pointing derived from spacecraft telemetry is an order of magnitude less accurate than pointing derived from star images. This degradation is reflected in both

the expected accuracy and the actual trajectory estimate of case 1 (Fig. 48) as compared to cases 2 and 3. The case 1 trajectory estimate is well behaved, when compared to its expected accuracy, until the last picture in POS II (No. 12). Then the large, nonrandom TV pointing errors (modeled as random errors) in the remaining pictures drove the trajectory estimate to a  $3-\sigma$  error. Improved trajectory accuracy may be possible by modeling the TV pointing errors as time-correlated processes.

These star-sensitivity results can be explained by examining the TV pointing errors. For a given picture, all sources of pointing errors can be modeled as three independent rotations about the axes of an orthogonal coordinate system (e.g., TV pointing has three degrees of rotational freedom). One star image (a pixel and line observation) yields two of the three degrees of rotational freedom. The third degree of freedom is obtained from a second star or from *a priori* TV pointing, which has an accuracy of a few tenths of a degree. *A priori* TV pointing to this accuracy can be obtained from either reduced spacecraft telemetry data (0.015 deg,  $1\sigma$ ) or from the desired pointing (0.15 deg,  $1\sigma$ ). Additional stars, however, do not improve the Deimos inertial reference information in a picture. Measurement errors in the Deimos image location control this accuracy and are not affected by star observations.

Even though only one star per picture is needed, it is desirable to have many. From a reliability standpoint, many stars per picture give independent checks on the TV pointing and also indicate the accuracy of the TV distortion model. Any discrepancy between image location residuals within a given picture would flag it for further evaluation.

2. **Sensitivity to TV distortion.** A comparison was made of OD performance as a function of the data type used to calibrate TV distortion and as a function of the order of polynomial used to model it. Data used included

- (1) Only reseau images from ground pictures.
- (2) Only reseau images from flight pictures.
- (3) Only star images from flight pictures.

Distortion polynomials of first and third order, determined from flight reseau images, were compared to results from the sixth-order polynomial.

In comparing calibration data, it was found that all three types gave equivalent trajectory estimation results.

The difference between reseau images from ground and flight pictures was an offset and rotation common to all reseaux. This difference was easily absorbed in the TV pointing error model. Approximately 200 star images from Pleiades pictures and optical navigation pictures were used to produce results equivalent to those from reseau data. In fact, stars are more desirable than reseau data because they enable the calibration of optical as well as electromagnetic distortion and are more easily detected than reseaux in pictures used for TV calibration and navigation.

The tradeoff between increased optical data linearity and reduced accuracy was examined, and it was found that a third-order distortion polynomial gave equivalent trajectory estimates to the nominal sixth-order model. The increased linearity was accompanied by a slightly noisier trajectory estimate behavior, which was, however, well within the predicted accuracy. The trajectory estimate obtained using a first-order distortion model was in error by only 15 km. Therefore, it was concluded that a first-order model would have sufficed if time constraints had not allowed iteration of the optical data. If time is available, which is generally the case, the sixth-order model will give the full accuracy potential of the optical data with iteration of the data.

**3. Sensitivity to the amount of radiometric data.** To evaluate the strength of optical data alone, a trajectory solution was made without the aid of any other tracking data. From the considerations of Section VI-E, it should be expected that POS I and II data alone would yield an accurate  $\mathbf{B} \cdot \hat{\mathbf{R}}$  and  $\mathbf{B} \cdot \hat{\mathbf{T}}$  solution, but that limited pictures and observed parallax would degrade the time-of-flight accuracy, whereas POS III data, containing both Deimos parallax and trajectory bending, would yield a complete trajectory determination from only the optical data.

A nominal trajectory was generated from Atlas/Centaur injection conditions. These injection conditions gave a 25,000-km aim-point bias at Mars for planetary quarantine. The use of this trajectory did not allow the optical data to "know," *a priori*, that a midcourse maneuver had been performed 5 days after launch. The midcourse maneuver changed the actual trajectory aim point by some 25,000 km and the arrival time by 19 h. In other words, this *a priori* trajectory indicated to the optical data that the spacecraft was going in the vicinity of Mars. Moreover, the pre-flight Deimos ephemeris having a 400-km error was used.

Initially, only POS I and II data were iterated because only they were available in real time. Five complete iterations of the POS I and II data were needed to obtain a converged solution because of the nonlinearity caused by the *a priori* trajectory error. After a converged solution was obtained for the POS I and II data, an additional solution was made which included the POS III data. This final solution allowed the full potential of the approach optical data to be evaluated.

The **B**-plane trajectory estimates are shown in Figs. 51 and 52 at the end of a complete iteration of POS I and II data. It can be seen that an accurate estimate of  $\mathbf{B} \cdot \hat{\mathbf{R}}$  and  $\mathbf{B} \cdot \hat{\mathbf{T}}$  can be obtained using only POS I and II data as expected. The **B**-plane estimate after five iterations was within 10 km and 16 s of the current best estimate. This estimate would easily have met mission accuracy requirements for inserting Mariner 9 into orbit about Mars. Adding the POS III data brought the **B**-plane estimates from optical data only to within 5 km and 3 s of the current best estimate.

The time-of-flight estimate and expected uncertainty from the final solution are shown in Fig. 53. It is seen that the uncertainty does not go below a few seconds until 10 h from MOI. This level of accuracy would be available about a day before MOI from radiometric data. It is concluded, therefore, that optical data only can yield an accurate trajectory estimate using data within 10 h from Mars MOI. By combining optical and radiometric data, an estimate of comparable accuracy can be obtained much earlier.

**4. Sensitivity to Mars ephemeris.** One major source of error in the use of radiometric data for navigation estimates is planetary ephemeris errors. The reason for this is that the data are taken by stations on Earth and must be related to the target planet using assumed station locations and a planetary ephemeris. However, from on-board optical data, the spacecraft state is directly related to the target planet. After the insertion of Mariner 9 into Mars orbit, there was an update to the planetary ephemeris affecting the position of Mars by about 40 km. The optical navigation estimates for the **B**-plane parameters remained essentially the same with this change in ephemeris.

To demonstrate the independence of optical navigation estimates from the planetary ephemeris errors, a solution was made with a Mars ephemeris error of about 500 km. The results of processing the optical data with this ephemeris error are shown in Fig. 54, which gives the **B**-plane solution history. The origin of the plot is at the current

best estimate. The figure shows that the first pass through the data moves the estimate from an *a priori* estimate more than 500 km away to within 10 km of the current best estimate. The final iteration moves the estimate to within 2 km of the current best estimate.

### I. Conclusions

The radiometric plus satellite/star trajectory estimate for Mariner 9 was the most accurate solution generated during any real-time approach operations. The new optical data navigation techniques were successfully demonstrated during real-time and post-flight analysis. Star and resseau images were used to reduce all systematic

TV pointing and distortion errors to arc-second accuracy. Consequently, satellite image location errors were random, with a measurement noise of 3"0 (1  $\sigma$ ). These satellite images allowed the Mariner 9 trajectory and the satellite ephemeris to be determined independent of *a priori* uncertainties in satellite ephemerides. The addition of the optical data to a few days of radiometric data allows the approach navigation process to reach its full accuracy potential and become insensitive to planetary ephemeris errors, nongravitational spacecraft accelerations, and Earth-based tracking station location errors. Thus, a demonstrated navigation capability now exists which can meet the demanding requirements of future missions.

## References

1. Madrid, G. A., et al., *Tracking System Analytic Calibration Activities for the Mariner Mars 1971 Mission*, Technical Report 32-1587, Jet Propulsion Laboratory, Pasadena, Calif. (in press).
2. Moyer, T. D., *Mathematical Formulation of the Double-Precision Orbit Determination Program (DPODP)*, Technical Report 32-1527, Jet Propulsion Laboratory, Pasadena, Calif., May 15, 1971.
3. O'Handley, D. A., et al., *JPL Development Ephemeris Number 69*, Technical Report 32-1465, Jet Propulsion Laboratory, Pasadena, Calif., Dec. 15, 1969.
4. Boggs, D. H., "A Partial Step Algorithm for the Nonlinear Estimation Problem," *AIAA J.*, Vol. 10, No. 5, pp. 675-679, May 1972.
5. Wong, S. K., and Reynolds, G. W., *Preliminary Orbit Determination Strategy and Accuracy, Mariner Mars 1971*, PD 610-33, Aug. 15, 1970 (JPL internal document).
6. Jordan, J. F., Madrid, G. A., and Pease, G. E., "The Effects of Major Error Sources on Planetary Spacecraft Navigation Accuracies," *AIAA/AAS Astrodynamics Conference*, Santa Barbara, Calif., Aug. 1968.
7. Zielenbach, J. W., and Jordan, J. F., "Orbit Determination Strategy and Results for the Mariner Mars 1971 Mission," *AAS Paper No. 71-391*, *Astrodynamics Specialists Conference*, Fort Lauderdale, Fla., Aug. 17-19, 1971.
8. Wong, S. K., Reinbold, S. J., and Sievers, G. L., *Mariner 9 Inflight Orbit Determination Analysis*, TM 391-342, July 17, 1972 (JPL internal document).
9. Wong, S. K., *Mariner 9 Postflight Interplanetary Orbit Determination Analysis*, TM 391-410, Feb. 14, 1973 (JPL internal document).

## References (contd)

10. Esposito, P. B., and Wong, S. K., "Geocentric Gravitational Constant Determined from Mariner 9 Radio Tracking Data," Paper presented at International Symposium on Earth Gravity Models and Related Problems, St. Louis, Mo., August 16-18, 1972.
11. Melbourne, W. G., "The Determination of Planetary Masses from Radio Tracking of Space Probes and Planetary Radar," paper presented at COSPAR-IAU-IAG/IUGG-IUTAM Symposium, Prague, 1969.
12. Hamilton, T. W., and Melbourne, W. G., "Information Content of a Single Pass of Doppler Data from a Distant Spacecraft," in *The Deep Space Network*, Space Programs Summary 37-39, Vol. III, pp. 18-23, Jet Propulsion Laboratory, Pasadena, Calif., May 31, 1966.
13. Ondrasik, V. J., and Rourke, K. H., "Applications of Quasi-VLBI Tracking Data Types to the Zero Declination and Process Noise Problems," AAS Paper No. 71-399 presented at AAS/AIAA Astrodynamics Specialists Conference, Fort Lauderdale, Fla., August 17-19, 1971.
14. Cordon, H. J., et al., *The Mariner VI and VII Flight Paths and Their Determination from Tracking Data*, Technical Memorandum 33-469, Jet Propulsion Laboratory, Pasadena, Calif., Dec. 1, 1970.
15. Wong, S. K., and Reynolds, G. W., *Preliminary Orbit Determination Strategy and Accuracy Mariner Mars 1971*, PD 610-33, Aug. 15, 1970 (JPL internal document).
16. Null, G. W., et al., *The Mariner IV Flight Path and Its Determination from Tracking Data*, Technical Report 32-1108, Jet Propulsion Laboratory, Pasadena, Calif., Aug. 1, 1967.
17. Bourke, R. D., McReynolds, S. R., and Thuleen, K. L., "Translational Forces on the Mariner V Spacecraft Stemming from the Attitude Control System," Paper presented at the AIAA 7th Aerospace Sciences Meeting, New York, Jan. 21, 1969.
18. Rourke, K. H., and Jordan, J. F., "Application of Advanced Filtering Methods to the Determination of the Interplanetary Orbit of Mariner 71," AIAA Paper No. 72-906, AIAA/AAS Astrodynamics Conference, Palo Alto, Calif., Sept. 11-12, 1972.
19. Mulhall, B. D., Chao, C. C., and Zielenbach, J. W., *Report of the Two-Station Doppler (QVLBI) Demonstration Conducted with Mariner 9, Part I Batch Filtering*, TM 391-413, Feb. 22, 1973 (JPL internal document).
20. Breckenridge, W. G., and Acton, C. H., "A Detailed Analysis of Mariner 9 TV Navigation Data," AIAA Paper No. 72-866, Aug. 1972.
21. Akmes, K., "On the Use of Hill Variables in Artificial Satellite Theory: Brouwer's Theory," *J. Astron. Astrophys.*, 17, 70, 1972.

**Table 1. Standard deviations of residuals based on a state-only solution from Run 000967**

DSS	F2, Hz <sup>a</sup>	MARK 1A, m	TAU, ns	MU, ns
12	0.00366	20.313		935.07
14	0.00433		569.89	
41	0.00345	21.895		
51	0.00349	23.233		
62	0.00474	22.887		

<sup>a</sup>1 Hz  $\approx$  6.5 cm/s at S-band.

**Table 3. A priori uncertainties in radio tracking parameters**

Parameters	Units	Considering	Estimating
r of state	km		10 <sup>5</sup>
v of state	km/s		1
Solar pressure	unitless ratios	0.03	0.05
Constant attitude control leaks	km/s <sup>2</sup>	10 <sup>-12</sup>	10 <sup>-12</sup>
r <sub>s</sub> of stations	m	3	50
$\lambda$ of stations	m	5	50
GM Moon	km <sup>3</sup> /s <sup>2</sup>	0.03	1
GM Mars	km <sup>3</sup> /s <sup>2</sup>	1	1
Ephemerides	radians or unitless ratios	*	10 <sup>-4</sup>

\*Covariances provided by the Ephemeris Development Group.

**Table 2. Transfer trajectory navigation accuracy requirements, 3  $\sigma$**

Time at which OD estimate is required	Allowable uncertainty in predicted magnitude of B vector, km
Launch + 5 days	750
MOI - 30 days	250
MOI - 6 h	150

**Table 4. A priori uncertainties in elements of the Martian natural satellites**

Parameter <sup>a</sup>	Units	Phobos	Deimos
a	km	3.0	5.0
e		0.01	0.01
M <sub>s</sub>	deg	2.0	1.0
i	deg	0.2	0.1
$\omega$	deg	10.0	10.0
$\Omega$	deg	5.0	5.0

<sup>a</sup>Referred to Mars true equator of date.

Table 5. Some typical parameter sets

Solution set	Parameter
A	State
B	State, solar pressure (SP)
C	State, SP, DSS
D	State, DSS
E	State, SP, DSS, GM of Moon (GMM) and/or Mars (GM4)
F	State, SP, DSS, attitude control (AC) leaks
G	State, SP, DSS, GMM and/or GM4, AC
H	State, SP, DSS, GMM, GM4, AC, Mars and barycenter ephemerides
I	State, satellite ephemerides
J	State, SP, GMM, GM4
K	State, SP, GMM, GM4, Mars and barycenter ephemerides, AC

Table 6. Comparison of nongravitational parameter solutions using pre-midcourse data

	A	B	C	D	E	F
Parameter	Post-flight post-midcourse (current best estimate)	Pre-flight a priori	Inflight pre-midcourse	Post-flight pre-midcourse	Post-flight a priori	
$SP_B$	1.2234	1.3249	1.3189	1.2406	1.2329	
$SP_x$	-0.0462	-0.0143	-0.0211	-0.0503	-0.0597	
$SP_y$	-0.0516	-0.0143	-0.0226	-0.0464	-0.0506	
$AC_B, \text{ km/s}^2$	0.2960 E-12	0	0	0.1847 E-12	0	
$AC_x, \text{ km/s}^2$	0.1166 E-11	0	0	0.1115 E-11	0.8916 E-12	
$AC_y, \text{ km/s}^2$	0.1831 E-11	0	0	0.1822 E-11	0.1502 E-12	
Run identification	00972L-C		PREM/C-10-C	PRE017-E		

Table 7. Pre-midcourse (pc-4-unilatch) results

Parameter	InFlight (PREM/C-10-C)			A priori			Estimated			Post-flight (PREO17-E)			Estimated		
	Value	$\sigma$	Units	Value	$\sigma$	Units	Value	$\sigma$	Units	Value	$\sigma$	Units	Value	$\sigma$	Units
X	251727.12	0.10 E+5	km <sup>3</sup>	251727.32	0.45		251726.89	0.10 E+5		251727.08	0.10 E+5		251727.08	0.76	
Y	-211593.70	0.10 E+5	km <sup>3</sup>	-211593.29	0.69		-211593.75	0.10 E+5		-211593.25	0.10 E+5		-211593.25	0.78	
Z	-180738.94	0.10 E+5	km <sup>3</sup>	-180738.56	0.82		-180738.53	0.10 E+5		-180738.77	0.10 E+5		-180738.77	1.40	
X̂	2.3811821	1.0	km/s <sup>2</sup>	2.3811826	0.37 E-5		2.3811826	1.0		2.3811803	1.0		2.3811803	0.67 E-5	
Ŷ	-1.7412558	1.0	km/s <sup>2</sup>	-1.7412571	0.53 E-5		-1.7412555	1.0		-1.7412585	1.0		-1.7412585	0.68 E-5	
Ẑ	-1.6063038	1.0	km/s <sup>2</sup>	-1.6063020	0.62 E-5		-1.6063032	1.0		-1.6063034	1.0		-1.6063034	1.12 E-4	
S <sub>P</sub>	1.3949000	0.50 E-1		1.3189836	0.46 E-1		1.2329000	0.50 E-1		1.2406346	0.50 E-1		1.2406346	0.28 E-1	
SP	-0.0143000	0.50 E-1		-0.0211228	0.43 E-1		-0.0597000	0.50 E-1		-0.0503297	0.50 E-1		-0.0503297	0.27 E-1	
SP	-0.0143000	0.50 E-1		-0.0226177	0.39 E-1		-0.0599000	0.50 E-1		-0.0463724	0.50 E-1		-0.0463724	0.25 E-1	
r <sub>11</sub>	5212.0502	0.80 E-2	km	5212.0504	0.53 E-2		5212.0484	0.25 E-1		5212.0474	0.25 E-1		5212.0474	0.12 E-1	
r <sub>12</sub>	3665.6280	0.10 E-1	km	3665.6240	0.97 E-2		3665.6280	0.15 E-1		3665.6240	0.15 E-1		3665.6240	0.15 E-1	
λ <sub>12</sub>	243.19457	0.10 E-3	deg	243.19457	0.55 E-4		243.19452	0.25 E-3		243.19450	0.25 E-3		243.19450	0.12 E-3	
r <sub>21</sub>	5203.9857	0.80 E-2	km	5203.9837	0.63 E-2		5203.9931	0.25 E-1		5203.9930	0.25 E-1		5203.9930	0.12 E-1	
r <sub>22</sub>	3677.0530	0.10 E-1	km	3677.0537	0.98 E-2		3677.0520	0.15 E-1		3677.0518	0.15 E-1		3677.0518	0.15 E-1	
λ <sub>11</sub>	243.11052	0.10 E-3	deg	243.11052	0.56 E-4		243.11048	0.25 E-3		243.11046	0.25 E-3		243.11046	0.12 E-3	
r <sub>31</sub>	5450.1982	0.80 E-2	km	5450.2003	0.40 E-2		5450.2009	0.25 E-1		5450.2030	0.25 E-1		5450.2030	0.12 E-1	
r <sub>32</sub>	-3302.2430	0.10 E-1	km	-3302.2408	0.97 E-2		-3302.2430	0.15 E-1		-332.2429	0.15 E-1		-332.2429	0.14 E-1	
λ <sub>21</sub>	136.88754	0.10 E-3	deg	136.88574	0.53 E-4		136.88748	0.25 E-3		136.88748	0.25 E-3		136.88748	0.12 E-3	
r <sub>41</sub>	5742.9418	0.80 E-2	km	5742.9364	0.44 E-2		5742.9399	0.25 E-1		5742.9378	0.25 E-1		5742.9378	0.13 E-1	
r <sub>42</sub>	-2768.7440	0.10 E-1	km	-2768.7440	0.10 E-1		-2768.7440	0.15 E-1		-2768.7439	0.15 E-1		-2768.7439	0.15 E-1	
λ <sub>22</sub>	27.68544	0.10 E-3	deg	27.68545	0.53 E-4		27.68540	0.25 E-3		27.68539	0.25 E-3		27.68539	0.12 E-1	
GMS	398601.30		km <sup>2</sup> /s <sup>2</sup>	398601.20			398601.20	1.0		398600.71	1.0		398600.71	0.36	
GMM	4902.7800		km <sup>2</sup> /s <sup>2</sup>	4902.7800			4902.7800	1.0		4902.8260	1.0		4902.8260	0.19	
AC <sub>2</sub>	0.0		km/s <sup>2</sup>	0.0			0.0			0.1847 E-12	0.1 E-11		0.1847 E-12	0.97 E-12	
AC <sub>3</sub>	0.0		km/s <sup>2</sup>	0.0			0.8918 E-12	0.1 E-11		0.1115 E-11	0.1 E-11		0.1115 E-11	0.95 E-12	
AC <sub>7</sub>	0.0		km/s <sup>2</sup>	0.0			0.1502 E-12	0.1 E-11		0.1822 E-11	0.1 E-11		0.1822 E-11	0.93 E-12	
B			km	32953.68	118.60					32916.58			32916.58	125.07	
B·B			km	19639.43	137.26					19850.09			19850.09	127.46	
B·F			km	27312.39	110.7					26257.85			26257.85	101.33	
F <sub>04</sub>			19+	34=43:15	55:5.5					34=25:29			34=25:29	50:18	
SMAA			km	250						133.15			133.15		
SMAA			km	175						93.72			93.72		
φ			deg	161.57						65.96			65.96		

\*Geocentric initial conditions on June 1, 1971, at 01:30:00:00, UTC.  
 †November 14, 1971.

Table 8. Pre-sporadic gas leak results

Parameter	Inflight (POSTMC-J0-E)			A priori			Estimated			A priori			Post-flight (00972L-G)			Estimated		
	Value	σ	Units	Value	σ	Units	Value	σ	Units	Value	σ	Units	Value	σ	Units	Value	σ	Units
X	1029054.70	0.10 E+5	km <sup>a</sup>	1029050.20	0.69		1029050.20	0.10 E+5		1029050.20	0.10 E+5		1029051.70	0.10 E+5		1029051.70	0.79	
Y	-778256.22	0.10 E+5	km <sup>a</sup>	-778256.30	0.76		-778256.30	0.10 E+5		-778256.30	0.10 E+5		-778256.26	0.10 E+5		-778256.26	0.96	
Z	704708.45	0.10 E+5	km <sup>a</sup>	-704707.46	1.50		-704707.46	0.10 E+5		-704709.65	0.10 E+5		-704708.02	0.10 E+5		-704708.02	1.50	
X	2.2118967	1.0	km/s <sup>a</sup>	2.2118979	0.77 E-6		2.2118979	1.0		2.2118970	1.0		2.2118961	1.0		2.2118961	0.82 E-6	
Y	-1.6187862	1.0	km/s <sup>a</sup>	-1.6187941	0.13 E-5		-1.6187941	1.0		-1.6187946	0.13 E-5		-1.6187951	0.13 E-5		-1.6187951	0.14 E-5	
Z	-1.4937248	1.0	km/s <sup>a</sup>	-1.4937140	0.15 E-5		-1.4937140	1.0		-1.4937132	0.15 E-5		-1.4937155	0.15 E-5		-1.4937155	0.16 E-5	
SP <sub>2</sub>	1.2400000	0.50 E-1	km/s <sup>a</sup>	1.2358664	0.55 E-2		1.2358664	0.50 E-1		1.2275000	0.50 E-1		1.2234083	0.50 E-1		1.2234083	0.19 E-1	
SP <sub>3</sub>	0.0150000	0.50 E-1	km/s <sup>a</sup>	-0.0149795	0.15 E-1		-0.0149795	0.50 E-1		-0.0406000	0.50 E-1		-0.0461950	0.50 E-1		-0.0461950	0.24 E-1	
SP <sub>7</sub>	0.0150000	0.50 E-1	km/s <sup>a</sup>	-0.0178877	0.13 E-1		-0.0178877	0.50 E-1		-0.0436000	0.50 E-1		-0.0515863	0.50 E-1		-0.0515863	0.22 E-1	
r <sub>2,12</sub>	5212.0502	0.50 E-1	km	5212.0486	0.19 E-2		5212.0486	0.50 E-1		5212.0484	0.25 E-1		5212.0491	0.25 E-1		5212.0491	0.21 E-2	
r <sub>2,13</sub>	3665.6280	0.15 E-1	km	3665.6257	0.15 E-1		3665.6257	0.15 E-1		3665.6280	0.15 E-1		3665.6283	0.15 E-1		3665.6283	0.15 E-1	
r <sub>2,14</sub>	243.19457	0.18 E-4	deg	243.19448	0.18 E-4		243.19448	0.18 E-4		243.19452	0.25 E-3		243.19446	0.19 E-4		243.19446	0.19 E-4	
r <sub>2,15</sub>	5203.9957	0.31 E-2	km	5203.9926	0.31 E-2		5203.9926	0.31 E-2		5203.9931	0.25 E-1		5203.9932	0.31 E-2		5203.9932	0.31 E-2	
r <sub>2,16</sub>	3677.0520	0.15 E-1	km	3677.05212	0.15 E-1		3677.05212	0.15 E-1		3677.0520	0.15 E-1		3677.05174	0.15 E-1		3677.05174	0.15 E-1	
λ <sub>2,14</sub>	243.11052	0.21 E-4	deg	243.11043	0.21 E-4		243.11043	0.21 E-4		243.11048	0.25 E-3		243.11040	0.22 E-4		243.11040	0.22 E-4	
r <sub>2,21</sub>	5450.1992	0.17 E-2	km	5450.2018	0.17 E-2		5450.2018	0.17 E-2		5450.2009	0.25 E-1		5450.2025	0.19 E-2		5450.2025	0.19 E-2	
r <sub>2,31</sub>	-3302.2430	0.15 E-1	km	-3302.2419	0.15 E-1		-3302.2419	0.15 E-1		-3302.2430	0.25 E-1		-3302.2430	0.15 E-1		-3302.2430	0.15 E-1	
λ <sub>2,31</sub>	136.88754	0.18 E-4	deg	136.88745	0.18 E-4		136.88745	0.18 E-4		136.88748	0.25 E-3		136.88742	0.19 E-4		136.88742	0.19 E-4	
r <sub>2,51</sub>	5742.9418	0.18 E-2	km	574.9371	0.18 E-2		574.9371	0.18 E-2		5742.9399	0.25 E-1		5742.9381	0.20 E-2		5742.9381	0.20 E-2	
r <sub>2,51</sub>	-2768.7440	0.14 E-1	km	-27.7428	0.14 E-1		-27.7428	0.14 E-1		-2768.7440	0.15 E-1		-2768.7440	0.15 E-1		-2768.7440	0.15 E-1	
λ <sub>2,51</sub>	27.68544	0.18 E-4	deg	27.68535	0.18 E-4		27.68535	0.18 E-4		27.68540	0.25 E-1		27.68533	0.19 E-4		27.68533	0.19 E-4	
r <sub>2,62</sub>	4860.8149	0.27 E-2	km	4860.8137	0.27 E-2		4860.8137	0.27 E-2		4860.8149	0.25 E-1		4860.8135	0.28 E-2		4860.8135	0.28 E-2	
r <sub>2,62</sub>	4116.9080	0.15 E-1	km	4116.9078	0.15 E-1		4116.9078	0.15 E-1		4116.9080	0.15 E-1		4116.9080	0.15 E-1		4116.9080	0.15 E-1	
λ <sub>2,62</sub>	355.63217	0.19 E-4	deg	355.63214	0.19 E-4		355.63214	0.19 E-4		355.63217	0.25 E-3		355.63211	0.20 E-4		355.63211	0.20 E-4	
GMM	4902.7835	1.0	km <sup>2</sup> /s <sup>2</sup>	4902.8028	0.78 E-2		4902.8028	1.0		4902.7835	1.0		4902.8027	0.83 E-2		4902.8027	0.83 E-2	
AC <sub>K</sub>	0.0		km/s <sup>2</sup>							0.0			0.2269 E-12	0.74 E-12		0.2269 E-12	0.74 E-12	
AC <sub>X</sub>	0.0		km/s <sup>2</sup>							0.6517 E-12			0.1168 E-12	0.89 E-12		0.1168 E-12	0.89 E-12	
AC <sub>Y</sub>	0.0		km/s <sup>2</sup>							0.8761 E-12			0.1831 E-11	0.84 E-12		0.1831 E-11	0.84 E-12	
B			km	8280.81	39.87		8280.81						8244.74	46.06		8244.74	46.06	
B•R			km	6076.32	53.23		6076.32						6054.53	60.56		6054.53	60.56	
B•T			km	5625.84	4.79		5625.84						5596.28	11.81		5596.28	11.81	
T <sub>C,1</sub> <sup>b</sup>			0+ +	31.22457	1.67		31.22457						31.00381	2.18		31.00381	2.18	
SMAA			km	53.23			53.23						60.58			60.58		
SMAA			km	4.69			4.69						11.73			11.73		
θ			deg	88.91			88.91						88.72			88.72		

<sup>a</sup>Geocentric initial conditions on June 5, 1971 at 01:00:00±0 UTC.

<sup>b</sup>November 14, 1971.

Table 9. Pre-unlatch results

Parameter	Units	Inflight (PREUNL-9-A)		Post-flight (UPBM17)				
		May 31, 1971, at 03 <sup>h</sup> 04 <sup>m</sup> 00 <sup>s</sup> 00 UTC		May 30, 1971, at 22 <sup>h</sup> 34 <sup>m</sup> 59 <sup>s</sup> 70 UTC				
		A priori	Estimated	A priori	Estimated			
X	km <sup>a</sup>	47134.52	47134.60	-6053.52	-6053.47	0.10 E+5	0.10 E+5	0.63 E-1
Y	km <sup>a</sup>	-59392.78	-59392.78	267.84	267.86	0.10 E+5	0.10 E+5	0.27 E-1
Z	km <sup>a</sup>	-41524.05	-41524.10	2475.59	2475.61	0.10 E+5	0.10 E+5	0.82 E-1
Ẋ	km/s <sup>a</sup>	2.9520881	2.9520845	-1.9974769	-1.9974933	1.0	1.0	0.41 E-4
Ẏ	km/s <sup>a</sup>	-2.3281361	-2.3281367	-10.7476580	-10.7477000	1.0	1.0	0.92 E-4
Ż	km/s <sup>a</sup>	-2.0602463	-2.0602486	-3.3885799	-3.3885147	1.0	1.0	0.20 E-3
SP <sub>z</sub>		1.3249000		1.2329000	1.2330742	0.30 E-1	0.30 E-1	0.30 E-1
SP <sub>x</sub>		-0.0143000		-0.0597000	-0.0594831	0.30 E-1	0.30 E-1	0.30 E-1
SP <sub>y</sub>		-0.0143000		-0.0598000	-0.0593701	0.30 E-1	0.30 E-1	0.30 E-1
r <sub>014</sub>	km	5203.9857		5203.9931	5203.9920	0.25 E-1	0.25 E-1	0.12 E-1
z <sub>14</sub>	km	3677.0520		3677.0520	3677.0538	0.15 E-1	0.15 E-1	0.15 E-1
λ <sub>14</sub>	deg	243.11052		243.11048	243.11044	0.25 E-3	0.25 E-3	0.13 E-3
r <sub>011</sub>	km	5450.1992		5450.2009	5450.2044	0.25 E-1	0.25 E-1	0.12 E-1
z <sub>11</sub>	km	-3302.2430		-3302.2430	-3302.2429	0.15 E-1	0.15 E-1	0.15 E-1
λ <sub>11</sub>	deg	136.88754		136.88748	136.88747	0.25 E-3	0.25 E-3	0.15 E-3
r <sub>011</sub>	km	5742.9416		5742.9399	5742.9380	0.25 E-1	0.25 E-1	0.14 E-1
z <sub>11</sub>	km	-2768.7440		-2768.7440	-2768.7431	0.15 E-1	0.15 E-1	0.15 E-1
λ <sub>11</sub>	deg	27.68544		27.68540	27.68541	0.25 E-3	0.25 E-3	0.13 E-1
r <sub>012</sub>	km	4860.8149		4860.8149	4860.8072	0.25 E-1	0.25 E-1	0.17 E-1
z <sub>12</sub>	km	4116.9080		4116.9080	4116.9079	0.15 E-1	0.15 E-1	0.15 E-1
λ <sub>12</sub>	deg	355.63217		355.63217	355.63220	0.25 E-3	0.25 E-3	0.17 E-3
GMM3	km <sup>2</sup> /s <sup>2</sup>	398601.20		398601.20	398600.67	1.0	1.0	0.23
GMM	km <sup>2</sup> /s <sup>2</sup>	4702.7800		4902.7835	4902.7853	1.0	1.0	0.20
AC <sub>z</sub>	km/s <sup>2</sup>	0.0		0.0	0.4136 E-14	0.10 E-11	0.10 E-11	0.10 E-11
AC <sub>x</sub>	km/s <sup>2</sup>	0.0		0.8918 E-12	0.8981 E-12	0.10 E-11	0.10 E-11	0.10 E-11
AC <sub>y</sub>	km/s <sup>2</sup>	0.0		0.1502 E-11	0.1512 E-11	0.10 E-11	0.10 E-11	0.10 E-11
B	km		32943.73		33033.29			155.00
B · $\hat{e}_z$	km		19843.28		19869.51			132.04
B · $\hat{e}_x$	km		26297.03		26389.41			149.53
T <sub>CA</sub> <sup>b</sup>	19 <sup>h</sup> + km		34 <sup>m</sup> 32 <sup>s</sup> 31		37 <sup>m</sup> 11 <sup>s</sup> 75			7788
SM <sub>AA</sub>	km		344.02		157.64			
SM <sub>IA</sub>	km		90.02		122.24			
σ	deg		20.00		30.092			

<sup>a</sup>Geocentric inertial conditions.

<sup>b</sup>November 14, 1971.

Table 10. Comparison of B-plane parameters for pre-unlatch orbits, adjusted for unlatch and maneuver  $\Delta$ 's

A	B	C	D	E	F
Parameter	Current best estimate	Inflight pre-unlatch	$\Delta(C-B)$	Post-flight pre-unlatch	$\Delta(E-B)$
$ B $ , km	8261.4	8233.6	-27.8	8315.6	54.2
$B \cdot \hat{R}$ , km	6081.8	6066.2	-15.6	6092.4	10.6
$B \cdot \hat{T}$ , km	5591.3	5567.2	-24.1	5659.6	68.3
$T_{CA}^a$ , 0 <sup>h</sup> +	31 <sup>m</sup> 08:72	29 <sup>m</sup> 16:26	-112:46	31 <sup>m</sup> 55:68	46:96
Run identification	MOI08A	PREUNL-9-A		UPBM17	

<sup>a</sup>November 14, 1971.

Table 11. Orbit changes caused by scan platform unlatch and engine gas line venting (Run UPBM16)

Velocity changes	B-plane changes
$\Delta V_x = 2.99 \pm 1.63$ mm/s	$\Delta B  = -25.82$ km
$\Delta V_y = 2.82 \pm 1.38$ mm/s	$\Delta B \cdot \hat{R} = 2.62$ km
$\Delta V_z = -0.13 \pm 2.64$ mm/s	$\Delta B \cdot \hat{T} = -34.34$ km
$ \Delta V  = 4.11$ mm/s	$\Delta T_{CA} = -0:70$

Table 12. Comparison of B-plane parameters for pre-midcourse orbits, adjusted for maneuver  $\Delta$ 's

A	B	C	D	E	F	G	H
Parameter	CBE	Inflight post-unlatch	$\Delta(C-B)$	Post-flight post-unlatch	$\Delta(E-B)$	Post-flight pre- and post-unlatch	$\Delta(G-B)$
$ B $ , km	8261.4	8260.3	-0.9	8231.1	-30.3	8288.7	27.3
$B \cdot \hat{R}$	6081.8	6055.6	-26.2	6066.3	-15.5	6121.0	39.2
$B \cdot \hat{T}$	5591.3	5618.0	26.7	5563.4	-27.9	5588.8	-2.5
$T_{CA}^a$ , 0 <sup>h</sup> +	31 <sup>m</sup> 08:72	29 <sup>m</sup> 27:61	-101:11	31 <sup>m</sup> 09:75	1:03	31 <sup>m</sup> 25:61	16:89
Run identification	MOI08A	PREM/C-10-C		PRE017-E		UPBM18	

<sup>a</sup>November 14, 1971.

Table 13. Differences between current best estimate of encounter orbit and final aiming point for the maneuver

Parameter	A	B	C	D	E	F
$B \cdot \hat{R}$ , km	18.8	14.9	-4.2	15.1	73.7	-80.7
$B \cdot \hat{T}$ , km	73.3	-34.9	-19.7	4.3	-137.8	-114.9
$T_{CA}$ , s	138.72	-3.64	105.98	-0.43	20.86	16.1

**Table 14. Commanded midcourse maneuver and current best estimate of achieved maneuver**

Parameter	Commanded	Current best estimate (UPPBM6)	$\Delta$ Commanded current best estimate
$\Delta V_x$ , m/s	2.707	2.695 $\pm$ 0.0013	0.012
$\Delta V_y$ , m/s	-4.682	-4.696 $\pm$ 0.0016	0.014
$\Delta V_z$ , m/s	-4.007	-3.997 $\pm$ 0.0018	-0.010
$ \Delta V $ , m/s	6.731	6.730	0.001

**Table 18. Predicted B-plane parameters at MOI - 2 h**

A	B	C	D
Parameter	Current best estimate MOI08A	Long-arc radio POSTMC-56-A	Short-arc radio POSTMC-57-A
$ B $ , km	8261.4	8231.1	8275.8
$B \cdot \hat{R}$ , km	6081.8	6036.5	6125.0
$B \cdot \hat{T}$ , km	5591.3	5595.5	5566.4
$T_{CA}$ , $^{\circ}0^h+$	31 <sup>m</sup> 08 <sup>s</sup> 72	31 <sup>m</sup> 03 <sup>s</sup> 27	31 <sup>m</sup> 07 <sup>s</sup> 3

<sup>a</sup>November 14, 1971.

**Table 15. Comparison of B-plane estimates using different ephemerides**

Orbit	POSTMC-32	POSTMC-39	$\Delta$ solution	$\Delta$ trajectory	POSTMC-48	POSTMC-50	$\Delta$ solution	$\Delta$ trajectory
Ephemeris	DE69	DE78	(DE78 - DE69)		DE78	DE79	(DE79 - DE78)	
$ B $ , km	8279.4	8209.0	-70.4	-51.4	8206.2	8232.5	26.4	25.3
$B \cdot \hat{R}$ , km	6080.7	6011.2	-69.5	-53.2	6007.7	6038.8	31.1	33.6
$B \cdot \hat{T}$ , km	5618.9	5590.4	-28.5	-18.1	5590.0	5595.3	5.2	0.9
$T_{CA}$ , $^{\circ}0^h+$	32 <sup>m</sup> 16 <sup>s</sup> 1	31 <sup>m</sup> 15 <sup>s</sup> 7	0.4	-10.9	31 <sup>m</sup> 04 <sup>s</sup> 2	31 <sup>m</sup> 03 <sup>s</sup> 2	-1.0	0.2

<sup>a</sup>November 14, 1971.

**Table 16. Comparison of AC coefficients using post-midcourse data**

A	B	C	D	E	F
Parameter	Post-flight post-midcourse current best estimate	AC subsystem engineers	$\Delta(B-C)$	Inflight post-midcourse	$\Delta(B-E)$
$AC_R$ , km/s <sup>2</sup>	0.2239 E-12	0.0	0.2269 E-12	0.0	0.2269 E-12
$AC_x$ , km/s <sup>2</sup>	0.1168 E-11	0.2401 E-12	0.0928 E-11	0.8918 E-12	0.0277 E-11
$AC_y$ , km/s <sup>2</sup>	0.1831 E-11	0.6254 E-12	0.1206 E-11	0.1502 E-11	0.0329 E-11
Run identification	00972L-C			SKW789A	

**Table 17. Predicted B-plane parameters at MOI - 12 h**

A	B	C	D	E	F
Parameter	Current best estimate MOI08A	Long-arc radio POSTMC-52-A	Short-arc radio POSTMC-53-A	Optical ODAP-POS12	Radio + Optical GH009
$ B $ , km	8261.4	8232.4	8291.0	8265.9	8260.1
$B \cdot \hat{R}$ , km	6081.8	6036.5	6149.2	6033.0	6079.3
$B \cdot \hat{T}$ , km	5591.3	5595.3	5561.3	5651.3	5592.0
$T_{CA}$ , $^{\circ}0^h+$	31 <sup>m</sup> 08 <sup>s</sup> 72	31 <sup>m</sup> 03 <sup>s</sup> 19	31 <sup>m</sup> 06 <sup>s</sup> 99	29 <sup>m</sup> 50 <sup>s</sup> 0	31 <sup>m</sup> 18 <sup>s</sup> 65

<sup>a</sup>November 14, 1971.

Table 19. Predicted B-plane parameters for selected radio-only solutions

A	B	C	D	E	F	G	H	I
Run identification, POSTMC-xx	Parameter set <sup>a</sup>	Time of last data point used (1971)	$ B $ , km	$B \cdot \hat{R}$ , km	$B \cdot \hat{T}$ , km	$T_{11}$ (11/14/71), h:min:s	Doppler/range <sup>b</sup>	Arce
1	A	06/05 135000	8770.10	6800.99	5537.25	00:34:39.86		L
2	A	06/05 195332	8345.26	6196.60	5589.76			L
3	A	06/07 150302	8279.73	6119.98	5576.71	00:29:41.90		L
4	A	06/08 152302	8322.75	6114.34	5646.51	00:30:06.35		L
4	C	06/08 152302	8272.17	6049.78	5641.71	00:30:00.38		L
4	A	06/08 152302	8333.74	6099.75	5678.41	00:30:08.16	D	L
4	C	06/08 152302	8289.18	6055.61	5660.40	00:30:02.58	D	I
5	A	06/10 143802	8258.79	6072.66	5598.00	00:29:50.47		L
5	C	06/10 143802	8279.84	6017.94	5686.34	00:30:03.96		L
6	A	06/14 144602	8225.27	6058.76	5562.95	00:29:48.82		L
6	C	06/14 144602	8244.98	6011.36	5642.99	00:30:16.53		L
7	A	06/17 152702	8279.55	6036.38	5666.85	00:30:16.43		L
7	C	06/17 152702	8213.21	6015.25	5592.28	00:30:51.99		L
8	A	06/21 144002	8240.66	6029.85	5616.88	00:30:18.50		L
8	C	06/21 144002	8188.88	5995.75	5577.52	00:30:16.50		L
8	A	06/21 144002	8274.50	6064.10	5629.74	00:30:09.19	D	L
8	C	06/21 144002	8265.76	6041.69	5640.99	00:30:34.35	D	L
9	A	06/21 144002	8200.49	6002.52	5587.29	00:30:05.77	R	L
9	C	06/21 144002	8245.87	6047.52	5605.51	00:30:30.72	R	L
10	A	06/23 164702	8200.25	6017.55	5570.75	00:30:21.14		L
10	C	06/23 164702	8181.62	5975.05	5589.08	00:30:08.72		L
10	A	06/23 164702	8245.15	6055.96	5595.34	00:30:19.53	D	L
10	C	06/23 164702	8264.19	6027.36	5654.00	00:30:33.16	D	L
12	A	06/25 171002	8201.95	6017.07	5573.76	00:30:24.68		L
12	C	06/25 171002	8178.04	5966.63	5592.82	00:30:04.43		L
12	A	06/25 171002	8247.34	6055.99	5598.53	00:30:32.34	D	L
12	C	06/25 171002	8262.27	6022.26	5656.63	00:30:36.91	D	L
14	A	06/29 164602	8201.12	6013.94	5575.92	00:30:23.22		L
14	C	06/29 164602	8182.96	5970.85	5595.52	00:30:19.68		L
14	A	06/29 164602	8247.73	6052.75	5602.61	00:30:31.75	D	L
14	C	06/29 164602	8283.09	6045.74	5662.03	00:30:55.68	D	L
14	E	06/29 164602	8263.01	6052.34	5625.53	00:31:01.80	D	L
15	C	07/01 145002	8254.41	6032.07	5634.66	00:30:38.44		L
15	E	07/01 145002	8261.27	6050.03	5625.45	00:30:47.89		L
15	C	07/01 145002	8295.64	6057.19	5665.25	00:30:59.38	D	L
15	E	07/01 145002	8271.45	6058.06	5631.77	00:31:01.48	D	L
15	C	07/01 145002	8255.79	6037.86	5630.48	00:30:41.64	R	L
15	E	07/01 145002	8242.91	6060.79	5586.80	00:30:59.78	R	L
16	C	07/06 223102	8285.45	6058.46	5651.88	00:30:56.41		L
16	E	07/06 223102	8254.03	6041.77	5623.71	00:30:47.32		L

<sup>a</sup>From Table 5.

<sup>b</sup>D = doppler only; R = range only; blank = doppler and range.

<sup>c</sup>L = long; I = intermediate; S = short.

Table 19 (contd)

A	B	C		D	E	F	G	H	I
Run identification, POSTMC-xx	Parameter set <sup>a</sup>	Time of last data point used (1971)		$ B $ , km	$B \cdot \hat{R}$ , km	$B \cdot \hat{T}$ , km	$T_{CA}$ (11/14/71), h:min:s	Doppler/range <sup>b</sup>	Arc <sup>c</sup>
16	C	07/06	223102	8334.88	6093.96	5686.29	00:31:12.53	D	L
16	E	07/06	223102	8289.20	6069.88	5645.11	00:31:00.91	D	L
18	C	07/13	155302	8368.72	6118.06	5710.07	00:31:21.88		L
18	E	07/13	155302	8305.09	6077.50	5660.25	00:30:59.02		L
18	C	07/13	155302	8367.90	6111.74	5715.63	00:31:30.66	D	L
18	E	07/13	155302	8294.24	6065.41	5657.32	00:31:07.83	D	L
19	E	07/15	165002	8316.46	6088.87	5664.73	00:31:02.02		L
20	E	07/20	212502	8357.23	6117.82	5693.16	00:31:23.26	D	L
21	E	07/20	212502	8379.02	6142.41	5699.01	00:31:17.92		L
22	E	07/26	150302	8343.31	6166.25	5620.34	00:31:21.88		L
22	E	07/26	150302	8514.28	6097.66	5652.06	00:31:09.54	D	L
23	E	07/26	150302	8299.09	6085.74	5642.57	00:30:57.16		L
24	E	08/04	201502	8293.80	6091.48	5626.59	00:31:22.09		L
24	F	08/04	201502	8290.30	6089.71	5625.33	00:31:22.45		L
25	E	08/10	203602	8285.10	6083.42	5624.49	00:31:31.76		L
25	F	08/10	203602	8264.25	6061.59	5618.42	00:31:21.78	D	L
26	E	08/14	101802	8282.84	6079.26	5625.65	00:31:22.62		L
26	E	08/14	101802	8260.45	6054.93	5618.97	00:31:22.27	D	L
26	E	08/14	101802	8301.91	6107.16	5623.55	00:31:20.31	R	L
27	E	08/22	212402	8282.27	6075.86	5628.48	00:31:23.78		L
27	E	08/22	212402	8258.72	6048.27	5623.59	00:31:23.68	D	L
28	E	08/31	170602	8265.68	6055.93	5626.28	00:31:24.55		L
28	E	08/31	170602	8250.92	6039.49	5621.58	00:31:23.11	D	L
30	E	09/12	231642	8280.81	6076.32	5625.84	00:31:22.57		L
30	E	09/12	231642	8259.14	6051.62	5620.62	00:31:22.21	D	L
31	A	09/28	233252	8281.60	6081.47	5621.44	00:31:16.42		L
31	E	09/28	233252	8266.14	6079.24	5601.06	00:31:16.11		L
32	A	10/07	040000	8279.36	6080.73	5618.95	00:31:16.11		L
32	E	10/07	040000	8275.00	6097.80	5593.97	00:31:15.56		L
32	G	09/15	000000	8274.95	6075.77	5617.81	00:31:17.42		L
35	A	10/13	162402	8234.56	6051.98	5584.04	00:31:14.70	D	L
35	G	10/13	162402	8240.19	6059.58	5584.11	00:31:13.23	D	I
37	A	10/13	000000	8252.02	6063.53	5597.27	00:31:03.32	R	L
38	A	09/15	000000	8240.24	6027.71	5618.57	00:31:06.55	D	L
38	G	09/15	000000	8199.14	5991.40	5597.23	00:31:05.55	D	L
39	A	10/31	000000	8208.98	6011.22	5590.41	00:31:15.74		L
39	G	10/31	000000	8180.92	6004.24	5556.67	00:31:17.81		L
39	A	11/01	070000	8218.54	6018.73	5596.37	00:31:04.84	D	L
39	A	09/15	000000	8231.49	6018.76	5615.32	00:31:18.70		L
41	A	11/07	000000	8279.04	6112.77	5583.59	00:31:01.15		I
41	C	11/07	000000	8173.53	6025.62	5522.33	00:31:10.17		I
42	A	11/07	000000	8203.41	6004.71	5589.22	00:31:46.64		L
43	A	11/07	000000	8207.54	6028.89	5569.21	00:31:07.36		I
43	C	11/07	000000	8234.87	6055.22	5580.99	00:31:05.34		I

Table 19 (contd)

A	B	C	D	E	F	G	H	I
Run identification, POSTMC-xx	Parameter set <sup>a</sup>	Time of last data point used (1971)	$B_1$ , km	$B \cdot \hat{R}$ , km	$B \cdot \hat{T}$ , km	$T_{11}$ (11/14/71), h:mm:ss	Doppler/range <sup>b</sup>	Arc <sup>c</sup>
44	A	11/08 140000	8227.83	6063.19	5561.91	00:31:07.07		I
44	C	11/08 140000	8221.18	6040.10	5577.18	00:31:06.16		I
45	A	11/10 190000	8284.64	6145.56	5555.84	00:31:06.40		I
45	C	11/10 190000	8444.29	6341.22	5576.28	00:30:58.41		I
45	C	11/10 190000	8313.21	6180.02	5560.29	00:30:48.45	D	I
46	A	11/10 190000	8200.96	6014.00	5588.84	00:31:04.24		L
46	A	11/10 190000	8224.38	6036.16	5586.16	00:31:03.54	R	L
48	A	11/12 000000	8206.17	6007.70	5590.05	00:31:04.19		L
50	A	11/13 061800	8232.53	6038.81	5595.29	00:31:03.19		I
50	A	11/13 061800	8226.46	6032.87	5592.77	00:31:05.16	D	L
51	A	11/13 061800	8260.46	6098.03	5572.19	00:31:03.75		S
51	F	11/13 061800	8305.98	6174.12	5556.03	00:31:03.19		S
51	A	11/13 061800	8056.49	5964.47	5415.92	00:30:53.24	D	S
51	F	11/13 061800	8194.75	6101.64	5470.28	00:30:59.00	D	S
52	A	11/13 101800	8232.36	6038.52	5595.35	00:31:03.19		L
52	A	11/13 101800	8226.66	6033.12	5592.79	00:31:05.12	D	L
53	A	11/13 101800	8290.97	6149.18	5561.27	00:31:06.99		S
53	F	11/13 101800	8336.28	6224.85	5544.80	00:31:06.48		S
53	A	11/13 101800	8152.69	6075.99	5435.87	00:31:01.44	D	S
53	F	11/13 101800	8313.43	6226.14	5508.93	00:31:04.93	D	S
54	A	11/13 141800	8231.70	6037.52	5595.47	00:31:03.23		L
54	A	11/13 141800	8226.93	6033.46	5592.83	00:31:05.08	D	L
55	A	11/13 141800	8286.25	6142.08	5562.08	00:31:07.04		S
55	F	11/13 141800	8314.44	6188.90	5552.25	00:31:06.78		S
56	A	11/13 161800	8230.97	6036.49	5595.51	00:31:03.28		L
56	A	11/13 161800	8226.96	6033.49	5592.84	00:31:05.07	D	L
57	A	11/13 161800	8275.84	6125.03	5565.39	00:31:07.31		S
57	F	11/13 161800	8275.79	6124.78	5565.44	00:31:07.31		S
57	A	11/13 161800	8280.14	6192.86	5496.29	00:31:04.67	D	S
57	F	11/13 161800	8280.06	6188.95	5500.57	00:31:04.83	D	S
58	A	11/13 201800	8261.27	6103.32	5567.60	00:31:11.49		S
59	A	11/13 214800	8261.85	6104.13	5567.56	00:31:07.87		S
59	F	11/13 214800	8261.81	6104.14	5567.50	00:31:07.88		S
60	A	11/13 234800	8262.43	6104.97	5567.51	00:31:07.92		S
60	F	11/13 234800	8262.27	6104.78	5567.48	00:31:07.93		S
60	A	11/13 234800	8262.59	6111.60	5560.47	00:31:07.67	D	S
60	F	11/13 234800	8262.21	6101.79	5570.61	00:31:08.04	D	S

Table 20. Solutions supporting current best estimate of B-plane parameters

A	B	C	D	E
Parameter	Long arc 001009-H	Long arc 001009-A	Short arc MOI 5d → MOI-45m E001WL	CBE short arc MOI-5d → MOI+10h MOI03A
B , km	8261.7	8269.8	8262.0	8261.4
$B \cdot \hat{R}$ , km	6083.0	6100.6	6087.0	6081.8
$B \cdot \hat{T}$ , km	5590.5	5583.2	5586.6	5591.3
$T_{OA}$ , <sup>a</sup> 0h+	31 <sup>m</sup> 09:52	31 <sup>m</sup> 08:50	31 <sup>m</sup> 05:54	31 <sup>m</sup> 08:72

<sup>a</sup>November 14, 1971.

Table 21. Comparison of estimated maneuver parameters<sup>a</sup>

A	B	C	D	E	F
Parameter	Commanded maneuver	A priori from telemetry	Strategy 1	Strategy 2	Strategy 3
$F_0$		$0.13290676 \times 10^4$	$0.13363450 \times 10^4$	$0.1331191 \times 10^4$	$0.13298025 \times 10^4$
$F_1$		$-0.70234773 \times 10^{-1}$	$-0.70679196 \times 10^{-1}$	$-0.70067575 \times 10^{-1}$	$-0.69835305 \times 10^{-1}$
$F_2$		$0.29411911 \times 10^{-3}$	$0.28530662 \times 10^{-3}$	$0.29473017 \times 10^{-3}$	$0.29352292 \times 10^{-3}$
$F_3$		$-0.41188397 \times 10^{-6}$	$-0.42682422 \times 10^{-6}$	$-0.41235486 \times 10^{-6}$	$-0.41060609 \times 10^{-6}$
$F_4$		$0.19269307 \times 10^{-9}$	$0.18995661 \times 10^{-9}$	$0.19246737 \times 10^{-9}$	$0.19385616 \times 10^{-9}$
$\alpha$ , rad		2.5365863	2.5361710	2.5364832	2.5366572
$\delta$ , rad		0.20075508	0.19982343	0.20028938	0.20052894
$T$ , s		( $ \Delta V $ cutoff)	( $ \Delta V $ cutoff)	914.7534	915.2659
$ \Delta V $ , m/s	1600.500	1600.685	1600.685	1601.853	1601.912
Roll turn, deg	42.765		42.519	42.557	42.578
Yaw turn, deg	124.898		125.206	125.215	125.221
Run identification			MOI91G	MOI08A	MOI05W

<sup>a</sup>For all the solutions, the other applicable burn parameters were:

$$\begin{aligned}
 T_0 &= \text{Nov. 14, 1971, } 0^{\text{h}}18^{\text{m}}20^{\text{s}}5111 \text{ ET} & \dot{M}_1 &= 72692513 \times 10^{-9} \\
 M_0 &= 995 \text{ kg} & \dot{M}_2 &= 0.11812921 \times 10^{-9} \\
 \dot{M}_0 &= 0.46951544 & \dot{M}_3 &= -0.24449644 \times 10^{-12}
 \end{aligned}$$

Table 22. Determinations of GM Earth from Mariner 9 data

Source	GM Earth, km <sup>3</sup> /s <sup>2</sup>	Standard deviation, km <sup>3</sup> /s <sup>2</sup>	Run identi- fication
Data span 1	398600.67	0.226	UPBM17
Data span 2	398600.67	0.150	UPBM18
Data span 3	398600.75	0.133	UPPBM6
Data span 4	398600.71	0.359	PRE017

Table 23. Influence of consider parameters on GM Earth determination

Consider parameter	Assumed uncertainty	Absolute value of change in GM Earth, km <sup>3</sup> /s <sup>2</sup>
$AC_R, AC_X, AC_Y$ , km/s <sup>2</sup>	$0.5 \times 10^{-11}$	0.06, 0.08, 0.10
$z$ (DSS 51), m	30.0	0.05
GM Moon, km <sup>3</sup> /s <sup>2</sup>	0.05	0.004
$J_2, J_3, J_4$	$0.5 \times 10^{-7}$	Negligible
$C_{2,2}, S_{2,2}$	$0.5 \times 10^{-7}$	0.001, 0.001
Earth orbital elements (set 3)	$1.0 \times 10^{-7}$	Negligible
Moon orbital elements (set 3)	$0.12 \times 10^{-5}$	Negligible
Astronomical unit	3.0 km	Negligible

Table 24. DSS locations determined from interplanetary data

Station	DSS 18	DSS 14	DSS 41	DSS 51	DSS 62
Base, deg	243.194xxx	243.110xxx	136.887xxx	27.685xxx	355.632xxx
A priori	5303	4804	4774	3956	1713
Pre-midcourse	5046 ± 1244	4599 ± 1247	4850 ± 1244	3904 ± 1243	
Post-midcourse	4567 ± 0188	4033 ± 0222	4198 ± 0187	3283 ± 0185	1093 ± 0199
Pre-encounter	4418 ± 0291	3982 ± 0331	4043 ± 0279		0853 ± 0295
Pre- and post-encounter	4458 ± 0181	3992 ± 0232	4058 ± 0160		0900 ± 0185
Base, km	5312.0 xxx	5203.9 xxx	5450.2 xxx	5742.9 xxx	4860.8 xxx
A priori	4837	9310	0091	3990	1487
Pre-midcourse	4770 ± 1211	9297 ± 1232	0296 ± 1249	3785 ± 1317	
Post-midcourse	4912 ± 0208	9320 ± 0316	0252 ± 0195	3809 ± 0205	1351 ± 0275
Pre-encounter	4859 ± 0090	9663 ± 0362	0396 ± 0089		1719 ± 0091
Pre- and post-encounter	4899 ± 0076	9754 ± 0342	0422 ± 0076		1774 ± 0079
Base, km	3663.6 xxx	3677.0 xxx	-3302.2 xxx	-2768.7 xxx	4116.9 xxx
A priori	2900	5990	4300	4400	0800
Pre-midcourse	2798 ± 1500	5178 ± 1500	4291 ± 1500	4392 ± 1500	
Post-midcourse	2630 ± 1492	5174 ± 1492	4304 ± 1500	4401 ± 1500	0799 ± 1500
Pre-encounter	2798 ± 0800	5200 ± 0800	4295 ± 0800		0799 ± 0800

Table 25. Torque directions around spacecraft axes caused by individual roll-jet thrusts

Label in Fig. 16	Direction jet exhaust points	Direction of spacecraft motion in roll caused by jet firing	Roll torque	Pitch torque	Yaw torque	Location of jet in spacecraft coordinates
a	CW	CCW	+	+	+	-X
b	CCW	CW	-	-	+	-X
c	CCW	CW	-	+	-	+X
d	CW	CCW	+	-	-	+X

Table 26. Current best estimate of accelerations during interplanetary phase induced by roll-jet leak

Date (1971)	Time, GMT h:m	$a$ , DN/s <sup>2</sup>	$T$ , N $\times 10^6$ ( $\mu$ lb)	$\Delta AC_x$ , km/s <sup>2</sup> $\times 10^{12}$	$\Delta AC_y$ , km/s <sup>2</sup> $\times 10^{12}$
9/15	13:55	$-0.14 \times 10^{-3}$	2.68 (5.9)	10.1	-26.3
	23:15	$-0.48 \times 10^{-3}$	0.91 (2.0)	3.4	-8.9
9/21	20:25	$-0.80 \times 10^{-4}$	1.54 (3.4)	5.8	-15.2
9/22	02:30	$-0.45 \times 10^{-4}$	0.86 (1.9)	3.3	-8.5
9/24	09:17	$-0.70 \times 10^{-4}$	1.36 (3.0)	5.1	-13.4
	12:48	$-0.45 \times 10^{-4}$	0.86 (1.9)	3.3	-8.5
10/03	21:36	$-0.82 \times 10^{-4}$	1.59 (3.5)	6.0	-15.6
10/04	05:10	$-0.37 \times 10^{-4}$	0.73 (1.6)	2.7	-7.1
10/25	04:16	$-0.20 \times 10^{-3}$	3.85 (8.5)	14.5	-38.0
	20:16	$-0.20 \times 10^{-3}$	3.85 (8.5)	14.5	-38.0
10/26	06:18	$-0.58 \times 10^{-4}$	1.13 (2.5)	4.3	-11.2
10/27	11:36	$-0.51 \times 10^{-4}$	1.00 (2.2)	3.6	-8.3
10/27	22:36	$-0.10 \times 10^{-3}$	1.91 (4.2)	7.2	-18.8
	23:34	$-0.50 \times 10^{-4}$	0.95 (2.1)	3.6	-9.4
10/28	21:42	$-0.80 \times 10^{-4}$	1.54 (3.4)	5.8	-15.2
11/02	16:00	$-0.65 \times 10^{-4}$	1.22 (2.7)	4.6	-12.1
11/05	03:19	$-0.60 \times 10^{-4}$	1.91 (4.2)	7.2	-18.8
	20:23	$-0.42 \times 10^{-4}$	0.82 (1.8)	3.1	-8.0
11/05	21:42	$-0.65 \times 10^{-4}$	1.27 (2.8)	4.8	-12.5
11/07	00:03	$-0.36 \times 10^{-4}$	0.68 (1.5)	2.6	-6.7
11/07	12:26	$-0.11 \times 10^{-3}$	2.04 (4.5)	7.7	-20.1
11/08	14:29	$-0.48 \times 10^{-4}$	0.91 (2.0)	3.4	-8.9
11/09	02:10	$-0.43 \times 10^{-4}$	0.82 (1.8)	3.1	-8.0
	03:09	$-0.40 \times 10^{-4}$	0.77 (1.7)	2.9	-7.6
11/09	10:10	$-0.75 \times 10^{-4}$	1.45 (3.2)	5.5	-14.3
11/10	13:21	$-0.56 \times 10^{-4}$	1.09 (2.4)	4.1	-10.7
11/11	16:49	$-0.20 \times 10^{-3}$	3.85 (8.5)	14.6	-37.9
	22:48	$-0.15 \times 10^{-3}$	2.46 (5.5)	9.4	-24.5
11/12	23:54	$-0.10 \times 10^{-3}$	1.91 (4.2)	7.2	-18.8
11/13	19:17	$-0.48 \times 10^{-4}$	0.91 (2.0)	3.4	-8.9
11/14	01:41	$-0.36 \times 10^{-4}$	0.50 (1.1)	1.9	-4.9
	03:51	$-0.36 \times 10^{-4}$	0.50 (1.1)	1.9	-4.9

**Table 27. Formation of certain radiometric data types**

Data type	Transmitter function	Spacecraft function	Receiver function	Formation of data
Doppler	Transmit signal with frequency ( $f_t$ ) generated by transmitting station frequency standard	Receive signal and retransmit via transponder	Receive signal with frequency $f_r$ , and compare with station frequency standard $f_s$	$f_r - f_s$
Range	Transmit range code at time $t_t$ as measured by transmitting station's clock	Receive signal and retransmit via transponder	Receive signal at time $t_r$ , as measured by receiving station's clock	$t_r - t_t$

**Table 28. Summary of data used in dual-station experiment**

Data type	DSS 12	DSS 41	Subtotal
Overlap F2	295	130	425
Meridian passage F2	130	65	195
F3	36	180	216
F2 - F3	35	170	205
MU	14	0	14
Total	510	385	895

Table 29. Estimated frequency offsets in mHz from F3, F2, and MU solutions

Solution code (Table 5)	Weight code <sup>a</sup>	Oct. 4		Oct. 23		Oct. 29		Nov. 6
		DSS 12	DSS 41	F3 12	DSS 41	DSS 12	DSS 41	DSS 41
A	1	4.86	3.42	-6.07	-8.63	5.13	2.41	-2.20
	2	4.97	3.58	-5.86	-8.42	5.25	2.55	-2.28
	3	5.70	4.35	-5.64	-8.20	5.24	2.58	-2.62
B	1	4.66	3.11	-5.97	-8.54	5.08	2.34	-2.24
	2	4.86	3.38	-5.82	-8.39	5.24	2.53	-2.30
	3	5.63	4.22	-5.62	-8.17	5.24	2.58	-2.64
J	1	4.82	2.74	-1.84	-4.41	5.38	2.59	-3.89
	2	4.78	2.89	-1.53	-4.10	5.53	2.77	-3.86
	3	5.04	3.08	-0.86	-3.44	5.90	2.84	-4.01
C	1	1.86	0.37	-6.94	-9.20	3.65	1.85	-4.17
	2	1.94	0.10	-6.82	-9.26	3.63	1.45	-4.45
	3	2.92	0.59	-6.16	-8.83	4.05	1.96	-4.41
E	1	2.09	0.56	-4.10	-6.41	3.58	1.62	-5.35
	2	2.24	0.49	-3.74	-6.20	3.56	1.26	-5.65
	3	3.03	0.95	-2.36	-4.99	4.12	1.37	-5.50
G	1	2.02	0.42	-4.07	-6.38	3.60	1.66	-5.28
	2	2.14	0.20	-3.79	-6.25	3.61	1.33	-5.62
H	1	2.03	0.41	-4.06	-6.38	3.61	1.66	-5.27
	2	2.13	0.24	-3.78	-6.24	3.61	1.33	-5.61
	3	1.88	-0.20	-2.80	-5.43	4.33	1.60	-5.31

<sup>a</sup>Weight code:

	F2	F3	MU
1	0.015 Hz	0.075 Hz	150 m
2	0.030 Hz	0.015 Hz	150 m
3	0.075 Hz	0.015 Hz	150 m

Table 30. Deimos coverage

Number in Fig. 44	POS	Time before insertion, h	Mean anomaly, deg	Number in Fig. 44	POS	Time before insertion, h	Mean anomaly, deg
1	I	66.0	95 <sup>a</sup>	10	II	29.0	176
2	I	53.0	180	11	II	26.0	196
3	I	57.0	204	12	II	26.0	212
4	I	55.0	228	13	II	22.0	271
5	I	54.0	243	14	III	16.5	285
6	I	53.0	256	15	III	16.4	287
7	II	36.0	98	16	III	12.0	18
8	II	65.0	104	17	III	10.0	43
9	II	64.0	116	18	III	9.0	89

<sup>a</sup>Lost during playback.

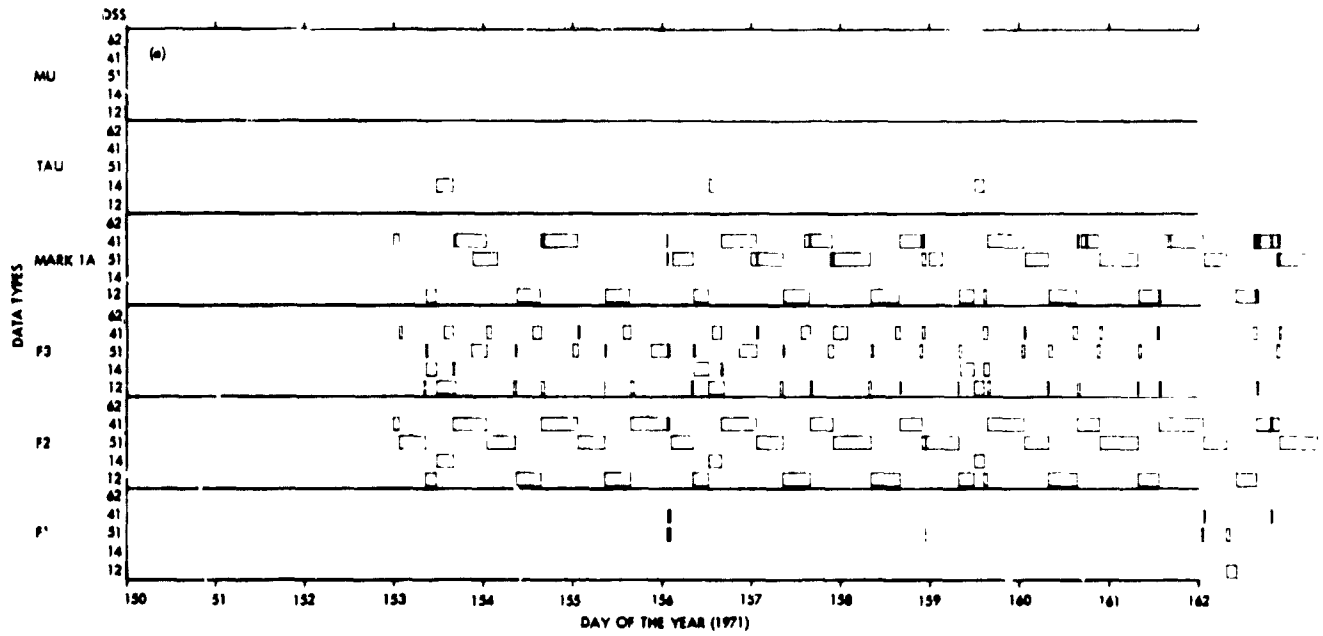


Fig. 1. Tracking coverage provided by the DSN for MM'71 interplanetary operations

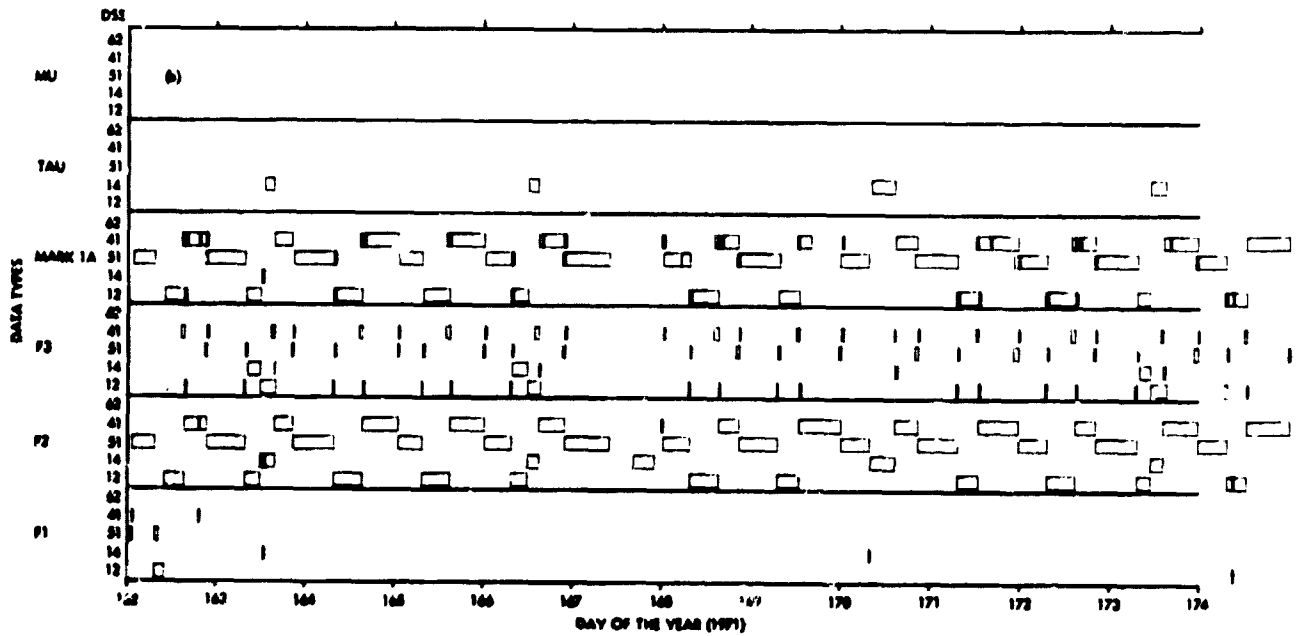


Fig. 1 (contd)

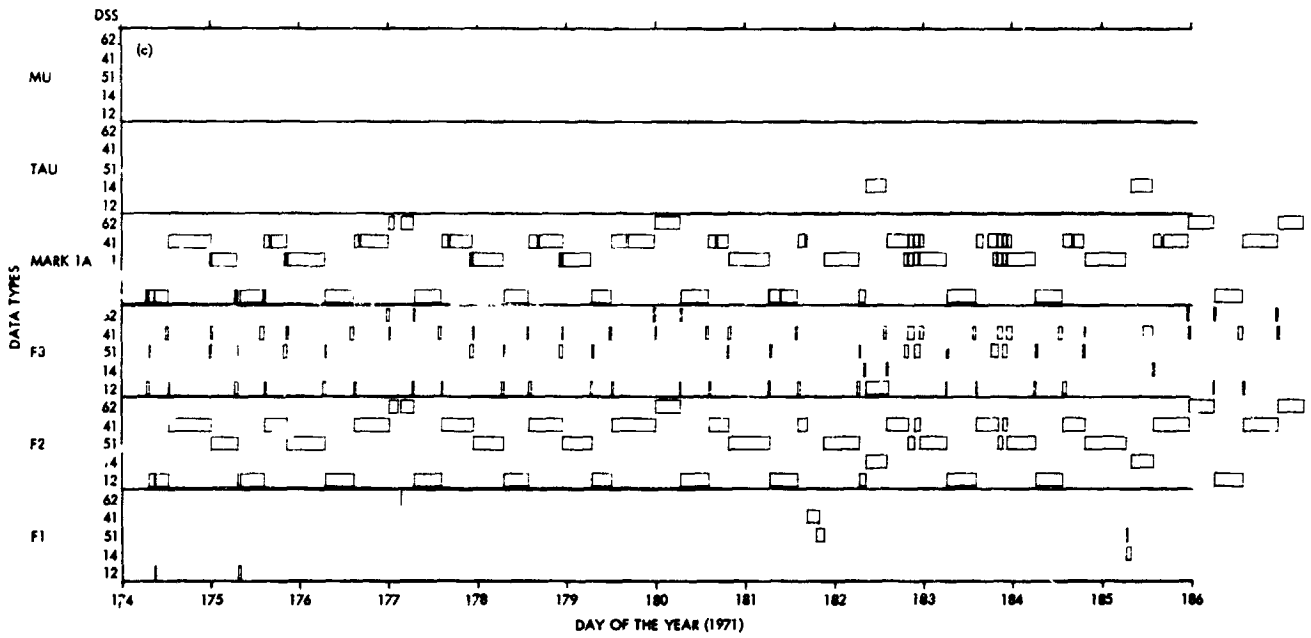


Fig. 1 (contd)

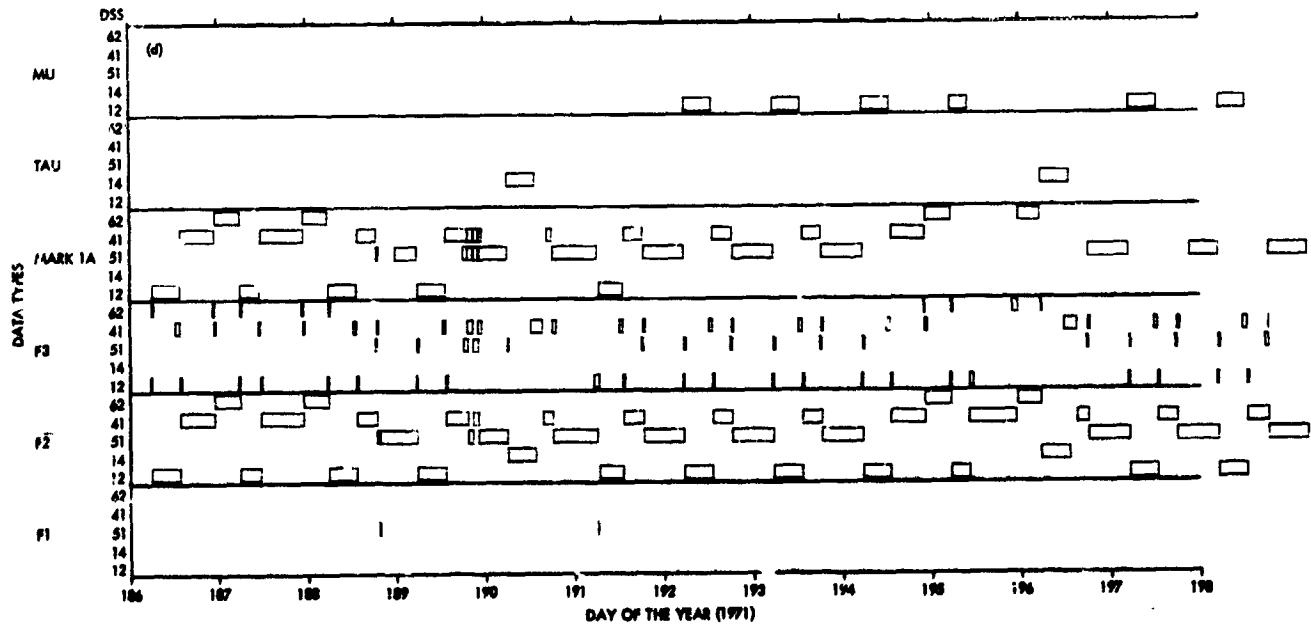


Fig. 1 (contd)

e-8

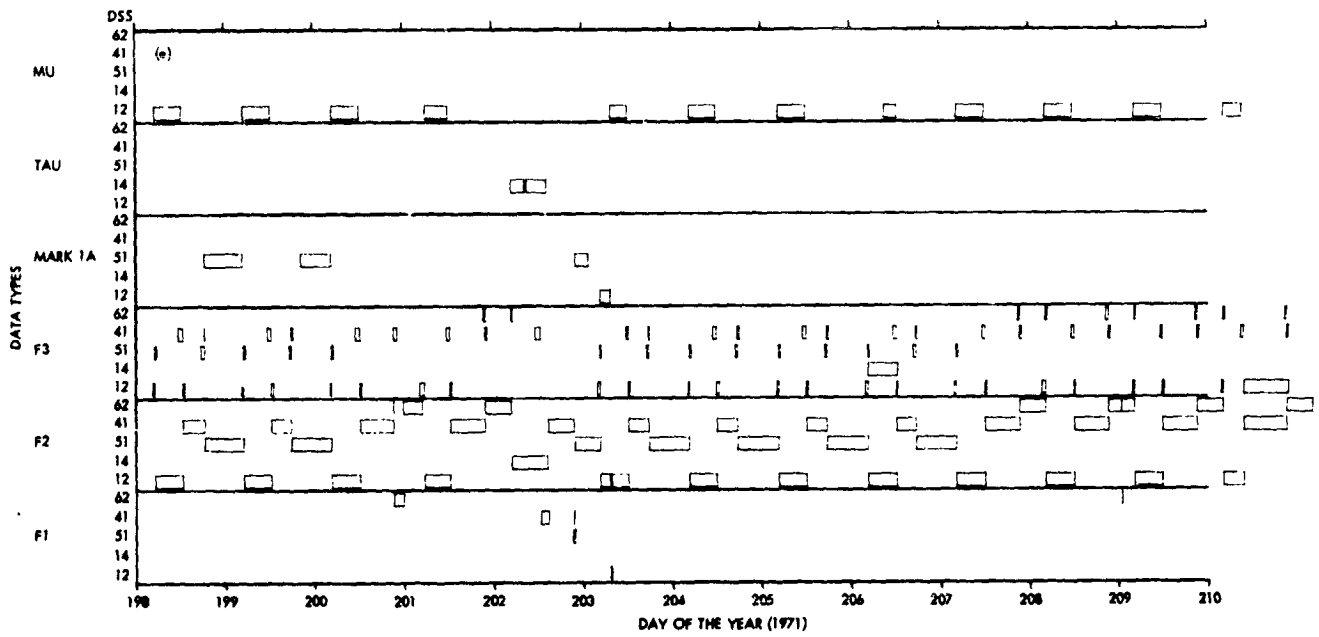


Fig. 1 (contd)

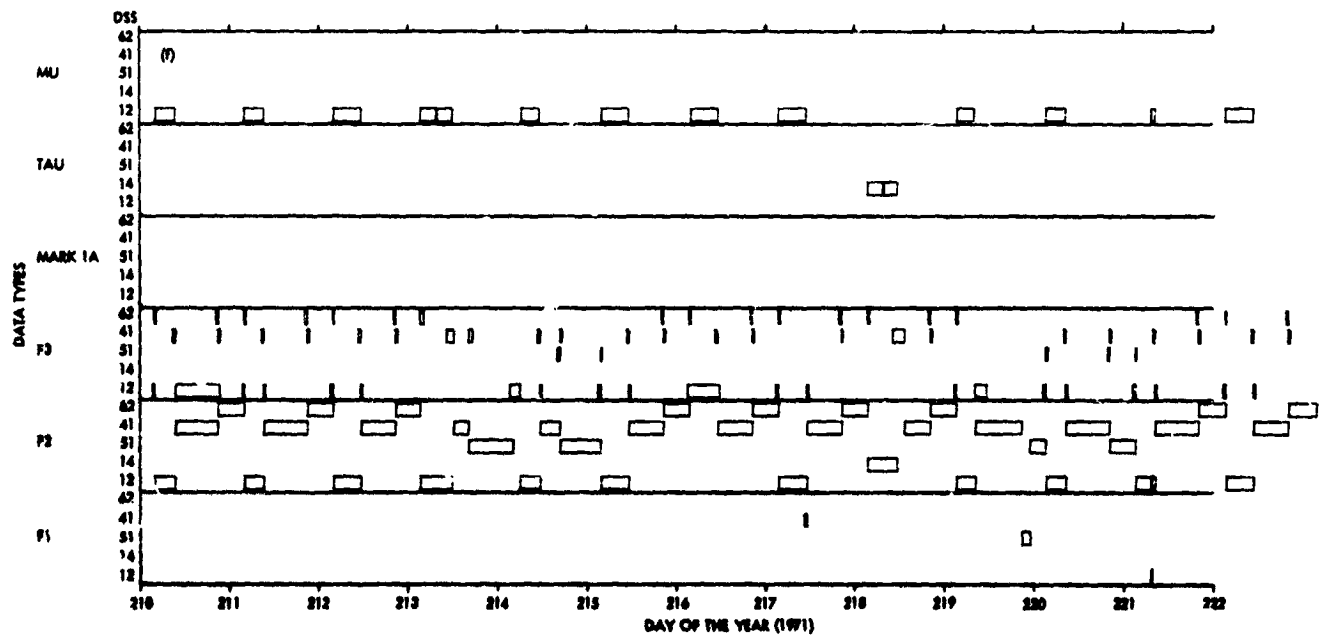


Fig. 1 (contd)

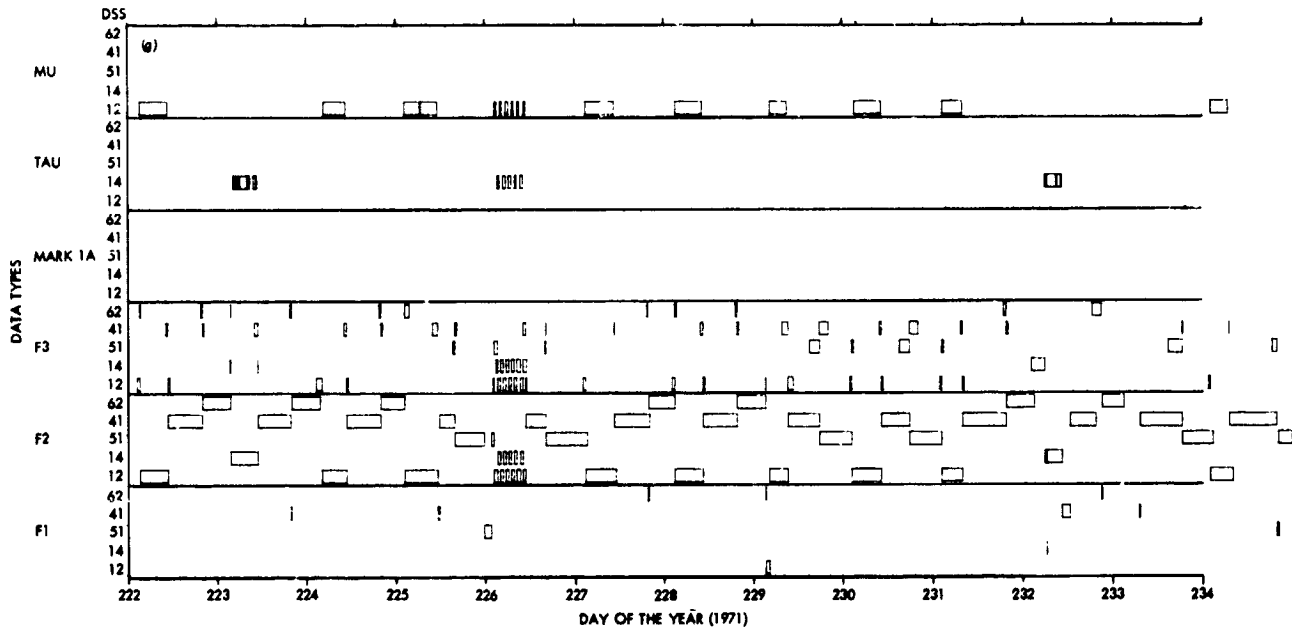


Fig. 1 (contd)

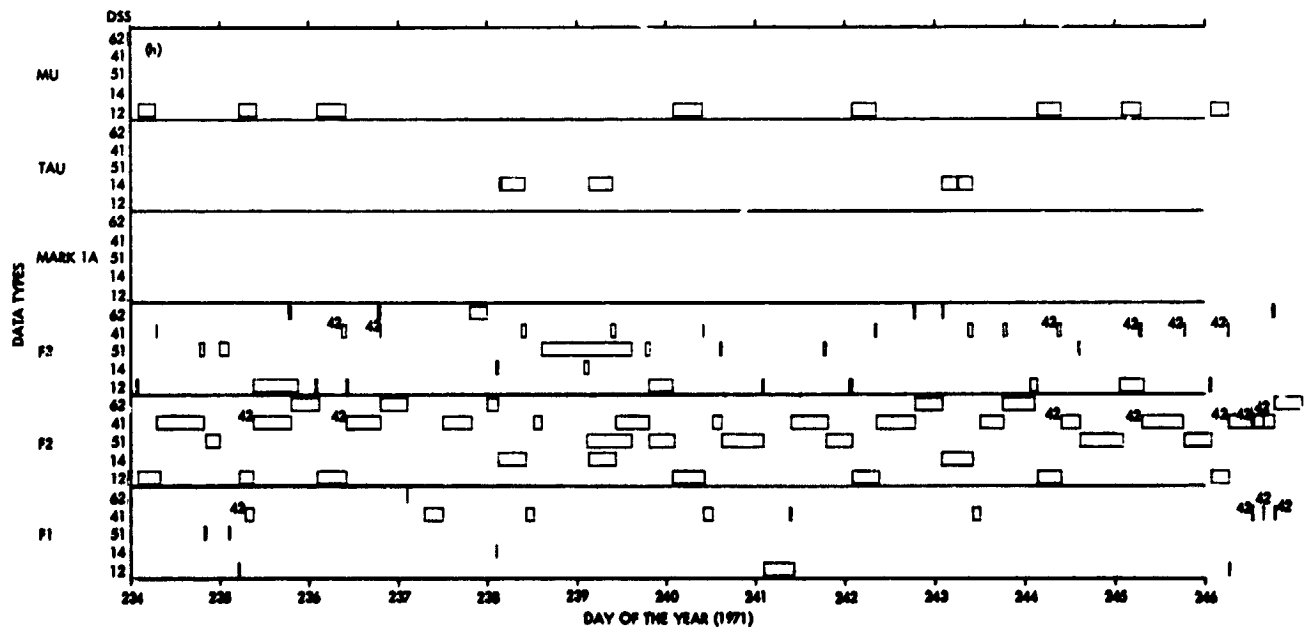


Fig. 1 (contd)

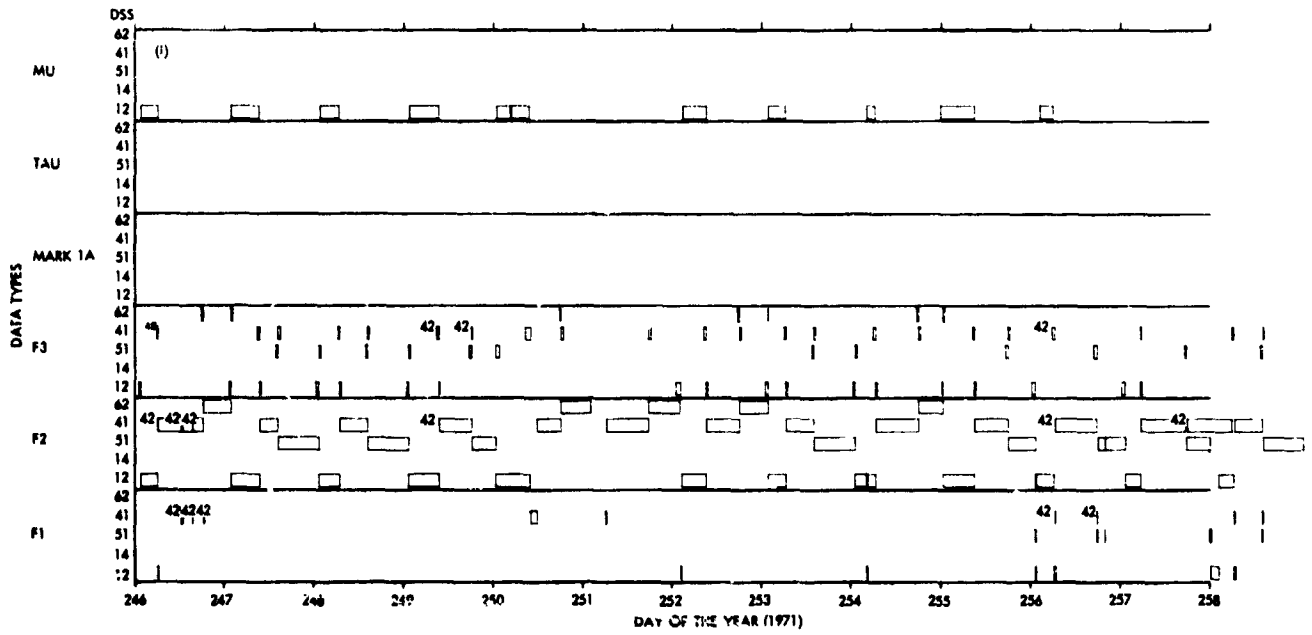


Fig. 1 (contd)

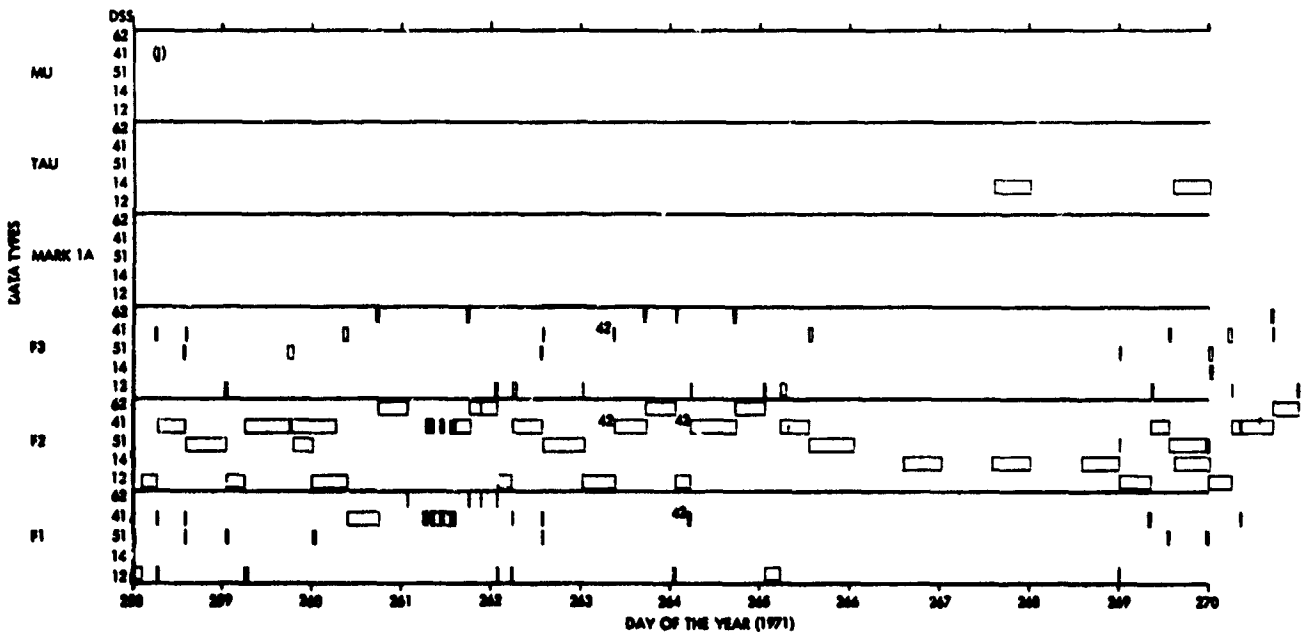


Fig. 1 (contd)

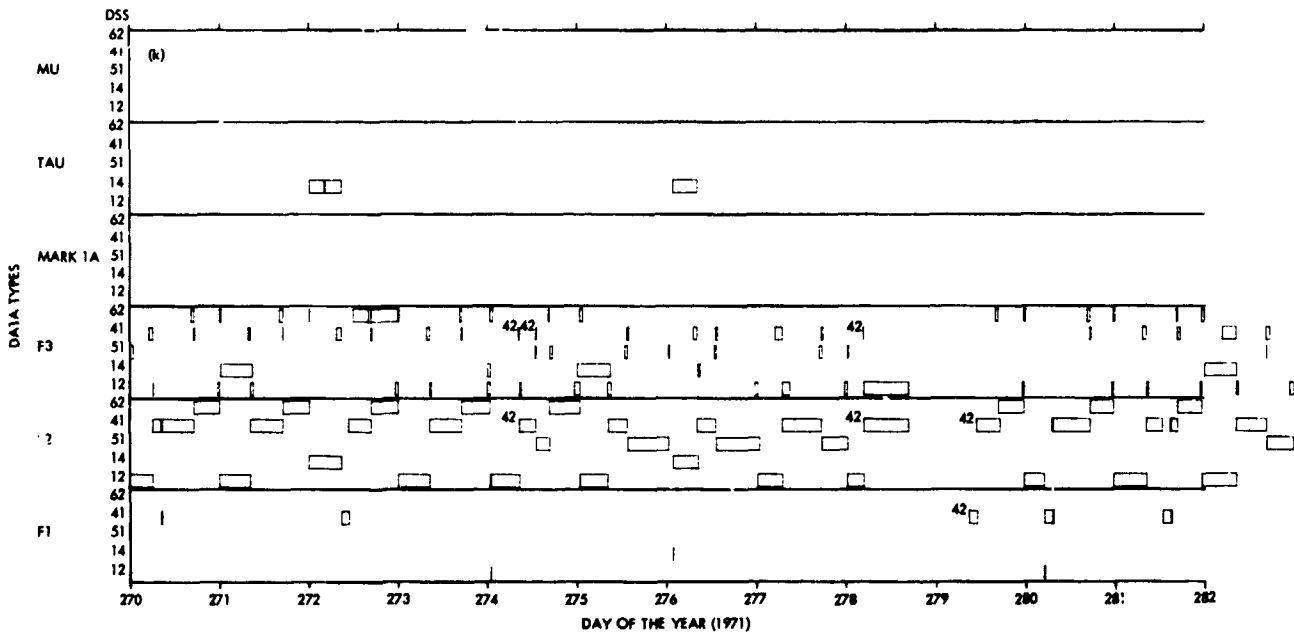


Fig. 1 (contd)

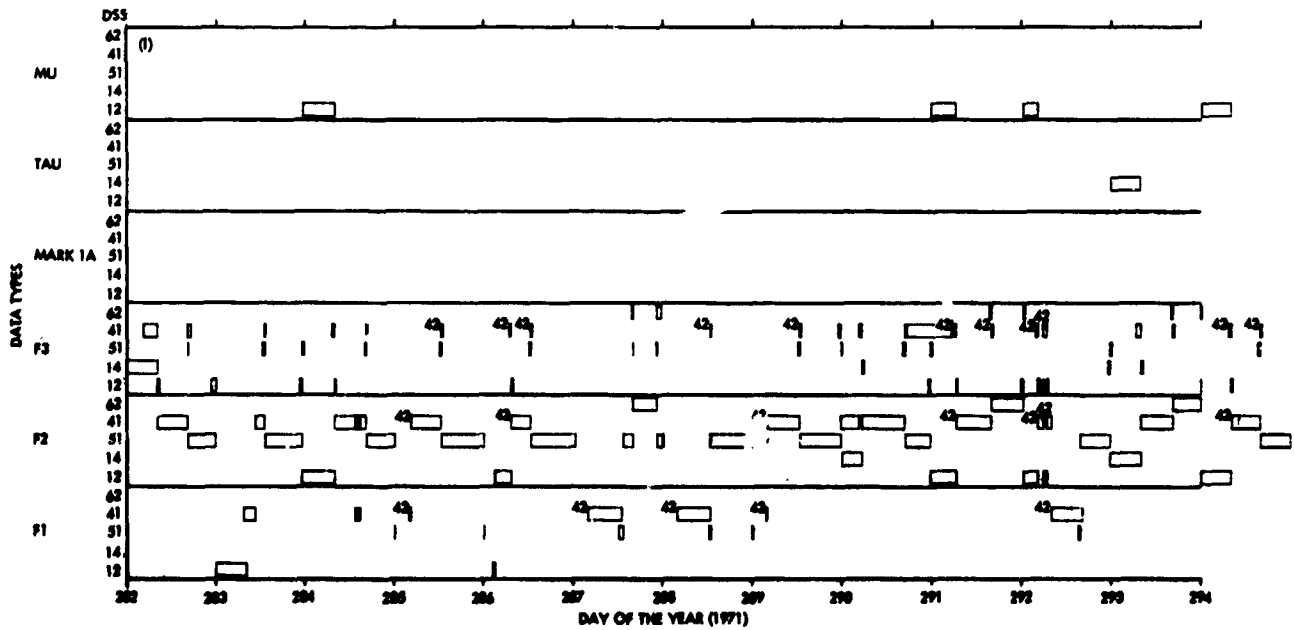


Fig. 1 (contd)

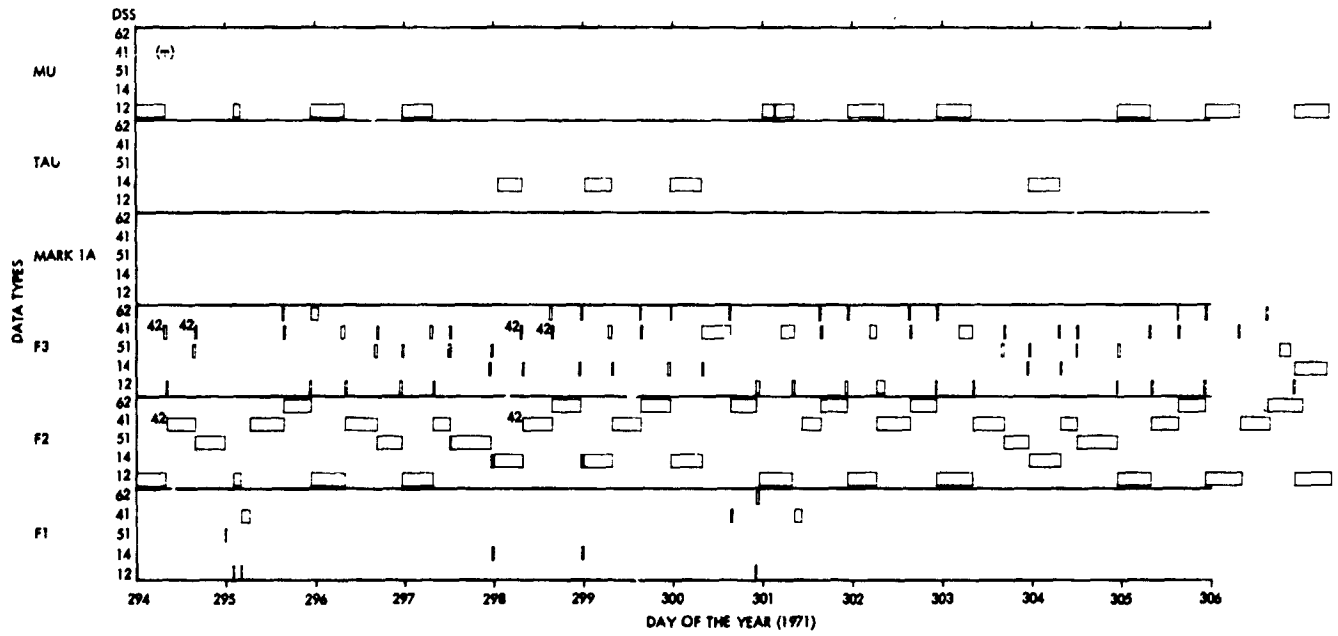


Fig. 1 (contd)

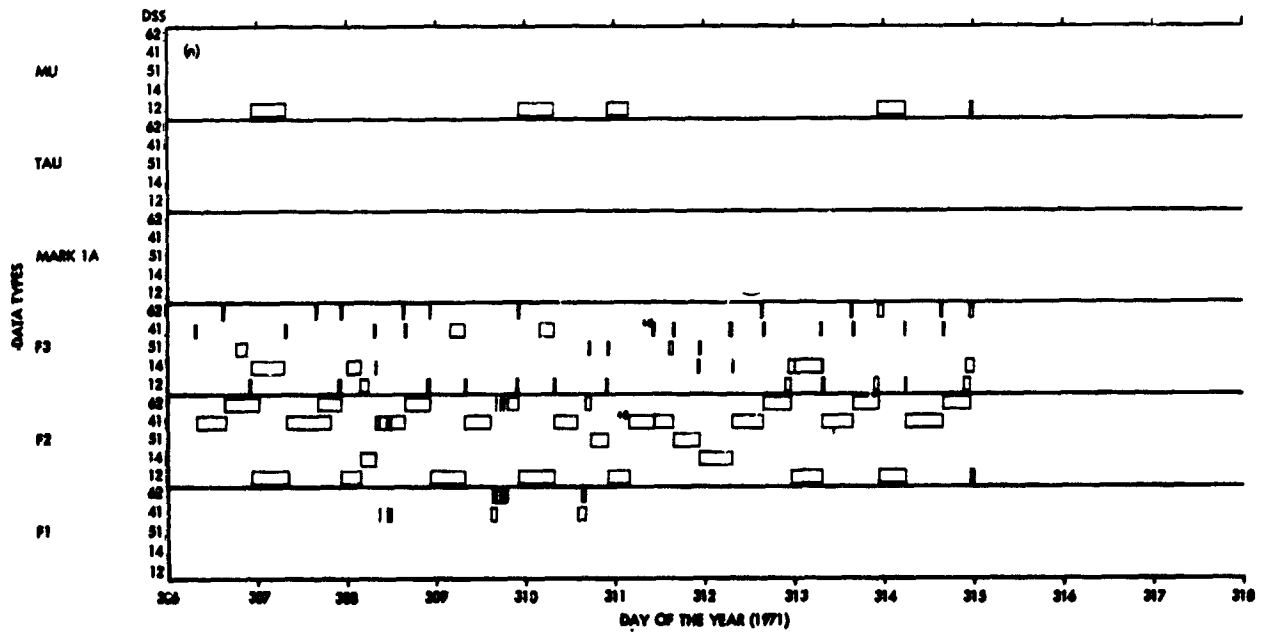


Fig. 1 (contd)

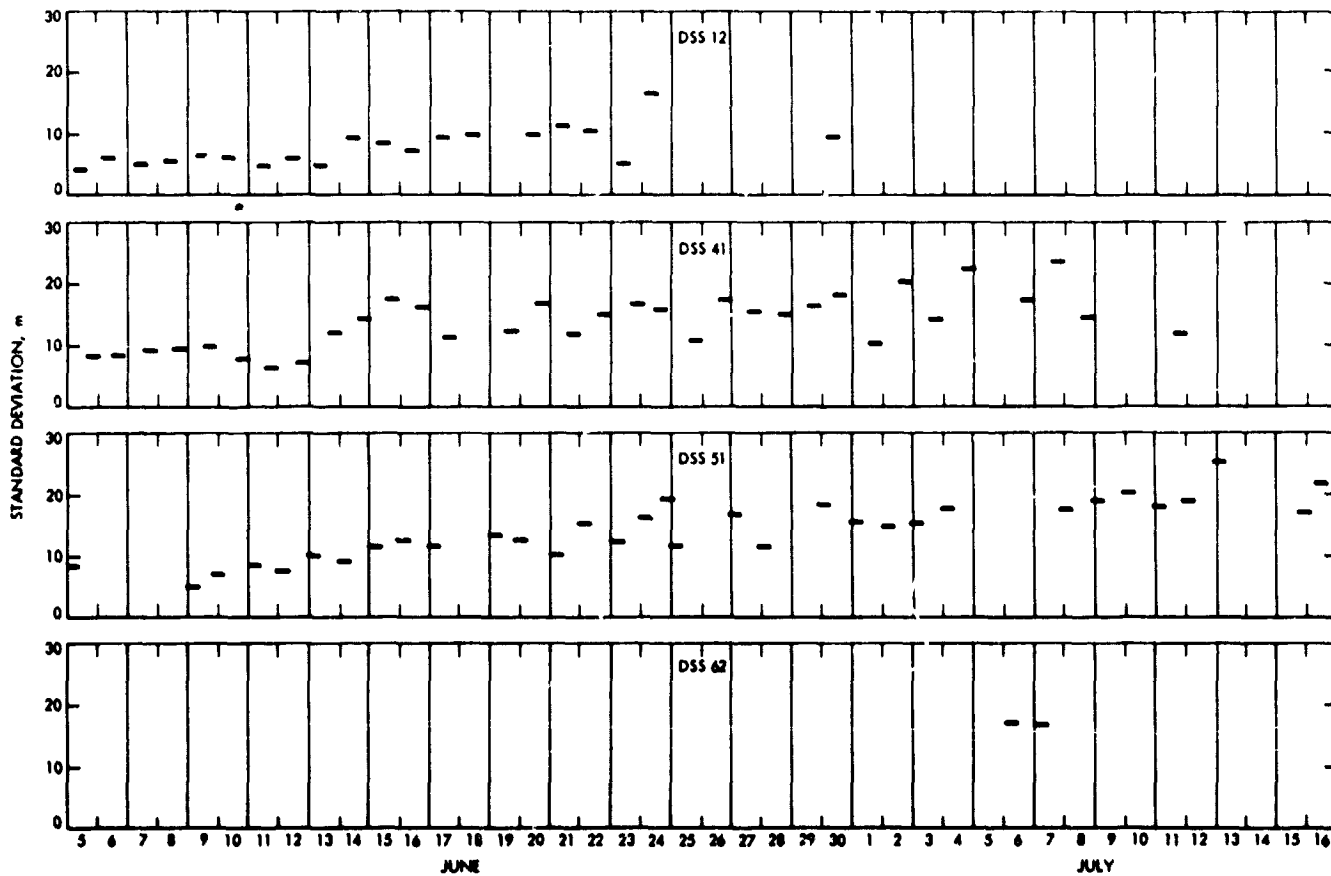


Fig. 2. Standard deviations of MARK 1A passes from the state-only solution of Run 000967



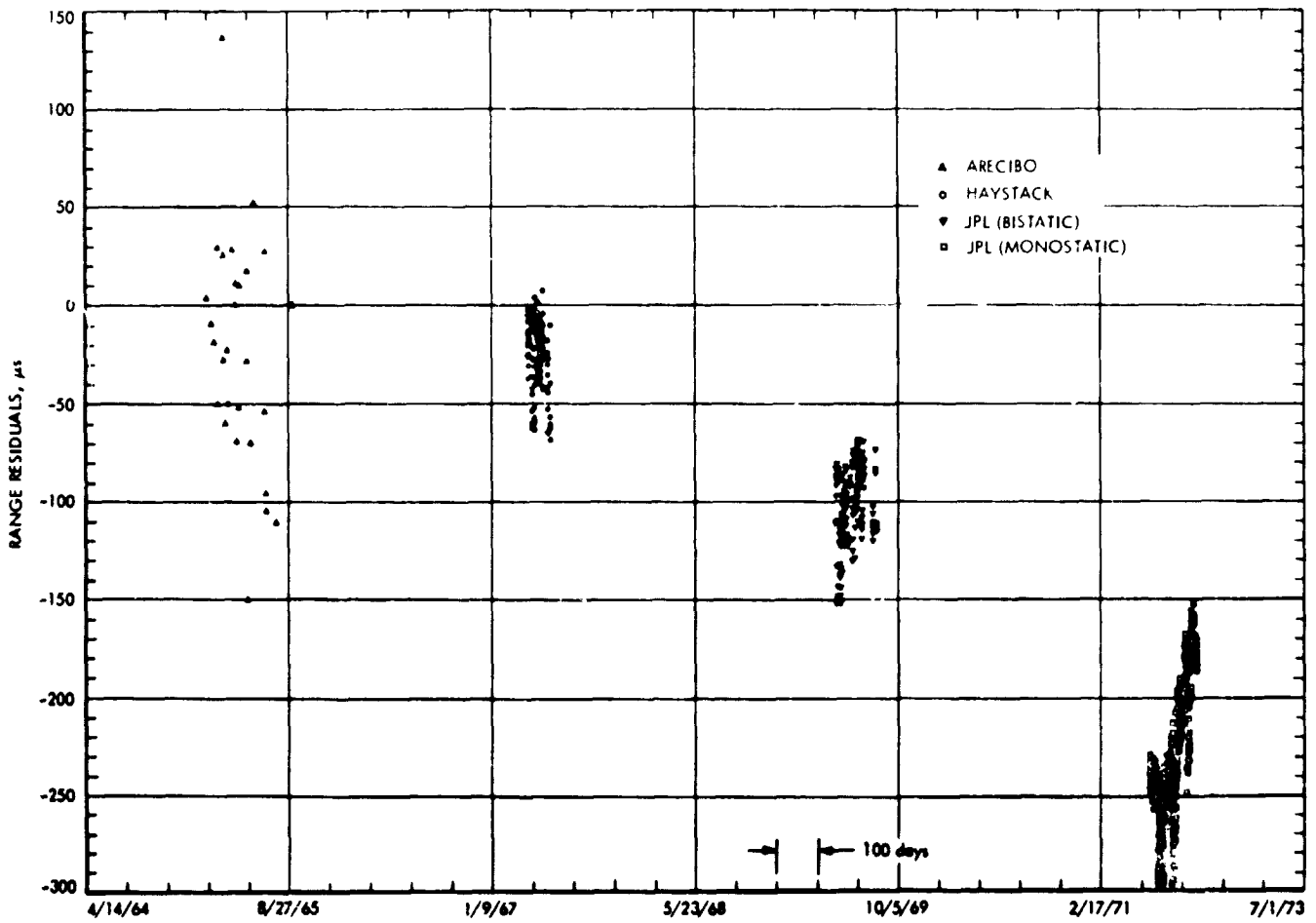


Fig. 4. Residuals of post-1969 planetary ranging data from DE09

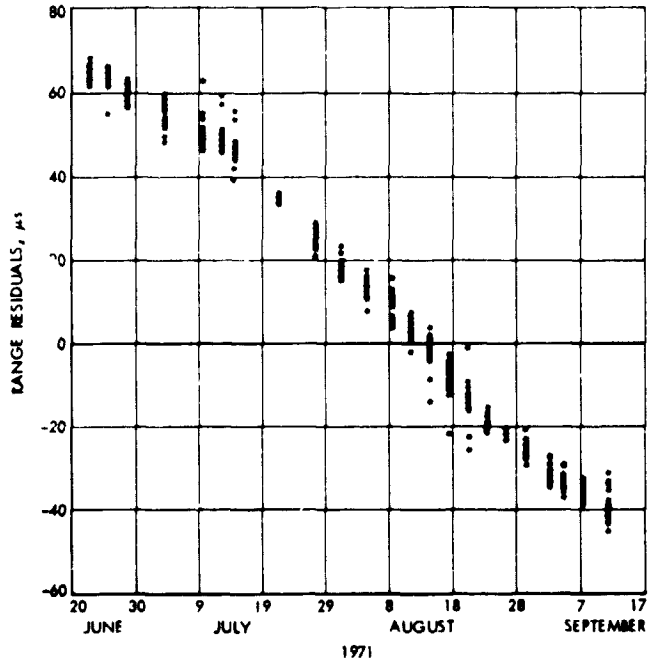


Fig. 5. Residuals of 1971 planetary ranging data from DE7B

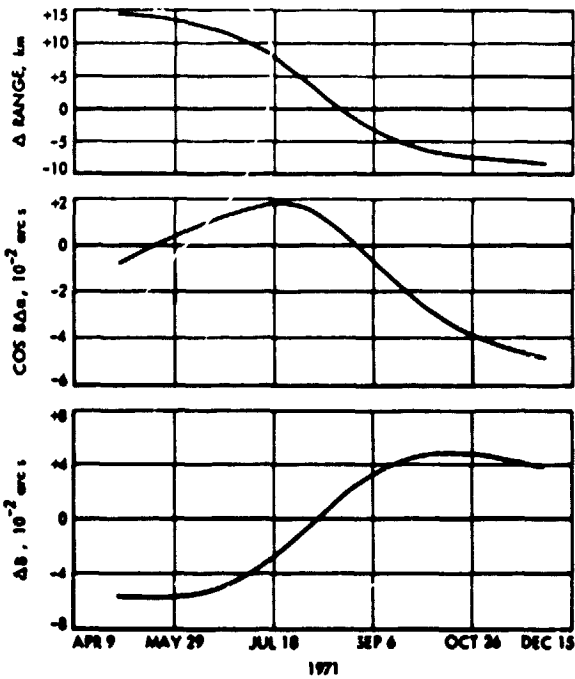


Fig. 6. Differences (DE79 - DE7B) in geocentric spherical coordinates of Mars

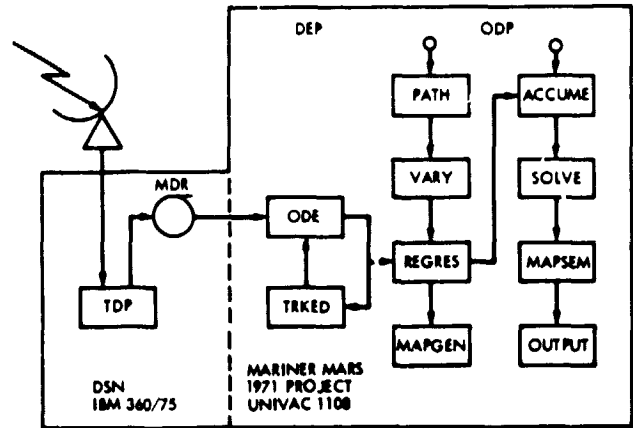


Fig. 7. Interaction of radiometric data processing programs

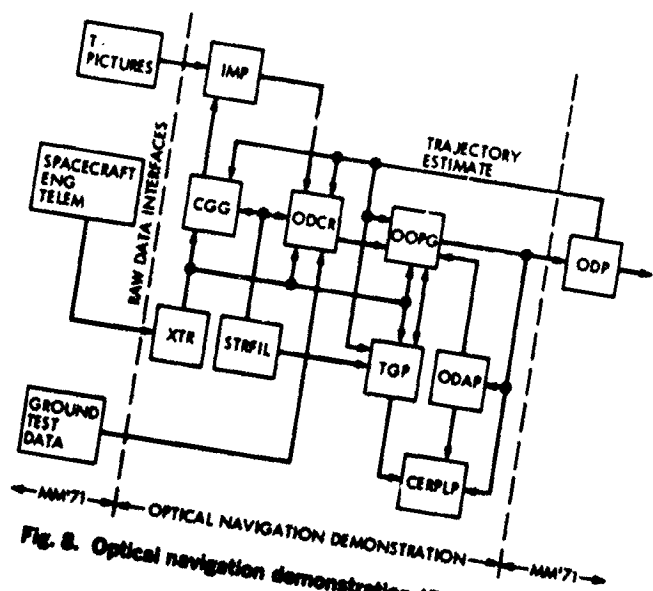


Fig. 8. Optical navigation demonstration (OND) software

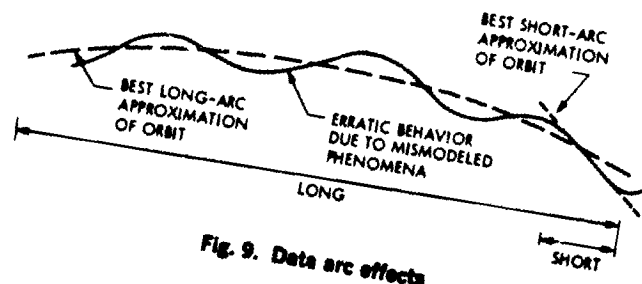


Fig. 9. Data arc effects

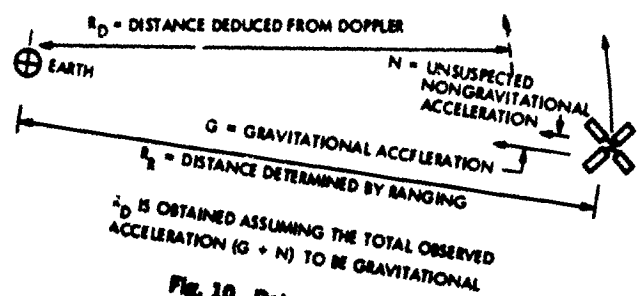


Fig. 10. Data type effects

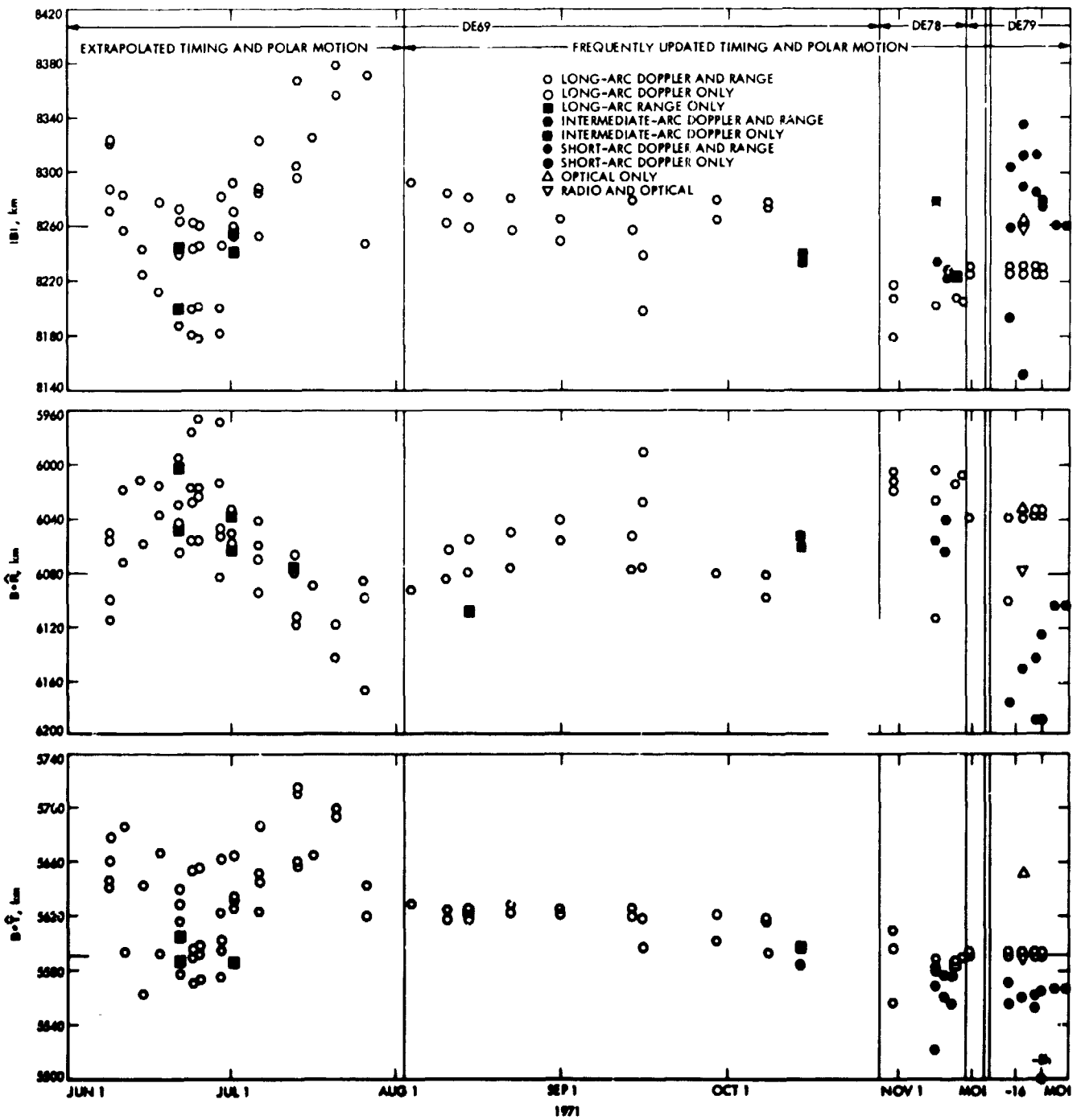


Fig. 11. B-plane behavior of state-only solutions during the interplanetary phase

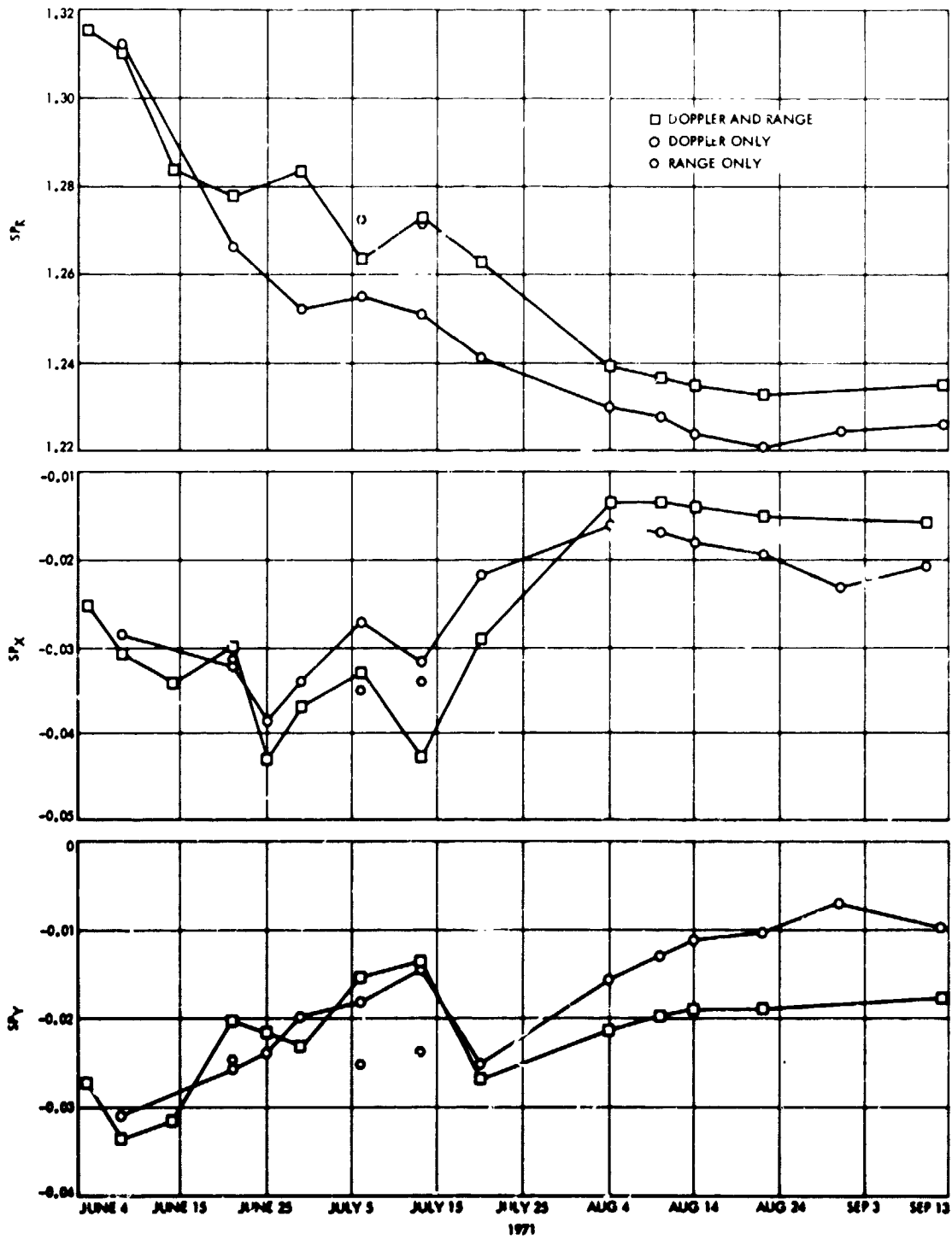


Fig. 12. Secular behavior of solutions for solar pressure coefficients

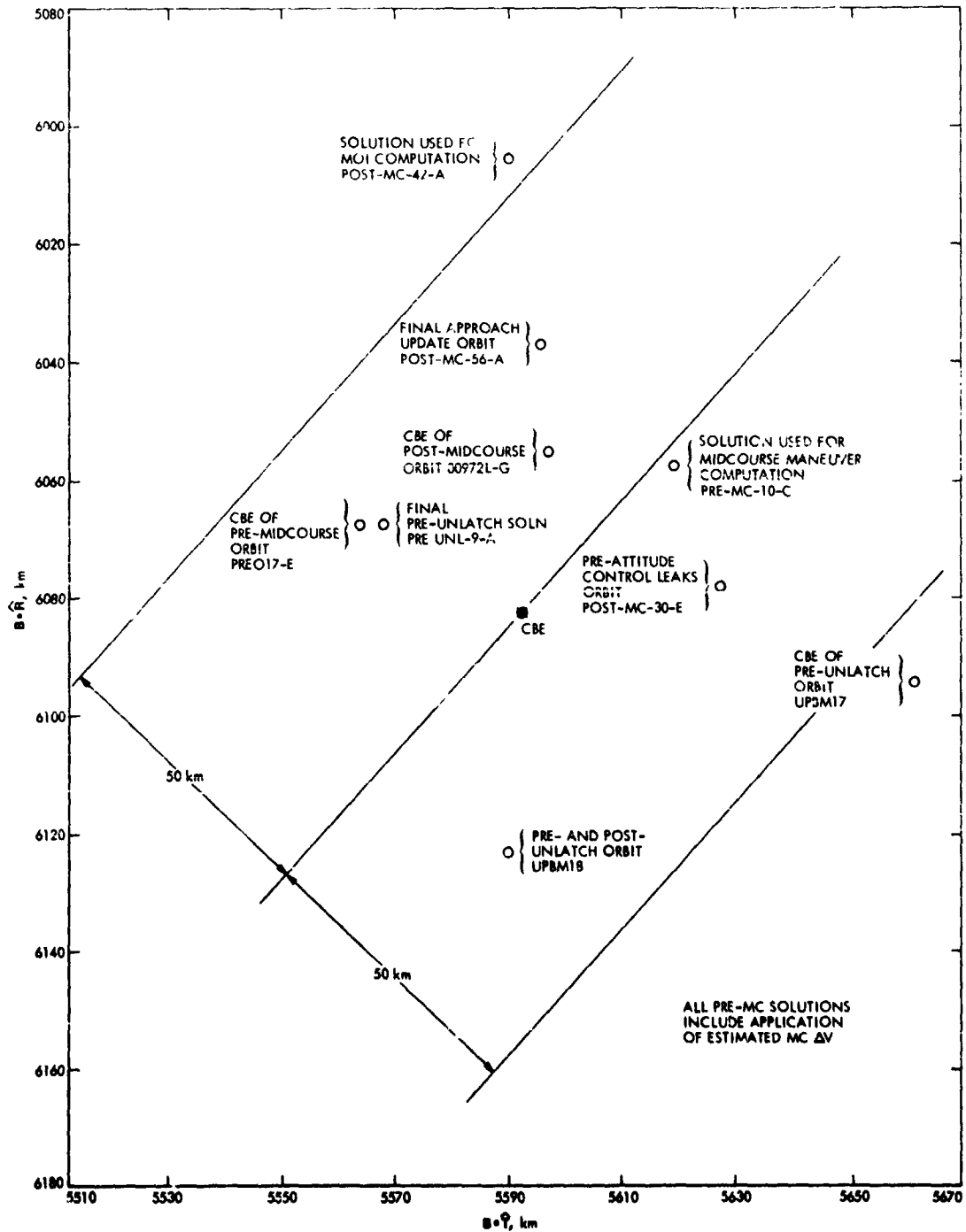


Fig. 13. Summary of inflight and post-flight B-plane predictions

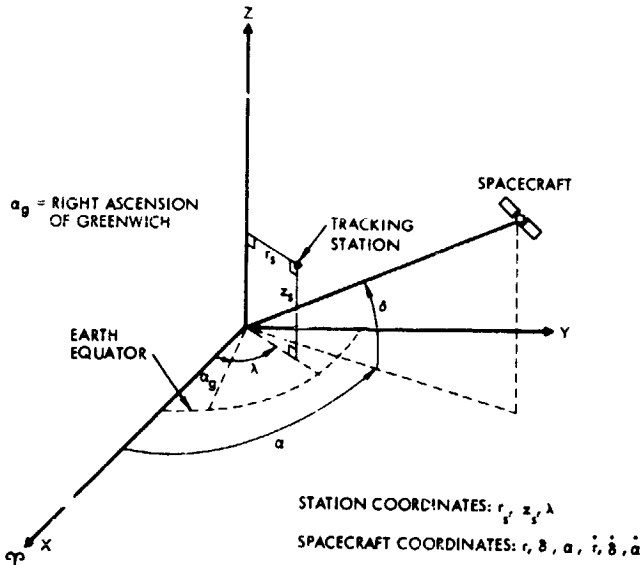


Fig. 14. Spacecraft and station coordinate systems

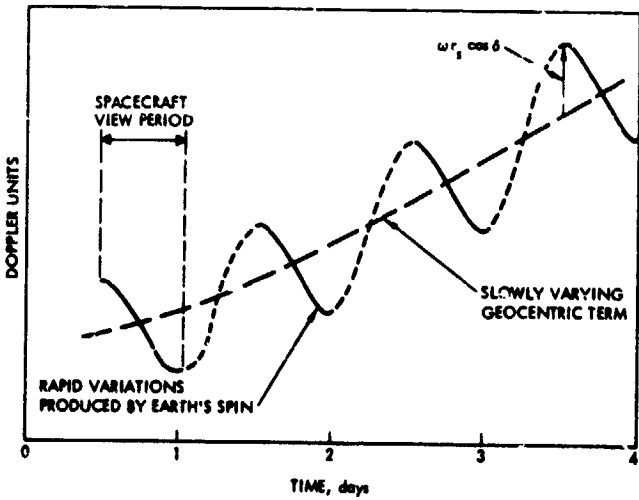


Fig. 15. Range rate observables

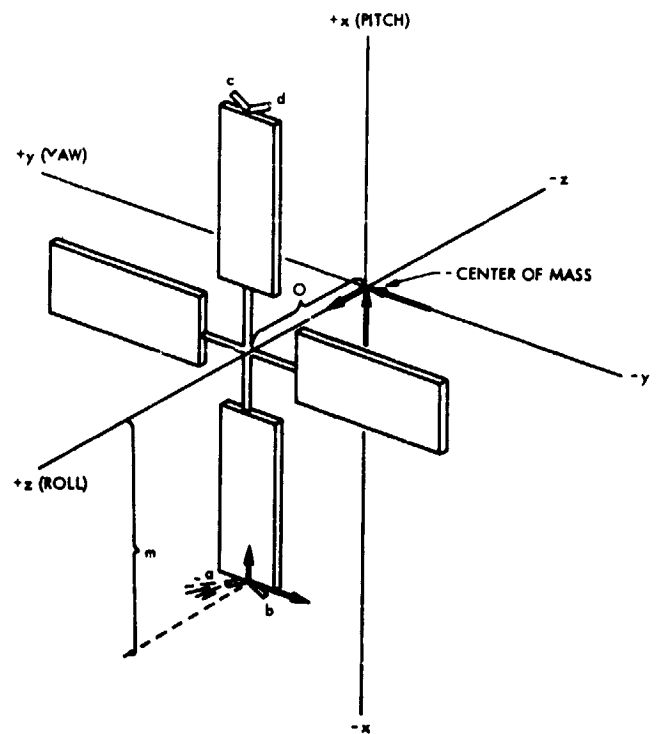


Fig. 16. Spacecraft AC roll jets and forces

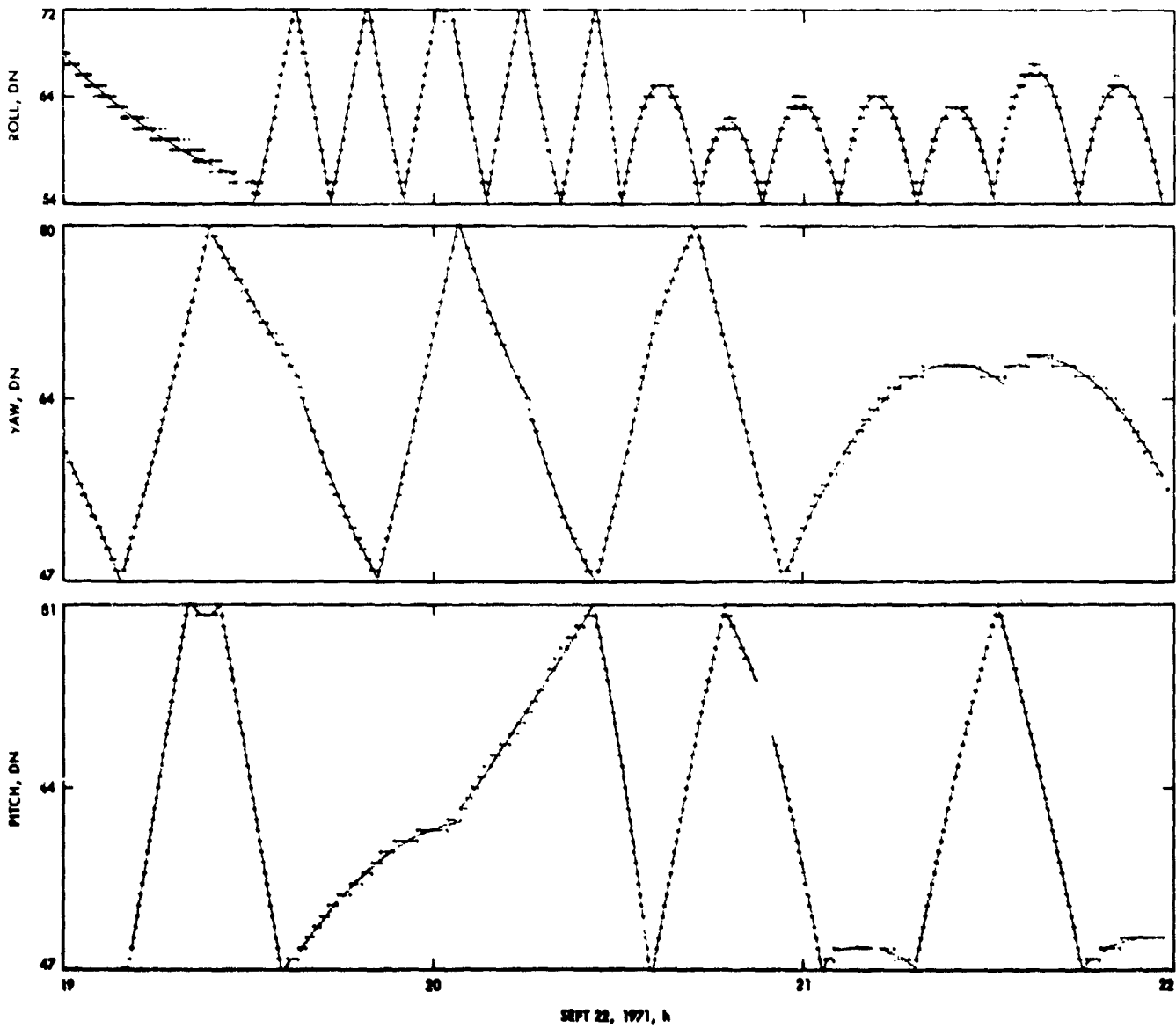


Fig. 17. Typical AC telemetry data represented by polynomials fit to them

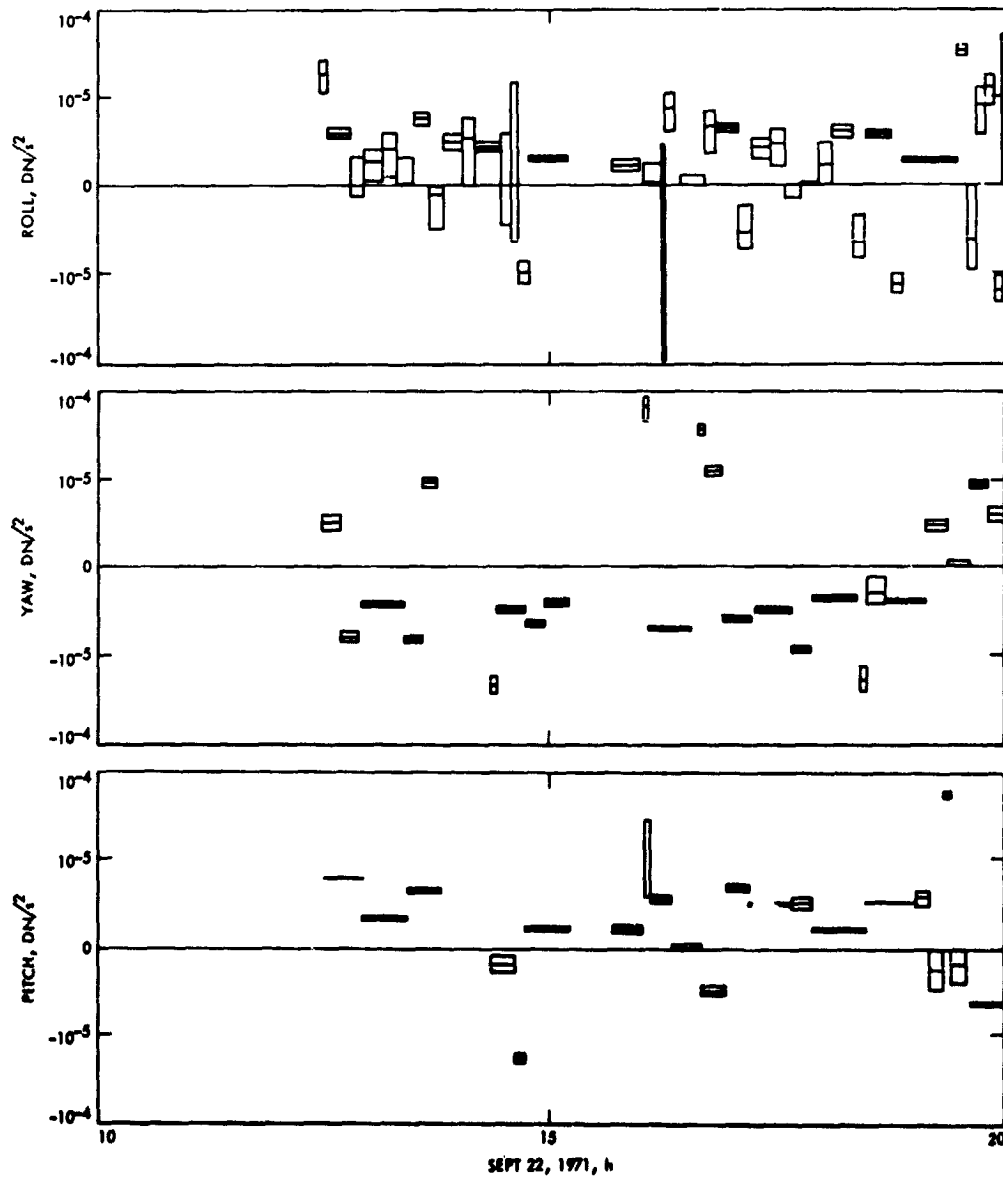


Fig. 18. Angular accelerations computed for a typical period of small ("constant") gas leaks

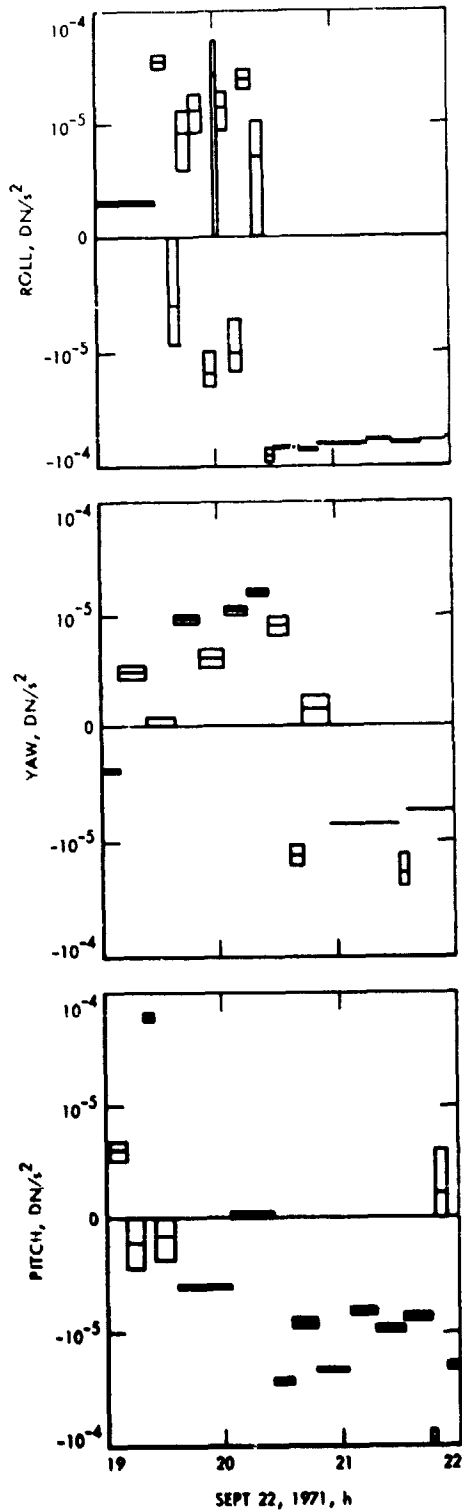


Fig. 19. Angular accelerations computed for a typical period of large roll-jet leaks

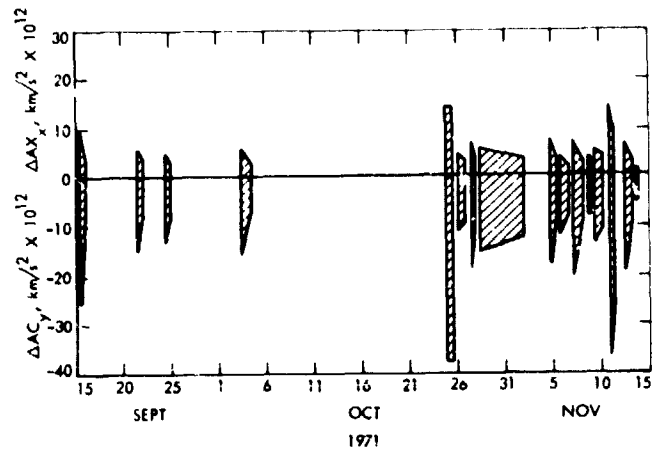


Fig. 20. Current best estimate of translational acceleration magnitudes caused by AC jet leaks during the interplanetary phase

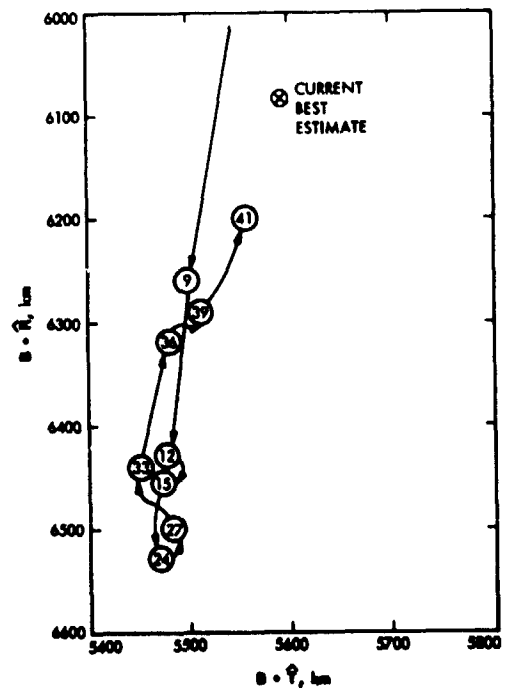


Fig. 21. Evolution of state estimates in the B-plane for the batch filter (set 1) (solutions labeled in days past October 4)

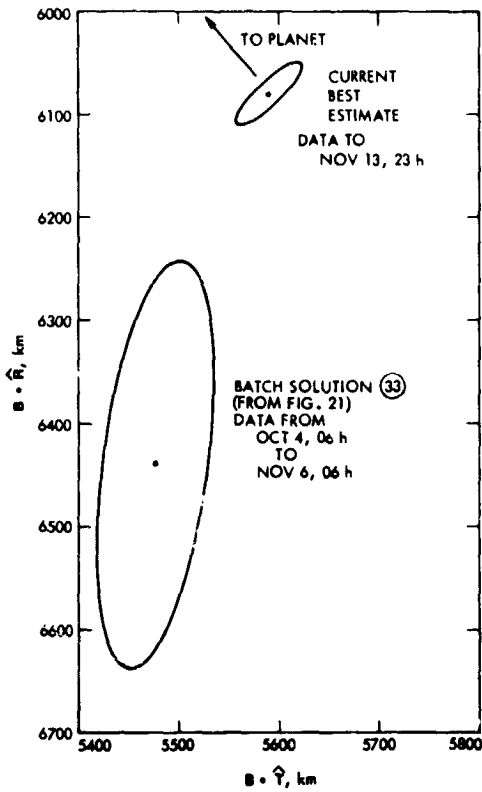


Fig. 22. Comparison of November approach solution with current best estimate

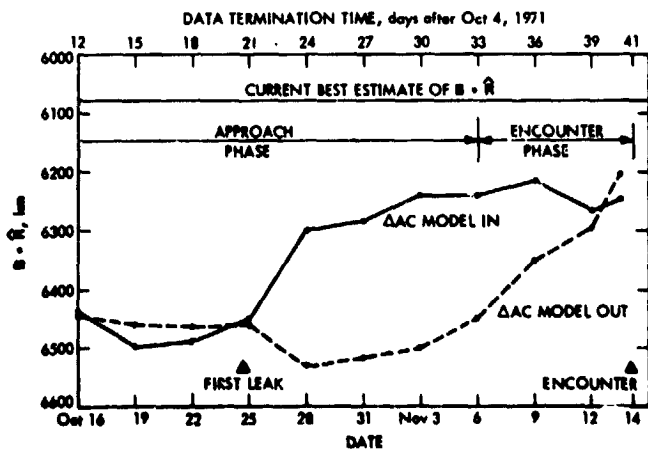


Fig. 23. Time history of  $B \cdot \hat{R}$  solutions from the batch filter (set 1)

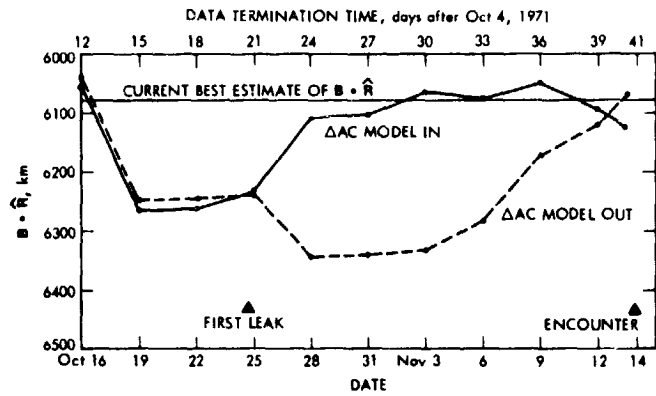


Fig. 24. Time history of  $B \cdot \hat{R}$  solutions from the batch filter (set 2)

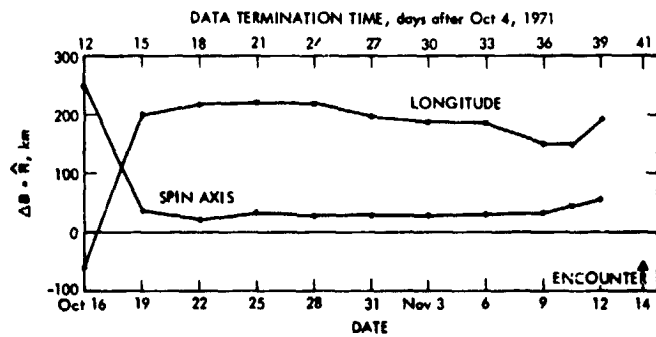


Fig. 25. Time history of perturbations in  $B \cdot \hat{R}$  caused by  $+7\text{-m } \lambda$  and  $+3\text{-m } r_e$  errors in all station locations using a batch filter

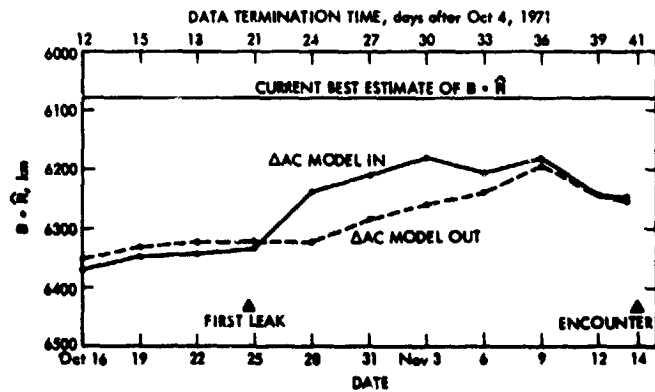


Fig. 26. Time history of  $B \cdot \hat{R}$  solutions for the  $10^{-15} \text{ km/s}^2$  process noise sequential filter (set 1)

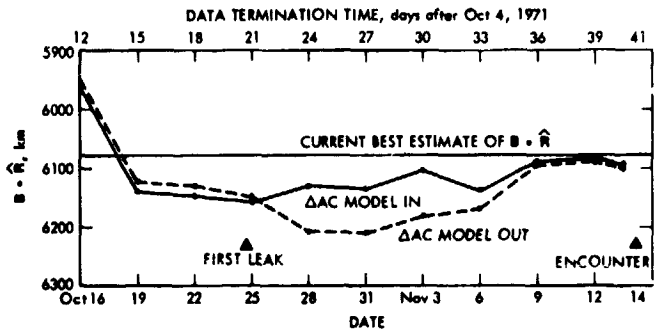


Fig. 27. Time history of  $B \cdot \hat{R}$  solutions for the  $10^{-12}$  km/s<sup>2</sup> process noise sequential filter (set 2)

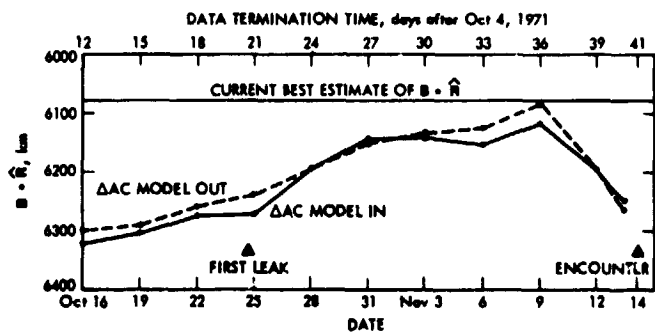


Fig. 28. Time history of  $B \cdot \hat{R}$  solutions for the  $10^{-11}$  km/s<sup>2</sup> process noise sequential filter (set 1)

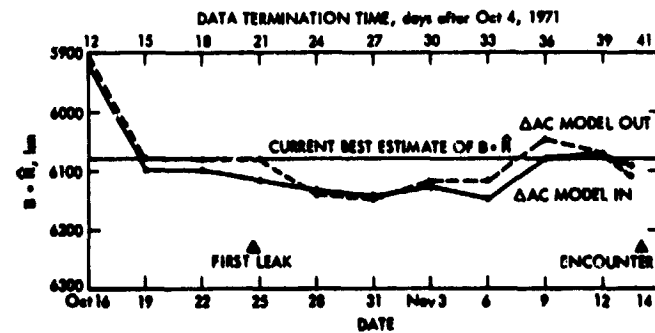


Fig. 29. Time history of  $E \cdot \hat{R}$  solutions for the  $10^{-11}$  km/s<sup>2</sup> process noise sequential filter (set 2)

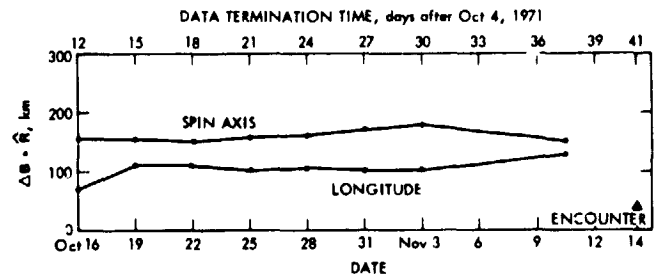


Fig. 30. Time history of perturbations in  $B \cdot \hat{R}$  due to  $+7\text{-m } \lambda$  and  $+3\text{-m } r_s$  errors in all stations located for the  $10^{-11}$  km/s<sup>2</sup> process noise sequential filter

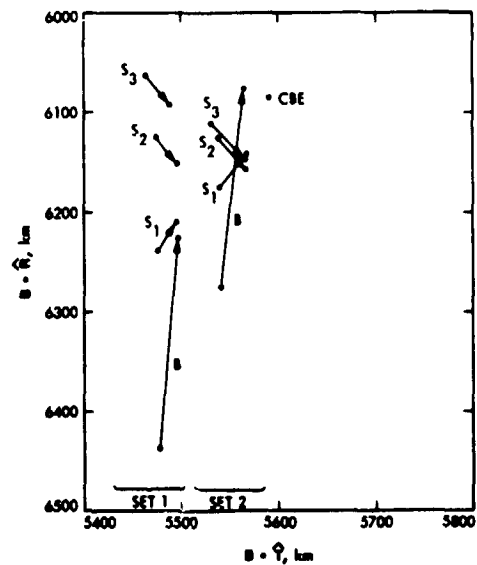


Fig. 31. Summary of November 6 solutions in the B-plane

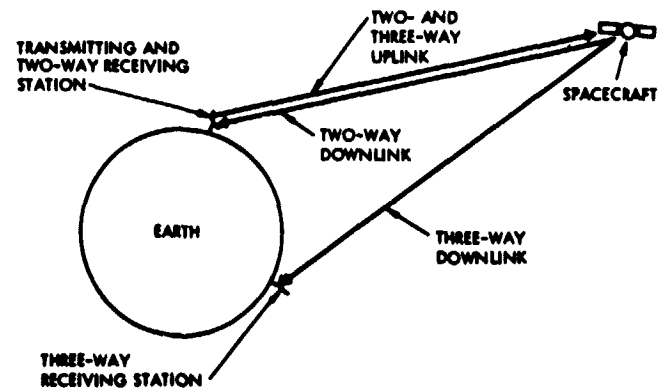


Fig. 32. Transmitting and receiving configuration for two-way and three-way data

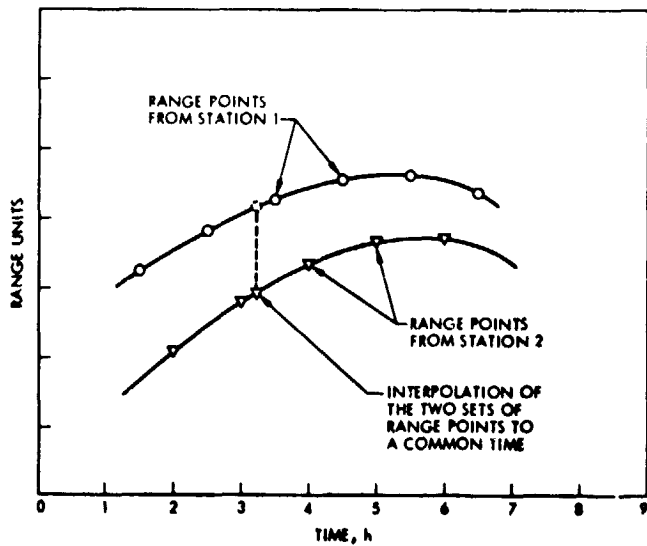


Fig. 33. Interpolation of near-simultaneous range points

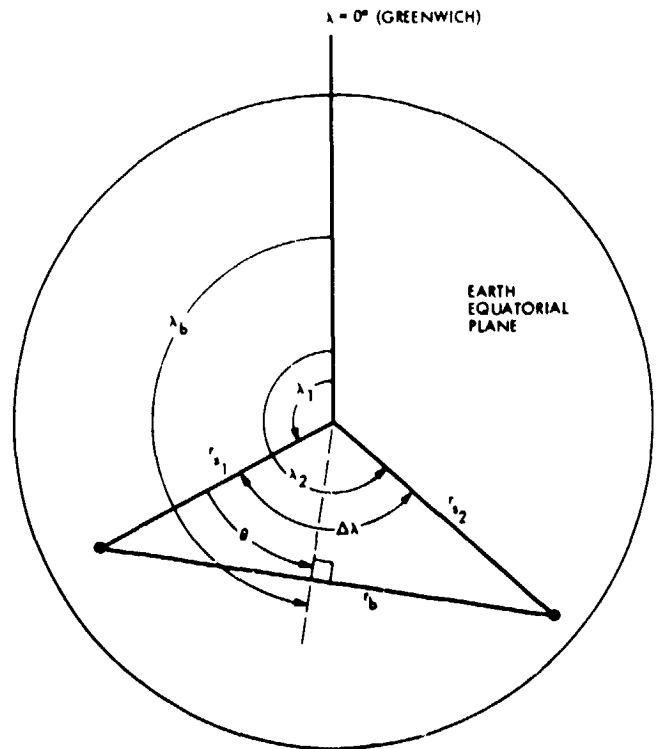


Fig. 34. Interrelationship of station location and baseline parameters

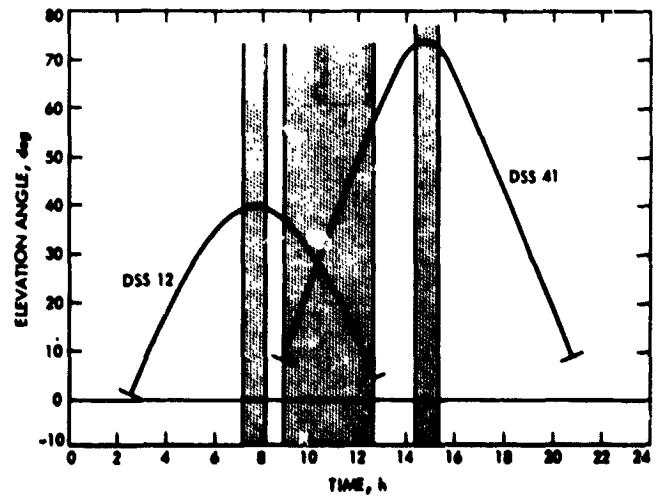


Fig. 35. Selection of two-way data for the dual-station experiment

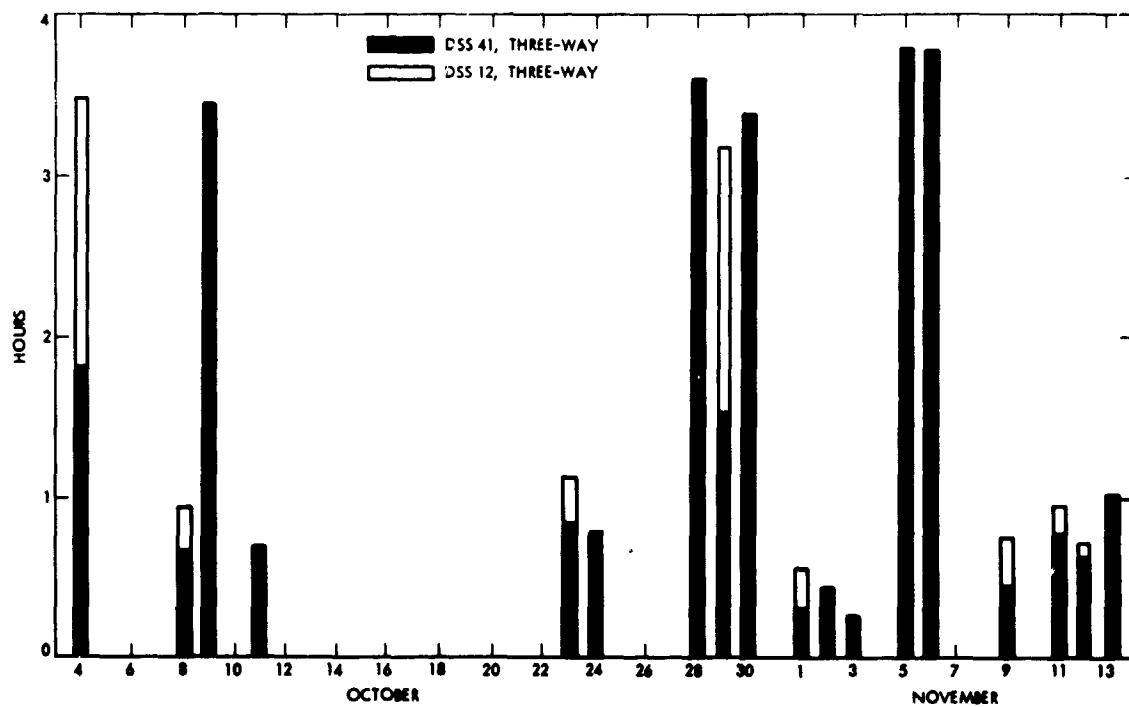


Fig. 36. Distribution of differenced data

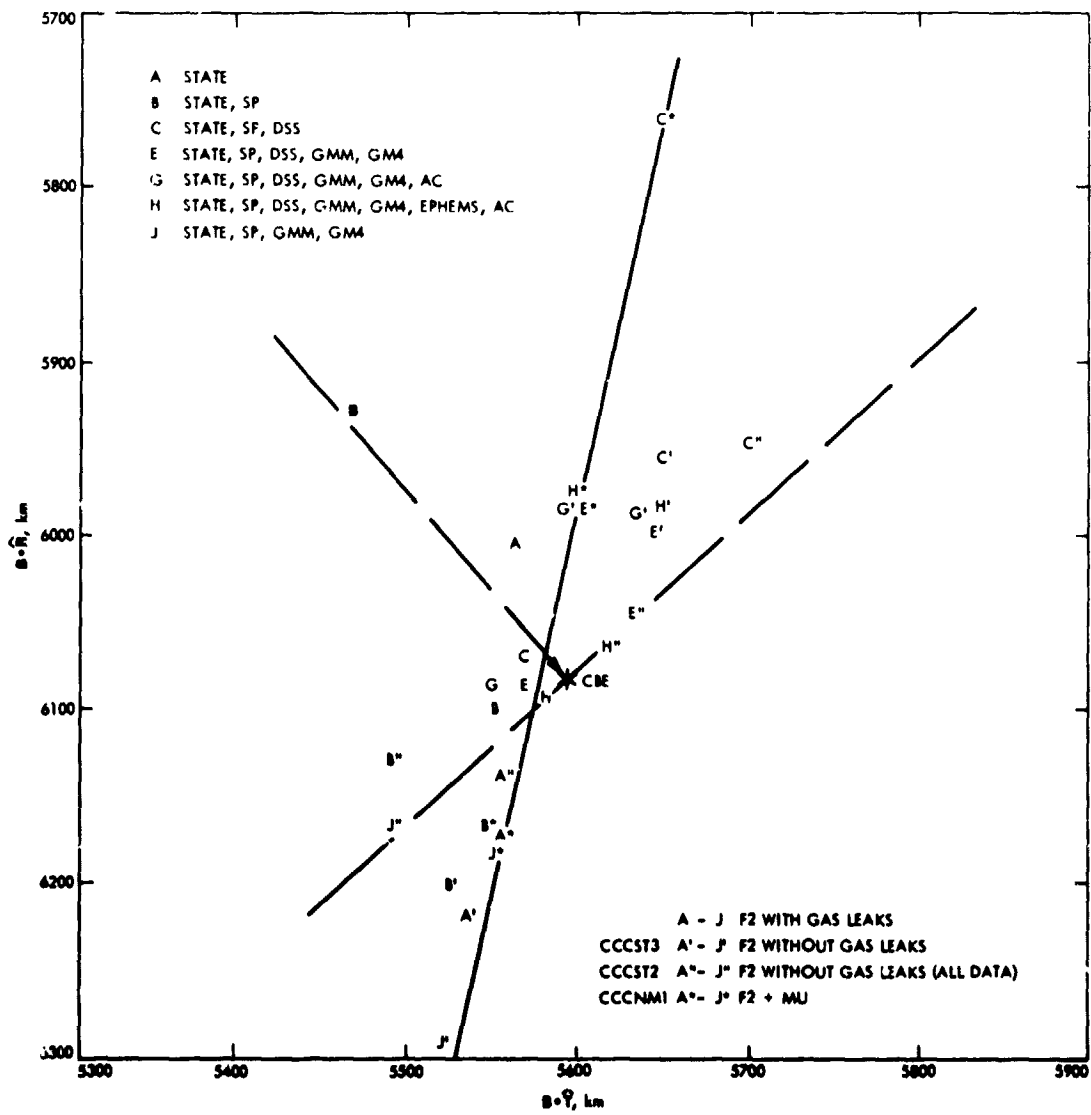
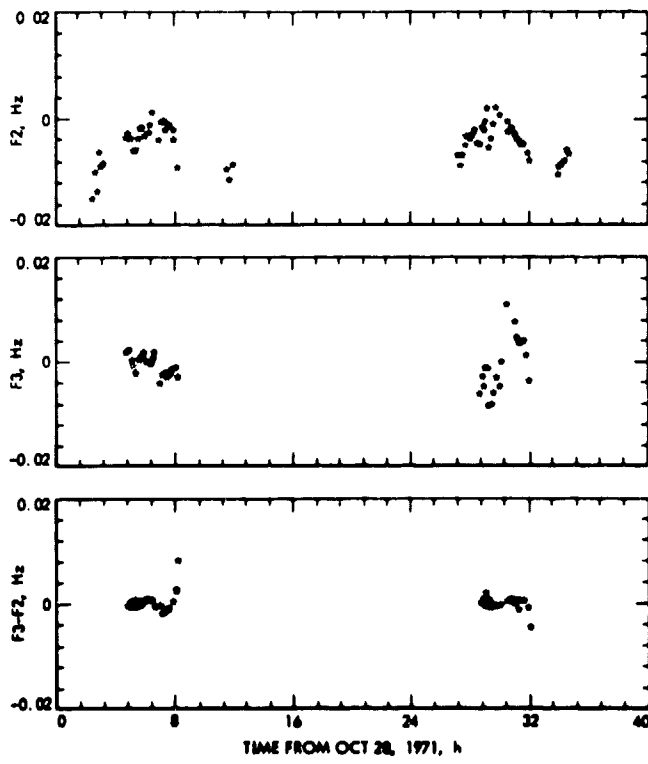


Fig. 37. B-plane results for the dual-station experiment



**Fig. 38. Typical residuals showing removal of process noise by differencing**

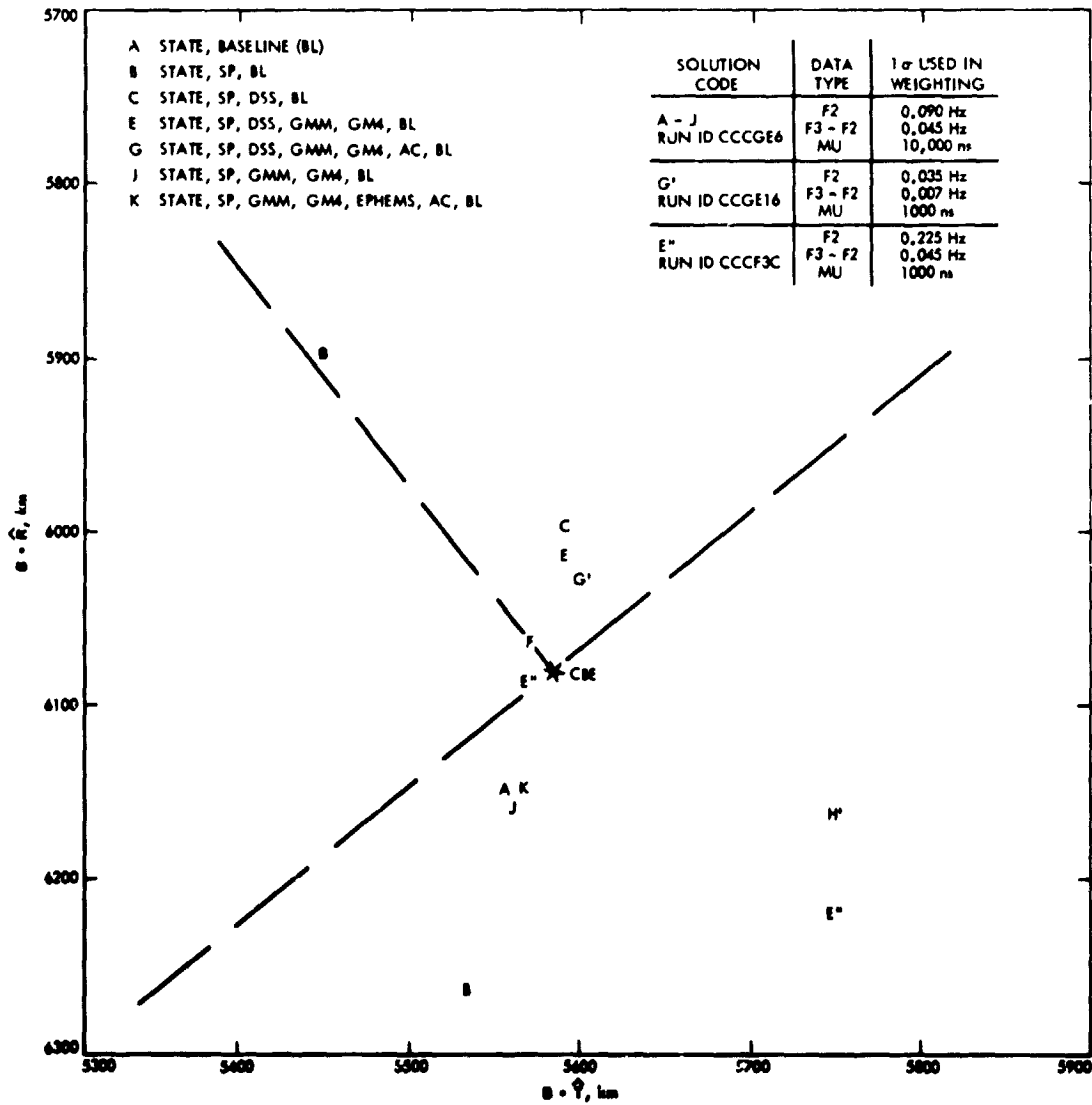


Fig. 39. B-plane solutions for various combinations of weights on F3-F2, F2, and MU data

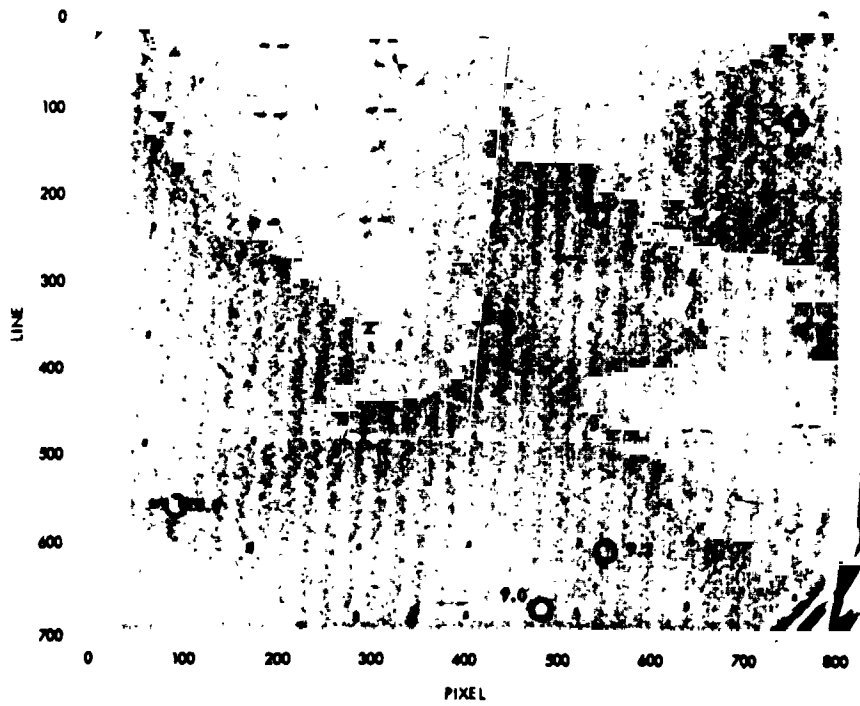


Fig. 40. Approach Deimos picture

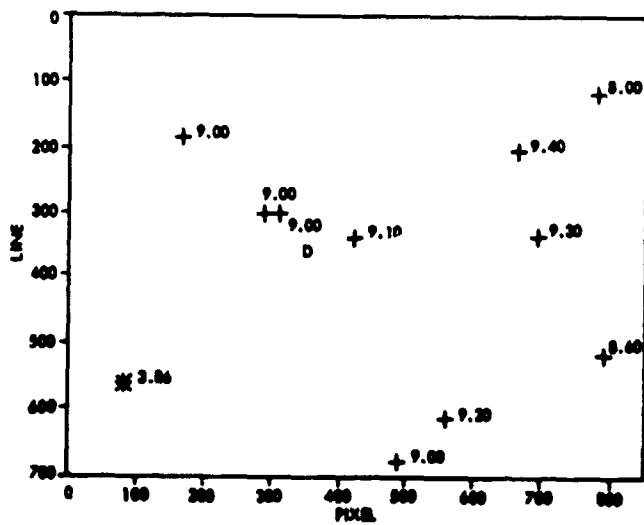


Fig. 41. Predicted approach Deimos picture

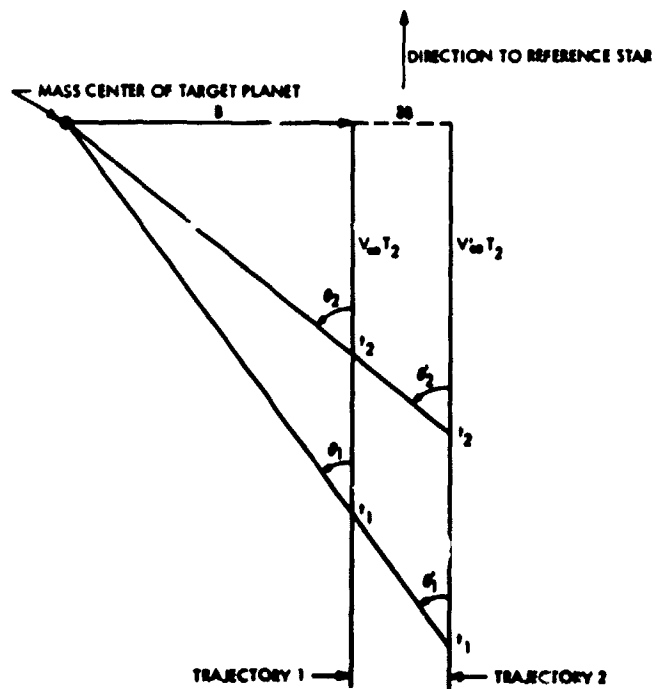


Fig. 42. Approach trajectory geometry

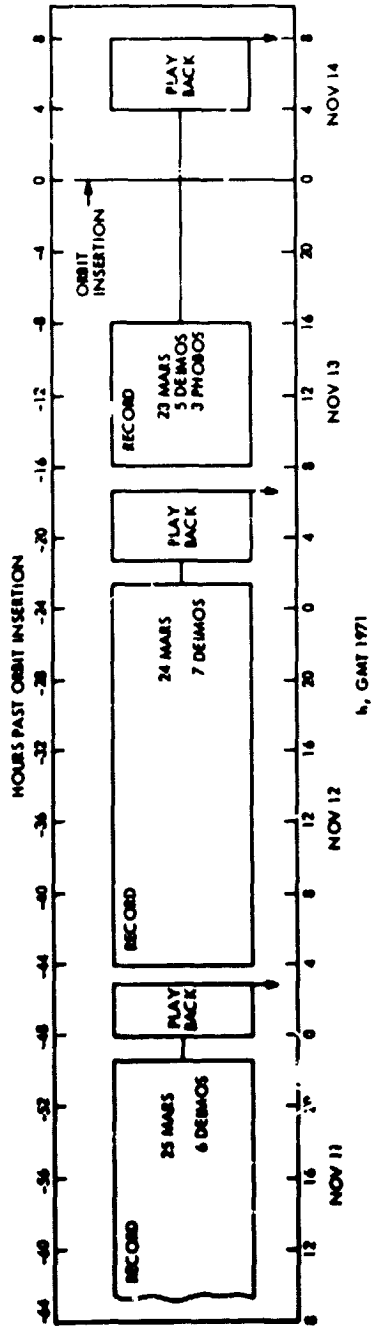


Fig. 43. Approach picture sequence

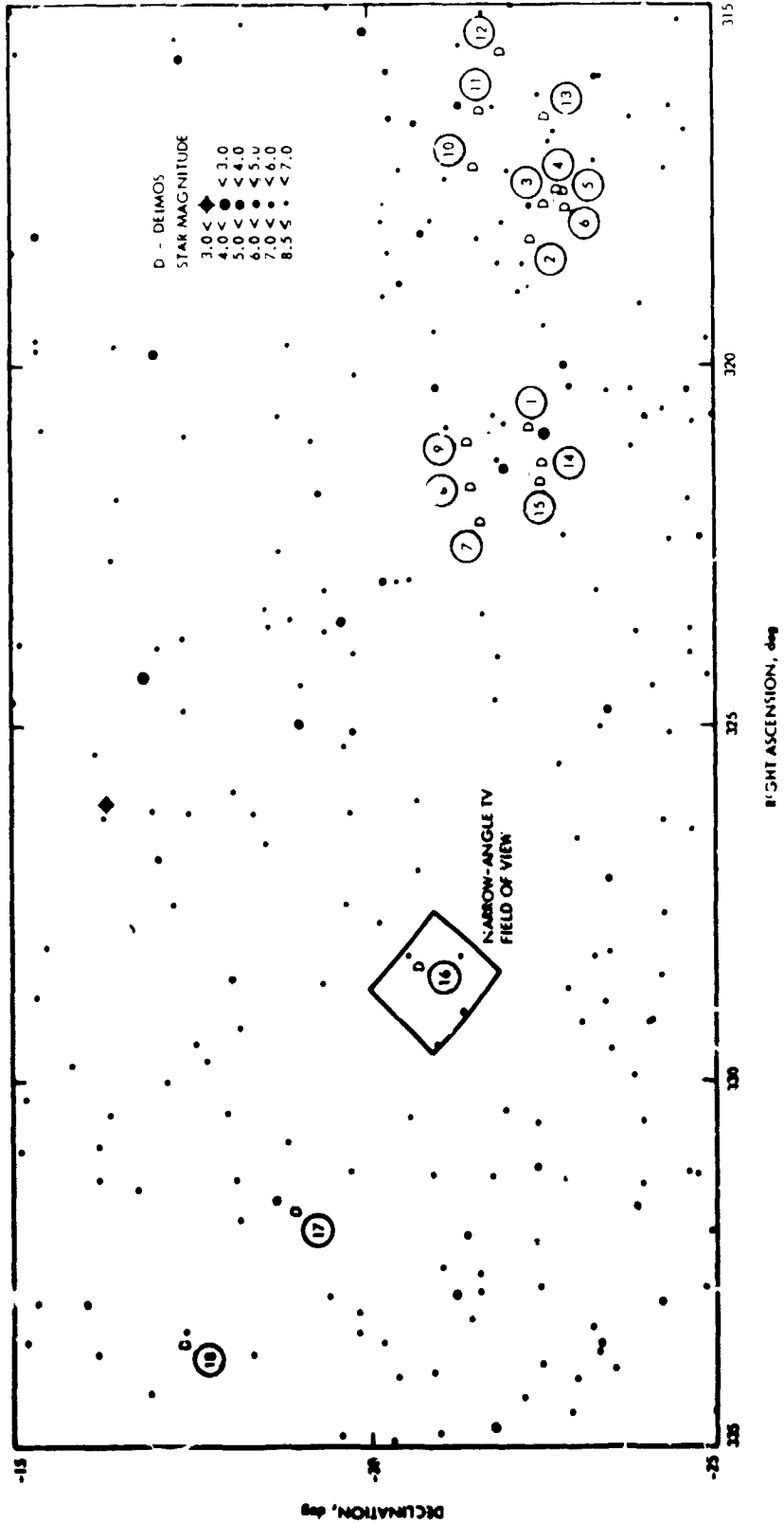


Fig. 44. Approach Deimos/star geometry

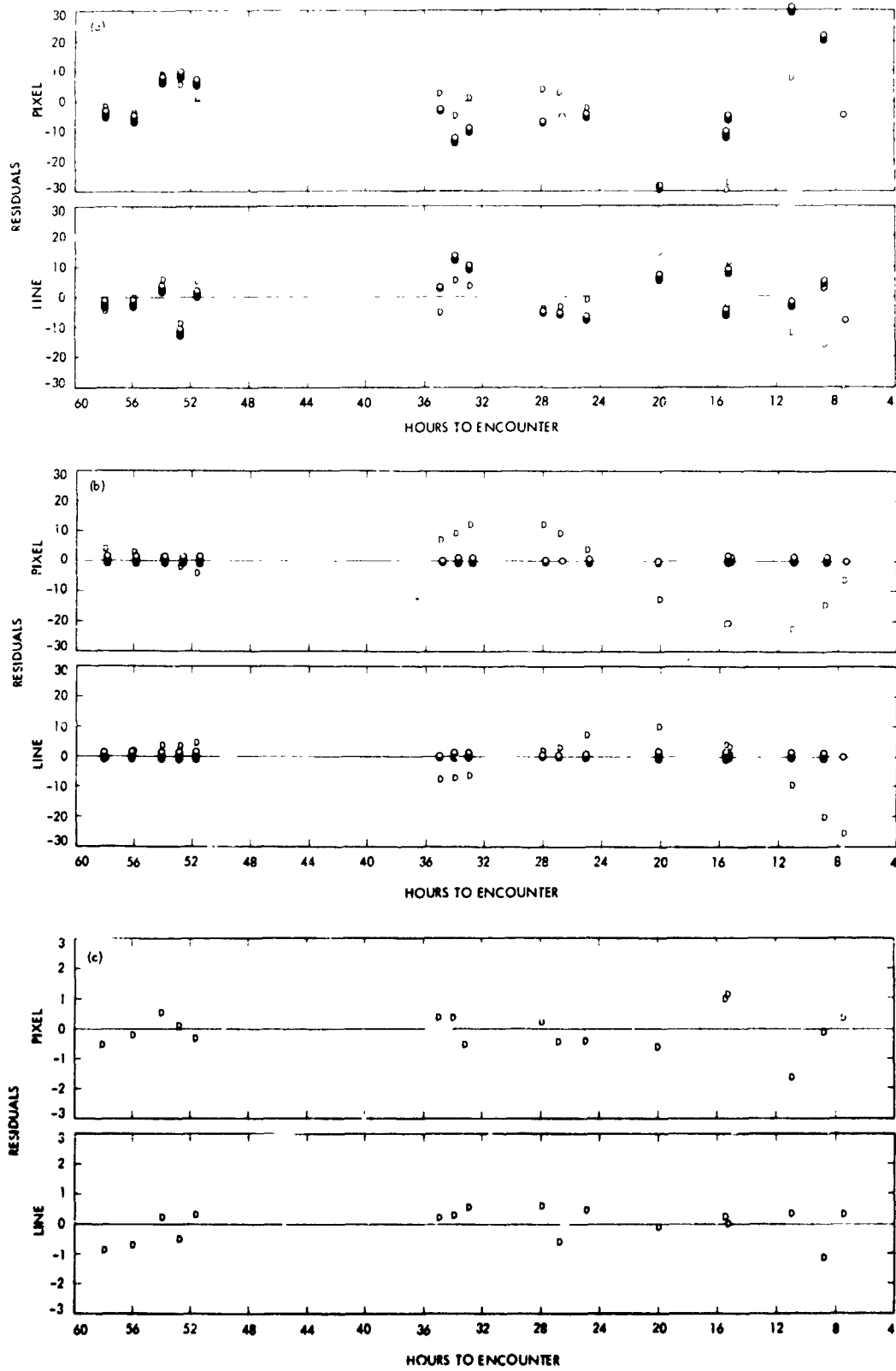


Fig. 45. Deimos observation residuals: (a) raw data, (b) with TV printing errors removed, (c) after fit

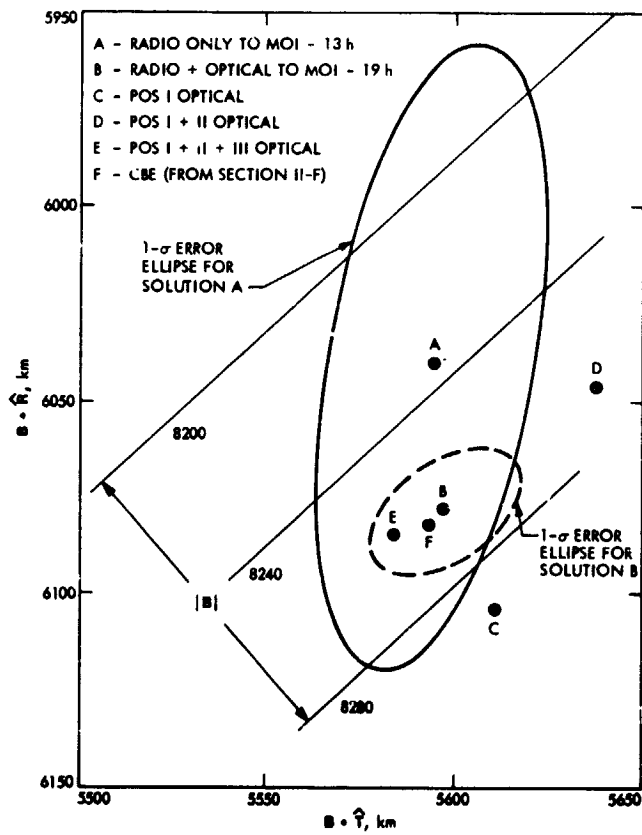


Fig. 46. Near-real-time trajectory estimates

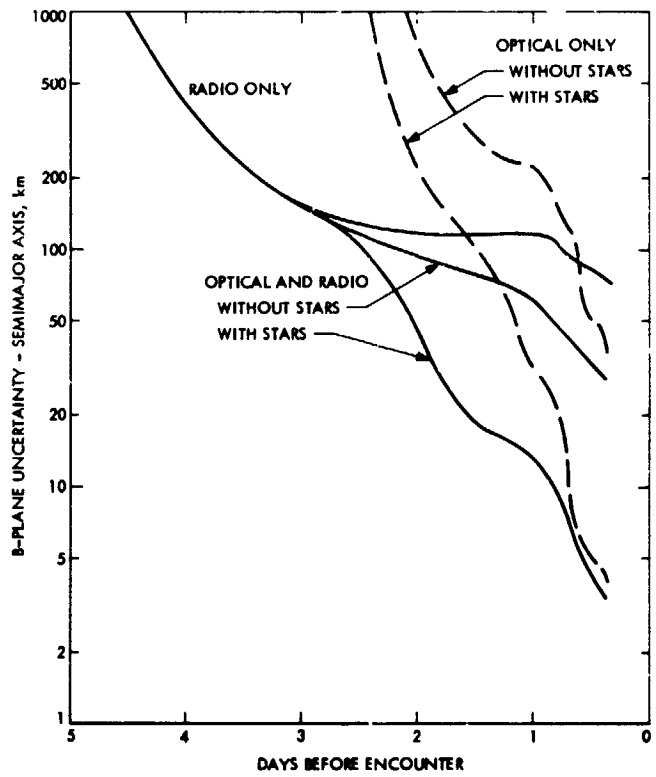


Fig. 47. Expected trajectory estimation accuracy

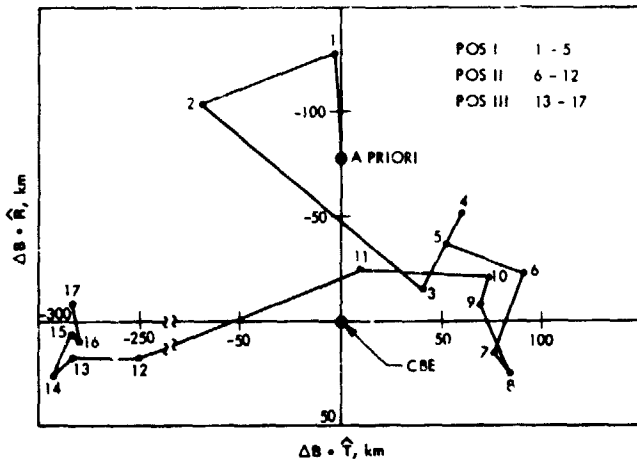


Fig. 48. Trajectory estimate using no stars

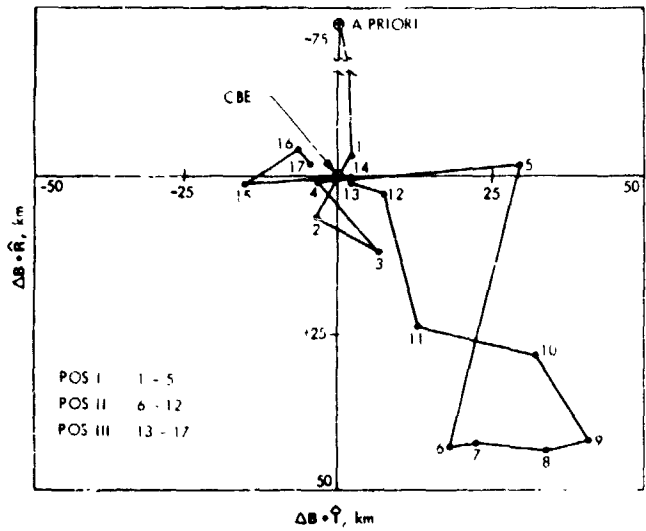


Fig. 50. Trajectory estimate using many stars per picture

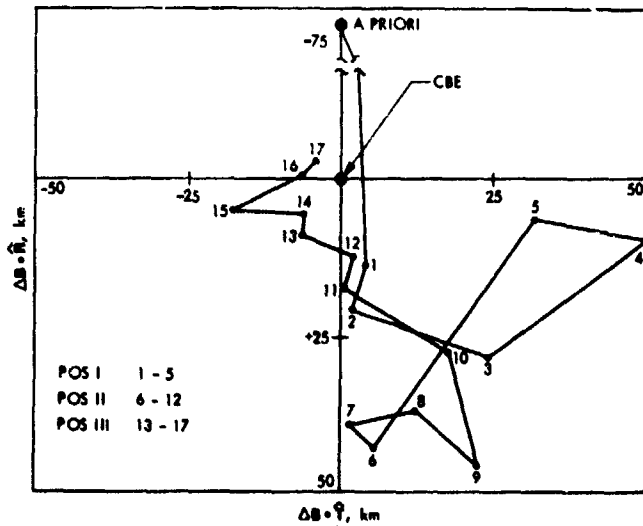


Fig. 49. Trajectory estimate using one star per picture

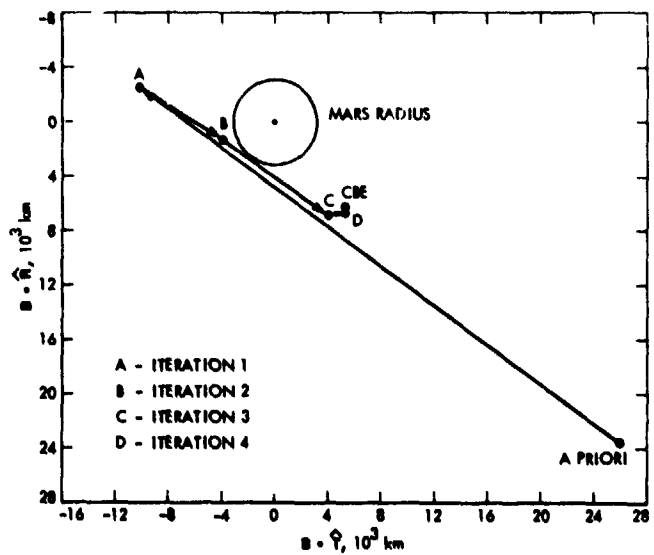


Fig. 51. Optical data solution (coordinates)

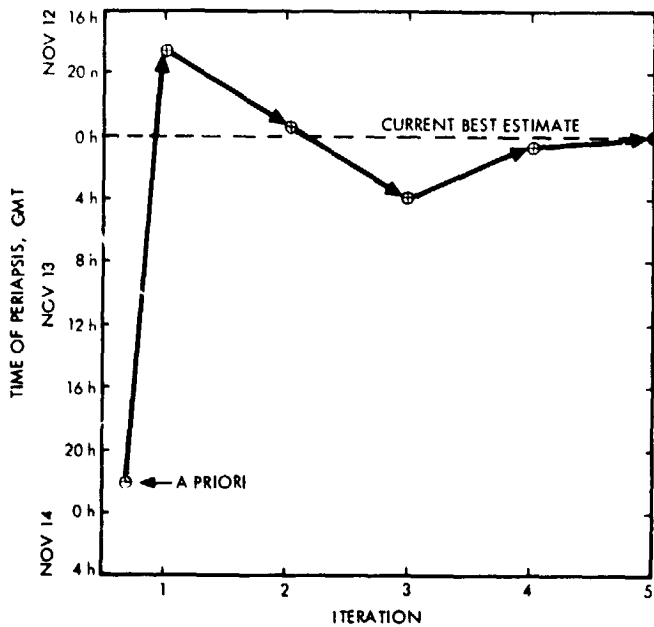


Fig. 52. Optical data solution (time of flight)

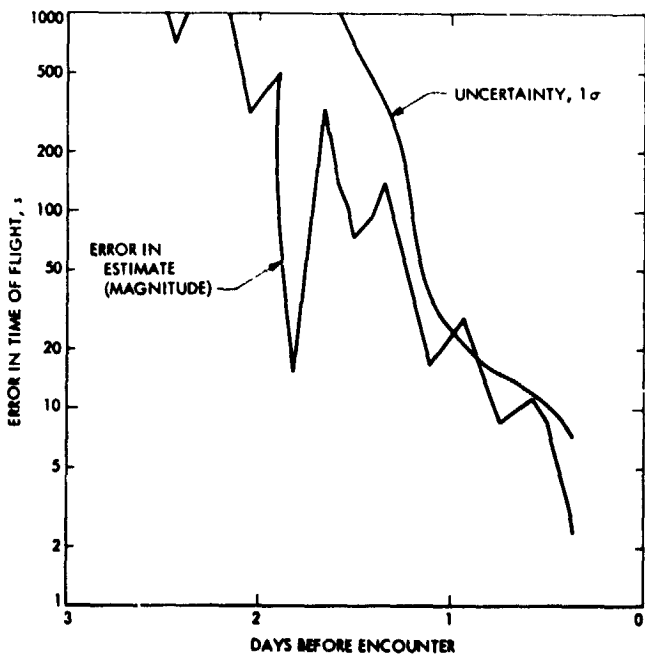


Fig. 53. Estimate of time of flight using optical data

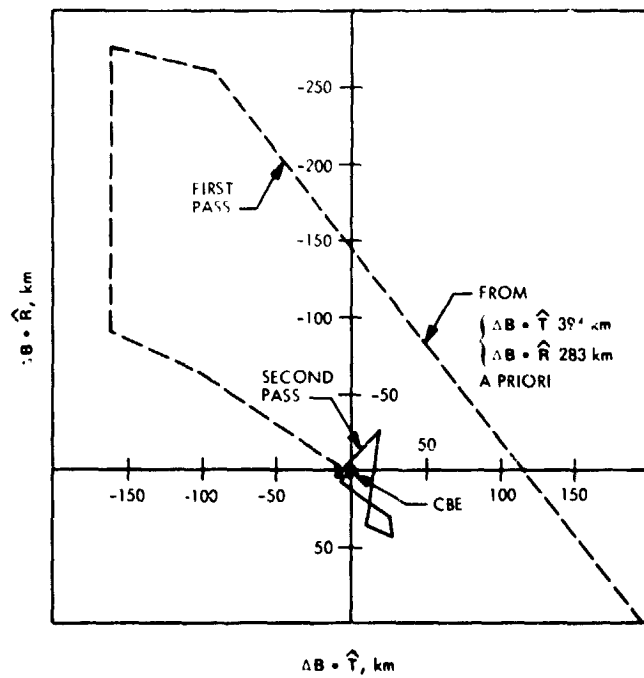


Fig. 54. Sensitivity to Mars ephemeris error

## Appendix A

### Definition of Spacecraft Trajectory Parameters and Associated Statistics at Closest Approach to Mars

- B** a vector from the center of Mars normal to the incoming asymptote of the spacecraft Mars-centered hyperbolic orbit (This conic is computed for the closest approach time.)
- S** a unit vector along the incoming asymptote
- T** a unit vector normal to **S** and lying in the ecliptic plane. **T** is directed very nearly toward the Sun.
- R** a unit vector making up a right-handed RST coordinate system
- $T_{CA}$  the actual closest approach time of the spacecraft to the center of Mars
- $R_{CA}$  the closest approach distance of the spacecraft to the center of Mars
- $\theta'$  the angle from the **+T** axis to the **B** vector measured positively toward **+R** (downward)
- SMAA** the square root of the largest eigenvalue of positional uncertainty in the **B**-plane (The **B**-plane is normal to **S**.)
- SMIA** the square root of the smallest eigenvalue of positional uncertainty in the **B**-plane
- $\theta$  the angle from the **+T** axis to the **SMAA** measured positive from **+T** toward **-R**. This is the opposite convention from the  $\theta'$  definition.

The **SMAA** and **SMIA** form the semimajor and semiminor axes of the 40% dispersion ellipse; i.e., there is a 40% probability that the predicted target point lies in a 40% dispersion ellipse centered about the "true" target point (see Fig.A-1).

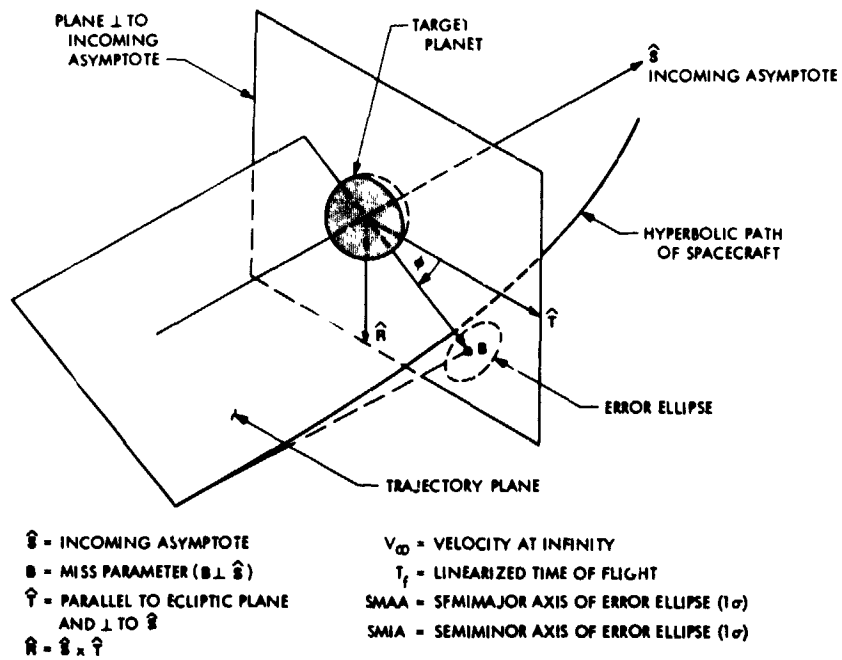


Fig. A-1. Definition of B-plane parameters

## Appendix B Mars Mission Lockfile

```

$ * * * * * MARS MISSION LOCKFILE * * * * *
$ PHASE C VERSION
$
$ THIS LOCKFILE IS DESIGNED FOR PROCESSING REAL DATA ON MARS MISSIONS
$ IT CONTAINS:
$
$ 1. THE 'UNIFIED' LOCKFILE (ODINA)
$
$ 2. TIMING AND POLAR MOTION INPUTS (ODINA)
$
$ 3. INPUT TO INSURE TRAJECTORIES (ODINA)
$ ACCURATE ENOUGH FOR O.D.
$
$ 4. MISCELLANEOUS INPUTS DESIRED (ODINA)
$ BY O.D. ON ALL MARS MISSIONS
$
$ 5. MISCELLANEOUS NON-TRAJECTORY (ODINB)
$ INPUTS
$
$ * * * * * 1. * * * * *
$
$DPODP
OPT='LOCKUP', AFIL='LOCK', BFILE='LOCK2',
;
$INPUT
$NOMINAL VALUES OF THE INPUT PARAMETERS -UNIFIED-C 0.2,
$DPTRAJ/DPODP ODINA- KHATIB- 3/24/71 ,
$ASTRODYNAMIC CONSTANTS ,
GM(1)=.22181597705 , RADI(1)=.243504 , FLAT(1)=0.000 ,
GM(2)=.32486010306 , RADI(2)=.605204 , FLAT(2)=0.000 ,
GM(3)=.398601206 , RADI(3)=.63791604 , FLAT(3)=.3352891865230-0,
GM(4)=.42828443905 , RADI(4)=.3393404 , FLAT(4)=.1050-1,
GM(5)=.12670771909 , RADI(5)=.7137205 , FLAT(5)=.6670-1,
GM(6)=.37926525808 , RADI(6)=.6040105 , FLAT(6)=.10500,
GM(7)=.57877234607 , RADI(7)=.2353505 , FLAT(7)=.6250-1,
GM(8)=.68905762707 , RADI(8)=.2232405 , FLAT(8)=.1770-1,
GM(9)=.73240893505 , RADI(9)=.701504 , FLAT(9)=0.000,
GM(10)=.1327124993908025012, RADI(10)=.E9599206 , FLAT(10)=0.000,
GM(11)=.49027834804 , RADI(11)=.17380904 , FLAT(11)=0.000,
AU(1)=149597893.000 , RE(1)=6378.149256927E1000 , C(1)=299792.500 ,
BETREL(1)=1.000 , GAMREL(1)=1.000 ,
$TIME AND POLAR MOTION TRANSFORMATIONS
STPD(1)=86400.000 , DT58(1)=32.1500 , DRFJ(1)=2433232.500,
RFJD(3)=3HET ,3HET , FRQC(1)=9192631770.000 , FAKE1=2,
$ EPOCH, SEC PAST 50, A.1-UTC, RATE, 12 SETS, REAL INPUT IS TP
IT(1)=510101, TP(1)=.31536E8,9.92,0.0,
IT(4)=990101, TP(4)=.15463008E10,9.92,0.0,
$EPOCH, SEC PAST 50, A.1-UT1, RATE, 12 SETS, PEAL INPUT IS TP., SAME EPOCHS
TP(40)=.31536E8,9.92,0.0, TP(43)=.15463038E10,9.92,0.0,
$POLAR MOTION, SAME EPOCHS,,SEC PAST 50 , X,Y,DX,DY, REAL TP, 12 SETS
TP(151)=.31536E8,0.0,0.0,0.0,0.0,0.0, TP(156)=.15463008E10,
$NEW TRIC AND COORDINATE TRANSFORMATION DATA
$NODE(3) FOR ALL PLANETS +SUN +MOON RESPECTIVELY
COMEGA(1,1)=-0.477385902,-0.1255900,-0.090-3,
COMEGA(1,2)=-0.7622296702,-0.2778500,-0.140-3,
COMEGA(1,3)=-0.1744095E03,-0.2416000,0.600-4,
COMEGA(1,4)=-0.491719302,-0.2947000,-0.0650-2,
COMEGA(1,5)=-0.999433502,-0.1672800,0.550-3,
COMEGA(1,6)=-0.1132201503,-0.2597300,0.620-3,
COMEGA(1,7)=-0.737452102,0.66710-1,-0.0680-2,
COMEGA(1,8)=-0.1312295903,-0.5740-2,-0.290-3,
COMEGA(1,9)=3*0.000,

```

COMEGA(1,10)=0.1744095603,-.2416600,0.60-4,  
 COMEGA(1,11)=0.1211279102,-0.193413992904,0.20810-2,  
 \$INCLINATION 50 FOR ALL PLANETS + SUN +MOON  
 CI50(1,1)=0.70038101,-0.5970-2,0.10-5,  
 CI50(1,2)=0.33941301,-0.860-3,-0.30-4,  
 CI50(1,3)=0.000,0.130760-1,-0.90-5,  
 CI50(1,4)=0.18500001,-0.2210-2,-0.20-4,  
 CI50(1,5)=0.13059201,-0.2050-2,0.30-4,  
 CI50(1,6)=0.24903601,0.1860-2,-0.30-4,  
 CI50(1,7)=0.7730000,-0.1360-2,-0.40-4,  
 CI50(1,8)=0.1774701,0.370-3,0.80-5,  
 CI50(1,9)=3.0.000,  
 CI50(1,10)=0.000,0.130760-1,-0.90-5,  
 CI50(1,11)=0.51453901,0.000,0.000,  
 \$EARTH-OBLIQ(4),RA50(4),DECS0(4),DELTA5L(4), HA CCEFF(6) RESPECTIVELY  
 CEPSBE(1)=23.445788861580338900,-.1301416695621594800-1,  
 CEPSBE(3)=-.9444816418530-6,+5000320391510-6,  
 CEARTH(1)=-.13435407922300-5,-.64027800907729573200,  
 CEARTH(3)=-.839480618953650-4,-.50003203915090-5,  
 CEARTH(5)=89.999998831731894600,-.55675002974884527500,  
 CEARTH(7)=-.1185066931585290-3,.116118551313940-4,  
 CEARTH(9)=89.999998656459206800,-.64027301000166763500,  
 CEARTH(11)=-.3042074711501730-3,-.50836590647010-5,  
 CEARTH(13)=0.100273790929401,0.24003,0.100075542604203,  
 CEARTH(16)=0.36000769312083305,0.38709330-3,0.5890-10,  
 \$EARTH- COEFF OF PA(4), ARGUM. CF PERIH.(3),EARTH LONGIT.(3), RESPECTIVELY  
 CERTH2(1)=0.358000681527803,0.35999045597505,-0.1550-3,-0.333330-5,  
 CERTH2(5)=0.2876709703,0.5649400,0.090-3,  
 CERTH2(8)=0.1744095603,0.11546901,0.370-3,  
 \$MERCURY-OBLIQ.(1), NUTATIONS IN LONG. AND OBLIQ.(2), HA COEF(2), RESPECTIVELY  
 CMERC(1)=3\*0.000, 0.343547203,0.613001,  
 \$RA50(2),DECS0(2),NUT.-LONG(2),NUT-OBLIQ(2),HA CCEF(2),RESPECTIVELY FOR  
 \$VENUS, MARS, JUPIT., SATUR., URAN., NEPTU., SUN, RESPECTIVELY.  
 PLANV(1)=0.980225502,0.000,-0.689887702,5\*0.000,  
 PLANV(9)=0.31769558403,0.148392401,  
 PLANM(1)=0.316853803,-0.9960-1,0.53006602,-0.5660-1,4\*0.000,  
 PLANM(9)=0.14867250103,0.35089196203,  
 PLANJ(1)=0.268044703,0.000,0.64552802,5\*0.000,  
 PLANJ(9)=0.23975103,0.8779002,  
 PLANS(1)=0.384131402,0.000,0.833104902,6\*0.000,0.844303,  
 PLANU(1)=0.7676102,0.000,0.149202,6\*0.000,0.79876703,  
 PLANN(1)=0.295571203,0.000,0.414663502,6\*0.000,0.61714303,  
 PLANSU(1)=0.286019303,0.000,0.63771802,5\*0.000,0.425422500,0.141643971602,  
 \$PLUTO- RA50(1), DECS0(1),MEAN AUTU. EQUIN.(1),OBLIQ.(1),NUTAT.(2), HA,  
 CPLUTO(1)=0.3132913603,0.66364202,0.691358702,3\*0.000,0.5633802,  
 \$MOON-LON OF NODE(E+1),ARG. PERIH(4), PA(4) M-OBLIQ(1), E50 M-OBLIQ(1),  
 \$MOON CONTINUED - FREE LIBRATION COEF(3), RESPECTIVELY  
 CMOON(1)=0.20-5,0.19673119803,0.600316362904,-0.124250-1,-0.140-4,  
 CMOON(6)=0.21553146303,0.4771988583106,0.92140-2,0.140-4,  
 CMOON(10)=0.667900701,0.234457889902,0.341900,0.345803,0.18702,  
 \$COEF OF LUNAR PHYSICAL LIBRATION TA(9), SB(5), RC(5)  
 TA(1)=1.7,91.7,-1.2,4.2,-3.5,-16.9,1.0,15.3,10.0,  
 SB(1)=-3.2,-10.6,-23.8,2.5,-100.7,  
 RC(1)=-3.2,-11.0,23.9,-1.9,-98.5,  
 \$TRAJECTORY CONTRL ,  
 TEND(3)=3MUTC,3MET , FBFL(1)=6HFORMRD, DTFL(1)=6HAUTO ,  
 CBFL(1)=6MPCB , RSPH(1)=1.205,2.506,2.506,2.006,5.007,5.007,  
 RSPH(7)=5.007,8.007,4.007,0.000,4.004,2.506,  
 \$INTEGRATION CONTROL ,  
 M(1)=10, PCOP=3, EPSL(1)=1.0E-6, TOLR=1.E-9, ERMX=1.E-9,  
 ERMN=1.E-14, HMAX(1)=691200.000, HMIN(1)=1.000,

RLD(1)=.3D2,.3D2,.3D2,.3D2,.6D2,.6D2,.6D2,.6D2,.3D2,.768D4,.3D2,  
 RLR(1,1)=5E3,12E3,22E3,38E3,62E3,96E3,140E3,1E20,4.0E0,  
 RLR(1,2)=8E3,16E3,30E3,80E3,120E3,400E3,800E3,1E6,1.8E6,2.8E6,  
 RLR(11,2)=1E20,0.0E0,  
 RLR(1,3)=8E3,16E3,30E3,80E3,120E3,400E3,600E3,1E6,1.8E6,2.8E6,  
 RLR(11,3)=1E20,0.0E0,  
 RLR(10,5)=3E6,5E6,1E20,  
 RLR(1,5)=100E3,200E3,300E3,400E3,600E3,800E3,1E6,1.2E6,2E6,  
 RLR(10,4)=2E6,1E20,0.0E0,  
 RLR(1,4)=6E3,12E3,25E3,60E3,100E3,300E3,500E3,800E3,1.2E6,  
 RLR(1,6)=100E3,200E3,300E3,400E3,600E3,800E3,1E6,1.2E6,2E6,  
 RLR(10,6)=3E6,5E6,1E20,  
 RLR(1,7)=100E3,200E3,300E3,400E3,600E3,800E3,1E6,1.2E6,2E6,  
 RLR(10,7)=3E6,5E6,1E20,  
 RLR(1,8)=100E3,200E3,300E3,400E3,600E3,800E3,1E6,1.2E6,2E6,  
 RLR(10,8)=3E6,5E6,1E20,  
 RLR(1,9)=8E3,16E3,30E3,80E3,120E3,400E3,600E3,1E6,1.8E6,2.8E6,  
 RLR(11,9)=1E20,0.0E0,  
 RLR(1,10)=1E20,11.0.0E0,  
 RLR(1,11)=5E3,12E3,20E3,30E3,45E3,70E3,1E20,5.0.0E0,  
 RLR(1,12)=12.0.0E0,

\$GRAVITATIONAL PERTURBATIONS ,  
 PERB=11\*1,EF1T(3)=2HET,2HET,EF2T(3)=2HET,2HET,EF3T(3)=2HET,2HET,  
 EF1B(1)=6H ,EF2B(1)=6H ,EF3B(1)=6H ,

OBAF=6HEARTH ,4,  
 OBAO = 2.000 ,  
 OBAR = .63781E04 ,  
 OBAJ(2)= .10827D-2, OBAC(2,2)= .1570D-5, OBAS(2,2)= -.8970D-6,  
 OBAJ(3)= -.2560D-5, OBAC(3,1)= .2100D-5, OBAS(3,1)= .1600D-6,  
 OBAJ(4)= -.1580D-5, OBAC(3,2)= .2500D-6, OBAS(3,2)= -.2700D-6,  
 OBAJ(5)= -.1500D-6, OBAC(3,3)= .7700D-7, OBAS(3,3)= .1730D-6,  
 OBAJ(6)= .5900D-6, OBAC(4,1)= -.5800D-6, OBAS(4,1)= -.4600D-6,  
 OBAJ(7)= -.4400D-6, OBAC(4,2)= .7400D-7, OBAS(4,2)= .1600D-6,  
 OBAC(4,3)= .5300D-7, OBAS(4,3)= .4000D-8,  
 OBAC(4,4)= -.6500D-8, OBAS(4,4)= .2300D-8,

OBBF=6HMOON ,2,2,2,  
 OBBD = 4.004 ,  
 OBBR = 0.173809D4 ,  
 OBBJ(2) = 2.054D-4 ,  
 OBBC(2,2) = 0.231D-4 ,  
 OBCF=6HMARS ,2,  
 OBCD = 2.006 ,  
 OBCR = 0.33934D4 ,  
 OBCJ(2) = 0.197D-2 ,

\$SOLAR PRESSURE ,  
 SC(1)=1.04D8 ,SAST(3)=3HUTC, CANO(1)=-.05034347D0,.63342983D0,  
 CANO(3)=-.79512962D0, SASP(1)=1.34D0, REFB(1)=6MCANOPU ,  
 \$ATTITUDE CONTROL ,  
 SAAT(3,1)=3HUTC,SAAT(3,2)=3HUTC,  
 \$EXPONENTIAL GAS LEAK ,  
 ISTREX(3,1)=3HUTC,3HET ,ISTREX(3,2)=3HUTC,3HET ,ISTREX(3,3)=3HUTC,2HET,  
 ISTPEX(3,1)=3HUTC,3HET ,ISTPEX(3,2)=3HUTC,2HET,ISTPEX(3,3)=3HUTC,2HET,  
 \$MOTOR BURNS ,  
 MA1T(3)=3HUTC,2HET,MA2T(3)=3HUTC,2HET,MA3T(3)=3HUTC,2HET,MA1K=.1D-2,  
 MA2K=.1D-2,MA3K=.1D-2,MB1T(3)=3HUTC,2HET,MB2T(3)=3HUTC,2HET,  
 MB3T(3)=3HUTC,2HET, BURN(1)=3\*1,  
 \$LIFT AND DRAG  
 SKF(1)=1.0D-6,  
 SMS = 3.004,  
 \$TRAJECTORY INITIAL CONDITIONS ,  
 IMES=6HCARTES,IXAX=6HSPACE ,ICEN=6HEARTH ,DIE0=1950.000,  
 IEQX(3)=3HET ,3HET ,IZAX=6HEARTH ,6HMEAN ,6HEQUATO,OE0X(3)=3HET ,

ORIGINAL PAGE IS POOR

```

OMES=6HCARTES,OXAX=6HSPACE,CCEN=6HEARTH,OZAX=6HEARTH,6HMEAN,
OZAX(3)=6HEQUATO,DOEQ=1950.000,PHIL=28.30900,ITIM(3)=3HUTC,
ITOP=6HSPHERI,OTOP=6HSPHERI,
$TRAJECTORY OUTPUT CONTROL,
FILE=1,HPEP=1.008,SKIP=1,EPSN=.10-5,PRT(1)=1,ETIM(3)=2HET,2HET,
LABL(1)=38*6H,PAGE(1)=19*6H,
WROSP=6HC-0,
ABST(3,1)=2HET,2HET,ABST(3,2)=2HET,2HET,ABST(3,3)=2HET,2HET,
ABST(3,4)=2HET,2HET,ABST(3,5)=2HET,2HET,ABST(3,6)=2HET,2HET,
ABST(3,7)=2HET,2HET,ABST(3,8)=2HET,2HET,ABST(3,9)=2HET,2HET,
ABST(3,10)=2HET,2HET,PCB(25,1)=2HET,2HET,PCE(25,2)=2HET,2HET,
CRFL(1)=6HEXTERN,
PCB(25,3)=2HET,2HET,PCB(25,4)=2HET,2HET,PCB(25,5)=2HET,2HET,
PCB(25,6)=2HET,2HET,PCB(25,7)=2HET,2HET,PRT(3,1)=2HET,2HET,
PRT(3,2)=2HET,2HET,PRT(3,3)=2HET,2HET,PRT(3,4)=2HET,2HET,
PRT(3,5)=2HET,2HET,PRT(3,6)=2HET,2HET,PRT(3,7)=2HET,2HET,
PRT(5,1)=6HSINGLE,PRT(5,2)=6HSINGLE,PRT(5,3)=6HSINGLE,
PRT(5,4)=6HSINGLE,PRT(5,5)=6HSINGLE,PRT(5,6)=6HSINGLE,
PRT(5,7)=6HSINGLE,
PCB(1,1)=6HSUN,PCB(3,1)=1,2,PCB(1,2)=6HEARTH,PCB(3,2)=1,2,
DPR(1,1)=1950.000,PRT(6,1)=6HEARTH,6HEARTH,6HMEAN,6HEQUATC,
PRT(12,1)=6HSUN,6HEARTH,6HMEAN,6HORBITA,PRT(24,1)=6HSUN,
PRT(6,2)=6HEARTH,6HEARTH,6HTRUE,6HEQUATC,PRT(12,2)=6HSUN,6HEARTH,
PRT(14,2)=6HTRUE,6HORBITA,PRT(24,2)=6HEARTH,
$EARTH STATIONS DATA, STATION LOCATION SET LS28- 12/29/70
AE=6378.1600,DPTES(1)=12*1900.0500,
STANAM(1,1)=24HGOLDSTONE PIONEER,
STANAM(1,2)=24HGOLDSTONE ECHO,
STANAM(1,3)=24HGOLDSTONE 210 FT,
STANAM(1,4)=24HMOONERA,
STANAM(1,5)=24HCANBERRA,
STANAM(1,6)=24HJOBURG,
STANAM(1,7)=24HROBLEDC,
STANAM(1,8)=24HCEBREROS,
ES(1,1)=11,6HHA-DEC,6HCYLIND,
ES(1,2)=12,6HHA-DEC,6HCYLIND,
ES(1,3)=14,6HAZ-EL,6HCYLIND,
ES(1,4)=41,6HHA-DEC,6HCYLIND,
ES(1,5)=42,6HHA-DEC,6HCYLIND,
ES(1,6)=51,6HHA-DEC,6HCYLIND,
ES(1,7)=61,6HHA-DEC,6HCYLIND,
ES(1,8)=62,6HHA-DEC,6HCYLIND,
ESDATA(1,1)=243.150613400,3673.76300,5206.34159300,
ESDATA(1,2)=243.194545300,3665.62800,5212.05319200,
ESDATA(1,3)=243.110499400,3677.05200,5203.99852600,
ESDATA(1,4)=136.887521800,-3302.24300,5450.19897400,
ESDATA(1,5)=148.98127500,-3674.64600,5205.35053700,
ESDATA(1,6)=27.6854110600,-2768.74400,5742.94206100,
ESDATA(1,7)=355.750977900,4114.88500,4862.60780600,
ESDATA(1,8)=355.6322170700,4116.90800,4860.81759400,
MVWANT(1)=2HET,2HET,
STACOF(1,1,1)=2.0,0.0,270.75,4*0.0,77.630284,
STACOF(1,2,1)=1.77,630284,-.10314291E2,-.20803256,.19486614E-1,
-.24040826E-3,.83630960E-6,113.0,
STACOF(1,3,1)=1.113,0,-.42574919E2,-.58284155,.25687248E-1,
-.20469425E-3,.48992056E-6,166.044515,
STACOF(1,4,1)=3.166,044515,311.616,4*0.0,200.05731,
STACOF(1,5,1)=1.200,05731,-.16963657E3,-.30570691,.76442280E-2,
.18166260E-4,-.13613741E-6,228.0,
STACOF(1,6,1)=1.228,0,-.14550392E2,.55495194,-.39397366E-3,
-.17835216E-4,.45287370E-7,272.80148,
STACOF(1,7,1)=2.272,80148,90.022,4*0.0,360.0,

```

STACOF(1,1,2)=1.,0.0,5.2,4\*0.0,360.0,  
 STACOF(1,1,3)=3.,0.0,48.684,4\*0.0,25.870692,  
 STACOF(1,2,3)=1.,25.870692,.33039522E1,-.12721327,.362966E9E-2,  
 -.47051634E-4,.1786E475E-E,58.049E27,  
 STACOF(1,3,3)=2.,98.049627,265.788,4\*0.0,180.0,  
 STACOF(1,4,3)=2.,180.0,96.246,4\*0.0,258.130E7,  
 STACOF(1,5,3)=1.,258.130E7,-.12487371E1,-.8362E709E-1,.36771227E-3,  
 .45273767E-6,-.21747013E-E,333.89425,  
 STACOF(1,6,3)=3.,333.88425,48.684,4\*0.0,360.0,  
 STACOF(1,1,4)=3.,0.0,47.992,4\*0.0,15.331349,  
 STACOF(1,2,4)=1.,15.331349,-.44611256E1,.11000933E1,-.48064202E-1,  
 .94749819E-3,-.63933543E-5,69.0,  
 STACOF(1,3,4)=1.,69.,.53716762E2,-.10029115E1,.27988004E-2,  
 .80397655E-4,-.46864056E-6,121.32450,  
 STACOF(1,4,4)=2.,121.32450,257.264,4\*0.0,180.0,  
 STACOF(1,5,4)=2.,180.0,100.262,4\*0.0,246.39012,  
 STACOF(1,6,4)=1.,246.39012,-.27832537E2,.71988679,-.85958835E-3,  
 .29368643E-6,.51562041E-9,336.79229,  
 STACOF(1,7,4)=3.,336.79229,47.992,4\*0.0,360.0,  
 STACOF(1,1,5)=3.,0.0,49.6,4\*0.0,27.014899,  
 STACOF(1,2,5)=1.,27.014899,.62466306E2,-.50234724E1,.15769151,  
 -.21396949E-2,.10636528E-4,69.0,  
 STACOF(1,3,5)=1.,65.0,-.34791256E2,.62662482,.8055E520E-2,  
 -.18321512E-3,.81250981E-6,104.02914,  
 STACOF(1,4,5)=2.,104.02914,265.774,4\*0.0,180.0,  
 STACOF(1,5,5)=2.,180.0,90.374,4\*0.0,265.03513,  
 STACOF(1,6,5)=1.,265.03513,.13867070E3,-.35475290,.11134807E-2,  
 -.21113009E-4,.55120421E-7,296.0,  
 STACOF(1,7,5)=1.,296.0,.42292366E1,-.63536572,.22671088E-2,  
 .53576139E-5,-.19133017E-7,334.99321,  
 STACOF(1,8,5)=3.,334.99321,49.6,4\*0.0,360.0,  
 STACOF(1,1,6)=2.,0.0,255.864,4\*0.0,54.772925,  
 STACOF(1,2,6)=1.,64.772825,-.23371603E2,.94217241,-.75527187E-3,  
 -.11967487E-3,.69163223E-6,118.0,  
 STACOF(1,3,6)=1.,118.0,-.23460736E2,.56132013,-.25681203E-2,  
 -.61584356E-5,.40169110E-7,174.17944,  
 STACOF(1,4,6)=3.,174.17944,311.144,4\*0.0,188.3940E,  
 STACOF(1,5,6)=1.,188.3940E,-.26884192E2,.16439455E1,-.12448171E-1,  
 .14023659E-4,.52171047E-7,218.0,  
 STACOF(1,6,6)=1.,218.0,-.21303883E1,-.45851290E-1,-.15E10107E-3,  
 .46421653E-5,-.11158741E-7,294.42224,  
 STACOF(1,7,6)=2.,294.42224,102.428,4\*0.0,360.0,  
 ST1262(1,1,1)=2.,0.0,266.840,4\*0.0,76.0,  
 ST1262(1,2,1)=3.,76.0,13.958,4\*0.0,78.0,  
 ST1262(1,3,1)=2.,78.0,270.05,4\*0.0,89.745845,  
 ST1262(1,4,1)=1.,89.745845,-.40655151E2,.92843309E-1,.71739722E-2,  
 .26767812E-5,-.41801529E-6,93.0,  
 ST1262(1,5,1)=1.,93.0,.52757641E2,-.92072283,.22093288E-2,  
 .32051217E-4,-.14295263E-E,156.83989,  
 ST1262(1,6,1)=3.,156.83989,311.45,4\*0.0,185.76166,  
 ST1262(1,7,1)=1.,185.76166,.19224893E2,-.10424344E1,-.3119482E-1,  
 .316E235E-3,-.78748585E-6,192.0,  
 ST1262(1,8,1)=1.,192.0,.1280E705E2,-.15108728,.39930036E-3,  
 .29883620E-5,-.11103625E-7,269.91486,  
 ST1262(1,9,1)=2.,269.91486,89.486,4\*0.0,281.0,  
 ST1262(1,10,1)=3.,281.0,13.958,4\*0.0,285.0,  
 ST1262(1,11,1)=2.,285.0,96.012,4\*0.0,360.0,  
 ST1262(1,1,2)=2.,0.0,255.47,4\*0.0,63.302922,  
 ST1262(1,2,2)=1.,63.302922,.51464513E2,-.80610698,-.10E41681E-1,  
 .25990119E-3,-.12176147E-5,112.0,  
 ST1262(1,3,2)=1.,112.0,-.21181374E3,.37240397E1,-.74297204E-2,  
 -.15358037E-3,.67208290E-6,151.0



```

DANAMS(1,13)='TAU',      DANAMS(1,14)='MU',      DANAMS(1,15)='ANGLE S',
DANAMS(1,16)='AZ',      DANAMS(1,17)='EL',      DANAMS(1,18)='HA',
DANAMS(1,19)='DEC',     DANAMS(1,20)='X30',     DANAMS(1,21)='Y30',
DANAMS(1,22)='X85',     DANAMS(1,23)='Y85',
DANUMS=0,5,10,11,12,13,14,21,30,31,32,33,34,35,50,51,52,53,54,55,56,57,58,
      $ REGRES INPUT
BASE= 2*20.06,960.06,2290.06, PARTLS=70* * , FLAND=2* * ,
BNDCON(1,1)=2298.506,1.00,104.253393665158400,1.06,104.253393665158400,
BNDCON(1,2)=2298.506,1.00,32.5791855203619300,1.06,32.5791855203619900,
LTCRIT=1.0-7,NOLT=5,
      $ OUTPUT INPUT
PLOTYP ='F2','TAU','MARK1A','PLSCAL=.1,2*100.,NH?=12,IPFLAG=3,E,5,4,5,2,5,2,5,
RSTA(1)='DSN 11','DSN 12','DSN 14','DSN 41','DSN 42','DSN 51','DSN 61',
      'DSN 62','SPCRFT',6* * ,PRSOL=266* * ,
PSTA(1)='DSN 11','DSN 12','DSN 14','DSN 41','DSN 42','DSN 51','DSN 61',
      'DSN 62','SPCRFT',6* * ,PLSOL=266* * ,
QPLOT=0, SECLIN=600,
      $ SOLVE INPUT
LUCON=86.3135019086591600,EST=70* * ,CCN=70* * ,EXCN=2* * ,APNAMS=70* * ,
QB=1.,QC=1.,
EPS1=1.E-30,EPS2=1.E-30,SVD=1,SOLPRP(4)=1, SOLPRP(8)=1,1,
SOLPRP(10)=1,
      $ UPDATE INPUT
TESTQ=1.,ITHAX=1,
      $ MAPGEN INPUT
CTOLR=1.E-5,CITLIM=5,
      $GENERAL INPUT
TOSSE=104,TOKEEP=6,TODRUG=43, EDFLAG=1,
RGLNO=17,45,46,47,48,
LABL=38* * ,
4ADD MM71*TSACDECKS.TROPCSTABLES/ICM-3913-352
      $MAPSEM INPUT
MAPRP=0,1,PRPOST='PRE',EIGEN=20* * ,
OPEND2=1,
$
;
$DPODP
OPT='ONMCO','AFILE='LOCK','BFILE='LOCK2',
OMNSTR='ODINA','COINB',
$
;
$INPUT
OPEND=1, $
;
$INPUT2
OPEND2=1, $
;
ENDCSP
$DPODP
OPT='STOP', $
;

```

# Satellite Orbit Determination

J. F. Jordan, D. H. Boggs, G. H. Born, E. J. Christensen, A. J. Ferrari, D. V. Green,  
R. K. Hylkema, S. N. Mohan, S. J. Reinbold, and G. L. Sievers

## I. Introduction and Summary

The satellite phase of the Mariner Mars 1971 (MM71) mission began on November 14, 1971, at 00 h 42 min UT, when the Mariner 9 spacecraft was injected into a Mars orbit by a 1600.5-m/s maneuver. The initial orbit had a period of approximately 12 h 37 min.

The selection of the original elements for the Mariner 9 orbit and the strategy of subsequent trim maneuvers were arrived at on the basis of science and propellant constraints (Ref. 1). The selected orbit maximized the longitudinal and latitudinal coverage of the planet, ensured early Earth occultations, no early Sun occultations, and no violation of propellant constraints.

The first orbital trim maneuver was performed by a 15.3-m/s burn near the fourth periapsis passage. The burn corrected the period to 11 h 58 min and synchronized the periapsis passage with the zenith of the Goldstone station to maximize the science data return, as discussed earlier.

After sufficient data were available to more accurately determine the mean orbital period, a 41.9-m/s trim was performed in revolution 94 to resynchronize periapsis passage with the Goldstone zenith and to increase the periapsis altitude. Approximate values of the initial, post-trim 1, and post-trim 2 orbital elements of Mariner 9 are given in Table 1.

Mariner 9 continued to orbit Mars as a "live" spacecraft until October 27, 1972, at 17 h 41 min UT, when the last

signal from the spacecraft was received. Thus, the live satellite phase of the mission endured for approximately 347 days 17 h.

A precise knowledge of the orbit of Mariner 9 was required throughout the satellite phase of the mission. The various necessary orbit determination tasks were to

- (1) Converge to an orbit solution using data in the first orbit revolution and supply, at that time and throughout the remainder of the mission, predicted trajectories for observable prediction and tracking station frequency tuning purposes.
- (2) Determine the predicted orbit, from data in the first three revolutions, to compute the first trim maneuver at the end of the fourth revolution. An acceptable trim was dependent on a predicted orbital period in the fifth revolution accurate to 3.0 s, and a determined height of periapsis passage accurate to 1.5 km. Orbit determination support was also required for the second orbit trim.
- (3) Provide trajectories which located the predicted position of the spacecraft to an accuracy of 10 km in the martian plane of the sky for a period of 1 week into the future. This requirement, the provision of predicted trajectories for science sequence planning, was the most stringent orbit determination (OD) requirement and was imposed at all times when scan platform maneuvers were imminent. The 10-km accuracy requirement is consistent

with a maximum science instrument pointing uncertainty of 0.5 deg. A total of more than 7000 TV images, 50,000 UV spectra, 20,000 IR spectra, and 400 S-band occultation measurements of the Martian surface were obtained on the basis of the predicted trajectories.

- (4) Provide final trajectories throughout the regions in which visual images and spectra were obtained. These "smooth" trajectories were determined from local doppler data and did not involve extrapolation beyond the data interval. The smooth trajectories provided the final best estimate of the spacecraft position at science data-acquisition times.
- (5) Supply Earth-to-Mars pseudo-range measurements for use in the relativity effort of the celestial mechanics experiment. These constructed Earth-Mars range data, referred to as "normal" data points, were obtained at the times of MU ranging and were constructed as described in Subsection IX.

Orbit Determination activities performed by the Satellite OD Group are outlined in Table 2. The staffing level shown in the table was maintained throughout most of the satellite phase of the mission.

The processing software used by the Satellite OD Group to process data was identical to that used by the Interplanetary OD Group. This software, which was operational on the UNIVAC 1108 computer, is described in the Interplanetary Orbit Determination section.

This section is concerned primarily with the history of the activities of the Satellite OD Group during the MM'71 mission and provides an assessment of the accuracy of the determined orbit of the Mariner 9 spacecraft. The results of the pre-flight studies are reviewed, and the major error sources described. The tracking and data-fitting strategy actually used in real-time operations is itemized. The Deep Space Network (DSN) data available for orbit fitting during the mission and the auxiliary information used by the Navigation Team, such as the nongravitational force models from attitude control sensor data, TV imaging data, planetary ephemerides, and astrodynamical constants, are described. A detailed orbit-fitting history of the first four revolutions of the satellite orbit of Mariner 9 is presented, with emphasis on the convergence problems and the delivered solution for the first orbit trim maneuver. The results of sensing the gravity field of Mars and the direction of its spin axis are discussed, and a summary history of the predicted and smooth determined

trajectories is given. Also included are a solution accuracy summary, the history of the spacecraft orbit osculating elements, the results of verifying the radio orbit solutions with TV imaging data, and a summary of the normal points generated for the relativity experiment.

## II. Satellite Orbit Determination Pre-flight Studies

### A. Scope and Methodology of Pre-flight Studies

The problem of determining the orbit of a spacecraft around a planet is vastly different than when the spacecraft is in interplanetary cruise phase. A spacecraft in cruise phase experiences very low accelerations; thus, the information content of Earth-based data is as much dependent on the motion of the tracking stations on the Earth's surface as on the motion of the probe itself. Therefore, the requirement for accurate station location values consistent with the planetary ephemerides is vitally important.

A spacecraft in a planetary orbit experiences relatively high and rapidly changing accelerations, which give Earth-based data a high content of information about the spacecraft motion relative to the planet. Dependence of the orbit solution accuracies on the motion of the stations is thus reduced considerably, while other sources of errors become dominant. Extensive pre-flight OD studies were performed prior to real-time operations for reasons that included the following:

- (1) To further an understanding of the technical aspects of the satellite OD task in terms of the sensitivities of the solution accuracy to quantity and pattern of tracking data and geometry.
- (2) To identify the most probable major model error sources for the OD task and to understand the influence of such model errors on the solution accuracies.
- (3) To develop an operational strategy, or sequence of solution computations, suitable for performing the OD task.
- (4) To demonstrate effectiveness of the personnel and software to complete the OD task in a competent and timely manner.

All of these aspects of flight readiness were addressed in the Mariner 9 pre-flight studies. The studies employed two distinct methods of analysis. In the 2 years prior to encounter with Mars, the dynamic and geometric properties of the satellite OD problem were studied using the

methods of covariance analysis. In the last few months before encounter, extensive simulation exercises were conducted in a simulated environment which was designed to reflect the predicted real-time conditions as accurately as possible. The simulation exercises were used to test procedures and verify the solution accuracies predicted from covariance analyses.

The results of the pre-flight studies disclosed two distinct OD-related difficulties of major importance in the satellite phase of the mission. The first was the convergence problem, which arises in the differential correction estimation procedure and is caused by the effects of nonlinearities. The second difficulty involved the limitations imposed on the accuracy of converged orbit estimates by the *a priori* lack of knowledge of the structure of the Martian gravity field. The remainder of this section summarizes the state of the art prior to the Mariner 9 mission in relation to these two problems and outlines the solution strategy that was eventually employed in actual operations.

## B. Orbit Convergence Problem and Partial-Step Algorithm

1. **Problem statement.** Nonlinearities result from the inability to accurately relate finite deviations in the data to deviations in the probe state with first-order partial derivatives. The convergence problem, which arises with a Mars orbiter because of the effects of nonlinearities, was recognized some time before the Mariner 9 mission. Full-step, weighted, least-squares differential corrections, which are entirely adequate for interplanetary OD, were shown to lead to divergent results in many cases, even for small initial state errors (Ref. 2). To deal with the difficulties associated with nonlinearities, a rank deficient, partial-step differential correction algorithm was implemented in the ODP. The partial-step method uses an *a priori* covariance matrix to automatically constrain the relative magnitudes of individual components of the solution step in the eigenvector space of the normal matrix, thereby reducing the probability of taking divergent steps. The theory of the partial-step algorithm is given in Ref. 2, where the results of a preliminary OD convergence study for MM71 are presented. The final preflight statistics of the tested ODP orbit convergence capability is given here in terms of the results of test cases on the mission. The region of convergence is compared with the preflight predicted orbit error caused by maneuver errors and encounter phase OD errors.

2. **Predicted OD accuracy at initial periapsis.** The orbit knowledge error at the termination of the Mars orbit

insertion (MOI) maneuver is composed of the encounter phase OD error and the state error caused by errors in executing the spacecraft insertion maneuver. Figure 1 illustrates the encounter phase OD uncertainty for doppler tracking of the spacecraft from  $E = 30$  days. Plotted in the figure are the rss position and rss velocity uncertainties at hyperbolic periapsis, in an areocentric cartesian coordinate system, as functions of the time at which the tracking is terminated. Error assumptions used to derive the curves in Fig. 1 are given in Table 3.

The accuracy obtained from the processing of tracking data up to  $E = 1$  h was taken as a nominal expected figure because roll maneuvers were to be made in the last hour in preparation for the MOI maneuver. At the initial periapsis, these accuracies were

$$3\sigma(\text{rss position}) \approx 30 \text{ km}$$

$$3\sigma(\text{rss velocity}) \approx 20 \text{ m/s}$$

3. **Maneuver errors.** The state knowledge uncertainties at the initial periapsis caused by errors in the MOI maneuver were expected to be well within the following tolerances:

$$3\sigma(\text{rss position}) \approx 17 \text{ km}$$

$$3\sigma(\text{rss velocity}) \approx 49 \text{ m/s}$$

Because the OD and maneuver errors were expected to be uncorrelated, these individual errors were combined to yield the following total 3- $\sigma$  state knowledge uncertainties at the initial periapsis:

$$3\sigma(\text{rss position}) \approx 34 \text{ km}$$

$$3\sigma(\text{rss velocity}) \approx 53 \text{ m/s}$$

4. **Results of partial-step method and worst direction for errors.** Several studies were completed using the partial-step algorithm to aid in OD convergence. Although errors in all directions in the state space led to convergence with the partial-step method, some directions appeared more favorable than others. A worst direction for errors at initial periapsis was found; the convergence region for this direction yielded a conservative estimate of the capabilities of the partial-step method. To get an intuition of the worst direction for an initial state error, the doppler time history for a planetary satellite like Mariner 9 (shown in Fig. 2) must be considered. If the solid line represents the real data and the broken line the predicted data based on an *a priori* state at periapsis,  $t_0$  and  $t_1$  are the first and second periapsis times of the true

trajectory—the generator of the real  $t_1$ . The following convergence characteristics were observed in almost all of the partial-step cases observed to date, where  $t$  represents the end of the data span processed (for all cases  $t < t_1$ —the predicted orbital period):

- (1) If the second periaapsis of the true trajectory is not included in the real data—i.e., if  $t < t_1$ —then convergence is obtained.
- (2) If the second periaapsis is included in the real data—i.e., if  $t > t_1$ —then convergence is not obtained.

These observations led to the conclusion that the presence of an unexpected periaapsis in the data interval is the most significant condition that can occur in terms of limiting the convergence of the partial-step algorithm. Thus, the worst initial direction error (where error = real minus predicted) is that which results in the predicted period being as much larger than the actual period as is possible for a given error magnitude. A worst-direction analysis, however, must be conditioned on the *a priori* probabilities associated with the direction of the initial error. Examination of Fig. 3, which heuristically depicts position-velocity phase space, might suggest that the worst direction is given by the vector  $\Delta$ , the shortest distance to the boundary of the nonconvergence region. However, if the *a priori* initial error dispersion is represented by the ellipse centered at the origin, then the probable worst direction may lie more in the direction of the vector  $B$ . This worst direction can be found analytically by minimizing the function

$$J = \mathbf{A}\Delta\mathbf{x} + \lambda(\Delta\mathbf{x}^T\Gamma_p^{-1}\Delta\mathbf{x} - 1) \quad (1)$$

where

$\Delta\mathbf{x}$  = worst-direction error (to be solved for)

$\mathbf{A} = \partial a / \partial (xyz, \dot{x}\dot{y}\dot{z})$  ( $a$  = semimajor axis)

$\Gamma_p$  = *a priori* state knowledge covariance matrix at periaapsis

The solution to the minimization of  $J$  in Eq. (1) is

$$\Delta\mathbf{x} = -\frac{\Gamma_p\mathbf{A}^T}{\sqrt{\mathbf{A}\Gamma_p\mathbf{A}^T}} \quad (2)$$

It was found from calculations using Eq. (2) that the worst direction is a dispersion in position opposite the position vector at periaapsis and a dispersion in velocity opposite the velocity vector at periaapsis. Thus, the worst direction lies in the orbit plane and results from negative perturbations in the semimajor axis and the eccentricity.

Multiples of the worst-direction vector were tested over various data spans to obtain the worst-direction convergence properties for the Mariner 9 orbit. The results of the tests are shown in Fig. 4 in the form of plots showing convergence and nonconvergence regions in terms of initial position error—convergence limits vs the tracking data span used. The initial position error is defined as the magnitude  $(\Delta x^2 + \Delta y^2 + \Delta z^2)^{1/2}$  of the position deviation in cartesian coordinates corresponding to the worst-direction perturbation. OD accuracies are also included on each plot. The rss position uncertainty at periaapsis  $(\sigma_x^2 + \sigma_y^2 + \sigma_z^2)^{1/2}$  is shown as a function of the data termination time. Tracking begins 1 h after periaapsis. The partial-step algorithm attained convergence from a worst-direction rss error of 100 km ( $\Delta V = 200$  m/s) fitting 4 h of data. After preliminary convergence with such a short data arc, finer "tuning," i.e., convergence to a more accurate solution, can be performed with a longer data arc. This procedure is illustrated in the Fig. 4, where an initial position error of 100 km remains easily in the convergence region until 4 h of data are processed, bringing the error to the 3- $\sigma$  OD level. From this point, more data can be added to the solution span, and the convergence procedure can be continued. After initial convergence has been obtained, the remaining error lies in the Earth's plane of the sky. (This phenomenon will be discussed later.) Hence, the convergence properties with additional data are even more optimistic than those suggested by the figure.

### C. Major Error Sources Affecting Converged Solution Accuracy

1. **Martian gravity.** It was determined on the basis of extensive covariance analyses that the probable major OD error source for the satellite phase of Mariner 9 would be the unmodeled accelerations caused by an incomplete mathematical model of the Martian gravity field. The classical treatment of fields involves expressing the gravitational potential as a series of spherical harmonics. The values of the harmonic coefficients of the Mars potential function were unknown, with the exception of  $C_{20}$ , which had been determined from observations of the Martian moons and from Mariner 4 radio tracking data (Ref. 3). Because it was felt that accurate values for the coefficients would not be determined until many revolutions of data had been processed, the bulk of the pre-flight studies were concerned with defining a solution strategy which minimized the effects of gravity anomalies.

2. **Theory of spherical harmonics.** In all of the pre-flight studies, the spacecraft acceleration was assumed to result from a gravitational potential represented by the spheri-

cal harmonic expansion obtained by solving Laplace's equation

$$\nabla^2 U = 0 \quad (3)$$

The solution for the gravity potential is

$$U = \frac{\mu_g}{r} \left\{ 1 + \sum_{l=1}^{\infty} \sum_{m=0}^l \left( \frac{R}{r} \right)^l P_l^m(\sin \phi) \times (C_{lm} \cos m\lambda + S_{lm} \sin m\lambda) \right\} \quad (4)$$

where

$r, \phi, \lambda$  = Mars-centered, body-fixed spherical coordinates

$\mu_g$  = Mars gravitation constant

$R$  = Mars mean equatorial radius

$P_l^m$  = associated Legendre polynomial of degree  $l$ , order  $m$

$C_{lm}, S_{lm}$  = harmonic coefficients

The coefficients  $C_{lm}$  and  $S_{lm}$  are related to the commonly used coefficients  $J_{lm}$  and  $\lambda_{lm}$  by the relations

$$\begin{aligned} C_{lm} &= J_{lm} \cos m\lambda_{lm} \\ S_{lm} &= J_{lm} \sin m\lambda_{lm} \end{aligned} \quad (5)$$

When this convention is used, Eq. (4) becomes

$$U = \frac{\mu_g}{r} \left\{ 1 + \sum_{l=1}^{\infty} \sum_{m=0}^l \left( \frac{R}{r} \right)^l P_l^m(\sin \phi) \times J_{lm} \cos m(\lambda - \lambda_{lm}) \right\} \quad (6)$$

In this notation,  $J_{lm}$  is a measure of the magnitude of the gravitational anomaly; and  $\lambda_{lm}$  orientates the anomaly relative to the prime meridian of the planet.

The first-order polynomials,  $P_l^0(\sin \phi)$ , are periodic on the surface of a unit sphere and vanish along  $l$  latitudinal nodes on the surface, dividing it into  $(l + 1)$  zones. The respective associated coefficients are referred to as zonal

harmonics. A node is defined as a point or locus of points where

$$P_l^0(\sin \phi) = 0 \quad (7)$$

The functions  $P_l^m(\sin \phi) \cos m\lambda$  and  $P_l^m(\sin \phi) \sin m\lambda$  are also periodic on the surface of a unit sphere. They vanish along  $(l - m)$  latitudinal nodes and along  $2m$  longitudinal nodes, thus dividing the surface into  $(l - m + 1)$  zones and  $2m$  sectors. These two families of nodal lines intersect orthogonally, dividing the surface into rectangular domains or tesserae; hence, they are called tesseral harmonics. The  $C_{lm}$  or  $J_{lm}$  are termed the zonal coefficients of the potential function, and the  $C_{lm}, S_{lm}$  or  $J_{lm}$  are known as the tesseral coefficients when  $m \neq l$ , and as sectoral coefficients when  $m = l$ .

It is possible to relate the lower-degree harmonic coefficients to physical properties of the planet. These coefficients are a function of the size, shape, and mass distribution of the planet, and, for a rigid body, are a set of constant characteristics of that body. For example,  $C_{10}, C_{11}$ , and  $S_{11}$  represent displacements of the center of mass along the  $z$ -,  $x$ -, and  $y$ -axes, respectively, where  $z$  is the planet's spin axis and  $r$  passes through the prime meridian. Furthermore,  $C_{21}, S_{21}$ , and  $S_{22}$  are proportional to the products of inertia  $I_{xz}, I_{yz}$ , and  $I_{xy}$ , respectively. Consequently, if the body-fixed coordinate system corresponds to the principal axes, these products of inertia and the corresponding harmonic coefficients are zero. If, in addition, the planet is axially symmetric about the  $z$ -axis, all coefficients not of order zero vanish; i.e.,  $J_{lm} = C_{lm} = 0$  if  $m \neq 0$ .

Insight into the effect of the individual terms in the expansion of the potential can be obtained by replacing the actual distributed mass with an equivalent body of uniform density. The approximate shape of this equivalent mass can be determined from a study of the variation of the potential with  $\phi$  and  $\lambda$  at a constant radial distance  $r$ . Values of  $U$  that are greater than  $\mu_g/r$  will indicate that the equivalent body has more mass in the region than it would have if it were a homogeneous sphere. Similarly, values of  $U$  less than  $\mu_g/r$  indicate a mass deficit.

For the purposes of this discussion, it is assumed that  $J_{lm} > 0$  and

$$\bar{U}_{lm} = \frac{U_{lm}}{(\mu_g R^l / r^{l+1}) J_{lm}} = P_l^m(\sin \phi) \cos m(\lambda - \lambda_{lm}) \quad (8)$$

is defined. Then  $\bar{U}_{lm}$  can be used to demonstrate the dependence of  $U$  on  $\phi$  or  $\lambda$ . For example, if

$$\bar{U}_{20} = P_2(\sin \phi) = -\frac{1}{2} + \frac{3}{2} \sin^2 \phi \quad (9)$$

the quantity has its maximum value at  $\phi = 90$  deg and  $-90$  deg, its minimum at  $\phi = 0$  deg, and zeros at  $\sin \phi = \pm(1/3)$  or  $\phi = 35$  deg and  $145$  deg. The results of plotting  $U_{20}$  radially on the surface of a sphere are shown in Fig. 5a. The shaded areas represent an excess of mass; the unshaded, a deficiency. The results of plotting  $U_{30}$  radially are shown in Fig. 5b. It is common practice to designate  $U_{20}$  as the prolateness ( $J_{20} > 0$ ) or oblateness ( $J_{20} < 0$ ) and  $U_{30}$ , for obvious reasons, as the "pear-shape" effect. As noted earlier, the zonal coefficients divide the body into  $l + 1$  latitudinal zones and, as shown in the figure,  $J_{20}$  divides the body into three, and  $J_{30}$  into four latitudinal zones. The figures presented in this section illustrating the harmonics are taken from Ref. 4.

An example of the sectoral harmonic  $\bar{U}_{22}$  is sketched in Fig. 5c. As seen in the figure, this harmonic produces no latitudinal nodes ( $l - m = 0$ ) and four longitudinal nodes ( $2m = 4$ ), thus dividing the body into one zone ( $l - m + 1 = 1$ ) and four sectors ( $2m = 4$ ).

Figure 5d presents a sketch of the tesseral harmonic coefficient  $\bar{U}_{32}$ . Again, as shown by the figure, there are one latitudinal node, four longitudinal nodes, two zones, and four sectors. In general, many harmonics are required to model the gravity field of a planet adequately. As a result, the composite equivalent mass model of the gravity field is an extremely complicated structure.

**3. A priori uncertainties in the gravity harmonic coefficients.** A pre-flight uncertainty model for the magnitudes of the Mars harmonic coefficients was developed based on an extrapolation of the Earth's gravity coefficients down to those of a planet whose size and mass coincide with Mars. It was assumed that the strength of the supporting material of Mars is similar to that of the Earth, and that equal stresses are supported (Ref. 5). The existence of equal stresses then implies that

$$|C_{nm} S_{nm}|_{\sigma} \approx \left(\frac{\mu_{\oplus}}{\mu_{\sigma}}\right)^2 \left(\frac{R_{\sigma}}{R_{\oplus}}\right)^4 |C_{nm} S_{nm}|_{\oplus} \quad (10)$$

Table 4 lists the *a priori* standard deviations of the Martian harmonic coefficients based on the premise that Eq. (10) gives a reasonable approximation of the expected absolute values but no information on the signs of the

coefficients. Consequently, the *a priori* estimate of each coefficient was zero.

Table 5 presents a comparison of the expected probe acceleration uncertainty caused by the gravity terms with the uncertainty caused by other error sources. The maximum expected magnitude of the unmodeled accelerations due to radiation pressure, lift and drag forces caused by the Mars atmosphere, and spacecraft gas and propellant leaks are listed along with the maximum expected unmodeled accelerations caused by gravitational uncertainties. The table shows that the acceleration errors resulting from an incomplete gravitational model of Mars are much larger than the ones caused by these other sources.

**4. Dependence of OD accuracy on the uncertainty of the gravity model.** To assess the relative effect of the inexact gravity model on the expected accuracy of the orbit solution, the formulation of the weighted least-squares estimate of the spacecraft state derived from Earth-based tracking data was examined. The data vector  $z$  (observed minus computed values) is related to the estimated state vector  $x$  and the parameters expected to be in error  $y$ , by

$$z = Ax + By + n \quad (11)$$

where  $n$  is the data noise vector.

If the standard deviation of the zero-mean data noise is given by  $R$ , then the minimum variance estimate of  $x$  is given by the familiar weighted least-squares form

$$\hat{x} = (A^T R^{-1} A)^{-1} A^T R^{-1} z \quad (12)$$

and the computed covariance matrix of the error in the state estimate is given by the equation

$$\Gamma = (A^T R^{-1} A)^{-1} \quad (13)$$

The error in the estimate of  $x$ , based on the neglected parameters  $y$  and the data noise, is given by

$$x - \hat{x} = -(A^T R^{-1} A)^{-1} A^T R^{-1} B y - (A^T R^{-1} A)^{-1} A^T R^{-1} n \quad (14)$$

The partial derivative or sensitivity matrix of the error in the estimate of  $x$  to the  $y$  parameters is given by

$$S = -(A^T R^{-1} A)^{-1} A^T R^{-1} B \quad (15)$$

and, if the  $y$  parameters have an *a priori* covariance matrix  $\Gamma_y$ , then the consider covariance matrix of the error in the estimate of  $x$  is

$$\Gamma_x = \Gamma + S\Gamma_y S' \quad (16)$$

If the  $y$  are uncorrelated, the expected error perturbation in one of the  $x$  components,  $x_i$ , caused by one of the  $y$  components,  $y_j$ , is given by

$$\Delta x_{i,j} = S_{x_i, y_j} \sigma_{y_j} \quad (17)$$

where  $S_{x_i, y_j}$  is the  $i, j$ th element of the  $S$  matrix.

To determine how errors in the harmonic coefficients would corrupt both the local and mapped state solution accuracies, many covariance analyses were performed on simulated state solutions in the early phases of the pre-flight studies. In these covariance analyses, the vector  $x$  in Eq. (11) was usually the deviation from the anticipated standard state vector (cartesian velocity and position) of the spacecraft at the periapsis passage time just preceding the interval of data, and  $y$  was usually a vector of harmonic coefficient deviations, as well as other model errors. The results of the covariance analyses have been published in the literature, most notably in Refs. 6 and 7.

In summary, the pre-flight covariance analysis led to the conclusion that if only the state vector is estimated, no more than a single revolution of tracking data can be processed without experiencing severe degradation of the solution accuracy because of errors in the gravity model. Furthermore, it was shown that the single revolution of tracking data could not contain any data points within an hour of a periapsis passage without the estimate of the orbital period being adversely affected. A poor estimate of the orbital period leads to poor trajectory extrapolation accuracies.

Table 6 lists the  $1-\sigma$  values of the rss position error at the periapses, bracketing a revolution of processed data, and the  $1-\sigma$  values of orbital period in the following revolution. The values were obtained from the formulas given above, applied to a simulated Mariner 9 orbit on November 14, 1971. The gravity coefficient uncertainties in Table 4 were used to construct the *a priori* covariance matrix  $\Gamma_y$ . Table 6 also lists the deviations in the estimates corresponding to the summed effects of the gravity coefficients of differing degrees. Second-degree coefficients dominate the uncertainty in both position and period.

The results of extending the data are to cover two revolutions of data and increasing the solution list to include low-degree gravity coefficients are also shown in Table 6. The period error is given for the first revolution after data termination. The position error is not changed with second-degree coefficients but is reduced if third-degree coefficients are included in the solution list. Marked period error reduction is seen if second-degree coefficients are included in the solution list, and estimating third-degree coefficients improves the estimate accuracy further.

#### D. Qualitative Description of Satellite OD Accuracy Properties

**1. Longitude of node in Earth's plane of the sky.** It was recognized that, of all the orbital elements determined locally from Earth-based tracking data, the longitude of the line of nodes in the Earth's plane of the sky is the most uncertain. The uncertainty in this poorly determined angle is equivalent to the uncertainty of  $\Omega$  as it is defined in Fig. 6, which illustrates the Earth-station, Mars-spacecraft tracking geometry. In the figure,  $z', r$ , and  $\Omega$  are cylindrical coordinates defining the position of the spacecraft relative to Mars at the time of tracking, and  $h_x, h_y$ , and  $h_z$  are components of the station in an Earth-centered cartesian coordinate system. They are given by the expressions

$$\begin{aligned} h_x &= r_s \sin \omega t \\ h_y &= h \cos \delta - r_s \sin \delta \cos \omega t \\ h_z &= h \sin \delta + r_s \cos \delta \cos \omega t \end{aligned} \quad (18)$$

where

$h$  = distance from station to Earth equator along the Earth spin axis

$\delta$  = geocentric declination of Mars

$\omega$  = angular rate of the Earth

$t$  = time from station meridian passage of Mars

$r_s$  = station distance from the spin axis

Figure 7 presents a geometric view of how a node error can affect the position error of the spacecraft. A node error is equivalent to mislocating the orientation of the orbit about the Earth-Mars line of sight, and the doppler data are relatively insensitive to such a rotation. The orientation error results in a total position error of  $r_s \Delta \Omega$  at periapsis. This position error is normally minimum in the

periapsis region and maximum in the apoapsis region for an eccentric orbit like that of Mariner 9. It should be noted that  $r\Delta\Omega$  constitutes almost the entire position error of the spacecraft, and that the errors in  $r$  and  $z'$  are small compared to  $r\Delta\Omega$ . Figure 8 presents the time history of the respective  $1-\sigma$  errors in  $r\Delta\Omega$ ,  $r$ , and  $z'$  for the pre-flight uncertainties in the Mars gravity coefficients. The uncertainties in  $r\Delta\Omega$  and  $r$  are seen to be minimum at periapsis, but the uncertainty in  $z'$  is maximum. The maximum  $\Delta z$  occurs at periapsis because of in-orbit downtrack errors in the trajectory in the periapsis region, where the erroneous accelerations caused by uncertainties in the gravity field are maximum.

**2. Predicted orbital period.** The least accurate predicted orbital element is the orbital period. If the estimated spacecraft state is integrated forward in time, past the region of available data, for several revolutions and compared to the actual trajectory of the spacecraft, the position error between the two can grow in the down-track direction. Such a position error results from the actual trajectory being perturbed by the unknown portions of the gravity field so that the actual period and times of periapsis passage change in a manner which is not predicted in the estimated trajectory; i.e., the actual orbit moves "out from under" the estimated orbit. The geometry of this error is illustrated in Fig. 9, where the constant initial position error caused by the node error is shown vector-summed with successive position errors, which lie along the instantaneous velocity direction. These successive position errors result from the successive periapsis passage time errors, and their contributions can dominate the total predicted periapsis position error after several revolutions. The in-track predicted position error can be approximated by the formula  $V_p\Delta T_p$ , where  $V_p$  is the magnitude of the velocity at periapsis, and  $\Delta T_p$  is the error in the time of periapsis passage.

### E. Simulation Studies

The final and most important step in the pre-flight studies was the fitting of simulated data in a simulated operations environment. The desirable method in such studies was to apply the OD strategy, observe the estimate behavior over several revolutions of data, and correlate the observed behavior with the results of the covariance analysis. A number of such studies were conducted as part of the pre-flight analysis; the results of one are presented here. Several revolutions of data were generated for a simulated trajectory with typical sample coefficients in the gravity field. The spacecraft orbit was determined from three successive revolutions of data. The

dispersion of the periapsis position estimates about the first solution is given in Fig. 10. The actual simulated position is also placed in the figure. The position determination appears to be consistent with the covariance results, with the estimates dispersed about the true value with errors in the 10-km range. The position estimates are plotted as a function of time in seconds, with the actual time of successive periapsis passages denoted by vertical lines. Predicted periapsis passage times are shown by the crossmarks on the extended (dashed) position bars. The mapping uncertainty is less than 1 s after one revolution and within 2 s after two revolutions. Gravity solutions from the simulated data led to smaller solution deviations, as predicted from the covariance analysis results.

### F. Orbit Determination Solution Strategy for the Satellite Phase of the Mission and Expected Accuracy

The results of the pre-flight covariance analyses and simulation studies led to the following definition of the solution strategy:

- (1) Using a batch-weighted, least-squares estimator, solve for the state (position and velocity) of the spacecraft from a single revolution of tracking data, omitting the data within an hour of periapsis, which are most sensitive to the gravity errors. Use the partial-step algorithm for convergence if necessary. If severe convergence problems arise, shorten the data span, and work up to a full revolution of data, as illustrated in Fig. 4.
- (2) Accumulate several successive revolutions of data. Then, using the conditions arrived at in step (1) as initial conditions, solve for the state plus low-order gravity coefficients.
- (3) As more data become available, resolve for the state from a single revolution of tracking data, with the gravity terms obtained from step (2) placed in the spacecraft trajectory integration model.

The three steps listed above are referred to as the pre-gravity sensing mode of operation, the gravity sensing mode, and the post-sensing mode, respectively.

The predicted uncertainties of the local and mapped estimated position at periapsis, based on the pre-flight simulation and covariance analyses, are summarized in Table 7. The predicted uncertainties are compared with the accuracy requirements. The uncertainty in the mapped time of periapsis has been corrected to an approximate downtrack position error by multiplying the time of periapsis uncertainty by the velocity magnitude at periapsis.

The results shown in Table 7 illustrate the most important characteristic of the Mariner 9 satellite orbit determination problem: that the high degree of OD accuracy required by the MM71 Project would be met only after multirevolution solutions for the gravity field of Mars

### III. Mariner 9 Data and A Priori Astrodynamic Constants

#### A. DSN Data

1. **Two-way doppler.** Almost all of the satellite orbit solutions for Mariner 9 were computed on the basis of two-way doppler measurements only. During the 11½ months Mariner 9 was in orbit, over 300,000 two-way doppler measurements at 1-min count times were recorded. In the first 280 revolutions, two-way doppler tracking data were obtained in a nearly continuous fashion by deep space station (DSS) 12 at Goldstone, California, DSS 41 at Woomera, Australia, and DSS 62 at Madrid, Spain. As the Earth-Mars distance increased during the orbit phase of the mission, the signal-to-noise ratio of the spacecraft communication link decreased. In March, increased data noise rendered the 26-m-diameter antennas ineffectual. Consequently, after revolution 280, only the 64-m antenna at DSS 14 was used for tracking the spacecraft. Figures 11a and b show the time history of the respective antenna elevation angles over a 1-day interval on November 15, 1971 (Fig. 11a), and again on May 5, 1972 (Fig. 11b), when only DSS 14 was tracking. Times of local periapses and apoapses are marked on the figures.

Figure 12 illustrates the evolution of the accuracy of the doppler data by showing the rms of the doppler residuals plotted against time through October 1972. Individual rms values have been obtained from short arc fits to the data. Also included on the figure is the magnitude of the Earth-Mars distance showing its increase from about  $1.2 \times 10^8$  km at insertion to about  $4 \times 10^8$  km after 600 orbits. It can be seen that, as the Earth-Mars distance approached  $3 \times 10^8$  km, the noise observed at the 26-m antenna increased markedly, whereas that at the 64-m antenna increased only slightly.

The quality of the doppler data during the month around superior conjunction was degraded sharply because of the effects of the rapidly varying quantities of charged particles along the signal path because of the solar corona. The rms of the doppler noise actually reached a maximum of 2 Hz on the day of conjunction,

when the Sun-Earth-Mars angle was 104 deg and the signal path passed within four solar radii of the Sun

The data from the DSN stations were sent over teletype to the Space Flight Operations Facility (SFOF), where they were stored on high speed magnetic drums. Data were then written on magnetic tape by the Network Analysis Team Tracking Group as requested by the Navigation Team. These tapes contained, in addition to two-way doppler observables, one- and three-way doppler count, MU ranging, and angular observables, all at specific times (usually 1-min samples), synthesizer frequency, transmitter on/off times, and ranging adjust coefficients and data quality indicators.

The Navigation Team processed these data tapes on the UNIVAC 1108 computer. The orbit data editing (ODE) program was used to reformat the data and to eliminate all of the unused data types, such as angular data. The output of the ODE was then processed by a medium-accuracy OD editing program, the tracking data editing orbit determination (TRKED) program. The printed and plotted output of this program was analyzed to locate and eliminate poor data. Data were compressed to 10-min intervals for regions of time at least 2 h away from a periapsis passage. Individual edited and compressed data records were merged with previously processed data records and stored on tape to produce complete satellite data records for use in the orbit estimation computations.

During the period of time in which all stations were tracking, radiometric data were obtained 24 h per day by the DSN. After revolution 280, a 10-h pass of data centered around periapsis was taken by DSS 14. The rate was generally one point every 60 s. During most of the orbit phase, the Satellite OD Group processed data two or three times per week to fulfill science or DSN requests for updated orbits.

2. **MU ranging data.** Navigation Team support of the relativity experiment required the processing of Earth-spacecraft range measurements. Two-way time delay measurements, which are proportional to station-spacecraft range, were obtained using the MU ranging machine at Goldstone throughout the mission. Range measurements were acquired several times per week from November 1971 until August 1972, at which time the frequency of independent range measurements was increased to several measurements per Goldstone pass. In all, a total of over 1300 individual range measurements were acquired during the satellite phase of the mission. Most of these

measurements were obtained in the 8 weeks bracketing superior conjunction. The ranging measurements, which are normally precise to a few meters, were perturbed by charged particles in the transmission media, which retarded the signal and thus contributed to a larger time delay than that predicted from the true coordinate range. As the signal path for Mariner 9 neared the Sun, both the amplitude of the steady-state charged particle content and that of the stochastic variations along the signal path increased. However, the effect of the steady-state content can be modeled, and so it caused few problems (Ref. 8). At closest proximity to the Sun on September 7, 1972, the average electron content of the signal path through the solar corona was at its maximum, which caused a time delay of about 20  $\mu$ s (out of a total round-trip light time of some 45 min). Because 1  $\mu$ s of time delay corresponds to about 150 m one-way range to the spacecraft, the maximum corona effect was some 3000 m in range. On the other hand, the stochastic variations in the corona induced a range uncertainty that is difficult, if not impossible, to model. On a scale of 1 day, the effect can be several microseconds.

**3. Differenced range vs integrated doppler technique calibrations.** The differenced range vs integrated doppler (DRVID) technique, discussed in more detail in Ref. 9, was used to calibrate charged particle activity in the signal path for small Sun-Earth-probe angles and to provide corrections for orbit computations. Raw DRVID data provide a time history of the observed range difference from the initial range observation in a continuous pass minus the integrated range rate from the doppler data. The data measure twice the round-trip range change during a pass because of charged particles, but they do not indicate the total group delay.

DRVID data were obtained by way of two modes of operation: (1) the MU ranging machine, because of its mechanization, output DRVID data automatically during any single range acquisition, or (2) the data were constructed externally from counted doppler and individual range acquisitions. DRVID data spanning entire passes were generated, using primarily the second mode, for the periods of August 10 to 25 and September 16 to October 12, 1972. Data nearer conjunction could not be obtained because of poor doppler quality. Data further from conjunction are now being processed. The data are least-squares fit with a polynomial of the lowest order, which reasonably represents its structure. The coefficients of this polynomial are used to adjust the doppler and range data in the spacecraft-orbit fitting software.

Figures 13a, b, and c illustrate the DRVID data for passes beginning on August 20, 23, and 25, respectively. Curves which show the least-squares-fit polynomial are superimposed on the actual data. On the days shown, the variation in observed range caused by charged particles in a single pass was as high as 300 m, with a maximum slope of 75 m/h.

## B. Spacecraft Data

**1. TV images of surface landmarks.** The radio orbit solutions of Mariner 9 were confirmed by solutions based on TV images of the Martian surface. The imaging system on board the Mariner 9 spacecraft consists of a wide-angle, low-resolution camera and a narrow-angle, high-resolution camera mounted on a scan platform with two degrees of freedom, which can be positioned relative to the spacecraft. The wide-angle camera has an effective focal length of 50 mm and a field of view of  $11 \times 14$  deg with a surface resolution of 1 km at a slant range of approximately 1750 km. The narrow-angle camera has an effective focal length of 500 mm and a field of view of  $1.1 \times 1.4$  deg with a surface resolution of 100 m at the same slant range of 1750 km. The basic landmark observables consist of picture coordinates of images (line, pixel locations) measured on  $8 \times 10$  in. photoproducts.

The criterion used for selection of pictures from the available collection transmitted by Mariner 9 while in orbit was based on redundancy of observation of some well identifiable surface features. The dust storm obscuration of the planet during the first 2 months of orbit left only the south polar cap and the volcanic prominences in the Tharsis region visible. Consequently, the TV science interests were focused on these regions, and it was possible to get data from these early pictures. Because the areas were photographed through the haze created by dust in the Martian atmosphere, a large portion of the early data was of poor visual quality. However, the pictures were still usable. The bulk of pictures received after the dust storm cleared in January were taken for the purpose of mapping the planet with a minimum observational redundancy. Thus, data became available only during special picture sequences, when the TV camera was trained on the south polar cap and on the volcanic prominences in Tharsis, namely, Nix Olympica, Pavonis Lacus, and Nodus Gordii. The data for Ascraeus Lacus were scanty and of poor quality, and were not used. Figure 14 shows the distribution of the total usable pictures relative to time of periapsis passage, the target sighted, and the type of camera used. A very large portion of the data is made up of wide-angle pictures of the

south polar region, all taken 30 min before periapsis. This part of the data allows observation of the south polar cap from a nearly fixed position in space while the planet rotates underneath the spacecraft at the rate of 9.5 deg per orbit of Mariner 9. The 13 landmarks sighted are shown in Figs. 15a, b, and c.

**2. TV pointing data.** The accuracy of OD solutions based on optical data is dependent on the acquisition of data which yield the inertial pointing of the target raster at the time of observation. These data are processed by two methods. The first consists of processing the engineering telemetry data, which contain quantized readouts of the scan platform gimbal angles in the cone and clock axes, readouts of the pitch and yaw angles from the sun sensor, and the star sensor readout of the roll angle. Figure 16 shows a sample plot of the yaw, pitch, and roll variations in the vicinity of a picture shuttering over a 100-s time interval. Because of a wide variety of situations arising from the spacecraft attitude motion and the response of the attitude control system, it was necessary to examine all the data available to determine the switching condition of the spacecraft attitude control system and, thereafter, to fit an appropriate segment of the data in the neighborhood of the shuttering instant. This procedure was adequate during the high-data-rate transmission, when the engineering data samples were obtained every 4.2 s. However, an appreciable portion of the pictures were taken when the engineering data sampling rate was four times slower than the 4.2 s sample rate. At this rate, it was not always possible to correctly deduce the trend of limit-cycle excursions within the allowed dead-band. Such data were therefore carefully examined to determine the nearest two data samples containing the shuttering interval, and the readout was obtained by linear interpolation. In addition, problems were occasionally encountered in obtaining the cone and clock gimbal-angle readouts. Because the sampling rate for these readouts was 42 s/sample, there were situations in which the scan platform was in the slewing mode when the telemetry channels were sampled. In such instances, the gimbal angle readouts were not available from the channels, but they were obtainable from the command values. The "open-loop" TV raster orientation had appreciable errors associated with its construction. Hence, a "closed-loop," second-stage determination of the TV-camera pointing errors was essential to obtain consistent solutions.

The second processing method consisted of solving for the most probable camera orientation at shuttering times using the estimated direction of inertial pointing from the

first method of processing. It was noticed during early landmark data fits that there was a significant discontinuity in the data residuals whenever the cameras were switched; i.e., the narrow-angle camera residuals were observed to be offset from the wide-angle camera residuals. The obvious inference was that the model for pointing errors needed an additional three degrees of freedom in the platform coordinates to describe the wide-angle camera offsets in relation to the narrow-angle camera optical axis. When these additional degrees of freedom were introduced, the discontinuity was noticeably reduced. In addition, a set of three fixed offsets of the narrow-angle TV target raster, relative to the scan platform pointing defined by the first-stage estimates, were estimated. Superimposed on these was a random component modeled as being in the yaw, pitch, and roll directions of the spacecraft. Thus, a total of nine parameters were estimated to adequately describe the "true" TV orientation with respect to the celestial reference made up by the spacecraft-Sun and spacecraft-Canopus directions. (Arcturus was not used as a reference star for the data span included here.)

In addition to the above-mentioned discontinuity, there was another source of error stemming from the sun sensor regulation problem. It was noticed, in fitting some close-range landmark data, that the data residuals were enormously large in comparison to the expected measurement error in the pictures shuttered within 20 min from the periapsis passage of the spacecraft. It was determined that this behavior was associated with the design of the sun sensor preamplifier circuitry. It was also found from some symptomatic behavior of the attitude control telemetry that the sun sensor went into an anomalous state whenever stray light from Mars became sufficiently strong in intensity. The incident stray light from the planet rendered the voltage-regulation mechanism of the acquisition sun sensors ineffective. The primary sun sensors were dependent on this same mechanism for voltage regulation. The result was a floating voltage and an unknown scale factor for the primary sun sensor output whenever the problem occurred. Because the sensor telemetry was rendered meaningless in these situations, data taken in the vicinity of periapsis passage could not be used for OD. This resulted in elimination of the high-resolution data. The alternative to the first method of processing, i.e., corrupting the covariance to solve for the camera pointing direction, was not very successful in these situations because the *a priori* uncertainty was too large.

**3. Nongravitational accelerations.** The problem of determining the history of thrusts caused by leaks from the

cold-gas attitude control system became more difficult in the orbital phase than it was in the cruise phase, as discussed in the preceding section. The insertion maneuver required a burn which expended a considerable mass of propellant, causing the center of mass of the spacecraft to move closer to the center of the roll-axis jet couple. This reduced the degree to which torques, caused by roll-axis jet leaks, were cross-coupled into the other axes. In addition, the effects of gravity gradient torques near periapsis produced periodic signatures in the pitch and yaw axes, which had to be separated from any cross-coupling effects. The net result was that the cross-coupling effects of roll-jet leaks were below the threshold of detection in the satellite phase of the mission. Therefore, the OD Group had to rely on assumptions of historical continuity. In particular, because the roll axis continued to exhibit occasional bursts of torque in the same direction as those seen prior to Mars encounter, it was assumed that the same roll jet was continuing to leak sporadically. Thrust directions were assigned on that basis.

The computation of the roll-axis torques was also complicated by the motion of the instrument scan platform because the reaction torques were large and the task of reconstructing them from the scan platform position telemetry was difficult. As a result, any gas leaks that occurred during the periods of scan platform slewing could not be effectively detected.

Figure 17 is a plot of the angular accelerations in each of the three spacecraft axes over a span of two orbits near the beginning of December 1971. Uncertainties in the accelerations are denoted by the height of the boxes bracketing each plotted value. A typical roll-axis leak can be seen between 10<sup>1</sup>/<sub>2</sub> and 11<sup>1</sup>/<sub>2</sub> h. The cross-coupled torques in the pitch and yaw axes, which were quite distinct in the cruise phase, are indistinguishable here. The torque signatures in the pitch and yaw axes, in which the angular accelerations are positive over most of each orbit but become negative near periapsis, are caused by gravity gradient torques. The large uncertainties in acceleration over the period of 2 to 3 h prior to each periapsis are due to the slewing of the scan platform.

The start and stop times and the magnitudes of the leaks were estimated by using acceleration profiles like those shown in Fig. 17. Figure 18 is a plot of the spacecraft accelerations caused by gas leaks over a typical period in mid-December 1971. Because the time scale of the plot makes the durations of the various leaks difficult to compare, the integrated velocity effect of each

leak (i.e., magnitude times duration) has also been plotted and is designated by  $\Delta$ .

4. **Spacecraft mass.** The mass of Mariner 9 was determined from telemetered information, which yielded the propellant expenditures of the various maneuver burns. The values of the spacecraft mass for the pre-trim 1 and post-trim 1 and 2 phases of the satellite mission are listed below:

- (1) Pre-trim 1, 563.775 kg.
- (2) Post-trim 1, 560.201 kg.
- (3) Post-trim 2, 551.890 kg.

5. **Solar radiation pressure.** The spacecraft reflectivity coefficients which relate the solar radiation to the pressure acting on the spacecraft were determined from analysis of the cruise data. The respective values of the coefficients which were used in the satellite phase of the mission were  $G_R = 1.2275$ ,  $G_y = -0.0406$ , and  $G_z = -0.0436$ . (See the preceding section for definitions of these parameters.)

#### C. Observer Location and Transmission Media Calibrations

The tracking system analytic calibrations for the satellite and cruise phases of the MM71 mission were comprised of calibration coefficients for timing, polar motion, and tropospheric refraction, supplied by the DSN. A discussion of these calibrations appears in the preceding section.

Station locations used during the satellite phase of the mission were determined on the basis of Mars encounter data from Mariner 6. These station locations are given in Table 8.

#### D. Martian Astrodynamic Constants

1. **Gravitational constant.** The mass constant associated with Mars which was used throughout the satellite OD operations had a value of 42,828.44 km<sup>3</sup>/s<sup>2</sup>. This value was determined by Null (Ref. 3) from analysis of Mariner 4 tracking data. It is in good agreement with values from Mariners 6 and 7, and is consistent with a Gaussian gravitational constant  $k = 0.01720209895$  and a velocity of light value of  $c = 299792.5$  km/s, given in Ref. 10.

2. **Oblateness.** The *a priori* Martian oblateness coefficient,  $J_2$ , had a value of  $1.97 \times 10^{-4}$ , which was determined by Wilkins (Ref. 11) from long-term observations of the Martian satellites. The corresponding mean radius of Mars for gravity scaling was taken as 3389.1 km.

3. **Spin-axis direction.** The direction of the Martian spin axis used at the beginning of the satellite operations can be stated in terms of the right ascension and declination value of the pole direction in the Earth mean equator coordinate system of 1950. These values are

$$\alpha = 316.8538 \quad 0.09997T$$

$$\delta = 53.0066 \quad 0.0566T$$

where  $T$  is in Julian centuries past 1950.0. The values were derived by de Vaucouleurs (Ref. 12) as an unweighted average of the results of Burton (Ref. 13), whose values were determined from Earth-based observations of the motion of Deimos and Phobos, and from Camichel (Ref. 14), whose values were determined from Earth-based observation of the motion of surface features on Mars.

Prior to the flight of Mariner 9, it was thought that the direction of the pole was known to an accuracy of 1 deg. Figure 19 shows the pole solution obtained by various observers using surface markings and orbits of Phobos and Deimos since 1877. These solutions were taken from Ref. 12 and mapped to the 1950 epoch. The pre-Mariner 9 adopted value was obtained by averaging the two Burton values and the single Camichel value shown in the figure.

#### E. Planetary Ephemerides

The planetary ephemerides used by the Satellite OD Group during operations were all recent, differentially corrected versions of the *JPL Planetary Export Ephemeris DE-69* (Ref. 15). The first of these versions, DE-79, included Mars radar time delayed data from June 20 to September 10, 1971. The second version, DE-80, was available on December 28, 1971, and included time delay measurements to October 11, 1971. The third ephemeris, DE-82, was available on September 18, 1972; it was based on existing radar and optical measurements to October 11, 1971, plus 88 "normal points," or reduced range measurements of Mariner 9 itself.

The values of the astronomical unit (AU) and solar mass constant for each ephemeris are given in Table 9.

## IV Pre-trim 1 Orbit Determination History and Support of Trims 1 and 2

### A. Initial Orbit Convergence

As stated in Section I, the first real-time duty of the Satellite OD Group was to obtain a converged orbit solution from data acquired during the first revolution of Mariner 9 about Mars. The pre-flight studies, reported in Section II, led to the conclusion that the partial-step algorithm would possibly be necessary to solve the problem of nonconvergence during the initial probe state determination immediately following Mars orbit insertion (MOI).

Pre-flight studies also showed that the mission OD software required the following capabilities to meet the possible error contingencies that could arise during initial orbit convergence:

- (1) Rapid near-real-time multiple iteration of the least-squares fitting procedure.
- (2) Immediate on-line visual output of the results of each individual iteration
- (3) The ability to wait in a "holding pattern" between any given iteration while the user answers the question of whether he has convergence or needs to continue the iteration.
- (4) The ability to execute the appropriate response depending on the user's answer to (3).

Therefore, these capabilities and the partial-step algorithm were added to the existing TRKED program, as well as to the ODP. The resulting version of TRKED was certified for mission use during the course of the pre-flight studies.

The computer time necessary to complete a typical (initial orbit phase) iteration was about 10 s for TRKED, as compared to 2 min for the ODP. This order-of-magnitude improvement in speed was due to TRKED's simplified models and computational shortcuts; the tradeoff was the difference in precision. Compared to the expected state knowledge uncertainties at the initial periapsis (as discussed in Section II), this difference was found to be small: under 10 km in rss position, with a corresponding discrepancy in velocity. Thus, the ODP could converge on the same set of data with two or three "fine-tuning" iterations using TRKED's converged state solutions as initial conditions.

Initial state convergence and refinement during the first actual orbit about Mars following the MOI maneuver was performed in the following manner. The data fitted was two-way, 1-mm doppler, which began immediately after the occultation period ended. Thus, the fitted data started approximately 66 min after the initial periapsis, which was chosen to be the epoch for all of the fits performed during this first orbit. For each case, the last best estimate available (at periapsis) was used as the nominal state; succeeding fits improved this state estimate. *A priori* sigmas used for all the fits were 250 km for the positional uncertainties and 100 m/s for the velocities. The first fit after the MOI was based on approximately 2 h of data and included 156 points covering the time span between November 14, 1971, 01 h 48 min 32 s and 04 h 29 min 32 s.

TRKED was used for this initial convergence case and was run in near-real-time, i.e., it was executed immediately after the last data point to be fitted was received and included on the proper OD data file. This initial convergence was completed in essentially two iterations and was notable only for its triviality. The cruise phase OD solutions and the Mars insertion itself were so accurately executed that the TRKED convergence yielded a state whose position moved from the initial *a priori* state by only 26 km. Thus, TRKED's extended partial-step solution and its full-rank solution (which was computed only for reference) are identical for each iteration of this case, because the total correction necessary to the *a priori* state values were well within the linear region of convergence. The conclusion is that, because the mission was so near the expected standards, the partial-step algorithm was not actually necessary; it was only a safeguard. The equality of the two different solution techniques can be seen in Fig. 20, which is a photocopy of the results of TRKED's first two iterations as seen on a remote terminal screen during the execution of the program on November 14, 1971. The number of data points used in the fit is  $M (= 156)$ , and OLDPER and NEWPER are the instantaneous two-body periods in hours before and after the iteration, respectively. PS-DQ and FR-DQ are the partial-step algorithm and full-rank corrections to the state computed for the particular iteration and are in the order  $x, y, z, \dot{x}, \dot{y}, \dot{z}$  in units of km and km/s. The two solutions are identical. The position state has moved from the *a priori* values of 825.0, -2438.7, and -4038.0 km to 836.1,

2419.7, and -4050.2 km, with computed sigmas of 39.12, and 67 km. (The coordinate system is the Mars-centered mean Earth equator of 1950.) Similarly, the total rss move in velocity is seen to be less than 3 m/s. The

converged two-body period of 12.59 h is equivalent to 12 h 35 min 24 s.

Following the initial TRKED convergence, the resulting solution was used as *a priori* state for reconverging over the same data span with the SATODP. This yielded the solution and uncertainties compiled in the 2-h data arc section of Table 10. The net rss position change between TRKED and SATODP solutions is about 10 km, this difference vector lies almost entirely in the instantaneous plane of sky and has a magnitude considerably within the corresponding uncertainty ellipsoid. After enough time had elapsed to allow an accumulation of about 4 h of data, the SATODP was used to fit this expanded arc, starting with the 2-h solution as the *a priori* state. This procedure was repeated two more times with the SATODP during the first orbit, once after 8 h of data had been accumulated, and again after 10.5 h. Table 10 summarizes SATODP position solution history for this first orbit. Convergence was obtained with two full-rank iterations for each of the four data arc solutions. The computed sigmas in the table are based on 1 mm/s random data noise, and the consider sigmas are derived from the harmonic coefficient uncertainty reported in Section I.

If the four converged states from Table 10 are differenced, it can be shown with the proper coordinate transformation that these difference vectors all lie almost entirely in the plane of sky. Because most of the state estimation error lies in the plane of sky, it is clear that the inclusion of additional data in the fits of the first orbit decreases and perhaps reorients this plane-of-sky error. Figure 21 summarizes the first orbit solution history in terms of positional plane-of-sky deviations resulting from fitting the data arcs, which are increasing in length. The location of the squares (TRKED) and circles (SATODP) shows  $r_{p\Omega}$  coordinate moves relative to an arbitrary zero ordinate value. The inscribed 0 or 1 indicates the iteration number yielding that particular value of  $r_{p\Omega}$ . For example, the ① appearing beneath the 6-h abscissa point corresponds to the  $r_{p\Omega}$  value resulting from the ODP's first iteration on the 4-h data-arc fit. The time evolution of the data noise (computed) and consider 1- $\sigma$  curves resulting from fitting the different data arcs are shown as functions of the time of the last data point for comparison.

Figure 22 similarly presents a summary of the solution history in terms of the computed anomalistic orbital period (elapsed time between successive periapsis passages). The zero ordinate point corresponds to a period

of 12 h and 34 min. The figures demonstrate properties of the satellite orbit convergence procedure which have been present throughout the history of the satellite phase of the mission. (1) the first iteration solution corrects the orientation of the orbit in the Earth's plane of the sky ( $\Omega$ ) to its final value while the orbital period is driven to an erroneous value, and (2) the second iteration solution usually corrects the period to its final value. All subsequent solution iterations in subsequent revolutions of the satellite mission were performed with the full-step algorithm in the ODP, and convergence was usually obtained with two solution iterations.

### B. Single-Revolution State Solutions

After the initial orbit solution was converged, the major task of the Satellite OD Group was to determine a predicted orbit on which to base the first orbit trim maneuver. This first maneuver was planned near the periapsis passage at the end of the fourth revolution,  $P_4$ . To allow time for data editing, data fitting, trajectory generation, maneuver computation, and generation of the spacecraft commands, the predicted orbit had to be determined on the basis of the first three revolutions of tracking data.

Three successive single-revolution fits were made over the first three revolutions. The consistency of the three solutions is shown in Fig. 23 in the same format as the pre-flight simulation fits presented in Fig. 10. The actual trajectory is not pictured in the figure because it is obviously unknown. The dispersion of  $r_p \Delta \Omega$  is, however, approximately 40 km instead of the 10 km seen with the simulated data, and predicted periapsis passage time mapping is poorer than with the simulated data. From the data fit in the first revolution, the time of periapsis passage one revolution later, at  $P_2$ , is in error by 3 s, whereas the same fit misestimates the periapsis passage at  $P_1$  by 8.5 s.

### C. Multi-Revolution Solutions

Because of the inconsistency between position estimates and between local and predicted passage times, the Navigation Team proceeded to sense the gravity field immediately. To do this, a state plus second- and third-degree coefficient solution was made over the first 2½ revolutions of data. The position of this long-arc solution, shown on Fig. 23, falls within the spread of the single-revolution solutions. The times of periapsis passages are consistent with those which are local to the single-revolution solutions (accurate to 0.1 s), even when the solution is mapped ½ revolution to  $P_1$ .

The trajectory from the long-arc fit was used to plan the first orbit trim maneuver. This first maneuver was designed to trim down the local orbital period from 12 h 35 min to 11 h 58 min. The trim controlled the period in the revolution  $P_1$  to  $P_2$  to within an error of 1 s.

### D. Conclusions of the Pre-trim Solutions

The pre-trim orbit determination was successfully carried out, but, as indicated by Fig. 23, when compared to Fig. 10, the following unexpected characteristics of the OD process and of the Martian gravity environment were observed:

- (1) The dispersion of successive periapsis position estimates in the plane of the sky was three to four times larger than predicted on the basis of pre-flight gravity uncertainty estimates.
- (2) The predicted times of periapsis passage were three times more inaccurate after a few revolutions than expected.
- (3) The harmonic coefficient estimates from the 2½-revolution long-arc solution were approximately four times larger than expected.

### E. OD Support for the Second Orbit Trim Maneuver

The first maneuver performed in the satellite phase trimmed the anomalistic period in revolution 5 to 11 h 58 min so that the orbital timing would be synchronized with Goldstone. The period of the Mariner 9 orbit, however, did not remain constant.

The gravity structure of Mars accounts for the variation in the period. This rough structure is characterized primarily by two strong gravity regions on opposite sides of the planet and two consistent, weak gravity regions removed 90 deg from the strong regions. These strong and weak gravity regions were manifested in the coefficient solutions as large values of  $C_{22}$  and  $S_{22}$ .

Because the orbital period of the spacecraft was approximately 12 h and the period of planetary rotation is 24.02 h, the spacecraft at periapsis passed almost over the same ground feature of the planet on every other revolution, and the gravity bulges caused by  $C_{22}$  and  $S_{22}$  then exerted a pumping effect on the planetocentric orbital energy and, hence, on the orbital period. This phenomenon, called resonance, can be intuitively illustrated by the diagrams in Fig. 24.

The figure presents a diagrammatic view of the planet-spacecraft geometry from along the Martian spin axis for four successive points in time. The first view (a) shows the periapsis occurring directly above the tesseral bulge. Thus, the perturbation is perpendicular to the velocity direction, and no period changes occur. Because the rotation rate of the planet does not quite keep pace with twice the orbital rate of the spacecraft, a few revolutions later the spacecraft at periapsis is ahead of the gravity bulge, as shown in (b). Now the gravity perturbation retards the energy of motion, pulling the orbital period down. In (c), the probe periapsis has advanced to a point above a gravity valley, and the period levels off. However, in (d), the spacecraft periapsis is approaching the opposite bulge; hence, the energy and period are increased. This alternating push and pull on the spacecraft resulted in an actual oscillatory period history for Mariner 9, one cycle of which is shown in Fig. 25. The period oscillated in a quasi-sinusoidal manner with an amplitude of 40 s and a wavelength of 37 orbital revolutions or 16½ days, the time taken for the spacecraft to cover the entire Martian surface. The high-frequency variations in the period curve can be attributed to the effects of third- and higher-order gravity coefficients.

The first orbit trim was performed when the period of Mariner 9 was near the top of the cycle shown in Fig. 25 but was falling by about 3 to 4 s per revolution. Since the mean period (as determined later) was then some 40 s less than the controlled period in revolution 5, synchronization of the spacecraft periapsis passage with Goldstone view was not properly achieved by the first trim.

A difference between the local period in revolution 5 and the mean period was suspected prior to the commanding of the first orbital trim. However, confidence in the estimated value of the mean period was low. Although the local period drift was observed, the determination of the mean period involved extrapolation of the orbit with a gravity model determined from only 2½ revolutions of data. Because the high values of  $C_{22}$  and  $S_{22}$  dominated the model, the accuracy of the determined mean period was almost totally dependent on the accuracy of these two global coefficients, which were currently estimated from orbital motion over only 6% of the surface of the planet. A 10% change in the magnitude of the  $C_{22}$ ,  $S_{22}$  effect— $J_{22}$ —would result in a 4-s mean period change, as would a 10-deg change in orientation,  $\lambda_{22}$ . Because the confidence in the values of  $C_{22}$  and  $S_{22}$  was not at the 10% level, it was decided to take the local period estimate as the predicted mean period when computing the desired trim maneuver ignition time.

Confidence in the gravity model increased markedly when longer-arc solutions, containing many revolutions of data, confirmed the gravity model from the first pre-trim 1 fit. The accuracy of the single revolution fits also improved as gravity models were included in the trajectory generation model. This improved accuracy is easily illustrated by an extension of Fig. 23 to include fits made after trim 1. This is shown in Fig. 26, where the fit consistencies are presented in terms of  $r_p \Delta \Omega$ ,  $\Delta r_p$ , and  $\Delta z'_p$  (see Fig. 6).

The first four revolutions are the same as those shown in Fig. 23, and were processed with only the pre-flight  $J_2$  value of 0.00197 in the gravity model. After the orbit trim was executed at  $P_4$ , the remaining revolutions shown in Fig. 26 were processed with a fourth-order gravity model, determined from a solution over the first four revolutions, included in the trajectory integration. The solution deviations in all of the state components are consistent with the error magnitudes predicted from the covariance studies. The position estimates made after  $P_4$  agree with neighboring estimates much more closely than those made before  $P_4$ , which indicates the extreme importance of in-orbit gravity modeling.

With the increased confidence in the gravity model and, hence, in the mean period of the orbit, the OD Group performed a single-revolution fit from data in revolution 93. This fit was used to command a second trim maneuver in revolution 94, which readjusted the mean period of the orbit to synchronize with Goldstone.

## V. Martian Gravity Analysis

### A. Gravity Solution Description

It was concluded from the findings during the pre-trim OD phase of the mission that the gravity sensing mode of the OD strategy would be a very important part of the entire OD system. This conclusion certainly proved to be true for the duration of the satellite operations. Hence, it is important to include a discussion of the characteristics of the gravity field solutions.

Many harmonic coefficient models were determined for Mars throughout the mission to meet the navigation requirements. These models varied in the length of the data arcs and estimated parameter sets. Pre-flight covariance analyses indicated that estimation of the spacecraft state and harmonic coefficients through the sixth degree with data from four to six orbital revolutions would be useful

for navigation purposes. Consequently, a total of 19 different sixth-order resonance models over separate data intervals were obtained during the first few months of the mission. These models were used for the data fits until around revolution 100, and they were also useful for consistency checks on the values of individual harmonic coefficients.

Because 38 orbital revolutions (19 days) were required for the periapsis point to cover 360 deg in longitude with respect to the Martian surface, this time span was a natural one to use in the solutions for harmonic coefficients. Two such 38-revolution fits were made. An eighth-degree harmonic model was generated by Lorell and Laing (Ref. 16) of the Celestial Mechanics Team over revolutions 4 to 42. Later, a tenth-degree harmonic model over revolutions 52 to 90 was generated by the Navigation Team.

Because a model based on 38 revolutions was valid for all subsequent ground tracks, it was sufficient for subsequent real-time navigation. On December 19, 1971, the eighth-degree harmonic model based on revolutions 4 to 42 was made available to the Navigation Team. This model was used for short-arc fits from revolutions 100 through 250. On March 28, 1972, the Navigation Team completed the tenth-degree model over revolutions 52 to 90. This model was used for all fits beyond revolution 250.

Table 11 lists all gravity models generated during the satellite phase of Mariner 9.

## B. Physical Description of the Gravity Field of Mars

The estimated values of the coefficients of the respective gravity models have differed from solution to solution because of the presence of higher-order unmodeled gravity coefficients, planetary ephemeris errors, and attitude control gas leaks on the spacecraft. However, solutions for several of the lower-order coefficients have been relatively consistent for all estimation lists and data intervals.

The solution for the second-order zonal coefficient,  $C_{20}$ , is  $(1.96 \pm 0.01) \times 10^{-3}$ , which is in good agreement with the value determined from Earth-based optical observations of the Martian satellites and from Mariner 4 data. The direction of the Martian spin axis has been estimated simultaneously with the gravity coefficients; hence, the values of the coefficients  $C_{21}$  and  $S_{21}$  are very small. However, the values of the resonance tesserals  $C_{22}$  and  $S_{22}$  are  $-5(\pm 0.5) \times 10^{-5}$  and  $3(\pm 0.5) \times 10^{-5}$ , respectively, which are approximately four times larger than expected from extrapolation of the Earth's potential. Physically,

the  $J_2$  term corresponds to a gravitational bulge around the Martian equator, which is symmetric about the Mars spin axis. When  $C_{22}$  and  $S_{22}$  combine, they produce a gravitational bulge at the Martian equator, which is superimposed on the  $J_2$  bulge but is symmetric about a plane in which the spin axis lies. Hence, the gravity bulge caused by  $C_{22}$ ,  $S_{22}$  can be thought of as placed on the front and back of the planet, with gravity valleys on the sides.

Third-degree terms,  $C_{30}$ ,  $S_{30}$ ,  $C_{31}$ , and  $S_{31}$ , have also shown relative consistency.

The harmonic coefficient values for the tenth-degree harmonic model are given in Table 12. It is emphasized that only the aforementioned stable terms ( $C_{20}$ ,  $C_{22}$ ,  $S_{22}$ ,  $C_{30}$ ,  $S_{30}$ ,  $C_{31}$ , and  $S_{31}$ ) are meaningful on an individual basis. However, the ensemble of coefficients has worked well for navigational purposes for the Mariner 9 orbit.

The gravitational structure of Mars, as represented by coefficients, whose values are given in Table 12, is characterized by an equipotential surface with a large equatorial bulge, whose height at the equator is approximately 18 km above the polar height if a mean radius of 3394 km is assumed. Superimposed on this equatorial bulge, the tesseral terms combine to form a 1.2-km bulge above the mean equatorial surface in the Tharsis region of the planet (110°W longitude). A corresponding high bulge of approximately 0.5 km occurs on the opposite side of the planet in the Syrtis Major region (280°W longitude), and low valleys, 0.6-km deep, are located at 30 and 180°W longitude.

## C. Consistency of Gravity Solutions

Figure 27 illustrates the dispersion range of all harmonic solutions as a function of degree and order of all coefficients through four. The values have been divided by their respective *a priori* uncertainties as derived by extrapolation from the Earth's value. The vertical lines cover the range of values of the sixth-degree solutions; the white circles indicate the tenth-degree fit, the dark circles the eighth-degree fit. The results for  $C_{20}$  are shown as a deviation from the pre-flight value. The dashed line represents 1- $\sigma$  variations in the estimation of the coefficients based on the extrapolated values for the Earth. As can be seen, many of the solution values are three to five times greater than pre-flight expectations. Note that  $C_{20}$ ,  $C_{22}$ ,  $S_{22}$ ,  $C_{31}$ ,  $S_{31}$ ,  $C_{33}$  and  $S_{33}$  all appear to be reasonably consistent but that estimates of the higher-degree coefficients are unstable. This instability is due to the fact that the effects of many of the harmonics have similar signa-

tures in the doppler data. Consequently, these coefficients are highly correlated and, to a degree, inseparable.

#### D. Error Sources for Gravity Field Solutions

Post-fit residuals of the Mariner 9 doppler data obtained after orbit insertion are one to two orders of magnitude larger than the post-fit residuals from the cruise portion of the mission. Furthermore, the residuals after orbit insertion show clear structure, especially for data obtained near periapsis passage. Consequently, the harmonic models generated thus far have deficiencies both from the point of view of serving as a navigation tool and of actually modeling the gravity field of Mars. The cause of this deficiency falls into four categories, which are discussed below.

**1. Limitations of the harmonic expansion.** The spherical harmonic expansion used to represent the Mars gravity potential must be truncated, usually after the first few tens of terms. In general, the effects of such omitted terms are partly "absorbed" by other components of the model, whose coefficients take on compensatory values. Thus, the value of the harmonic coefficients obtained in a particular solution will depend both on the span of data used and on the number of terms retained in the harmonic expansion. With data from only one spacecraft orbit available, many harmonic coefficients leave similar signatures in the data, which causes certain combinations of coefficients to be nearly linearly dependent. It may be possible to alleviate this problem by adding different data types, such as landmark and natural satellite observations, and data from the occultation experiment.

**2. Gas leaks and radiation pressure.** Sporadic gas leaks in the attitude control system produced accelerations on the order of  $10^{-11}$  to  $10^{-12}$  km/s<sup>2</sup>. Such leaks are extremely difficult to model accurately, and engineering data on them have been refined only for revolutions prior to trim 2. Studies over this region indicate that unmodeled gas leaks are an insignificant factor on the harmonic coefficient solutions compared to other model deficiencies. The unmodeled part of the solar radiation pressure, together with Mars reflected and reradiated energy, produces an acceleration which is somewhat smaller than that caused by the gas leaks.

The effects on the estimates of the harmonic coefficients of unmodeled gas leaks are illustrated in Fig. 28, where the differences between two coefficient models determined from the same four-revolution data arc, one with no gas leaks modeled and the other with gas leaks modeled

(as described in Section III-B), are denoted by the vertical bars. The ordinate scale is the same as that in Fig. 27. Although this model has a relatively small effect on  $J_2$ , the changes in many of the higher-degree terms seem more significant relative to the assumed *a priori* uncertainties.

**3. Ephemerides.** The ranging, or time delay, measurements indicate that the ephemerides used to analyze the Mariner 9 data in Section III are in error in the Earth-Mars direction by several kilometers. Figure 29 illustrates the effects of such errors on the estimates of the harmonic coefficients, where the differences between two harmonic coefficient sets, determined using DE 79 and DE 80, respectively, are denoted by the vertical bars as in Fig. 28. The two ephemerides differ by about 8 km and 0.5 mm/s in the Earth-Mars range and range rate, respectively. Coefficient solution differences are mostly smaller than those caused by the gas leaks, and hence they show the lower sensitivity of the estimates of the harmonic coefficients to this order of ephemeris error. The two data arcs for Figs. 28 and 29 were different; thus, the solutions for the higher-degree coefficients do not agree.

**4. Station locations.** Another source of model error is introduced by the uncertainties in the geocentric locations of tracking stations, which are on the order of 3 m in longitude (in the system defined by the planetary ephemerides) and 2 m in distance from the Earth's spin axis (Ref. 17). These errors, being diurnal, are highly correlated with those of the models used to describe the effects of the Earth's atmosphere and ionosphere on the propagation of the tracking signal. Analyses, especially of the cruise data, are being undertaken to reduce this error source.

## VI. Science Support Orbit Determination History

### A. Solution Procedures

The great bulk of orbit solutions which were generated by the Satellite OD Group were in support of science sequence planning and science data-reduction efforts. Prediction trajectories had to be provided to locate the predicted Mars periapsis position of the spacecraft to an accuracy of 10 km in the Martian plane of the sky for a period of 1 week into the future. These trajectories were used to align the scan platform prior to sensing the Martian surface. Therefore, the predicted trajectory requirement was imposed at all times at which scan platform maneuvers were imminent. The 10-km accuracy

requirement is consistent with a maximum science instrument pointing uncertainty of 0.5 deg. Using the predicted trajectories supplied by the Satellite OD Group, the mission obtained a total of more than 7000 TV images, 50,000 UV spectra, 20,000 IR spectra, and 400 S-band occultation measurements of the Martian surface.

Prediction orbits were generated on the basis of short-arc data fits defined by the strategy discussed in Section III. Data were fit once or twice per week in accordance with mission needs. While the 26-m antennas were tracking, the basic strategy was to process a single revolution of data. These fits contain enough data to minimize the effects of data noise and still yield accurate state solutions. After the spacecraft went out of range of the 26-m antennas, many of the short-arc fits contained data from two successive revolutions, which provided enough information for adequate orbit determination. These single-station, two-revolution fits, however, are not as accurate as the single-revolution multi-station fits. During the entire satellite phase of the mission, approximately 190 short-arc fits were performed in support of mission objectives.

It was also necessary to provide final trajectories throughout the regions in which visual images and spectra were obtained. These smooth trajectories were determined from local doppler data and involved extrapolation only a few revolutions beyond the data interval. The time of periapsis passage was held to a maximum allowable error of 0.1 s throughout the extrapolation, rendering the  $\Omega$ -error the dominant position uncertainty. The trajectories provided the final best estimate of the spacecraft position at science data acquisition times, and thus they were used by the science experimenters in the reduction of the instrument data.

Smooth orbits were generated from multi-revolution, long-arc fits to the data. Early in the satellite mission, most of these trajectories were derived from data fits which had been originally used to generate harmonic solutions. As the mission progressed, state-only fits, with a proper harmonic coefficient set in the dynamic model, proved suitable. Most long-arc fits were determined over six revolutions of data until revolution 191, after which one or two revolutions of data proved adequate because of the availability of a more complete harmonic model. The long-arc fit activity was suspended after revolution 277.

## B. Solution Summaries and Accuracies

1. **Accuracy criteria.** Since the accuracy of the location of the spacecraft in the periapsis region was of prime im-

portance to science, the discussion of the accuracy of both the predicted and smooth orbits will be limited here to the position accuracy at periapsis. The pre-flight studies indicated that the error in the spacecraft estimated position at periapsis is comprised almost entirely of the vector sum of the local position error which results from the imprecision of the determined longitude of node in the Earth's plane of the sky and the mapping error caused by an erroneous predicted time of periapsis. These two position errors, denoted respectively by  $r_p \Delta \Omega$  and  $v_p \Delta T_p$ , thus will be used as criteria for judging the accuracy of local and predicted orbits.

Because a local time of periapsis passage (i.e., a time of periapsis either within or near the ends of a processed span of data) is determined to within 0.1 s, the errors in the predicted periapsis times are easily measured by comparison with updated passage times determined after local data are available. Thus, values of  $\Delta T_p$ , the periapsis passage time error, were easy to compute for all predicted trajectories at any future periapsis. Errors in  $\Omega$  are more difficult to assess because the true value, or a more accurate value, of  $\Omega$  is not available. For purposes of indicating the accuracy of the  $\Omega$  value for a particular estimated orbit, the concept of the average or mean  $\Omega$  will be employed. Thus, the node error,  $\Delta \Omega$ , will be referenced to a mean  $\Omega$  value, which has been determined from averaging many  $\Omega$  solutions made throughout the satellite mission. Values of  $\Delta \Omega$ , then, do not necessarily represent the actual error in  $\Omega$  for a particular estimated orbit but indicate only the deviations from average.

2. **Short-arc fit summary.** A partial list of the short-arc fits which were computed during the satellite phase of the mission is given in Table 13. Included in the table are deviations from a mean orbit at periapsis in the determined position, which lies almost entirely in the Earth's plane of the sky. The mean orbit is determined from all of the short-arc fits. Values of the  $\Omega$  deviations in degrees are also given. The  $\Omega$  error is related to the position error by  $r_p$ , the distance of the spacecraft at periapsis from the Mars-Earth line of sight. The evolution of  $r_p$  throughout the satellite mission is presented in Fig. 30. Also included in the figure is the evolution of the component of the Mars-spacecraft vector at periapsis along the Earth-Mars line  $z'_p$ .

Deviations in the plane of the sky position may also be related to in-track and out-of-plane position deviations by using Fig. 31, which shows the evolution of the ratios of the in-track and out-of-plane position deviations to  $r_p \Delta \Omega$ .

Around revolution 280, the  $\Omega$  error contributed almost exclusively to an in-track position error, while around revolution 390, the  $\Omega$  error fell entirely out of the orbit plane. At this particular time, the Earth viewed the Mariner orbit "edge-on." (The  $\Omega$ -error vector never has a component in the local altitude direction.)

Table 13 includes a column which lists the number of revolutions for which the predicted time of periapsis was accurate to within 2 s. Since the velocity magnitude at periapsis was 3.8 km/s, the 2-s error tolerance corresponds to an in-track position error of 7.6 km, which is close to the flight accuracy requirements of 10 km. Thus, the number of mapped revolutions for which the  $\Delta T_p$  is less than 2 s corresponds roughly to the number of revolutions for which the predicted orbit was satisfactory for science sequence command generation.

**3. Long-arc fit summary.** Table 14 is a complete list of the long-arc, or smooth-orbit, estimates, which were generated by the Satellite OD Group. As in Table 13, values of the position deviation  $r_p \Delta \Omega$  and the angular deviation  $\Delta \Omega$  from the mean of the long-arc fits are given. Also included in the table is a column for the periapsis to which extrapolation of the fit was allowed; i.e., the tolerance of 0.1-s time-of-periapsis passage was not violated for the periapsis listed.

**4. Local position accuracy.** Figure 32 displays the time history of the deviations in  $\Omega$  from the mean values of  $\Omega$  for the short-arc solutions of Table 13. The values in the figure are taken directly from the table. Little sensitivity of the consistency of the  $\Omega$  solution to the degree of the gravity coefficient model can be seen in the figure. However, when only the 64-m station was tracking, the two-revolution, apoapsis-to-apoapsis data span fits were not as accurate as the single-revolution, three-station fits.

The rms local position error from the mean was approximately 5 km, while both the 26- and 64-m tracking stations were receiving data. After the loss of the 26-m stations, the rms position error rose to 8 km.

The rms local position deviation from the mean for the long-arc or smooth solutions was slightly less than 2 km, which indicates that the long-arc mode of processing yields the more consistent local position estimates. The mean position estimate from long-arc fits agreed within 1 km with the mean position from short-arc fits when the averaging included all fits made between trim 1 and trim 2. The difference between the respective mean positions, based on fits after trim 2, was just less than 2 km.

**5. Prediction accuracy.** As the time of prediction increases, the in-track or timing errors dominate those caused by errors in  $\Omega$ . Figure 33 is typical of the error growth for  $T_p$  for the tenth-degree harmonic model. It was generated by performing a short-arc fit and solving for state only. The resulting solution was integrated forward in time, and the predicted  $T_p$  was compared with more accurate values obtained from numerous short-arc fits throughout the subsequent tracking data. The error exhibits a 19-day periodic variation, indicating a deficiency in the even-order tesseral harmonics. The accompanying secular error is attributed to errors in the gravity field combining with errors in the initial state to yield an incorrect mean period.

Another manifestation of in-track errors is seen in predicted doppler residuals. Figure 34 shows doppler residuals associated with a one-revolution fit and the subsequent 20 revolutions of prediction. The prediction residuals exhibit peaks in the periapsis regions which follow a secular trend and reach a maximum of 50 Hz, equivalent to a 5-s error in  $T_p$ . As can be seen from the insert, the residuals within the fit also have a systematic structure of about 0.1 Hz, reflecting model deficiencies.

Figure 35 shows the mapping accuracy history of the short-arc fits in terms of the number of revolutions for which the predicted time of periapsis was accurate to within 2 s. The plot is taken directly from the values in Table 13. It is important to note that the feasible prediction interval increased markedly as the sixth-degree gravity field was replaced by the eighth-degree field. The average number of revolutions that could be predicted to within the 2-s tolerance rose from 6 to 14. The commencement of the use of the tenth-degree field, however, coincided with the loss of the 26-m stations, and no noticeable prediction improvement was achieved. Later in the mission, as solution procedures were somewhat refined, the prediction capability increased, so that predicted orbits were accurate to within 2 s for as many as 40 revolutions.

## VII. Perturbed Orbital Motion of Mariner 9

A history of the Mariner 9 Kepler elements relative to the Mars true equator of date is analyzed here to determine the short-period and long-period characteristics in the evolution of the orbit. The short-period variations are found by performing a one-revolution fit and integrating that solution for one satellite period between two successive apoapses. The long-period orbital element variations are obtained by sampling short-arc OD solutions once per satellite revolution at periapsis and apoapsis. Only the

apoapsis history is shown since periapsis results were noisier because of the interaction between short- and long-period effects. The Kepler elements discussed span Mariner 9 orbits 5 through 502 (approximately 250 days)

## A. Theoretical Considerations

The perturbations in the Mariner 9 orbit arose from the noncentral properties of the Mars mass distribution and from disturbing effects of the Sun, solar radiation pressure, and other planets. Although these perturbing effects were small (at least 500 times less than the inverse attraction of Mars), each induced a distinct variation in the orbital elements. In order of importance, the major perturbations were:

- (1) Mars gravity
  - (a) Equatorial bulge,  $C_{20}$ .
  - (b) Equatorial ellipticity,  $C_{22}$ ,  $S_{22}$ .
  - (c) Other resonance harmonics,  $m$  even.
  - (d) Other tesseral harmonics,  $C_{31}$ ,  $S_{31}$ ,  $C_{33}$ ,  $S_{33}$ .
  - (e) Higher-order harmonics.
- (2) N-body perturbations
  - (a) Solar gravity.
  - (b) Solar radiation pressure.
  - (c) Other planets (Jupiter, etc.).

The time dependence induced in each of the Kepler elements by these perturbations is given by the Variation of Parameters Equations (Ref. 18):

$$\frac{dk}{dt} = \sum_{l,m} F(a, e, i) [C_{lm} \cos \psi + S_{lm} \sin \psi] + \dot{k}_O + \dot{k}_J + \dot{k}_{SR} \quad (19)$$

where  $\mathbf{k}$  is the six-vector of orbital elements;  $\dot{k}_O$ ,  $\dot{k}_J$ , and  $\dot{k}_{SR}$  are the solar gravity, Jupiter, and solar radiation pressure perturbations,

$$\psi = [(l - 2p)\omega + (l - 2p + q)M + m(\Omega - \theta)] \quad (20)$$

$l$ ,  $m$ ,  $p$  and  $q$  are dummy indices, and  $\theta$  is the sidereal time. Using first-order perturbation theory, solutions to these equations can be approximated. If only the variations arising from the Mars noncentral gravity are considered, the following solution can be postulated:

$$\delta \mathbf{k}(t) = \sum_m \frac{F(a, e, i)}{i} [C_{lm} \sin \psi(t) + S_{lm} \cos \psi(t)] \Big|_{t_0} \quad (21)$$

where

$$\dot{\psi} = (l - 2p)\dot{\omega} + (l - 2p + q)\dot{M} + m(\dot{\Omega} - \dot{\theta}) \quad (22)$$

and

$$\psi(t) = \psi(t_0) + \dot{\psi}(t - t_0) \quad (23)$$

The terms in Eq. (21) will generate nearly periodic variations in the orbital elements having the characteristics shown in Table 15. Since the orbital rate of Mariner 9 and the rotation rate of Mars are nearly commensurable (2:1), a resonance condition exists. In the notation of Eq. (21), the commensurability of the rotation rates is

$$(\dot{\Omega} - \dot{\theta}) \approx -\frac{\dot{M}}{2} \quad (24)$$

Because Mariner 9 was very near critical inclination, the argument of perifocus rate was very small relative to the other rates; hence, it is assumed to be zero for this calculation. Using the commensurability condition and setting  $\dot{\omega} = 0$ , the following relationship is obtained:

$$\left[ (l - 2p + q) - \frac{m}{2} \right] \dot{M} \approx 0 \quad (25)$$

For resonance,

$$(l - 2p + q) = \frac{m}{2} \quad (26)$$

Any tesseral harmonic in the gravity field fulfilling this relationship generates a resonant perturbation in the orbital elements (Ref. 18). Using these concepts from perturbation theory, an analysis of the orbital element variations can now be performed.

## B. Analysis of Orbit Evolution

**1. Short-period effects.** The short-period variations in the orbital elements of Mariner are shown in Fig. 36. These variations cover one orbital period as measured from apoapsis to apoapsis. Because the orbit has a highly elliptical shape, the short-period variations are all concentrated in a region very near the periapsis ( $T_p \pm 100$  min).

These short-period variations result from a superposition of all the harmonics in the Mars gravity field. The short-period variations in semimajor axis of +21 and -24 km correspond to osculations in the period of 105 and 120 s. The associated short-period variations in eccentricity correspond to local changes in the periapsis height of 7.5 and 8.0 km. The trends associated with each of the orientation angles ( $i, \omega, \Omega$ ) are due to the perturbing effects of the zonal terms in the Mars gravity and N-body perturbations.

**2. Long-period effects.** The long-period osculating orbit elements of Mariner 9 are illustrated in Fig. 37, (a) showing the in-plane elements ( $a, e, P$ ) and (b) the orientation angles ( $i, \omega, \Omega$ ). Each part shows the variation in the orbital elements from an epoch value. The semimajor axis and anomalistic period variations are referenced to an epoch value at apoapsis 5. Since the second trim maneuver was performed in orbit 94, the remaining elements,  $e, i, \omega,$  and  $\Omega$ , are referenced to two different epochs to show periodic variations on this scale. From apoapsis 5 through 94, they are differenced from apoapsis 5, whereas from apoapsis 95 through 502, they are differenced from values at apoapsis 95. It can be noted directly from the figures that the second trim maneuver increased the mean value of the semimajor axis about 16 km.

The discontinuities experienced in each of the orientation angles are a manifestation of both gravity model errors and observability problems associated with  $\Omega_{\text{POS}}$ . During the early phases of the mission, very preliminary gravity models were used, and, as a result, adjacent solutions did not extrapolate continuously. As the mission progressed and improved models were obtained, the extrapolation quality of the models markedly improved until loss of the 26-m antennas. The observability problem previously discussed projects onto each of the orientation angles relative to Mars equator.

**3. Effects of oblateness.** Because the gravity field of Mars possesses a large oblateness term, a regression of both the argument of perifocus and ascending node was experienced by Mariner 9. The results for  $\Delta\omega$  and  $\Delta\Omega$ , presented in Fig. 37, have had a rate (approximately the first-order secular rate of  $C_{20}$ ) subtracted. The values used in this calculation are given in Table 16.

The regression of the ascending node was the largest and most dominant perturbation affecting the orbit (about 0.16 deg/day). The presence of oblateness caused a difference between the observed anomalistic period and the equivalent two-body period based on an average semi-

major axis  $a_0$ . The difference in period caused by  $C_{20}$  is found as follows:

$$\Delta P = 2 - \left[ \frac{1}{n} - \frac{1}{n} \right] \quad (27)$$

where

$$n_0 = \sqrt{\frac{\mu}{a_0^3}} \quad (28)$$

$$n = n_0 \left[ 1 - \frac{3}{4} C_{20} \left( \frac{R}{a_0} \right)^2 \frac{(3 \cos^2 i - 1)}{(1 - e^2)^{3/2}} \right] \quad (29)$$

The value of the difference in the period is 4.4 s.

**4. Resonance effects.** The resonance condition induced by the tesseral harmonics in the Martian gravity field generates a periodic perturbation in each of the orbital elements. Since all even-order tesseral harmonics satisfy the resonance relationship, they superimpose to generate the 39-revolution periodic effects observed. Analysis has shown that 90% of the resonance variations arise from  $C_{22}$  and  $S_{22}$ , the equatorial ellipticity terms. To illustrate this point, an analytical trajectory generator (Ref. 19) was used to predict the mean anomaly at time of periapsis passage for one resonance cycle. Three gravity models were employed in this study:

- (1) Equatorial oblateness only ( $C_{20}$ ).
- (2) Triaxial ( $C_{20}, C_{22}, S_{22}$ ).
- (3) Complete eighth-degree model.

Figure 38 shows the errors in mean anomaly and  $T_p$  using these three models. As can be seen, the triaxial model reduces the errors by a large percentage. The addition of higher-degree harmonics (through degree and order eight) provides enough resonance harmonics to reduce these errors to 0.01 deg and 2 s, respectively. The resonance harmonics induce a periodic variation in the anomalistic period with an amplitude of 40 s and an associated variation in the semimajor axis with an amplitude of 8 km (see Fig. 37). This corresponds to an in-track position variation with an amplitude of 1000 km.

**5. Effects of nonresonance tesserals.** Analysis of the variation in the orbital elements reveals that high-frequency oscillations are superimposed on the basic resonance cycle. The effects are particularly noticeable in the semimajor axis and anomalistic period variations. These variations (shown in Fig. 25) are generated by the odd-

ordered tesseral harmonics, principally  $C_{22}$ ,  $S_{22}$ , and  $C_{42}$ ,  $S_{42}$ . At a maximum, these terms induce variations of 0.5 km in the semimajor axis at apoapsis and period changes of 2.5 s.

**6.  $N$ -body effects.** The long-term trends experienced by the orbital elements  $e$ ,  $i$ ,  $\omega$ ,  $\Omega$  are due to  $N$ -body perturbations, solar radiation pressure, and the effects of gravity coefficients. To separate these effects, the perturbations of the Sun, Jupiter, and solar radiation pressure have been numerically integrated and are shown in Fig. 37. For the case of each of these orbit parameters, the  $N$ -body effects are indicated by solid lines on the figures. Assuming that all other perturbations are negligible, the difference between the  $N$ -body effects and the value of the osculating elements at any point is the variation arising from the Mars gravity field. A large amount of the long-period variation experienced by the orbit elements is due to  $N$ -body effects. The solar gravity and radiation pressure perturbations are near-periodic, with a frequency proportional to a Martian year (1.8 Earth years). Solar gravity perturbations are an order of magnitude larger than those of solar radiation pressure.

The change in apoapsis height over revolutions 92–502 was computed to illustrate the long-term effects of all perturbations on Mariner 9. The long-term change in eccentricity over this period is  $\Delta e = -0.9 \times 10^{-3}$ . The corresponding change in apoapsis height is

$$\Delta r_a = a \Delta e = -11.4 \text{ km}$$

To calculate the long-term effect of the Mars gravity field on the apoapsis height, the  $N$ -body effects were subtracted from the osculating eccentricity. The resultant long-term change in eccentricity was  $\Delta e = 0.375 \times 10^{-3}$  or  $\Delta r_a = 4.7 \text{ km}$ . Corresponding calculations result in a long-term inclination change of  $\Delta i = 0.1 \text{ deg}$ . These changes in  $e$  and  $i$  result primarily from the interaction effects of sectorial harmonics  $C_{22}$  and  $S_{22}$  in the Mars gravity field.

**7. Effects of solar occultation.** The solar occultation period, which occurred between values of eccentric anomaly of 240 to 277 deg, also caused a perceptible change in the energy of the orbit, which is manifested in a change in mean semimajor axis and anomalistic period. For the orbits during which the spacecraft was in full sunlight, the change in energy caused by solar radiation averaged to zero over the period of the orbit.

The rather subtle effect of solar occultation can be seen in Fig. 39, where the error in mean anomaly and time of periapsis passage are shown for an analytical ephemeris generator, which does not model the effects of solar radiation pressure. An epoch state vector at periapsis 95, the eighth-degree harmonic mode, and the correct average mean motion were supplied for the analytical program. The states were then obtained at periapsis times gathered from local OD solutions over revolutions 105 to 505. The figure shows that the error in  $T_p$  is small and oscillates about zero until the spacecraft enters solar occultation at about revolution 285, after which the rate increases steadily. This change in the mean period of the orbit is revealed because the analytical program makes no attempt to model solar radiation effects. After solar occultation (revolution 402) the mean rate of error growth in  $T_p$  becomes constant, indicating that the spacecraft mean orbital period was again constant.

From the slope of the error growth in  $M$  after solar occultation, it is possible to compute the change in mean period during solar occultation.

$$\frac{\Delta M}{\text{rev}} = 0.135 \times 10^{-4} \frac{\text{rad}}{\text{rev}}$$

and

$$\frac{\Delta M \text{ rev}}{n} = 0.0154 \frac{\text{min}}{\text{rev}} = 0.924 \frac{\text{s}}{\text{rev}}$$

where  $n = 0.873329 \times 10^{-2} \text{ rad/min}$  is the average mean motion.

Hence, solar occultation increased the mean anomalistic period by approximately 0.9 s. Equivalently, it changed the mean semimajor axis  $a$  by

$$\Delta a = \frac{na \Delta P}{3\pi} = 0.185 \text{ km}$$

The above results may be verified analytically by averaging the planetary equation for semimajor axis given by

$$\frac{da}{dt} = -\frac{2}{n \sqrt{1-e^2}} \left( S e \sin f + a \frac{(1-e^2)}{r} T \right) \quad (30)$$

where

$S$  = radial component of acceleration caused by solar radiation pressure

$T$  tangential component of acceleration caused by solar radiation pressure

Averaging Eq. (30) over the period yields

$$\Delta a = \frac{2F}{n} [A \cos E - B \sqrt{1-e^2} \sin E] \Big|_{F(\text{exit})}^{F(\text{entrance})} \quad (31)$$

where

$FA$  component of solar radiation acceleration in direction of periapsis

$FB$  component of solar radiation acceleration normal to periapsis direction

The magnitude of the solar radiation force for Mariner 9 is approximately  $4.5 \times 10^{-11}$  km s<sup>2</sup>. Evaluating Eq. (31) yields

$$\Delta a = 0.166 \times 10^{-2} \text{ km rev}$$

or

$$\Delta a_{\text{TOTAL}} = 0.19 \text{ km}$$

This value corresponds very well with the value computed earlier from the observed period change, indicating that the solar radiation force model for the Mariner 9 spacecraft is quite good. From Eq. (31), it is seen that there is no net change in  $a$  if the orbit is always in full sun.

If a similar averaging procedure is carried out for eccentricity (detailed in Ref. 20), the result is

$$\Delta e = \frac{-F \sqrt{1-e^2}}{an^2} \frac{1}{4} A \sqrt{1-e^2} \cos 2E \quad (32)$$

$$+ B \left( \frac{1}{4} \sin 2E - 2e \sin E + \frac{3}{2} E \right) \Big|_{F(\text{exit})}^{F(\text{entrance})}$$

Evaluating Eq. (32) for the period of occultation yields

$$\Delta e_{\text{TOTAL}} = 0.71 \times 10^{-5}$$

The change in radius of periapsis is given by

$$\Delta r_p = [a \Delta e + e \Delta a]$$

$$\Delta r_p = 0.214 \text{ km}$$

Consequently, the period of solar occultation from revolutions 282 to 402 resulted in an increased mean energy

and in increased lifetime for Mariner 9. The effect of occultation on the other orbital elements is small. For example,

$$\Delta \omega = 0.008 \text{ deg}$$

## VIII. Confirmation of Doppler-Determined Orbits With TV Imaging Data

During the satellite mission, the Mariner 9 spacecraft transmitted over 7000 pictures covering the entire planet. A select subset of these picture data has been processed with a view to improving existing knowledge of the physical properties of Mars, as well as verifying the knowledge of the topocentric position of the spacecraft itself.

### A. Data-Processing Method

The selected subset of observed landmarks was used to differentially correct the orbit of Mariner 9 in the first 191 revolutions of the satellite phase of the mission. The landmark data processor made use of radio-determined solution segments as *a priori* orbits throughout the 176-revolution interval. These *a priori* solution segments were selected from the harmonic coefficient solutions reported in Section V and the long-arc solutions in Section VI. Because none of the radio-determined solution segments contained extrapolated orbits,  $\Omega$  was the only orbital element for which the various segments were inconsistent. Hence,  $\Omega$  was the only spacecraft orbital element which was corrected from visual observations of the planet surface.

The chosen optical data span was covered by a total of 16 probe ephemerides generated from the long-arc and harmonic coefficient fit. Most of the segments were generated from tracking of less than 8 revolutions. The only exception was the 39-revolution coefficient fit made prior to the second orbit trim maneuver.

The data filter used to process the landmark data was more general than the weighted least-squares algorithm used for radio data during the satellite mission. The solution list for the landmark processor includes

- (1) A constant correction to the node in the plane of the sky associated with each probe ephemeris segment.
- (2) The right ascension and declination of the Martian spin axis referred to Earth mean equator and equinox of 1950 coordinates. (Secular variations are assumed known.)

(3) Heliocentric latitude and longitude, of each landmark, and the radius of Mars referred to the planet center of mass at each of the landmark locations.

(4) TV pointing errors made up of

(a) A set of three constant offsets of the narrow-angle target raster in the platform coordinate system described by the increasing cross-cone, cone, and twist directions.

(b) A set of three constant offsets of the wide-angle target raster with respect to the narrow-angle target raster, defined in the platform coordinate system.

(c) A set of three random variations of the scan platform with respect to the celestial coordinate system described in the yaw, pitch, and roll direction.

The filter was then required to estimate a set of constant parameters over discrete time segments made up by the length of each of the available probe ephemerides and, additionally, to model the discontinuity in the trajectory information by treating it as discrete process noise acting on  $\Omega$  between segments.

The measurement equation can be given, as in Eq. (11), by

$$z = Ax + By + n$$

where the vector  $y$  here consists of random but time-correlated variables of the solution vector and is modeled by

$$y(t + \Delta t) = \rho(\Delta t)y(t) + \sqrt{T} \rho^{-1}q \quad (33)$$

$$\rho(\Delta t) = \exp\left(-\frac{\Delta t}{\tau}\right) \quad (34)$$

where  $q$  is normally distributed, uncorrelated random variable. In the limit that  $\tau \rightarrow 0$ ,  $y$  represents random uncorrelated variables. If  $\tau \rightarrow \infty$ ,  $y$  is a set of constants.

The solution vector contains both  $x$  and the correlated coefficients,  $y$ . Defining estimates and covariances in usual filter theory notation, the filter equations are stated as follows:

$$P = P - P A' (A P A' + R)^{-1} A P \quad (\text{measurement update of covariance}) \quad (35)$$

$$x = x + K(z - Ax) \quad (\text{update of estimate}) \quad (36)$$

$$K = P A' (A P A' + R)^{-1} \quad (\text{optimal filter gain}) \quad (37)$$

Whenever a new trajectory segment is encountered,

$$P = P + D Q D' \quad (38)$$

and

$$\Delta\Omega = 0$$

In addition to the measurement update equations given above, the final solution consists of the final values of the constant parameters  $x$  and solutions  $y$  at each observation time, as well as the node correction for each probe ephemeris segment. The post-fit data residuals are computed on a picture-to-picture basis with these final values.

## B. A Priori Parameter Values

The spacecraft node for the various trajectory segments has discontinuities on the order of 0.05 deg. Thus, the *a priori* 1- $\sigma$  value was based on this state-of-the-art uncertainty.

Although preliminary values of the right ascension and declination of the spin axis of Mars were determined from approach and satellite data and the values obtained were within an 0.05-deg spread, the *a priori* value for the spin axis direction uncertainty was left wide open at 10 deg.

The areographic latitudes and longitudes of observed landmarks were relatively unknown; therefore, their *a priori* values were set at 10 deg (1  $\sigma$ ), approximately equivalent to a surface location uncertainty of 600 km. The polar longitude uncertainties were set at 60 deg to impart the same order of surface location uncertainty. The radii from the center of Mars to the various observed landmarks were assumed to be known to an accuracy of 10 km (1  $\sigma$ ).

The TV pointing uncertainties were described by (1) a set of constant offsets of the narrow-angle TV camera optic axis with respect to an inertial reference and of a

magnitude of 0.03 deg ( $1\sigma$ ), (2) a similar set of constant offsets describing the angle between the wide-angle and narrow-angle TV camera optic axes, set at 0.05 deg ( $1\sigma$ ), and (3) a set of random variations in the spacecraft yaw, pitch, and roll axes which would correct the telemetry readouts of the sun sensor and Canopus sensor, respectively. The *a priori* values were set at 0.03 deg ( $1\sigma$ ), being comparable to the quantization step in the star sensor readout.

The data were weighted independently for each of the various landmarks sighted. One-sigma measurement uncertainties are listed in Table 17.

### C. Corrections to the Mariner 9 Orbit

Figure 40 shows a plot of the variation in  $\Omega$  corresponding to each of the probe ephemerides, referred to a mean and continuous evolution of the node, as in Fig. 32. The figure contains both pre-trim 2 and post-trim 2 regions of data. Doppler-only orbit solution differences are shown by a dashed line, while solutions based on the inclusion of landmark data are depicted by solid lines. The spread of values is contained in the  $\pm 0.05$ -deg band, which was chosen as the  $1\sigma$  *a priori* knowledge uncertainty. As described earlier, the covariance was corrupted at the start of each trajectory segment, and a new solution for  $\Omega$  was sought. These solutions were added as corrections (solid lines) to the values plotted with dashed lines in the figure. The *a posteriori* variations in the node solutions for each of the probe ephemeris segment are listed in Table 18.

The landmark solutions show slight improvement in the consistency of the determined values of  $\Omega$  within the *a priori* orbit segments. The rms  $\Omega$  deviation is reduced from 0.022 to 0.018 deg before trim 2, and from 0.03 to 0.022 deg after trim 2. More important than the improvement in  $\Omega$  discrepancies is the consistency between the doppler-only and landmark solutions, which differ by 0.017 deg before trim 2 and by only 0.003 deg after trim 2. Thus, visual observations appear to verify the doppler-determined orbits.

### D. Estimated Landmark Locations in Areographic Coordinates

The observed landmarks are shown in Fig. 15, and estimates of latitude, longitude, and radii for each are listed in Table 19. TV line and pixel residuals corresponding to each of the landmarks in Pavonis Lacus, Nodus Gordii, Nix Olympica, and the south polar cap are shown in Fig. 41, and the temporal distribution of all data residuals is presented in Fig. 42. The  $1\sigma$  values of these residuals,

when reduced to equivalent wide-angle residuals, are well bounded by the *a priori*  $1\sigma$  value. The only exceptions are observations affected by the sun sensor regulation difficulties, which are discussed in Section III. These data were deleted from the data fit.

The results indicate that the landmark coordinates are obtained to an accuracy of 0.03 deg, equivalent to 1.8 km ( $1\sigma$ ) at the surface. These values compare favorably with the wide-angle camera resolution limit of 2 km at a slant range of about 3500 km.

To obtain correlation between solutions resulting from landmark data and those from occultation, planetary radar ranging, ultraviolet spectrometer (UVS) pressure, and infrared radiometry data, it is necessary to construct the absolute radii of Mars in the vicinity of the observed landmarks. Both planetary radar ranging data and UVS pressure data yield information on relative heights of topographic features, whereas occultation data yield the absolute radius both at signal extinction and reacquisition. Infrared radiometry provides indirect inference of slopes of topographic features from measured temperature profiles, which may be integrated to obtain relative height information.

Figure 43 (derived from longitudinal profiles like those in Ref. 21) shows a radar-based elevation map of Mars, and Fig. 44 (from Ref. 22) presents the UVS pressure map calibrated to show relative heights. Both figures have occultation positions plotted in areographic coordinates (Ref. 23). By matching occultation values of the radii of Mars at each of these positions with the nearest interpolated contour value, it is possible to calibrate the contour maps to show absolute information on heights instead of relative height information. This procedure yields 3393.4 km as the zero contour value in the UVS map and 3397.5 km in the radar map. Since both figures are drawn on a large scale in comparison to the landmarks used in this analysis, the contour values are assumed to reflect base radii in the vicinity of Nix Olympica, Pavonis Lacus, and Nodus Gordii. The base radii are 3401.0, 3403.0, and 3402.0 km, respectively, from the UVS map and 3402.5, 3403.5, and 3403.5 km, respectively, from the radar map. The relative height from base to summit is available from a detailed UVS profile of Pavonis Lacus and from an IRR profile of Nodus Gordii (Ref. 24). These altitudes are shown in Figs. 45 and 46, respectively. Direct comparison of values for the main caldera (identified as 2 in Fig. 45) in Pavonis Lacus shows that the estimated radius is within 0.7 km of the combined UVS occultation value, and within 1.2 km of the combined radar occultation value. Similar comparisons for Nodus Gordii show the estimated radius

to be within 2.5 km of the combined UVS occultation infrared radiometer (IRR) value, and within 3.5 km of the combined radar occultation IRR value. The formal  $1-\sigma$  uncertainties are given in Table 19. Figure 15a shows a map of the south polar region bounded by the  $65^\circ$  latitude band. As shown, the exit occultation position labeled 414x is the closest point to the south polar landmarks. Comparisons of radius values to that of 3383.9 km show that the estimate at LM66 is within 0.5 km and at LM661 within 1.2 km. The associated formal uncertainty of 2.0 km ( $1-\sigma$ ) appears quite representative. No comparisons are available for Nix Olympica.

The landmark elevations obtained from Mariner 9 visual observations agree with values from other data sources to within 2 km. It must be pointed out that the accuracy limits of the various data types were not considered when making the comparisons, and that the values were obtained by combining the occultation radii with relative height information from radar, UVS, and IRR wherever available. Although no comparative values exist for Nix Olympica, landmark data for this region indicate an absolute radius of  $3419.2 \pm 2.6$  km at the summit caldera, which is equivalent to a relative height of 18.2 km to the summit from the base.

Various pointing offsets were determined simultaneously with the landmark and spacecraft positions. However, no comparisons are available in the absence of simultaneous stellar imaging. The corrections are limited by the *a priori* uncertainty of 0.03 deg for the narrow-angle offsets and 0.05 deg for the mutual offsets between the wide-angle and narrow-angle cameras. These corrections would be applicable after ground and inflight calibration.

### E. Mars Spin-Axis Direction Solutions

New values for the direction angles of the Martian spin axis were determined from the landmark data. The new values of the 1950 right ascension and declination relative to the Earth mean equator of 1950 are

$$\alpha = (317.3 \pm 0.15 \text{ deg}) - 0.101 T$$

$$\delta = (52.7 \pm 0.15 \text{ deg}) - 0.057 T$$

where the new angle rates have been derived using the Mariner 9 value of the Martian  $J_2$ .

1. Comparison with pre-Mariner 9 values. As stated in Section III, the adopted values of the pre-Mariner 9 Martian spin-axis direction were derived from an average of the Laplacian poles of Deimos and Phobos, determined by Burton (Ref. 13), and a spin-axis direction derived by Camichel (Ref. 14).

It is known that the dynamical oblateness effect of Mars on its satellite orbits causes a precession of the orbits about the maximum axis of inertia of the planet. It can be shown that, in the presence of significant solar perturbation of the orbit in addition to the dynamical oblateness effect, the precessional axis (Laplacian pole) is moved towards the celestial pole (defined by the normal to the ecliptic) along the great circle connecting the spin axis to the celestial pole (Ref. 11). It can further be shown that the magnitude of such a separation, denoted  $I$ , is calculable from

$$\tan 2I = \frac{(C_1/C_2) \sin 2\gamma}{1 + (C_1/C_2) \cos 2\gamma} \quad (39)$$

where  $C_1$  and  $C_2$  are constants associated with the solar perturbation and the dynamical oblateness effect, respectively, and  $\gamma$  is the inclination of the equator of Mars to its ecliptic. It can be shown that the ratio  $C_1/C_2$  is proportional to the fifth power of the semimajor axis of the satellite orbit. Thus, the solar perturbation effect is more pronounced on the orbit of Deimos than on the orbit of Phobos. In fact, the calculated separation between the Laplacian pole of Deimos' orbit and the planet spin axis is 0.89 deg, and 0.0093 deg for Phobos' orbit.

It appears that an offset was introduced in the pre-Mariner 9 spin-axis direction angle values by not accounting for the fact that the Laplacian pole of Deimos is separated from the Martian spin axis by 0.89 deg as a result of the significant solar perturbation on the orbit of Deimos.

Figure 47 shows the spin axis of Mars (in the  $\mathcal{L}_0$ -plane) referred to the respective Laplacian poles of Phobos and Deimos. The larger of the two circles in the diagram represents the retrograde path of the instantaneous angular momentum vector of Deimos' orbit, with an inclination of 1.8 deg to its Laplacian pole, completing one period approximately every 54.36 years. The smaller circle shows similar details for the orbit of Phobos, which has an inclination of 0.9 deg and a period of 2.26 years.

It may be observed that the spin axis corresponding to the Laplacian pole of Deimos, whose inclination is measurable to greater precision from Earth-based telescopic observations than the inner satellite (Phobos) inclination, correlates very well with the pole solutions obtained from Mariner 9 landmark data. One would hope to see the Laplacian pole of Phobos coincide with the spin-axis solutions. Compared to the Deimos location, however, the Laplacian pole of Phobos, as determined by Wilkins, appears offset by 0.43 deg in a direction normal to the great circle containing the celestial pole and the spin axis of the planet. If the reasoning thus far reflects the truth of the situation, one may expect to see a correction to the orbit of Phobos from Mariner 9 data. This confirmation has been obtained from detailed analysis of all Phobos picture data transmitted. The conclusion is implicit in the discussion presented in Ref. 25.

The work of Sinclair (Ref. 26) provides a similar confirmation since the orbits of Phobos and Deimos are referenced to a spin axis orientation which agrees closely with that determined from imaging data given earlier in this section.

**2. Determination of the spin-axis direction from other Mariner 9 data.** The direction angles of the Martian spin axis have been determined from several types of data from Mariner 9. Two values of the direction of the spin axis have been determined from analysis of the doppler data. Data from orbital revolutions 4 through 10 were reduced with the parameters for a sixth-degree harmonic model, and data from revolutions 5 through 42 were reduced with the harmonic model increased to the eighth degree. These fits were reported in Section V as harmonic coefficient fit numbers 3 and 21, respectively. Two optical solutions were generated from approach data. The first solution was obtained by viewing Deimos against the fixed star background during planetary approach and relating the estimated inclination of the orbit of Deimos relative to the Earth equator to the Deimos Laplacian pole and, hence, to the spin axis. The second spin-axis direction angle values were obtained by viewing surface features in the south polar cap region during planetary approach.

The various new solutions for the Mars spin-axis direction are shown in Fig. 48 as they lie on the Martian celestial sphere. All of the recently determined spin-axis values, with the exception of the approach landmark value, agree to within 0.05 deg in right ascension and 0.15 deg in declination. All of the new values differ by approximately 0.5 deg from pre-Mariner 9 (1964) values.

## IX. Determination of Normal Points for the Relativity Experiment

### A. Definition of Normal Points

The relativity experiment is based on Mariner 9 tracking data acquired by the DSN and processed by the Satellite OD Group. The data consist of doppler measurements proportional to the tracking station-spacecraft range rate, and round-trip time-delay measurements proportional to the station-spacecraft range. Ideally, the total combined data set of range and range rate measurements could be processed simultaneously to estimate the relativity parameters affecting both the radio signal and the motion of the spacecraft and planets. However, since Mars is gravitationally very rough, with second-order tesseral harmonics four to five times larger than expected before flight, it is difficult to construct a gravity model with a finite number of parameters which is accurate enough to integrate the probe motion over hundreds of revolutions. The computer expense of such regression analyses is also a limiting factor. Hence, a data compression scheme has been employed to alleviate the accuracy and cost difficulties of a direct estimation approach. The compression scheme consists of first using the doppler data to solve for the spacecraft orbit and to relate the spacecraft position to the center of mass of Mars, and then combining this result with the station-spacecraft range measurements to obtain measurements of the Earth-Mars distance. These Earth-Mars pseudorange measurements, called normal data points, contain virtually all of the information in the individual time-delay measurements and the local doppler data which is pertinent to a detailed knowledge of the Earth-Mars motion. The Earth-Mars angular information content of the doppler is weak because of uncertainties in the locations of the tracking stations on the Earth, and it has not been exploited.

### B. Computation of the Normal Points

The station-spacecraft coordinate range  $\rho$  (see Fig. 6) is related to the Earth-Mars coordinate vector  $\mathbf{R}$  by the exact expression

$$\rho = |\mathbf{R} + \mathbf{R}_{sc} - \mathbf{R}_s| \quad (40)$$

where the vector  $\mathbf{R}_{sc}$  is the planet-centered coordinate vector of the spacecraft, which is determined from doppler tracking. The quantity  $\mathbf{R}_s$  is the accurately known, Earth-centered coordinate vector of the station. Equation (40) can be written in the following approximate form, accurate to 0.1 m, for the Mariner 9 geometry:

$$\rho = R - z' - h = \frac{1}{2R} \{ (r \sin \Omega - h_s)^2 + (r \cos \Omega - h_e)^2 \} \quad (41)$$

where  $z'$ ,  $r$ , and  $\Omega$  are defined as in Section II and designated here as cylindrical coordinates of the position of the spacecraft relative to Mars at the time of range observation. Components of the station in the Earth-centered cartesian coordinate system defined in Fig. 6 are  $h_e$ ,  $h_s$ , and  $h$ . Equation (41) can be solved directly for the Earth-Mars distance  $R$  from a measured value of the station-spacecraft coordinate time delay, using the expression

$$c \Delta t = \rho + (1 - \gamma) m \ln \frac{r_s + r_p + \rho}{r_s - r_p - \rho} \quad (42)$$

$$\rho = \frac{r_s^2 - r_p^2}{c} \quad (43)$$

where  $r_s$  and  $r_p$  are coordinate distances representing the Sun-observer distance and the Sun-spacecraft distance, respectively, to convert to range  $\rho$ .

In practice, an initial value of  $R$  is chosen from the currently employed planetary ephemeris, and the difference between the observed and predicted values of  $\rho$  is then related to a differential correction in  $R$ . The correction is then added to the initial value, yielding a pseudo-measured value of  $R$  at the time of the spacecraft ranging. Equation (42) is then used again to convert  $R$  into a relativistically consistent pseudo-observable in terms of coordinate time  $c \Delta t$ . It should be noted that  $\gamma$  is set nominally to unity in this computation, but that the charged particle delays are included in the value of  $c \Delta t$ .

### C. Normal Point Accuracy

The error in the determined value of  $R$  can be related to the error in the range measurement  $\Delta \rho$ , the error in the station locations  $(\Delta h_e, \Delta h_s, \Delta h)$ , and the error in the doppler-determined spacecraft position relative to Mars  $(\Delta z', \Delta r, r \Delta \Omega)$  by the following approximate expression, which is accurate to 0.1 m:

$$\Delta R = \Delta \rho + \Delta h_e - \Delta z' - \frac{1}{R_s} \{ (r - h_e \cos \Omega - h_s \sin \Omega) \Delta r + (h_s \sin \Omega - h_e \cos \Omega) r \Delta \Omega \} \quad (44)$$

Since the distance of the station from the Earth's spin axis and the station longitude are known to within an uncertainty of 10 m from analysis of data acquired during

planetary encounters on past Mariner missions, the error in the distance of the station from the Earth's equator is the only term which contributes more than 10 m to  $\Delta h$ . Hence,  $\Delta h$  can be expressed as  $\Delta h \sin \delta$  plus terms which contribute less than 10-m errors.

The remaining errors in Eq. (44) are due to the uncertainty in the doppler-determined spacecraft position relative to Mars. The coefficients of the errors of the spacecraft position in the Earth's plane of sky,  $\Delta r$  and  $r \Delta \Omega$ , are of the order of 10%. Thus, Eq. (44) can be reduced to the form

$$\Delta R = \Delta \rho + \Delta h \sin \delta - \Delta z' + (10^{-1}) \Delta r + (10^{-1}) r \Delta \Omega + (< 10\text{-m terms}) \quad (45)$$

The pre-flight predicted accuracies of  $z'$ ,  $r$ , and  $\Omega$  are given in Section II, and the consistency of solutions for these coordinates is shown in Section IV. The effect of errors in  $z'$ ,  $r$ , and  $\Omega$  on the errors of the computed normal points is discussed in Ref. 26. A summary of this information is given in Tables 20 and 21. The 1- $\sigma$  uncertainties of the components of position,  $r$ ,  $r \Delta \Omega$ , and  $z'$ , along with their respective contributions to the error in the normal data point  $R$ , are listed.

Pre-flight values, actual pre-gravity-sensing results from revolutions 1 through 4, and post-gravity-sensing results from both the three-station and single-station tracking configurations are shown in the tables, along with the maximum uncertainties caused by the stochastic solar corona near superior conjunction. Contributions from  $r \Delta \Omega$  and  $\Delta r$  are seen to be negligible throughout the mission, leaving the contributions from  $\Delta z'$  the only spacecraft position error of importance. Equation (45) can then be further reduced in the form

$$\Delta R = \Delta \rho + \Delta h \sin \delta - \Delta z' + (< 10\text{-m terms}) \quad (46)$$

where neither the contributions from the measurement error  $\Delta \rho$  nor from the spacecraft position error  $\Delta z'$  are highly correlated in time. The station location error  $\Delta h$  is a constant.

### D. Normal Point Residuals

The local orbit of Mariner 9 and the values of  $r$ ,  $\Omega$ , and  $z'$  have been estimated from the doppler data for virtually every revolution in which range measurements have been acquired. These orbit estimates have been used to predict values of  $\rho$ . Observed residuals in the observed  $\rho$  have

been related to values of  $R$  and, hence,  $c\Delta t$  at the times of the range measurements.

Residuals of the normal points over the 11 months of the mission are given in Fig. 49, where the elements of the orbits of both the Earth and Mars have been fit with the normal points obtained prior to July 31 to yield planetary ephemeris DE-82 (Section III). The dashed line indicates the apparent drift in the DE-82 extrapolated ephemeris. The sampled rms of the normal points is 0.1 s in the three-station configuration region and 0.2 s in the one-station region before July 31.

The effects of the charged particles due to the solar corona were observed in the 8 weeks bracketing superior conjunction. The apparent two-way time delay increased to a value near  $20 \mu\text{s}$ . In addition, daily variations of several microseconds can be observed which appear to be almost as large as the steady-state delay itself. The insert in the figure illustrates, on a larger scale, the normal point residuals before and after DRVID corrections for the time period from August 23 to August 25 (Section III). Drifts in the residuals of almost 2 s are seen on August 24 and 26 if DRVID corrections are not applied, but the total residual spread of a single pass is limited to  $0.5 \mu\text{s}$  by the application of DRVID corrections.

## References

1. Haynes, N. R., O'Neil, W. J., and Bollman, W. E., "The Mariner Mars 1971 Mission Design," presented at the AAS AIAA Astrodynamics Conference, Santa Barbara, Calif., Aug. 19-20, 1970.
2. Boggs, D. H., "A Partial-Step Algorithm for Enlarging the Convergence Region of the Nonlinear Estimation Problem," AIAA Paper No. 71-121, presented at the 9th AIAA Aerospace Sciences Meeting, New York, Jan. 25-27, 1971.
3. Null, G. W., "A Solution for the Mass and Dynamical Oblateness of Mars Using Mariner IV Doppler Data," *Bull. Amer. Astron. Soc.*, Vol. I, No. 4, 1969.
4. Hildebrand, C., *A Discussion of Two General Perturbation Methods and of Their Application to Artificial Satellite Theory*, Technical Report 1004 of the Applied Mechanics Research Laboratory, University of Texas at Austin, June 1969.
5. Kaula, W. M., "Plans for Analysis of Lunar Satellite Orbits," *Proceedings of Symposium on the Trajectories of Artificial Celestial Bodies*, Springer-Verlag, Berlin, New York, 1966.
6. Reynolds, G. W., Russell, R. K., and Jordan, J. F., "Earth Based Orbit Determination for a Mars Orbiting Spacecraft," AIAA 9th Aerospace Sciences Meeting, New York, Jan. 25-27, 1971.
7. Zielenbach, J. W., and Jordan, J. F., "Orbit Determination Strategy and Results for the Mariner Mars 1971 Mission," AAS Paper No. 71-391, presented at the AAS/AISS Astrodynamics Specialists Conference 1971, Fort Lauderdale, Fla., Aug. 17-19, 1971.
8. Muhleman, D. O., Anderson, J. D., Esposito, P. B., and Martin, W. L., "Radio Propagation Measurements of the Solar Corona and Gravitational Field: Applications to Mariner 6 and 7," *Proceedings of the Conference on Experimental Tests of Gravitation Theories*, R. Davies, ed., Technical Memorandum 33-499, Jet Propulsion Laboratory, Pasadena, Calif., Nov. 1, 1971.
9. MacDoran, P. F., and Martin, W. L., "DRVID Charged-Particle Measurements with a Binary Coded Sequential Acquisition Ranging System," in *Flight Projects. Space Programs Summary 37-57*, Vol. II, Jet Propulsion Laboratory, Pasadena, Calif., May 31, 1969, pp. 72-81.
10. Melbourne, W. G., et al., *Constants and Related Information for Astrodynamical Calculations, 1968*, Technical Report 32-130b, Jet Propulsion Laboratory, Pasadena, Calif., July 15, 1968.
11. Wilkins, G. A., "Orbits of the Satellites of Mars," H. M. Nautical Almanac Office, Tech. Note 1, August 1965.
12. de Vaucouleurs, G. H., "The Physical Ephemeris of Mars," *Icarus*, Vol. 3, No. 3, Sept. 1964, pp. 236-247.
13. Hall, A., and Burton, H. E., "Corrections to the Elements of the Satellites of Mars," *Astron. J.*, Vol. 39, No. 18, 1929, pp. 151-163.
14. Camichel, H., "Détermination Photographique du Pole de Mars, de son Diamètre et des Coordonnées Areographiques," *Bull. Astron.*, Sec. 2, Vol. 18, 1954, Fasc. 2, pp. 183-174; Fasc. 3, pp. 175-191.

## References (contd)

15. O'Handley, D. A., et al., JPL *Development Ephemeris Number 69*, Technical Report 32-1465, Jet Propulsion Laboratory, Pasadena, Calif., Dec. 15, 1969.
16. Lorell, J., et al., "Gravity Field of Mars from Mariner 9 Tracking Data," *Icarus*, Vol. 18, 1973.
17. Mottinger, N. A., and Zielenbach, J. W., *Station Locations Provided for Mariner 9*, Technical Memorandum 391-324, Jet Propulsion Laboratory, Pasadena, Calif., May 15, 1972 (JPL internal document).
18. Kaula, W. M., *Theory of Satellite Geodesy*, Blaisdell Publishing Company, Waltham, Mass., 1966.
19. Born, G. H., and Tapley, B. D., "An Approximate Solution for the Short Term Motion of a Lunar Satellite," *J. Spacecraft and Rockets*, Vol. 6, No. 5, May 1969.
20. Kozai, Y., *Effects of Solar Radiation Pressure on the Motion of an Artificial Satellite*, Smithsonian Institution, Special Report No. 56, Jan. 1961.
21. Pettengill, G. H., Shapiro, I. I., and Rogers, A. E. E., "Topography and Radar Scattering Properties of Mars," *Icarus*, Vol. 18, No. 1, Jan. 1973, pp. 22-28.
22. Hord, C. W., Barth, C. A., Stewart, A. I., and Lane, A. L., "Mariner 9 Ultraviolet Spectrometer Experiment: Photometry and Topography of Mars," *Icarus*, Vol. 17, No. 2, Oct. 1972, pp. 443-456.
23. Kliore, A. J., Cain, D. L., Fjeldbo, G., Seidel, B. L., Sykes, M. G., and Rasool, S. I., "The Atmosphere of Mars from Mariner 9 Radio Occultation Measurements," *Icarus*, Vol. 17, No. 2, Oct. 1972, pp. 484-516.
24. Kieffer, H. H., Chase, S. C., Miner, E., Münch, G., and Neugebauer, G., "Preliminary Report on Infrared Radiometric Measurements from the Mariner 9 Spacecraft," *J. Geophys. Res.*, July 1973.
25. Born, G. H., "Mars Physical Parameters as Determined From Mariner 9 Observations of the Natural Satellites," paper presented at AAS/AIAA Astrodynamics Conference, Vail, Colo., July 16-18, 1973.
26. Sinclair, A. T., "The Motions of the Satellites of Mars," *Monthly Notices of the Royal Astronomical Society*, Vol. 155, 1972, pp. 249-274.
27. Jordan, J. F., Melbourne, W. G., and Anderson, J. D., "Testing Relativistic Gravity Theories Using Radio Tracking Data from Planetary Orbiting Spacecraft," Paper No. a13, presented at XV Plenary Meeting of COSPAR, May 10-24, 1972, Madrid, Spain.

**Table 1. Approximate areocentric orbital elements of Mariner 9**

Orbital elements	Initial parameters, Nov. 14 to 16	Post-trim 1, Nov. 16 to Dec. 31	Post-trim 2, Dec. 31
Semimajor axis $a$ , km	13055.	12631.	12647.
Eccentricity $e$	0.63	0.62	0.60
Mean orbital period $P$ , h	12 62	11.97	11 99
Longitude of ascending node <sup>a</sup> $\Omega$ , deg	42.3	42.1	34.2
Argument of periaapsis $\omega$ , deg	-24.9	24.3	26.0
Inclination $i$ , deg	64.6	64.8	64.4
Height above surface at periaapsis <sup>b</sup> $h_p$ , km	1396	1387.	1641.
Latitude of sub-periaapsis passage $\phi_p$ , deg	22.3	21.9	23.3

<sup>a</sup>Keplerian elements referenced to Mars true equator of date.  
<sup>b</sup>Mean radius of Mars used in computing  $h_p = 3394$  km.

**Table 2. Satellite OD Group staffing levels**

Task descriptions	Staffing level, men
Satellite OD Group coordination activities	1
Direction and coordination of Group activities, assessment of solution accuracies, certification of probe ephemeris tapes, interface with Navigation Team Chief and science users.	
Data handling	1
Reformatting of doppler and ranging data for navigation team use, editing and compressing of data, storage of data on FASTRAN files.	
Orbit estimation	5
Data fitting for both smooth and predicted trajectories, trajectory generation, gravity and Mars spin-axis direction sensing and assessment, generation and maintenance of FASTRAN files of astrodynamical constants, gravity models, nongravitational forces, Tracking System analytic calibration (TSAC) data, etc.	
Normal point generation	1

**Table 3. Error source standard deviations for encounter OD results**

Error source	Standard deviation
Range-rate data noise	3 mm/s
Mass constant of Mars	0.1 km <sup>3</sup> /s <sup>2</sup>
Mars ephemeris errors (Brower, set III)	10 <sup>-7</sup>
Nongravitational acceleration (constant)	10 <sup>-12</sup> km/s <sup>2</sup> per axis
Tracking station longitude	5 m
Tracking station radius	3 m

**Table 4. Standard deviations for Mars harmonics based on dimensional analysis**

Zonal harmonic	1- $\sigma$ uncertainty	Tesseral harmonic	1- $\sigma$ uncertainty
$C_{20}$	$0.22 \times 10^{-4}$	$C_{21}, S_{21}$	$0.233 \times 10^{-4}$
		$C_{22}, S_{22}$	$0.111 \times 10^{-4}$
$C_{30}$	$0.202 \times 10^{-4}$	$C_{31}, S_{31}$	$0.828 \times 10^{-5}$
		$C_{32}, S_{32}$	$0.250 \times 10^{-5}$
		$C_{33}, S_{33}$	$0.107 \times 10^{-5}$
$C_{40}$	$0.130 \times 10^{-4}$	$C_{41}, S_{41}$	$0.410 \times 10^{-5}$
		$C_{42}, S_{42}$	$0.960 \times 10^{-6}$
		$C_{43}, S_{43}$	$0.258 \times 10^{-6}$
		$C_{44}, S_{44}$	$0.910 \times 10^{-7}$

**Table 5. Comparison of unmodeled acceleration magnitudes at periaapsis**

Type of acceleration and total magnitude, km/s <sup>2</sup>	Maximum expected unmodeled acceleration (periaapsis) due to each source, km/s <sup>2</sup>
Mars gravity	
Central mass force <sup>c</sup> ( $2 \times 10^{-3}$ )	$5 \times 10^{-9}$
Noncentral gravity forces ( $2 \times 10^{-5}$ )	$2 \times 10^{-7}$
Environmental	
Solar radiation	$3 \times 10^{-12}$
Drag	$2 \times 10^{-10}$
Spacecraft	
Propulsion	$5 \times 10^{-12}$
Attitude control	$1 \times 10^{-12}$

**Table 6. Local position and extrapolated period error caused by low-order gravity coefficient errors**

Estimation list, data arc	State, one revolution	State, second-degree harmonics, two revolutions	State, second-degree and third-degree harmonics, two revolutions
1- $\sigma$ total position error at periapsis, km	6.0	6.0	3.0
Perturbations caused by			
Second-degree gravity coefficients, km	5.0		
Third-degree gravity coefficients, km	3.3	5.4	
Fourth-degree gravity coefficients, km	1.2	0.6	3.0
1- $\sigma$ period error in first mapped revolution, s	1.1	0.11	0.04
Perturbations caused by			
Second-degree gravity coefficients, s	0.94		
Third-degree gravity coefficients, s	0.12	0.08	
Fourth-degree gravity coefficients, s	0.05	0.03	0.04

**Table 7. Pre-flight required and predicted OD accuracy summary (pre-gravity sensing/post-sensing)**

	MM'71 requirement	Pre-flight results
Local position uncertainty, km	10	10/5
Mapped time of periapsis uncertainty, s (revolutions)	2 (14)	106 (14)/2 (14)
Mapped position uncertainty, km (revolutions)	10 (14)	400 (14)/7 (14)

**Table 8. Approximate station location values for MM'71 satellite mission**

Parameters	Station location values
Spin-axis radius, km	
DSS 12	5212.05
DSS 14	5203.99
DSS 41	5450.20
DSS 62	4860.82
Longitude deg	
DSS 12	243.1945
DSS 14	243.1105
DSS 41	136.8875
DSS 62	355.6322
Distance from equator, km	
DSS 12	3665.63
DSS 14	3677.05
DSS 41	-3302.24
DSS 62	4116.91

**Table 9. Values of the AU and GM used with Earth-Mariner planetary ephemeris**

Ephemeris	AU, km	GM, km <sup>3</sup> /s <sup>2</sup>
DE-79	149597894.00	132712502083.05
DE-80	149597894.38	132712503061.83
DE-82	149597891.01	132712494095.18

Table 10. SATODP first orbit convergence history

Data arc, h	Data points	DSS	Interval, d, h, m, s	State, km	Computed $\sigma$ , km	Consider $\sigma$ , km
2	156	14	14, 1, 48, 32 → 14, 2, 24, 32	839.0	39.7	39.7
		12	14, 2, 39, 32 → 14, 4, 29, 32	-2410.0	125.6	125.7
				-4055.2	66.7	66.8
4	238	14	14, 1, 48, 32 → 14, 2, 24, 32	831.4	23.4	23.5
		12	14, 2, 39, 32 → 14, 5, 58, 32	-2434.7	78.4	78.9
				-4042.2	40.3	40.7
8	447	14	14, 1, 48, 32 → 14, 2, 24, 32	823.7	1.11	2.36
		12	14, 2, 39, 32 → 14, 6, 55, 32	-2459.3	3.08	7.13
		41	14, 7, 25, 32 → 14, 9, 58, 32	-4028.8	1.99	6.35
10.5	564	14	14, 1, 48, 32 → 14, 2, 24, 32	827.7	0.58	1.84
		12	14, 2, 39, 32 → 14, 6, 55, 32	-2445.5	1.89	6.4
		41	14, 7, 25, 32 → 14, 12, 15, 32	-4036.2	1.01	3.3

Table 11. Mariner 9 harmonic solutions

Model number	Orbital fits	Description of harmonics, resonance order	Date available
1	$P_0-P_4$	4th	11/16/71
2	$P_0-P_4$	6th	11/17/71
3 <sup>a</sup>	$P_4-P_{10}$	6th	11/24/71
4	$P_{15}-P_{19}$	6th	11/24/71
5	$P_{19}-P_{23}$	6th	11/29/71
6	$P_{27}-P_{31}$	6th	11/30/71
7	$P_{31}-P_{37}$	6th	12/06/71
8	$P_{37}-P_{43}$	6th	12/10/71
9	$P_{52}-P_{56}$	6th	12/28/71
10	$P_{43}-P_{51}$	6th	1/19/72
11	$P_{44}-P_{54}$	6th	1/20/72
12	$P_{52}-P_{64}$	6th	1/23/72
13	$P_{108}-P_{112}$	6th	1/26/72
14	$P_{64}-P_{70}$	6th	2/01/72
15	$P_{72}-P_{78}$	6th	2/04/72
16	$P_{114}-P_{120}$	6th	2/05/72
17	$P_{122}-P_{128}$	6th	2/09/72
18	$P_{80}-P_{86}$	6th	2/11/72
19	$P_{88}-P_{94}$	6th	2/16/72
20	$P_{130}-P_{136}$	6th	2/16/72
21 <sup>a, b</sup>	$P_4-P_{42}$	8th	12/19/71
22	$P_{32}-P_{82}$	10th	3/14/72
23 <sup>b</sup>	$P_{32}-P_{80}$	10th	3/28/72

<sup>a</sup>Solution list includes Mars spin-axis direction angles.

<sup>b</sup>Determined over one resonance cycle.

Degree	Order				
	0	1	2	3	4
2	$0.19637604 \times 10^{-2}$	$0.82880823 \times 10^{-6}$ $0.38389742 \times 10^{-6}$	$0.54865648 \times 10^{-4}$ $0.31342373 \times 10^{-4}$		
3	$0.16702033 \times 10^{-4}$	$0.26350573 \times 10^{-5}$ $0.28141315 \times 10^{-4}$	$-0.54675236 \times 10^{-5}$ $0.26696797 \times 10^{-5}$	$0.48830455 \times 10^{-5}$ $0.37141632 \times 10^{-5}$	
4	$0.53410858 \times 10^{-4}$	$0.35286608 \times 10^{-5}$ $0.64779491 \times 10^{-5}$	$0.11379641 \times 10^{-5}$ $0.15689429 \times 10^{-5}$	$0.51197116 \times 10^{-6}$ $0.81116264 \times 10^{-7}$	$-0.14152993 \times 10^{-7}$ $-0.27684856 \times 10^{-6}$
5	$0.23164585 \times 10^{-4}$	$0.89319295 \times 10^{-6}$ $0.63512161 \times 10^{-5}$	$-0.24889816 \times 10^{-5}$ $0.59425099 \times 10^{-6}$	$0.22608158 \times 10^{-6}$ $0.63012291 \times 10^{-7}$	$-0.56199295 \times 10^{-7}$ $-0.20601205 \times 10^{-7}$
6	$0.11245375 \times 10^{-4}$	$0.57621663 \times 10^{-5}$ $0.41707502 \times 10^{-5}$	$0.58842912 \times 10^{-6}$ $0.14282701 \times 10^{-5}$	$0.14304231 \times 10^{-6}$ $-0.14674199 \times 10^{-6}$	$0.53615922 \times 10^{-8}$ $0.24952049 \times 10^{-7}$
7	$0.19117505 \times 10^{-5}$	$0.68380163 \times 10^{-5}$ $-0.43256804 \times 10^{-5}$	$0.22617700 \times 10^{-5}$ $0.25320829 \times 10^{-5}$	$0.25555787 \times 10^{-7}$ $0.25738444 \times 10^{-6}$	$0.32678534 \times 10^{-7}$ $0.14322185 \times 10^{-7}$
8	$0.22460446 \times 10^{-4}$	$0.75394716 \times 10^{-5}$ $0.30335715 \times 10^{-5}$	$0.24985728 \times 10^{-5}$ $0.33521262 \times 10^{-5}$	$0.17253395 \times 10^{-6}$ $0.97131307 \times 10^{-7}$	$0.26615292 \times 10^{-7}$ $0.47830983 \times 10^{-7}$
9	$-0.45438015 \times 10^{-4}$	$0.74077120 \times 10^{-5}$ $0.99596139 \times 10^{-5}$	$0.60035209 \times 10^{-7}$ $0.18427201 \times 10^{-5}$	$0.19482533 \times 10^{-6}$ $0.59156130 \times 10^{-8}$	$0.11462030 \times 10^{-8}$ $0.21146237 \times 10^{-7}$
10	$0.12146101 \times 10^{-4}$	$0.10605017 \times 10^{-4}$ $-0.75161187 \times 10^{-5}$	$-0.39758291 \times 10^{-6}$ $0.73665544 \times 10^{-6}$	$-0.32582780 \times 10^{-7}$ $-0.37591059 \times 10^{-7}$	$-0.71218216 \times 10^{-8}$ $0.55791204 \times 10^{-10}$

Table 12. Coefficients for the tenth-degree harmonic gravity model (C/S)

Order					
5	6	7	8	9	10
-0.71092642 × 10 <sup>-8</sup>					
0.47087929 × 10 <sup>-8</sup>					
0.12473048 × 10 <sup>-8</sup>	0.86275381 × 10 <sup>-9</sup>				
-0.30622927 × 10 <sup>-8</sup>	-0.34340824 × 10 <sup>-9</sup>				
-0.13389670 × 10 <sup>-8</sup>	-0.30652077 × 10 <sup>-9</sup>	-0.41013469 × 10 <sup>-10</sup>			
-0.42902814 × 10 <sup>-8</sup>	-0.43898135 × 10 <sup>-9</sup>	0.39439971 × 10 <sup>-10</sup>			
-0.38899155 × 10 <sup>-8</sup>	-0.28403351 × 10 <sup>-9</sup>	0.43473828 × 10 <sup>-11</sup>	0.12291580 × 10 <sup>-11</sup>		
-0.14389265 × 10 <sup>-8</sup>	-0.18637042 × 10 <sup>-9</sup>	0.43212145 × 10 <sup>-10</sup>	0.54698644 × 10 <sup>-11</sup>		
0.27636240 × 10 <sup>-8</sup>	-0.13687388 × 10 <sup>-9</sup>	-0.10366049 × 10 <sup>-11</sup>	0.37252880 × 10 <sup>-11</sup>	0.12034184 × 10 <sup>-12</sup>	
0.48277638 × 10 <sup>-9</sup>	-0.20504467 × 10 <sup>-9</sup>	0.19875240 × 10 <sup>-10</sup>	0.11827967 × 10 <sup>-11</sup>	-0.43508199 × 10 <sup>-12</sup>	
-0.94128357 × 10 <sup>-9</sup>	-0.80089751 × 10 <sup>-10</sup>	0.33561106 × 10 <sup>-11</sup>	0.11016686 × 10 <sup>-11</sup>	-0.95379180 × 10 <sup>-13</sup>	0.16796570 × 10 <sup>-14</sup>
0.31033661 × 10 <sup>-9</sup>	-0.11098738 × 10 <sup>-9</sup>	0.55400811 × 10 <sup>-11</sup>	-0.23991272 × 10 <sup>-12</sup>	-0.13343572 × 10 <sup>-12</sup>	0.62183627 × 10 <sup>-14</sup>

Table 13. Short-arc solution summary

Orbits fit	Harmonic model number	$r_p \Delta \Omega$ from mean, km	$\Delta \Omega$ from mean, deg	Number of revolutions for which $\Delta T_p$ was within 2 s	Orbits fit	Harmonic model number	$r_p \Delta \Omega$ from mean, km	$\Delta \Omega$ from mean, deg	Number of revolutions for which $\Delta T_p$ was within 2 s
$P_6 - P_7$	2	0.86	-0.013	12	$P_{101} - P_{102}$		0.01	0.014	13
$P_7 - P_8$	2	1.38	0.018	10	$P_{103} - P_{104}$		7.53	0.142	9
$P_{10} - P_{11}$	2	-1.29	0.060	6	$P_{105} - P_{106}$		11.47	0.207	12
$P_{13} - P_{14}$	2	3.50	0.045	3	$P_{107} - P_{108}$		1.12	0.015	33
$P_{15} - P_{16}$	3	3.26	0.042	4	$P_{111} - P_{112}$		4.95	0.096	24
$P_{18} - P_{19}$	5	4.45	0.057	7	$P_{113} - P_{114}$		1.87	0.038	38 + <sup>b</sup>
$P_{19} - P_{20}$	3	1.35	0.018	6	$P_{115} - P_{116}$		3.38	0.067	40 + <sup>b</sup>
$P_{20} - P_{21}$	3	3.19	0.039	2	$P_{117} - P_{118}$		6.76	0.136	24
$P_{23} - P_{24}$	5	-7.02	-0.086	6	$P_{119} - P_{120}$	21	8.56	0.175	10
$P_{24} - P_{25}$	6	1.15	0.014	9	$A_{122} - A_{123}$	22	3.46	0.053	23
$P_{27} - P_{28}$	5	2.25	0.027	8	$P_{122} - A_{122}$		-3.09	-0.128	15
$P_{28} - P_{29}$	3	-0.42	-0.005	10	$A_{125} - A_{126}$		-0.26	0.046	21
$P_{29} - P_{30}$	1	-1.52	0.083	5 + <sup>a</sup>	$A_{111} - A_{112}$		3.40	0.054	11
$P_{30} - P_{31}$	5	-2.42	0.029	7	$A_{113} - A_{114}$		12.19	0.281	11
$P_{100} - P_{101}$	5	-1.93	-0.013	5	$A_{105} - A_{106}$		-3.21	0.081	31
$P_{106} - P_{107}$	7	1.50	0.023	13	$A_{127} - A_{128}$		2.02	0.036	15
$P_{114} - P_{115}$	21	-7.28	-0.079	25	$A_{108} - A_{109}$		-24.36	-0.558	9
$P_{120} - P_{121}$	21	7.71	0.094	37 + <sup>b</sup>	$A_{105} - A_{106}$		0.744	-0.055	21
$P_{127} - P_{128}$	9	4.48	0.057	9	$A_{111} - A_{112}$		22.88	0.345	8
$P_{132} - P_{133}$	5	5.72	0.072	8	$A_{120} - A_{121}$		6.44	0.078	13
$P_{132} - P_{133}$	6	-6.23	-0.070	8	$A_{128} - A_{129}$		0.49	-0.016	21
$P_{143} - P_{144}$	21	-5.21	-0.059	32 + <sup>b</sup>	$A_{114} - A_{115}$		-4.03	-0.084	32
$P_{146} - P_{147}$		-3.56	-0.039	13	$A_{112} - A_{113}$		7.94	0.089	17
$P_{162} - P_{163}$		-6.89	-0.080	30	$A_{145} - A_{146}$		0.87	-0.009	21
$P_{170} - P_{171}$		-16.82	-0.205	12	$A_{150} - A_{151}$		1.05	-0.008	42
$P_{171} - P_{172}$		-3.53	-0.036	26	$A_{170} - A_{171}$		6.97	0.070	28
$P_{177} - P_{178}$		2.67	0.045	30 + <sup>b</sup>	$A_{184} - A_{185}$		1.39	-0.035	32
$P_{184} - P_{185}$		3.29	0.014	23	$A_{194} - A_{195}$		-6.27	-0.093	46 +
$P_{187} - P_{188}$		-1.63	-0.013	14	$A_{202} - A_{203}$		-7.44	-0.108	19
$P_{191} - P_{192}$		6.90	0.105	14	$A_{220} - A_{221}$		-5.80	-0.088	42 +
$P_{197} - P_{198}$		3.19	0.053	44 + <sup>b</sup>	$A_{242} - A_{243}$		-4.18	-0.069	36 +
$P_{201} - P_{202}$		-3.33	-0.041	32 + <sup>b</sup>	$A_{250} - A_{251}$		0.49	-0.017	44 +
$P_{205} - P_{206}$		-9.49	-0.131	38 +	$A_{268} - A_{269}$		-12.03	-0.159	8
$P_{211} - P_{212}$		-12.99	-0.184	5	$A_{250} - A_{251}$		0.84	-0.005	58
$P_{215} - P_{216}$		2.19	0.050	21	$A_{628} - A_{633}$		4.01	0.037	45 +
$P_{219} - P_{221}$		1.64	0.042	35 + <sup>b</sup>	$A_{646} - A_{651}$	22	6.37	0.073	40 +

<sup>a</sup>Predicted trajectory information beyond this point was not available because of the second trim maneuver performed at  $P_{64}$ .

<sup>b</sup>Predicted trajectory information based on this fit was not available beyond this point.

<sup>c</sup>As defined in Table 11.

Table 14. Long-arc solution summary

Orbits fit	Description of fit	$r_p \Delta \Omega$ from mean, km	$\Delta \Omega$ from mean at periaapsis, deg	$\Delta T_p < 0.1$ s to
$P_{10}-P_1$	State + 4th-order resonance	-	-	$P_1$
$P_{11}-P_{110}$	State + 6th-order resonance	6.67	0.053	$P_{110}$
$P_{111}-P_{111}$	State + 4th-order resonance	3.30	0.047	$P_{111}$
$P_{112}-P_{119}$	State + 6th-order resonance	-0.90	0.005	$P_{119}$
$P_{116}-P_{121}$		-1.91	0.019	$P_{121}$
$P_{117}-P_{121}$		1.09	0.020	$P_{121}$
$P_{118}-P_{121}$		2.82	0.013	$P_{121}$
$P_{119}-P_{121}$		-2.55	-0.043	$P_{121}$
$P_{121}-P_{121}$		1.86	0.013	$P_{121}$
$F_{121}-P_{121}$		2.08	0.036	$P_{121}$
$P_{122}-P_{121}$		0.15	-0.008	$P_{121}$
$P_{123}-P_{122}$		4.54	0.045	$P_{122}$
$P_{124}-P_{125}$		-1.43	-0.027	$P_{125}$
$P_{126}-P_{126}$		-2.97	-0.046	$P_{126}$
$P_{127}-P_{127}$	State + 6th-order resonance	-2.99	-0.046	$P_{127}$
$P_{128}-P_{128}$	State/harmonic model 3	3.03	0.036	$P_{128}$
$P_{129}-P_{100}$	State + 6th-order resonance	2.58	0.031	$P_{100}$
$P_{102}-P_{100}$		2.59	0.031	$P_{100}$
$P_{105}-P_{112}$		-1.68	-0.017	$P_{112}$
$P_{111}-P_{129}$		-3.77	-0.041	$P_{129}$
$P_{122}-P_{128}$		-1.32	-0.013	$P_{122}$
$P_{130}-P_{130}$	State + 6th-order resonance	-1.61	-0.016	$P_{130}$
$P_{135}-P_{134}$	State/harmonic model 7	1.42	0.019	$P_{132}$
$P_{136}-P_{136}$	State/harmonic model 8	3.27	0.042	$P_{138}$
$P_{136}-P_{162}$	State + 6th-order resonance	0.09	0.003	$P_{167}$
$P_{165}-P_{171}$	State/harmonic model 12	-0.51	-0.005	$P_{175}$
$P_{171}-P_{179}$	State/harmonic model 22	0.06	0.003	$P_{185}$
$P_{181}-P_{189}$	State/harmonic model 22	0.02	0.002	$P_{191}$
$P_{191}-P_{192}$	State/harmonic model 22	0.54	0.009	$P_{198}$
$P_{195}-P_{197}$	State/harmonic model 23	0.78	0.012	$P_{211}$
$P_{209}-P_{211}$	State/harmonic model 23	0.43	0.007	$P_{221}$
$P_{219}-P_{221}$	State/harmonic model 23	0.06	0.002	$P_{224}$
$P_{231}-P_{231}$	State/harmonic model 23	-0.79	-0.013	$P_{242}$
$P_{238}-P_{249}$	State/harmonic model 23	-0.64	-0.010	$P_{254}$
$P_{252}-P_{254}$	State/harmonic model 23	-1.31	-0.023	$P_{256}$
$P_{257}-P_{259}$	State/harmonic model 23	-1.60	-0.029	$P_{274}$
$P_{272}-P_{277}$	State/harmonic model 23	-1.65	-0.030	$P_{282}$

Table 15. Characteristics of periodic variations

Term	Type	Period
$(l - 2p + q) \dot{M}$	Short-period	12 h or less
$m(\dot{\Omega} - \dot{\theta})$	Medium-period	24 h or less
$(l - 2p) \dot{\omega}$	Long-period	Years
$m = 0$	} Secular (Constant rate)	
$(l - 2p) = 0$		
$(l - 2p + q) = 0$		

Table 16. Secular rates, rad/s

Apoapses (5-94)	Apoapses (95-502)
$\dot{\omega} = -0.405 \times 10^{-6}$	$\dot{\omega} = -0.235 \times 10^{-6}$
$\dot{\Omega} = -0.349 \times 10^{-7}$	$\dot{\Omega} = -0.386 \times 10^{-7}$

**Table 17. One-sigma measurement uncertainties for observed landmarks**

Landmark identification	Narrow-angle camera		Wide-angle camera	
	Pixel	Line	Pixel	Line
6	20.0	20.0	3.0	3.0
66	— <sup>a</sup>	— <sup>a</sup>	3.0	3.0
661	— <sup>a</sup>	— <sup>a</sup>	3.0	3.0
49	— <sup>a</sup>	— <sup>a</sup>	3.0	3.0
9	10.0	10.0	3.0	3.0
2	10.0	10.0	5.0	5.0
201	5.0	5.0	3.0	3.0
202	3.0	3.0	— <sup>a</sup>	— <sup>a</sup>
3	5.0	5.0	3.0	3.0
51	4.0	4.0	3.0	3.0
53	4.0	4.0	3.0	3.0
54	4.0	4.0	3.0	3.0

<sup>a</sup>Observations of the indicated type were not made.

**Table 18. Variation of  $\Omega$  relative to a mean continuous node evolution**

Probe segment	<i>A priori</i>		<i>A posteriori</i>	
	$\Delta\Omega_0$ , deg	$\Delta\Omega_0$ average, deg	$\Delta\Omega$ , deg	$\Delta\Omega$ average, deg
Post-trim 1				
1	0.05	+0.026	+0.035	+0.025
2	0.03	+0.006	+0.035	+0.025
3	0.00	-0.024	-0.005	-0.015
4	0.05	+0.026	+0.015	+0.005
5	0.04	+0.016	-0.010	-0.020
6	0.00	-0.024	0.005	-0.015
7	0.00	-0.024	+0.000	-0.010
Average	0.024		+0.010	
Rms		0.022		0.018
Post-trim 2				
8	0.00	-0.005	+0.000	-0.008
9	0.03	+0.025	+0.040	+0.032
10	0.05	+0.045	+0.030	+0.022
11	0.03	+0.025	+0.035	+0.027
12	0.03	+0.025	+0.010	+0.002
13	-0.02	-0.025	+0.000	-0.008
14	-0.04	-0.045	-0.025	-0.033
15	-0.02	-0.025	-0.010	-0.018
16	-0.02	-0.025	-0.015	-0.023
Average	+0.005		+0.008	
Rms		+0.030		+0.022
Combined rms		+0.0265		+0.0202

Table 19. Elevation results from landmark data processing

Landmark	Identification	Latitude $\pm 1\sigma$ , deg	W longitude $\pm 1\sigma$ , deg	Radius $\pm 1\sigma$ , km	Combined UVS and occultation radius, km	Combined radar and occultation radius, km
South polar cap	6	-86.02 $\pm$ 0.01	357.11 $\pm$ 0.14	3384.67 $\pm$ 2.0	Exit occultation value at -78.8° latitude and 346.6°W longitude is 3383.9 km	Outside limits of Earth-based radar observability
	9	-84.12 $\pm$ 0.01	57.69 $\pm$ 0.11	3382.44 $\pm$ 2.0		
	66	-80.22 $\pm$ 0.03	354.11 $\pm$ 0.10	3383.41 $\pm$ 2.0		
	661	-81.00 $\pm$ 0.02	341.42 $\pm$ 0.11	3382.71 $\pm$ 2.0		
	49	-76.97 $\pm$ 0.03	1.33 $\pm$ 0.11	3384.97 $\pm$ 3.5		
Pavonis Lacus	2	1.50 $\pm$ 0.04	113.17 $\pm$ 0.03	3410.81 $\pm$ 2.5	3411.5	3412.0
	201	1.58 $\pm$ 0.03	113.00 $\pm$ 0.03	3413.07 $\pm$ 2.4	Nearest available value is 3417.5	Nearest available value is 3418.0
	202	0.28 $\pm$ 0.03	113.96 $\pm$ 0.03	3414.95 $\pm$ 2.3	Base 3403.0	3403.5
Nodus Gordii	3	-10.25 $\pm$ 0.03	120.82 $\pm$ 0.03	3412.05 $\pm$ 2.3	Base 3402.0	3403.5
					3414.5	3415.5
Nix Olympica	51	17.21 $\pm$ 0.03	133.73 $\pm$ 0.03	3419.20 $\pm$ 2.6	Base 3401.0	3402.5
	53	17.91 $\pm$ 0.03	133.70 $\pm$ 0.03	3416.22 $\pm$ 2.7	No relative information available	
	54	17.77 $\pm$ 0.03	133.45 $\pm$ 0.03	3418.51 $\pm$ 2.6	No relative information available	

Table 20. One-sigma uncertainties in Mariner 9 position when ranging is taken

Position components	Pre-flight	Actual pre-gravity sensing, revolutions 1-4	Post-gravity sensing (3 stations), revolutions 4-280	Post-gravity sensing (1 station), revolutions 280-695	Post-gravity sensing (conjunction region)
$r\Delta\Omega$ , km	30	120	5	10	< 30
$\Delta r$ , m	100	400	20	60	< 150
$\Delta s'$ , m	50	200	20	60	< 150

Table 21. Effect of position uncertainties on Earth-Mars measurement

Position components	Pre-flight	Actual pre-gravity sensing, revolutions 1-4	Post-gravity sensing (3 stations), revolutions 4-280	Post-gravity sensing (1 station), revolutions 280-695	Post-gravity sensing (conjunction region)
$r\Delta\Omega$ , m	3	13	0.5	1	< 3
$\Delta r$ , m	0.01	0.04	0.008	0.006	< 0.015
$\Delta s'$ , m	50	200	20	60	< 150

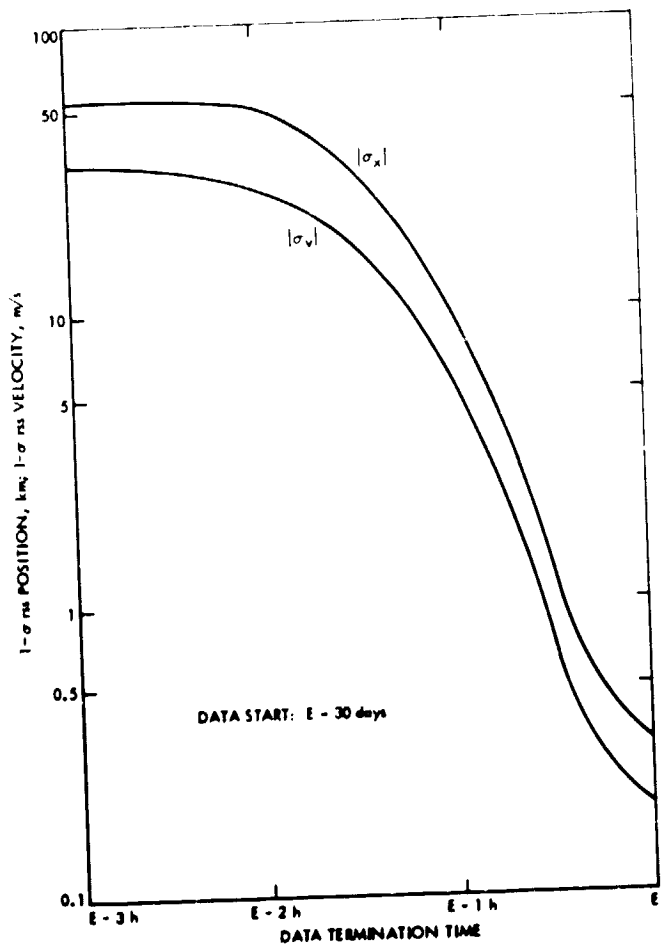


Fig. 1. Encounter OD position error at periaapsis as a function of data termination time

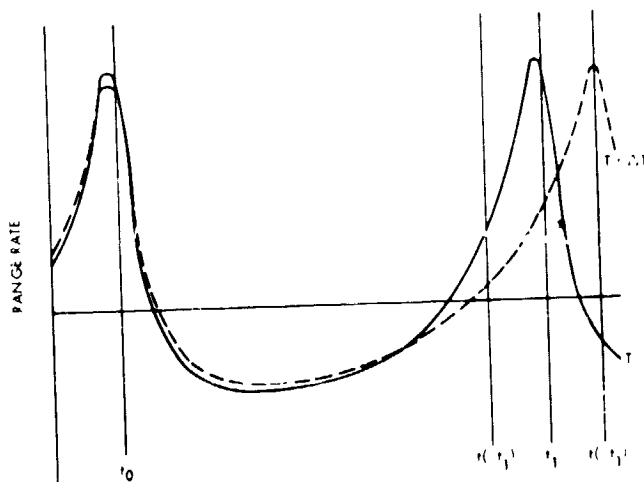


Fig. 2. Range-rate time history for two different values of orbital period

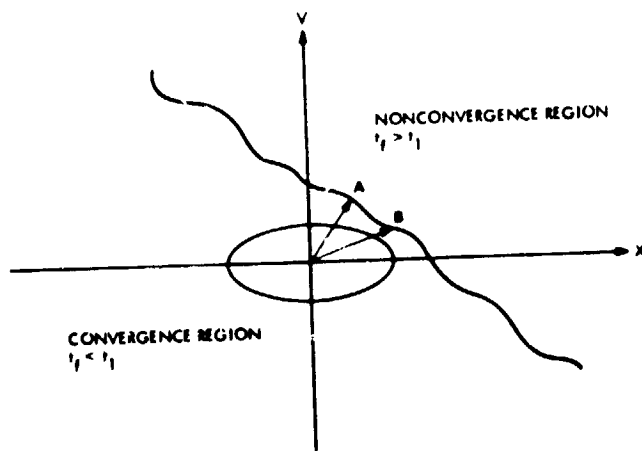


Fig. 3. Worst-direction diagram in phase space

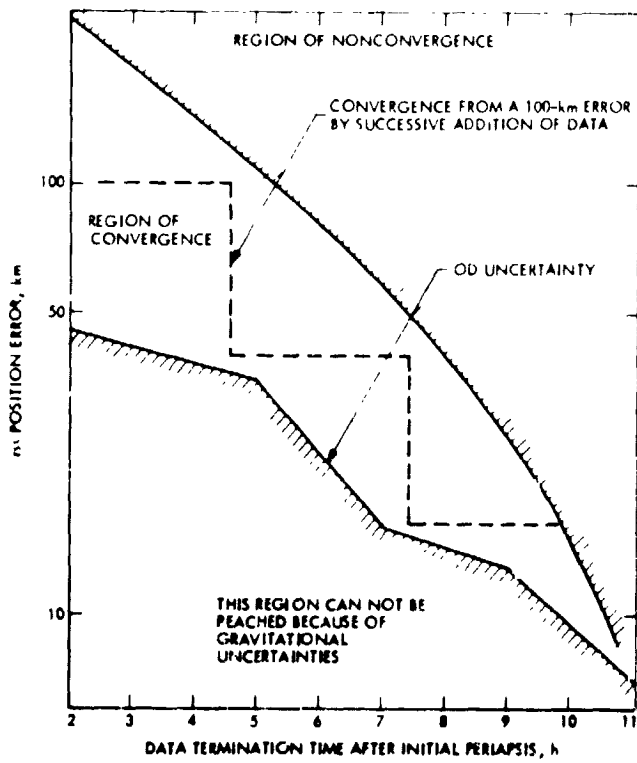


Fig. 4. Worst-direction convergence profile as a function of data termination time

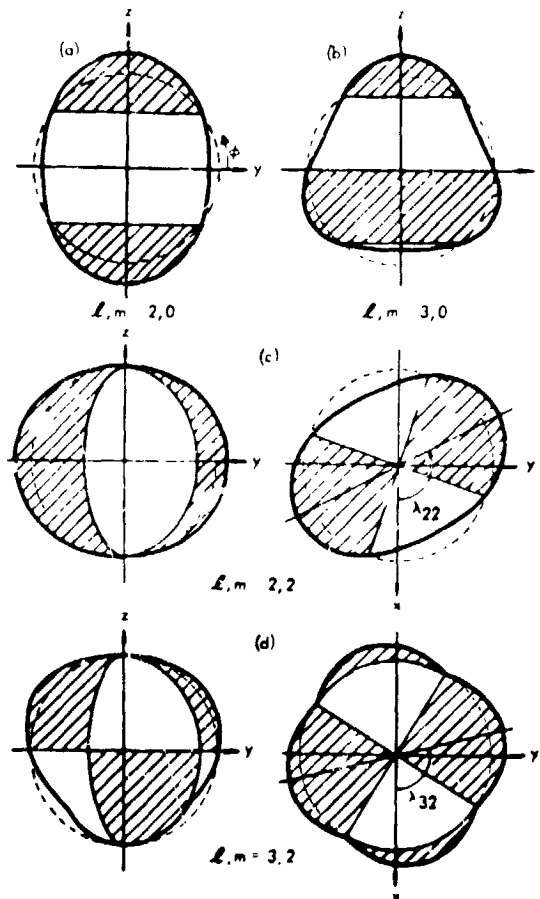


Fig. 5. Geometric shape of low-order U-functions.

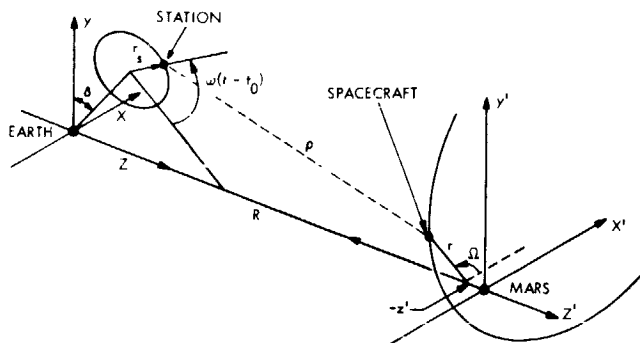


Fig. 6. Earth-station/Mars-spacecraft configuration

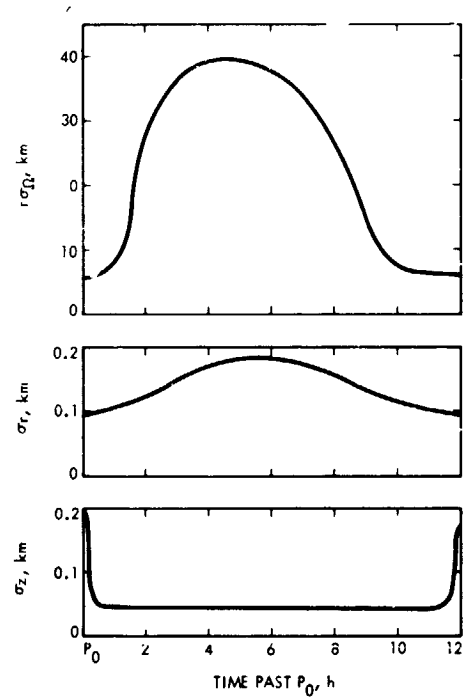


Fig. 8. Time histories of pre-flight state estimate uncertainty over a single revolution (November 14, 1971)

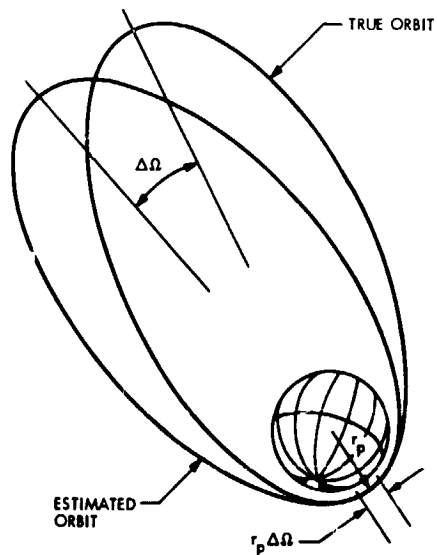


Fig. 7. Projection of true and estimated orbit in Earth's plane of sky

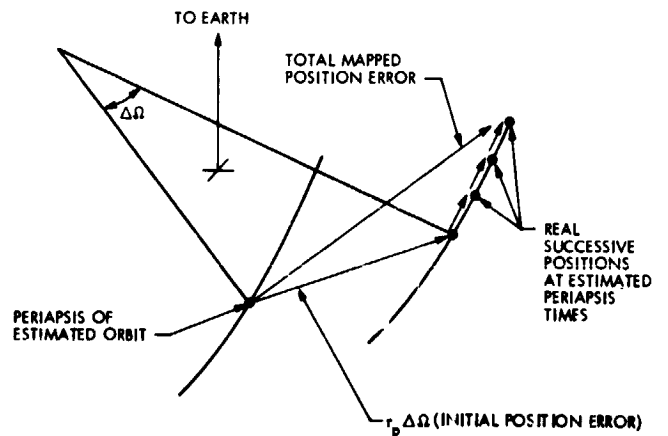


Fig. 9. Effect of period error on mapped position error at periaapsis

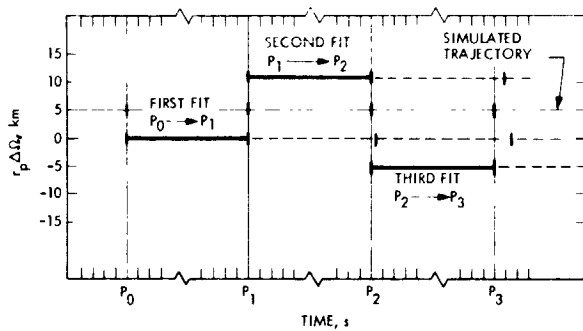


Fig. 10. Pre-gravitation sensing solution history (pre-flight simulated data)

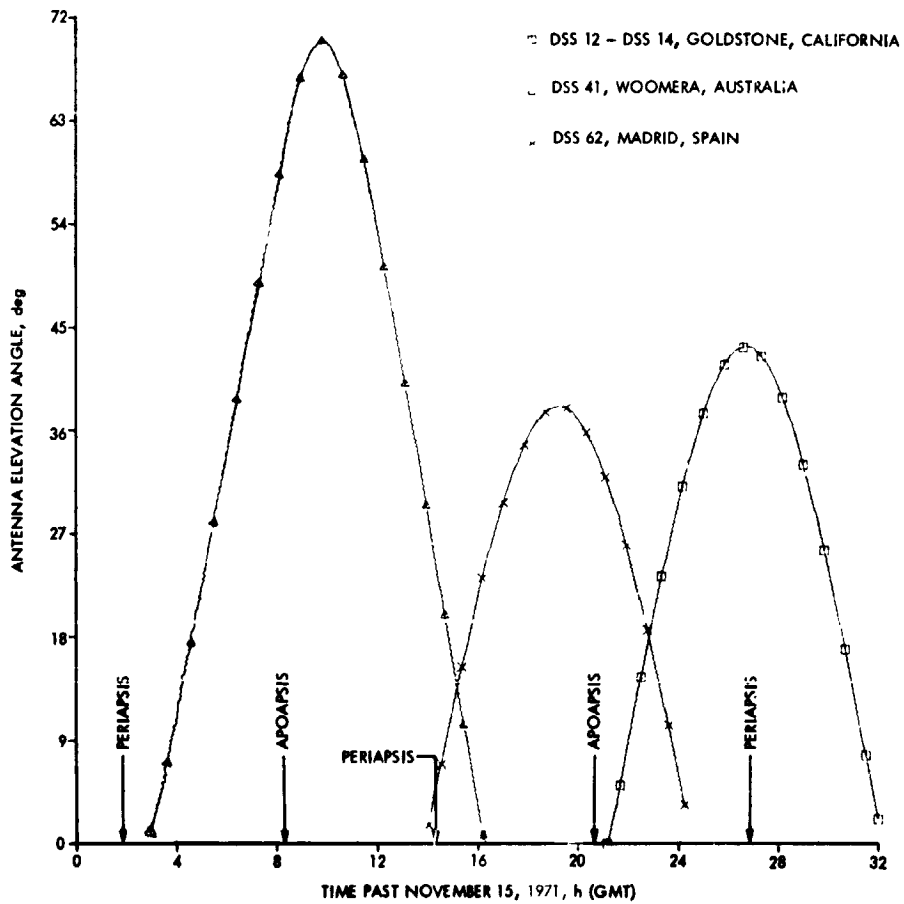


Fig. 11. Antenna elevation angle vs time: (a) November 15, 1971, (b) May 5, 1972

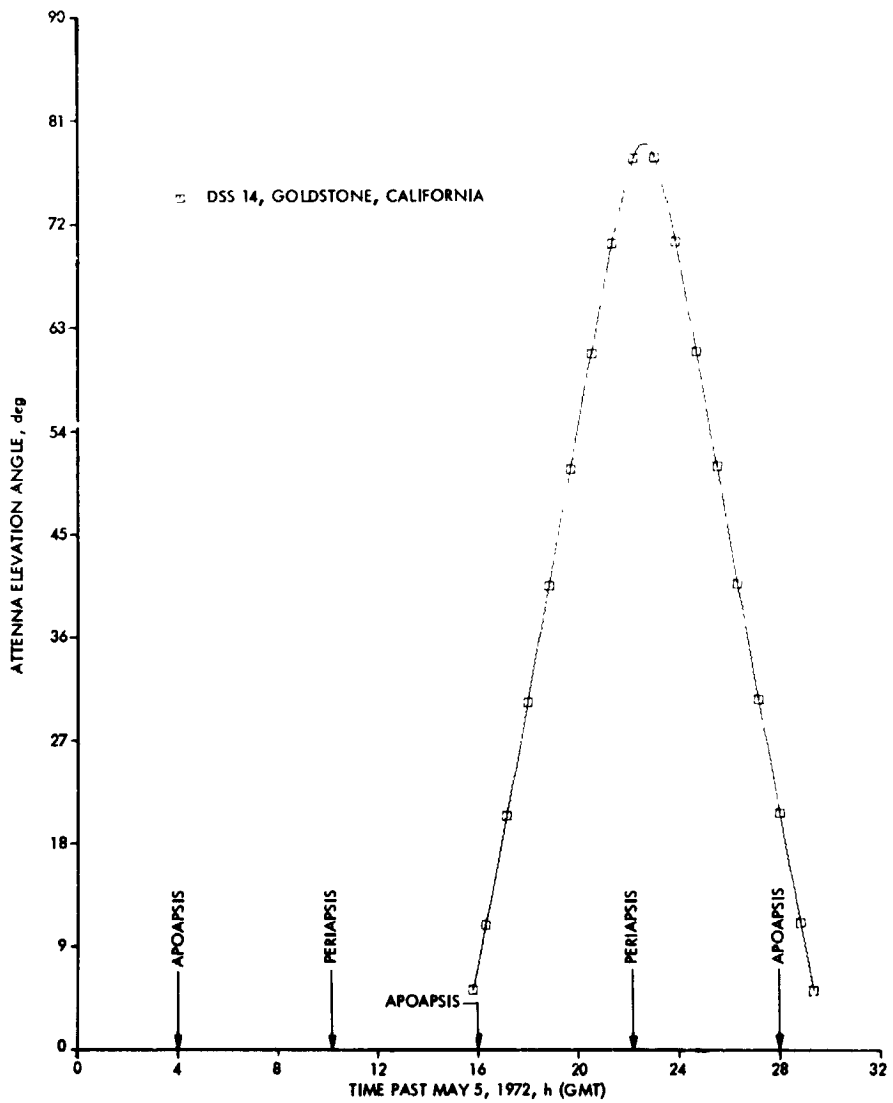


Fig. 11 (contd)

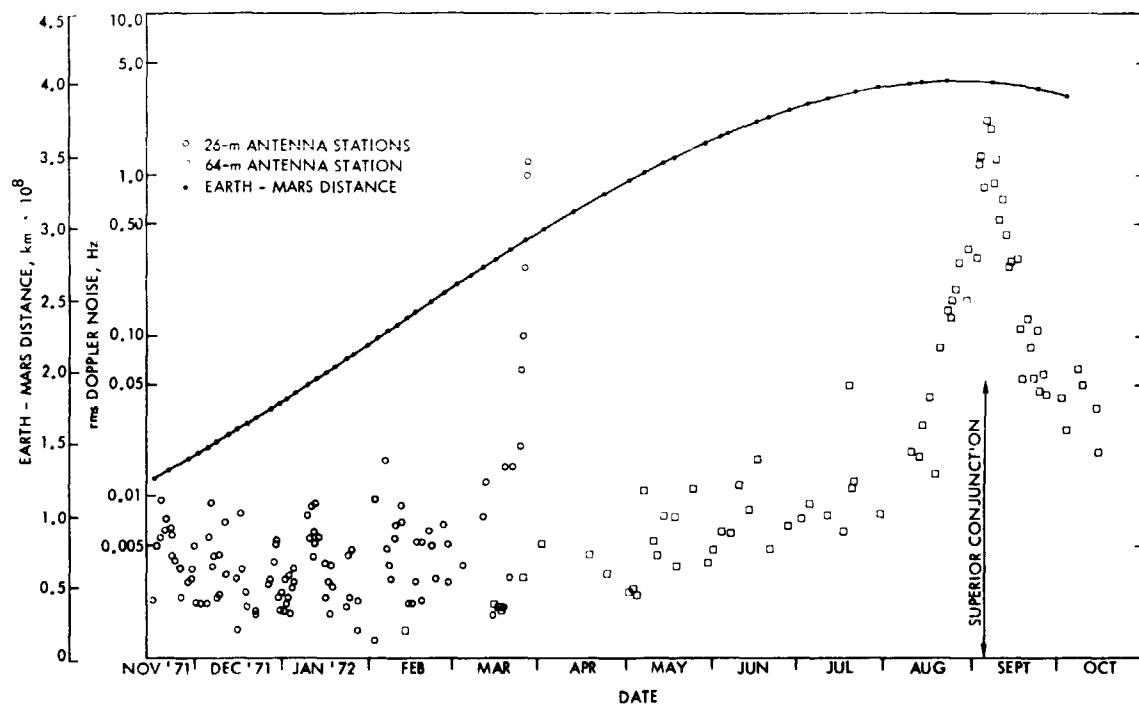


Fig. 12. Evolution of doppler data accuracy

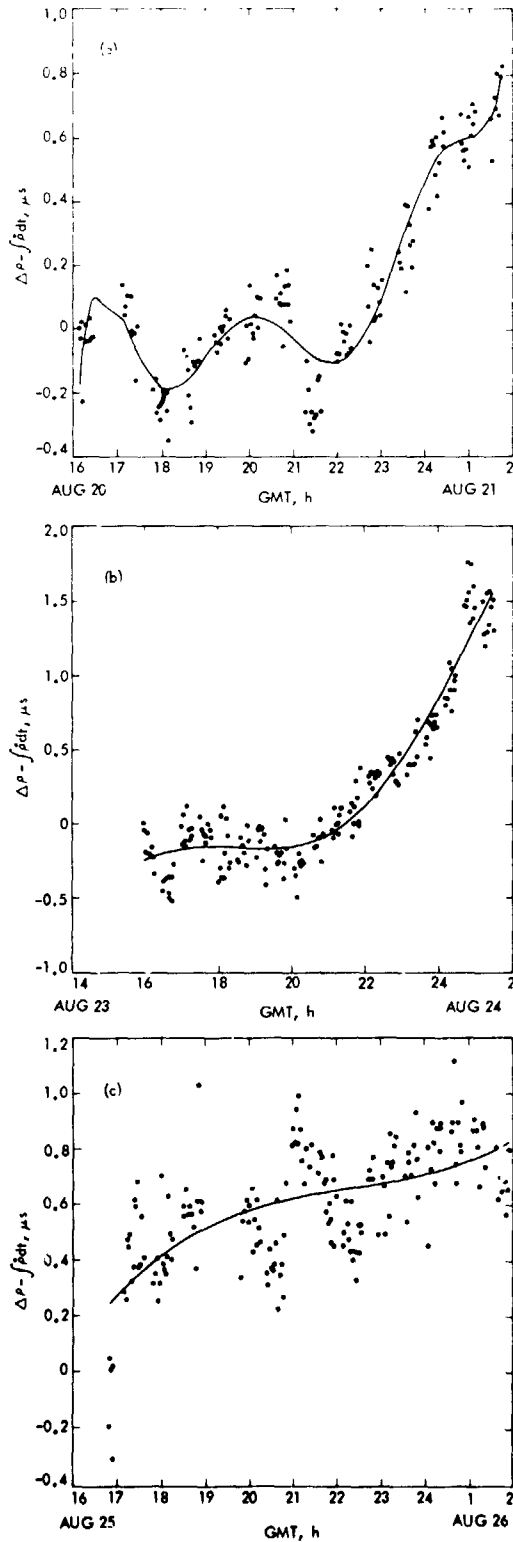


Fig. 13. Differenced range minus integrated doppler time histories: (a) August 20 (order fit 8), (b) August 23 (order fit 3), (c) August 25 (order fit 3)

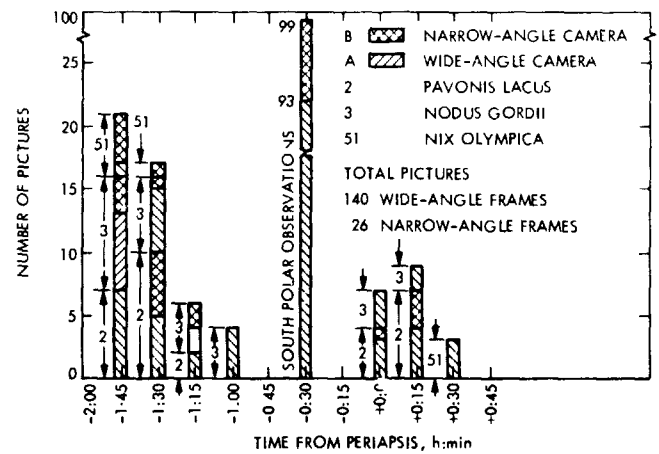
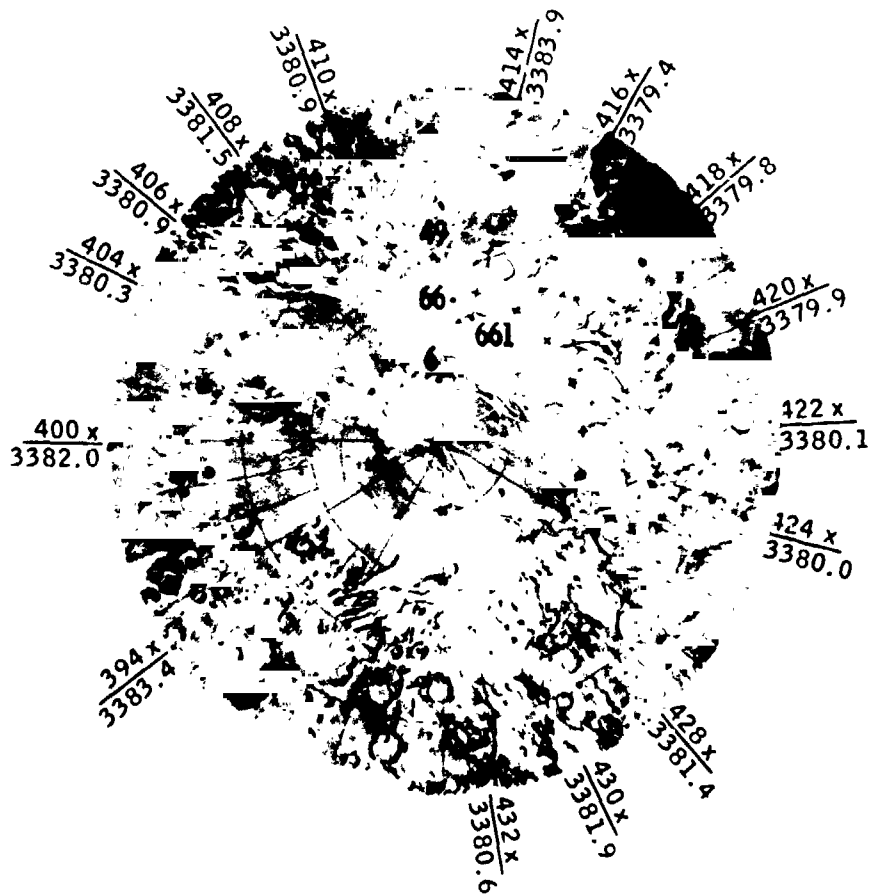


Fig. 14. Distribution of observation times relative to time of periapsis passage of spacecraft for pictures used in optical OD



RESOLUTION NUMBER  
MEASURED RADIUS

Fig. 15. Landmark locations: (a) South polar region, (b) Pavonis Lacus, (c) Nodus Gordii

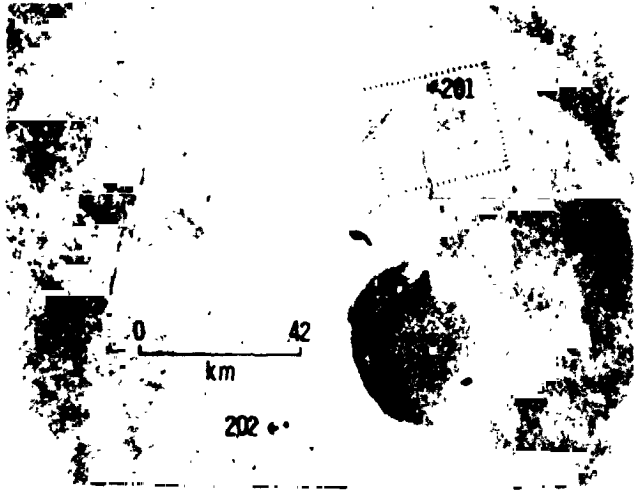


Fig. 15 (contd)



Fig. 15 (contd)

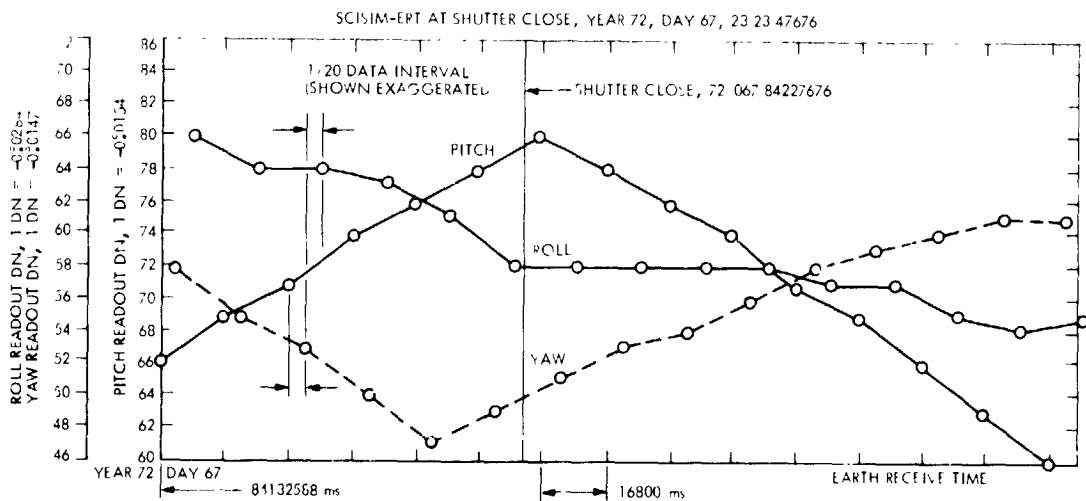
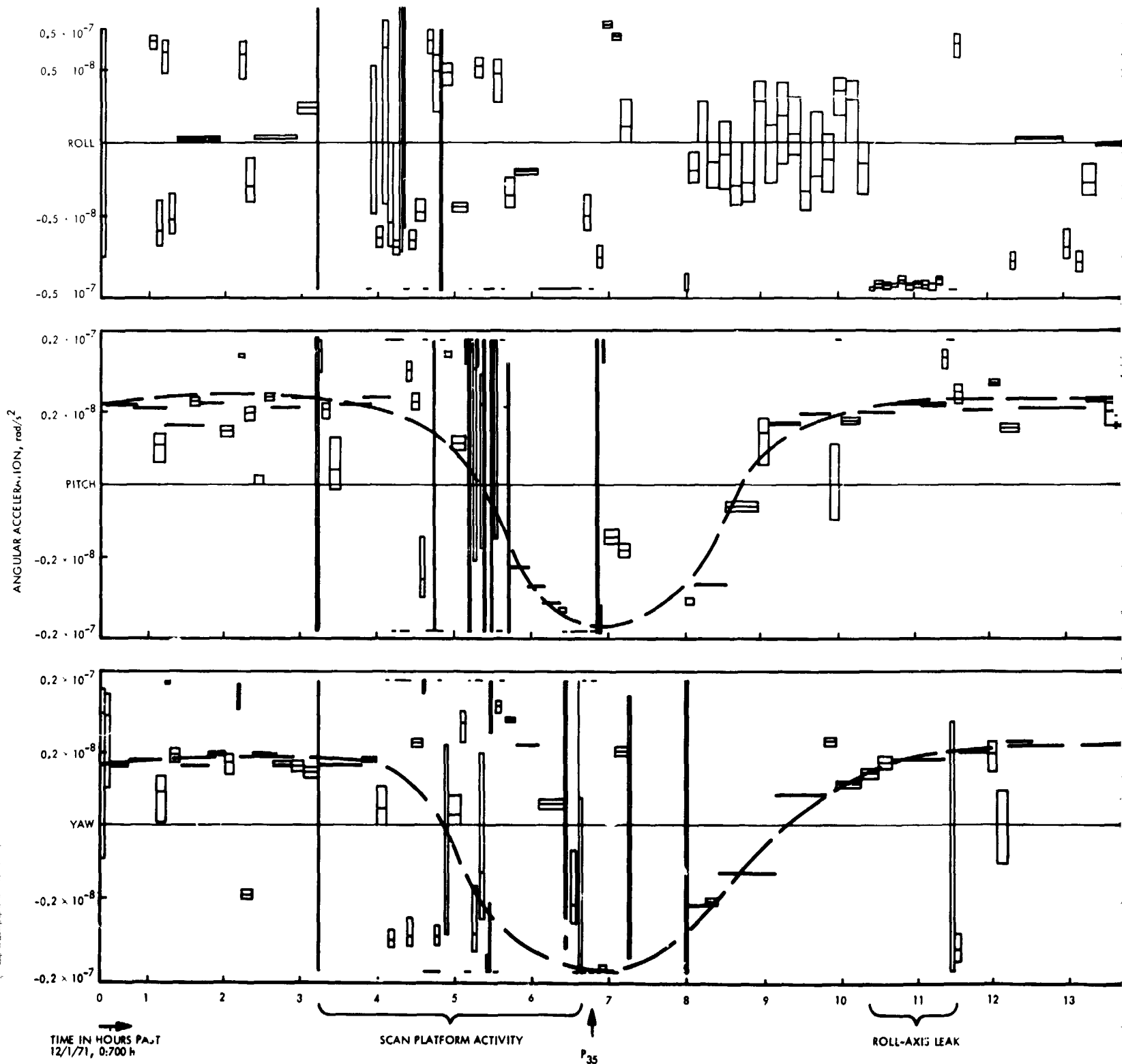


Fig. 16. Engineering telemetry data



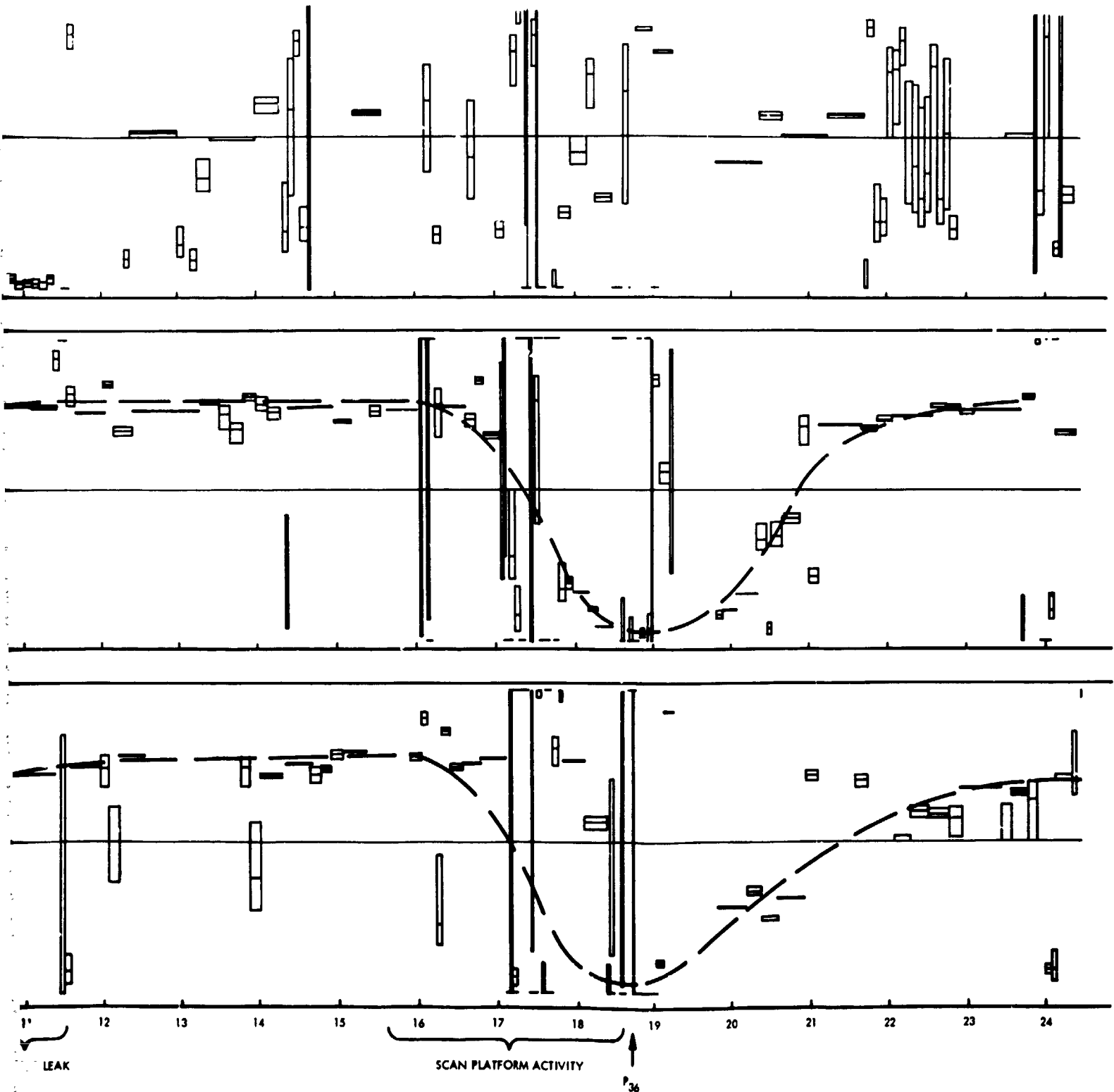


Fig. 17. Typical roll-axis leak

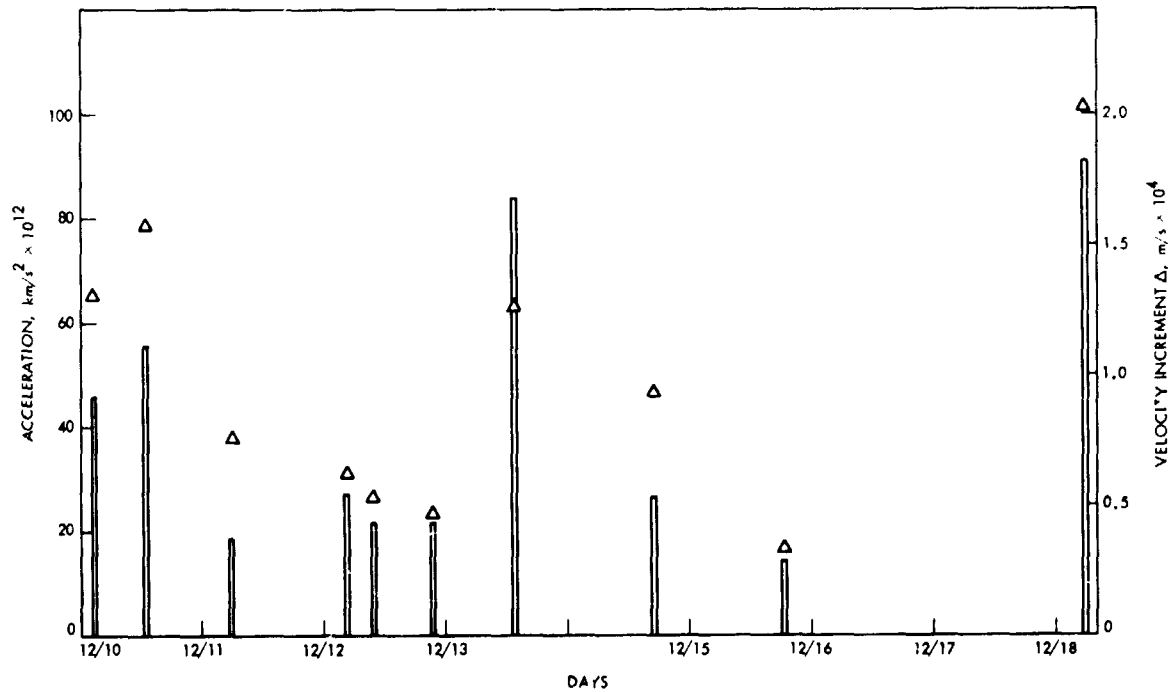


Fig. 18. Gas leak acceleration and  $\Delta V$  history for mid-December 1971

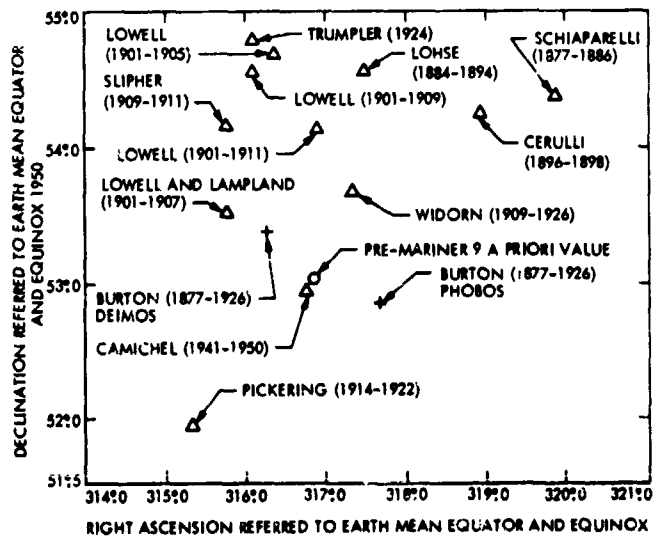


Fig. 19. Celestial coordinates (1950.0) of Martian north pole



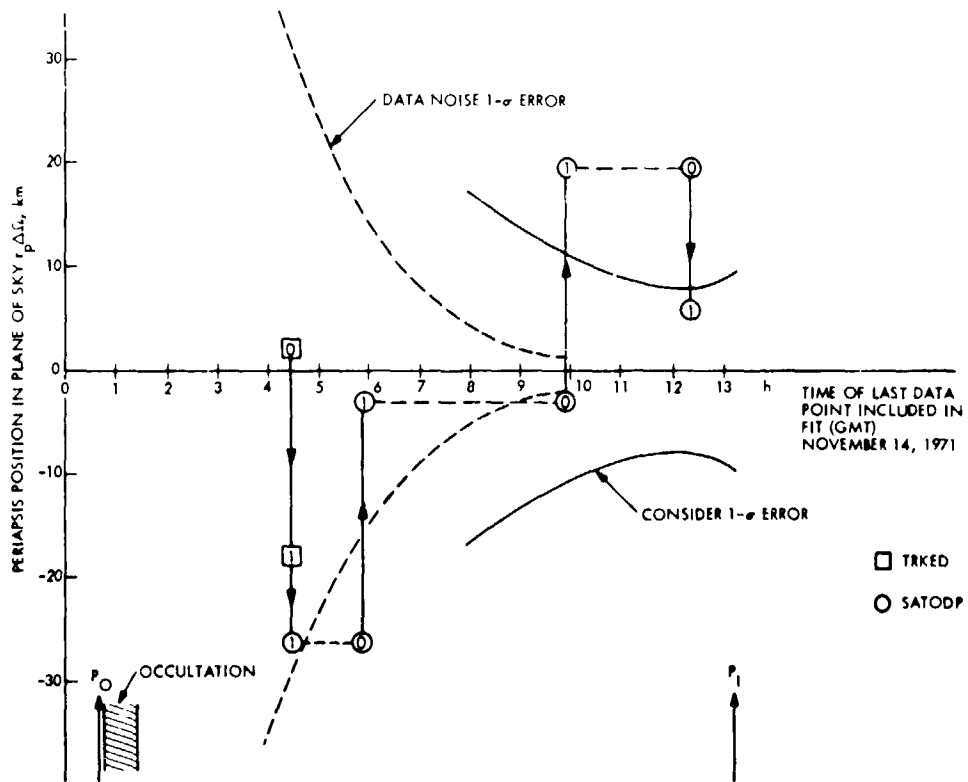


Fig. 21. First orbit convergence history (position)

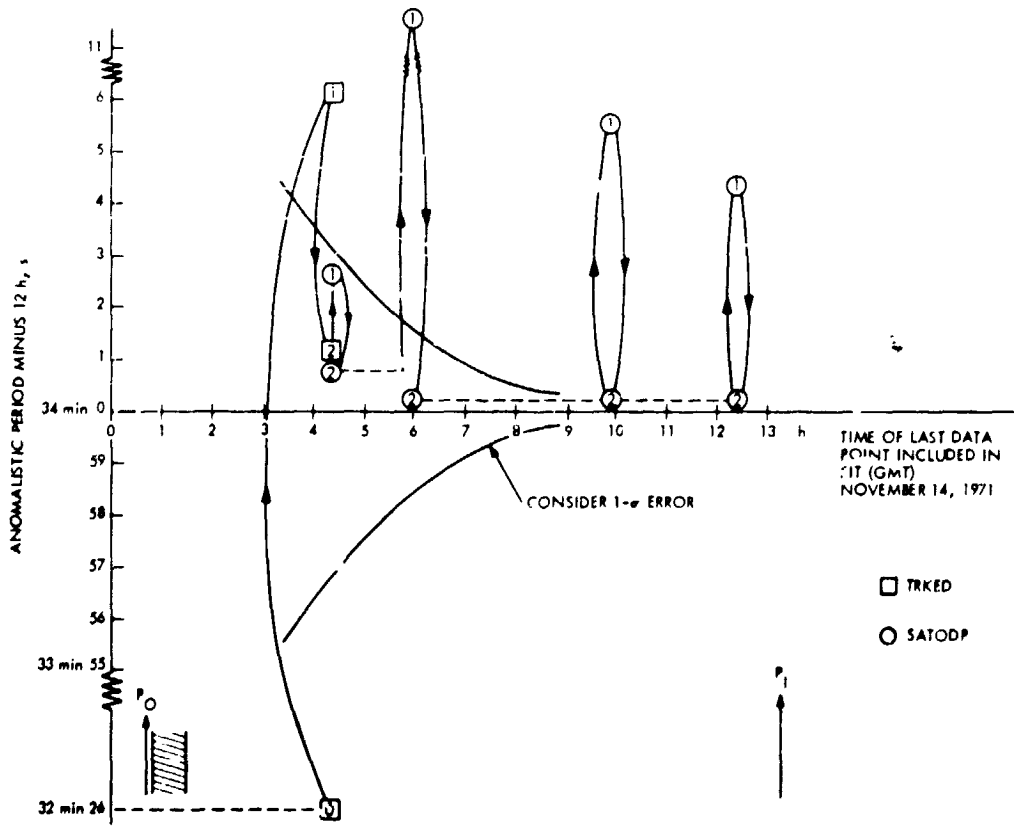


Fig. 22. First orbit convergence history (period)

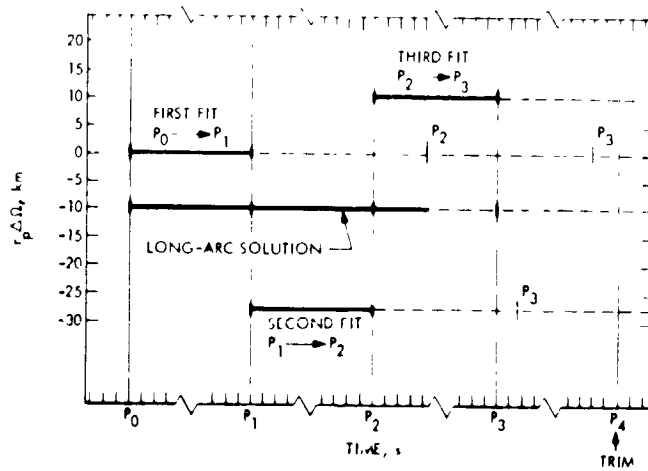


Fig. 23. Near-real-time pre-gravity-sensing solution history

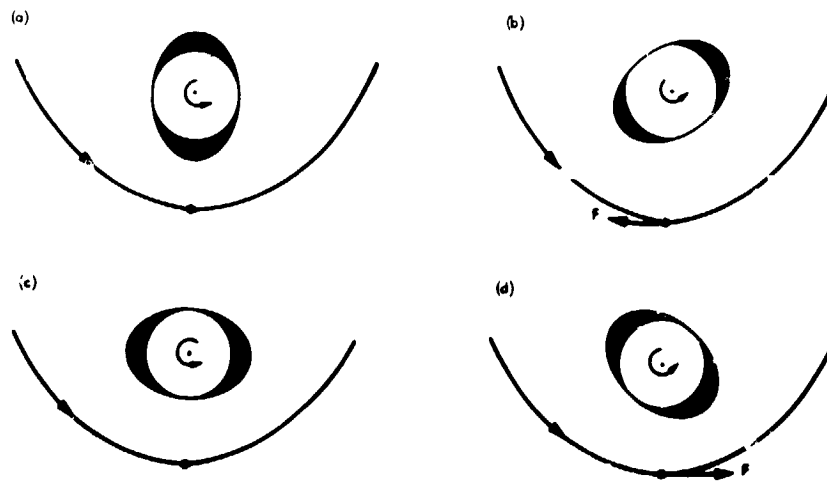


Fig. 24. Effects of  $C_{22}$  and  $S_{22}$  on orbit of Mariner 9 (view along Martian spin axis): (a) Unstable equilibrium, (b) Energy of probe decreases, (c) Stable equilibrium, (d) Energy of probe increases

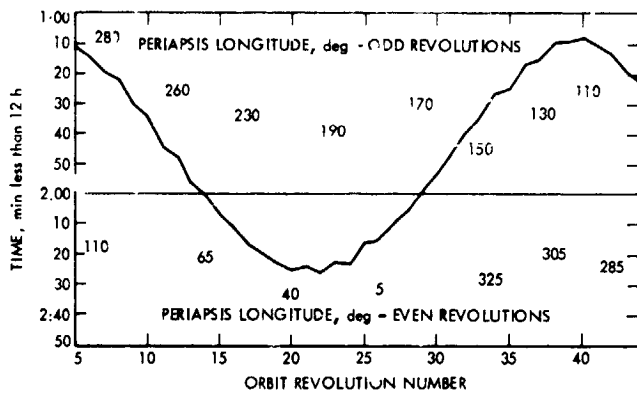


Fig. 25. Variation in Mariner 9 post-trim 1 orbit period

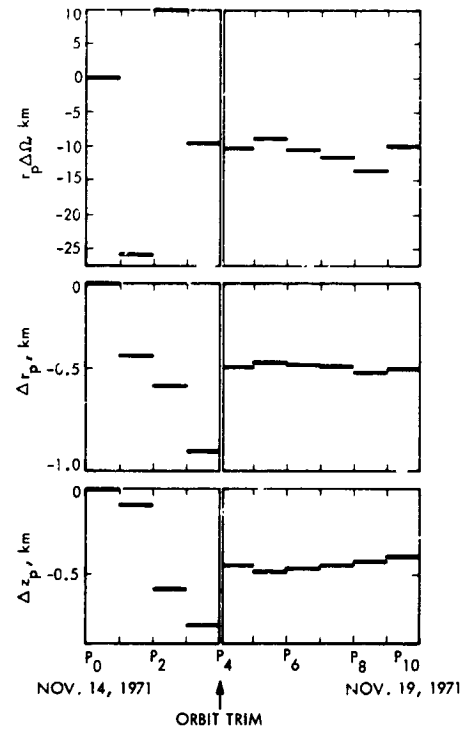


Fig. 26. Estimated differences of single-revolution state at periapsis for first 10 revolutions

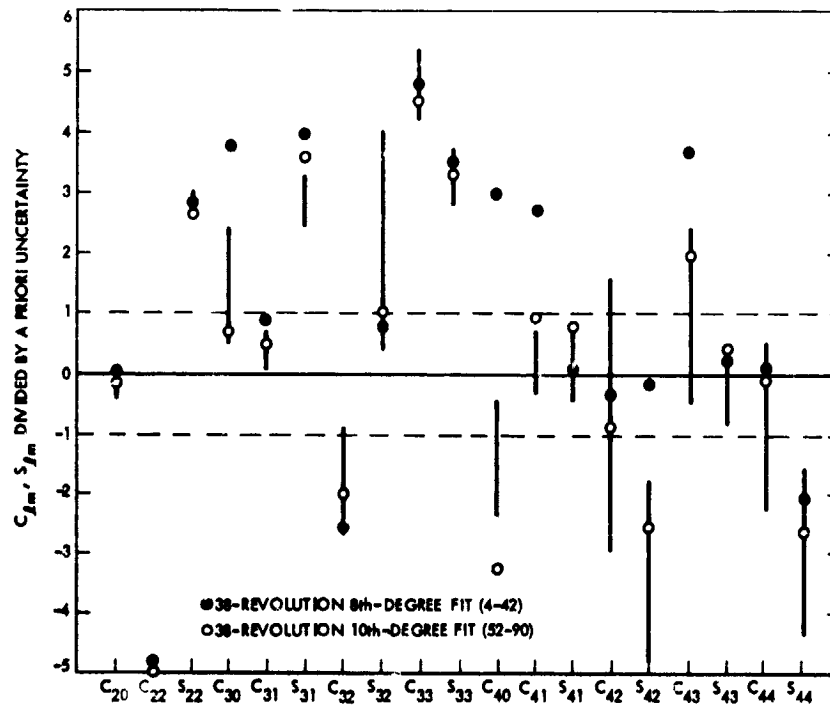


Fig. 27. Variation in estimates of harmonic coefficients

C-3

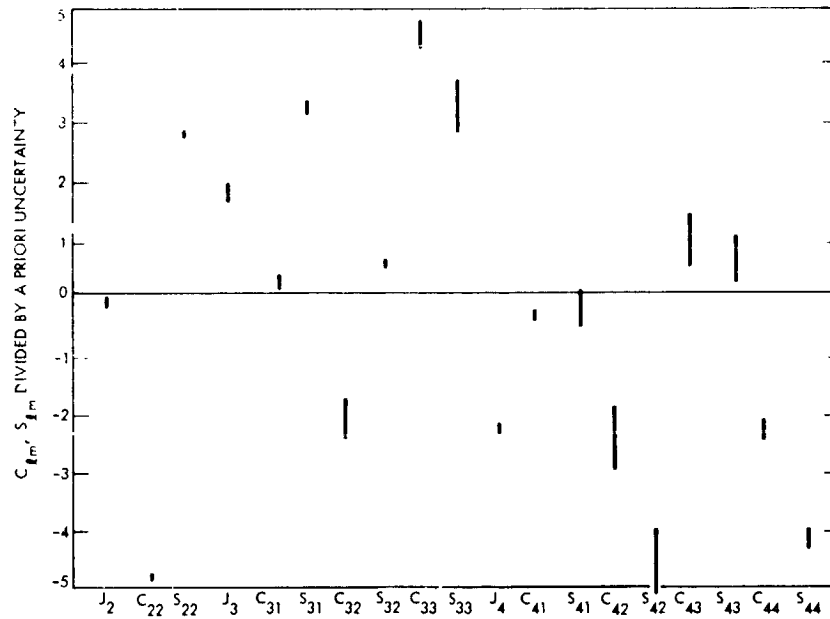


Fig. 28. Effect of gas leak modeling on estimate of harmonics

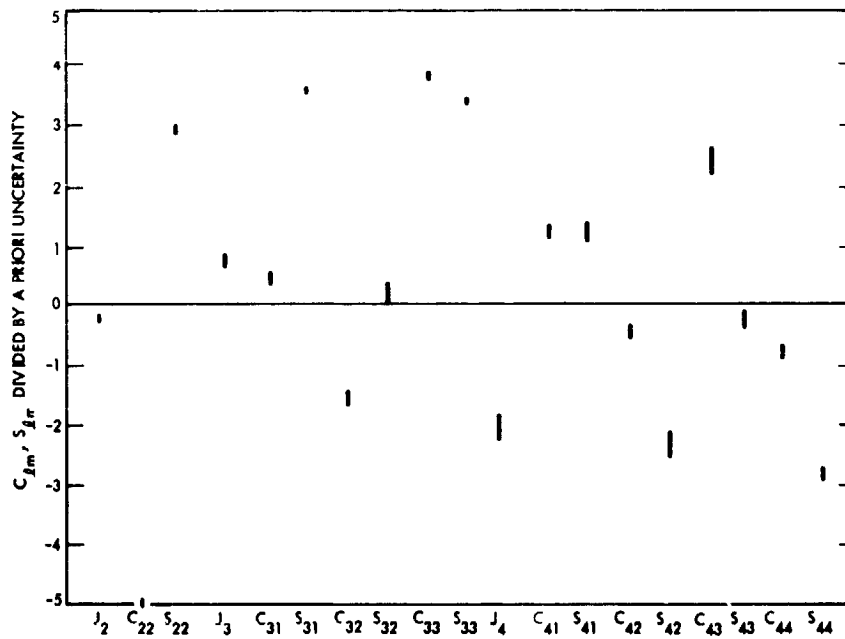


Fig. 29. Effect of ephemeris errors on estimate of harmonics

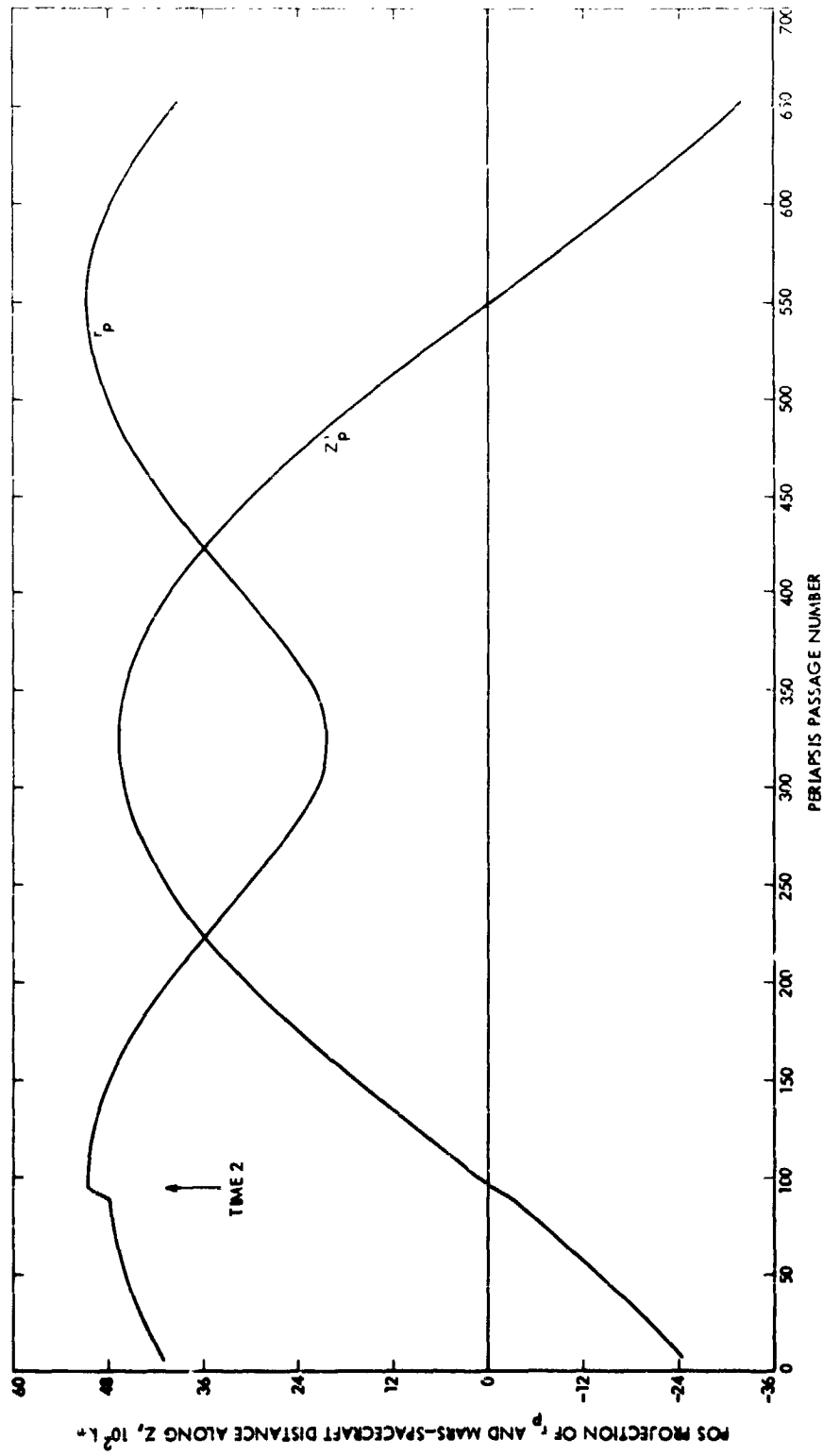


Fig. 30. Time history of  $r_p$  and  $z'_p$

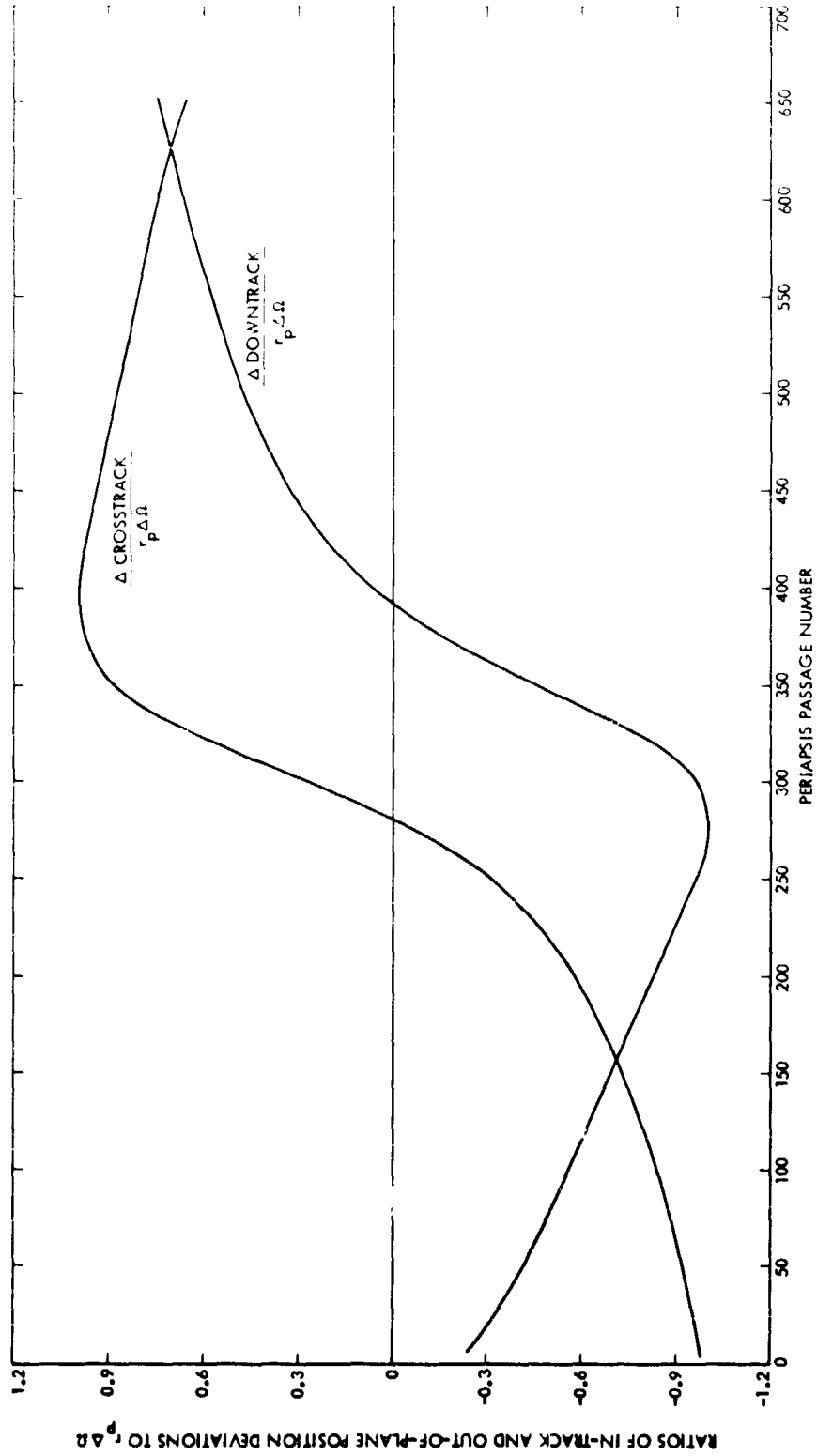


Fig. 31. Time history of ratios of in-track and out-of-plane position deviations to  $r_p \Delta \Omega$ .

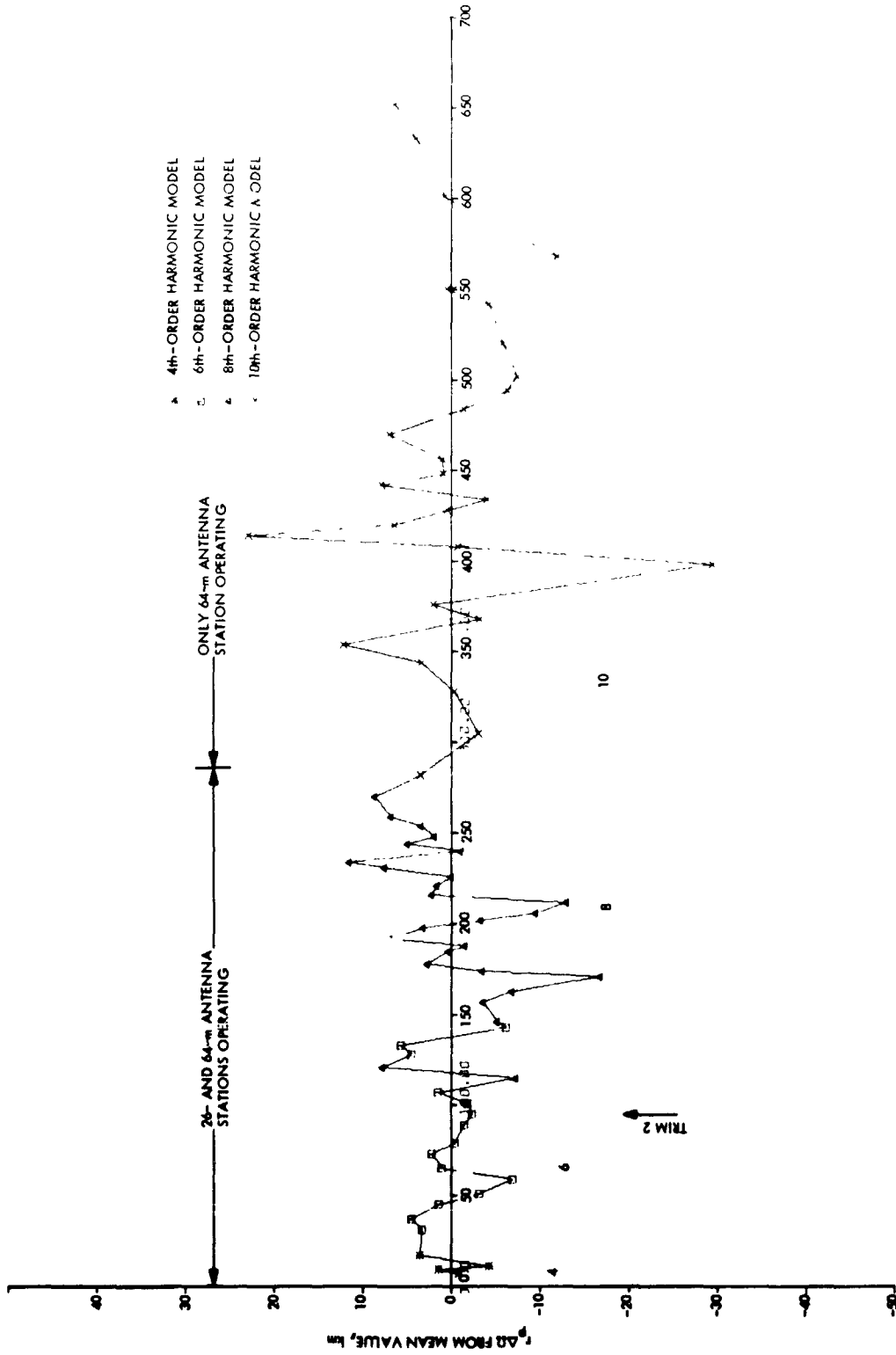


Fig. 32. Time history of  $r_p - \Delta\Omega$  from mean for short-arc fits

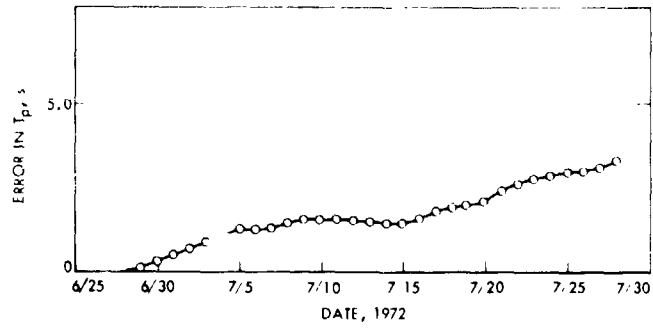


Fig. 33. Prediction error in  $T_p$  for tenth-degree harmonic model

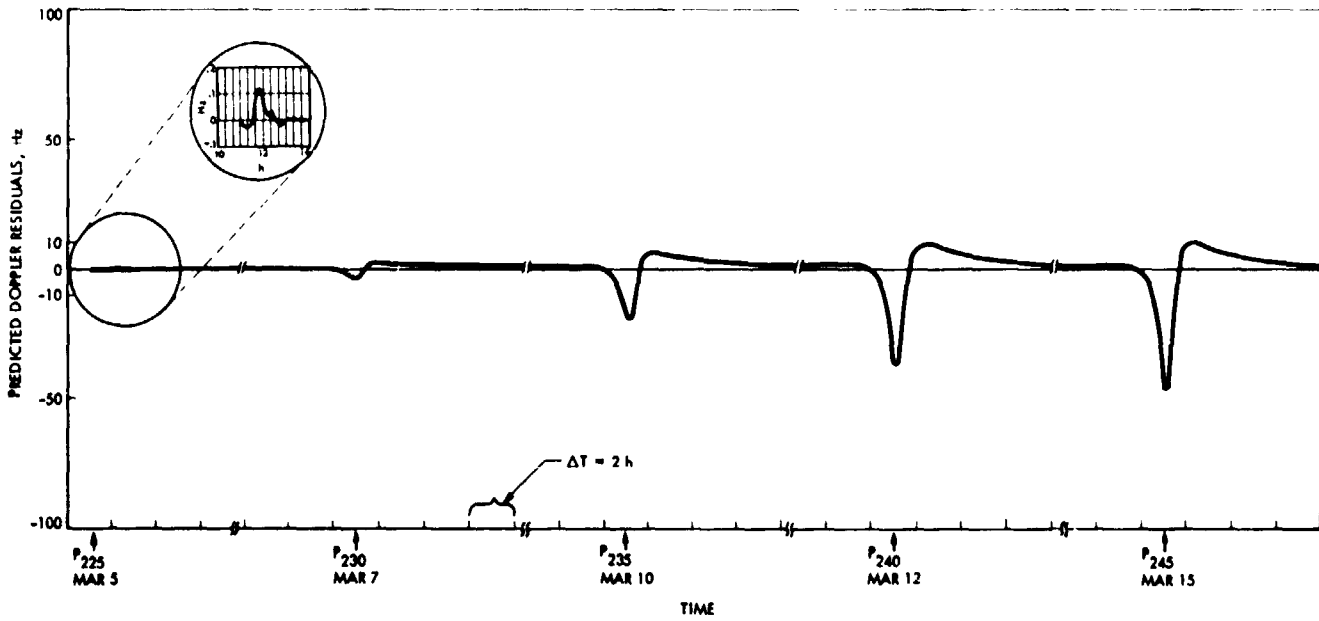


Fig. 34. Typical fit and predicted doppler residuals

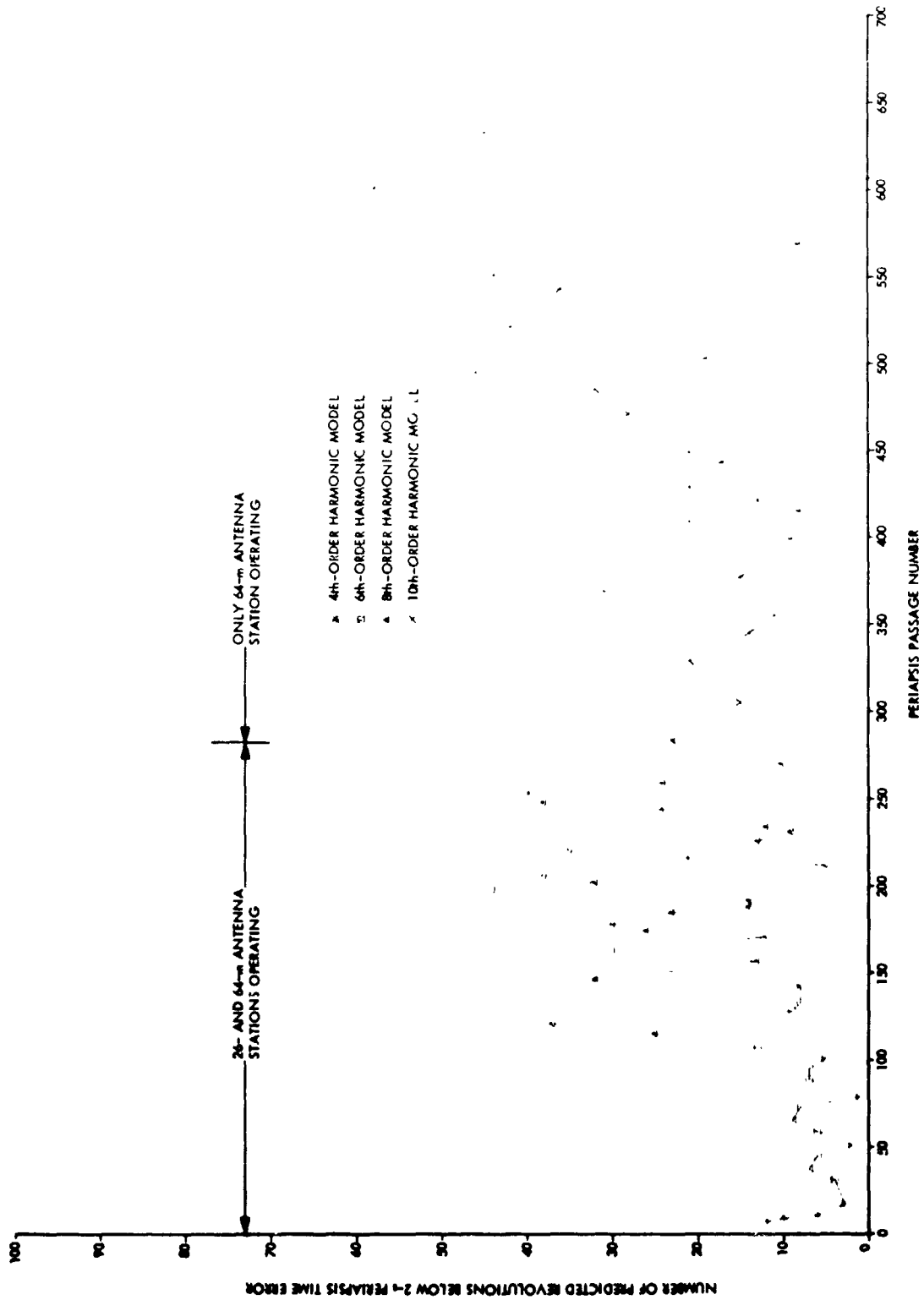


Fig. 35. Time history of predicted revolutions below 2-s time error

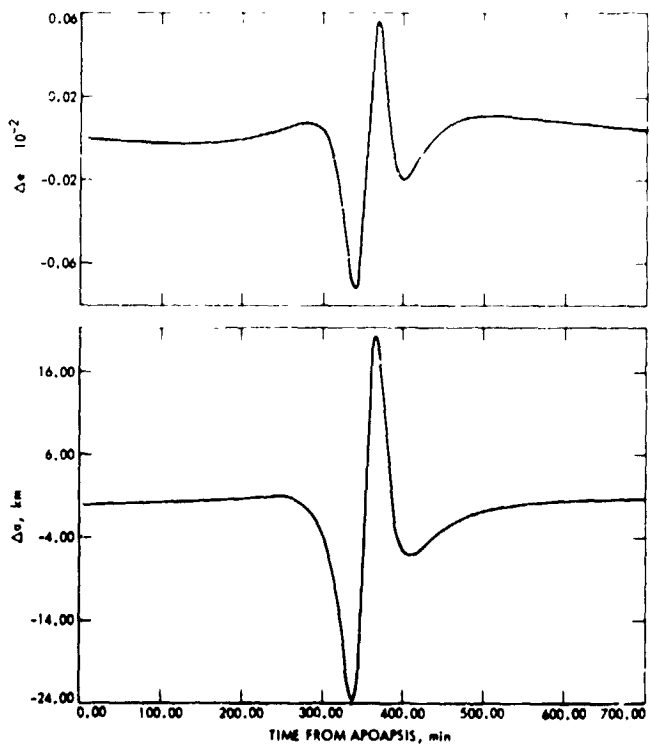


Fig. 36. High-frequency orbital element variations

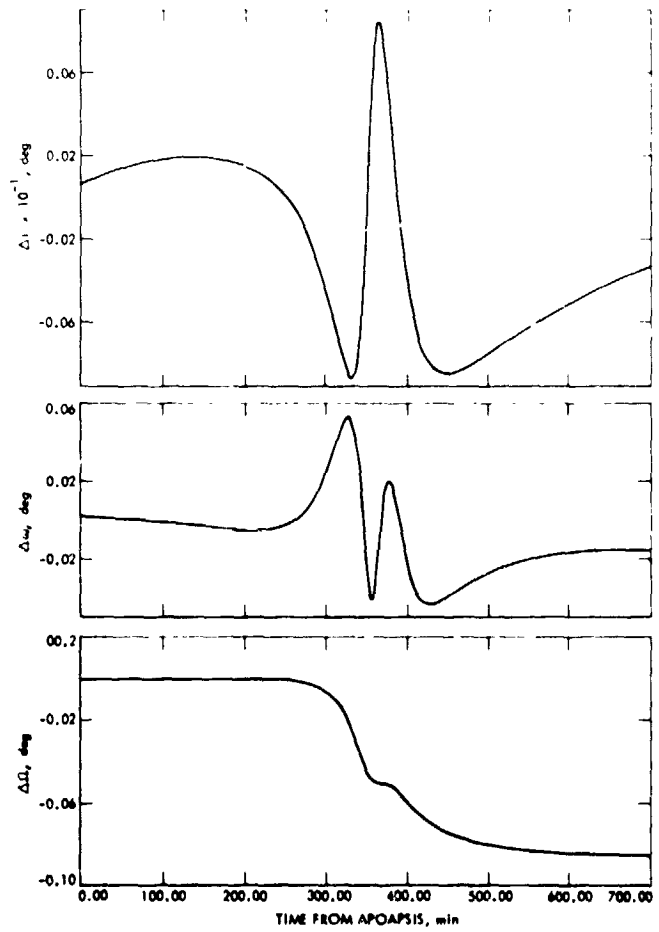


Fig. 36 (contd)

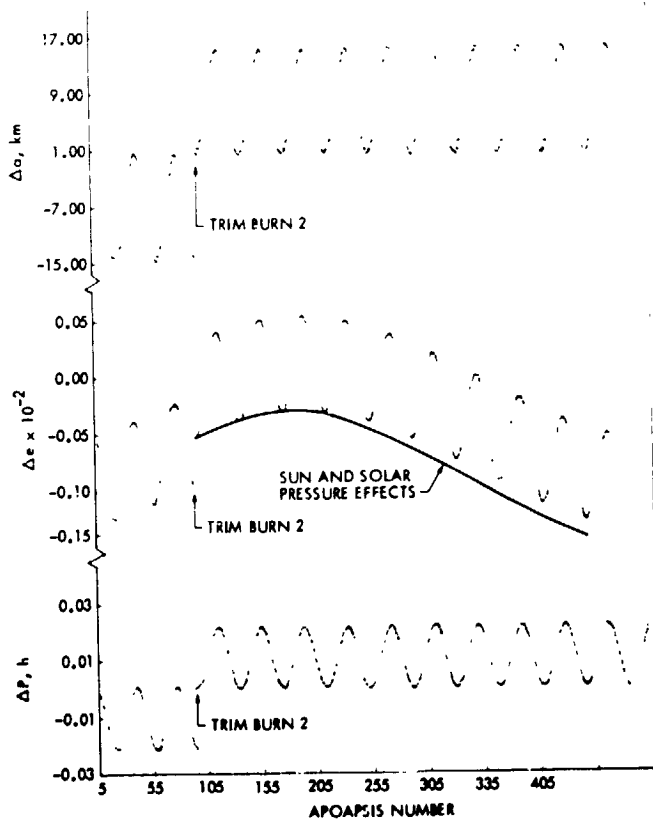


Fig. 37. Long-period osculating orbit elements: (a) In-plane elements, (b) Orientation angles relative to Mars true equator

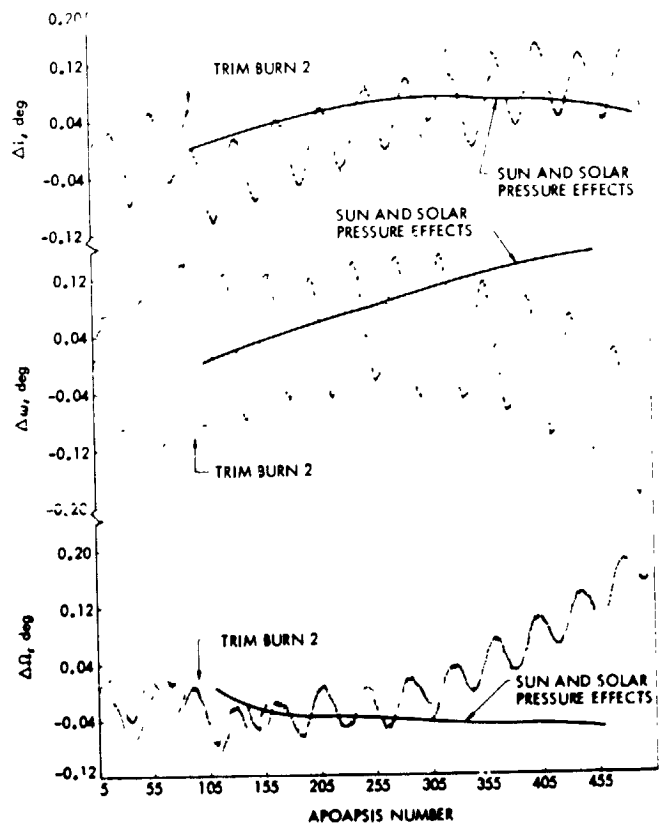


Fig. 37 (contd)

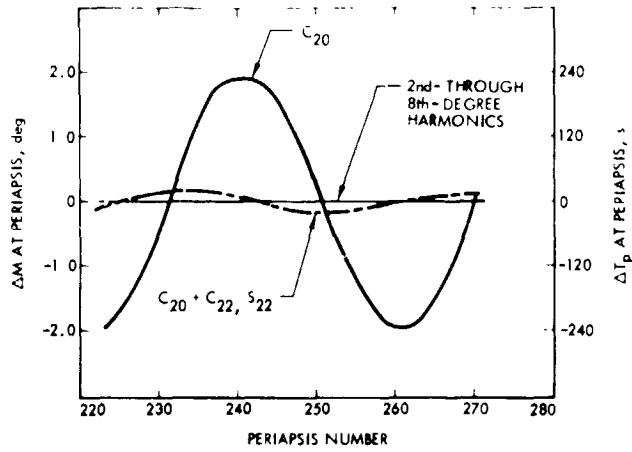


Fig. 38. Error in predicted mean anomaly and  $T_p$  using various gravity models

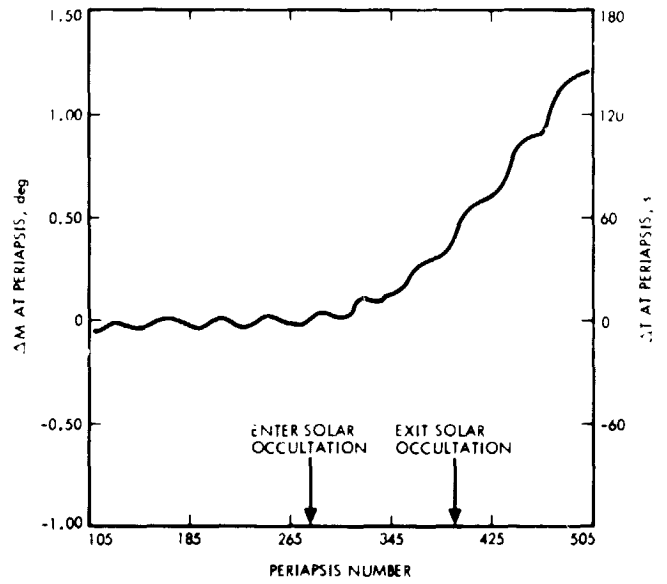


Fig. 39. Error in predicted mean anomaly at periaapsis

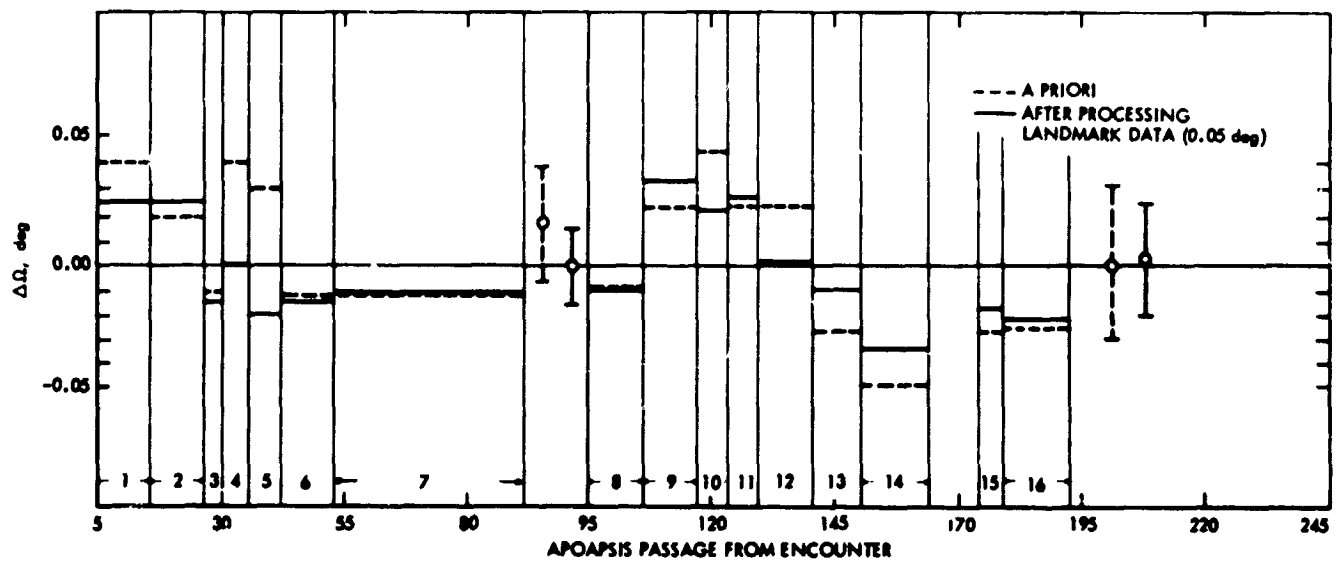


Fig. 40.  $\Omega$  correction time history

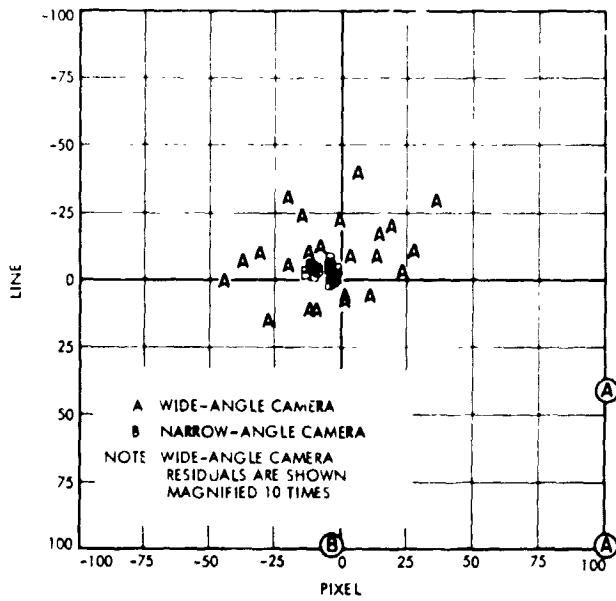


Fig. 41. TV image residuals: (a) Pavonis Lacus, (b) Nodus Gordii, (c) Nix Olympica, (d) South polar region

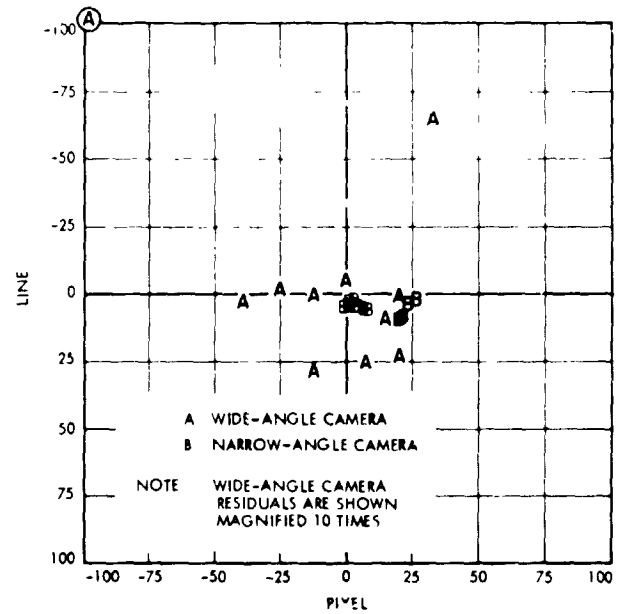


Fig. 41 (contd)

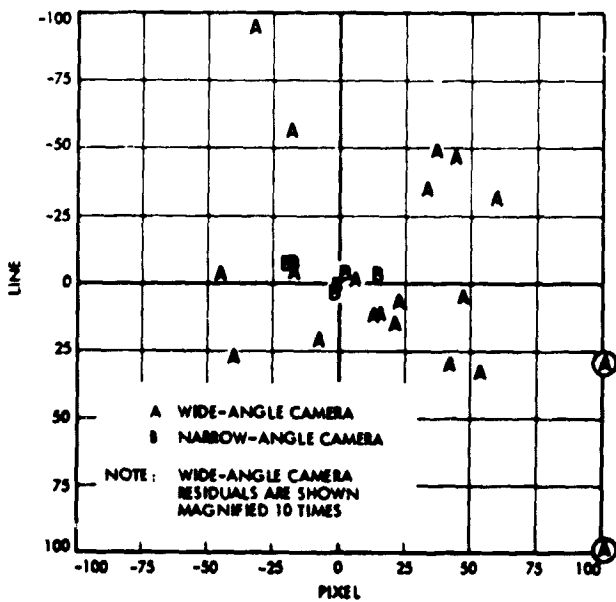


Fig. 41 (contd)

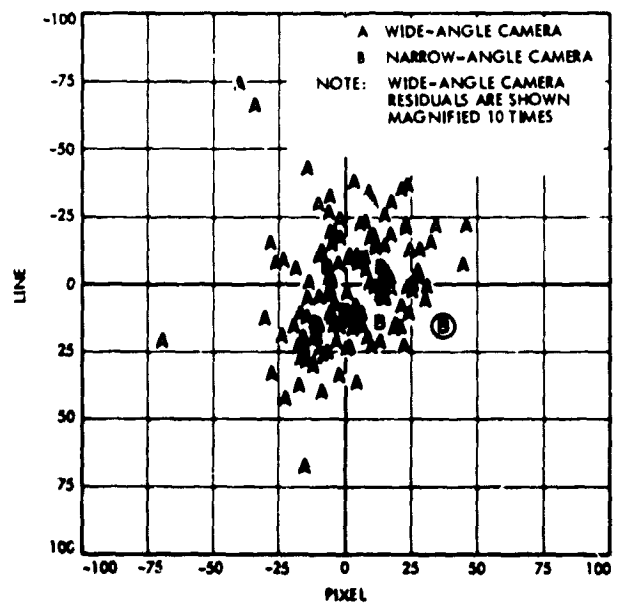


Fig. 41 (contd)

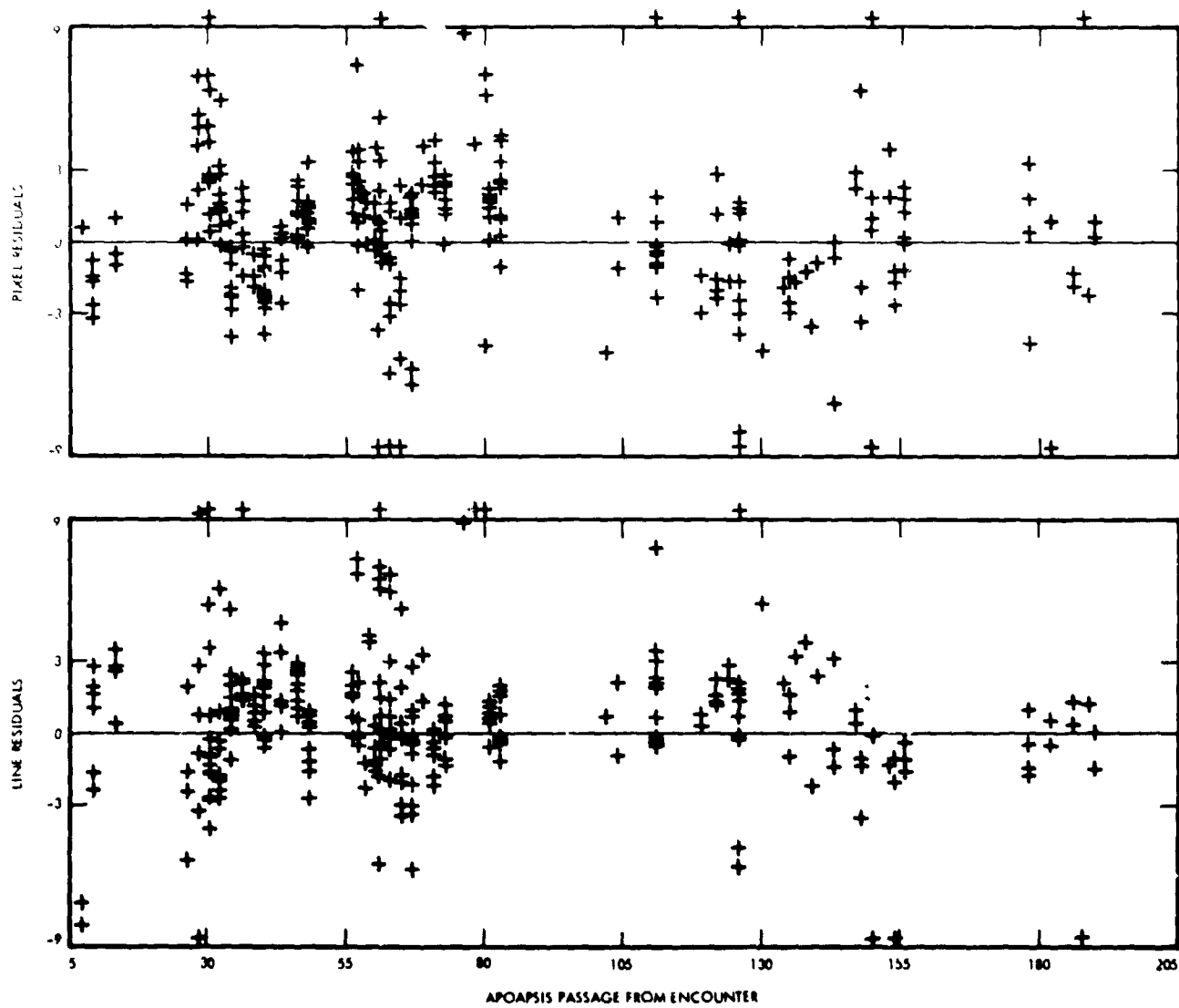


Fig. 42. Time history of landmark image residuals

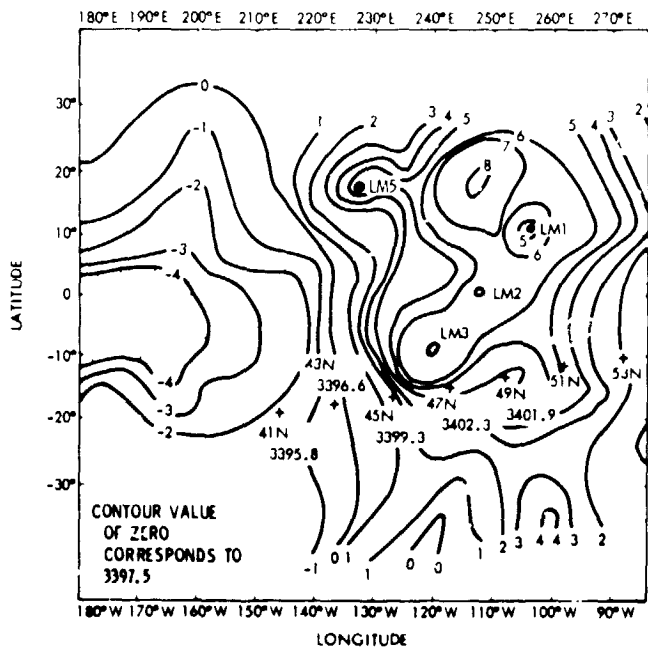


Fig. 43. Topography of Mars (from radar-ranging data) relative to center of mass

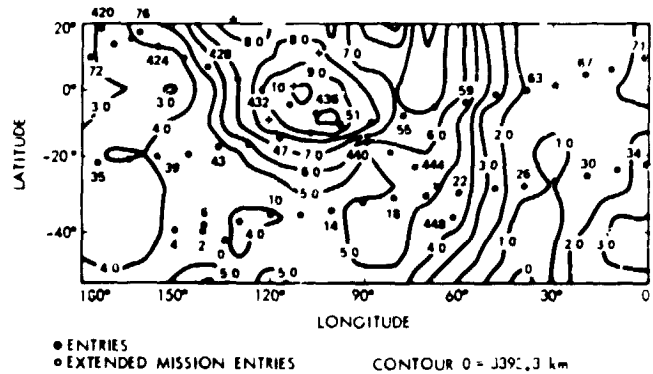


Fig. 44. Topography of Mars (from UVS and occultation data) relative to an equipotential surface

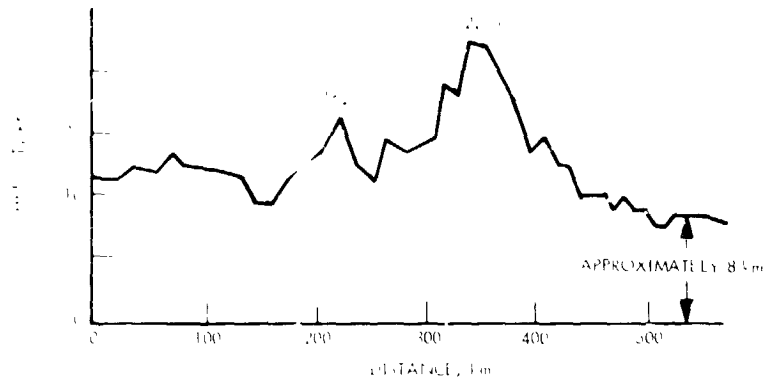


Fig. 45. Altitude profile of Middle Spot

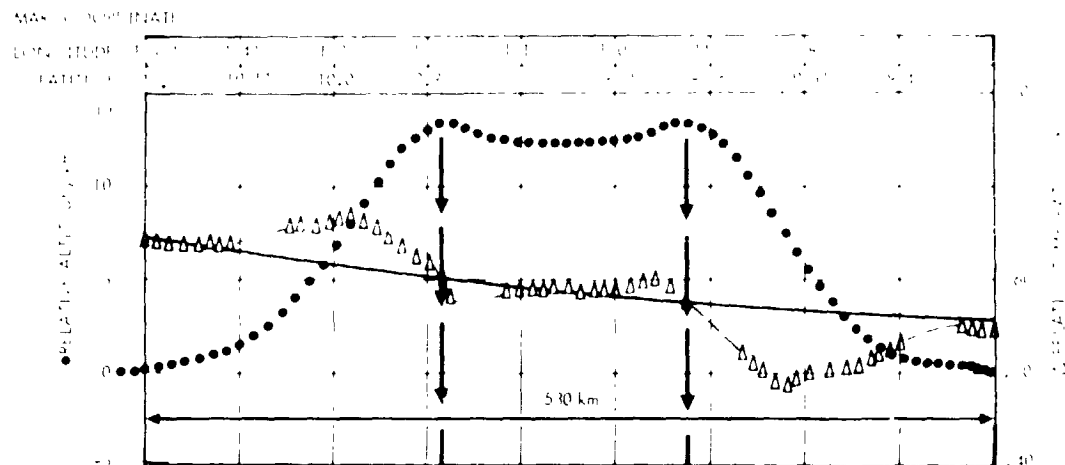


Fig. 46. IRR view of South Spot

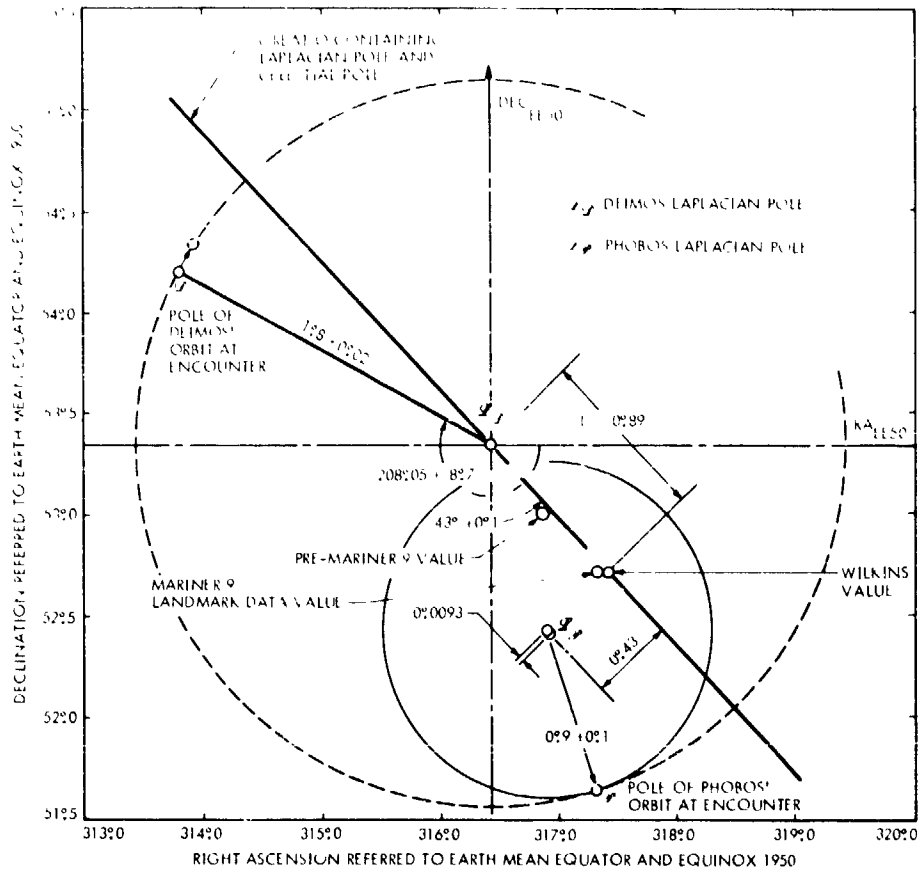


Fig. 47. North pole of Mars in Laplacian plane of Deimos

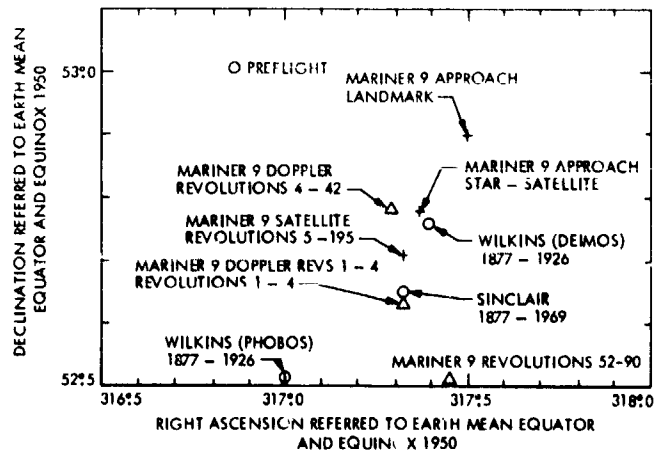


Fig. 48. Mars spin-axis direction solutions from Mariner 9 data

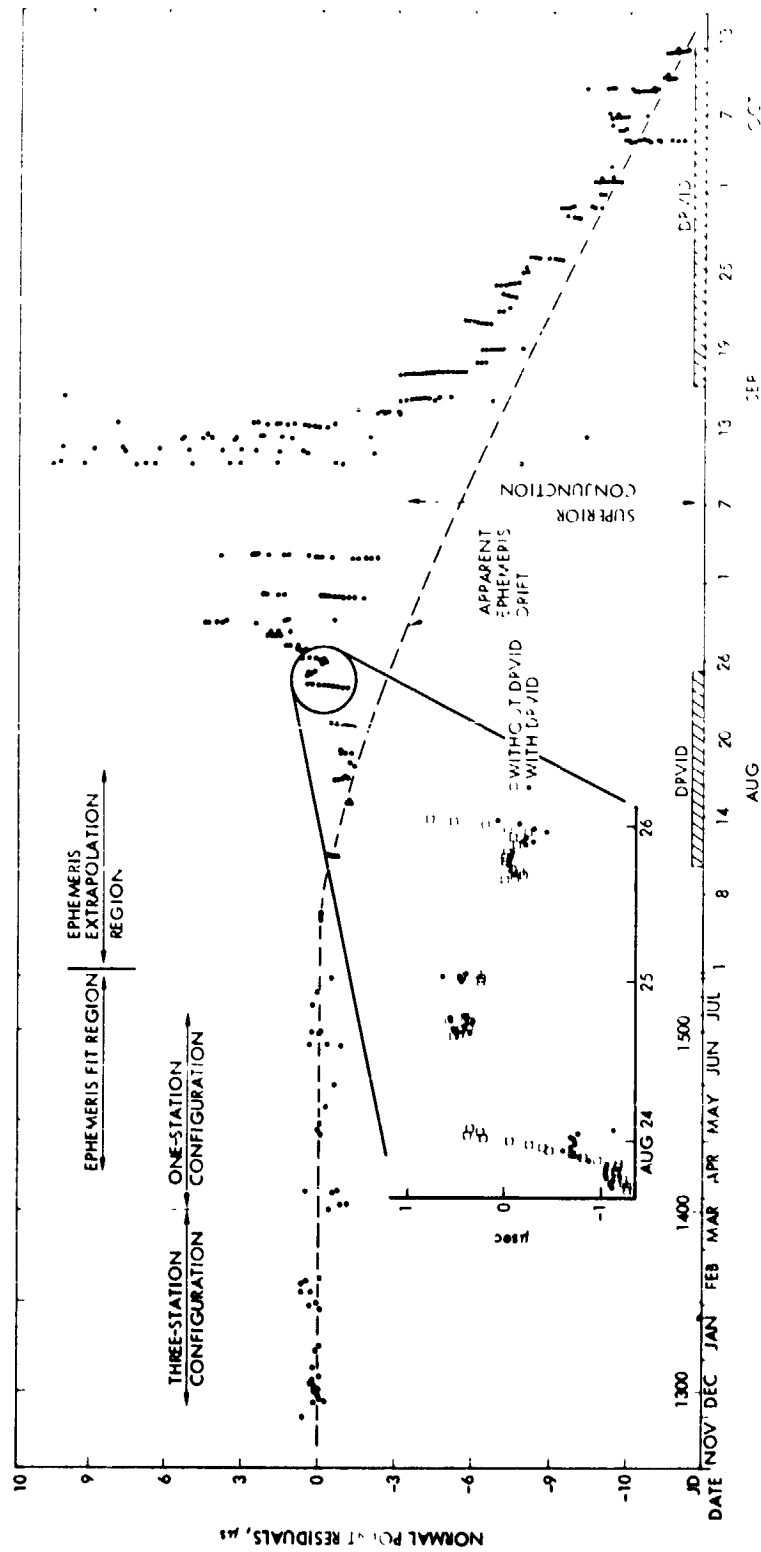


Fig. 49. Normal-point residuals referenced to fit to data through July 31, 1972 (Insert shows DRVID improvement through August 23 to 26, 1972.)

# Maneuver Analysis

R. T. Mitchell, G. R. Hintz, and G. Preston

The maneuver analysis for the Mariner 9 mission, both pre-launch and in-flight, was different from that of previous Mariners because of the requirement to insert the spacecraft into orbit about Mars and to trim the orbit to an unprecedented accuracy. The most apparent differences were in the spacecraft design, the software development, and the maneuver strategy required for each phase of the mission. This section describes the analysis that was performed and the software that was developed, with emphasis on the maneuver strategy and actual in-flight results.

## I. Strategy Evolution

The development of the maneuver strategy began early in mission planning and extended well into the interplanetary flight. Initial strategies were varied because analysis indicated different techniques for increasing

accuracy and reducing velocity-correction requirements. Additional changes were made as the scientific objectives evolved and became final, thus changing trajectory requirements and delivery accuracy specifications. The loss of Mariner 8 at launch, leaving only one spacecraft with which to perform the Mariner Mars 1971 (MM71) mission, also led to significant changes in the manner in which maneuvers were designed and implemented. The selection of the final target values for the orbit about Mars was completed about 2 months after launch, when the final experimenter inputs became available.

Initially, the two missions were identified as A and B, with target values of 1250- and 850-km periapsis altitude, 80- and 50-deg inclination, and about 12- and 33-h periods, respectively. The apsidal rotation, defined as the angle between the incoming asymptote and the elliptical periapsis direction, was specified as 130 and 155 deg, respectively.

The original plan for interplanetary maneuver targeting was to select aim points that would yield an orientation corresponding to the desired inclination, thereby allowing the orbital maneuvers to be planar, and to give **B**-magnitudes for minimum insertion velocity requirements. Previous work indicated that out-of-plane errors caused by orbit determination (OD) and maneuver execution errors were within specifications and would not require correcting. The insertion was to be targeted directly to the desired period, orientation, and periapsis altitude. Since post-insertion trajectory errors were expected to be large, primarily because of OD uncertainty on the approach hyperbola, two trim maneuvers were planned. The first was to correct periapsis altitude and orientation. The remaining period error would then cause the periapsis passage time to migrate into the Goldstone view period. A second trim would be performed at periapsis when the desired timing was achieved. This second trim would adjust the orbital period to about 12 h, thereby causing every other periapsis passage to occur near the middle of the Goldstone view period. The orbit would then be "synchronized" with Goldstone, maximizing the data return capability, as discussed in the *Introduction*.

The first change in this plan came early in the analysis, when it was observed that by biasing the target period at insertion to a larger value than was ultimately desired, two benefits could be obtained. First,  $\Delta V$  requirements were reduced because the probability of needing to restore energy to the orbit with a trim after removing too much at insertion could be reduced from 50% to nearly zero. The second benefit came from the fact that nearly synchronous post-insertion orbital periods would require more time to get into proper phase than those with larger period errors, since the periapsis migration would be slower. When starting with periods well above the synchronous value, the trim sequence would proceed much more rapidly and efficiently. Details of the actual implementation of this strategy are discussed later in this section.

After the failure of Mariner 8 at launch, a mission redesign took place to maximize the data that could be obtained with the single remaining spacecraft. The final orbit selected had a periapsis altitude of 1300 km, a period of about 12 h, an inclination of 65 deg, and the maximum achievable apsidal rotation ( $\psi$ ), which was a little over 142 deg for this orbit. It was determined that the delivery accuracy of the in-plane orientation of the orbit after insertion would be acceptable for meeting the mission objectives. This increased the overall mission reliability by requiring only one trim maneuver, which would correct the period, in those cases where the post-insertion

periapsis altitude was within tolerance. The Mariner 9 spacecraft was launched and the first midcourse maneuver performed under these ground rules.

The final decision on the desired orbit was made by the experimenters in July 1971, 2 months after launch. The periapsis altitude requirement was changed to allow any altitude in the range of 1200 to 1500 km, and the desired apsidal rotation was fixed at 140 deg. Based on this, a value of a 1350-km periapsis height was chosen to minimize the likelihood of requiring a post-insertion altitude correction. Changing these two target parameters also slightly changed the optimum **B** of the approach hyperbola from that in effect when the midcourse maneuver was performed. However, a fortuitous combination of execution and OD errors at the time of the first maneuver, plus an update of the Mars ephemeris during flight, resulted in a near-optimum spacecraft trajectory. Consequently, a second midcourse maneuver was not needed.

Additional details on maneuver strategy as it relates to actual maneuver implementation may be found in the following discussion of the design and performance of each maneuver. Further descriptions are also presented in Ref. 1.

## II. Maneuver Mechanization

The planned maneuver sequence for the Mariner 9 spacecraft was a gyro warmup period followed by a roll turn, yaw turn, and burn. Turns could be made of either polarity and for durations exceeding a complete revolution about either axis. The duration of the turns was controlled by counting a specified number of pulses, each 1 s in length. Hence, the computed turns to implement a correction had to be quantized to an integer number of seconds in duration, and could not be mechanized precisely. With a turn rate of about 0.18 deg/s, the maximum resolution error was 0.09 deg about both the roll and yaw axes. A similar situation existed for controlling the magnitude of the velocity correction. An accelerometer was used, which issued pulses for each 0.03 m/s (0.98 m/s for insertion), corresponding to a maximum resolution error of 0.015 m/s (0.48 in/s for insertion).

Two degrees of freedom existed, which allowed the effect of these resolution errors to be minimized. One was to alter the time of motor ignition, thus changing slightly the pointing and magnitude requirements. The second was to modify the direction of the maneuver in such a way

that critical target parameters were unchanged, and resolution errors were mapped into less important parameters. For the first midcourse maneuver, the sensitivity of the maneuver parameters to motor ignition time was so slight that no advantages could be obtained without changing ignition time to the point that it affected other operational considerations. The accuracy with which the **B**-vector magnitude was controlled was improved, however, by altering the arrival time so that the accelerometer resolution was eliminated. The errors caused by quantization of the insertion maneuver parameters were negligible when compared with expected execution and orbit determination errors and, hence, were simply rounded to the nearest integer pulse. A further motivation for doing this was the fact that the target parameters were interrelated in such a manner that it was not possible to absorb errors into a single one of them. The sensitivity to ignition time for the trim maneuvers was large enough that ignition time changes were used very effectively both to reduce resolution errors and to account for late changes in the orbit estimate.

A number of alternatives existed for controlling the start of motor burn, all of which involved use of the computer and/or sequencer on board the spacecraft. For the midcourse and trim maneuvers, when an aborted maneuver did not mean mission failure and was preferred to an anomalous maneuver, the spacecraft was operated in the tandem mode. In this mode, the computer and sequencer counted down simultaneously and aborted the maneuver if the count was out of synchronization. A ground command (DC-52) was issued to initiate the countdown for the tandem maneuvers. This flexibility was not available for the insertion maneuver because an abort meant total mission failure. Instead, the spacecraft was operated in a parallel mode, wherein both the computer and sequencer counted down to motor ignition without a fail-safe check, and either could initiate the burn. This countdown was initiated by a stored onboard command.

The execution errors associated with the mechanization of a maneuver may be classified as proportional to the maneuver magnitude, and fixed, and therefore independent of the magnitude. Resolution errors, caused by the quantization of commands, are included statistically

<sup>1</sup>Two independent roll/yaw turn sets exist that will achieve the desired thrust pointing direction, although, in general, the spacecraft orientation after implementation of each set would be different. By taking different combinations of turns, including the long way around (>180 deg), eight different turn sets are found which yield the required thrust pointing.

with the fixed errors. The  $3\sigma$  execution errors in both magnitude and pointing for Mariner 9 are shown in Table I.

### III. Maneuver Constraints

A number of constraints existed on the design of each of the maneuvers primarily on the turns that could be performed and on the timing of the maneuvers. Turn constraints were determined by the need to have down-link communications during the motor burn, and the requirements that certain of the instruments not be pointed to the Sun, Earth, or Mars. Figure 1 indicates the manner in which violation of turn constraints was checked. By superimposing on this figure the trace of the Sun, Earth, or Mars during the turns, an appropriate set of turns from among the eight possible could be determined.<sup>1</sup>

Specific instruments which imposed constraints were the infrared interferometer spectrometer (IRIS), TV, and Canopus sensor sun shutter. The constraint imposed by the latter instrument was precautionary because the purpose of the shutter was to protect the Canopus sensor from light sources such as the Sun. The precaution was necessary because, if the shutter failed either in the open position and the sensor was damaged by being exposed to direct sunlight or in the closed position, the spacecraft would be unable to maintain its star reference. Communication constraints, which required that the appropriate antenna be directed, with varying tolerances, to the Earth direction, were satisfied by incorporating this factor in the maneuver strategy at the outset. The aim points at launch and first midcourse were biased for the first and second midcourses so that, if the second midcourse were not needed, the bias would not have to be removed. Additional details on this biasing scheme are given later in this section. The medium-gain antenna was mounted so that it was aligned with Earth when the spacecraft was in the necessary orientation for insertion and for a phasing maneuver to reduce the period, in accordance with the orbital strategy discussed earlier. The only maneuver, based on the final strategy, with pointing requirements that would not allow use of the medium-gain antenna, was an apoapsis maneuver to lower periapsis altitude. Had the need for this maneuver arisen, the low-gain antenna would have been used. Spacecraft orientations in which neither antenna could have been used existed, but never would have been needed for the strategies employed.

The constraints on maneuver timing were that each maneuver be completed over a single tracking station and that near-Mars maneuvers be performed over the 64-m

antenna at Goldstone for better telemetry data. A final constraint, which applied only to the first maneuver, was that the magnitude exceed 5.6 m/s. This constraint was imposed to provide proper propellant settling and relocation of the gas bubble within the bladder because the spacecraft was "upside-down" at launch.

#### IV. Maneuver Software

The entire software package for the Mariner 9 mission, including that for preflight analysis and in-flight operations, consisted of many programs. The preflight design and analysis (D&A) programs were used for evaluation of various strategies and constraints, determination of propellant-loading requirements and delivery capability, and for providing insight to potential problems during operations. Operations programs were placed in two categories: category I programs had a formal certification and documentation schedule and consisted of the main programs used for decision-making and generation of commandable quantities, category II programs, which went through an equally thorough, though less formal, verification process generally were smaller programs used for checks, generation of supporting data and plots, printing of magnetic tapes, etc. A brief description of the D&A and category I programs follows.

##### A. Design and Analysis Midcourse

The D&A midcourse program used the selected sampling technique, rather than Monte Carlo, for generating statistics. The program had the capability to analyze two successive maneuvers and satisfy the planetary quarantine constraint by adaptively selecting aim points according to a specified strategy. Three such strategies existed with differing criteria for optimization. All execution and OD errors, and velocity requirements were computed in three dimensions, except that the second maneuver corrected only the B-plane miss resulting from the first maneuver. The principal output from this program was a three-dimensional histogram on  $B \cdot R$ ,  $B \cdot T$ , and velocity requirement. Single variable histograms were obtained by summing along the other two perpendicular axes.

##### B. Design and Analysis Insert

The D&A program for insertion studies used the three-dimensional histogram, or box, from the D&A midcourse maneuver program as input, and processed each entry, along with its associated probability, to determine insertion velocity requirements and delivery accuracy for the insertion maneuver. The program simulated a finite

burn for each point of the input box using numerical integration and supplied, as principal output, delivery statistics on the post-insertion orbital elements and associated total velocity statistics to this point in the mission.

##### C. Design and Analysis Trim

Two D&A trim programs were developed, one to analyze one-trim strategies and the other for two-trim strategies. Both programs accepted as input the velocity and delivery statistics from the insertion program and used two-body conic equations and impulsive maneuver models to determine velocity requirements, final delivery statistics, and optimum strategies in the presence of time constraints and requirements. These programs contained sophisticated algorithms for trim maneuver analysis and optimization, and provided a valuable insight to the overall trim problem. Their utility was limited, however, after the simplified strategy was developed following the loss of Mariner 8.

##### D. Command Midcourse

The command midcourse program was used for the calculation of the maneuver parameters for the interplanetary trajectory corrections. It required an interface with each of the following programs, also used in operation

- (1) Double precision trajectory program (DPTRAJ).
- (2) Orbit determination program (ODP).
- (3) Double precision analytic partials (DPAP).
- (4) Iterative search package (SEARCH).
- (5) Telecommunication performance (TPAP).
- (6) Trajectory monitor (TRAM).

The command midcourse program computed the precise maneuver parameters required to achieve the desired encounter, including compensation for the accelerometer resolution error, and printed other data required for off-line analysis of constraints and turn resolution error decisions. An impulsive burn model was used with the results verified by a finite burn simulation using DPTRAJ.

##### E. Command Insert

The command insertion program performed a similar function for the orbit insertion maneuver. The interface with other programs was the same, except for the addition

of the propulsion subsystem operations program (PSOP) needed for the finite burn modeling, and a different search routine to allow nonsquare searches to be performed. The nonunique convergence problem was handled by a weighted least-squares criterion.

#### F. Command Trim

The command trim program was similar to the injection program in overall structure and interfaces. A sophisticated strategy for selection of target values was developed within the program, but it was used only minimally with the final strategy selected.

### V. Injection

The launch vehicle was sufficiently accurate at injection that, after the aim point was biased to satisfy navigation constraints, the spacecraft orientation for the first maneuver was not random. As a result, it was possible to select a launch trajectory which would satisfy all the imposed constraints (discussed below) and lead to a midcourse maneuver with a preferred spacecraft orientation. A detailed description of the injection targeting process will indicate how this was accomplished.

The target selection process included specification of the launch vehicle orientations for launch vehicle/spacecraft separation, launch vehicle deflection, and the desired post-separation encounter parameters of the spacecraft, subject to a number of launch vehicle, spacecraft, and mission-related constraints.

A review of the near-injection sequence of events will prove helpful at this point. At main engine cutoff (MECO), when the launch vehicle/spacecraft was on a trajectory to Mars, the launch vehicle began to turn to a prespecified direction for separation, commonly referred to as the *a*-direction. Separation occurred at MECO plus 95 s. At 250 s after separation, the spacecraft ejected a radiation-absorbing plug from the medium-gain antenna. Sun and Canopus acquisitions occurred soon after separation. The launch vehicle coasted on a ballistic trajectory for 460 s following separation, maintaining its inertial attitude along *a*. At this point, the vehicle began to turn to a specified direction for a deflection maneuver designed to ensure that it was placed on a trajectory with no chance of impacting Mars. The deflection maneuver, whose thrust direction is commonly referred to as the *b*-direction, was initiated 95 s after the beginning of the turn to *b*, with a duration of about 20 s.

The selection of the *a*-direction had to be made in such a manner as to satisfy the following criteria:

- (1) The low-gain antenna of the spacecraft must be pointed in the earthward hemisphere of the spacecraft to achieve acquisition of signal.
- (2) The post-separation orientation of the spacecraft must be such that the Sun is acquired before the spacecraft enters the Earth's shadow, if possible.
- (3) The orientation must not cause the Sun track in spacecraft coordinates to pass through the TV field of view during Sun acquisition.
- (4) To satisfy the planetary quarantine constraint, the medium-gain antenna plug must not be ejected from the spacecraft into a trajectory which will impact Mars.
- (5) The maximum turning angle between the launch vehicle longitudinal axis at MECO and at separation must be about 90 deg to ensure that the launch vehicle is not still turning at separation.

The final value for *a* was chosen by turning the launch vehicle nose-down 90 deg from its MECO attitude in the trajectory plane, which provided the best possible geometry for criterion (1) subject to (5), and was entirely satisfactory for (2) and (3). The means of satisfying criterion (4) will be discussed later.

Constraints governing the selection of *b* were:

- (1) The launch vehicle must be turned far enough from its separation attitude to ensure that the deflection thrust does not accelerate the launch vehicle into the spacecraft.
- (2) The launch vehicle orientation at deflection must prevent exhaust gases from impinging on spacecraft optics.
- (3) The launch vehicle must not be deflected in a direction which would bring it within the field of view of the spacecraft Canopus sensor.
- (4) The deflection direction should map as nearly as possible, subject to criteria (1), (2), and (3), along the negative gradient of the probability density function of the injection error distribution, thus minimizing the risk of impacting the planet.
- (5) It is desirable to prevent the launch vehicle and the ejected antenna plug from colliding.
- (6) The maximum turn from the separation attitude should be about 90 deg.

The encounter conditions to be targeted for at injection were determined by the following considerations:

- (1) The constraint must be placed on the spacecraft system that the first maneuver magnitude be at least 5.6 m/s, as mentioned above.
- (2) The probability of impact associated with the selected encounter parameters, combined with the reliability of the spacecraft maneuver system, must satisfy the planetary quarantine constraint.
- (3) The targeting should be such that the maneuver required to remove the bias imposed by considerations (1) and (2) is oriented to minimize the effects of execution errors on the more critical encounter parameters.
- (4) The nominal maneuver to remove the bias, or any statistically likely dispersed maneuvers, must not violate any constraints on the first maneuver. In particular, it is desirable to bias in such a way as to provide favorable communications during the first maneuver.

Pre-launch statistical analyses of the launch vehicle injection characteristics indicated that a nominal bias velocity of about 8 m/s should satisfy the requirement of (1) to the 99% level. Since the low-gain antenna and the nozzle of the propulsion system are parallel, a maneuver which accelerated the spacecraft along the Earth-to-spacecraft direction would exactly align the antenna axis with the Earth. Further, it was determined that all statistical dispersions about this nominal velocity, caused by injection dispersions, satisfied all first maneuver constraints. The spatial miss correction in the B-plane associated with an 8-m/s maneuver along the Earth direction was larger than the bias required in that direction for planetary quarantine, thus satisfying the requirements of consideration (2). In fact, the required aim point at launch for such a maneuver was sufficiently far from the planet that, for even the most unfavorable spacecraft orientation at plug ejection, the plug could not have been put on an impact trajectory (see item 4 under selection of a). Because, for Mariner 9, pointing errors were the dominant source of execution errors, (3) was optimized by having the nominal maneuver lie in the plane of the gradients of the miss parameters. The Earth direction in general does not possess this property. However, over the MM71 launch opportunity, the Earth's angular distance away from this plane was relatively small, and the encounter parameter sensitivities at the first maneuver were not appreciably degraded by performing an Earth-line maneuver. Consequently, the injection targeting parameters were selected

to require an 8-m/s Earth-line maneuver at launch plus 5 days. Figure 2 indicates the  $B \cdot R$  and  $B \cdot T$  parameters as a function of time throughout the launch opportunity. The bias in arrival time, not shown in Fig. 2, was about 24 h later than the desired post-maneuver encounter time for each day in the launch period. Figure 3 shows the pertinent targeting data for the actual Mariner 9 launch date of May 30, 1971.

## VI. Interplanetary Maneuvers

The targeting parameters to be controlled by the one or more midcourse maneuvers are the B-vector magnitude, the inclination of the approach hyperbola, and the time of closest approach. The primary criteria for selection of these parameters are:

- (1) Select values which will be optimum for the insertion and trim strategy, including maximizing the likelihood of not needing more than one trim.
- (2) Satisfy the planetary quarantine constraint.
- (3) Bias the first maneuver aim point in such a way that the second maneuver will
  - (a) Have the effect of minimizing execution errors.
  - (b) Have favorable antenna pointing.
  - (c) Not have to be performed to remove this bias, if not needed for other reasons.

Based on the mission requirements at the time of the first maneuver and on the data of Fig. 4, a target value of 8200 km was selected for B-magnitude. This value would yield a  $\psi$  near the maximum, with a very low probability of  $\psi$  being less than 138 deg, and a high likelihood of achieving an  $h_p$  near 1300 km. The plan was for the insertion and trim maneuvers to lie in the trajectory plane of the spacecraft, thereby minimizing maneuver velocity requirements. Accordingly, a hyperbolic inclination of 65 deg, equal to the desired final orbital inclination, was selected.

A number of considerations governed the selection of the target arrival time. The first was to bias the first maneuver aim point to provide desired characteristics for the second maneuver. The magnitude of a second maneuver, performed within 30 days of encounter to correct for orbit determination and execution errors at the time of the first maneuver, was small, the 99% upper limit being less than 0.75 m/s. For maneuvers this small, the fixed magnitude execution error dominates the proportional errors. It will be shown later that the pre-insertion arrival

time can vary up to  $\pm 30$  min and be compensated for by the orbital strategy with very little effect on final delivery errors or on the one-trim probability. For this reason, a strategy that would direct the fixed magnitude error along the flight time direction is desirable. The need for such a strategy is demonstrated by noting that a  $3\sigma$  error of 0.1 m/s on a maneuver applied in the gradient plane of the miss parameters (critical plane) 30 days before encounter results in a miss of over 250 km. The same error perpendicular to the critical plane (noncritical direction) results in no miss and a change in arrival time of less than 1.5 min. By designing a maneuver with a large component along the noncritical direction and the required projection onto the critical plane, the component of the fixed error projecting onto the critical plane can be made arbitrarily small. This is illustrated in Fig. 5. There is a limit on how far such a process can be taken advantageously because, as the magnitude increases, the proportional errors increase. For a maneuver nearly along the noncritical direction, the pointing errors, which map onto the critical plane, are most significant. Figure 6 illustrates the technique used to determine that velocity component along the noncritical direction which gave minimum execution errors in the critical plane for an in-plane component of 0.75 m/s. A parametric analysis indicated that the minimum point of about 2 m/s was quite insensitive to variations in the in-plane component, and accordingly, a bias of 25 min, corresponding to 2 m/s, was introduced in the first maneuver target arrival time. Based on these accuracy considerations, there was no preference for biasing late or early. However, because a second maneuver to decrease flight time gave favorable antenna pointing, the first maneuver was targeted for a late arrival.

Two other considerations for selecting the arrival time were the requirement of the orbital strategy that the first periapsis after insertion occur about 2.5 h before Goldstone zenith, and the fact that the unbraked hyperbolic periapsis time would occur 10 min prior to the first elliptical periapsis. The determination of a target arrival time based on these three considerations is illustrated in Fig. 7.

The necessary maneuver parameters were calculated to correct the trajectory from that achieved at injection (Fig. 3) to one that would meet the target values given above. The magnitude, after compensation for the accelerometer resolution, was 6.731 m/s. The computed turns and the choices of commandable turns are shown in Table 2. Figure 8 demonstrates the rationale behind the decision to go to the next-larger turn in both roll and yaw, where it is seen that this combination gives not only the minimum miss but also a miss nearly perpendicular to the

B-vector, or in the inclination direction. This is a desirable situation, since B-magnitude control had a tighter requirement than inclination.

The estimated delivery results are given in Table 3. The *a priori* delivery statistics shown are based on having performed only one maneuver, and the estimated delivery was taken from OD solutions made within 2 weeks of the maneuver to allow separation of the maneuver execution errors from such items as ephemeris updates and non-gravitational forces. For this reason, these statistics will differ from other solutions shown elsewhere. The estimated maneuver parameters are presented in Table 4. It is important to note that the turn error estimates are not estimates of actual errors in performing the turns but rather a measure of the total pointing error expressed in equivalent roll and yaw errors. They therefore include the effects of such error sources as limit-cycle position and gyro drifts.

By the time a second midcourse maneuver would have been performed, about a month before encounter, the final orbital requirements had been set. The previous values of maximum apsidal rotation and a 1300-km periapsis, on which Fig. 4 was based, were changed to new values of 140 deg of rotation and an altitude of 1350 km. These new values increased the optimum value of B-magnitude to a little over 8200 km and allowed some savings in insertion velocity near this value, as shown in Fig. 9. The change in orbital requirements had very little effect on the interplanetary delivery target. Because the first maneuver was executed quite accurately and erred in the now preferred direction of increasing B-magnitude, it appeared that little was to be gained by performing a second maneuver, especially in view of the risk attendant in performing any maneuver. Nevertheless, a more quantitative investigation was performed, with the results shown in Fig. 10 and Table 5. The criteria for determining the need for this maneuver were (1) how it affected the probability of requiring only one trim and (2) its impact on the trim velocity budget. The result of considering (2) is presented in Fig. 10, where the trim velocity requirement is shown as a function of the post-insertion period, with and without the second maneuver. The discontinuity around 13 h is due to the fact that, at about this point, it would be desirable to allow periapsis to migrate completely around the planet with the loss of one revolution rather than to force a direction reversal in periapsis timing to achieve synchronization. It is apparent that no appreciable reduction in velocity requirements could be achieved by a second maneuver.

Table 5 indicates the changes that would be made and the resulting trim probabilities if the second maneuver were performed. The difference of 0.4 h in TBIAS (the difference in time between the first post-insertion periapsis and Goldstone zenith) is due to the 25-min bias introduced at the first midcourse, and the different target periods compensate for this bias. The total 99% velocity requirement is the same in either case, since the savings for insertion and trims, if the correction is made exactly, coincidentally equals the magnitude of the second maneuver. The trim probabilities are, for practical purposes, unchanged. Based on these data and the risk factor mentioned above, a decision was made not to perform the second maneuver.

## VII. Orbit Insertion Maneuver

In the earlier discussion concerning the evolution of the maneuver strategy, mention was made of the fact that an orbital strategy had been developed which required that the insertion be targeted to a period larger than the final desired value. The advantage of this is best described by explaining a graphical technique that was developed for analyzing and understanding this strategy. The ordinate of Fig. 11 is the difference between the time of periapsis and Goldstone zenith, and the abscissa is the number of revolutions the spacecraft has made in orbit. For convenience, the periapsis nearest insertion is defined as the zeroth periapsis; thus, the  $n$ th periapsis occurs after the  $n$ th revolution is completed. The box in the figure is bounded on the ordinate by the requirement that the final periapsis of the synchronized orbit occur within the time period from Goldstone zenith to zenith plus 1 h, and a final synchronizing maneuver made near periapsis must be made within, or at least very close to, this time span. The abscissa indicates a Project-imposed constraint that all trim maneuvers be performed between the fourth and 16th periapses. The one exception allowed is described in the next subsection. The time of periapsis is indicated for each even-numbered revolution, with a trim made at the sixth passage. Although the ordinate is defined only for integer values of the abscissa, lines are used on this type of figure for added clarity. A horizontal line indicates no change in passage time relative to Goldstone zenith with increasing revolutions, i.e., a synchronous period. Lines sloping upward to the right correspond to a less than synchronous period, and lines sloping down represent greater periods. To achieve a synchronous period with one trim maneuver, it is necessary that the line representing the period achieved at insertion pass through the box in Fig. 11. The *a priori* likelihood of the line intersecting this box ranged from 24% when no timing offset

was introduced up to a maximum of 64% for a bias of about 2.5 h (as shown in the figure), with a value of 59% for the bias of 2.1 h achieved as a result of not performing the second midcourse maneuver. If no timing bias is present, the probability of needing no trims is less than 1%.

The near-encounter geometry, including the Earth and Sun directions, motor thrust direction, and relative orientation of the hyperbola and ellipse, is shown in Fig. 12. A more detailed near-encounter sketch is presented in Fig. 13.

The delivery accuracy of the post-insertion ellipse is determined by the execution errors associated with the insertion maneuver, and by the OD errors associated with estimating the approach hyperbola. Figure 14 indicates the delivery statistics on period, periapsis altitude, eccentricity, and rotation based on the execution errors of Table 1, OD statistics on arrival time, and parametric in  $B$ -magnitude and the uncertainty in  $B$ . Sensitivity studies not shown indicated that, for values of  $\sigma_B$  greater than about 25 km, insertion delivery statistics are determined almost entirely by how well  $B$ -magnitude is known.

For reasons of reliability, Project policy stipulated that the orbit insertion maneuver commands were to be loaded in the spacecraft at least 24 h before the maneuver was performed, and that these commands were not to be updated subsequently unless the trajectory estimate changed so drastically that it would not be possible to trim the post-MOI orbit to the final desired orbit with the propellant remaining after execution of the MOI commands currently on board the spacecraft. This policy required the maneuver calculations to be performed well before the spacecraft was close enough to the planet to allow the Mars gravitational attraction on the spacecraft to provide an accurate trajectory estimate. As a result, the  $B$ -magnitude uncertainty at the time of the maneuver calculations was about 100 km ( $1\sigma$ ).

Table 6 shows the estimate of the approach trajectory at the time the maneuver was calculated, at the last possible time a change could have been made, and the final post-flight result. The errors shown are those which would result from applying the calculated maneuver to the later trajectory estimates. Figure 15 illustrates the expected trim situation by applying the calculated maneuver to the trajectory estimated at the last time the maneuver could have been updated. Although the nominal trim time was now on the fourth periapsis instead of the sixth, this was an acceptable result, and the errors of Table 6 were small

compared to the expected 1- $\sigma$  errors after insertion, therefore, the decision was made to not update the parameters.

The orbital values achieved by the insertion maneuver are shown in Table 7, together with the errors in delivery and their *a priori* statistics. The fact that the errors are nearly those predicted based on the final hyperbola of Table 6 indicates that the spacecraft performance was near nominal.

The estimated spacecraft performance in implementing the insertion maneuver is shown in Table 8. It is important to note again that the estimates of the turns shown are equivalent turns, which account for all sources of pointing error, and not estimates of the turns that were actually performed.

## VIII. Trim Maneuvers

### A. First Trim Maneuver

The objective of the trim maneuvers was to control the period and periapsis altitude of the spacecraft orbit to within specified tolerances and to satisfy constraints on the time of periapsis passage. It was desirable to have the spacecraft make two revolutions around Mars for each pass of Mars over the Goldstone tracking station. With appropriate periapsis passage timing, this would allow a tape recorder load of pictures to be taken on the nadir pass and played back early on the zenith pass. Another set would then be taken and played back during the zenith pass, leaving the tape recorder ready for the next picture-taking sequence on the nadir pass. This requirement was satisfied by synchronizing the orbit with the Goldstone view period such that every other periapsis passage would occur between Goldstone zenith and zenith plus 1 h. Altitude corrections were required only when the altitude was outside the 1200- to 1500-km range.

The trim maneuver strategy was designed to attain the required objectives while satisfying the maneuver constraints discussed earlier. According to this strategy, a sequence of up to three orbit trim maneuvers was to be performed to remove planned parameter biases and the effects of OD and maneuver execution errors remaining after the insertion maneuver. The sequence of maneuvers and the planned parameter biases determined by the trim strategy are discussed below.

The mission requirements were such that only orbital period, periapsis passage time, and possibly the height at periapsis required correction by orbit trims. As discussed

previously, the angle  $\zeta$  (and equivalently, the argument of periapsis  $\omega$ ) was controlled at insertion to an acceptable accuracy, and the inclination  $i$  of the orbit was adequately controlled by the midcourse maneuver. Given  $\zeta$  and  $i$  and the hyperbolic approach geometry, the longitude of the ascending node  $\Omega$ , which was uniquely determined based on a coplanar insertion, was completely satisfactory.

For the necessary parameter corrections, one, two, or three trims could have been required.

1. **No  $h_p$ -corrective sequences.** The insertion maneuver was targeted for an orbit having  $h_p = 1350$  km to maximize the probability that no  $h_p$ -corrective trims would be required. The desired initial periapsis time and mean orbital period were chosen to maximize the probability of requiring only one trim maneuver at periapsis to achieve the final orbit. If the initial periapsis time and period produced a timing curve that intersected the outlined box in Fig. 11, corresponding to a periapsis occurring satisfactorily over Goldstone, only one trim maneuver would be needed.

A periapsis time and period combination that missed the box would require two period-change trim maneuvers. These misses could be

- (1) To the left resulting from too large a period at insertion (pre-insertion probability = 18%).
- (2) To the right resulting from too small a period (pre-MOI probability = 18%).

The expected post-insertion errors for periapsis time ( $\sigma_t \approx 0.25$  min) were much less than the expected post-insertion period dispersions. Therefore, in computing trim probabilities, the "zeroth" periapsis time dispersions were ignored. The initial period was assumed to be a normal random variable.

2. **With  $h_p$ -corrective sequences.** If the post-insertion height at periapsis had been greater than 1500 km, it would have been necessary to correct it down to 1500 km, and if less than 1200 km, up to 1200 km. Hence, it was necessary to consider those cases in which correction of this parameter was required.

Whereas the period-change maneuvers discussed above are most efficiently made at periapsis, it is impossible to correct  $h_p$  by a maneuver at this location. In fact, the most efficient location for correcting  $h_p$  is at apoapsis.

The maneuver sequence selected to meet the  $h_p$  requirement consisted of one or two (as needed) period-change maneuvers, followed by an  $h_p$  correction at the 19th apoapsis passage after insertion. This situation was the one exception allowed to the constraint that all trims be performed by the 16th revolution. The periapsis maneuvers in this sequence are the same as those discussed above, except that it is necessary to anticipate the change in period caused by correcting  $h_p$ . This makes it necessary to introduce a bias in the phase time with respect to Goldstone zenith experienced at  $P_{19}$ , and in the orbital period. The final trim maneuver at the 19th apoapsis is then executed to simultaneously correct  $h_p$ , correct the orbital period to 11 980 h, and adjust the phase time to within the acceptable interval.

As mentioned above, the necessary corrections to achieve the final orbit could have required one, two, or three orbital trims. Figure 16 shows the number of orbital trims that would have been required as a function of post-insertion period and  $h_p$ . It should be noted that regions of high period and low  $h_p$  dispersions (and vice versa) in Fig. 16 are of no concern because of the high correlation between the post-insertion period and  $h_p$ .

Figure 16 also indicates total velocity cost contours for the trim maneuver sequence. For example, if the post-MOI period and  $h_p$  values had been 12.6 h and 1590 km, respectively, then 30 m/s would have been needed to execute a three-maneuver sequence. The determination of the probability that only one trim maneuver would be required for given predicted or estimated values of period,  $h_p$ ,  $\sigma_p$ , and  $\sigma_{h_p}$  was made as follows. It was assumed that the post-insertion period and  $h_p$  had a positive unit correlation. Hence, the set of possible period and  $h_p$  values lie along a line in period vs  $h_p$  space. A transparent overlay, consisting of a line with slope  $100 \text{ km}/0.407 \text{ h} = 245.7 \text{ km/h}$ , determined from a knowledge of the sensitivities of period and altitude with respect to B errors, was constructed. This overlay was superimposed on Fig. 16 to determine the period values at the points of intersection of this line with the boundary lines in the figure. For the line shown in the figure, the probability of requiring only one trim is equal to the probability that the period (a normal random variable) would fall between 12.11 and 12.75 h. The probabilities of requiring two or three trims were determined in a similar manner.

The probability of requiring only one trim at  $P_1$  or  $P_2$  was determined by integrating the probability density over the interval for which one such trim could be performed. For a time of periapsis passage at  $P_1$  of 2.1 h

before Goldstone zenith, one trim could be performed at  $P_1$  if  $12.51 < \text{period} < 12.76 \text{ h}$  or one could be performed at  $P_2$  if  $12.33 < \text{period} < 12.49 \text{ h}$ .

An important operational consideration was the need to use the latest OD solution to calculate the maneuver parameters. After the spacecraft was inserted into orbit, tracking data were processed to predict the orbital parameters at the time of the trim maneuver. The collecting and processing of tracking data was to continue during, and subsequent to, the calculation of the trim maneuver. Hence, it was expected that the spacecraft orbit estimate would be updated after the time when a maneuver had to be loaded into the spacecraft onboard computer. The desired period correction for achieving a Goldstone-synchronous orbit might therefore change subsequent to maneuver loading.

It was important to use the updated OD solution because it did not require predicting as far ahead to the maneuver time as the original solution. Predicting far ahead could result in significant OD errors because of the large uncertainty in the Mars gravity field as it was then known.

In loading the maneuver into the spacecraft, three maneuver parameters (the velocity magnitude, the roll turn, and the yaw turn) had to be specified well in advance of implementing the maneuver. The maneuver sequence was then started by receipt of a ground command (DC-52). Hence, the capability to increase or decrease the period change resulting from the trim, based on updated orbit estimates, had to be achieved by adjusting only the maneuver start time. However, because a period correction can most efficiently be performed at periapsis, adjusting the start time of a maneuver designed for periapsis can only decrease the resulting period change. Therefore, it was decided that the maneuver would be computed for a point near, but not at, periapsis. It was determined parametrically that the point 20 min prior to the desired periapsis would give sufficient flexibility to update the required period change without paying a significant velocity penalty for performing the maneuver away from periapsis.

The capability to change the orbital period by merely adjusting the maneuver sequence start time (equivalently, the ignition time) is illustrated in Fig. 17. For a velocity increment of 16 m/s and fixed spacecraft orientation, it was possible to decrease the period by about 1.5 min, or to increase it by up to 3.5 min. Figure 17 also shows that there are two ignition times corresponding to a desired

period change. This fact provided a backup capability because it was possible to send a command for the motor to ignite at the second point if it had not already done so at the first. The effect of early or late motor ignition is shown in Fig. 18.

Finally, the knowledge of the sensitivity of the orbital parameters to maneuver parameters, shown in Figs. 19 to 22, was used to demonstrate that performing the maneuver 20 min before periapsis passage would not produce unacceptable values for other parameters ( $h_p$ ,  $\omega$ ,  $i$ , and  $\Omega$ ). Therefore, the point 20 min before periapsis passage was selected for the optimum maneuver ignition time. The information presented in Figs. 19 to 22 also proved useful in other situations while the trim strategy was being developed and studied. The velocity coordinate system used in these figures is defined in Fig. 23.

Very precise period control was achieved by using the ground-based maneuver-start command. The period was the main orbit parameter of interest because period errors would accumulate in periapsis timing errors. Motor ignition for the first trim maneuver occurred on November 16, 1971, at 02:36:53 GMT at the spacecraft, with a burn duration of 6.25 s. The commanded velocity correction was 15.25 m/s, corresponding to a discrete pulse count of 506. The spacecraft turns required to achieve the pointing for implementing the computed velocity vector were a roll of 34.49 deg and a yaw of 128.76 deg. These turns were quantized to a commandable roll turn of 34.443 deg and a commandable yaw turn of 128.732 deg. The maneuver performance for the first trim is summarized in Tables 9 and 10. The maneuver parameters are presented in Table 9, which gives the commanded values and estimates of the actual values for each parameter, together with associated errors and statistics. The achieved orbit elements are shown in Table 10, together with associated errors and statistics.

The actual maneuver parameters were estimated by reconstructing the maneuver from the best OD estimates of the pre-maneuver and post-maneuver orbits. The OD estimates were computed some time after the performance of the maneuver, utilizing the best data and model available. Again, turn estimates are to be interpreted as equivalent turns accounting for the total pointing error.

OD data indicate that the important orbital parameter, the period, was achieved to within 1 s of the desired value (Table 10). This precision was produced by adjusting the maneuver start time by a ground-based command, as

described above. OD data up to a few hours before the maneuver were utilized in computing this updated start command, which was sent exactly 1 min earlier than the value previously planned. This 1-min adjustment was required to produce about a 15-s change in the period correction (see Fig. 17).

## B. Second Trim Maneuver

The delivery accuracy of the first trim maneuver was very good, as shown in Table 10, and was well within the mission requirement. Normally, the objective of performing only one trim maneuver would have been satisfied. However, as the mission progressed, it became apparent that a second maneuver would be needed because (1) the presence of a dust storm made it necessary to extend the planned 90-day orbital mapping mission, and (2) the unexpected nature of the Mars gravity field caused the period of the orbit to behave in a sinusoidal manner, with a mean period 25 s smaller than the desired synchronous period. As a result, the periapsis time was moving through the Goldstone view period and would have been well out of the required time zone before the end of the now-extended mission.

Based on data obtained in the first part of the mission and on the fact that a second trim was required anyway, the science team decided to raise periapsis altitude to 1650 km. The most efficient technique, in terms of  $\Delta V$  expenditure, for adjusting both period and periapsis altitude is to perform two maneuvers, each parallel to the local spacecraft velocity, one at periapsis and one at apoapsis. The apoapsis maneuver corrects the altitude and will change the period. The second maneuver at periapsis then adjusts to the desired period. With this technique, the corrections planned for the second trim would have required about 22 m/s. An alternative method was to perform a single correction at either of the two points of intersection of the current and the desired orbit, which would require a velocity change of about 42 m/s. Because of the standard performance throughout the mission, there was ample  $\Delta V$  capability remaining at this point. Therefore, a decision was made to use the single-impulse option for reliability reasons.

An analysis of the geometry involved indicated that the maneuver would have to be performed at the second intersection (true anomaly  $> 180$  deg) to provide for communications. By adding a small out-of-plane component to the maneuver and rotating the target orbit slightly, it was possible to align the axis of the medium-gain antenna along the spacecraft-to-Earth direction for

excellent communications. The strategy employed for this maneuver is best explained by noting that in-plane perpendicular and colinear components of the maneuver velocity relative to the local spacecraft velocity map independently to altitude and period changes, respectively. Further, since the desired changes were about 250 km in altitude and 79 s in period, the maneuver would be, essentially, all in the perpendicular direction. Accordingly, the maneuver was designed so that the inertial spacecraft orientation would both align the medium-gain antenna with Earth and orient the spacecraft thrust vector perpendicular to the local velocity at the intersection of the pre- and post-trim orbits. Thus, small variations in the ignition time, allowing the local velocity to rotate, would give the required projection of the correction velocity onto the local spacecraft velocity for the desired period correction. By incorporating last-minute OD data in the calculations of the ignition time and using the ground command capability, this technique resulted in very good delivery accuracy. The geometry of the second trim, and its effects and implementation are shown in Fig. 24. Tables 11 and 12 indicate spacecraft performance and delivery accuracy, respectively, for the second trim.

By mid-March of 1972, the planned mapping mission was completed, and the spacecraft was still performing essentially as planned. However, by this time, the Earth-Mars-Sun alignment had changed to the point that the high-gain antenna could no longer transmit data to Earth while the spacecraft was Sun-oriented; furthermore, the instruments could no longer view Mars with Canopus used for the spacecraft roll reference. The latter problem was solved by using, at various times, the stars Vega, Arcturus, and Canopus as the roll reference. To extend the mission data return after mid-March, spacecraft turns were performed to align the antenna axis to Earth to play back the data now made available by the different roll reference. One or the other of two turn sequences, either a roll-yaw or yaw-roll, would have been able to give the desired orientation. However, a constraint on the turns that could be performed was the need not to turn the solar panels too far off the Sun, which would cause the spacecraft to draw too much energy from the battery. By using a roll-yaw-roll turn sequence to minimize the required magnitude of the yaw turn, or equivalently, the angle of the panels off the Sun, satisfactory spacecraft orientations could be found. This technique was used 13 times between March 23 and October 17 to permit data playback. Thus, the useful mission duration was extended by about 7 months.

## IX. Contingency Insertion Planning

To successfully implement the insertion maneuver, it was necessary to transmit the maneuver parameters to the spacecraft from the ground. An unlikely but possible failure mode of the spacecraft could make it impossible to transmit such commands at some time during the mission. To ensure the maximum probability of placing the spacecraft in orbit, the decision was made to load a set of insertion maneuver commands in the spacecraft soon after the first midcourse maneuver. These commands could be updated as required when the trajectory estimate changed or subsequent maneuvers were performed. If command capability were then lost, the loaded maneuver would accomplish an insertion—though perhaps significantly different than desired—from which the mission could be salvaged if command capability were later restored. Table 13 indicates the maneuver commands that were first loaded and the time history of their updates. Because command capability was not lost, this contingency plan was not used.

The implications of the planetary quarantine constraint on loading a maneuver in the spacecraft motivated a study to ensure that this constraint was indeed satisfied. Three possible failure modes during cruise which could lead to possible impact were identified as (1) motor ignition while the spacecraft was in the cruise attitude, (2) motor ignition after performance of the commanded turns, and (3) motor ignition with the spacecraft in any random orientation. Each of these modes could be further subdivided into cases wherein the stored  $\Delta V$  magnitude was implemented and in which the fuel was burned to depletion. However, these distinctions proved unnecessary because the computed  $\Delta V$  magnitude was greater than 95% of the remaining capability. The three failure mode cases defined are discussed individually below:

- (1) *Case 1.* It was determined that a motor ignition at any time from the first midcourse to encounter with the spacecraft in the cruise attitude would not result in an impact trajectory.
- (2) *Case 2.* There existed a small region near encounter where an impact trajectory would have resulted if the loaded turns had been implemented and the motor ignited. Very few quantitative data were available on the probability of such an event occurring prematurely, and estimates provided by the Spacecraft Team ranged from the most pessimistic of  $10^{-4}$  down to "impossible." Assuming that the occurrence of such an event was equally likely at any time after the commands were loaded until encounter, the probability of its taking place within

the time span in which an impact would occur times  $10^4$  gave a final impact worst-case probability well below that allocated to insertion.

- (3) *Case 3.* From the first maneuver time until about 10 days before encounter, a premature burn would have required a specific pointing direction with tight tolerances to achieve an impact trajectory. By dividing the area that this pointing cone traces out on a unit sphere by  $2\pi$  steradians, the probability is shown to be well below the constraint level, without any allowance for the likelihood of such an event occurring. Near encounter, two pointing directions can lead to impact. A  $\Delta V$  applied nearly

along the spacecraft velocity can deflect the spacecraft into the planet, and a  $\Delta V$  approximately along the negative spacecraft velocity will slow the spacecraft, thus increasing the capture area and leading to impact. Figure 25 indicates the pointing directions relative to the incoming asymptote that would cause impact, and Fig. 28 illustrates the probability of achieving these pointing directions, assuming the pointing to be uniformly distributed over a sphere. By multiplying these probabilities by the likelihood of a random orientation and motor ignition occurring, conservatively estimated at  $10^{-3}$ , the resulting probabilities are found to be well below the constraint level.

## Reference

1. Mitchell, R. T., and O'Neil, W. J., "Maneuver Design and Implementation for the Mariner 9 Mission," AIAA/AAS Astrodynamics Conference, Palo Alto, Calif., Sept. 11-12, 1972.

**Table 1. Maneuver-execution error statistics, 3  $\sigma$**

	Midcourse	Insertion	Trim
Proportional magnitude, %	0.15	0.13	0.12
Fixed magnitude, m/s	0.1	0.84	0.1
Pointing, mrad	23.8	20.2	22.8

**Table 2. Ideal and commandable turns**

Turn	Commandable	Ideal	Commandable
Roll, deg	-140.887	-140.88	-140.806
Yaw, deg	-44.907	-44.79	-44.725

**Table 3. Interplanetary delivery results**

	Target	Achieved	Error	A priori 1 $\sigma$ *	Ratio of error to $\sigma$
B-direction	8200 km	8281 km	61 km	100 km	0.2
Inclination	65 deg	64.23 deg	0.77 deg	3 deg	0.3
Time of closest approach	11/14 00:29:00	11/14 00:31:09	2 min, 9 s	7.5 min	0.3

\*Based on one-maneuver statistics.

**Table 4. First midcourse maneuver performance**

Maneuver parameter	Estimated actual value	Command value	Error	A priori 1 $\sigma$	Ratio of error to $\sigma$
Roll turn	-140.717 deg	-140.806 deg	-0.089 deg	0.289 deg	0.31
Yaw turn	-44.725 deg	-44.628 deg	0.097 deg	0.289 deg	0.34
$\Delta V$	6.723 m/s	6.731 m/s	0.008 m/s	0.036 m/s	0.22

**Table 5. Second midcourse maneuver tradeoffs**

Parameter	Without midcourse maneuver 2	With midcourse maneuver 2
TBIAS ( $T_{r_0} - T_{e_s}$ ), h	-2.1	-2.5
MOI* target period, h	12.43	12.50
$\Delta V$ total 99% high, m/s	1661.0	1661.0
Rotation angle $\pm 3 \sigma$ , deg	140.0 $\pm$ 2.4	140.0 $\pm$ 2.4
Inclination $\pm 3 \sigma_{inc}$ , deg	64.3 $\pm$ 2.7	65.0 $\pm$ 2.7
Trim probabilities, %		
One trim	59	63
One P6 trim	15	15
Two trims	29	30
Three trims	12	7

\*Mars orbit insertion.

**Table 6. Pre-insertion OD results and predicted errors**

	Calculation	Decision	Final
Results			
B, km	8209	8235	8281
Inclination, deg	63.87	64.02	64.23
Time of closest approach, GMT	00:31:07	00:31:03	00:31:09
Predicted errors			
$\delta P$ , min:s		7:24	14:52
$\delta h_p$ , km		21	40
$\delta \psi$ , deg		-0.1	-0.1

Table 7. Insertion results

	Target	Achieved	Error	A priori 1 $\sigma$	Ratio of error to $\sigma$
Period	12 h 25 min	12 h 34 min	9 min	17 min	0.53
$h_p$	1350 km	1398 km	48 km	69 km	0.69
$\psi$	140.0 deg	139.7 deg	-0.3 deg	0.6 deg	0.5
Inclination	64.1 deg	64.36 deg	0.26 deg	0.8 deg	0.33

Table 8. Insertion performance

Maneuver parameter	Estimated actual value	Commanded value	Error	A priori 1 $\sigma$	Ratio of error to $\sigma$
Roll turn	42.591 deg	42.765 deg	-0.174 deg	0.273 deg	0.637
Yaw turn	125.220 deg	124.898 deg	0.322 deg	0.273 deg	1.18
$\Delta V$	1600.647 m/s	1600.50 m/s	0.147 m/s	0.733 m/s	0.201
$T_{ign}$ , GMT	318,00:17:39	318,00:17:39	0	-	-

Table 9. First trim performance

Maneuver parameter	Estimated actual value	Commanded value	Error	A priori 1 $\sigma$	Ratio of error to $\sigma$
Roll turn	34.462 deg	34.443 deg	0.019 deg	0.285 deg	0.067
Yaw turn	128.807 deg	128.732 deg	0.075 deg	0.285 deg	0.263
$\Delta V$	15.26 m/s	15.25 m/s	0.01 m/s	0.038 m/s	0.263
$T_{ign}$ , GMT	320,02:36:53	320,02:36:53	0	-	-

Table 10. First trim results

	Target	Achieved	Error	A priori 1 $\sigma$	Ratio of error to $\sigma$
Period	11 h 58 min 48 s	11 h 48 min 49 s	1 s	3.5 s	0.29
$H_p$	1367 km	1367 km	~0	0.3 km	~0
$\psi$	140.3 deg	140.3 deg	~0	0.03 deg	~0
Inclination	64.37 deg	64.37 deg	~0	0.03 deg	~0

**Table 11. Second trim performance**

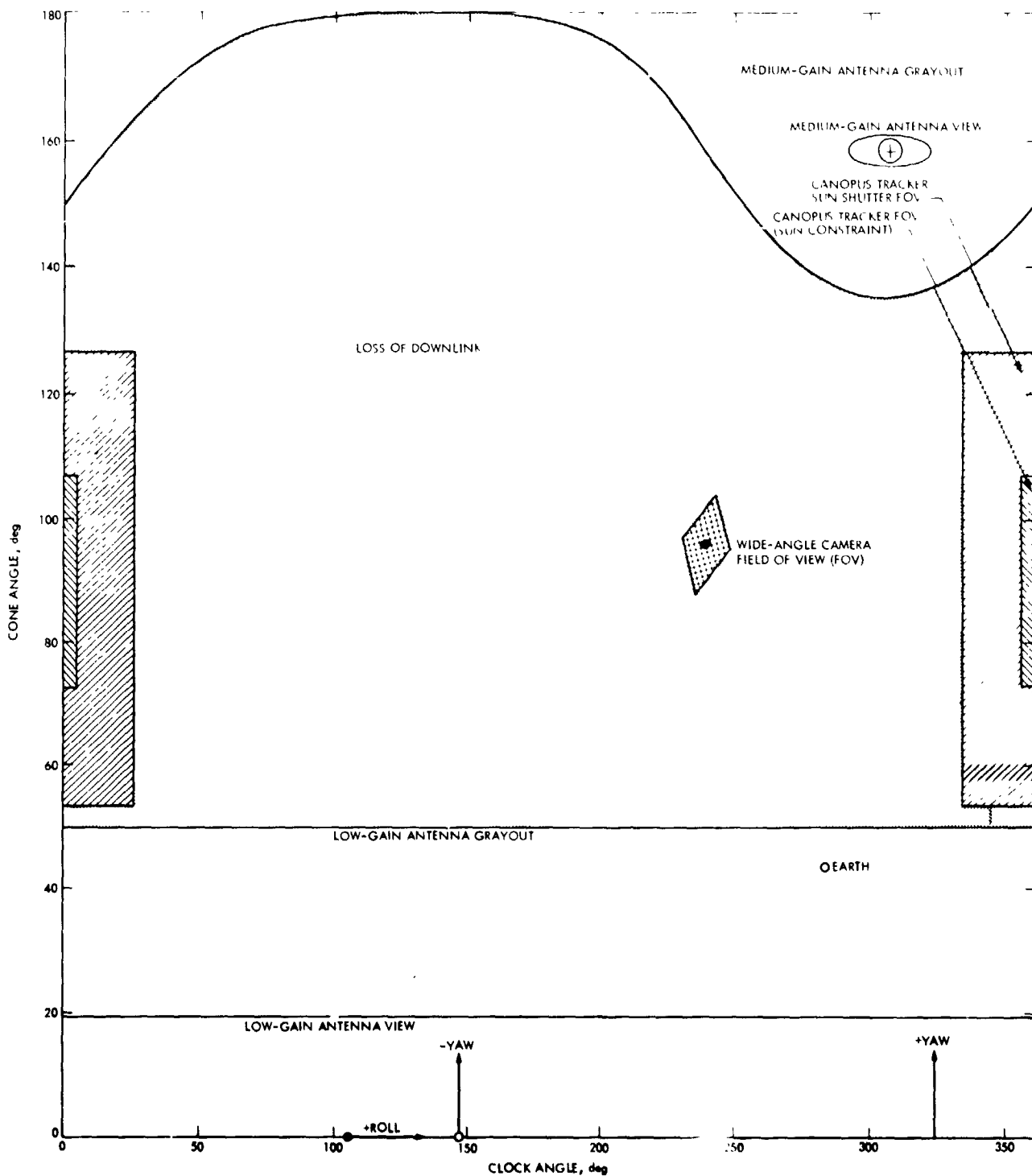
Maneuver parameter	Estimated actual value	Commanded value	Error	A priori 1 $\sigma$	Ratio of error to $\sigma$
Roll turn	33.746 deg	32.996 deg	0.750 deg	0.285 deg	2.63
Yaw turn	118.730 deg	118.255 deg	0.475 deg	0.285 deg	1.67
$\Delta V$	41.925 m/s	41.81 m/s	0.115 m/s	0.041 m/s	2.80
$T_{1,GN}$ , GMT	364, 21:48:59	364, 21:48:59	0	—	—

**Table 12. Second trim results**

	Target	Achieved	Error	A priori 1 $\sigma$	Ratio of error to $\sigma$
Period	11 h 58 min 58 s	11 h 58 min 52 s	-6 s	13.2 s	0.45
$h_p$	1650 km	1650 km	~0	0.3 km	~0
$\omega$	-26.09 deg	-26.02 deg	0.07 deg	0.1 deg	0.7
Inclination	64.43 deg	64.40 deg	-0.03 deg	0.1 deg	0.3

**Table 13. Contingency insertion maneuver data**

Parameters	Original insertion maneuver commands	First update	Second update
<b>Trajectory estimate</b>			
Approximate date	Mid-June	Mid-July	Early October
B • R, km	6011.4	6064.8	6081.5
B • T, km	5643.0	5640.3	5621.4
B, km	8245.0	8282.2	8281.6
Time of closest approach, (GMT), Nov. 14, 0 h, min:s	30:58.4	30:55.8	31:16.4
<b>Maneuver parameters</b>			
Roll turn, deg	41.32	No change	No change
Yaw turn, deg	125.57	No change	No change
$\Delta V$ , m/s	1617.13	1621.94	No change
$T_{1,GN}$ , (GMT), Nov. 14, 0 h, min:s	14:41.4	15:11.1	15:24.0



1. PLATFORM STOWED (23 deg CLOCK, 96.4 deg CONE)
2. ROLL/YAW TANDEM MANEUVER
3. TELECOMMUNICATION AREAS FOR DOWNLINK ONLY
4. BATTERY SHARE AT 25 deg CONE AND BATTERY ONLY AT 85 deg CONE
5. MARS NOT TO BE IN FOV OF CANOPIUS STAR TRACKER AT END OF EITHER TURN

Fig. 1. Maneuver constraints on Mariner 9 orbit trim 2, December 30, 1971

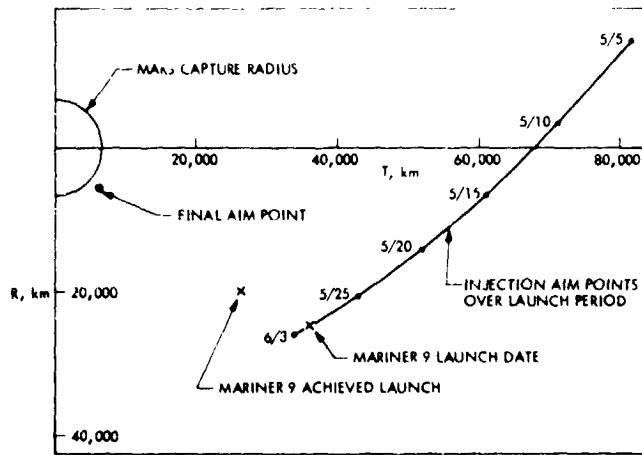


Fig. 2. Targeting data at injection

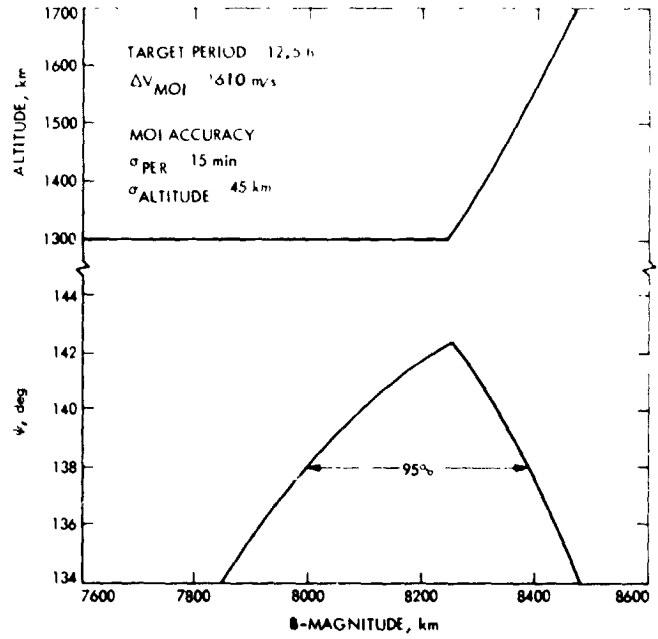


Fig. 4. Mars orbit insertion

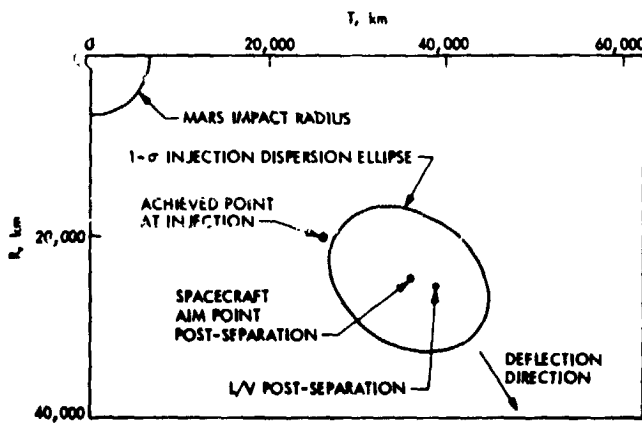


Fig. 3. Targeting data for launch

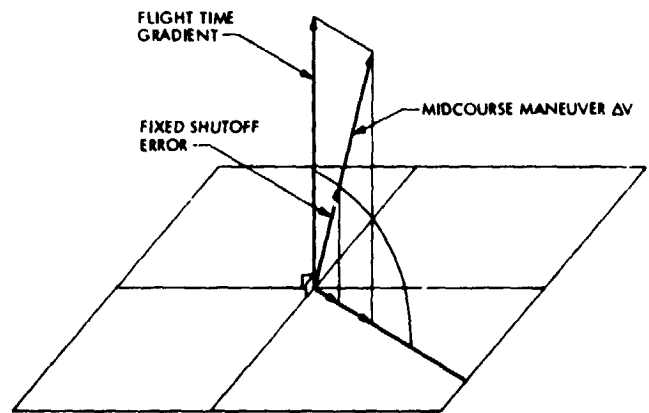


Fig. 5. Second midcourse maneuver accuracy improvement

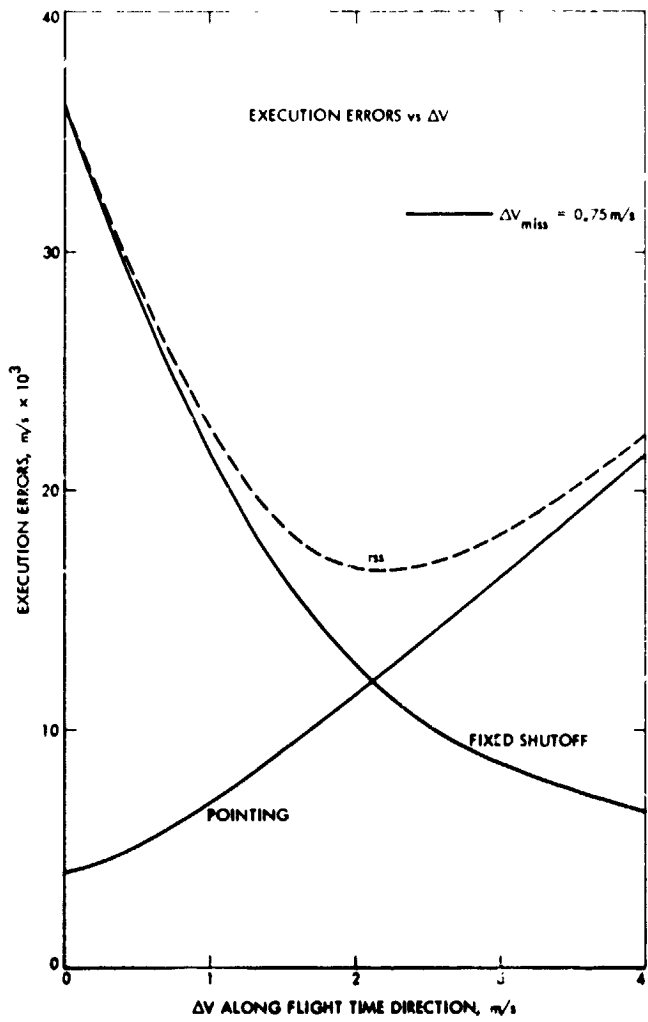


Fig. 6. Execution errors vs  $\Delta V$

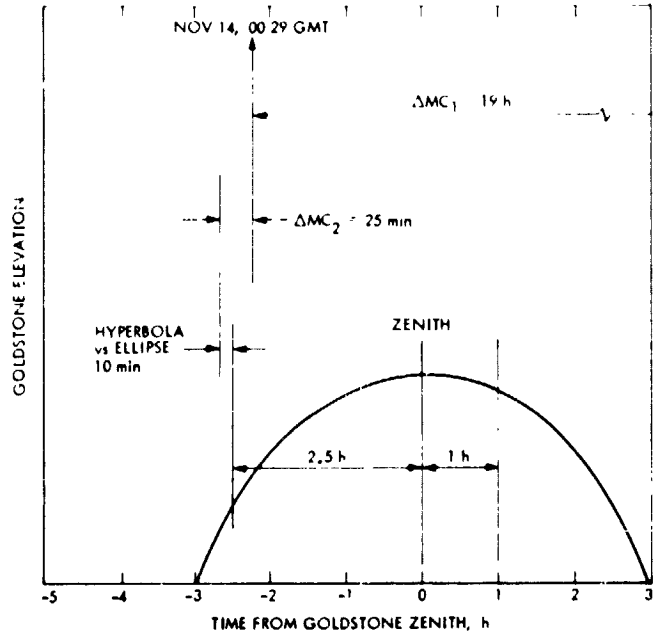


Fig. 7. Arrival time target

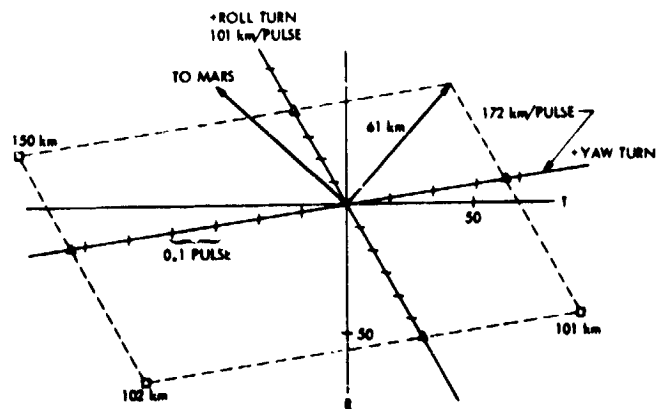


Fig. 8. Turn quantization

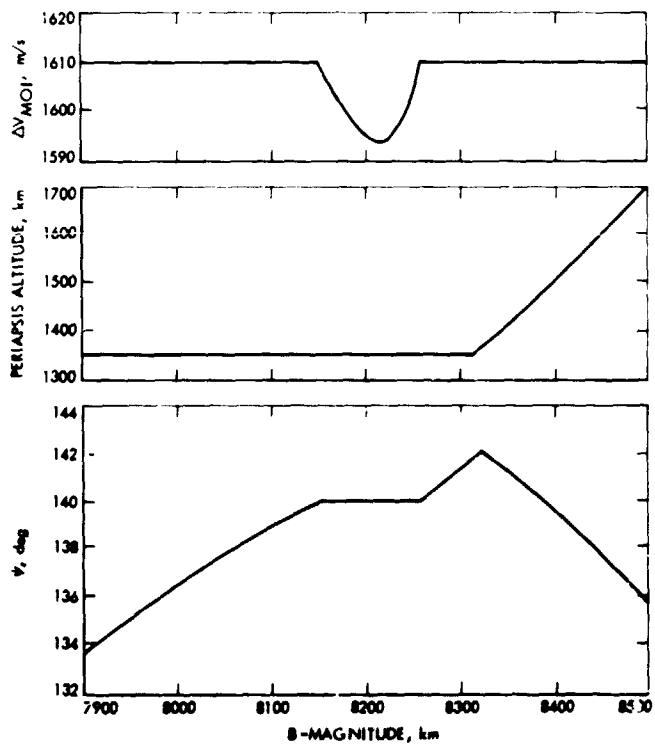


Fig. 9. Mars orbit insertion target criteria

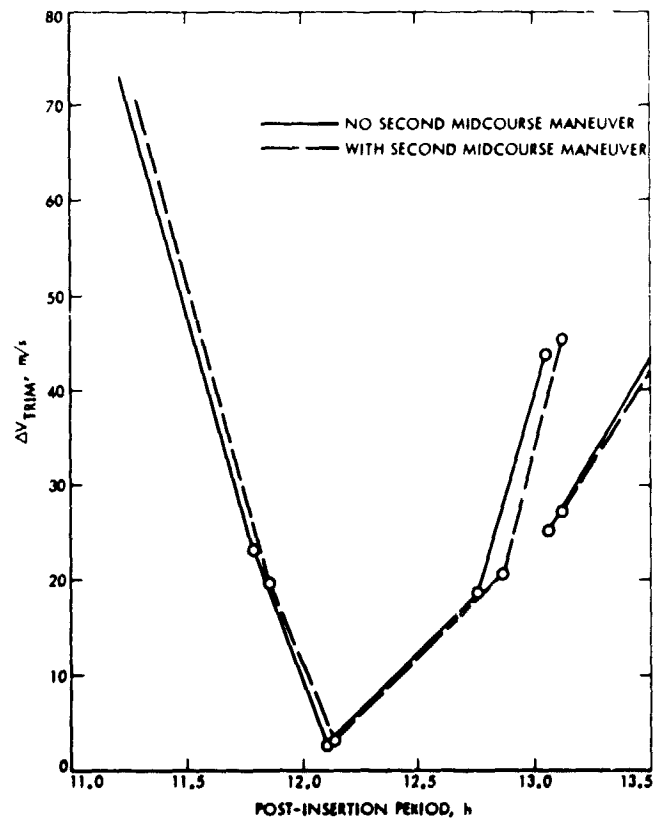


Fig. 10.  $\Delta V$  trim

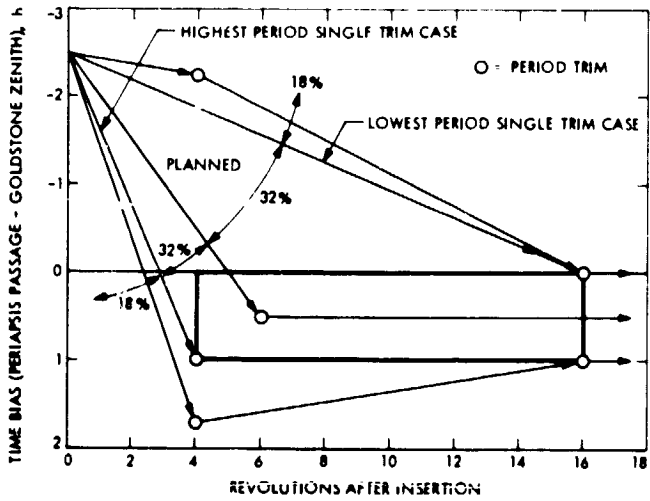


Fig. 11. Orbit trim strategy

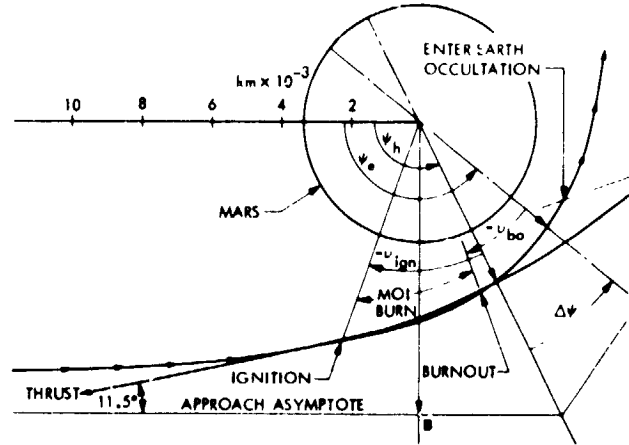


Fig. 13. MOI geometry

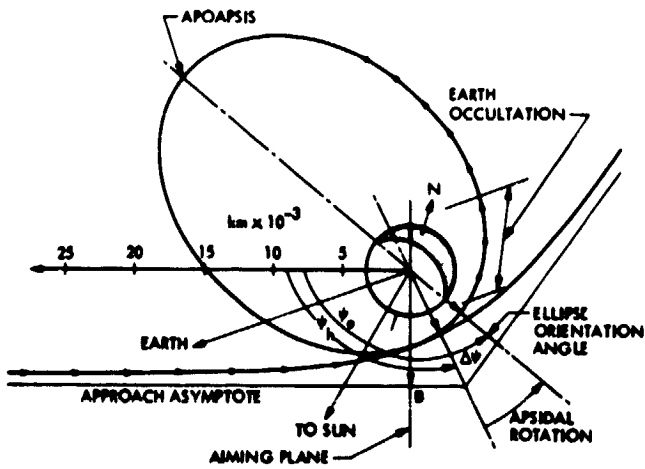


Fig. 12. Encounter conditions

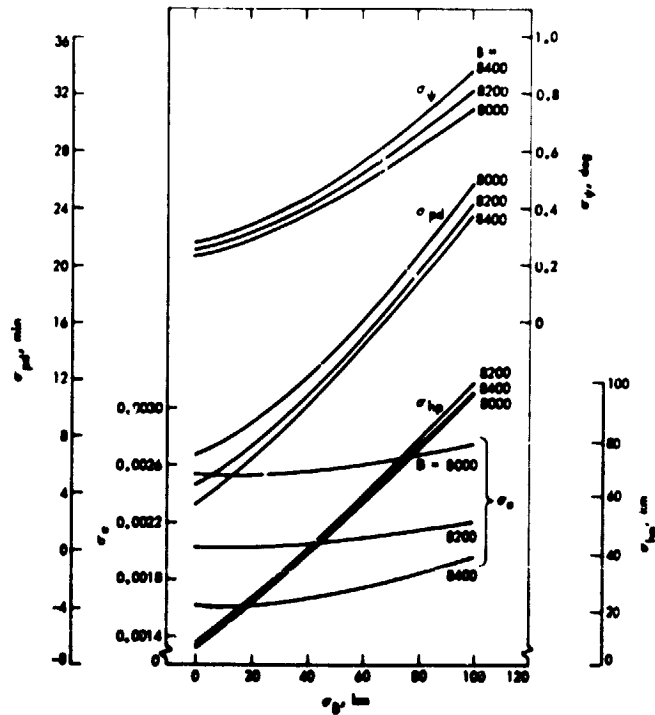


Fig. 14. MOI statistical relationships

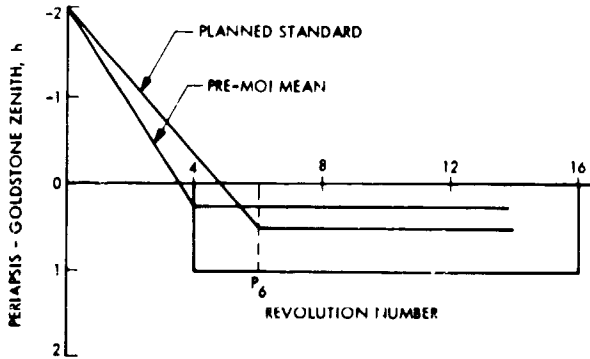


Fig. 15. Predicted trim situation pre-MOI

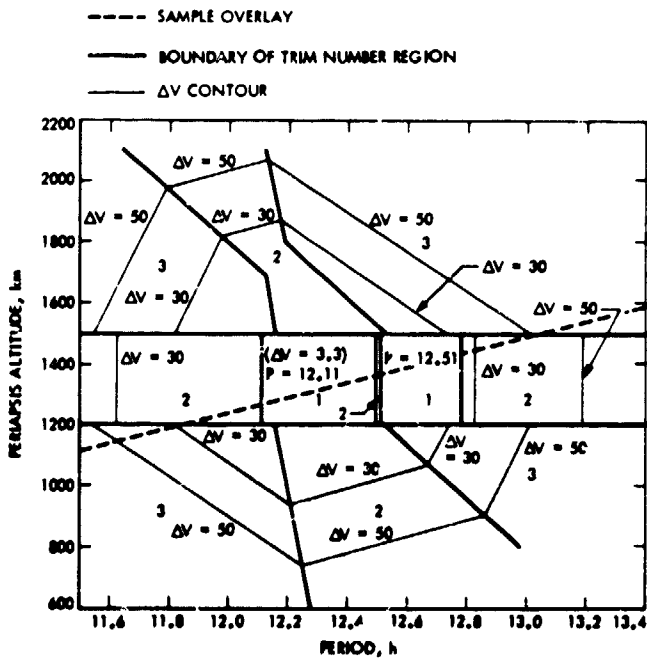


Fig. 16. Number of required orbital trims as a function of post-injection period and  $h$ ,

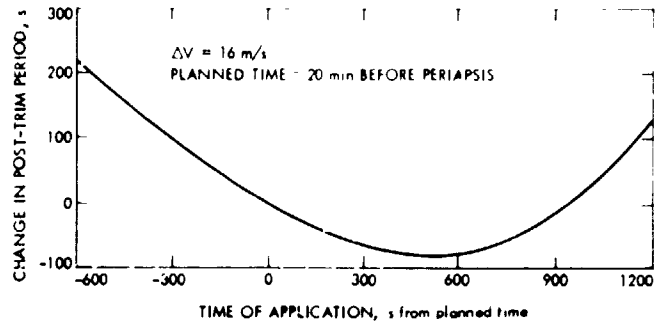


Fig. 17. Period sensitivity to ignition time

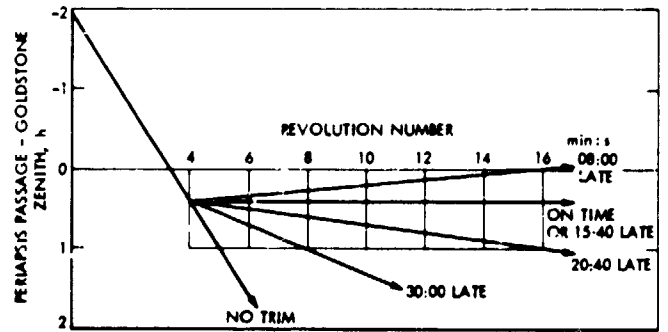


Fig. 18. Trim situation

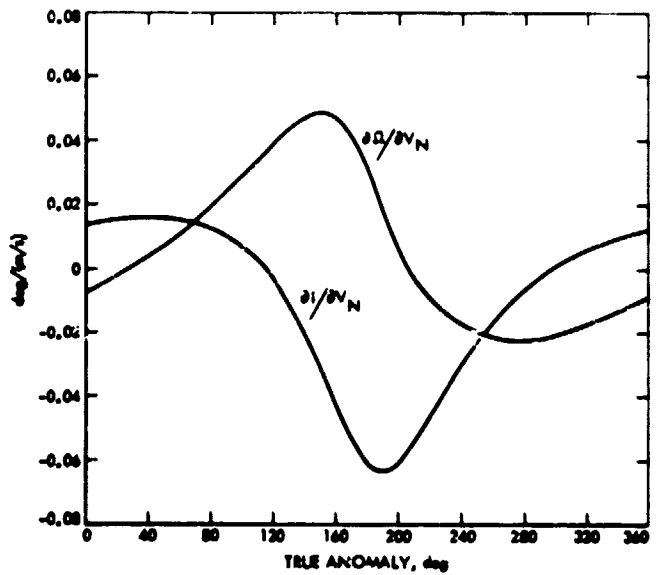


Fig. 19. Node ( $\Omega$ ) and inclination ( $i$ ) gradients

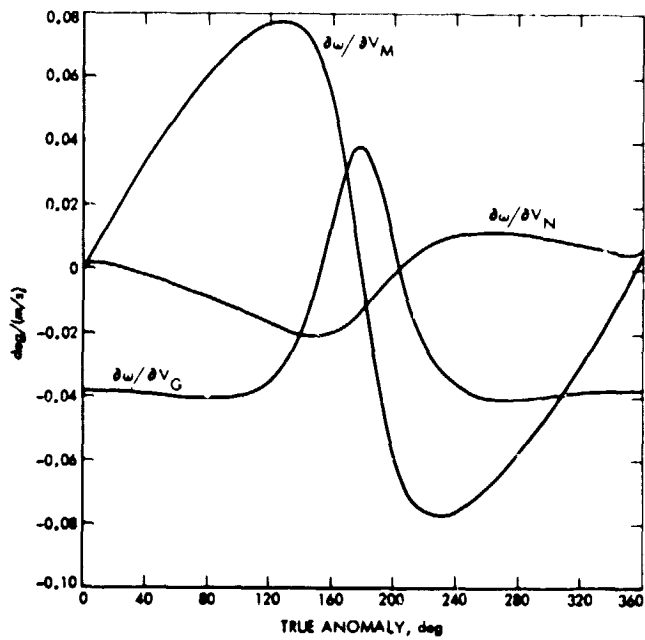


Fig. 20. Argument of perapsis ( $\omega$ )

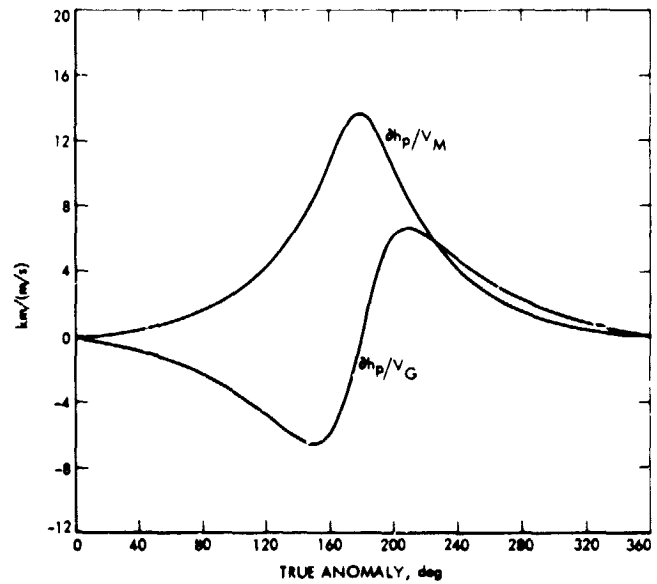


Fig. 22. Periapsis altitude ( $h_p$ ) gradient

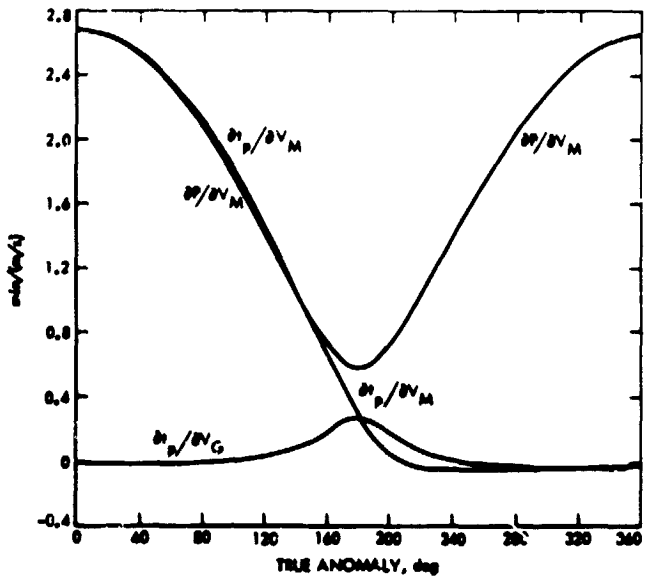
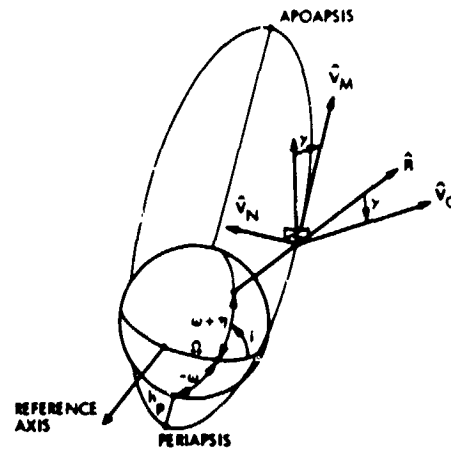


Fig. 21. Period ( $P$ ) and time ( $t_p$ ) of periapsis passage gradients



$\hat{V}_G$  = UNIT VECTOR NORMAL TO NOMINAL VELOCITY VECTOR IN ORBIT PLANE DIRECTED AWAY FROM PLANET  
 $\hat{V}_M$  = UNIT VECTOR ALONG NOMINAL VELOCITY VECTOR  
 $\hat{V}_N$  = UNIT VECTOR NORMAL TO ORBIT PLANE IN ANGULAR MOMENTUM DIRECTION  
 $\hat{R}$  = UNIT VECTOR ALONG THE RADIUS VECTOR  
 $\gamma$  = FLIGHT PATH ANGLE  
 $\nu$  = TRUE ANOMALY

Fig. 23. Flight plane velocity space

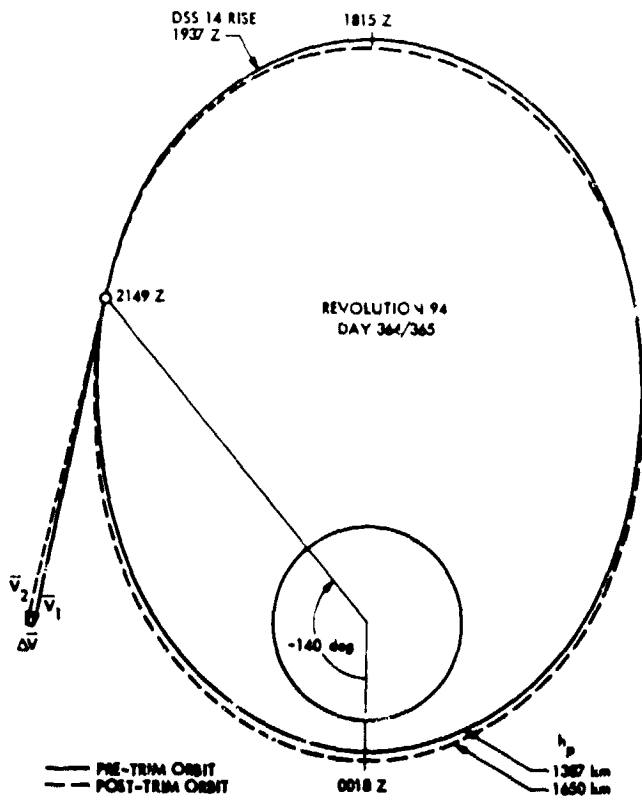


Fig. 24. Orbit trim 2 geometry

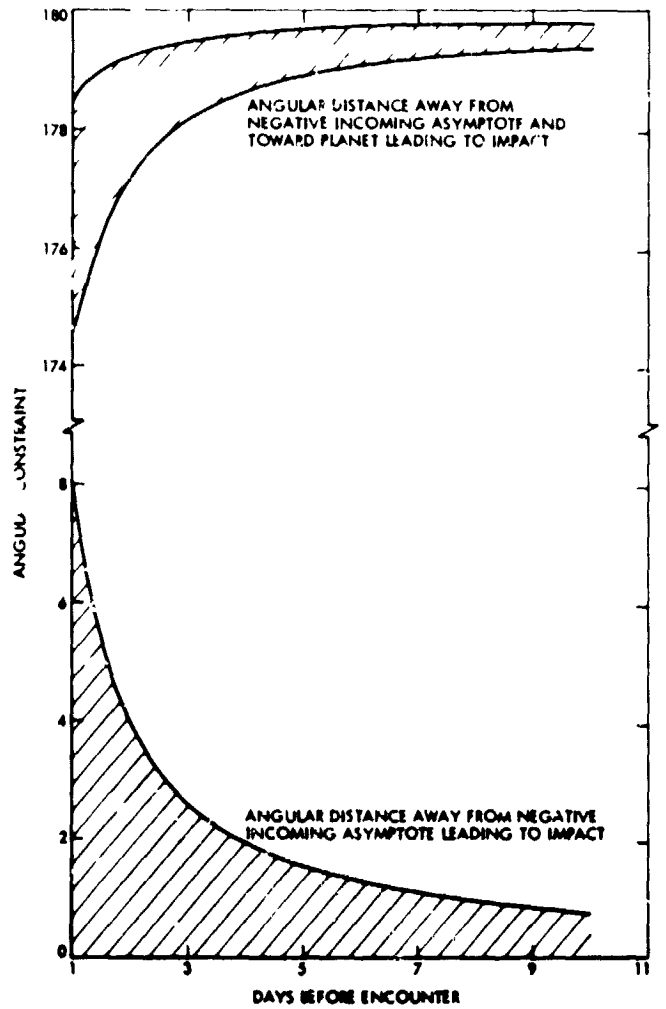
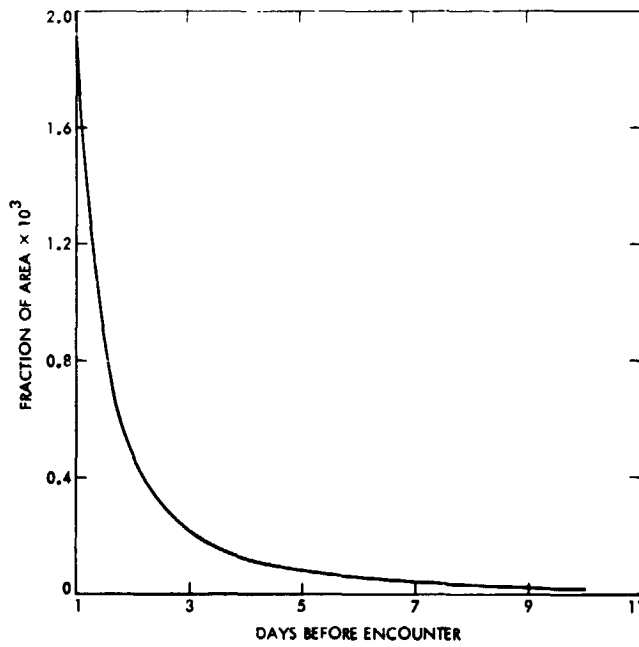


Fig. 25. Pointing directions resulting in planetary impact



**Fig. 26. Fraction of all possible pointing directions leading to planetary impact**

# Trajectory Description

W. A. Webb

## I. Launch Phase

The Mariner 9 spacecraft was launched by an Atlas/Centaur launch vehicle (AC-23) on a direct-ascent trajectory from the Air Force Eastern Test Range (AFETR) launch complex 36B on May 30, 1971. Liftoff occurred at 22 h 23 min 04.5 s GMT, slightly more than 6 min after the opening of a 60-min launch window. The vehicle rose vertically for approximately 15 s, during which time, a programmed roll to a launch azimuth of 92.74 deg was performed. After the initial vertical rise, the vehicle, guided by the open-loop Atlas autopilot, began to pitch over into a zero-lift trajectory. The first of three main powered phases was terminated by booster engine cutoff (BECO) at 22 h 25 min 35.5 s. After the Atlas booster engine package was jettisoned 3 s later, the flight continued under the power of the Atlas sustainer engine and guided by the Centaur guidance system operating in a closed-loop mode.

Because of an unusual launch geometry situation for the Mariner Mars 1971 (MM71) launch opportunity, it was possible to hold the launch azimuth constant during each daily launch window. However, a small yaw "dog-leg" maneuver had to be performed so that the vehicle would attain the correct departure direction. At BECO

+8 s, a launch-time-dependent yaw command was issued. The magnitude of the yaw maneuvers was measured in yaw index units. A unit positive value of yaw index indicated a main engine cutoff (MECO) position 58.69 km (186,000 ft) to the right (looking downrange) of a typical nonyawed (planar) trajectory. The yaw index for the Mariner 9 launch was  $-0.34$ .

After rising above a significant portion of the atmosphere, the Centaur insulation panels and nose fairing, which protected the vehicle during ascent, were jettisoned at 22 h 26 min 20.5 s and 22 h 27 min 02.6 s, respectively. The Atlas sustainer phase was ended normally by propellant depletion at sustainer engine cutoff (SECO) at 22 h 27 min 07.5 s. The Atlas sustainer stage was separated from the Centaur at 22 h 27 min 10.5 s.

After a 10.7-s coast, the main engines of the Centaur were ignited at 22 h 27 min 21.2 s. At main engine start +4 s, the guidance steering loop, which was interrupted at SECO, was again closed. No additional yaw maneuvers were performed during this phase. Centaur MECO was commanded by the Centaur guidance system at 22 h 34 min 46.9 s. Centaur MECO occurred at 702.4 s after liftoff.

After MECO, the Centaur guidance system initiated a turning maneuver to bring the vehicle into alignment with the predetermined separation direction. A spring deflection separated the spacecraft from the Centaur at 22 h 36 min 22.6 s, and Mariner 9 was injected into a Mars transfer trajectory. Launch phase event times are summarized in Table 1. The current best estimates of the spacecraft's geocentric orbital elements at injection are presented in Table 2.

Shortly before separation from the Centaur, at 22 h 35 min 47.5 s, Mariner 9 entered the shadow of the Earth. Solar panel deployment was completed at 22 h 42 min 02.9 s, and the spacecraft began Sun acquisition at 23 h 08 min 46.0 s, when it exited the Earth's shadow. Sun acquisition was achieved at 23 h 15 min 59.8 s. At this time, spacecraft power was being supplied entirely by the solar panels.

Upon acquiring the Sun, the spacecraft was fully stabilized in pitch and yaw and was drifting without a reference for the roll axis. The search for Canopus, the roll-reference star, was initiated by turning on the Canopus sensor. On the first roll, Achernar was acquired instead of Canopus, as expected. A ground command was transmitted to disacquire Achernar and continue the search for Canopus. At 02 h 25 min 10.2 s on May 31, 1971, Canopus was acquired.

## II. Interplanetary Cruise Phase

Approximately 24 h after launch, on May 31, 1971, at 22 h 31 min 01.0 s, the scan platform, on which the science instruments were mounted, was unlatched from its stowed position. The unlatching involved the releasing of compressed nitrogen, and the resulting velocity vector change slightly altered the spacecraft trajectory.

Several hours after scan unlatch, a propulsion system engine vent sequence was initiated. At 01 h 28 min 29.3 s, on June 1, 1971, the main engine valve of the propulsion system was opened for 2 s to allow undesired gases trapped upstream of the valve to escape to the vacuum of space. The spacecraft trajectory was again slightly changed. The best estimates of the post-engine-vent geocentric orbital elements of the trajectory are presented in Table 3.

### A. Aiming Point

The aiming point at Mars is typically defined by the polar coordinates  $B$  and  $\theta$  in the aiming plane. The aim-

ing plane is the areocentric plane normal to the incoming asymptote of the approach hyperbola. The parameter  $B$  is the miss distance, and the angle  $\theta$  specifies its orientation in the aiming plane. The aiming plane coordinate system is depicted in Fig. 1.

The launch aiming point was biased farther from the planet than the final required actual aiming point to satisfy planetary quarantine and other requirements. The particular biasing direction chosen was dictated by spacecraft and propulsion system constraints and a desire to minimize the post-midcourse trajectory dispersions, as was discussed in the preceding section, which would result from injection errors. The bias was then removed by the mid-course maneuver.

The specified injection aiming point selected for the Mariner 9 spacecraft was  $B \cdot R = 25,072.0$  km and  $B \cdot T = 35,596.0$  km. The selected closest approach time was 23 h 33 min 00.0 s on November 14, 1971. The actual injection aiming point achieved was  $B \cdot R = 19,869.5$  km and  $B \cdot T = 26,389.4$  km. Without a midcourse maneuver, the closest approach time would have been 19 h 37 min 11.7 s on November 14, 1971. Figure 1 shows that the Atlas/Centaur launch vehicle would have delivered Mariner 9 only 10,600 km (well within specified tolerance) from the specified injection aiming point.

### B. Midcourse Maneuver

The midcourse correction maneuver was performed 6 days after launch on June 5, 1971, to remove the injection aiming point bias and to deliver the spacecraft to the proper aiming point for insertion into orbit about Mars. The aiming point, determined by the desired orbit about Mars and the orbit insertion criteria, was  $B \cdot R = 6106.4$  km,  $B \cdot T = 5472.9$  km. The selected time of closest approach was 0 h 28 min 58.6 s on November 14, 1971.

The engine was ignited at 00 h 22 min 06.0 s for a 5.1-s motor burn to provide a  $\Delta V$  of 6.723 m/s. The resultant change in the spacecraft trajectory is illustrated by a comparison of aiming point coordinates:  $B \cdot R$  was now 6085.9 km,  $B \cdot T$  was 5587.5, and closest approach time was 00 h 31 min 8.554 s on November 14, 1971. The accuracy of the maneuver was better than  $0.5 \sigma$  based upon *a priori* statistical estimates, sufficient to eliminate the need for a planned second midcourse maneuver, which would have been performed about a month before encounter. Figure 1 shows a comparison of the desired and actual injection and post-midcourse aiming points. The best estimates of the post-midcourse heliocentric orbital elements are given in Table 4.

After leaving the vicinity of the Earth, Mariner 9 moved along an approximately elliptical path about the Sun until it reached the vicinity of Mars. Initially, the spacecraft moved ahead of the Earth along its orbit toward Mars but gradually slowed and was passed by the Earth. The heliocentric transfer angle was 129.12 deg (Type I trajectory), and the flight time was 168 days.

A projection of the transfer trajectory in the ecliptic plane is shown in Fig. 2. Figures 3 to 5 show several pertinent characteristics of the transfer trajectory presented as a function of calendar date. The parameters presented are celestial latitude and longitude, and the geocentric, heliocentric, and areocentric range to the spacecraft.

### III. Encounter Phase

On November 8, 1971, Mariner 9 was only 2 million km from Mars and proceeding toward an encounter with the "red" planet with an areocentric speed of about 3.2 km/s. During the near-encounter phase, the spacecraft trajectory may be characterized by a hyperbola with the center of Mars located at the focus. The approach direction at Mars may be specified by the vectorial difference between the heliocentric velocity of Mars and the heliocentric velocity of the spacecraft near encounter. As Mariner 9 approached Mars along the incoming asymptote, the Sun was approximately 70 deg behind and to the right, and the Earth approximately 25 deg behind and to the same side. The near-encounter geometry for the Mariner 9 trajectory is illustrated in Fig. 6. The best estimates of the areocentric orbital elements of the near-encounter trajectory are presented in Table 5.

On November 10, 1971, with Mars still over 1 million km away, the spacecraft onboard computer initiated the

first of three preprogrammed science sequences, which were scheduled to be performed before insertion into orbit about Mars. These sequences included wide- and narrow-angle TV pictures and spectral data from the ultraviolet spectrometer (UVS), the infrared interferometer spectrometer (IRIS), and the infrared radiometer (IRR) instruments, which were mounted on the scan platform.

During pre-orbit science sequence 1 (POS-1), 25 narrow-angle TV pictures of the full Martian disk were taken on 62-min centers. Five narrow-angle pictures of the satellite Deimos were taken by ground command from the Earth. All of these pictures, plus spectral data, were recorded on the tape recorder aboard the spacecraft and transmitted back to Earth via the Goldstone 64-in-diameter antenna. On November 12 and 13, 1971, the next science sequence (POS-2) was taken. This sequence was similar to POS-1, with 24 pictures of Mars and 6 of Deimos. As the pictures from the first two sequences were received, it became clear that, unfortunately, the surface of Mars was obscured by a massive atmospheric storm.

The final sequence (POS-3) consisted of 23 wide- and narrow-angle pictures of portions of Mars taken at 2-h intervals designed to produce a mosaic of most of the planet. Five more pictures of Deimos and two of Phobos were also obtained. These pictures and spectral data were recorded to be played back to Earth after orbit insertion.

On November 14, 1971, Mariner 9 was maneuvered (roll and yaw) to the correct attitude, and at 00 h 24 min 22.0 s, the main engine valve was opened, causing the hypergolic propellants to ignite for a planned burn of over 15 min. This motor burn produced a velocity vector change of approximately 1600 m/s, slowing the spacecraft and placing it into the proper orbit about Mars.

**Table 1. Mariner 9 launch sequence of events**

Event	Time from liftoff, s
Liftoff <sup>a</sup>	0
Cut off Atlas booster engine	151.0
Jettison Atlas booster engines	154.0
Jettison Centaur insulation panels	196.0
Jettison Centaur nose fairing	238.1
Cut off Atlas sustainer and vernier engine	243.0
Separate Centaur stage from Atlas	246.0
Start Centaur main engine	256.7
Cut off Centaur main engine	702.4
Separate Centaur/spacecraft	798.1
Begin Centaur tank reorientation	1258.3
Begin Centaur retro thrust	1353.3
End Centaur retro thrust	1373.3
Start tank blowdown	1702.6
End tank blowdown, energize power changeover	1953.6

<sup>a</sup>At 22 h 23 min 04.5 s GMT on May 30, 1971.

**Table 2. Geocentric orbital elements at injection**

Orbital element	Best estimate
Periapsis radius, km	6,544.9
Semimajor axis, km	-43,358.3
Eccentricity	1.1509
Inclination <sup>a</sup> , deg	28.79
Argument of periapsis <sup>a</sup> , deg	127.45
Longitude of ascending node <sup>a</sup> , deg	45.39
Time of periapsis passage, GMT	May 30, 1971, 22 h 34 min 47.94 s

<sup>a</sup>With respect to the Earth true equator and equinox of date.

**Table 3. Post-engine-vent geocentric orbital elements**

Orbital element	Best estimate
Periapsis radius, km	6,532.8
Semimajor axis, km	-43,495.8
Eccentricity	1.1502
Inclination <sup>a</sup> , deg	28.80
Argument of periapsis <sup>a</sup> , deg	127.63
Longitude of ascending node <sup>a</sup> , deg	45.20
Time of periapsis passage, GMT	May 30, 1971, 22 h 35 min 02.87 s

<sup>a</sup>With respect to the Earth true equator and equinox of date.

**Table 4. Post-midcourse heliocentric orbital elements**

Orbital element	Best estimate
Periapsis radius, 10 <sup>6</sup> km	150.83
Semimajor axis, 10 <sup>6</sup> km	186.80
Eccentricity	0.1926
Inclination <sup>a</sup> , deg	1.29
Argument of periapsis <sup>a</sup> , deg	164.71
Longitude of ascending node <sup>a</sup> , deg	68.64
Time of periapsis passage, GMT	May 16, 1971, 06 h 19 min 04.26 s

<sup>a</sup>With respect to the true ecliptic and equinox of date.

**Table 5. Areocentric orbital elements at encounter**

Orbital element	Best estimate
Periapsis radius, km	5116.4
Semimajor axis, km	-4112.2
Eccentricity	2.2441
Inclination <sup>a</sup> , deg	64.65
Argument of periapsis <sup>a</sup> , deg	311.87
Longitude of ascending node <sup>a</sup> , deg	42.50
Time of periapsis passage, GMT	Nov. 14, 1971, 0 h 31 min 06.62 s

<sup>a</sup>With respect to the Mars true equator and vernal equinox.

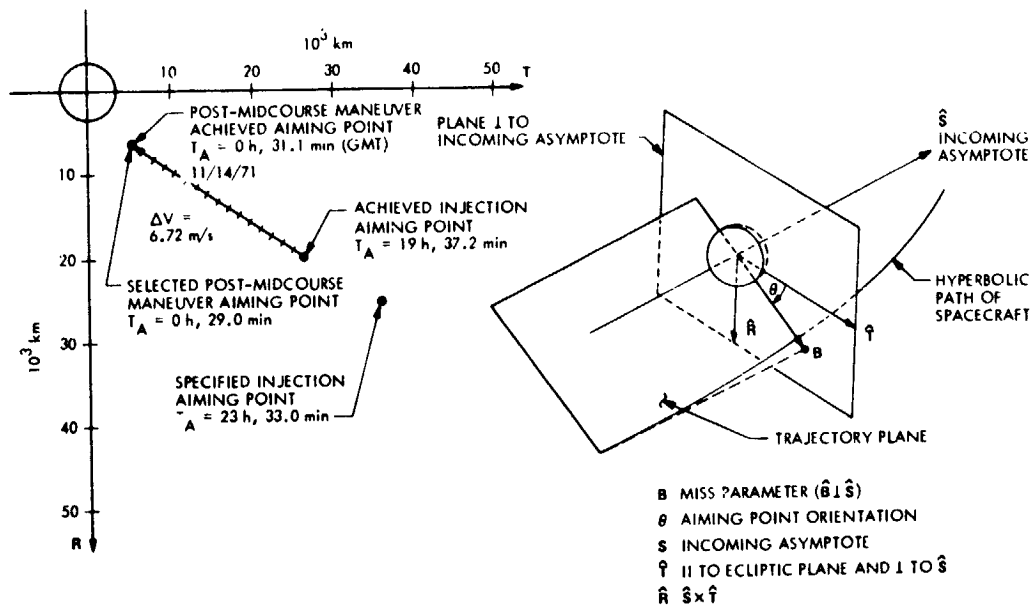


Fig. 1. Mariner 9 injection and midcourse aiming points

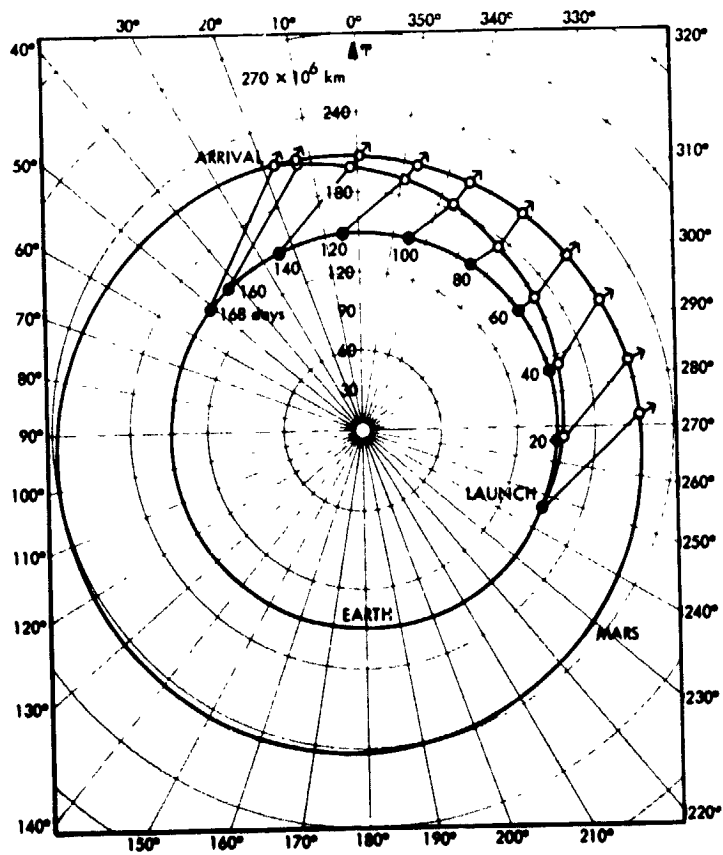
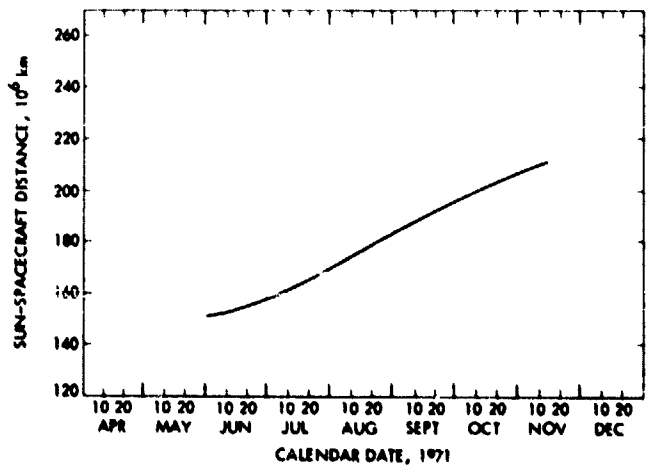
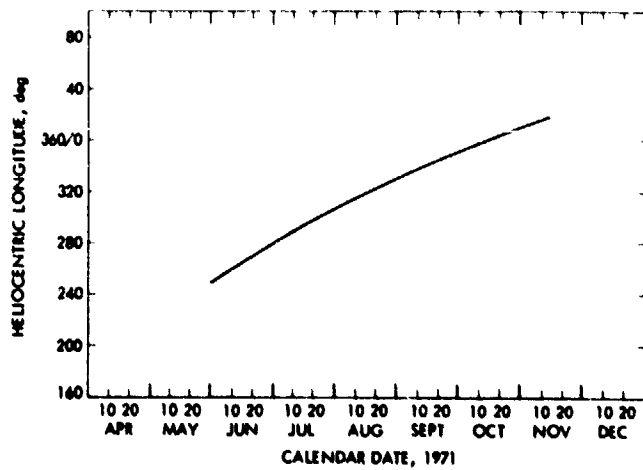
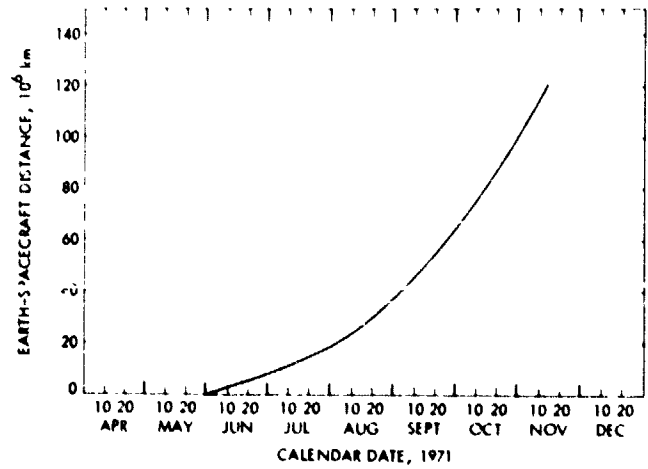
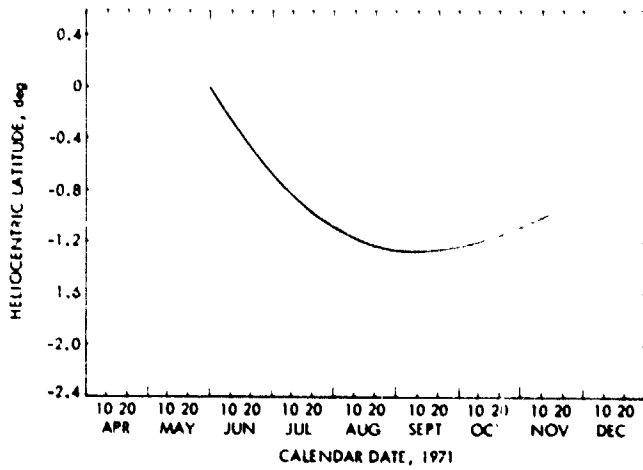


Fig. 2. Projection of heliocentric trajectory in the ecliptic plane (launch, May 5, 1971; arrival, November 14, 1971)



**Fig. 3. Transfer trajectory as a function of calendar date:**  
 (a) Helio-centric latitude, (b) Helio-centric longitude

**Fig. 4. Mariner 9 distance as a function of calendar date:**  
 (a) Earth-spacecraft, (b) Sun-spacecraft

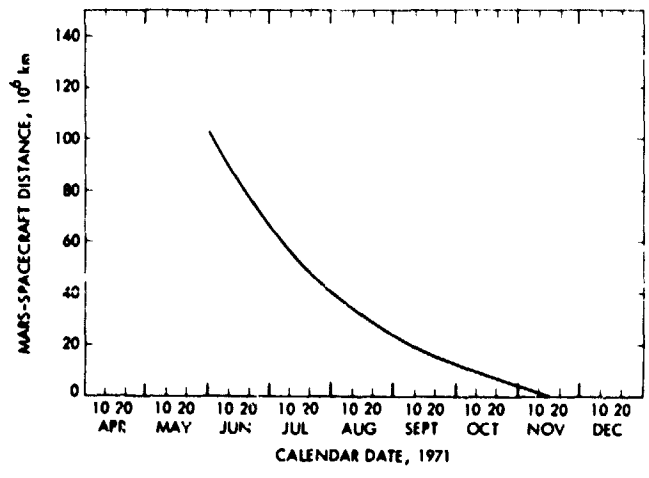


Fig. 5. Mars-spacecraft distance as a function of calendar date

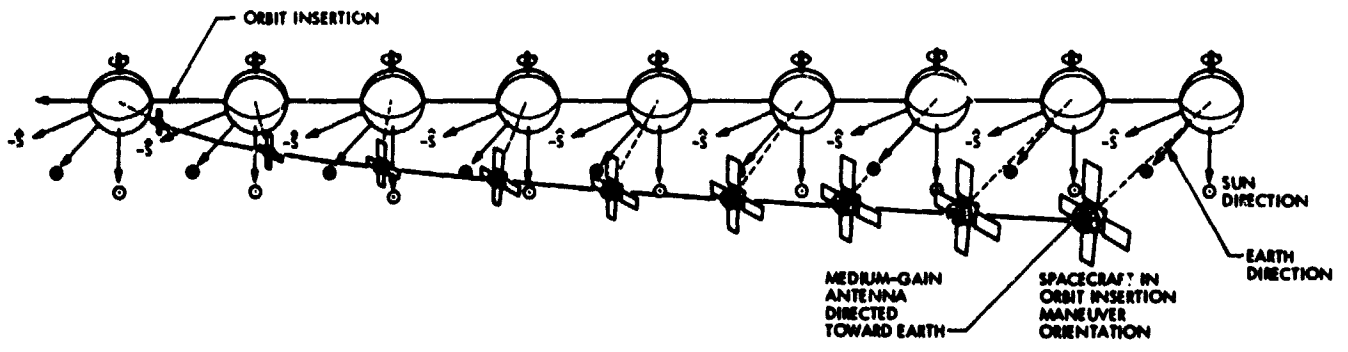


Fig. 6. Near-encounter geometry

# Science Sequence Design

P. E. Koskela, W. E. Bollman, J. E. Freeman, M. R. Helton, R. J. Reichert, E. S. Travers, and S. J. Zawacki

## I. Introduction

The primary objective of the Mariner Mars 1971 mission was to study the characteristics of Mars for at least 90 days. The mission was highly successful in that 70 to 80% of Mars was mapped during the first 262 revolutions. The extended mission later brought this coverage to nearly 100%.

The activities of the following members of the Navigation Team are recorded in this section: the Science Sequence Design Group, responsible for preparing the final science sequence designs; the Advance Sequence Planning Group, responsible for sequence planning; and the Science Recommendation Team (SRT) representatives, responsible for conducting the necessary sequence design interfaces with the teams during the mission. The interface task included science support in both advance planning and daily operations. The science sequences designed during the mission are also discussed in this section.

## II. Software

The Planetary Observation Geometry and Science Instrument Sequence (POGASIS) system of programs used for science sequence planning and design was comprised of POGASIS, POGASIS plot, Library POGASIS Program (LIBPOG), SCOUT, summary programs, POGASIS plot driver, and POGASIS data package driver. A description of the major functions of each program follows.

### A. POGASIS

The POGASIS program is a single-precision Fortran V program that was used to generate the Mariner 9 observational geometry. POGASIS formed the basis of all science sequence design computations. The program operated on the UNIVAC 1108 computer.

POGASIS computes the spacecraft orbit either by processing a numerically integrated ephemeris tape that has

been generated by the double precision trajectory program (DPTRAJ), or by using a two-body orbit modified to include general perturbation expressions for the major perturbative effects of solar gravity and Mars oblateness. All trajectory-related quantities of interest can be computed, including spacecraft maneuver attitude information, occultation parameters of Sun and Earth, and look angles to Earth-based tracking stations.

The instrument scan geometry portion of POGASIS, given the pointing directions and times, projects the images of up to 10 onboard instruments onto the surface of Mars. It also computes the pointing angles and times necessary to satisfy specified observational criteria. This portion of POGASIS computes all instrument-related quantities of interest.

## B. POGASIS Plot

The POGASIS plot program provides graphical representation of instrument viewing geometry for all instruments. The program uses a data tape generated by POGASIS or LIBPOG as input, and outputs graphical data in mercator, orthographic, cartesian, or conical projection form. The plots could be viewed on the Tektronix T4002 (and hard-copied if desired) or directed to the Stromberg-Carlson (SC) 4020 plotter.

## C. LIBPOG

LIBPOG was used for post-processing by the Science Data Team to provide high-precision data. The program is equivalent to POGASIS, except that it has no triggering capability. Program input data are modified by the Scan Platform Operations Program (SPOP) to reflect all known biases to the pointing angles, including the platform limit cycle. Spacecraft position and planet position are obtained from the probe ephemeris tape and the planetary ephemeris tape, respectively.

## D. SCOUT

The SCOUT program rapidly computes and illustrates spacecraft viewing geometry for an instrument mounted on the scan platform. Its primary application was in the advance sequence design process. The program operated on the UNIVAC 1106 computer, and it could produce plots on the Tektronix T 4002 or the SC 4020 plotter.

The program computed spacecraft position, using mean elements corrected for Mars oblateness; this approximation proved to be accurate enough for planning purposes. Its various scan-pointing and plotting options, including

the spacecraft cone/clock grids, made SCOUT useful for design purposes, and its ability to immediately produce plots on the Tektronix made it invaluable for rapid iterative design work.

## E. In-flight Enhancements

As orbital operations progressed, a series of auxiliary programs were developed to automate the more routine computer-related activities. These programs were designed initially to help the POGASIS engineers check the output of the computer runs, and later, to assist in the generation of input for the POGASIS runs and plots. This automation eliminated much tedious manual checking and input preparation.

**1. Summary programs.** Several summary programs, useful for checking output, came into use soon after orbital operations began. Their purpose was to pinpoint problem areas immediately. The output from these summaries was generally printed on the Tektronix screen by the POGASIS forecast engineer as soon as the computer run closed and before printout was delivered. They enabled the forecast engineer and the SRT Representative to check picture shuttering times, slew times, and cone- and clock-angle limit violations. Another summary program formatted output exactly like the sequence generator (SEQGEN) output. This helped validate the POGASIS data package.

**2. POGASIS plot driver.** This input generator came into use after orbital operations were well under way. It eliminated manual preparation of the input necessary for each plot by extracting data from the POGASIS output adaptive mode planning system (AMPS) tape. The plot driver aided both the POGASIS forecast engineer and the POGASIS data package engineer in creating orthographic, conic, and mercator plots. The plot driver results comprised the input to the POGASIS plot program.

**3. POGASIS data package driver.** This input-formation aid came into use about two-thirds of the way through the primary mission, eliminating the tedious coding of input for POGASIS data package runs. The driver also automatically set up the correct input for a POGASIS case when provided the slews, camera pointings, and corresponding times from SEQGEN.

The ultimate refinement in POGASIS data package generation was developed in time for the extended mission. This program read the SEQGEN output tape. The data package engineer no longer had to manually type in the slew and picture shuttering data. With this driver to set up the POGASIS case and the POGASIS plot driver

to set up the plots, the data package engineer could at times prepare the data package in ½ h, as opposed to the 6 to 10 h typically required at the beginning of orbital operations.

### III. Procedures

The procedures involved in preparing the science sequence designs for Mariner 9 are given below.

For several weeks prior to encounter and orbit insertion, tentative operations procedures were tested by the POGASIS group of engineers and SRT representatives. Some of these readiness tests encompassed the entire Navigation Team, while others were conducted within the POGASIS group only.

Base cases for the TV sequence designs were prepared in advance for the first 40 revolutions. Decisions regarding the TV science beyond the first 40 revolutions were postponed because of the uncertainties resulting from the dust storm. It was intended that, during the first 40 revolutions after encounter, TV and spectral science sequences and base cases for subsequent revolutions would be prepared as the requirements of the scientists became known.

Upon insertion into Mars orbit, the sequence designs for the first 40 revolutions were changed entirely because of the dust storm. New sequence designs had to be prepared in near-real time.

The Advance Sequence Planning Group worked closely with the SRT representatives and helped prepare advance details of the TV-science sequences; the Science Sequence Design (POGASIS operations) Group handled everyday operations, along with unexpected problems and requests requiring immediate action.

#### A. Advance Planning

*1. Science Recommendation Team Representatives.* The SRT Representatives responsible for preparing unified requests for science data based on a 20-day-cycle mission plan, were involved with a variety of functions and interfaces, requiring a working knowledge of the various Mariner 9 systems, particularly the spacecraft. Because the SRT Representatives had to interface with each of the scientific experimenters or their representatives, they also had to understand the objectives of the various experiments. During the primary mission, 3.5 men were necessary to support this function 7 days per week.

The Mission Design Team was responsible for producing the basic 20-day-cycle mission plans. These plans had to reflect not only the experimenters' desires but also the constraints as dictated by the various Project systems. The plans specified the number and order of the various science sequence links, their science objectives, the structure of each link, plus system guidelines from the spacecraft and mission operations representatives. The Mission Design Team meetings were attended by: (1) SRT members, (2) Mission Engineers responsible for spacecraft operating characteristics and constraints, (3) Mission Operation System (MOS) Representatives with implementation guidelines, and (4) the SRT Representative from the Navigation Team.

The SRT Representatives were expected to provide trajectory-related information, including viewing characteristics, constraints and capabilities, in support of advance planning. As the science desires became known, the SRT Representatives, along with members of the Advance Sequence Planning Group, would design basic sequences to satisfy these requirements, and then present them to the Mission Design Team. The Mission Engineers would present the spacecraft constraints in conjunction with the proposed science sequences. Upon final iteration of the SRT desires and system constraints, a mission plan, with the basic science sequence link structure for a 20-day cycle, was prepared jointly with the Mission Engineers. When approved, this mission sequence plan would go to the Mission Sequence Working Group for implementation. An example of such a sequence plan is shown in Fig. 1.

*2. Advance Sequence Planning Group.* The Advance Sequence Planning Group worked closely with the SRT Representatives and, on occasion, with the experimenters to work out sequence designs that would meet the objectives of each science cycle. The end product was an inter-related collection of science sequences, which were then translated into POGASIS program input. This POGASIS standard (or base) case often required only minor changes (for example, in cone and clock angles or surface point locations), when used for daily operations by the Science Sequence Design Group.

Preliminary design studies were generally started at least one entire 20-day cycle in advance. Both the SCOUT and POGASIS programs were used in this iterative process, along with the Tektronix video display terminals. The SRT Representatives were the interface between the Advance Planning Sequence Group and the SRT. Changes were made until a satisfactory final design was achieved.

Once the final design for two revolutions was complete, the POGASIS standard case was compiled. The final step was to make the actual POGASIS run for the first day (two orbital revolutions) of the new science cycle as a final check for design flaws and also to effect a smooth transition between cycles and the two POGASIS groups. Preliminary work on the next science cycle was then begun.

At times, the Advance Sequence Planning Group performed design studies on a phase of the mission more than one cycle ahead. This work affected future and, on occasion, current planning and often served to shape the science objectives of a cycle.

## B. Daily Operations

**1. Science Recommendation Team Representatives.** The SRT Representatives functioned on a daily basis as the interface between the Science Sequence Design Group, the Mission Sequence Working Group, and the SRT. They coordinated the daily preparation of an orbital sequence plan that reflected the SRT desires and satisfied the operational and spacecraft constraints. The interface and orbital sequence problem-solving function made this a full-time endeavor, partially because of the sequence redesign necessitated by the dust storm and the failure of AMPS, which led to handwritten orbital sequence plans. These interface functions are listed below:

- (1) **Science Recommendation Team.** This group consisted of the science experimenters of the various disciplines and instruments and their representatives. The SRT stated the daily science sequence requirements for every data-taking revolution, including the specification of the target and/or coverage for every spectral instrument scan and TV picture link in the sequence plan for a particular mission cycle. The SRT Representative advised the SRT of the daily target viewability as a function of revolution. The final product of the SRT meetings was an orbital sequence plan, with the science requests specified for a particular revolution pair.
- (2) **Science Sequence Design Group.** This group consisted of the POGASIS operation engineers, who were responsible for designing the daily science sequences in coordination with the SRT Representative, from whom they received the science requests. Any problems that appeared during the sequence design process requiring consultation outside the Navigation Team were handled by the SRT Representatives. Upon completion of the sequence design process, the POGASIS forecast run

was submitted to the SRT Representative for double-checking and orbital sequence plan submittal.

- (3) **Mission Sequence Working Group.** This group consisted of representatives from the various mission operations teams such as the Spacecraft Team, SRT, and the Navigation Team. Actual implementation of the daily science sequences began in this group, when the science sequence plan was reviewed and approved for execution.

**2. Science Sequence Design Group (POGASIS operations).** The Science Sequence Design Group handled the everyday tasks associated with the Mariner 9 POGASIS activities. The operations task was divided into three specific tasks, performed by the forecast engineer, the data package engineer, and the duty engineer. Each of these positions was manned 7 days a week and approximately 12 h per day. The tasks were rotated among the members of the group every 8 days. A description of each of the POGASIS operations tasks, and their principal duties, follows:

- (1) **Forecast engineer.** It was the responsibility of the forecast engineer to begin the daily sequence design process by using the POGASIS base case and inputting the science requests. It typically took 8 h to accomplish this task of designing sequences which did not violate any constraints for a pair of revolutions.
- (2) **Data package engineer.** Data packages were distributed the day of playback, and it was the responsibility of the data package engineer to meet that schedule. The POGASIS run contained in the data package represented the best *a priori* model of the sequences executed by the spacecraft. Part-way through the primary mission, programs were written that simplified the production of the data packages (see Subsection IIE).
- (3) **Duty engineer.** It was the responsibility of the duty engineer to identify all forecast problems and, if necessary, to complete the sequence design begun by the forecast engineer by working with the SRT Representative in an attempt to eliminate these problems. In addition, the duty engineer was required to perform any impromptu studies that might arise. He also acted as a focal point for POGASIS activities and was the on-duty leader of the Science Sequence Design Group.

### C. Evolution of a Zenith/Nadir Orbital Sequence

The complete science sequence design process is shown in Fig. 2. It is assumed that a mission plan for the subject 20-day cycle has been formulated. The plan would specify the general science sequence structure, including all data-taking (D/T) link times, picture link descriptions, slew times, ground-commanded picture capability, and the flexibility allowed for sequence structure change requests. A POGASIS base case modeling this science sequence structure would have been prepared by the Advance Sequence Planning Group. The procedures used for producing an orbital sequence plan follow in chronological order for a typical zenith/nadir revolution pair:

- (1) The SRT representative attended the daily SRT meeting to discuss the targeting for the science sequences to be taken 6 days later. The science requests were recorded on the orbital sequence plan forms (see Fig. 3). When filled out, these forms contained the detailed sequence design information to be implemented by the Spacecraft Team.
- (2) The SRT Representative then attended the Mission Sequence Working Group meeting to review the orbital sequence plan brought in by the SRT Chief. Any foreseeable implementation problems (e.g., MOS or spacecraft) were resolved at this time. After approval by the Mission Sequence Working Group, copies of the sequence plan forms were made, and the original was given to the SRT Representative.
- (3) Next, the SRT Representative presented a copy of the sequence plan forms to the forecast engineer, along with any necessary explanation concerning the science requests.
- (4) Once the science requests were understood, the forecast engineer loaded the POGASIS base case into the computer and modified it (using the text editor mode at the Tektronix) to model these requests. Additional items the forecast engineer had to include prior to his first computer run were: (a) the calendar date and day of year of the particular revolutions; (b) the DA's automation subsystem (DAS) reference time for these revolutions from B-frame start listings provided by the Spacecraft Team; (c) the number of the latest probe ephemeris tape, with the difference between universal and ephemeris time corrections, if applicable.
- (5) After execution, the POGASIS output was checked by the forecast engineer. Typically, a number of

computer runs were made before one was obtained that fully satisfied the science requests. In some cases, the science requests were impossible to satisfy because of some spacecraft or geometrical constraint. Spacecraft constraints included scan platform viewing limits and slew duration limitations. Such problems were described in a note to the next day's duty engineer; the note was left with the output from the last POGASIS run and copies of all plots.

- (6) The following day, the duty engineer and the SRT Representative reviewed any problems encountered the preceding day by the forecast engineer. If no viable strategy or solution could be found, the SRT Representative brought the target or sequence problem to the attention of the Mission Sequence Working Group. The group, consulting with the SRT Representative, proposed an SRT target change or a sequence structure modification. These sequence amendments could be proposed throughout the day if the responsible working group individuals were available. Otherwise, the amendments would be proposed at the 4:00 p.m. meeting. The proposed change was then brought back to the duty engineer, who made the necessary changes to the POGASIS case and checked the feasibility of the revised sequence. The rest of the day was used for finishing the sequence design and producing plots for all the sequences.
- (7) When the duty engineer completed the POGASIS forecast run containing the required sequences (usually the following morning), it was given, with the plots, to the SRT Representative to double-check to ensure that the science requests and all system constraints were satisfied. These system constraints included: (a) scan platform limits, (b) slew duration limitations between links, (c) minimum picture link timing separations, and (d) the ultraviolet spectrometer (UVS) "zap" problem. The UVS zap problem was not known before encounter. The constraint was imposed that the UVS instrument, when operating, never be slewed from black space onto the illuminated limb of the planet because of its sensitivity to such an abrupt exposure to UV radiation.
- (8) UVS zap checking was done by the SRT Representative in conjunction with the duty engineer. Perspective views (with superimposed cone and clock grids) of the planet at 5-min intervals were pro-

vided by the Advance Sequence Planning Group for this purpose. All slews in a sequence were checked for potential violations. SCOUT and POGASIS were used to check marginal cases. If a violation was detected, a slew strategy to prevent the zap was devised, which might include slewing earlier or later, or possibly incorporating an extra slew into the sequence to slew around to the dark side of the planet.

- (9) After the checking was completed, the SRT Representative filled out the orbital sequence plan forms with the data from the final POGASIS forecast run. The duty engineer assisted in this, if required. The data provided on the forms included the picture link times, all cone and clock angles, floating slew strategies and times, and periapsis times. (See Fig. 3 for a sample orbital sequence plan for a zenith revolution in mapping cycle III.)
- (10) The SRT Representative then attended the daily 4:00 p.m. Mission Sequence Working Group meeting to submit for approval the prepared orbital sequence plans for the science sequences to be taken 4 days later. After review and Working Group approval, the sequences went to the Spacecraft Team for implementation.
- (11) If no unforeseen implementation problems appeared, the next step was initiated 1½ to 2 days before the sequence D/T, when the EQGEN output, consisting of the actual times and cone and clock angles that were loaded into the central computer and sequencer (CC&S), was available. The data package engineer used these values to construct a POGASIS input case, which would model the spacecraft sequences using the precise times they would be executed. A final check of the UVS zap problem was also included in this last POGASIS case. This check was made early enough so that emergency commands could be sent to the spacecraft if a UVS problem was detected. Plots were constructed on the SC 4020 plotter with the final run. The plots were labeled and the data package was assembled, reproduced, distributed, and ready for use before playback began.

The preceding procedures were in a continuing state of development throughout the mission. Once a mission cycle had begun, the procedures would overlap so that, during any one day, three data-taking sequences were being worked on.

## IV. Science Sequences

Mariner 9 science sequence design can be discussed in three different phases: (1) the pre-insertion planning, which took place after the loss of Mariner 8 because of a launch vehicle failure, (2) the post-insertion planning and changes necessitated by the dust storm; and (3) the sequences as they actually were taken.

### A. Pre-insertion Planning

The launch failure of Mariner 8 led to the first of several redesigns of the science sequences. The two phases of the Mariner Mars 1971 mission represented by Mariners 8 and 9, each with its own science objectives, had to be combined into a single compromise mission. This revised mission had to satisfy the minimum requirements of each scientific discipline, while receiving about one-half the data that would have been available from the two separate spacecraft.

An example of the tradeoffs made in re-designing the mission was the selection of a 65-deg-inclination orbit. This represented a compromise between a high-inclination orbit, which would have provided excellent south polar coverage, and a low-inclination orbit, which would have provided better variable feature observations near Martian high noon. The orbit period was chosen to be approximately 12 h to maximize the amount of data return. The planned apsidal orientation was 140 deg and the periapsis altitude, 1300 km.

Communication requirements dictated that the science data be played back through the 64-m-diameter antenna at the Goldstone Deep Space Station. The orbit period was synchronized as closely as possible to the Goldstone view period to maximize the data return. The time period when the science instruments could view the planet was dependent on the instrument platform scan constraints. The TV data and high-rate spectral data recorded during the Goldstone nadir pass had to be played back during the following zenith pass. In addition, real-time high-rate spectral data could be received during the zenith pass. A total of 30 TV pictures, the tape recorder capacity, were planned for each pass.

To follow this sequence of events, the spacecraft was to be maneuvered into an orbit with a period which maintained the periapsis passage of every other revolution (or a 12-h period) close to the time of zenith of the Goldstone view period. Depending on the resultant orbit period following orbit insertion, one or more orbit trim maneuvers were planned to achieve synchronization with

the Goldstone view period. The first science data-taking cycle was to begin after the final orbit trim maneuver. Subject to when and how many trim maneuvers would be needed, various science instrument calibrations and simple mapping sequences were planned for the period between orbit insertion and the final trim.

A fortuitous situation existed in that an orbit period synchronized with Goldstone zenith would result in a shift of spacecraft longitude between successive zenith or successive nadir passes which permitted contiguous TV mapping with the low-resolution camera. About 20 days of orbital operations were necessary to complete one cycle of mapping swaths around the planet. Because mapping of the Martian surface was one of the prime science objectives, the science sequence planning cycle was tied to the mapping cycle. Prior to orbit insertion, detailed mission design plans for the first mapping cycle were completed. This plan accommodated a final orbit trim maneuver as late as revolution 16.

Four mapping cycles were planned to cover the Martian surface from a latitude of  $65^{\circ}\text{S}$  to about  $25^{\circ}\text{N}$ . In addition to this TV mapping, various other kinds of data taking, both TV and spectral, were a part of the first cycle, as indicated in Figs. 4 and 5. Time ticks relate the position of the spacecraft to periapsis passage. The approximate time periods during which the instruments would acquire data are shown as planned for the first cycle.

## B. Post-insertion Planning

Upon arrival of Mariner 9 at Mars, the mission plan was changed again because of the planet-wide dust storm. The start of the mapping cycles was delayed, and a reconnaissance mode of operation was initiated instead to seek areas that were clear enough to photograph.

During the reconnaissance cycles, advance studies were performed to accomplish the primary science objectives after the dust storm ceased. For example, a minimum of 40 days was determined as the time period required to contiguously map the planet from  $65^{\circ}\text{S}$  to  $45^{\circ}\text{N}$ . However, almost all available pictures would be required to accomplish the task, and all other TV requests would have to be ignored, which was untenable. The spectral experimenters also had competing desires, which influenced the science sequence design. Further analysis indicated that, if the periapsis altitude were raised from the achieved value of 1390 km to about 1650 km and the mapping cycles extended over 60 days (three cycles), the

number of low-resolution pictures required to map the planet could be held to about 10 per orbit for the first two 20-day cycles and 12 for the last cycle.

The amount of scan platform slewing required during the mapping was also dependent on the periapsis altitude; i.e., the higher the altitude, the fewer the number of slews needed to get forward-lap with the low-resolution camera.

Because the spectral experimenters desired as few slews as possible during any link of picture taking, an effort was made to minimize the number of slews consistent with the other requirements (e.g., keeping the view angle to less than 20 to 25 deg). If the periapsis altitude was about 1650 km, only two slews would be needed during a mapping swath. Therefore, to raise the periapsis altitude from 1390 to 1650 km and to correct the orbital period to adjust the shifting of periapsis passage time with respect to Goldstone zenith, an orbit trim maneuver was performed on revolution 94, prior to the start of the first mapping cycle on revolution 100.

Mission plans redesigned after arrival were greatly influenced by the limited capabilities of mission operations. Sequences that had been fairly intricate before arrival were simplified by maintaining the same sequence design throughout a mapping cycle. Epochs (measured from periapsis) at which the science links took place were fixed for every zenith orbit and for every nadir orbit. Also, the epochs and the number of scan platform slews to accomplish the science links were held constant for each orbit. Then the sequence design was optimized from the standpoint of the science objectives. Determining where to point many of the links became a daily activity based on inputs from the SRT.

Assuming that no maneuvers to change the attitude of the spacecraft to point the high-gain antenna at Earth would be executed during the primary mission, the three mapping cycles had to be finished by early March 1972 because of degraded communication capability. This consideration dictated a starting date early in January for the mapping mode, which was compatible with the expected subsidence of the dust storm to the point that good pictures could be taken.

As can be seen from the sequence designs presented in Subsection IVC, there was a variety of TV science objectives, including geodesy, atmospheric sequences, variable surface feature geology, and Martian satellite astronomy. In addition, the sequence designs included scans made specifically for the spectral experimenters.

### C. Science Sequence Summaries

The Mariner 9 science data through revolution 262 were acquired in eight major cycles. A description of the science cycles and the revolutions included within each cycle, and a brief outline of the objectives of each cycle follow. Figure 6 provides a key to aid in reading Figs. 7 through 20, which contain complete sequence summaries for the nadir and zenith revolutions for each cycle. Sample orthographic plots for TV pictures taken on a zenith and nadir revolution for each cycle are presented in Figs. 21 through 35. A complete set of orthographic and/or mercator plots, and numerical data for every TV picture received during the first 262 revolutions are provided in Ref. 1.

**1. Post-orbital insertion mapping, calibration, and phase function cycle (revolutions 1-15).** The planet-wide dust storm to which Mariner 9 was exposed at arrival had a profound effect on the original science plan. While work progressed on replacement science sequences, a series of mapping sequences, taken near periapsis, were initiated to fill the gap left by the abandonment of the original plan. These mapping sequences, consisting of narrow-angle (B-camera) and wide-angle (A-camera) pairs, were relatively ineffective because of the dust storm. An orbit trim maneuver was performed on revolution 4 of this first cycle (no TV science data taken) and a calibration and phase function sequence on revolution 7. (See Fig. 7 for a complete sequence summary.)

**2. Interim cycle (revolutions 16 to 23).** While advanced planning continued, an interim sequence was adopted which afforded more possibility for planetary reconnaissance than BA mapping. This sequence consisted of a combination of two orbits from pre-insertion planning sequences, one nadir and one zenith. The same sequences were repeated continuously from revolutions 16 through 23. Figure 8 contains a complete sequence summary.

**3. Reconnaissance I (revolutions 24 to 33).** The new science plan was implemented on revolution 24. The primary feature of this cycle was the global coverage afforded by 10 wide-angle pictures on each zenith revolution and five on each nadir revolution. Specific targets in relatively dust-clear areas were identified in these pictures and were subsequently examined with two groups of four high-resolution pictures in each orbit. Each revolution also included a pair of overlapping high-resolution limb pictures, coverage of the south polar region with three BA pairs, and two or more BA pairs with the last A-frame vertical and 10 deg from the terminator. (See Figs. 9 and 10 for complete nadir and zenith revolution sequence summaries).

**4. Reconnaissance II (revolutions 64 to 99).** Reconnaissance of the planet continued, with a new science sequence beginning with revolution 64. The plan was similar to that for reconnaissance I, i.e., global coverage with eight A-frames on each revolution and a series of B-frames to investigate dust-free areas. On each zenith revolution, there were two tetrads (four Bs) and on each nadir revolution, a tetrad, a triad (three Bs), and a dyad (two Bs) for high-resolution limb pictures. Polar coverage continued with three BA pairs on each revolution. Near the end of this cycle, it was determined that a periapsis altitude of 1650 km would facilitate the mapping objective and also allow an orbital period adjustment for periapsis synchronization with Goldstone; therefore, a second orbital trim maneuver was ordered for revolution 94 (no TV science data taken). For two revolutions preceding the trim, and for all revolutions following the trim to the end of the cycle, BA mapping was substituted for the standard reconnaissance II format. (See Figs. 11 and 12 for nadir and zenith revolution sequence summaries).

**5. Mapping cycle I (revolutions 100 to 138).** The dust storm that had delayed Mariner 9's primary mission of mapping the surface began to abate during reconnaissance I and reconnaissance II. By revolution 100, the surface was clear enough to begin the surface mapping with mapping cycle I. Each revolution in the cycle had two mapping sequences. The first began at approximately  $P - 19$  min, with one A and three BA pairs. The second was at approximately  $P - 10$  min, 36 s, with one A and five BA pairs. The first mapping sequence was taken at a cone and clock angle such that the fourth A-frame was directed vertically, and the second sequence, such that the third A-frame was vertical. In addition to the mapping sequences, each revolution had five global pictures and a tetrad of mixed A and B frames. Each zenith revolution had a pentad of two AB and one A, and each nadir revolution had two dyads of one AB pair and a single B-frame, dubbed "TLR." This cycle was marked by one of the few hardware failures on Mariner 9. Near the end of the cycle, the filter wheel on the wide-angle camera failed to step. Analysis showed that the filter wheel was in position 5, a polarizing filter, for the remainder of the mission. Figures 13 and 14 present the nadir and zenith revolution sequence summaries.

**6. Mapping cycle II (revolutions 139 to 177).** Surface mapping continued at a higher latitude band with mapping cycle II. Each revolution again had two mapping sequences. The first was at  $P + 2$  min and the second at  $P + 13$  min, 54 s. The first sequence had one A, four BA pairs, and one B, and the second sequence, five BA

pairs. The first sequence was taken at a cone and clock angle such that the fourth A-frame was viewing vertically, and the second sequence was such that an imaginary sixth A-frame would have been vertical. Again, each revolution had a tetrad of mixed A and B frames and, in addition, each revolution had a dyad of one BA pair and two Bs, and two single B-frames. Each nadir revolution had a triad of one AB pair and one B, and three single B-frames. Figures 15 and 16 contain the nadir and zenith revolution sequence summaries.

**7. Mapping cycle III (revolutions 178 to 217).** Mapping of the planet continued with mapping cycle III. Surface features located at higher latitudes than those mapped on mapping cycle II were observed. Again, each revolution had two mapping sequences. The first was at  $P - 2$  min, 12 s and the second, at  $P + 30$  min. On each zenith revolution, two A-, one B-, and four A-frames were taken on the first sequence, followed by three AB pairs on the second sequence. On zenith revolution 206 and nadir revolution 207, and all mapping cycle III revolutions following, the B-frames in the first mapping sequence were omitted. In addition to the mapping, each revolution in the cycle contained two tetrads of mixed A- and B-frames, one dyad of one AB pair, and one dyad of two B-frames. In addition, each zenith revolution had a tetrad and a single B-frame, referred to as TEC, between mapping sequences. Each nadir revolution had two additional dyads, one consisting of an AB pair and one of two B-frames. Toward the end of this cycle, the increasing distance between Mars and Earth and the movement of Earth away from the high-gain antenna boresight caused a continued lowering of the signal-to-noise ratio, forcing selection of lower playback rates. This had the effect of decreasing the number of pictures that could be played back from approximately 30 on each revolution at the beginning of the cycle to approximately 20 at the end of the cycle. Figures 17 and 18 contain complete nadir and zenith revolution sequence summaries.

**8. Extended mission phase I (revolutions 218 to 262).** With the end of mapping cycle III, the major mission objectives were completed. However, with the exception of the inoperative A-camera filter wheel and an ever-dwindling supply of attitude control gas, the spacecraft continued to be in excellent condition to acquire data. The mission progressed to the extended mission phase beginning with revolution 218. At the start of this cycle, approximately 20 pictures could be played back on each zenith revolution. By revolution 242, this number had decreased to approximately 10. For each nadir revolution, approximately 15 to 16 pictures could be played back at the

beginning of the cycle, and 10 near the end. To increase the playback to an average of 22 pictures per day, five high-gain antenna maneuvers were planned every 2 days, starting on revolution 246. On the maneuver 1 zenith revolution, the sequence was constrained to straight mapping with limited slewing. Each zenith and nadir revolution was divided nominally into five triads, three with three Bs and two with a B and one AB pair. These triads were not constrained in time, and, in addition, provision was made to insert several ground-commanded sequences for special purposes. Two-thirds of the way through the cycle, CC&S checksum errors prevented taking data for several days, while the failure was investigated. Data-taking resumed on revolution 259, and ended on the only maneuvered revolution, 262, as the spacecraft entered solar occultation. This marked the end of the planned mission. (See Figs. 19 and 20 for nadir and zenith revolution sequence summaries).

The sequence summary tables show at a glance every TV sequence and picture taken during the first 262 revolutions and represent an orbit-by-orbit summary of the orbital sequence designs. The frame numbers (consecutive picture numbers) are in the upper left-hand corner of each "box." These frame numbers correspond to the frame numbers found on the sample orthographic and mercator plots shown in Figs. 21 to 35.

The orthographic plots, representing a perspective view from infinity, are obtained by projecting along lines parallel to the central optic path of one picture. The middle picture of a sequence gives this projection (viewing) direction, whereas its time defines the sub-spacecraft point, the terminator, and the solar subpoint. Any portion of the limb within a picture's field of view is also drawn. This generally differs from the outline of the globe. The orthographic plots provide an overall view of the geometry at the time the picture or sequence was taken. The terminator is denoted by a line of asterisks, the subsolar point by S, and the sub-spacecraft point by +. Each plot is provided with a science link title, which has the numbers of the pictures contained in the plots in parentheses. Pictures are also numbered on the plots themselves.

## V. Accuracy of TV Camera Targeting

An analysis of Mariner 9 targeting accuracy is presented in this subsection. In general, targeting was determined 5 days before initiation of the spacecraft science instruments to allow adequate time for reprogramming the spacecraft CC&S. Despite this time delay, adequate targeting accuracy was achieved.

Targeting is defined here as the process of determining the scan platform pointing necessary to provide coverage of a desired area. The accuracy attained must be sufficiently high to ensure coverage of high-resolution photography. The degree of accuracy attainable was limited by the following items:

- (1) Spacecraft position with respect to the planet
  - Position in orbit (time from periapsis)\*
  - Orbital definition
- (2) Pointing direction
  - Pointing direction within limit cycle ( $\pm 0.25$  deg)\*
  - Controllability ( $\pm 0.25$  deg)\*
  - Achievable pointing directions ( $\pm 0.125$  deg)\*
- (3) Planetary model
  - Pole direction\*
  - Mean radius and planetary oblateness
  - Local height variation
- (4) Camera shutter time
  - Reference time definition
  - Spacecraft DAS clock time drift ( $-0.146$  s/12 h)

The asterisk indicates the items which have the most significant effects on targeting accuracy. A discussion of each of these items follows.

The lack of a good definition of the detailed Martian gravitational potential early in the orbital phase limited the accuracy of the determination of spacecraft position within its orbit and, consequently, time of periapsis passage. The periapsis time error was the most significant item affecting targeting accuracy. As the mission proceeded, the gravitational potential became better defined, and more accurate periapsis time predictions were achieved. The targeting periapsis time error was reduced to less than 10 s on every orbit after revolution 157, and to less than 2 s (with a few exceptions) after revolution 186. A periapsis time error of 10 s, when the spacecraft is at the periapsis position, would result in a 1.3-deg pointing direction error, and a 2-s error would cause a 0.26-deg pointing error. The probe position errors due to out-of-plane (inclination and nodal position) errors were usually less than 2 km and therefore had a relatively small effect on targeting accuracy.

The scan platform pointing direction is another source of error. The possible pointing direction error caused by the limit cycle (the deadband boundaries of spacecraft attitude stabilization) may be 0.25 deg in clock and cone

angle. The limit-cycle deadband may be reached more often during times of high slew activity. Much less likely and more infrequent are controllability errors. These errors are caused by system hysteresis, control calibration, and mechanical errors which may total 0.25 deg in clock and cone angle. Approximately 34% of clock and cone angles skewed for TV picture data were in error by 0.2 deg or more because of limit cycle and controllability, and less than 1% by 0.4 deg or more. The difference between the desired and achievable pointing directions (quantizations in commanding mechanization) could be as large as 0.125 deg in clock and cone angle.

The error in the planetary rotational axis of approximately 0.5 deg on the celestial sphere could involve a pointing direction error of about 1 deg in the worst case for surface feature targeting. This case would occur at periapsis about 12 h out of phase with the 24.6 h of Mars rotation from a reference position. If surface features are targeted for times close to Mars rotation intervals, the targeting error caused by the pole error could be taken into account. A description of latitude and longitude corrections for the new rotational pole with the longitude reference consistent with the old pole is given in Ref. 2. A mean planetary radius of 3387 km was utilized for the entire mission. This value may differ by 10 km from the actual radius, and the resulting maximum pointing error, which would occur at periapsis with a 90-deg viewing angle (limb view), would be about 0.3 deg.

A camera shutter time error would contribute a maximum pointing direction error at periapsis. A time error of 1 s at periapsis would correspond to a pointing direction error of about 0.13 deg. The reference time could be in error by 0.6 s if the DAS clock is reset before engineering data are received. However, most camera shutter reference times were predicted to less than 0.1 s even with a DAS clock reset.

Three examples of B-frame targeting are shown in Fig. 36. The frame marked "target" is the planned target coverage, with symbol *T* representing the desired target point. The target frame utilizes the desired cone and clock angles as computed 5 days before the execution of this picture. The probe ephemeris data used for probe position definition were, therefore, more than a 5-day extrapolation. The "predicted" frame was made 1 day before execution, with the same cone and clock angle as the target frame, but usually with updated probe ephemeris data. The "processed" frame reflects the actual coverage (accounting for pointing direction corrections), with a final probe ephemeris. The final probe ephemeris corrects

the probe's position with respect to periapsis from an interpolated fit consisting of probe position data before and after photographic execution. The "new pole" frame indicates the processed frame latitude and longitude grid, with the provisional Mars pole as given in Ref. 3. Perti-

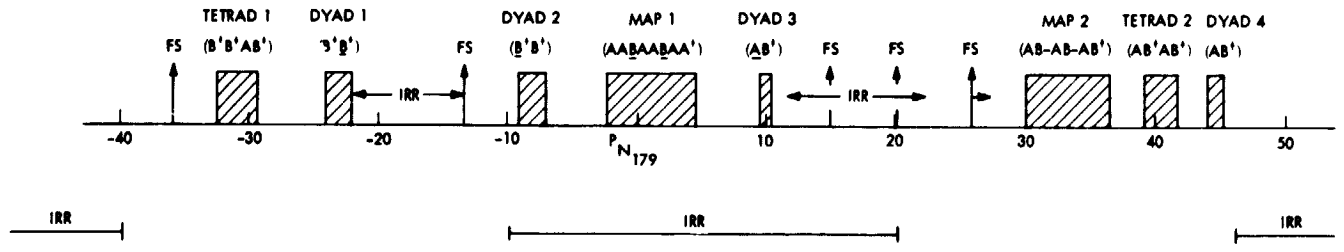
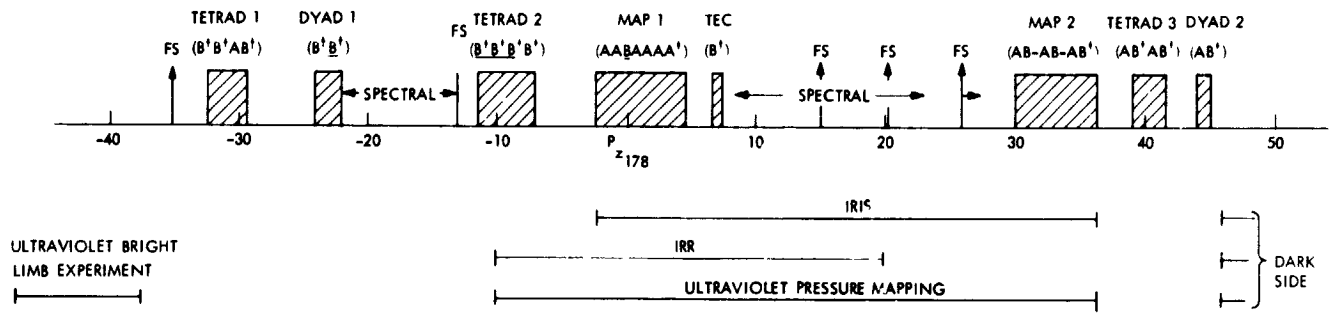
nent data for the examples shown in Fig. 36 are listed in Table 1. The pointing on revolution 157 represents a worst-case targeting because of the periapsis time and pointing direction errors. Revolutions 173 and 175 represent more typical performance.

## References

1. Koskela, P. E., Helton, M. R., Seeley, L. N., Zawacki, and S. J., *Mariner Mars 1971 Television Picture Catalog, Vol. II*, Technical Memorandum 33-585, Jet Propulsion Laboratory, Pasadena, Calif., Dec. 15, 1972.
2. Sturms, F. M., Jr., *Latitude and Longitude Corrections for New Mars Pole*, IOM 392.88, Jet Propulsion Laboratory, Pasadena, Calif., June 13, 1972 (JPL internal document).
3. Sturms, F. M., Jr., *Revised Mars Pole and Transformations for MM'71 Mapping*, IOM 392.4-657, Jet Propulsion Laboratory, Pasadena, Calif., Apr. 10, 1972 (JPL internal document).

**Table 1. Data for narrow-angle frame targeting**

Revo- lution	Time from periapsis			Target frame periapsis time error, s	Predicted frame periapsis time error, s	Delta cone, deg	Delta clock, deg
	h	min	s				
157	-0	14	38	-24.94	-1.18	0.48	0.06
173	-0	13	47	2.96	0.52	0.16	0.24
175	-0	13	42	0.25	0.25	0.01	0.37



FS = FLOATING SLEWS  
 A = WIDE-ANGLE CAMERA  
 B = NARROW-ANGLE CAMERA  
 UNDERLINED FRAMES  
 DELETED BEFORE END OF CYCLE III

Fig. 1. Mission sequence plan (profile) for mapping cycle III

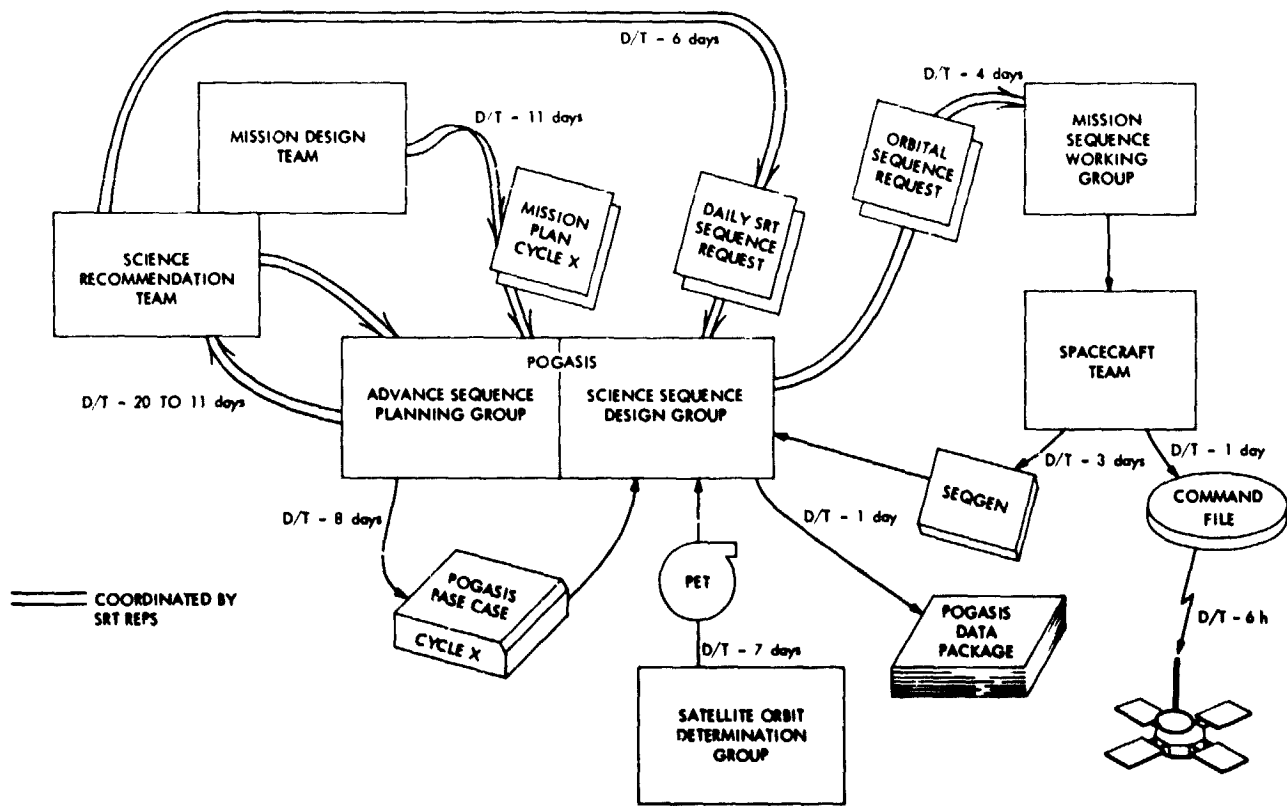


Fig. 2. Science sequence design process

ZENITH PFT HD 249 C E IIIA RECORD FALSE SHUTTER 1  
 REV. 192 DATE/TIME ORBITAL SEQUENCE PLAN DATE/TIME  
 SRC EMC 042 2300 TRIME P. TYPES Exp # 30 NAV Planchet 4/2/60  
 MSWG MJK 043/0003 1 → 28 Approved M. Kacina 4/4/60

LINK	TIME	LAT	LONG	CLOCK	CORE	B Expos (msec)	A Expos (msec)	PIX #	DESCRIPTION/COMMENTS
Playback of the Ions Madir Revolution									<u>PA</u> Data Rate Switch between Max 180K
Set Up Slew	P-31 <sup>2</sup>			141.	104.				Min. Res. Ter. after scan
End LINK	P-50 <sup>2</sup> Approx.								Before limb in view.
Floating Set-up Slew for Tetrad #1	P-35 <sup>2</sup>								Min. Res. as close to Tetrad as possible.
TETRAD #1 S <sup>1</sup> A <sup>1</sup> B <sup>1</sup> C <sup>1</sup> D <sup>1</sup> E <sup>1</sup> F <sup>1</sup> G <sup>1</sup> H <sup>1</sup> I <sup>1</sup> J <sup>1</sup> K <sup>1</sup> L <sup>1</sup> M <sup>1</sup> N <sup>1</sup> O <sup>1</sup> P <sup>1</sup> Q <sup>1</sup> R <sup>1</sup> S <sup>1</sup> T <sup>1</sup> U <sup>1</sup> V <sup>1</sup> W <sup>1</sup> X <sup>1</sup> Y <sup>1</sup> Z <sup>1</sup>	P-32 <sup>2</sup> 13 <sup>2</sup> 4/12/51 19 G <sup>1</sup>	-71° S	29° W	130.46 133.39 135.8 ↓	111.25 116.21 119.13 ↓	24 24 24 ↓	6 ms record 96 ms not recorded	1 2 3 4	 S. Polar Map
Set Up Slew for Tetrad #1	P-29 <sup>2</sup> 24 <sup>2</sup>								B-frame
DIAD #1 S <sup>1</sup> A <sup>1</sup> B <sup>1</sup> C <sup>1</sup> D <sup>1</sup> E <sup>1</sup> F <sup>1</sup> G <sup>1</sup> H <sup>1</sup> I <sup>1</sup> J <sup>1</sup> K <sup>1</sup> L <sup>1</sup> M <sup>1</sup> N <sup>1</sup> O <sup>1</sup> P <sup>1</sup> Q <sup>1</sup> R <sup>1</sup> S <sup>1</sup> T <sup>1</sup> U <sup>1</sup> V <sup>1</sup> W <sup>1</sup> X <sup>1</sup> Y <sup>1</sup> Z <sup>1</sup>	P-23 <sup>2</sup> 49 <sup>2</sup>	-80.6	34.0	126.73 127.63	134.63 138.19	24 24	6 ms Not Recorded	5 6	Inner Solar Hemisphere
Set Up Slew for Spectral	P-22 <sup>2</sup> 24 <sup>2</sup>			167.2	122.1				B-frame MORNING SPECTRAL
Floating Slew	F-13 <sup>2</sup>								Min. Res. as close to Tetrad as possible.

NOTE: Underlined frames (and associated slews) are to be deleted at the same time before the end of the cycle.

ZENITH PFT HD 249 C E IIIA RECORD FALSE SHUTTER 2  
 REV. 192 DATE/TIME ORBITAL SEQUENCE PLAN DATE/TIME  
 SRC EMC NAV Planchet 4/3/60  
 MSWG MJK Approved MJK

LINK	TIME	LAT	LONG	CLOCK	CORE	B Expos (msec)	A Expos (msec)	PIX #	DESCRIPTION/COMMENTS
TETRAD #2 S <sup>1</sup> A <sup>1</sup> B <sup>1</sup> C <sup>1</sup> D <sup>1</sup> E <sup>1</sup> F <sup>1</sup> G <sup>1</sup> H <sup>1</sup> I <sup>1</sup> J <sup>1</sup> K <sup>1</sup> L <sup>1</sup> M <sup>1</sup> N <sup>1</sup> O <sup>1</sup> P <sup>1</sup> Q <sup>1</sup> R <sup>1</sup> S <sup>1</sup> T <sup>1</sup> U <sup>1</sup> V <sup>1</sup> W <sup>1</sup> X <sup>1</sup> Y <sup>1</sup> Z <sup>1</sup>	P-11 <sup>2</sup> 13 <sup>2</sup>	-38.3	330.7	177.71 182.43 197.66 207.67	122.61 125.42 129.76 130.9	C ↓ ↓ ↓	6 ms Not Recorded	7 8 9 10	Intersecting Centers 
Set Up Slew for Map #1	P-7 <sup>2</sup> 00 <sup>2</sup>								B-frame
Periapas (ONE)	P-00 4/29/23								
MAP #1 A A B A A A A	P-27 <sup>2</sup> 57 <sup>2</sup>	-30° S	314.2	216.86 ↓	141.96 ↓	Auto ↓	Auto	11 ↓ 17	Do not record false shutter
Set Up Slew for T.E.C.	P-4 <sup>2</sup> 24 <sup>2</sup>					relax setting time 5 <sup>2</sup>			A-frame
T.E.C. S	P-0 <sup>2</sup> 57 <sup>2</sup>	-6.4° S	304.0	237.9	136.63	6	6 ms Not Recorded	18	Gullies
Set Up Slew for Spectral	P-1 <sup>2</sup> 24 <sup>2</sup>			269.6	135.5				B-frame MORNING SPECTRAL
Floating Slew	F-13 <sup>2</sup>			294.91	102.7				Min. Res.

NOTE: Underlined frames (and associated slews) are to be deleted at the same time before the end of the cycle.

Fig. 3. Sample taken from orbital sequence plan

ZENITH  
 Rev. 12  
 CYCLE IIIA  
 RECORD FALSE SHUTTER  
 DATE/TIME \_\_\_\_\_ ORBITAL SEQUENCE PLAN \_\_\_\_\_ DATE/TIME \_\_\_\_\_  
 SRT EMC  
 NAV R. B. ... 9/2/71  
 MSWG ZJK  
 Approved ZJK

LEAK	TIME	LAT	LONG	CLOCK	CONE	B Expos (msec)	A Expos (msec)	PIX #	DESCRIPTION/NOTES
Waiting Set-Up Slew	P+25m			279.5	76.2		Setup for Dyad # 2		Min. Res. as close to 1 p as possible
FRAMES 1-4	P+30m 00s	29°N	234.7	274.41	103.8	Auto	Auto	↓ ↓ ↓ ↓	2 x B-frame between pairs <u>Do not record false shutters</u>
Slew	P+30m 04s								B-frame
FRAMES 5-8	P+33m 00s			277.6 + 273.1	96.2° ↓ ↓	24	16	25 ↓ 28	2nd B on TIME UVIS gap? UVS gap?
Slew	P+33m 00s			277	103.				B-frame show to ... UVS gap
FRAMES 9-12	P+45m 24s	180°N		279.5	16.2°	24	16	27 ↓ 30	RETURN TO AUTO PH
Slew	P+45m 24s			277.75	76.2				B-frame NIGHT SIDE SPECTRAL
Slew	P+45m 24s								Min. Res.
Point of Zenith	P+20m								16-8 active 1F219
FRAMES 13-15	P+20m			278	103.96				Lo-rate
FRAMES 16-18	P+20m			278	103.96				Min. Res. 10 LAC
FRAMES 19-21	P+20m			278	103.96				Begin Inter-Resolution

NOTE: Underlined frames (and associated slews) are to be deleted at the same time before the end of the cycle.

Fig. 3 (contd)

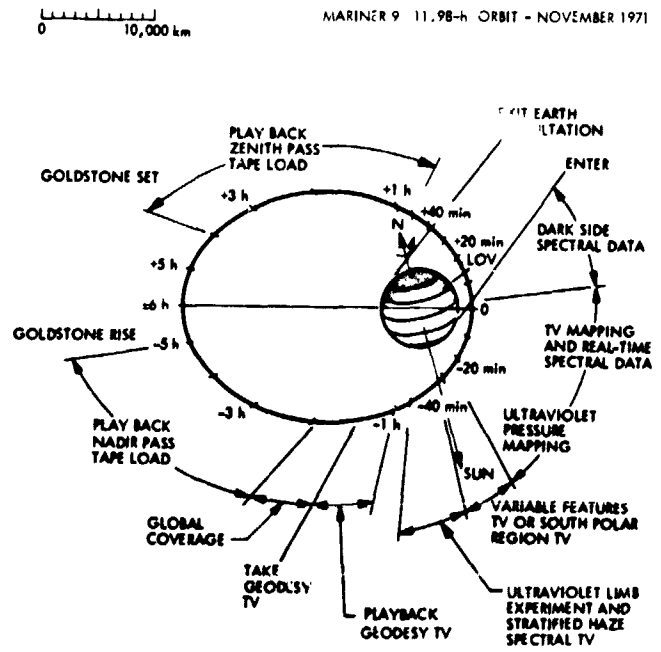


Fig. 4. Typical Goldstone zenith science sequence

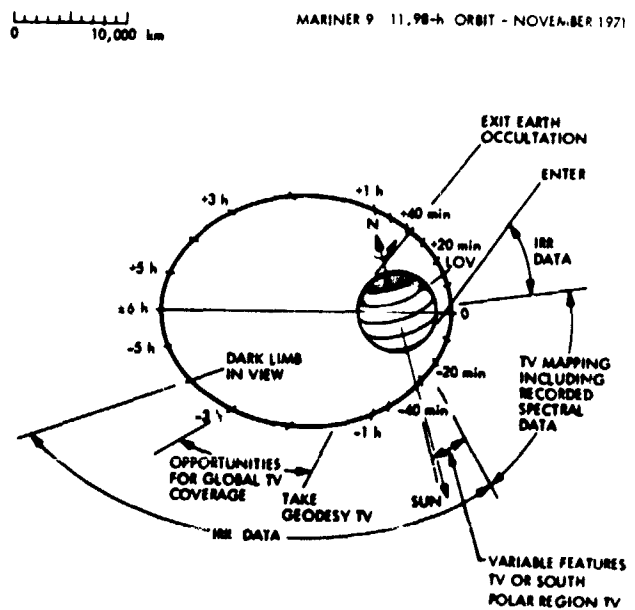
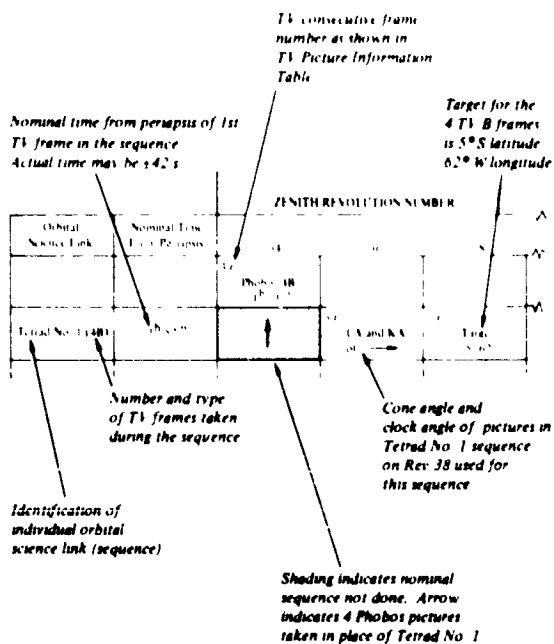
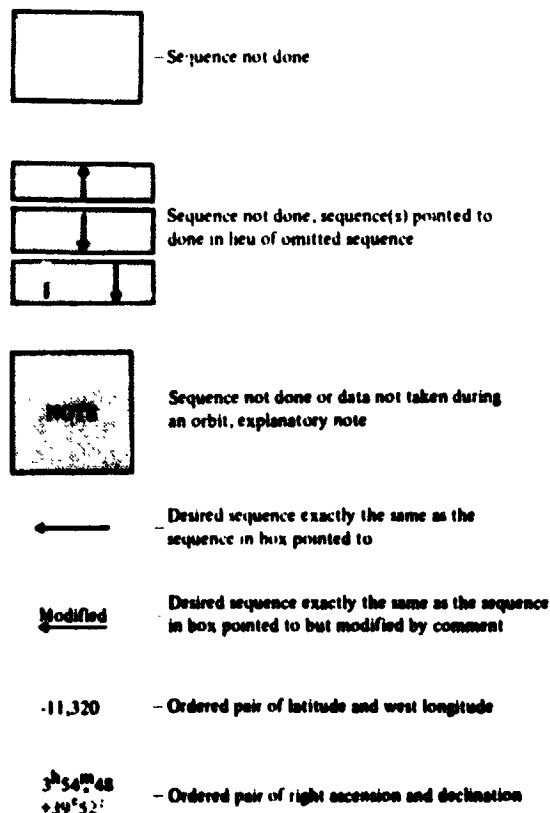


Fig. 5. Typical Goldstone nadir science sequence

## KEY TO SEQUENCE SUMMARY TABLES



## SYMBOLS USED IN THE SEQUENCE SUMMARY TABLES:



## ABBREVIATIONS USED IN THE SEQUENCE SUMMARY TABLES

Adj	Adjacent
B	Blue Filter
CA	Cone Angle
Cal	Calibration
Chg	Change
E	East
Ecl	Eclipse
Even	Evening
Exp	Exposure
Filt	Filter
G	Green Filter
Geod	Geodesy
Gnd Cmd	Ground Command
IRIS	Infrared Interferometer Spectrometer Experiment
IRR	Infrared Radiometer Experiment
KA	Clock Angle
km	Kilometer
Lat	Latitude
Long	Longitude
Lt	Lighted
Max	Maximum
Min	Minimum
Morn	Morning
N	North
NSS	Night Side Spectral
O	Orange Filter
Occul	Occultation
Pict	Picture
Press	Pressure
Ref	Reference
S	South
SB	Single B
Sext	Sextad (3 BA pairs)
Spect	Spectral
Sub-SC	Sub-spacecraft
Term	Terminator
Tet	Tetrad (4 TV frames)
Traj	Trajectory
UVBL	Ultraviolet Bright Limb Experiment
UVPM	Ultraviolet Spectrometer Pressure Mapping
UVS	Ultraviolet Spectrometer
V	Violet Filter
Vert	Vertical
View	Viewing Angle
W	West

## SYMBOLS USED ON PLOTS:

S	Sub-Solar Point
+	Sub-Spacecraft Point
••••	Terminator

Fig. 6. Key to sequence summaries



Orbital Science Link	Nominal Time From Periapas	24	26	28	30	32	34	36	38	40	42
Limb TV (2B)	1 <sup>h</sup> 59 <sup>m</sup>	1 2 Extreme N Limb	2 15°S Limb	←	←	Extreme N Limb	84 4°S E Limb	← (OK) N4 possible	←	E Limb S as possible	Extreme N Term
Tetrad No. 1 (4B)	1 <sup>h</sup> 42 <sup>m</sup>	3 4 Target 20 135	3 4 Target 12 106	3 4 Target 20 135	3 4 Target 12 106	3 4 Target 8 122	Phobos 4B 1 <sup>h</sup> 51 <sup>m</sup>	3 4 CA and KA of →	3 4 Target 5 62	3 4 Target 12 11	3 4 Target 1 45
Global TV (5A)	-1 <sup>h</sup> 44 <sup>m</sup>	7 11 Mosaic of Disk (V)	←	←	←	←	←	←	←	←	←
Global TV (5A)	1 <sup>h</sup> 33 <sup>m</sup>	12 16 Mosaic of Disk (O)	←	←	←	←	←	←	←	←	←
Tetrad No. 2 (4B)	1 <sup>h</sup> 24 <sup>m</sup>	17 20 Target 8 122	17 20 Target 2 116	17 20 Target 8 122	17 20 Target 2 116	17 20 Target 11 119	17 20 Target 19 50	17 20 CA and KA of →	17 20 Target 7 94	17 20 Target 7 95	17 20 Target 16 5 45 5
UVS Mapping	Start after Tet 2 Ends at P-38 <sup>m</sup>	Morn Limb Traj Plane	←	←	←	←	←	←	←	←	←
Polar TV (3 BA Poles)	-34 <sup>m</sup>	21-26 1st B on S Pole (D,G,B)	←	←	←	←	←	21 26 (enter on 84 4, 21 CA and KA of →	21 26 (enter on 84 4, 11	21 26 2nd B on 75, 150	21 26 2nd B on 10, 0
UVS Bright Limb	Start after Polar Ends at P-9 <sup>m</sup>	Align slit at 150 km	←	←	←	←	←	←	←	←	←
TV Mapping (2" BA Poles)	-3 <sup>m</sup>	27-33 Last A vert 10° from Term	←	←	←	←	←	←	←	←	←
Lyman α-1	12 <sup>m</sup>	3 <sup>h</sup> 54 <sup>m</sup> 48 +39°51'	3 <sup>h</sup> 32 <sup>m</sup> 30 +4°54.3	3 <sup>h</sup> 30 <sup>m</sup> 37 +6°19.1	3 <sup>h</sup> 30 <sup>m</sup> 37 +4°51.8	3 <sup>h</sup> 50 <sup>m</sup> 30 +31°44.1	3 <sup>h</sup> 32 <sup>m</sup> 30 +4°54.3	CA and KA of →	3 <sup>h</sup> 54 <sup>m</sup> 48 +39°52.0	3 <sup>h</sup> 25 <sup>m</sup> 15 +28°33.9	3 <sup>h</sup> 53 <sup>m</sup> 45 +40°27.5
Lyman α-2	4 <sup>h</sup> 39 <sup>m</sup>	4 <sup>h</sup> 28 <sup>m</sup> 0 +18°	23 <sup>h</sup> 26 <sup>m</sup> 12°	←	4 <sup>h</sup> 28 <sup>m</sup> 0 +18°	19 <sup>h</sup> 30 <sup>m</sup> +72°	23 <sup>h</sup> 26 <sup>m</sup> 12°	→	Start CA, KA of Rev 34	4 <sup>h</sup> 28 <sup>m</sup> 0 +18°	19 <sup>h</sup> 16 <sup>m</sup> +73°

**Footnotes:**

- ① All TV Pictures 1-sec and 84 sec. Interval later than nominal shown.
- ② SEDR data for picture 20 appears to be inconsistent with rest of Tetrad.

	38	40	42	44	46	48	50	52	54	56	58	60	62	64
							1 2 Phobos 4B 1 <sup>h</sup> 14 <sup>m</sup>							
	← 1 2 E Limb S as possible	1 2 Extreme N Term	1 2 20 <sup>h</sup> N Limb	2 Extreme S Limb	1 2 30 <sup>h</sup> N Limb	1 2 30 <sup>h</sup> N Limb	↑ 1 2 Extreme N Term	1 2 N Polar Term	1 2 In dark ←	1 2 N Limb Min CA	1 2 N Limb Term	1 2 ←		
Target	5 6 Target 12 71	5 6 Target 1 45	5 6 Target 28 52	5 6 Target 45 15	5 6 Target 46 21	5 6 IRIS Target	5 6 Target 43 10	5 6 Target 27 346	5 6 Ear S Limb	5 6 Target 22 334	5 6 2nd Bon 39.4 326.5	5 6 Target all 27 323		
11	← 7 11	← 7 11	← 7 11	← 7 11	← 7 11	← 7 11	← 7 11	← 7 11	← 7 11	← 7 11 Last A CA Limit	← 7 11	← 7 11	← 7 11 Last 2A CA Limit	
14	← 12 16	← 12 16	← 12 16	← 12 16	← 12 16	← 12 16	← 12 16	← 12 16	← 12 16	← 12 16	← 12 16	← 12 16	← 12 16	
							17 20 Phobos 4B 1 <sup>h</sup> 14 <sup>m</sup>							Start of Recon II Cycle
20	← 17 20 Target 7 94	← 17 20 Target 16.5 45.5	← 17 20 Target 45 45	← 17 20 Target 12.0	← 17 20 Target 47 353	← 17 20 Target 50 9	← 17 20 Target 46 336	← 17 20 Target 85 23	← 17 20 Target 60.4 208.8	← 17 20 2nd Bon 76 297	← 17 20 2nd Bon 31 320			
	←	←	←	←	←	←	←	←	←	←	←	←	←	
26	← 21 26 Center on -84.4 21	← 21 26 2nd Bon 75 350	← 21 26 2nd Bon 10 0	← 21 26 2nd Bon 77.7 14	← 21 26 2nd Bon 84 25	← 21 26 2nd Bon 30 140	← 21 26 2nd Bon 33 340	← 21 26 2nd Bon 87 2 5	← 21 26 2nd Bon 76 360	← 21 26 2nd Bon 88 1 325	← 21 26 2nd Bon 87 2 5	← 21 26 2nd Bon 77.1 281.5	← 21 26 2nd Bon N Limb, 247 <sup>m</sup>	
													27 UVBL IV (1B) P 20 <sup>m</sup>	
	←	←	←	←	←	←	←	←	←	←	←	←	←	
30	← 27 30	← 27 30	← 27 30	← 27 30	← 27 30	← 27 30	← 27 30	← 27 30	← 27 30	← 27 30	← 27 30	← 27 30	← 27 30	
	←	←	←	←	←	←	←	←	←	←	←	←	←	
35	← 3 <sup>h</sup> 54 <sup>m</sup> 48 +39 <sup>o</sup> 52'0"	← 5 <sup>h</sup> 25 <sup>m</sup> 11 +28 <sup>o</sup> 33'9"	← 6 <sup>h</sup> 53 <sup>m</sup> 65 +60 <sup>o</sup> 27'5"	← 5 <sup>h</sup> 34 <sup>m</sup> 66 +21 <sup>o</sup> 67'1"	← 21 <sup>h</sup> 28 <sup>m</sup> 02 +70 <sup>o</sup> 20'2"	← 3 <sup>h</sup> 54 <sup>m</sup> 48 +39 <sup>o</sup> 52'0"	←	← 5 <sup>h</sup> 32 <sup>m</sup> 39 +49 <sup>o</sup> 54'3"	← 20 <sup>h</sup> 30 <sup>m</sup> 72 +45 <sup>o</sup> 5'0"	← 5 <sup>h</sup> 38 <sup>m</sup> 24 +49 <sup>o</sup> 56'7"	← 5 <sup>h</sup> 54 <sup>m</sup> 31 +37 <sup>o</sup> 12'0"	← 20 <sup>h</sup> 35 <sup>m</sup> 04 +37 <sup>o</sup> 52'3"	← 21 <sup>h</sup> 46 <sup>m</sup> 27 +16 <sup>o</sup> 21'4"	
	← Base CA, KA of Rev 34	← 0 <sup>h</sup> 28 <sup>m</sup> 0 +18 <sup>o</sup>	← 19 <sup>h</sup> 16 <sup>m</sup> +73 <sup>o</sup>	← 23 <sup>h</sup> 24 <sup>m</sup> 12 <sup>o</sup>	← 0 <sup>h</sup> 28 <sup>m</sup> 0 +18 <sup>o</sup>	← UVBL Background	← 19 <sup>h</sup> 16 <sup>m</sup> +73 <sup>o</sup>	← 23 <sup>h</sup> 24 <sup>m</sup> 12 <sup>o</sup>	← 0 <sup>h</sup> 28 <sup>m</sup> 0 +18 <sup>o</sup>	← UVBL Background	← 19 <sup>h</sup> 16 <sup>m</sup> +73 <sup>o</sup>	← 23 <sup>h</sup> 24 <sup>m</sup> 12 <sup>o</sup>	← 0 <sup>h</sup> 28 <sup>m</sup> 0 +18 <sup>o</sup>	

Fig. 9. Zenith revolutions 24 to 62, reconnaissance I

BOLDON RAME

2

Orbital Science Link	Nominal Time From Periapsis	25	27	29	31	33	35	37	39	41	43	45	
		1-2 Deimos IBA P 2 <sup>h</sup> 43 <sup>m</sup>	1-2 Phobos IBA P 2 <sup>h</sup> 34 <sup>m</sup>										
IRR Scan No. 1	Start Slew at A+1 <sup>h</sup> 01 <sup>m</sup>	↑	↑	Morning Term at 30°N	←	←	←	←	←	←	←	←	
							1-2 Deimos IBA P 2 <sup>h</sup> 36 <sup>m</sup>			1 Phobos 1B P 2 <sup>h</sup> 20 <sup>m</sup>	1-2 Phobos IBA P 2 <sup>h</sup> 41 <sup>m</sup>		
IRR Scan No. 2	-2 <sup>h</sup> 30 <sup>m</sup>	Morning Term at 0°N	←	←	←	←	↑	Morning Term at 0°N	←	↑	↑ ↓	Morning Term at 0°N	
										2-3 Phobos 2B P 1 <sup>h</sup> 59 <sup>m</sup>	3-4 Phobos IBA P 2 <sup>h</sup> 36 <sup>m</sup>		
Limb TV (2B)	-1 <sup>h</sup> 59 <sup>m</sup>	3-4 Extreme N Limb	1-4 Equatorial Limb	1-2 30°S Limb	1-2 15°S Limb	1-2 Extreme N Limb	3-4 84.4°S W Limb	1-2 CA and KA of →	1-2 15°N Limb	↑	5-6 75°S Limb	1-2 20°N Limb	1-2 Exit S. Limb
Tetrad No. 1 (4B)	-1 <sup>h</sup> 52 <sup>m</sup>	5-8 Target 15, 340	5-8 Target -44, 314	3-6 Target -36, 315	3-6 Target -52, 315	3-6 Target -25, 290	5-8 Target 12, 180	3-6 CA and KA of →	3-6 Target -5, 262	① 4-7 Target -5, 222	7-10 Target 10, 245	3-6 Target 23, 213	3-6 Target 20, 213
Global TV (5A)	-1 <sup>h</sup> 45 <sup>m</sup>	9-13 Mosaic of Disk (O)	9-13 ←	7-11 ← (V)	7-11 ← (O)	7-11 ← (V)	9-13 ← (O)	7-11 ← (V)	7-11 ← (V)	8-12 ← (O)	11-15 ← (V)	7-11 ← (O)	7-11 ← (V)
										13-16 Phobos 1B 3A P-1 <sup>h</sup> 24 <sup>m</sup>			
Tetrad No. 2 (4B)	-1 <sup>h</sup> 35 <sup>m</sup>	14-17 Target -60, 345	14-17 Target -42, 324	12-16 Target 60, 345	12-16 Target -45, 312	12-16 Target 0, 270	14-17 Target 7, 269	12-16 CA and KA of →	12-16 Target 5, 270	↑	16-19 Target 2, 245	12-16 Target 30, 225	12-16 Target -12, 213
					16-17 Phobos IBA P-54 <sup>m</sup>	16-17 Phobos IBA P-51 <sup>m</sup>							16-17 Phobos P-4
IRR Limb Scan	Slew after Tet 2 Ends at P-40 <sup>m</sup>	Morn Limb Traj Plane	←	←	↑	↑	Morn Limb Traj Plane	←	←		Morn Limb Traj Plane	←	
Polar TV (3 BA Pairs)	-34 <sup>m</sup>	18-23 1st B on S Pole (O,G,B)	18-23 ←	16-21 ←	18-23 ←	18-23 ←	18-23 Center on -78, 143	16-21 CA and KA of →	16-21 Center on -78, 143	17-22 2nd B on -86, 27	20-26 2nd B on -79, 139	16-21 2nd B on -60, 180	16-21 2nd B on -60, 180
TV Mapping (4 BA Pairs)	-6 <sup>m</sup>	24-32 Last A Vert 10° from Term	24-32 ←	22-32 ←	24-32 ←	24-32 ←	24-32 ←	22-32 ←	22-32 ←	23-32 ←	26-32 Tape ← Limb	22-31 ←	24-32 ←

Footnotes:

- ① Error made in targeting: -5° read as -50 in Orbital Sequence Sheet for Rev. 39.
- ② Targets missed due to cone and clock angle errors during S/C ejection.
- ③ Remain Mars 3 Landing Site.

Fig. 10. Nadir revolutions 25 to 63, reconnaissance I

43	45	47	49	51	53	55	57	59	61	63	65
										1 Deimos 1B P-3 <sup>h</sup> 27 <sup>m</sup>	
←	←	←	←	←	Morning Term 15°S	A' CA Limit	←	←	←	↓ ↑	
-2 Phobos 1BA P-2 <sup>h</sup> 51 <sup>m</sup>								1 Phobos 1B P-2 <sup>h</sup> 47 <sup>m</sup>		2-7 Deimos 5BA P-2 <sup>h</sup> 48 <sup>m</sup>	
↓	Morning Term at 0°N	←	←	←	Morning Term 30°S	←	←	←	←	←	
-4 Phobos 1BA P-2 <sup>h</sup> 36 <sup>m</sup>											
-6 75°S Limb	1-2 20°N Limb	1-2 Extreme S Limb	1-2 30°N Limb	1-2 35°N Limb	1-2 Extreme N Term	1-2 N Polar Term	1-2 N Polar Term	2-3 N Limb CA Limit	1-2 Target 20, 134.5	8-9 Extreme N Limb	
							3-6 Phobos 4B P-1 <sup>h</sup> 52 <sup>m</sup>				
-10 245	3-6 Target 23, 213	3-6 Target 20, 192	3-6 Target 44, 200	3-6 Target 20, 192	3-6 Target 3, 173	3-6 Target 20, 135	↑	4-7 2nd B on 20, 134.5	3-6 2nd B on 20, 134.5	10-13 2nd B on 20, 134.5	Start of Recon II Cycle
-15	7-11 (O) ←	7-11 (V) ←	7-11 (O) ←	7-11 (V) ←	7-11 (O) ←	7-11 (V) ←	7-11 Last A CA Limit	8-12 (V) ←	7-11 (O) ←	14-18 Last 2A CA Limit	
-19 245	12-15 Target -30, 225	12-15 Target -2, 191	12-15 Target 37, 182	12-15 Target 16, 167	12-15 Nix Olym on Limb	12-15 20°N+2° 10° in dark	12-15 Target 20, 135	13-16 2nd B on -8, 121	12-15 Target -1, 113	19-22 ←	
		16-17 Phobos 1BA P-42 <sup>m</sup>			16-17 Phobos 1BA P-45 <sup>m</sup>						
Morn Limb Traj Plane	←	↑	Morn Limb Traj Plane	←	↑	Morn Limb Traj Plane	←	←	←	←	
-26 on 139	16-21 2nd B on -10, 180	18-23 2nd B on -46, 170	16-21 2nd B on -84, 23	16-21 2nd B on -33, 155	18-23 2nd B on -75, 187	16-21 2nd B on -88.1, 325	16-21 Mars 3 -45, 158	17-22 2nd B on -87.2, 5	16-21 2nd B on Limb, 121°W	23-28 ←	
	22-31 ←	24-32 ←	22-32 ←	22-32 ←	24-32 ←	22-32 ←	22-32 ←	23-32 ←	22-32 ←	29-32 Tape Limit	

Orbital Science Link	Nominal Time From Periapsis	64	66	68	70	72	74	76	78	80
						3 <sup>h</sup> 44 <sup>m</sup> 5 <sup>s</sup> +24 <sup>o</sup> 15'				
Tetrad No 1 (4B)	-1 <sup>h</sup> 30 <sup>m</sup>	1-4 Last B on Limb 85 <sup>o</sup> S	1-4 Target 15, 305	1-4 2nd B on 11, 320	1-4 Target 47, 271	1-4 ↑ Star Cal	1-4 2nd B on 0, 270	1-4 2nd B on 26.5, 233.4	1-4 Adjacent to ←	1-4 Adjacent to ←
						4 <sup>h</sup> 33 <sup>m</sup> +16 <sup>o</sup> 26'				
Global TV (1B, 8A, 1B)	-1 <sup>h</sup> 21 <sup>m</sup> 36 <sup>s</sup>	5-14 Mosaic of Lighted Disk	5-14 ← (V)	5-14 ← (O) Last B on 58.2, 197.12	5-14 Mosaic of 11. Disk	5-8 ↑ 1/2 Star Cal 10-14 ↑ 1/2	① 5-14 Mosaic of L1. Disk	5-14 Calibration 30, 230	5-1 Mosaic of 11. Disk	5-14 ←
						5 <sup>h</sup> 23 <sup>m</sup> 13 <sup>s</sup> +28 <sup>o</sup> 33'9"				15-18 Phobos 4 P 1 <sup>h</sup> 06 <sup>m</sup>
Tetrad No 2 (4B)	-1 <sup>h</sup> 06 <sup>m</sup> 12 <sup>s</sup>	15-18 2nd B on 75, 310	15-18 2nd B on -75, 301	15-18 2nd B on -58.2, 197.12	15-18 2nd B on -75, 292	15-18 RETURN to PLANE F	15-18 2nd B on 75, 283	15-18 Adj to Tet. 1 26.5, 230	15-18 2nd B on 75, 274	↑
Spectral Scan	-1 <sup>h</sup> 02 <sup>m</sup>	Spectral Scan	UVBL 2nd B on Sext	Slew to 58.2, 197.12	UVBL 2nd B on Sext	UVS Morn Map	UVBL 2nd B on Sext	Mapping	UVS Limb	Mapping
Sextad (3BA)	-34 <sup>m</sup>	19-24 2nd B on -72.3, 30.	19-24 2nd B on Limb UVBL	19-24 1st B on -58.2, 197.12	19-24 2nd B on Limb UVBL	19-24 Calibration Light = 60 <sup>o</sup>	19-24 2nd B on Limb UVBL	19-24 2nd B on 75, 160	19-24 ←	19-24 2nd B on 60, 180
									P 26 <sup>m</sup> Night Side Spect	
TV Mapping (1A, 3BA, 1B)	-17 <sup>m</sup> 54 <sup>s</sup>	25-32 5th A on Nadir vert	←	25-32 1st B on -58.2, 197.12	25-32 5th A on Nadir vert	←	25-32 P+6 <sup>m</sup> 1st B on -9, 119	25-32 P+5 <sup>m</sup> ← -8, 120	25-32 P+5 <sup>m</sup> ← 1.7, 112.4	25-32 P+3 <sup>m</sup> ←
Spectral Scan	-2 <sup>m</sup>	Night Side Spectral	←	←	←	←	Discontinued in order to move TV Mapping.			
Lyman α-1	30 <sup>m</sup>		5 <sup>h</sup> 32 <sup>m</sup> 39 <sup>s</sup> +9 <sup>o</sup> 54'3"	0 <sup>h</sup> 10 <sup>m</sup> 66 <sup>s</sup> +14 <sup>o</sup> 54'59"	5 <sup>h</sup> 32 <sup>m</sup> 39 <sup>s</sup> +9 <sup>o</sup> 54'3"	3 <sup>h</sup> 54 <sup>m</sup> 48 <sup>s</sup> +39 <sup>o</sup> 52'20"	5 <sup>h</sup> 34 <sup>m</sup> 06 <sup>s</sup> +21 <sup>o</sup> 07'1"	1 <sup>h</sup> 50 <sup>m</sup> 76 <sup>s</sup> +63 <sup>o</sup> 25'9"	22 <sup>h</sup> 37 <sup>m</sup> 01 <sup>s</sup> +38 <sup>o</sup> 47'6"	6 <sup>h</sup> 34 <sup>m</sup> 83 <sup>s</sup> +16 <sup>o</sup> 26'9"
Lyman α-2	4 <sup>h</sup> 35 <sup>m</sup>		19 <sup>h</sup> 16 <sup>m</sup> +73 <sup>o</sup>	22 <sup>h</sup> 37 <sup>m</sup> 01 <sup>s</sup> +38 <sup>o</sup> 47'6"	0 <sup>h</sup> 10 <sup>m</sup> 66 <sup>s</sup> +14 <sup>o</sup> 54'59"	↑	↑	↑	↑	
Lyman α-3	5 <sup>h</sup> 35 <sup>m</sup>		↑	23 <sup>h</sup> 24 <sup>m</sup> -12 <sup>o</sup>	0 <sup>h</sup> 28 <sup>m</sup> +18 <sup>o</sup>	UVBL Background	19 <sup>h</sup> 16 <sup>m</sup> +73 <sup>o</sup>	23 <sup>h</sup> 24 <sup>m</sup> 12 <sup>o</sup>	0 <sup>h</sup> 28 <sup>m</sup> +18 <sup>o</sup>	UVBL Background

Footnotes:

- ① Picture 9 taken during slew.
- ② Only 6 BA-pairs of data received on earth due to Goldstone antenna difficulties.

	74	76	78	80	82	84	86	88	90	92	94	96	98	100
	1-4 2nd B on 0 270	1-4 2nd B on 26 5 2334	1-4 Adjacent to ←	1-4 Adjacent to ←	1-4 1st B on 55 225	1-4 CA and KA ←	1-4 1st B on 55 207	1-4 1st B on 55 202	1-4 1st B on 55,194					
①	5-14 Mosaic of Lt Disk	5-14 Calibration 30 230	5-14 Mosaic of Lt Disk	5-14 ←	5-14 ←	5-14 ←	5-14 ←	5-14 ←	5-14 ←					
				15-8 Phobos 4B P-1 <sup>h</sup> 06 <sup>m</sup>										
	15-18 2nd B on 75, 287	15-18 Adj to Tet I 26 5 230	15-18 2nd B on 75 274	↑	15-18 1st B on 75, 220	15-18 CA and KA ←	15-18 1st B on 75 202	15-18 Target 46, 164	15-3 1st B on -45, 158					
	UVBL 2nd B on Sext	Mapping	LVS Limb	Mapping	UVBL	←	←	Morning Spect Map	UVBL					
	19-24 2nd B on Limb UVBL	19-24 2nd B on 75, 160	19-24 ←	19-24 2nd B on 60, 180	19-24 ←	19-24 CA and KA ←	19-24 2nd B on 58, 210	19-24 2nd B on 87 7, 96 9	19-24 2nd A on 34, 151					
			P 26 <sup>m</sup> Night Side Spect											
	25-32 P+6 <sup>m</sup> 1st B on 9 119	25-32 P+5 <sup>m</sup> ← 8, 120	25-32 P+5 <sup>m</sup> ← 17, 112,4	25-32 P+3 <sup>m</sup> ←	25-32 P 0 <sup>m</sup> ← 10 <sup>h</sup> 5	25-32 ←	25-32 P+1 <sup>m</sup> ←	25-32 P 1 <sup>m</sup> ← 1:0 <sup>s</sup>	25-32 P-0 <sup>m</sup> ←	1-12 P-36 <sup>m</sup> 16BA	①			
	Discontinued in order to move TV Mapping.													
	5 <sup>h</sup> 34 <sup>m</sup> 66 +21 <sup>o</sup> 07'1	1 <sup>h</sup> 50 <sup>m</sup> 76 +63 <sup>o</sup> 25'9	22 <sup>h</sup> 37 <sup>m</sup> 01 +38 <sup>o</sup> 47'6	6 <sup>h</sup> 34 <sup>m</sup> 83 +16 <sup>o</sup> 26'9	22 <sup>h</sup> 22 <sup>m</sup> 72 +1 <sup>o</sup> 07'3	CA and KA ←	5 <sup>h</sup> 37 <sup>m</sup> 01 +41 <sup>o</sup> 10'4	6 <sup>h</sup> 38 <sup>m</sup> 24 +9 <sup>o</sup> 56'7	0 <sup>h</sup> 57 <sup>m</sup> 79 +28 <sup>o</sup> 48'9			22 <sup>h</sup> 59 <sup>m</sup> 61 +42 <sup>o</sup> 3'1	0 <sup>h</sup> 34 <sup>m</sup> 17 +53 <sup>o</sup> 37'5	
	↑	↑	↑	↑	↑	↑	↑	↑	↑			↑	↑	
	19 <sup>h</sup> 16 <sup>m</sup> +73 <sup>o</sup>	23 <sup>h</sup> 24 <sup>m</sup> 12 <sup>o</sup>	0 <sup>h</sup> 28 <sup>m</sup> +18 <sup>o</sup>	UVBL Background	Ref. Position	Ref. Position	19 <sup>h</sup> 16 <sup>m</sup> +73 <sup>o</sup>		23 <sup>h</sup> 24 <sup>m</sup> 12 <sup>o</sup>			↑	↑	

ORBITAL TRIM MANEUVER NO SCIENCE DATA

Start of Mapping Cycle I

Fig. 11. Zenith revolutions 64 to 98, reconnaissance II

FOLDOUT FRAME

2

Orbital Science Link	Nominal Time From Periapsis	65	67	69	71	73	75	77	79	81	83	85	87	89	91
						1-2 Dempos 2B P 1 <sup>h</sup> 17 <sup>m</sup>									
IRR Scan No. 1	-5 <sup>h</sup> 12 <sup>m</sup>	Morning Term	←	←	←	↑ ↓	Track thru S. Spot	←	Track thru Middle Spot	Morning Term.	←	←	←	↓	Morning Term.
						3 Phobos 1B P 2 <sup>h</sup> 0 <sup>m</sup>								1-6 Phobos 3BA P 2 <sup>h</sup> 11 <sup>m</sup>	
IRR Scan No. 2	-2 <sup>h</sup>	Morning Term	←	←	←	←	S. Spot 8, 120	←	Middle Spot 1.5, 112.4	Morning Term.	←	←		IRR No. 1 Morn Term	
													1-4 Phobos 4B P 1 <sup>h</sup> 32 <sup>m</sup>		
Tetrad (4B)	-1 <sup>h</sup> 31 <sup>m</sup> 24 <sup>s</sup>	1-4 Target -1, 113	1-4 2nd B on 13, 105	1-4 3rd B on -7, 95	1-4 3rd B on 12, 71	4-7 2nd B on 10, 75	1-4 Adjacent ←	1-4 Adjacent ←	1-4 2nd B on -8, 48	1-4 Adjacent ←	1-4 2nd B on -30, 40	1-4 CA and KA ←	↑	7-10 2nd B on 55, 20	1-4 2nd B on -55, 11
Global TV (8A)	-1 <sup>h</sup> 20 <sup>m</sup> 54 <sup>s</sup>	5-12 Mosaic of Lighted Disk	5-12 (V) ←	5-12 (O) ←	5-12 (V) ←	8-15 (O) ←	5-12 (B) ←	5-12 (O) ←	5-12 (V) ←	5-12 (O) ←	5-12 (V) ←	5-12 (O) ←	5-12 (V) ←	11-18 (V) ←	5-12 (O) ←
Trad (3B)	-1 <sup>h</sup> 5 <sup>m</sup> 44 <sup>s</sup>	13-15 2nd B on -8, 121	13-15 2nd B on 17, 110	13-15 2nd B on -8, 121	13-15 2nd B on -15, 61	16-18 Contiguous with Tet.	13-15 Adjacent ←	13-15 Adjacent ←	13-15 Contiguous with Tet.	13-15 Adjacent ←	13-15 2nd B on -55, 30	13-15 CA and KA ←	13-16 1st B on -4.7, 6.5	19-21 2nd B on -46, 355	13-15 2nd B on -46, 351
Dyad (2B)	-5 <sup>h</sup> 7 <sup>m</sup> 20 <sup>s</sup>	16-17 1st B on -7, 95	16-17 N. Limb at 105°W	16-17 ←	16-17 45°S Limb	19-20 S. Term. at Limb	16-17 Target -29.5, 42.5	16-17 65°S Limb	16-17 48°S Limb	16-17 N. Limb Term	16-17 5°N Limb in Dark	16-17 CA and KA ←	16-17 S. Limb in Dark	22-23 N. Limb 0°W	16-17 ←
IRR Scan No. 3	-5 <sup>h</sup> 5 <sup>m</sup> 26 <sup>s</sup>	IRR Limb Scan	←	←	←	←	←	←	←	←	←	←	←	←	←
Sextad (3BA)	-3 <sup>h</sup> 3 <sup>m</sup> 32 <sup>s</sup>	18-23 2nd B on -87.2, 5	18-23 2nd B on -40, 60	18-23 1st B on S. Pole	18-23 3rd B on -87.2, 5	21-26 2nd B on -40, 90	18-23 2nd B on -60, 345	18-23 ←	18-23 3rd B on -82.7, 3	18-23 3rd B on -82.7, 3	18-23 1st B on -73, 8	18-23 CA and KA ←	18-23 1st B on -73, 325	24-29 B's on Limb A's on Term.	18-23 ←
								24-31 Phobos 1A 3BA 1B P-17 <sup>m</sup>							
TV Mapping (1A, 4BA)	-1 <sup>h</sup> 7 <sup>m</sup> 26 <sup>s</sup>	24-32 5th A Vertical	24-32 ←	24-32 ←	24-32 ←	27-31 Tape Limit	24-31 1A 3BA 1B	↑	24-31 Rev. 77 Map 1.4 3BA 1B	24-31 "5th A" Vert.	24-31 ←	24-31 ←	24-31 ←	30-32 Tape 1 mH	24-31 ←
IRR Scan No. 4	-2 <sup>h</sup>	Night Side Spectral	←	←	←	←	←		Night Side Spectral	←	←	←	←	←	←

Fig. 12. Nadir revolutions 65 to 99, reconnaissance II

	85	87	89	91	93	95	97	99	101
	←	←	↓	Morning Term.					
			1-6 Phobos 3BA P-2 <sup>h</sup> 1 <sup>m</sup>						
	←		IRR No. 1 Motn Term						
		1-4 Phobos 4B P-1 <sup>h</sup> 32 <sup>m</sup>							
	1-4 CA and KA ←	↑	7-10 2nd B on -55, 20	1-4 2nd B on -55, 11					
									Start of Mapping Cycle I
	5-12 ← (O)	8-12 ← (V)	11-18 ← (V)	5-12 ← (O)					
	13-18 CA and KA ←	13-18 1st B on -4.7, 6.5	18-21 2nd B on -46, 355	13-18 2nd B on -46, 351					
	16-17 CA and KA ←	16-17 S. Limb in Dark	22-23 N. Limb 0 <sup>h</sup> W	16-17 ←					
	←	←	←	←					
	18-23 CA and KA ←	18-23 1st B on -73, 325	24-28 B's on Limb A's on Term.	18-23 ←					
	24-31 ←	24-31 ←	30-32 Tape ← Limit	24-31 ←	1-23 P-16 <sup>m</sup> 16BA	1-33 P-35 <sup>m</sup> 16BA	1-35 P-36 <sup>m</sup> 16BA	1-32 P-36 <sup>m</sup> 16BA	
	←	←	←	←					

Orbital Science Link	Nominal Time From Periapsis	100	102	104	106	108	110	112	114	116	118
Global TV (5A)	-59 <sup>m</sup> 36 <sup>s</sup>	1-5 N-S Mosaic Light Disk	1-5 1st A on 12, 122	1-5 Light Angle 50° 55°	1-5 Same as	1-5 N-S Mosaic Light Disk	1-5	1-5	1-5	1-5	1-5
Spectral Scan	-53 <sup>m</sup> 54 <sup>s</sup>	Morning Spect. Map	UVBL	Morning Spect. Map	UVBL	Morning Spect. Map	UVBL	Morning Spect. Map	UVBL	Morning Spect. Map	←
Pentad (2 AB 1A)	-33 <sup>m</sup>	6-10 Gore Fill Revs 97&98	6-10 1st B on Limb	6-10 Target 50, 40	6-10 Target -62, 107	6-10 Gore Fill S. Polar	6-10 Target 60, 345	6-10 Target 50, 40	6-10 1st B on Limb Same as Rev 102	6-10 B Frames -86.5, 5	6-10 Target -30, 345
Spectral Scan	-30 <sup>m</sup> 06 <sup>s</sup>	Evening Spect. Map				Evening Spect. Map	Same CAA ← KA of Pent	Ends at ← P 25 <sup>m</sup>	←	←	←
TV Mapping No. 1 (1A 3BA)	-19 <sup>m</sup>	11-17 4th A Taken Vertically	11-17	11-17	11-17	11-17	11-17	11-17	11-17	11-17	11-17
TV Mapping No. 2 (1A 5BA)	-10 <sup>m</sup> 36 <sup>s</sup>	18-28 3rd A Taken Vertically	18-28	18-28	18-28	18-28	18-28	18-28	18-28	18-28 P-7 <sup>m</sup>	18-28 P-8 <sup>m</sup>
Spectral Scan	-3 <sup>m</sup> 30 <sup>s</sup>	Evening Spect. Map	←	←	←	←	←	←	←	P-1 <sup>m</sup>	←
Tetrad (1A 1BA 1A)	16 <sup>m</sup>	28-33 B on N. Limb at Term	28-33	28-33 Target 38, 340	28-33 Target 15, 325	28-33 Target 40, 330	28-33 B on Dark Limb	28-33 Target B 23, 295	28-33 2nd A on 16, 287	28-33 Target 10, 280	28-33 N. Limb and Term
Spectral Scan	18 <sup>m</sup> 54 <sup>s</sup>	Night Side Spectral	← P+23 <sup>m</sup>	←	←	←	←	←	←	Nominal Time	←
Lyman α-1	1 <sup>h</sup> 12 <sup>m</sup>	0 <sup>h</sup> 53 <sup>m</sup> 65 <sup>s</sup> +60°27.5	3 <sup>h</sup> 4 <sup>m</sup> 91 <sup>s</sup> +40°45.8	3 <sup>h</sup> 55 <sup>m</sup> 70 <sup>s</sup> +35°38.8	0 <sup>h</sup> 34 <sup>m</sup> 17 <sup>s</sup> +15°37.5	3 <sup>h</sup> 55 <sup>m</sup> 70 <sup>s</sup> +55°38.8	6 <sup>h</sup> 38 <sup>m</sup> 24 <sup>s</sup> +9°56.7	0 <sup>h</sup> 5 <sup>m</sup> 79 <sup>s</sup> +28°48.9	3 <sup>h</sup> 54 <sup>m</sup> 48 <sup>s</sup> +39°32.0	23 <sup>h</sup> 2 <sup>m</sup> 27 <sup>s</sup> +14°56.1	7 <sup>h</sup> 31 <sup>m</sup> 42 <sup>s</sup> +31°59.9
Lyman α-2	5 <sup>h</sup> 22 <sup>m</sup>	23 <sup>h</sup> 24 <sup>m</sup> -12°	19 <sup>h</sup> 16 <sup>m</sup> +73°	23 <sup>h</sup> 24 <sup>m</sup> -17°	0 <sup>h</sup> 28 <sup>m</sup> 0 <sup>s</sup> +18°	19 <sup>h</sup> 16 <sup>m</sup> +73°	UVBL Background	23 <sup>h</sup> 24 <sup>m</sup> -12°	UVBL Background	0 <sup>h</sup> 28 <sup>m</sup> 0 <sup>s</sup> +18°	19 <sup>h</sup> 16 <sup>m</sup> +73°

**Footnotes:**

- ① Pentad changed from 2AB 1A to 1B 2BA and Tetrad from 1A 1BA to 2BA on this rev and all succeeding revs in this cycle because of frozen filter wheel on α-owners. Nominal Time for Pentad changed to P-32<sup>m</sup>06<sup>s</sup> and for Tetrad from 16<sup>m</sup> to 15<sup>m</sup>28<sup>s</sup>.

	114	116	118	120	122	124	126	128	130	132	134	136	138	140
	1-5 ←	1-5 ←	1-5 ←	1-5 ←	1-5 ←	1-5 ←	1-5 ←	1-5 ←	1-5 Utter Y <sub>3</sub> ←	1-5 ←	1-5 ←	1-5 ←	1-5 ←	
	UVBL	Morning Spect Map	←	UVBL	←	Morning Spect Map	UVBL	Morning Spect Map	UVBL	Morning Spect Map	UVBL	Morning Spect Map	UVBL	
	6-10 1st B on Limb Same as Rev. 102	6-10 B Frames -86.5.5	6-10 Target 30, 345	6-10 B's on Limb Morn Term.	6-10 ←	6-10 Target 85.8, 5	6-10 Target 70.6, 255.3	6-10 Target 66.5, 126	6-10 ←	6-10 Target -72.0°W	6-10 Target 40, 270	6-10 2nd B on 40, 270	6-10 Target B's -40, 270	
	←	←	←	←	←	←	Endsat P 27 <sup>m</sup>	Endsat P 25 <sup>m</sup>	←	←		Same CAA KA of Pent.	←	
	11-17 ←	11-17 ←	11-17 ←	11-17 ←	11-17 ←	11-17 ←	11-17 ←	11-17 ←	11-17 ←	11-17 ←	11-17 ←	11-17 ←	11-17 ←	
	18-28 ←	18-28 P-7 <sup>m</sup>	18-28 P-8 <sup>m</sup>	18-28 ←	18-28 ←	18-28 ←	18-28 ←	18-28 ←	18-28 ←	18-28 ←	18-28 ←	18-28 ←	18-28 ←	
	←	P-1 <sup>m</sup>	←	←	←	←	←	←	←	←	←	←	←	
	28-33 2nd A on 16, 287	28-33 Target 10, 280	28-33 N. Limb and Term	28-33 ←	28-33 Target 15, 258	28-33 Target 15, 249	28-33 Target 15, 240	28-33 1st Limb and Term	28-33 Target 15, 205	28-33 ←	28-33 2nd B on 24.4, 213.2	28-33 1st A on 40, 185	28-33 Target 40, 185	
	←	Nominal Time	←	←	←	←	←	←	←	←	←	←	←	
	3 <sup>h</sup> 54 <sup>m</sup> 48 +39°52'0	23 <sup>h</sup> 2 <sup>m</sup> 27 +14°56'1	7 <sup>h</sup> 31 <sup>m</sup> 42 +31°59'9	0 <sup>h</sup> 10 <sup>m</sup> 66 +14°54'9	21 <sup>h</sup> 15 <sup>m</sup> 85 +34°41'5	4 <sup>h</sup> 48 <sup>m</sup> 04 +66°15'6	21 <sup>h</sup> 16 <sup>m</sup> 58 +43°43'6		21 <sup>h</sup> 44 <sup>m</sup> 94 +49°55'1	23 <sup>h</sup> 17 <sup>m</sup> 80 +7°58'0		3 <sup>h</sup> 4 <sup>m</sup> 91 +40°45'8	1 CAS φ Per	
	UVBL Background	0 <sup>h</sup> 28 <sup>m</sup> 0 +18°	19 <sup>h</sup> 16 <sup>m</sup> +73°	UVBL Background	←	0 <sup>h</sup> 28 <sup>m</sup> 0 +18°	2 <sup>h</sup> 24 <sup>m</sup> +12°	0 <sup>h</sup> 28 <sup>m</sup> 0 +18°	UVBL Background	19 <sup>h</sup> 16 <sup>m</sup> +73°	23 <sup>h</sup> 24 <sup>m</sup> -12°	3 <sup>h</sup> 32 <sup>m</sup> 03 +48°2'5	19 <sup>h</sup> 16 <sup>m</sup> +73°	

UVBL  
Background

Fig. 13. Zenith revolutions 100 to 138, mapping cycle I

FOLDBOUT FRAME

2

Orbital Science Link	Nominal Time From Periapas	101	103	105	107	109	111	113	115	117	119	121
							1 Demos 1B P-3h22m			1 Phobos 1B P-2h02m		1 Demos 1B P-1h15m
IRR Scan	-5h12m	Morning Term Scan	←	←	←	←	P-3h35m	P-2h15m	←	P-2h	P-2h15m	P-1h30m
Global TV (5A)	-5h036s	1-5 N-S Mosaic Light Disk	1-5 Light Angle 50° 55°	←	←	←	1-5 N-S Mosaic Light Disk	2-6	←	←	←	←
IRR Scan	-5h54s	IRR Limb Scan	←	←	←	←	←	←	←	←	←	←
TLR (1B)	-37m54s	6 Target -40, 270	8 Limb 300°W	←	6 Limb 270°W	6 Target -85, 50	7 Target -58, 223	6 Target -76.7, 155.7	6 Limb Min. CA	7 Target -58.9, 180.1	6 77°S, 10° in Light	7 Target -65.2, 207
Tetrad (2A 1BA)	-33m	7-10 B on -40, 270	7-10 B on Limb 250°W	←	7-10 B on Limb 295°W	7-10 Target B -85, 50	8-11 Target -58, 223	7-10 Target -75, 160	7-10 B on Limb at Term.	8-11 Target B -58.9, 180.1	7-10 B 77°S, 10° in Light	8-11 Target -65.2, 207
TV Mapping No. 1 (1A 3BA)	-10m	11-17 4th A Taken Vertically	←	←	←	←	←	←	←	←	←	←
TV Mapping No. 2 (1A 5BA)	-10m36s	18-28 3rd A Taken Vertically	←	←	←	←	←	←	←	←	← P-8m	← P-7m
Dyad No. 1 (1AB)	9m	28-30 B on 25, 190	28-30 Target B 0, 160	29-30 Target B 10, 146	28-30 Target B 20, 135	28-30 Target B -9.3, 123.8	30-31 Target B 1, 112.5	28-30 Target B -16, 109.5	28-30 Target B -8.8, 94.7	30-31 Target B 1, 112.5	28-30 Target B -5, 82.5	30-31 Target B -12, 70
Dyad No. 2 (1AB)	18m48s	31-32 B on N. Limb Term.	31-32 B at 50°N Min. CA	31-32 Target B 10, 146	31-32 Target B 20, 135	31-32 Target B 20, 134.5	30 Target B 1, 112.5	31-32 Target B 12.3, 104.3	31-32 Target B 46, 116	30 Target B 14, 92	31-32 B at 45°N Min. CA	32
IRR Scan	20m18s	IRR Night Side Scan	←	←	←	←	←	←	←	←	←	←

① Tetrad changed from 2A 1BA to 2BA for this rev and all succeeding revs in this cycle.

Fig. 14. Nadir revolutions 101 to 137, mapping cycle I

117	119	121	123	125	127	129	131	133	135	137	139
Phobos 1B P-2 <sup>h</sup> 0 <sup>m</sup>		Deimos 1B P-1 <sup>h</sup> 35 <sup>m</sup>					Phobos 1B P-1 <sup>h</sup> 33 <sup>m</sup>	Phobos 1B P-1 <sup>h</sup> 30 <sup>m</sup>			
P-2 <sup>h</sup>	P-2 <sup>h</sup> 15 <sup>m</sup>	P-1 <sup>h</sup> 30 <sup>m</sup>	P-2 <sup>h</sup> 15 <sup>m</sup>	←	←	←	P-1 <sup>h</sup> 30 <sup>m</sup>	P-1 <sup>h</sup> 27 <sup>m</sup>	P-2 <sup>h</sup> 15 <sup>m</sup>	←	
←	←	←	←	←	←	←	←	←	←	←	
←	←	←	←	←	←	←	←	←	←	←	
←	←	←	←	←	←	←	←	←	←	←	
							Phobos 1B P-3 <sup>h</sup> 27 <sup>m</sup>				
6 Target -180.1	7 77°S, 1° in Light Target -65.2, 207	7 Target -34.8, 186.6	6 Target -76.8, 230.1	6 Target -60.6, 144.7	6 Target -70.6, 81.2	7 Target -87.101	7 Target -87.101	7 Target -65.4, 123.8	6 Target -80.149		
							7-10 Phobos 2A 1BA P-33 <sup>m</sup>				
	7-10 B 77°S, 1° in Light	8-11 Target -65.2, 207	7-10 Target B -34.151	7-10 Target B -60.6, 144.7	8-11 S. Polar Limb Term	8-11 Target -87.101	7-10 2nd B on -65.4, 123.8	7-10 Target B's -80.149			Start of Mapping Cycle III
←	←	←	←	←	←	←	←	←	←	←	
←	←	←	←	←	←	←	←	←	←	←	
P-6 <sup>m</sup>	10-20 P-7 <sup>m</sup>	10-20 P-8 <sup>m</sup>	10-20	10-20 P-7 <sup>m</sup>	10-20 P-8 <sup>m</sup>	10-20	10-20	10-20	10-20	10-20	10-20
←	←	←	←	←	←	←	←	←	←	←	←
20-30 Target B -5, 82.5	20-31 Target B -12, 70	20-30	20-30 Target A 20, 65	20-30 Target A -3, 62	20-30 Target A -28.2, 53.1	20-31 Target B 3, 53	20-31 Target B -0.5, 48	20-30 Target B 10, 18	20-30 Target A 0, 0		
31-32 B at 45°N Min. CA	32	31-32 Target B 28, 62	31-32 Target A 20, 65	31-32 N. Polar Limb -60, 80	31-32 B on Limb Near Term.	30 Target B 45, 45	30 Target A 40, 30	31-32	31-32 Target A -10, 0		
←	←	←	←	←	←	←	←	←	←	←	

BOLDOUT FRAME

2

Orbital Science Link	Nominal Time From Periapis	140	142	144	146	148	150	152	154	156	158
Spectral Scan	3 <sup>h</sup> 17 <sup>m</sup>	Morning Term Scan	UVBI	Morning Term Scan	UVBI	Morning Term Scan	UVBI	Morning Term Scan	UVBI	Morning Term Scan	UVBI
		1 1B P 38 <sup>m</sup> 79.7 242.8									
Tetrad No. 1 (1BA 2B)	33 <sup>m</sup> 42 <sup>s</sup>		1 4 Target 78.3 300	1 4 Target 73.1 227	1 4 Target 62.3 254.6	1 4 Target 69.3 225	1 4 Target BA 75.4 162.8 Target 2B 74.9 159.7	←	1 4 Target 58.8 180	←	1 4 Target 49.7 192
		2 4 2A 1B P 33 <sup>m</sup> 41.5 314.5									
Spectral Scan	-30 <sup>m</sup> 48 <sup>s</sup>	UVS Press Mapping	UVPM	Same CA, KA of SB No. 1	UVPM	←	←	←	←	Same CA, KA of SB No. 1	←
Single B No. 1	-19 <sup>m</sup> 42 <sup>s</sup>	5 Same CA, KA of Press Map	5 Target 55.9 203.2	5 Target 58.1 199.2	5 Target 59.6 196.2	5 Target 50.8 168.4	5 Target 56.9 172.7	5 Target 57.9 167	5 Target 59.9 159.3	5 Target 59.9 149.3	5 Target 56.6 157
Single B No. 2	-14 <sup>m</sup> 06 <sup>s</sup>	6 Same CA, KA of Press Map	6 Target 34.1 187.4	6 Target 55.1 199.2	6 Target 59.6 196.2	6 Target 45.158	6 Target 38.1 140.3	6 Target 37.5 130.5	6 Target 11 120.5	6 Target 35.3 110.8	6 Target 34.4 1
Spectral Scan	-14 <sup>m</sup>	IRR Map P 14 <sup>m</sup>	←	←	←	←	←	IRIS Vertical	←	Vertical Mapping	←
TV Mapping No. 1 (1A 4BA 1B)	2 <sup>m</sup>	7 16 4th A Taken Vertically	7 16 ←	7 16 ←	7 16 ←	7 16 ←	7 16 ←	7 16 ←	7 16 ←	7 16 ←	7 16 ←
TV Mapping No. 2 (5 BA)	13 <sup>m</sup> 54 <sup>s</sup>	17 26 "6th A" Taken Vertically	17 26 ←	17 26 ←	17 26 ←	17 26 ←	17 26 ←	17 26 ←	17 26 ←	17 26 ←	17 26 ←
Tetrad No. 2 (1A 1AB 1A)	24 <sup>m</sup> 24 <sup>s</sup>	27 30 A Overlap Min CA	←	←	←	←	←	←	←	←	←
Dyad (1AB)	30 <sup>m</sup>	31 32 B on 45°N Min CA	31 32 B on 40°N Min CA	31 32 B on 60°N Min CA	31 32 B on 20°N Min CA	31 32 B on 50°N Min CA	↑ 31 32 Target B 45.116	31 32 Target B 45.101	31 32 Target A 30.95	31 32 Target A 30.80	
Spectral Scan	30 <sup>m</sup> 48 <sup>s</sup>	Same CA, KA of Dyad	Night Side Spectral	←	←	←		Night Side Spectral	←	←	←
		3 <sup>h</sup> 39 <sup>m</sup> 34 +47°37'N									
Lyman α-1	1 <sup>h</sup> 22 <sup>m</sup>	3 <sup>h</sup> 54 <sup>m</sup> 48 +39°52'N	3 <sup>h</sup> 16 <sup>m</sup> 20 +41°20'N	3 <sup>h</sup> 39 <sup>m</sup> 34 +47°37'N	←	←	←	←	3 <sup>h</sup> 36 <sup>m</sup> 73 +5°22'N	0 <sup>h</sup> 53 <sup>m</sup> 45 +60°27'N	←
		19 <sup>h</sup> 16 <sup>m</sup> +73°									

**Footnote**

① Targets missed due to cone and clock angle errors during S/C execution.

	152	154	156	158	160	162	164	166	168	170	172	174	176	178
Morning Term Scan	UVBI	Morning Term Scan	UVBI	Morning Term Scan	UVBI	Morning Term Scan	UVBI	Morning Term Scan	UVBI	Morning Term Scan	UVBI	Morning Term Scan	UVBI	Morning Term Scan
	1-4 Target 58.8, 180	1-4 ←	1-4 Target 49.7, 192	1-4 Target 52.5, 219	1-4 Target 59, 169	1-4 Target BA 77.1, 149.5 Target B 78.3, 147.5 Target B 78.3, 152.7	1-4 Target BA 38.3, 147.2 Target B 85.2, 12	1-4 Target BA 86.6, 65 Target B 84.2, 23	1-4 Target 57, 136	1-4 Target BA 75.9, 96.3 Target B 75.2, 91.5 Target B 76.88	1-4 Target BA 71.5, 101.5 Target B 77.8, 92 Target B 77.3, 86.3	1-4 Target BA 86.6, 65 Target B 86.3, 89 Target B 87.3, 78		
	←	Same CA, KA of S/B No. 1	←	Same CA, KA of Ter No. 1	Same CA, KA of S/B No. 1	←	Same CA, KA of Ter No. 1	←	←	←	←	←	←	
M 167	5 Target 59.9, 159.3	5 Target 58.9, 149.3	5 Target 56.6, 136.4	5 Target 58.4, 130.8	5 Target 56, 116.4	5 Target 57.3, 109	5 Target 61, 108	5 Target 61.6, 100.3	5 Target 58, 83.3	5 Target 61.3, 70.8	5 Target 57.5, 62	5 Target 58.3, 55.4		Start of Mapping Cycle III
M 130.5	6 Target 11, 120.7	6 Target 35.3, 110.8	6 Target 34.4, 100.7	6 Target 33.4, 90.6	6 Target 56, 116.4	6 Target 42.4, 80.4	6 Target 50.5, 81	6 Target 51.5, 81.2	6 Target 50.5, 68.5	6 Target 56.8, 47	6 Target 26.9, 29.6	6 Target 25.7, 19.6		
	←	Vertical Mapping	←	←	←	←	←	←	←	←	←	←		
	7-16 ←	7-16 ←	7-16 ←	7-16 ←	7-16 ←	7-16 ←	7-16 ←	7-16 ←	7-16 ←	7-16 ←	7-16 ←	7-16 ←		
	17-26 ←	17-26 ←	17-26 ←	17-26 ←	17-26 ←	17-26 ←	17-26 ←	17-26 ←	17-26 ←	17-26 ←	17-26 ←	17-26 ←		
	27-30 ←	27-30 ←	27-30 ←	27-30 ←	27-30 ←	27-30 ←	27-30 ←	27-30 ←	27-30 ←	27-30 ←	27-30 ←	27-30 ←		
	31-33 Target B 45, 101	31-33 Target A 30, 95	31-33 Target A 30, 80	31-33 Target B 22.8, 64.3	31-33 Target B 57.5, 65	31-33 Target B 42, 63	31-33 Target B 55, 53	31-33 Target A 40, 30	31-33 ←	31-33 Target 45, 14	31-33 Target 50, 15	31-33 Target 55, 15		
	←	←	←	←	←	←	←	←	←	←	←	←		
	7 <sup>h</sup> 36 <sup>m</sup> 73 +5 <sup>s</sup> 22 <sup>3</sup>	0 <sup>h</sup> 33 <sup>m</sup> 65 +60 <sup>s</sup> 27 <sup>5</sup>	←	←	←	23 <sup>h</sup> 56 <sup>m</sup> 45 +55 <sup>s</sup> 29 <sup>0</sup>	1 <sup>h</sup> 40 <sup>m</sup> 49 +50 <sup>s</sup> 26 <sup>3</sup>	5 <sup>h</sup> 3 <sup>m</sup> 01 +41 <sup>s</sup> 10 <sup>4</sup>	10 <sup>h</sup> 3 <sup>m</sup> 73 +12 <sup>s</sup> 12 <sup>6</sup>	←	5 <sup>h</sup> 23 <sup>m</sup> 13 +28 <sup>s</sup> 33 <sup>9</sup>	21 <sup>h</sup> 28 <sup>m</sup> 02 +70 <sup>s</sup> 20 <sup>2</sup>		

Fig. 15. Zenith revolutions 140 to 176, mapping cycle II

FOLDOUT FRAME

Orbital Science Link	Nominal Time From Perapsis	139	141	143	145	147	149	151	153	155	157
Lyman 2	5 <sup>h</sup> 18 <sup>m</sup>			2 <sup>h</sup> 24 <sup>m</sup> 12 <sup>s</sup>	0 <sup>h</sup> 28 <sup>m</sup> +18 <sup>s</sup>	UVBI Background	↓	2 <sup>h</sup> 24 <sup>m</sup> 12 <sup>s</sup>	0 <sup>h</sup> 28 <sup>m</sup> +18 <sup>s</sup>	UVBI Background	1 <sup>h</sup> 16 <sup>m</sup> +33 <sup>s</sup>
					1 <sup>h</sup> 28 <sup>m</sup> P 1 <sup>h</sup> 48 <sup>m</sup>		1 <sup>h</sup> 28 <sup>m</sup> P 4 <sup>h</sup> 48 <sup>m</sup>				
IRR Scan No. 1	2 <sup>h</sup>	Morning Term Scan	←	←	←	←	←	←	←	←	←
IRR Scan No. 2	55 <sup>m</sup>	Morning Spectral	↓	Morning Spectral	←	←	←	←	←	↑	↑
			1, 2 S Spot 1BA P 49 <sup>m</sup>								
Single B No. 1	-37 <sup>m</sup> 54 <sup>s</sup>	1 Target 77.92	2 Target 75.1, 67.9	1 Target 69.8, 90.5	2 Target 86.6, 50	1 Target 67.3, 82	2 Target 64.2, 147	1 Target 85.7, 100	1 Target 61.1, 153.1	1 Target 58.2, 41.3	1 Target 71.5, 0
		2-4 Phobos 2A 1BA P 33 <sup>m</sup>	4-6 Triad 1A 1AB 75.1, 67.9								
Triad (1AB 1B)	-33 <sup>m</sup> 42 <sup>s</sup>			2-4 Target AB 50, 40 Target B 48, 47.3	3-5 Target AB 88.5, 90 Target B 88, 55	2-4 Target A 50, 40 Target B's 57.5, 41	3-5 Target A 60, 145 Target B's 60.6, 146.6	2-4 Target AB 85.4, 80 Target B 85.7, 100	2-4 Target A 60, 145 Target B's 60.6, 146.6	2-4 Target AB 57.2, 41.4 Target B 56.6, 40.3	2-4 Target 71.5, 0
Single B No. 2	-10 <sup>m</sup> 45 <sup>s</sup>	5 Target 57.7, 40.5	7 Target 61.5, 31.1	8 Target 62, 27.7	6 Target 59.2, 13.5	6 Target 58.4, 157.9	6 Target 59, 158.8	6 Target 54.5, 142.6	6 Target 57.6, 339.2	6 Target 58.5, 132	6 Target 57.2, 322.9
Single B No. 3	-14 <sup>m</sup> 06 <sup>s</sup>	5 Target 51.4, 30.1	6 Target 61.5, 31.1	8 Target 49.7, 358	7 Target 49.1, 357.8	6 Target 49.7, 356.7	7 Target 54.2, 357.9	6 Target 54.5, 142.6	6 Target 44.5, 318.2	6 Target 37.2, 312.5	6 Target 57.2, 322.9
IRR Scan No. 3	-14 <sup>m</sup>	IRR Mapping	←	←	←	←	←	←	←	←	←
TV Mapping No. 1 (1A 4BA 1B)	2 <sup>m</sup>	16 4th A Taken Vertically	8-16	9-16	8-17	7-16	8-17	7-16	9-16	7-16	7-16
TV Mapping No. 2 (5BA)	13 <sup>m</sup> 44 <sup>s</sup>	17-20 "5th A" Taken Vertically	16-20	17-20	18-27	17-20	16-27	17-20	17-20	17-20	17-20
		27-30 Goodyear 3A P 24 <sup>m</sup>									
Tetrad (1A 1AB 1A)	24 <sup>m</sup> 34 <sup>s</sup>		29-32 A Overlay Min. CA	27-30	30-31	27-30	30-31	27-30	27-30	27-30	27-30
		30-32 Triad 1A 1AB P 27 <sup>m</sup>									
Dyad (1AB)	30 <sup>m</sup>		31-32 B on 60°N Min. CA	32 A on 60°N Min. CA	31-32 B on Lamb ~70°N	32 A on 60°N Min. CA	31-32 Min. CA	31-32 Min. CA	31-32 Target A 33, 280	31-32 Min. CA	31-32 Target A 43, 260
IRR Scan No. 4	30 <sup>m</sup> 40 <sup>s</sup>	Night Side IRR	←	←	←	←	←	←	←	←	←

**Footnote:**

- ① Same as in mapping, -7.7° read as -77° in Orbital Egress Sheet for Rev. 139.
- ② TV Picture Data shows only 2A 1B taken during this exposure.
- ③ TV Picture Data shows 2A 1B taken during this exposure.
- ④ TV Picture Data shows additional B frame (over) at start of Mapping No. 1

Fig. 16. Nadir revolutions 139 to 177, mapping cycle N

	155	157	159	161	163	165	167	169	171	173	175	177	179
	UVBI Background	$19^h 16^m 43^s$	$19^h 28^m 41^s$	$20^h 24^m 19^s$	$19^h 16^m 47^s$	$19^h 28^m 18^s$	$20^h 24^m 12^s$	$19^h 16^m 47^s$	$19^h 28^m 18^s$	$20^h 24^m 12^s$	$19^h 16^m 47^s$	$19^h 28^m 18^s$	
			1 Demos 1B $19^h 28^m 41^s$	1 Photos 1B $19^h 16^m 47^s$									
	←	←	←	↑	Morning Term Scan	←	←	←	←	←	←	←	
	↑	↑	↑	↓	↑	↑	↑	↑	↑	↑	↑	↑	
				2 Photos 1B $19^h 41^m$									
1	Target 58.2, 41.3	Target 71.5, 0	Target 85.7, 33	↑	Target 59, 10	Target 65.6, 326.1	Target 59.2, 335.3	Target 67.2, 325.7	Target 68, 323.5	Target 87.2, 340	Target 72, 325	Target 57, 283	
2-4	Target AB 57.2, 41.4 Target B 56.6, 40.1	Target 71.5, 0	Target AB 84.7, 31 Target B 85.7, 33	Target A 30, 345 Target B's 38.7, 350.2	Target 59, 10	Target A 65.6, 324.6 Target B 64.6, 325.5 Target B 65.1, 323.9	2-4 $\sqrt{60^\circ N}$ , 180 Limb	Target A 65.6, 324.6 Target B 66.4, 323.7 Target B 65.7, 322.3	Target A 69, 336 Target B 67.2, 322 Target B 66.1, 320.7	Target A 77, 300 Target B 75.5, 288.5 Target B 76.5, 292.3	Target A 74, 280 Target B 77.2, 288.5 Target B 76.3, 285	Target A 40, 270 Target B's 44.8, 265.5	
5	Target 58.5, 332	Target 57.2, 322.9	Target 56.4, 310.3	Target 59.1, 306.7	Target 58, 292.6	Target 56, 282	Target 59.8, 280.7	Target 59, 270.5	Target 52.7, 261	Target 56.5, 244.8	Target 59.8, 241.5	Target 59.7, 233	
6	Target 47.2, 312.5	Target 57.2, 322.9	Target 56.4, 310.3	Target 50.8, 219.9	Target 53.6, 281.7	Target 55, 275	Target 51, 262.8	Target 40.2, 253.5	Target 52.7, 261	Target 52.8, 31.5	Target 52.8, 231.5	Target 44, 220	
	←	←	←	←	←	←	←	←	←	←	←	←	
7-16	←	←	←	←	←	←	←	←	←	←	←	←	
17-20	←	←	←	←	←	←	←	←	←	←	←	←	
27-30	←	←	←	←	←	←	←	←	←	←	←	←	
31-32	Min. CA Max. KA	Target 43, 268	A on 43 <sup>PM</sup> Min. CA	Target A 60, 250	Target A 27, 229 Target B 27, 226	Target A 30, 225	←	A on 205 <sup>PM</sup> Max. KA	↑	Target A 40, 185	←	Target 62.2, 172	
	←	←	←	←	←	←	←	←	←	Night Side IRL	←	←	

Start of Mapping Cycle III

Orbital Scan: Link	Nominal Time From Perseus	178	180	182	184	186	188	190	192	194	196
Spectral Scan	-3 <sup>h</sup> 17 <sup>m</sup>	UVBI	Morning Term Scan	←	←	UVBI	Morning Term Scan	UVBI	Morning Term Scan	UVBI	Morning Term Scan
Tetrad No. 1 (2B 1AB)	-32 <sup>m</sup> 18 <sup>s</sup>	1-4 Target 52.9, 97.8	1-4 Target B's 82.62 82.6, 70 83.8, 68	1-4 Target B's 76.66 76.8, 71 Target A 70.68	1-4 Target B's 84.8, 65 84.3, 76 84.2, 53	1-4 Target 2B 57.5, 41 Target A 50.40	1-4 Target B's 86.6, 21 86.2, 1 88.8, 351	1-4 2B on Limb -50°W	1-4 Target 71.29	1st 2 B's 1-2 Target A 50.43	1-4 Target B's 83.5, 13 83.6, 25 84.42
Dyad No. 1 (2B)	-23 <sup>m</sup> 54 <sup>s</sup>	5-6 Target 58.1, 61.3	5-6 Target 80.8, 54 81.2, 72	5-6 Targets -83.2 84.2	5-6 Targets 73.8, 3 -74.8, 4	5-6 S. Limb 5 <sup>th</sup> from Term	5-6 Targets -68.6, 358 68.5, 355	5-6 Targets 68.2, 350 68.8, 448	5-6 Targets 80.8, 345 80.6, 338	3-4 Target 62.1, 344.4	3-6 Targets 82.6, 348 81.7, 355
Spectral Scan	-22 <sup>m</sup> 24 <sup>s</sup>	UVS Scan	←	←	←	←	Morning Spectral	←	←	←	←
Tetrad No. 2 (4B)	-11 <sup>m</sup> 18 <sup>s</sup>	7-10 Occul Point 25.8, 19.6	7-10 Target 41.5, 8	7-10 Target 24.5, 19	7-10 Target -21.5, 10.5	7-10 Target 23, 343	7-10 4B's in line between -31.6, 336.6 30.6, 335.5	7-10 4B's Along Spect Scan 3rd B on 39.2, 326.5	7-10 Target -38.3, 330.7	5-8 4B's Along Spect Scan 3rd B on -40.3, 319	7-10 2nd B on 46.2, 311
TV Mapping No. 1 (2A 1B 4A)	-2 <sup>m</sup> 12 <sup>s</sup>	11-17 1st A at -30, 19	11-17 ← -30, 8.8	11-17 ← -30, 359.5	11-17 ← -30, 350.2	11-17 ← -30, 341.1	11-17 ← 30, 331.9	11-17 ← 30, 323.2	11-17 ← -30, 314.2	9-15 ← 30, 305.3	11-17 ← -30, 296
TEC (1B)	6 <sup>m</sup> 54 <sup>s</sup>	18 Target 2.5, 358.5	18 Target -5.5, 358	18 Target -5.5, 340.5	18 Target -8.1, 335	18 Target -8.2, 334.7	18 Target -8.6, 323.2	18 Target -1.9, 306.4	18 Target 6.4, 304	18 Target 4.5, 294	18 Target 4.9, 275.7
Spectral Scan	7 <sup>m</sup>	Spectral Map	←	←	P+9 <sup>m</sup> ←	P+11 <sup>m</sup> ←	Evening Spectral	←	←	←	←
TV Mapping No. 2 (3AB)	30 <sup>m</sup>	19-24 1st A at 29, 349.3	19-24 ← 29, 340.1	19-24 ← 29, 330.9	19-24 ← 29, 321.7	19-24 ← 29, 312.4	19-24 ← 29, 303.2	19-24 ← 29, 294	19-24 ← 29, 284.8	17-22 ← 29, 275.6	19-24 ← 29, 266.3
Tetrad No. 3 (2AB)	39 <sup>m</sup> 48 <sup>s</sup>	25-28 1st B on 63.1, 347	25-28 Min CA Max. K.A	25-28 Extend Mapping	25-28 2nd B on Limb	25-28 Extend Mapping	25-28 2nd B on Limb	25-28 Extend Mapping	25-28 2nd B on Limb	23-26 Extend Mapping	25-26 1st Limb 2nd B
Dyad No. 2 (1AB)	45 <sup>m</sup> 24 <sup>s</sup>	29-30 ~70°N Min. CA	29-30 Target A at N. Pole	29-30 ~50°N Term	29-30 Limb Min. CA	29-30 ~80°N Min. CA	29-30 A and B on Limb	29-30 ~70°N Min. CA	29-30 ~80°N Min. CA	27-28 ←	
Spectral Scan	46 <sup>m</sup> 12 <sup>s</sup>	Night Side Spectral	←	←	←	←	←	←	←	←	←
Lyman α	1 <sup>h</sup> 32 <sup>m</sup>	3 <sup>h</sup> 54 <sup>m</sup> 48 <sup>s</sup> +12°52'0	←	10 <sup>h</sup> 5 <sup>m</sup> 73 <sup>s</sup> +12°12'6	←	0 <sup>h</sup> 30 <sup>m</sup> 16 <sup>s</sup> +62°39'5	0 <sup>h</sup> 28 <sup>m</sup> 0 <sup>s</sup> +18°	0 <sup>h</sup> 10 <sup>m</sup> 66 <sup>s</sup> +14°54'9	22 <sup>h</sup> 37 <sup>m</sup> 01 <sup>s</sup> +38°47'8	3 <sup>h</sup> 39 <sup>m</sup> 34 <sup>s</sup> +47°37'8	4 <sup>h</sup> ← +68°

190	192	194	196	198	200	202	204	206	208	210	212	214	216	218
UVBI	Morning Term Scan	UVBI	Morning Term Scan	Star Occul	Morning Term Scan	Star Occul - Cas	Morning Term Scan	←	UVBI	Morning Term Scan	←	←	←	
				1-2 Gnd Cnd BA A on 79.5 P 29 <sup>m</sup>		1-2 Gnd Cnd AB 76.326 P 29 <sup>m</sup>				1-2 Gnd Cnd BA P 38 <sup>m</sup>	1-2 Gnd Cnd BA P 35 <sup>m</sup>	1-2 45°N Min - A		
Lamb W	1-4 Target 71.29	1st 2 B's 1-2 Target A 50.44	1-4 Target B's 83.5.13 83.6.25 84.5.2	↑	1-4 Target B's 70.2.358 71.8.5 71.2.358	↑	1-4 Target B's 63.1.321.5 63.8.323.5 64.3.321.5	1-4 Target B's 86.2.0 85.1.337 85.7.295	1-4 Target B's 84.7.305 83.5.299 82.1.295.5	3-6 Target B's 80.9.293 80.5.285 81.8.284	3-6 Target B's 83.3.288.5 84.6.289 82.8.275	3-6 Target B's 86.5.273 85.3.275 84.2.276	1-4 Target B's 82.6.266 81.7.274 80.3.276	
S 350 48	5-6 Targets 80.8.345 80.6.338	3-4 Target 62.1.344.4	5-6 Targets 82.6.348 81.7.355	3-4 Targets 66.8.319.2 66.2.321.7	5-6 Targets 65.2.320.4 65.5.324.6	3-4 Target 58.7.335.2	5-6 Targets 84.5.349 83.5.339	5-5 Targets 87.6.324 86.3.313	5-6 Target 40.7.257.2		7-8 Targets 84.1.263 85.6.257			
←	←	←	←	←	←	←	←	←	←	←	←	←	←	←
Along Scan 15, 326.5	7-10 Target -38.3.330.7	5-8 4B's Along Spect Scan 3rd B on 40.3.319	7-10 2nd B on 46.2.311.5	5-8 Target 29.5.290.5	7-10 Target 32.6.282.7	5-8 Target 34.7.274.9	7-10 Target 40.2.269.2							
										7-8 P 8 <sup>m</sup> Dyad 2B 36.248.2		7-8 P 8 <sup>m</sup> Dyad 2B 35.216	5-6 P 8 <sup>m</sup> Dyad 2B 27.5.214.7	
3.2	11-17 30.314.2	9-15 30.305.3	11-17 30.296.5	9-15 30.287.4	11-17 30.278.5	9-15 30.269.3	11-17 30.260.1	7-12 Omit B 30.250.9	7-12 30.241.7	9-14 30.232.5	9-14 30.223.3	9-14 30.214.1	7-12 30.204.9	Start of Extended Mission - Phase I
5.4	18 Target -6.4.304	16 Target 4.5.294	18 Target 4.9.275.7	16 Target 0.4.270.2	18 Target 2.260.3	16 Target 1.9.249.9	18 Target 7.3.245.4	13 Target 2.4.238.8	13 Target -3.231.4	15 Target 5.2.214.9	15 Target 8.4.208.4	15 Target 7.8.192	13 Target -1.1.186	
←	←	←	←	←	←	←	←	←	←	←	←	←	←	
←	19-24 29.284.8	17-22 29.275.6	19-24 29.266.3	17-22 29.257.1	19-24 29.247.9	17-22 29.238.7	19-24 29.229.5	14-19 29.220.2	14-19 29.211	16-21 29.201.8	16-21 29.192.6	16-21 29.183.4	14-19 29.174.1	
	25-28 2nd B on Lamb	23-26 Extend Mapping	25-28 1st AB on Lamb 2nd AB	23-26 Extend Mapping	25-28 1st AB on Lamb 2nd AB	23-26 Extend Mapping	25-28 1st AB on Lamb 2nd AB	20-23 Extend Mapping	20-23 Extend Mapping	22-25 Extend Mapping	22-25 1st A on 40.185	22-25 Extend Mapping	20-23 1st A on 52.177.4	
	29-30 ~ 80°N Min. CA	27-28				27-28 Extend Mapping		24-28 Extend Mapping						
←	←	←	←	←	←	←	←	←	←	←	←	←	←	
				P+4 <sup>m</sup>	P+4 <sup>m</sup>	P+4 <sup>m</sup>	P+4 <sup>m</sup>	P+4 <sup>m</sup>	P+4 <sup>m</sup>			NSS P+4 <sup>m</sup>	←	
	22 <sup>h</sup> 37 <sup>m</sup> 01 +38°47'6	3 <sup>h</sup> 39 <sup>m</sup> 34 +47°37'8	4 <sup>h</sup> 49 <sup>m</sup> 04 +66°15'6	10 <sup>h</sup> 30 <sup>m</sup> 19 +9°33'6	3 <sup>h</sup> 39 <sup>m</sup> 34 +47°37'8	0 <sup>h</sup> 51 <sup>m</sup> 79 +28°48'6	0 <sup>h</sup> 53 <sup>m</sup> 65 +60°27'5	19 <sup>h</sup> 16 <sup>m</sup> +73°	←	←	0 <sup>h</sup> 28 <sup>m</sup> 0 +18°	←	←	

Fig. 17. Zenith revolutions 178 to 216, mapping cycle III

OLDOUT FRAME

J

Orbital Science Link	Nominal Time From Perapsis	179	181	183	185	187	189	191	193	195	197	199
IRR Scan No. 1	-3 <sup>h</sup>	IRR Term Scan	←	←	P 2 <sup>h</sup>	P 3 <sup>h</sup>	←	P 2 <sup>h</sup>	P 3 <sup>h</sup>	←	1 Dermis 1B P 3 <sup>h</sup> 14 <sup>m</sup>	IRR Term Scan
			3-2 Gnd Cmd BA P 3 <sup>m</sup> S Pole Lamb								Term Scan P 2 <sup>h</sup>	
Tetrad No. 1 (2B 1AB)	-32 <sup>m</sup> 18 <sup>s</sup>	1-4 Target 70.1, 253.6	←	1-3 Target B's 80.6, 265 79.9, 258 79.1, 250.5	1-4 Target B's 81.8, 261.5 81.1, 252.5 81.7, 244	1-4 Target 2B 79.7, 250.5 80.6, 237 Target A 87, 180	1-4 Target B's 71.8, 227.3 73, 223 71, 215	1-4 2nd B on 74.9, 159.7 3rd B on 75.4, 162.8		1st 2 B's 1-2 Target B 58.8, 180		1-2 1st 2 B's 3-4 Target A 67, 143
											Morn Spect P 30 <sup>m</sup>	
Dyad No. 1 (2b)	-23 <sup>m</sup> 54 <sup>s</sup>	5-6 Target 60, 233.5	7-8 Targets 74.6, 229.5 75.5, 227.2	5-6 Targets 71.8, 212.7 73, 215.5	5-6 Targets 72.7, 210.5 72.7, 207	5-6 Targets 73.5, 212.7 73.7, 209	5-6 Targets 74.8, 212.7 74.5, 207.8	5-6 Targets 73.3, 205 74.3, 203.5	1-2 Target 58.8, 180	3-4 Target 76.1, 152 76.6, 148		5-6 Targets 76.6, 145.5 77.4, 143
IRR Scan No. 2	-22 <sup>m</sup> 24 <sup>s</sup>	IRR Scan	←	←	←	←	Morning Spectral	←	←	←		Morning Spectral
Dyad No. 2 (2B)	-8 <sup>m</sup> 30 <sup>s</sup>	7-8 Target 39.5, 204.2	9-10 Target 34.2, 187	7-8 Target 25.9, 183.7	7-8 Target 34.5, 177.5	7-8 S Spot on Limb 120.4W	7-8 1st B on Limb 180W	7-8 Target 25.8, 140.4	3-4 Target 25.1, 131.6	5-6 Target 35.2, 136.7	2-3 Target 38.8, 119.7	7-8 Target 37.2, 109.4
TV Mapping No. 1 (2A 1B 2A 1B 2A)	-2 <sup>m</sup> 12 <sup>s</sup>	9-16 1st A at 30, 194.3	11-18 ← 30, 184.1	9-16 ← 30, 174.9	9-16 ← 30, 165.6	9-16 ← 30, 156.5	9-16 ← 30, 147.6	9-16 ← 30, 138.7	5-12 ← 30, 129.8	7-14 ← 30, 120.9	4-11 ← 30, 112	9-16 ← 30, 102.9
Dyad No. 3 (AB)	10 <sup>m</sup> 24 <sup>s</sup>	17-18 Target B -5.7, 174.5	19-20 Target B 25, 210	17-18 Target B -0.3, 164.3	17-18 Target B 1.3, 156.5	17-18 Target B -17.6, 133	17-18 Target B -9, 120	17-18 Target A -9.2, 120.4	13-14 Target B 3.1, 121.3	16-18 Target B 24, 111.2	12-13 Target B 13.4, 90.7	17-18 Target B 10.9, 104.6
IRR Scan No. 3	11 <sup>m</sup> 12 <sup>s</sup>	IRR Scan		IRR Scan	←	←	Evening Spectral	Morning Spectral	←	Evening Spectral	←	←
TV Mapping No. 2 (3AB)	30 <sup>m</sup>	19-24 1st A at 29, 164.8	21-26 ← 29, 155.6	19-24 ← 29, 146.4	19-24 ← 29, 137.2	19-24 ← 29, 127.9	19-24 ← 29, 118.7	19-24 ← 29, 109.5	16-20 ← 29, 100.3	17-22 ← 29, 91.1	14-19 ← 29, 81.8	19-24 ← 29, 72.6
Tetrad No. 2 (2AB)	39 <sup>m</sup> 48 <sup>s</sup>	26-28 1st B on 56.4, 163	27-30 Targets 52, 151 58, 153	26-28 1st B on 50, 135	26-28 Extend Mapping	26-28 1st B on 41.2, 109.8	26-28 Extend Mapping	26-28 2nd B on Limb	21-24 Extend Mapping	23-26 1st AB on Limb	20-23 Extend Mapping	25-26 1st AB Term-Limb 27-28 2nd AB
Dyad No. 4 (AB)	45 <sup>m</sup> 24 <sup>s</sup>	29-30 B Dark Limb		29-30 A on 85, 180	29-30 A on -75°N Min. CA	29-30 Limb Min. CA	29-30 A on 78°N Min. CA					24-26 Target A 80, 0
IRR Scan No. 4	46 <sup>m</sup> 12 <sup>s</sup>	Night Side IRR	P+42 <sup>m</sup>	P+46 <sup>m</sup>	←	←	←	←	P+42 <sup>m</sup>	P+46 <sup>m</sup>	←	P+45 <sup>m</sup>

**Footnotes:**

①-② These frames were not planned but were taken. Many of these unplanned frames were not received. See TV Picture Data to determine if they were received on earth.

**Fig. 18. Nadir revolutions 179 to 217, mapping cycle III**

	197	199	201	203	205	207	209	211	213	215	217	219	
	Demos IB P 3 <sup>h</sup> 14 <sup>m</sup>	IRR Term Scan	←	←	←	Phobos IB P 1 <sup>h</sup> 47 <sup>m</sup>	IRR Term Scan	←	←	←	←		
	Term Scan P 2 <sup>h</sup>					Phobos IB P 1 <sup>h</sup> 16 <sup>m</sup>	Gnd Cmd BA P 3 <sup>h</sup> 38 <sup>m</sup>				Gnd Cmd BA P 3 <sup>h</sup> 38 <sup>m</sup>		
	1-2 1st 2 B's 3-4 Target A 67 193	①		1st 2 B's 1-2 AB S Pole Limb Term		3-6 Target B's 85 131.5 86 3, 125 85 9, 97	3-6 Target B's 79 9, 141 -79 3, 136 -80, 132	1-4 Target B's 84 1, 116 83 4, 103 84 3, 92	1-4 Target B's 82 5, 92.5 81 4, 84 82 1, 78.5	1-2 1st 2 B's 3-4 Target B 83 6, 82	①	3-6 Target B's 78 1, 83 78 7, 79.5 79 4, 77.5	
	Morn Spect P 30 <sup>m</sup>		IRR Scan P 30 <sup>m</sup>		IRR Scan P 30 <sup>m</sup>								
	5-6 Targets 76 6, 145.5 77 4, 143		3-4 Targets 79, 144 -78 3, 139				7-8 Target 30 7, 123 9	5-6 Target 51 4, 80 4					
						IRR Scan P 29 <sup>m</sup>			IRR Scan P 29 <sup>m</sup>	←	←		
	Morning Spectral		Morning Spectral			Morning Spectral	P 24 <sup>m</sup> ←						
												Start of Extended Mission - Phase I	
	2-3 Target 38 8, 119 7	7-8 Target 37 2, 109 4	1-2 Target 22 6, 100 7	5-6 Target -40 5, 95 2	1-2 Target 24 7, 83 5	7-8 Target -40 9, 83 9			5-6 Target 27 5, 42 7	5-6 Target 30 1, 37 8	7-8 Target 22 6, 28 8 P-2 <sup>m</sup>		
	4-11 ← 30, 112	9-16 ← 30, 102 9	3-10 ← -30, 93 8	7-14 ← 30 94 7	3-10 ← 30, 75 5	9-14 ← Omit B's 30 66 7	9-14 ← 30 57 1	7-12 ← 30 47 9	7-12 ← 30 78 7	7-12 ← 30 29 5			
						15 Single B -7 5, 48 8	15 ← P+11 <sup>m</sup> 8 9, 33 4	13 ← 4.5, 30 1	13 ← 2.5, 17.7	13 ← 10.9, 4 6	Even. Spect P+5 <sup>m</sup>		
	12-13 Target B 13 4, 90 7	17-18 Target B 10 9, 104 6	11-12 B on Limb 9, 120 4	15-16 Target B 21 7, 71 3	11-12 Target B 24 3, 61 5	↑	16-17 Gnd Cmd BA P+16 <sup>m</sup> 11, 42				9 Single B P+11 <sup>m</sup> CA, KA of Spectral		
	←	←	P+15 <sup>m</sup> ←	P+11 <sup>m</sup> ←	←	←		Evening Spectral	←	←			
							IRR Scan P+18 <sup>m</sup>						
	14-19 ← 29, 81 8	19-24 ← 29, 72.6	13-18 ← 29, 63 4	17-22 ← 29, 54 2	13-18 ← 29, 45	16-21 ← 29, 35 7	18-23 ← 29, 26.5	14-19 ← 29, 17.3	14-19 ← 29, 8.1	14-19 ← 29, 35 8 9	10-16 2nd B on 36.9, 344.4		
	20-23 Extend Mapping	25-28 1st AB Term-Limb 27-30 2nd AB	19-22 Extend Mapping		18-22 Extend Mapping	27-23 A of 1st AB 41 5, 30 2		20-21 B of 1st AB 56 5, 9 0	20-21 B of 1st AB 63 5, 148 1	20-23 1st B on 63 5, 148.1	16-19 1st B on 51, 328		
						①		①	①	①			
	24-26 Target A 80, 0										20-21 Extend Coverage		
	←	P+45 <sup>m</sup> ←	P+42 <sup>m</sup> ←	P+36 <sup>m</sup> ←	P+42 <sup>m</sup> ←	←	P+36 <sup>m</sup> ←	P+42 <sup>m</sup> ←	←	←	P+46 <sup>m</sup> ←		

2

Orotal Science Link	218	220	222	224	226	228	230	232	234	236	238	240	
Spectral Scan	Star Occultat P 60 <sup>m</sup>	Limb Term Scan P 60 <sup>m</sup>	←		Limb Term Scan P 60 <sup>m</sup>		Limb Term Scan P 60 <sup>m</sup>		Limb Term Scan P 60 <sup>m</sup>	←			
							1-2 Gnd Cmd BA P 30 <sup>m</sup> 75.4 162.8		1-2 Gnd Cmd A P 30 <sup>m</sup> 80.60				
Triad No. 1 (3B)	1-3 P 25 <sup>m</sup> Targets 80.6, 260 80, 250.3 81.1 248.5	1-3 P 33 <sup>m</sup> Targets 80.1, 255.5 77.9 251.5 78.5 247	1-3 P 32 <sup>m</sup> Targets 82.5 257 83.7 25.5 82.9 24.	1-3 P 32 <sup>m</sup> Targets 87 253 88.3 249 88.9 292	1-3 P 33 <sup>m</sup> Targets 89.5 100 88.9 216 87.3 230	1-3 P 32 <sup>m</sup> Targets 73.7 232.7 74.6 233 75.7 233.5	3-5 P 25 <sup>m</sup> Targets 58.8 180	1-3 P 33 <sup>m</sup> Targets 74 212.5 72.8 214 71.9 215.3	3-5 P 32 <sup>m</sup> Targets 75.6 174 74.7 168.5 73.8 165.5	1-3 P 33 <sup>m</sup> Targets 86.4 201 87.7 200 86.1 187	1-3 P 22 <sup>m</sup> Targets 74.5 155.5 72.3 157 71.5 155	1-3 P 5 <sup>m</sup> Targets 7.85.6	1-3 P 5 <sup>m</sup> Targets 7.85.6
	4 Gnd Cmd A P 15 <sup>m</sup> S Pole Limb		Spectral Scan P 29 <sup>m</sup>	←		4-5 Gnd Cmd BA P 24 <sup>m</sup> 58.8 180	IRR Morn Scan P 21 <sup>m</sup>		IRR Spectral		IRR Morn Scan P 21 <sup>m</sup>	IRR Scan P 4 <sup>m</sup>	
Triad No. 2 (3B)	5-7 P 8 <sup>m</sup> Target 29.2, 192.4	4-6 P 27 <sup>m</sup> Target 70.1, 253.6	4-6 P 2 <sup>m</sup> Target 4.4 149.8	4-6 P 4 <sup>m</sup> Target 25.4, 183.7	4-6 P 27 <sup>m</sup> Targets 86.2 242 85.2 242 84.3 245.5	6-8 P 5 <sup>m</sup> Target 25.8 140.2	6-8 P 5 <sup>m</sup> Targets 11.7 121 11.3 121.4 10.8 121.8	4-6 P 23 <sup>m</sup> Target 72.8 152	6-8 P 6 <sup>m</sup> Targets 15 108.8 14.5 108.5 14 108	4-6 P 23 <sup>m</sup> Targets 88.4 162 86.9 173 87.1 151	4-6 P 13 <sup>m</sup> Targets 7.2, 87.1	4-6 P 6 <sup>m</sup> Targets 7.3 85.7 6.9 85.4 6.5 85.1	4-6 P 6 <sup>m</sup> Targets 7.3 85.7 6.9 85.4 6.5 85.1
		7-8 Gnd Cmd BA P 20 <sup>m</sup> 70.5, 258.5			IRR Scan P 14 <sup>m</sup>			IRR Morn Scan P 19 <sup>m</sup>		IRR Map P 20 <sup>m</sup>	Gnd Cmd A P 19 <sup>m</sup> 0, 81		
Triad No. 3 (IB 1AB)	9-10 P 6 <sup>m</sup> 1st B on 26.3, 182.6	9-11 P 5 <sup>m</sup> 1st B on 25.8, 190 Max Slew	7-9 P 4 <sup>m</sup> Target 4.4, 150.4 Max Slew	7-9 P 5 <sup>m</sup> 2nd B on 5.6, 150.5 Max Slew	7-9 P 12 <sup>m</sup> 1st B on 32.5, 150.8 Max Slew	9-11 P 3 <sup>m</sup> Target 9.5, 121.5 Max Slew	9-11 P 6 <sup>m</sup> Target 14.9, 130 Max Slew	7-9 P 5 <sup>m</sup> Target B's 0.1, 112.8 3.8, 111.5 Max Slew	9-11 P 6 <sup>m</sup> 2nd B on 9.4, 105.7 Max Slew	7-9 P 5 <sup>m</sup> 1st B on 11, 105.7 Max Slew	7-9 P 24 <sup>m</sup> Target 5, 66.2 7.7, 61.9 Max Slew	7-9 P 13 <sup>m</sup> Target 7.85.6 Max Slew	7-9 P 13 <sup>m</sup> Target 7.85.6 Max Slew
	11-12 Gnd Cmd BA P 13 <sup>m</sup> 2,165 (B)						IRR Scan P 8 <sup>m</sup>		IRR Scan P 8 <sup>m</sup>	10-11 Gnd Cmd BA P 15 <sup>m</sup>	IRR Map P 26 <sup>m</sup>	IRR Map P 5 <sup>m</sup>	
Triad No. 4 (3B)	13-15 P 24 <sup>m</sup> 2nd B on 15.2, 179.3	12-14 P 5 <sup>m</sup> 2nd B on 3,161	10-12 P 4 <sup>m</sup> 1st B on 16.4, 133.9 Other close as Possible	10-12 P 12 <sup>m</sup> Target B's 6, 151 5.6, 150.6 5, 150.3	10-12 P 2 <sup>m</sup> 2nd B on 9.5, 121.5 N S Overlap	12-14 P 20 <sup>m</sup> Targets 17.4, 125.9 18, 125.9 18.9, 125.2	12-14 P 20 <sup>m</sup> Target 2B 14.9, 130 18.1, 133.3	10-12 P 19 <sup>m</sup> Targets 0.4, 112.9 0.3, 112.7 0.5, 112.5		12-14 P 23 <sup>m</sup> Target 24.2, 97.5			
				13-14 Gnd Cmd BA P 19 <sup>m</sup> Target B 16.5, 138.8		IRR Scan P 23 <sup>m</sup>		13-14 Gnd Cmd BA P 27 <sup>m</sup> 11.2, 104.2	12-16 Gnd Cmd 3A Start +33 <sup>m</sup> End +41 <sup>m</sup> All 50 <sup>0</sup> W			10 Gnd Cmd BA P 32 <sup>m</sup> 50, 63	
Triad No. 5 (IB 1AB)	16-18 P 31 <sup>m</sup> Target A 36,155	15-17 P 11 <sup>m</sup> 1st B on 1, 138.7	13-15 P 26 <sup>m</sup> Target 38.2, 140.7		13-15 P 19 <sup>m</sup> Target B's 22, 132.2 23.4, 131		15 P 26 <sup>m</sup> 1st B on 17.9, 125.7	16-17 AB					
	19-20 Gnd Cmd BA P 38 <sup>m</sup> B on Limb	Morn Scan 18-21 Gnd Cmd 4A P 32 <sup>m</sup>	16-18 Gnd Cmd 3A Start +33 <sup>m</sup> End +55 <sup>m</sup>	18-19 Gnd Cmd 3A Start +37 <sup>m</sup> End +45 <sup>m</sup> 40, 110	16-18			IRR Scan P 27 <sup>m</sup> Even Scan P 40 <sup>m</sup>				Night Side Spectral P 38 <sup>m</sup>	
Lyman-α	P 1 <sup>h</sup> 47 <sup>m</sup> 0 <sup>h</sup> 28 <sup>m</sup> 0 +12 <sup>0</sup>	P 1 <sup>h</sup> 48 <sup>m</sup>	← 0 <sup>h</sup> 28 <sup>m</sup> 0 +18 <sup>0</sup>		P 1 <sup>h</sup> 48 <sup>m</sup> 0 <sup>h</sup> 28 <sup>m</sup> 0 +18 <sup>0</sup>	← 19 <sup>h</sup> 16 <sup>m</sup> +73 <sup>0</sup>	←	←	P 1 <sup>h</sup> 48 <sup>m</sup> 0 <sup>h</sup> 28 <sup>m</sup> 0 +18 <sup>0</sup>	← 19 <sup>h</sup> 16 <sup>m</sup> +73 <sup>0</sup>	← 0 <sup>h</sup> 28 <sup>m</sup> 0 +18 <sup>0</sup>	← 19 <sup>h</sup> 16 <sup>m</sup> +73 <sup>0</sup>	

Footnotes:

- ① TV Picture Data shows these frames taken.
- ② TV Picture Data shows a BA-pair taken during this sequence.
- ③ TV Picture Data shows BAB + 2A taken during this sequence.
- ④ This frame not taken.
- ⑤ TV Picture Data shows only A-frame taken during this sequence.
- ⑥ TV Picture Data shows 12 frames taken on this revolution at constant cone and clock.
- ⑦ TV Picture Data shows 8BA-pairs of data taken during this revolution at constant cone and clock.

230	232	234	236	238	240	242	244 <sup>1</sup>	246	248 <sup>1</sup>	250	252	254	256	258	260	262
1st Term Scan P-6 <sup>m</sup>		1st Term Scan P-6 <sup>m</sup>	←												1st Term Scan P-1 <sup>m</sup> 10 <sup>m</sup>	1st Term Scan P-1 <sup>m</sup> 10 <sup>m</sup>
2nd Cmd BA P-30 <sup>m</sup> -75.4 162.5		1 2 Gnd Cmd A P-36 <sup>m</sup> 86.60													1 2 Dvad (BA) P-26 <sup>m</sup> Target B 81.9 49	1 16 S. Polar Mapping P-25 <sup>m</sup> 3BA B A 4BA 3rd A on 86.5 13.5
3-6 -25 <sup>m</sup> Targets -58.8 180	1 3 P-3 <sup>m</sup> Targets 74.212.5 72.8 214 71.9 215.5	3 5 P-3 <sup>m</sup> Targets 75.6 174 74.7 168.5 73.8 165.5	1 3 P-3 <sup>m</sup> Targets 86.4 201 87.7 200 86.1 187	1 3 P-2 <sup>m</sup> Targets 74.5, 188.5 71.3 185	1 3 P-5 <sup>m</sup> Target 7, 85.6	1 3 P-5 <sup>m</sup> Max Slew										
1st Morn Scan P-21 <sup>m</sup>		IRR Spectral		IRR Morn Scan P-21 <sup>m</sup>	IRR Scan P-4 <sup>m</sup>										3 4 Dvad (2B) P-19 <sup>m</sup> Targets 60.7 34.5 60.2 34	Spect Scan
4-6 -5 <sup>m</sup> Targets -11.7, 121 -11.3 121.4 -10.8 121.8	4 6 P-2 <sup>m</sup> Target 72.8, 152	6 8 P-6 <sup>m</sup> Targets 15, 108.8 14.5 108.5 14 108	4-6 P-2 <sup>m</sup> Targets 88.4 162 86.9, 173 87.1 151	4 6 P-1 <sup>m</sup> Target 7.2 87.1	4 6 P-6 <sup>m</sup> Targets 7.3, 85.7 6.9 85.4 6.5, 85.1	4 6 P-6 <sup>m</sup> Adjacent										
	IRR Morn Scan P-19 <sup>m</sup>		IRR Map P-20 <sup>m</sup>	Gnd Cmd A P-19 <sup>m</sup> 0, 81											5 6 Gnd Cmd P-5 <sup>m</sup> Target A 23, 344	
7-9 -1 -9, 130 Max Slew	7 9 P-5 <sup>m</sup> Target B 0.1 112.8 3.8, 111.5	9 11 P-6 <sup>m</sup> 2nd B on 9.4, 108.5 Max Slew	7-9 P-5 <sup>m</sup> 1st B on 11 105.7 Max Slew	7 9 P-24 <sup>m</sup> Target B 21.5, 66.2 23.7 61.9	7-9 P-1 <sup>m</sup> Target 7.85, 6 Max Slew	7-9 P-24 <sup>m</sup> Target 1st B 23.7 61.9 Max Slew									7 9 Triad (3B) P-4 <sup>m</sup> Target 10.8, 358.3	
IRR Scan P-8 <sup>m</sup>		IRR Scan P-8 <sup>m</sup>	10-11 Gnd Cmd BA P-15 <sup>m</sup>	IRR Map P-26 <sup>m</sup>	IRR Map P-15 <sup>m</sup>	IRR Map P-26 <sup>m</sup>										
10-14 -20 <sup>m</sup> Target 2B -9, 130 at B -1, 133.3	10 12 P-19 <sup>m</sup> Targets 0.4, 112.9 0.3, 112.7 0.5, 112.5		12-14 P-23 <sup>m</sup> Target 24.2, 97.5												10-11 Dvad (2B) P-14 <sup>m</sup> Target 5.8, 34.3	
	13-14 Gnd Cmd BA P-27 <sup>m</sup> 11.2, 104.2	12-16 Gnd Cmd 3A Start +33 <sup>m</sup> End +41 <sup>m</sup> AH 50°N			10 Gnd Cmd BA P-32 <sup>m</sup> 50, 63	10-11 Gnd Cmd BA P-33 <sup>m</sup> 50, 30										
16 <sup>m</sup> Bon 7.9, 125.7															12 14 Triad (3B) P-22 <sup>m</sup> Target 16.4, 344.9	
	IRR Scan P-27 <sup>m</sup> Even Scan P-40 <sup>m</sup>				Night Side Spectral P-36 <sup>m</sup>	← CA, KA of Gnd Cmd BA									15-16 Dvad (AB) P-51 <sup>m</sup> Star Cal.	
		P-1 <sup>m</sup> 48 <sup>m</sup> 0 <sup>m</sup> 28 <sup>m</sup> 0 +18 <sup>o</sup>	← 19 <sup>h</sup> 16 <sup>m</sup> +73 <sup>o</sup>	← 0 <sup>m</sup> 28 <sup>m</sup> 0 +18 <sup>o</sup>	← 19 <sup>h</sup> 16 <sup>m</sup> +73 <sup>o</sup>	← 0 <sup>m</sup> 28 <sup>m</sup> 0 +18 <sup>o</sup>									Night Side Spect. 19 <sup>h</sup> 16 <sup>m</sup> +73 <sup>o</sup>	

CC&S Checksum Errors - No Data Taken During Investigation

Fig. 19. Zenith revolutions 218 to 262, extended mission phase I

FOLDOUT FRAME

2

Orbital Science Link	219	221	223	225	227	229	231	233	235	237	239	241	243	
Spectral Scan	Limb/Term Scan P 60 <sup>m</sup>		Limb/Term Scan P 1 <sup>h</sup> 20 <sup>m</sup>		Limb/Term Scan P 1 <sup>h</sup> 20 <sup>m</sup>	←	←	←	←	←	←	←	←	
		1 4 Gnd Cmd 2BA Phobos Ecl P 42 <sup>m</sup> to P 37 <sup>m</sup>	Gnd Cmd A P 32 <sup>m</sup> -85, 25				1 2 Gnd Cmd BA P 32 <sup>m</sup> 86, 357 (B) IRR Scan P 30 <sup>m</sup>							
Triad No. 1 (3B)	1 3 P 32 <sup>m</sup> Targets -81 4, 88 80 3, 75 80.9, 80	5 7 P 33 <sup>m</sup> Targets 77 8, 68 5 78 7, 67 79 3, 63 5	2 4 P 27 <sup>m</sup> Targets 78 2, 63 77 4, 64 5 76 7, 66		1-2 1st 2B 3P 33 <sup>m</sup> Target 83 5, 39	1 3 P 33 <sup>m</sup> Targets 84 2, 337 85 2, 14 83 4, 355	3 5 P 6 <sup>m</sup> Target 20 6, 305 6	1 3 P 32 <sup>m</sup> Targets -81, 350 -81 4, 342 80 8, 358						
	IRR Morn Scan P 28 <sup>m</sup>		IRR Spect 5 6 Gnd Cmd BA P 2 <sup>m</sup> -23, 343				6 7 Gnd Cmd BA P 6 <sup>m</sup> Target B -13 9, 303 8	IRR Morn Scan P 28 <sup>m</sup>						
Triad No. 2 (3B)	4 6 P 5 <sup>m</sup> Target 10 6, 345 6	8 10 P 27 <sup>m</sup> Targets -79 8, 69 -78 7, 67 79 3, 63 5	7 9 Triad (3B) P 3 <sup>m</sup> 15, 340		4 6 P 30 <sup>m</sup> Targets 80 8, 59 81 9, 56 82 9, 53	4 6 P 19 <sup>m</sup> Targets -47 2, 329 1 -47 6, 329 8 47 9, 330 4		4 6 P 19 <sup>m</sup> 1st 2 B's 4, 294 3rd Bon 6 5, 292 5	1 3 P 33 <sup>m</sup> Targets 70 7, 17 70 2, 14 69 2, 14 5	1 3 P 32 <sup>m</sup> Targets -85 3, 222 84 3, 223 83 1, 226	1 3 P 32 <sup>m</sup> Targets 80 4, 330 81 5, 328 82 1, 327	1 3 P 32 <sup>m</sup> Targets -81, 323 80 3, 325	1 3 P 32 <sup>m</sup> Targets -81, 323 80 3, 325	
		11-14 Gnd Cmd A P 21 <sup>m</sup> 49 7, 40 7 IRR Morn Scan P 19 <sup>m</sup>		7 8 Gnd Cmd BA P 23 <sup>m</sup> 60 6, 346 IRR Scan P 22 <sup>m</sup>	IRR Scan P 15 <sup>m</sup>	IRR Scan P 15 <sup>m</sup>	IRR Scan P 15 <sup>m</sup>			IRR Scan P 28 <sup>m</sup> 4 5 Gnd Cmd BA P 15 <sup>m</sup> 45 6, 305 2			IRR Scan P 28 <sup>m</sup>	
Triad No. 3 (1B 1AB)	7-9 P 5 <sup>m</sup> Target B's -7 5, 338.7	15-17 P 5 <sup>m</sup> Target -3 5, 356 3 Max Slew	10-12 P 10 <sup>m</sup> 1st Bon -4, 348 3 Max Slew		9-11 P 5 <sup>m</sup> Target -9 4, 330.3 Max Slew	7-9 P 6 <sup>m</sup> Target B's 10 2, 305.5		7 9 P 24 <sup>m</sup> 1st Bon 10 9, 283.5 2nd Bon 13, 283	4 6 P 23 <sup>m</sup> Target B's -72 5, 6 5 -73 6, 6 5	6 8 P 6 <sup>m</sup> 1st Bon 6,291 Max Slew	4 6 P 22 <sup>m</sup> 1st Bon 83 2, 316 A on 82 5, 310	1 3 P 22 <sup>m</sup> 1st Bon 64 3, 323 Max Slew	4 6 P 6 <sup>m</sup> 1st Bon 20 8, 240 Max Slew	
		IRR Map Scan P 7 <sup>m</sup>	IRR Spect P 12 <sup>m</sup>						Gnd Cmd A P 15 <sup>m</sup> -45, 310 IRR Scan P 13 <sup>m</sup>		IRR Morn Scan P 20 <sup>m</sup>	7-8 Gnd Cmd BA P 14 <sup>m</sup> B on Limb at -90° IRR Scan P 9 <sup>m</sup>	IRR Scan P 4 <sup>m</sup>	
Triad No. 4 (3B)	10-12 P 20 <sup>m</sup> Targets 10 7, 346.3 10 4, 346 9 10 9, 347 1	18-20 P 33 <sup>m</sup> Targets 39 8, 312 6 40 5, 312 5 41 1, 312 9	13-15 P 33 <sup>m</sup> Target 40 8, 312 5		12-14 P 5 <sup>m</sup> Target -10, 329.8	10-12 P 5 <sup>m</sup> 1st Bon -10, 305.2 Max Slews	8-10 Triad (3B) P 20 <sup>m</sup> Target 8 7, 293 2		7-9 Triad (3B) P 5 <sup>m</sup> Targets -15 3, 300 9 -15 7, 300 5 -15 8, 300 1	9 11 P 20 <sup>m</sup> Targets 15 5, 281 3	7-9 P 20 <sup>m</sup> Target 12 2, 270 8	7-11 Triad (3B) P 20 <sup>m</sup> Targets 18 2, 4 5 18 4, 234 8 19 8, 235 1	7-9 P 33 <sup>m</sup> Targets 30 1, 228 8 29 5, 227 8 29 227	
	IRR Map Scan P 24 <sup>m</sup>				IRR Scan P 14 <sup>m</sup>		IRR Scan P 23 <sup>m</sup>	10-11 Gnd Cmd BA P 30 <sup>m</sup> 28 5, 289 5	IRR Scan	IRR Scan P 24 <sup>m</sup>	IRR Map Scan P 23 <sup>m</sup>			
Triad No. 5 (1B 1AB)	13-15 P 37 <sup>m</sup> Target B's 40, 330						11-13 Triad (1B 1AB) P 38 <sup>m</sup> 60 2, 270 3	IRR Map Scan P 31 <sup>m</sup>				10-12 P 55 <sup>m</sup> 1st Bon 85, 330 Overlap B's 11 to Term.		
	16 Gnd Cmd BA P 54 <sup>m</sup> 80,0	21 Gnd Cmd A P 40 <sup>m</sup> 47 8, 333 8		1-14 Calibration Mapping (7BA) P 44 <sup>m</sup> Target 65,301				12 Gnd Cmd A P 53 <sup>m</sup> 77,315	10-11 Gnd Cmd 2 BA P 36 <sup>m</sup> 50 (310, 285)	12 Gnd Cmd A P 38 <sup>m</sup> 50,270		IRR Scan P 24 <sup>m</sup>		
	IRR Even Scan P 55 <sup>m</sup>	←	←		IRR Even Scan P 54 <sup>m</sup>	←	←	←	←	←	←	←	←	
		P 41 <sup>m</sup>	P 37 <sup>m</sup>			P 50 <sup>m</sup>	P 40 <sup>m</sup>	P 55 <sup>m</sup>	P 43 <sup>m</sup>	P 50 <sup>m</sup>	P 58 <sup>m</sup>	P 59 <sup>m</sup>	P 37 <sup>m</sup>	

Footnotes:

- ① TV Picture Data shows 2BA pairs taken.
- ② These frames shown in TV Picture Data.
- ③ This frame not taken.
- ④ TV Picture Data shows BA + 1A taken during this sequence.
- ⑤ This frame shown in TV Picture Data.
- ⑥ TV Picture Data shows a full 'ape' load of data taken during this revolution

Fig. 20. Nadir revolutions 219 to 261, extended mission phase I

239	241	243	245 <sup>Ⓢ</sup>	247	249	251	253	255	257	259	261	
←	←	←										
											1-2 Flyad (BA) P+25 <sup>m</sup> Target B -71.1 217.5	
											3-4 Dyad (2B) P+6 <sup>m</sup> Target 5, 150.5	
1-3 P+12 <sup>m</sup> Targets 80.4, 330 81.5, 325 82.1, 32.		1-5 1st B P+31 <sup>m</sup> Targets 81, 323 80.3, 325										
		IRR Scan P+26 <sup>m</sup>	CC&S Checksum Errors - No Data Taken During Investigation							1-2 Gnd Cmd BA P+12 <sup>m</sup> Fixed CA, KA	5-6 Dyad (BA) P+12 <sup>m</sup> Target 18.1, 133.3	
4-6 P+22 <sup>m</sup> 1st Bon 83.2, 316 A on 82.5, 310	1-3 P+22 <sup>m</sup> 1st Bon 64.3, 323 Max Slew	4-6 P+6 <sup>m</sup> 1st Bon 20.8, 240.8 Max Slew										7-8 Gnd Cmd BA P+9 <sup>m</sup> Target A 40, 110
IRR Morn Scan P+20 <sup>m</sup>	7-8 Gnd Cmd BA P+14 <sup>m</sup> Bon Lumb at 90° IRR S P+9 <sup>m</sup>	IRR Scan P+4 <sup>m</sup>									3-8 Gnd Cmd 3BA P+54 <sup>m</sup> Fixed CA, KA	
7-9 P+20 <sup>m</sup> Target 12.2, 270.8	9-11 Trad (3B) P+20 <sup>m</sup> Targets 18, 234.5 18.4, 234.8 18.8, 235.1	7-9 P+33 <sup>m</sup> Targets 30.1, 228.1 29.5, 22.1 29.227										
IRR Map Scan P+23 <sup>m</sup>												
-12 P+55 <sup>m</sup> 1st Bon 85, 330 Overlap B's 11 to Term												
	IRR Scan P+24 <sup>m</sup>											
← P+58 <sup>m</sup>	← P+59 <sup>m</sup>	← P+37 <sup>m</sup>										

FOLDOUT FRAME

2

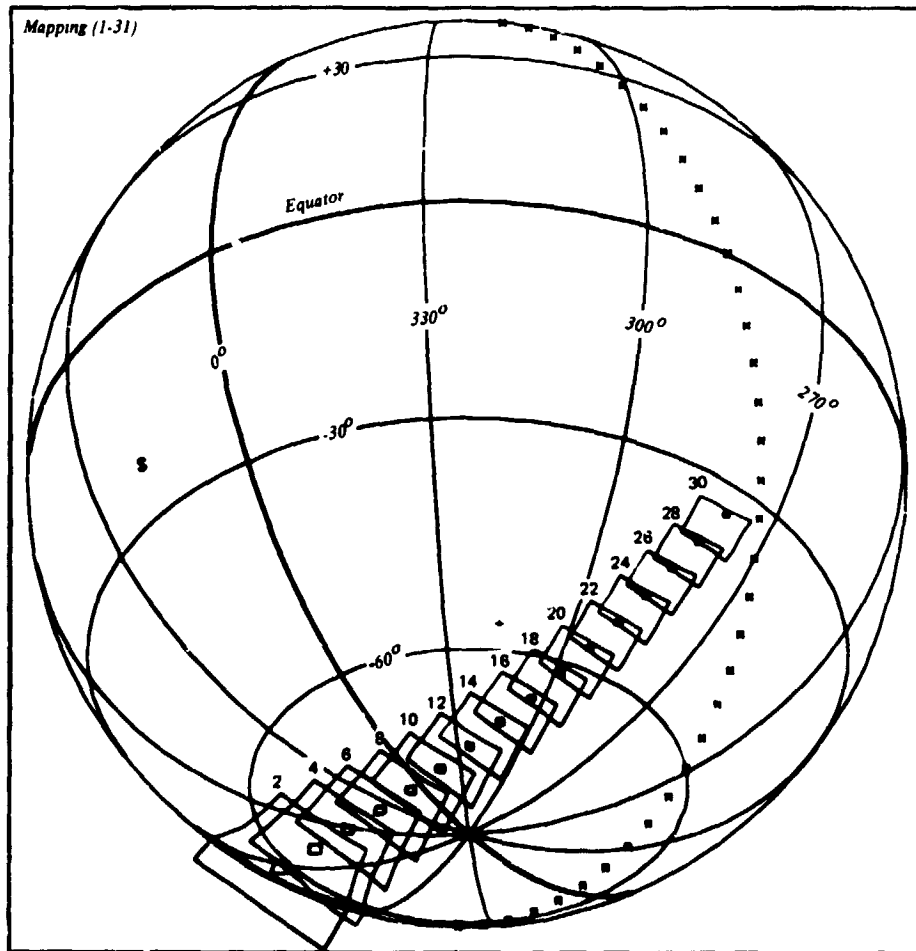


Fig. 21. Post-orbital insertion mapping sequences, revolution I

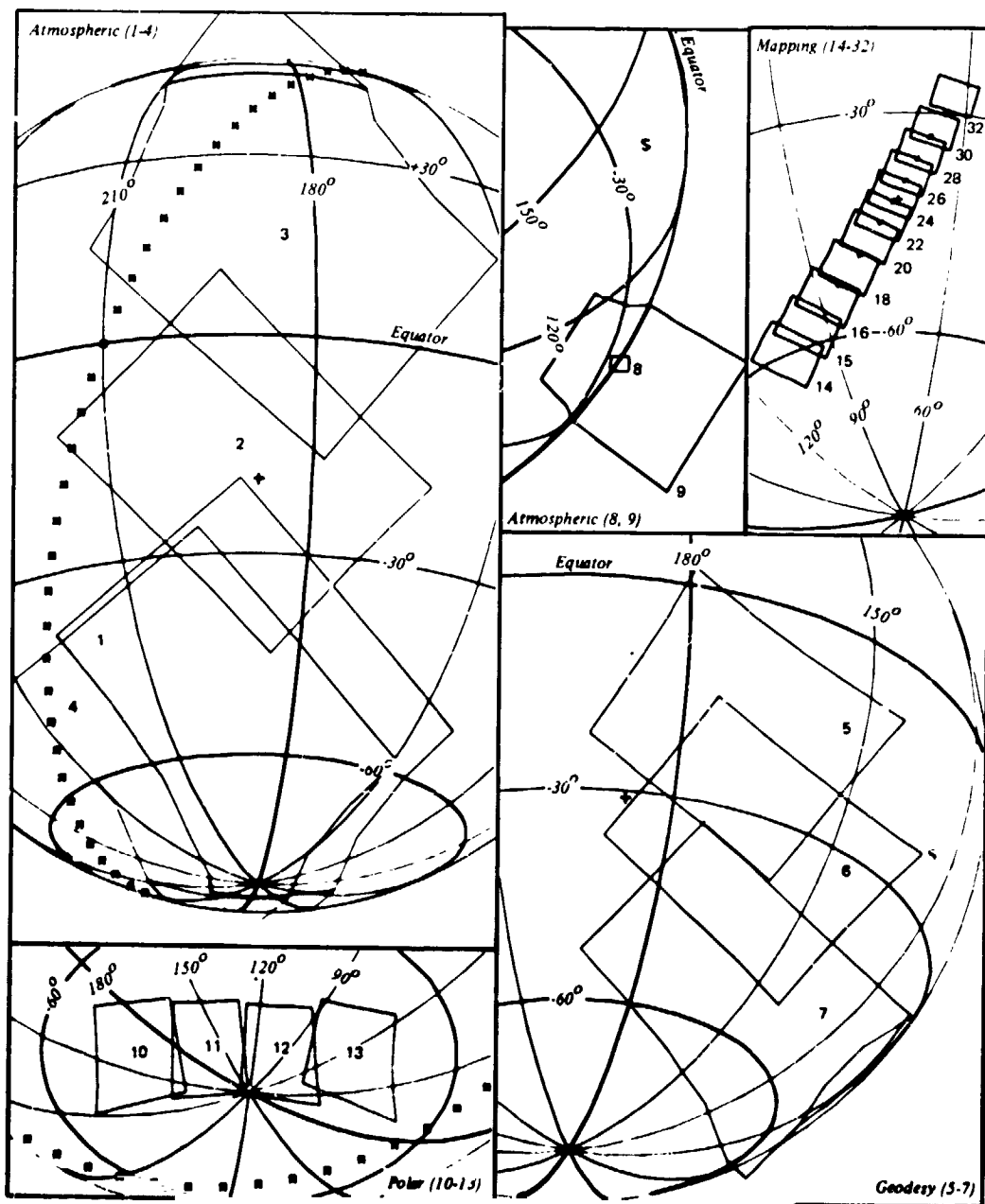


Fig. 22. Interim sequences, zenith revolution 16

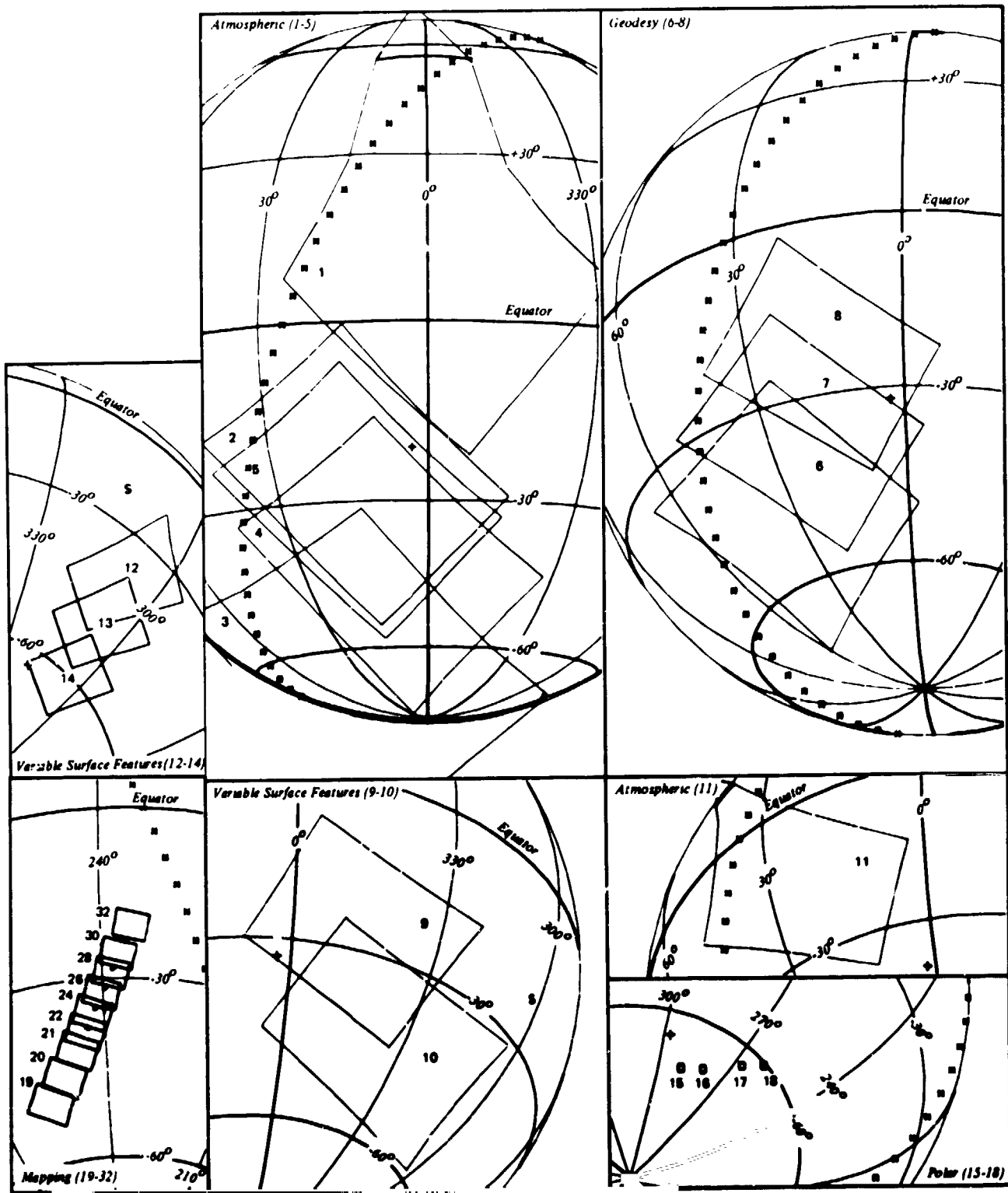


Fig. 23. Interim sequences, nadir revolution 17

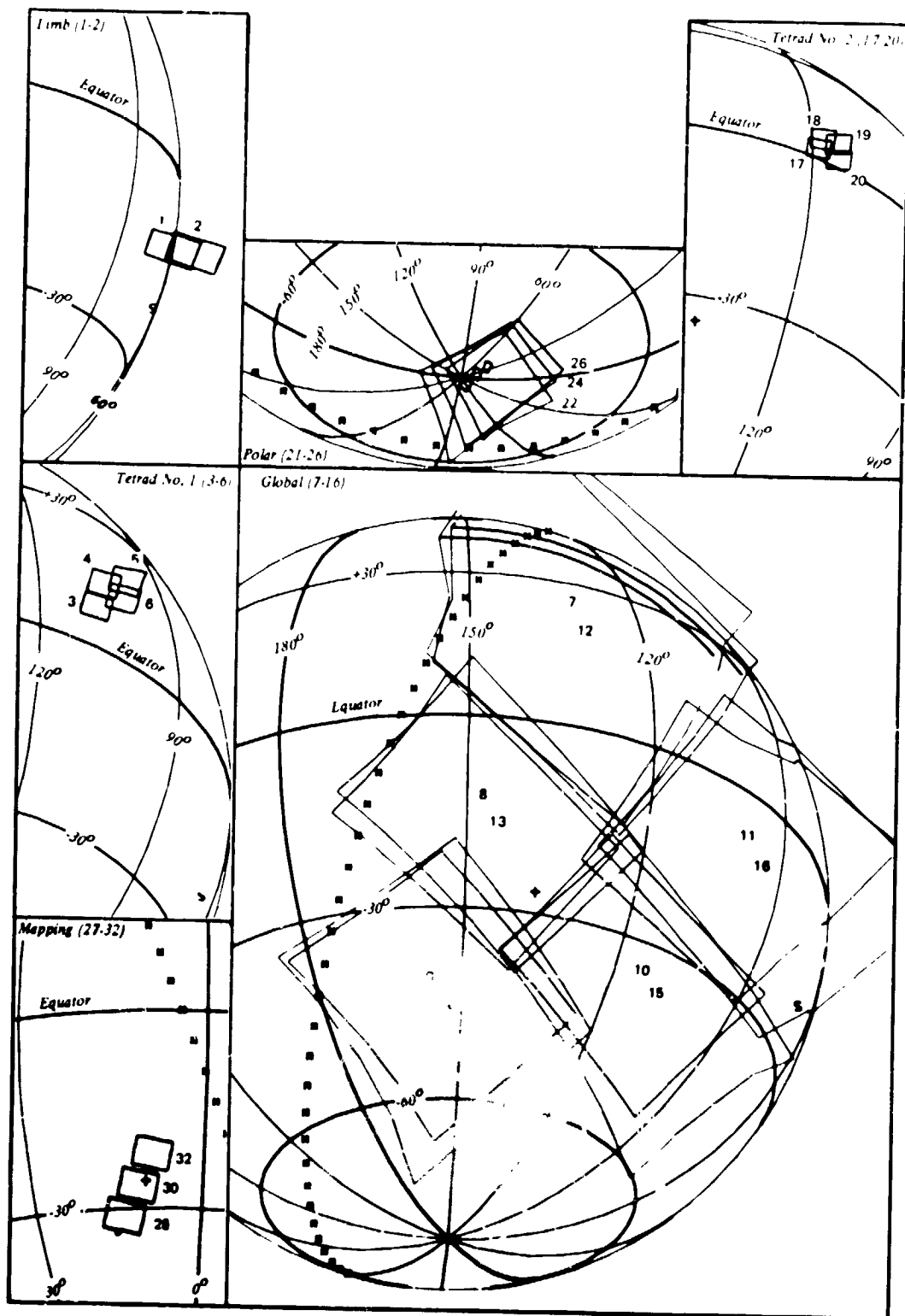


Fig. 24. Reconnaissance I, zenith revolution 26

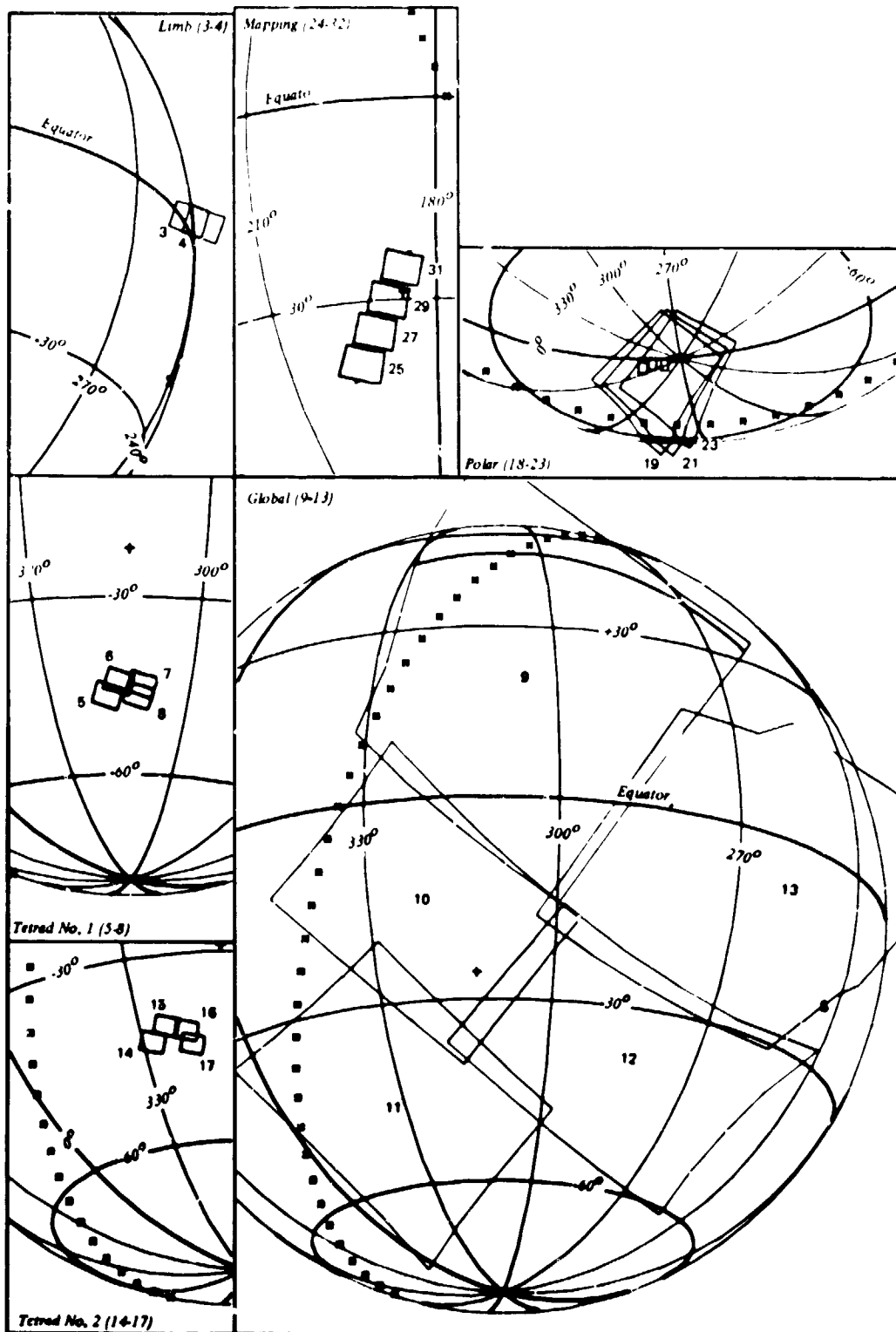


Fig. 25. Reconnaissance I, nadir revolution 27

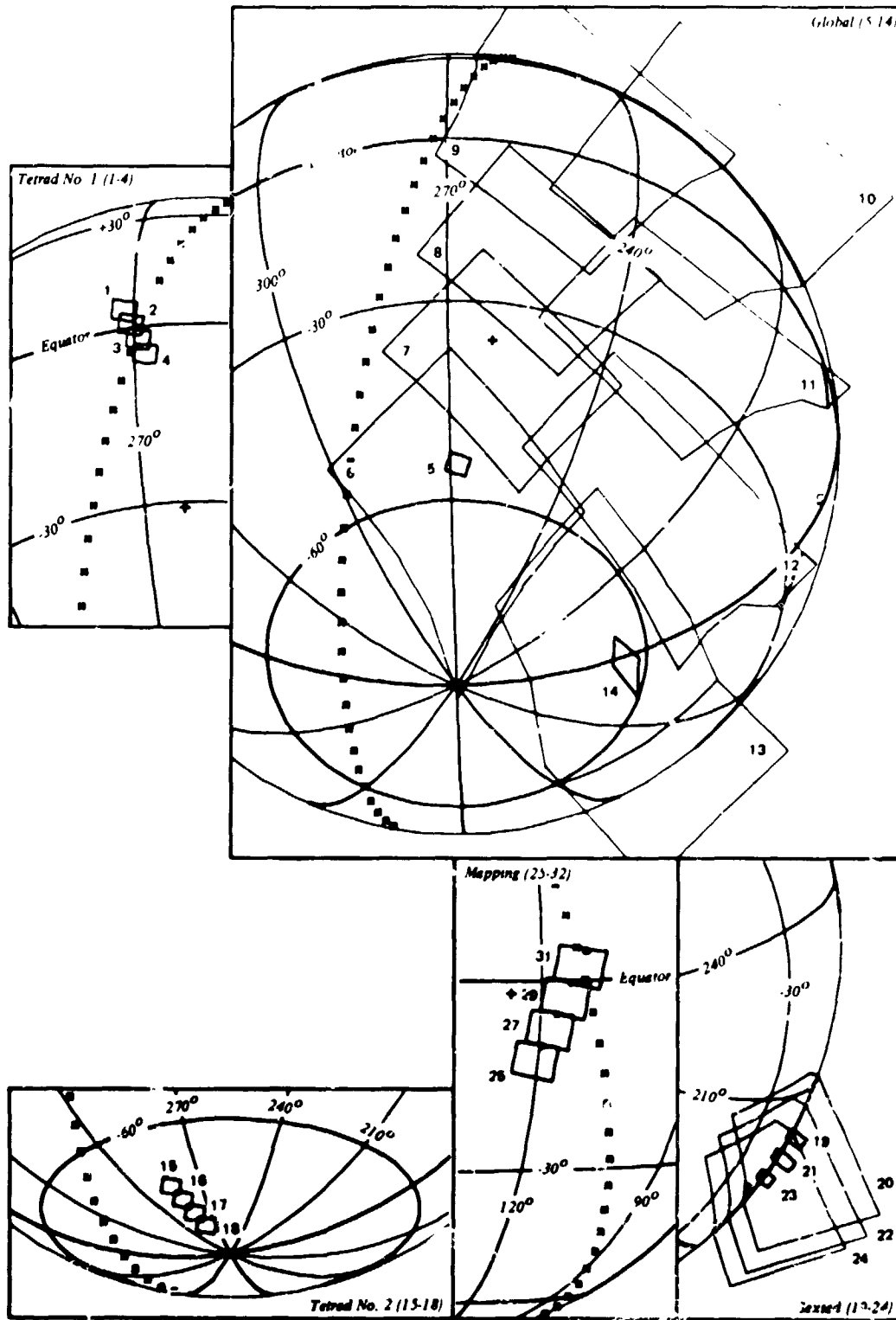


Fig. 26. Reconnaissance II, zenith revolution 7/2

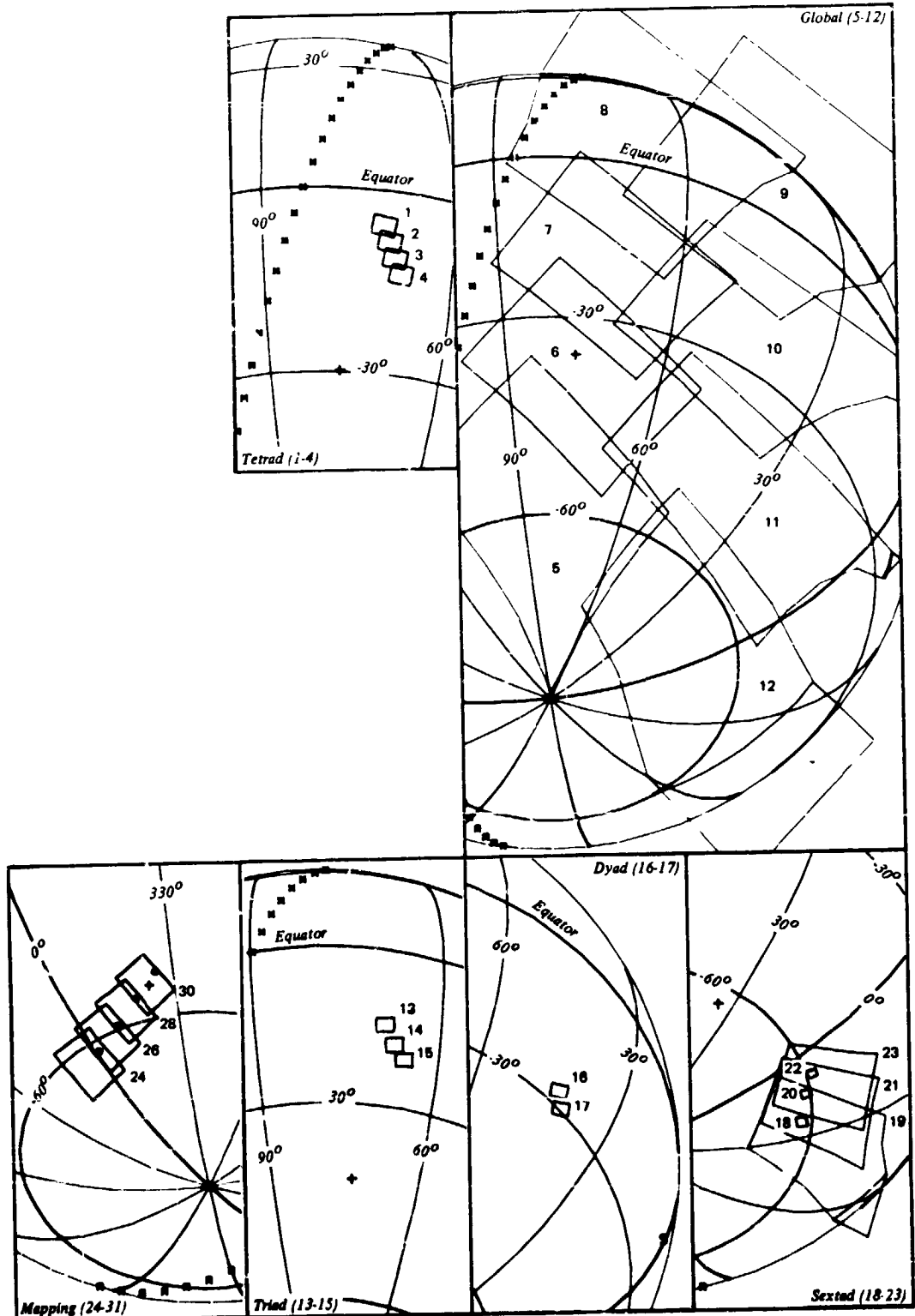


Fig. 27. Reconnaissance II, nadir revolution 75

11-4

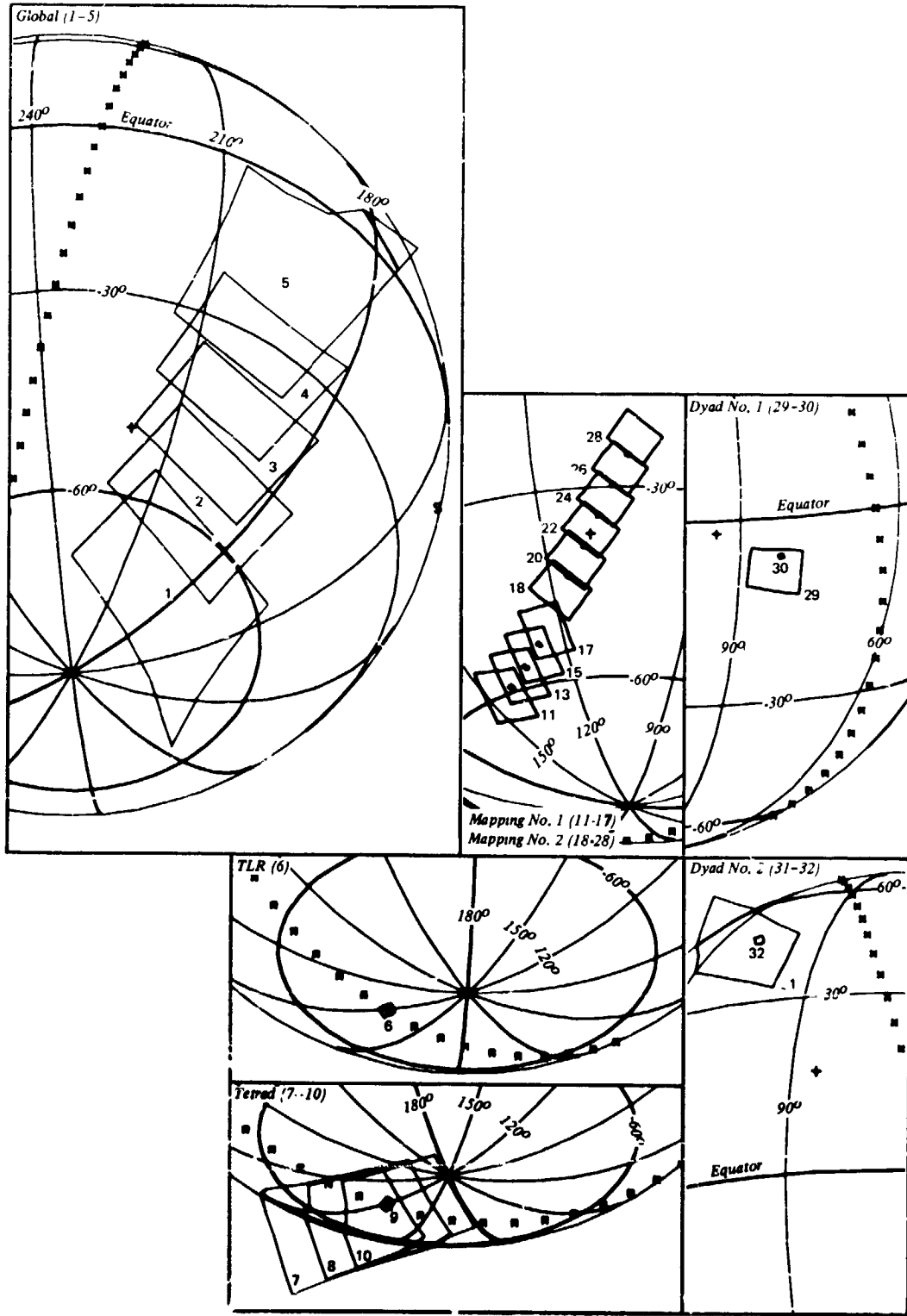


Fig. 28. Mapping cycle I, nadir revolution 119

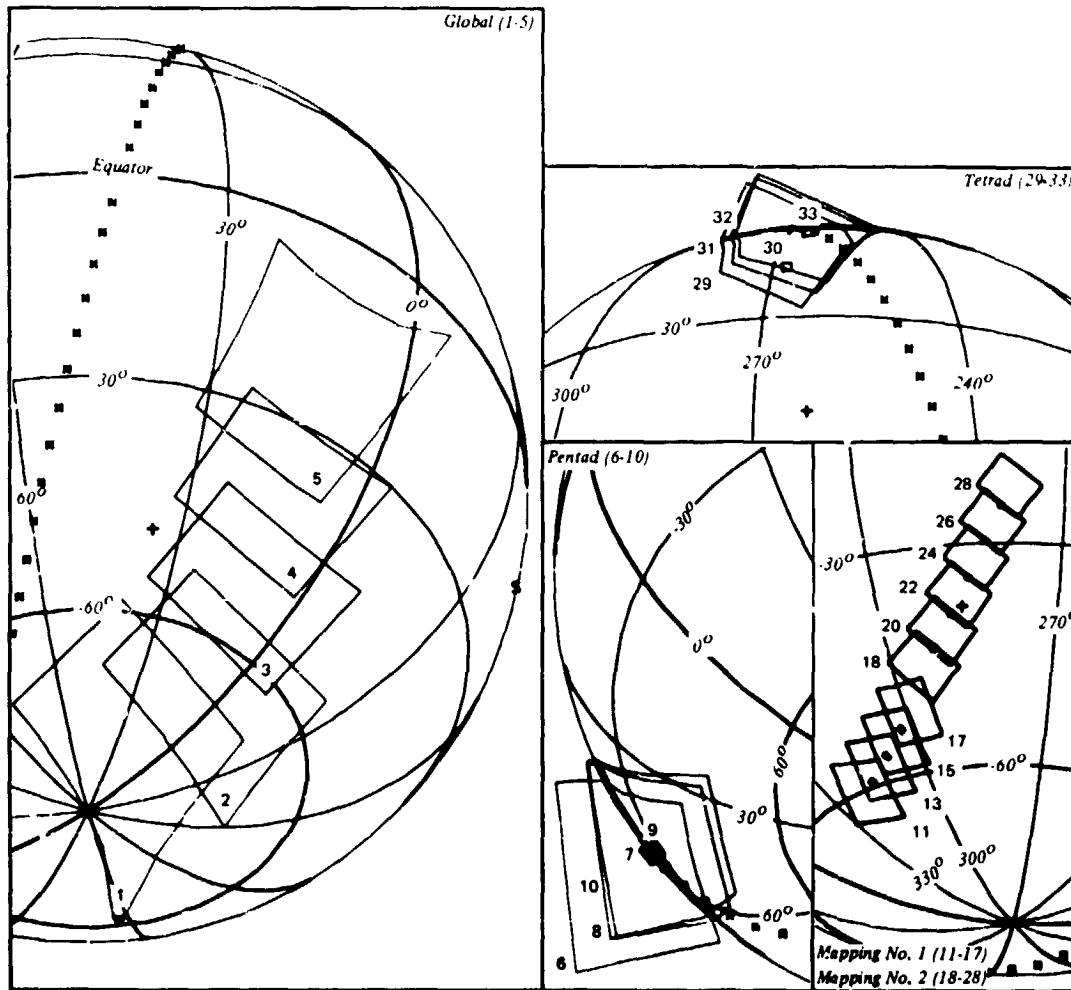


Fig. 29. Mapping cycle I, zenith revolution 120

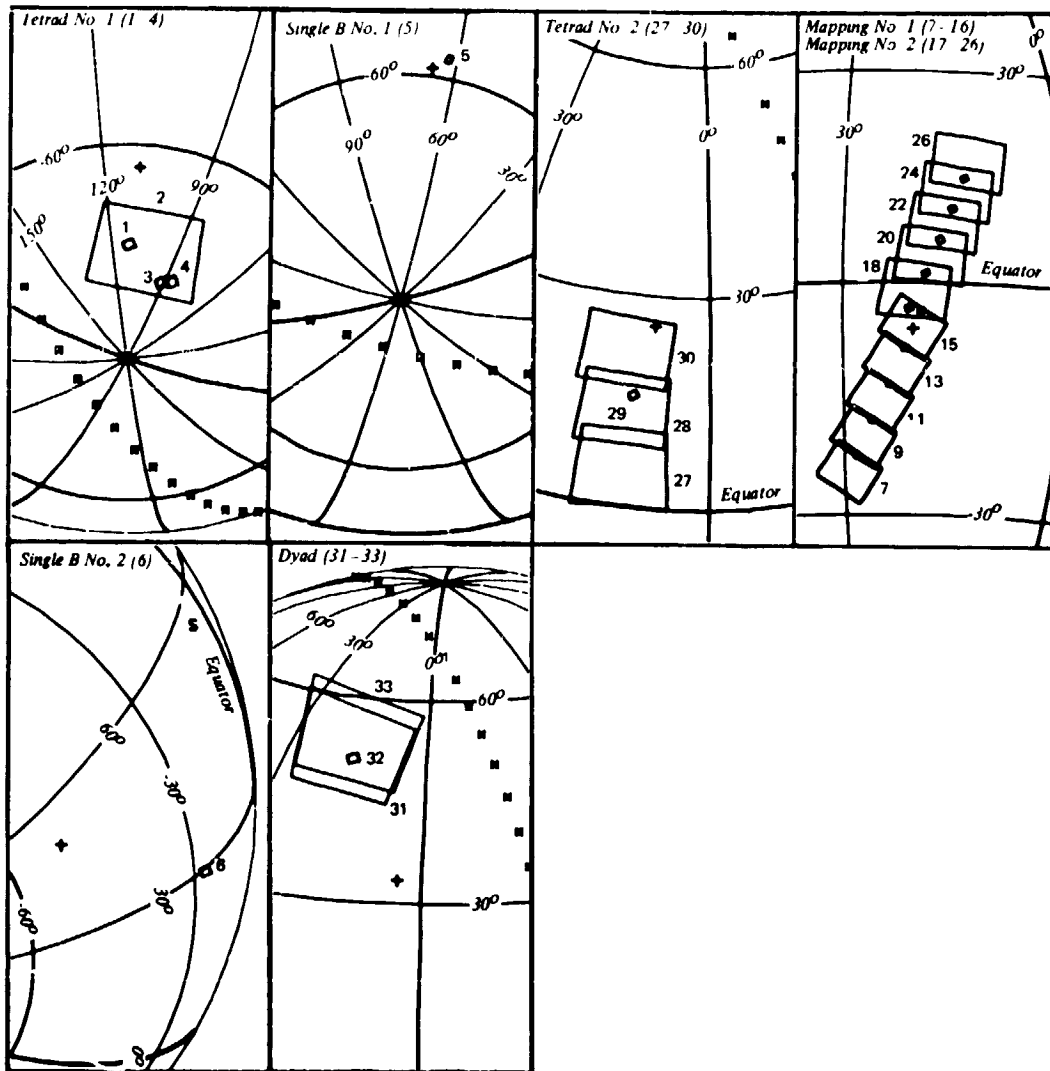


Fig. 30. Mapping cycle II, zenith revolution 174

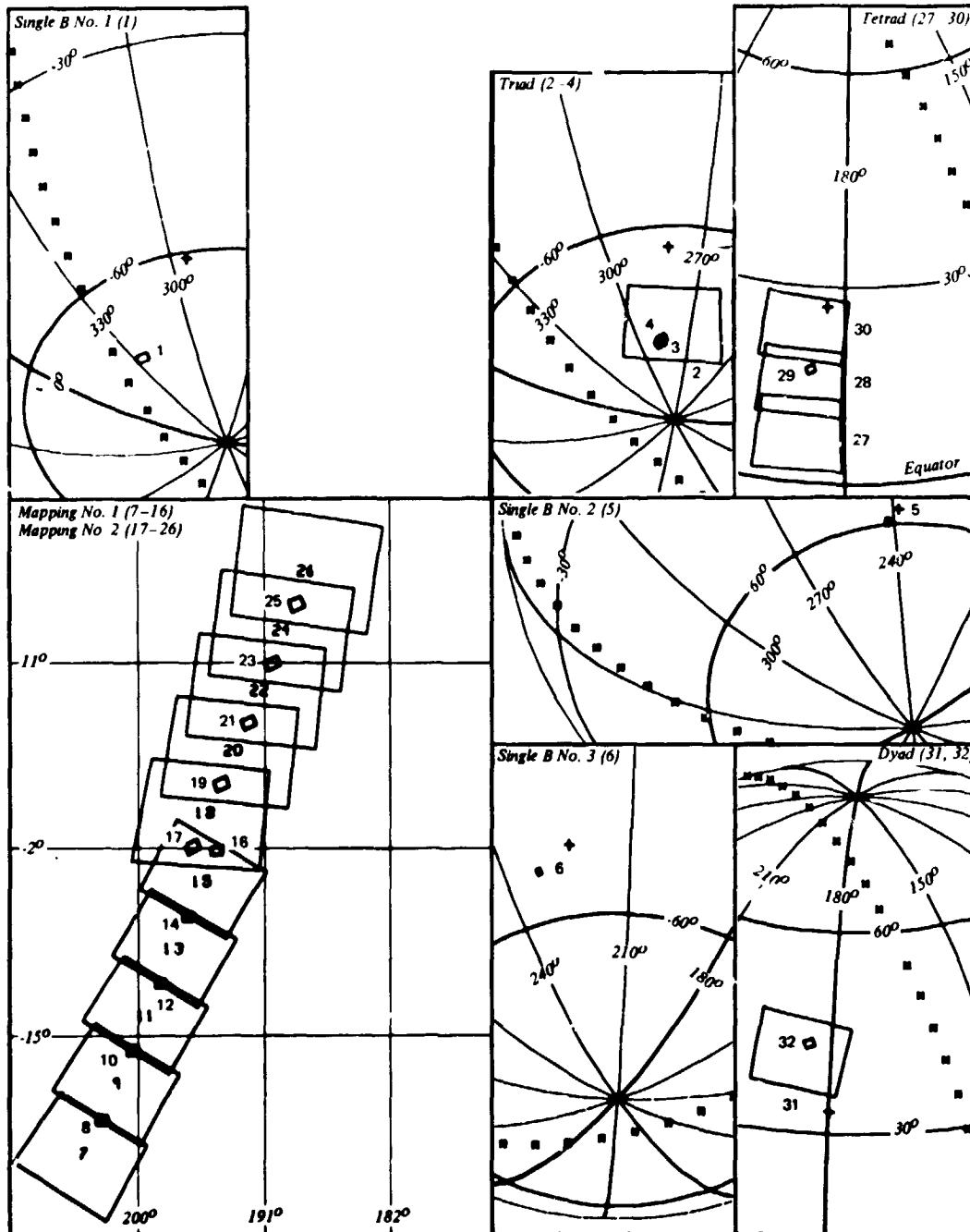


Fig. 31. Mapping cycle II, nadir revolution 175

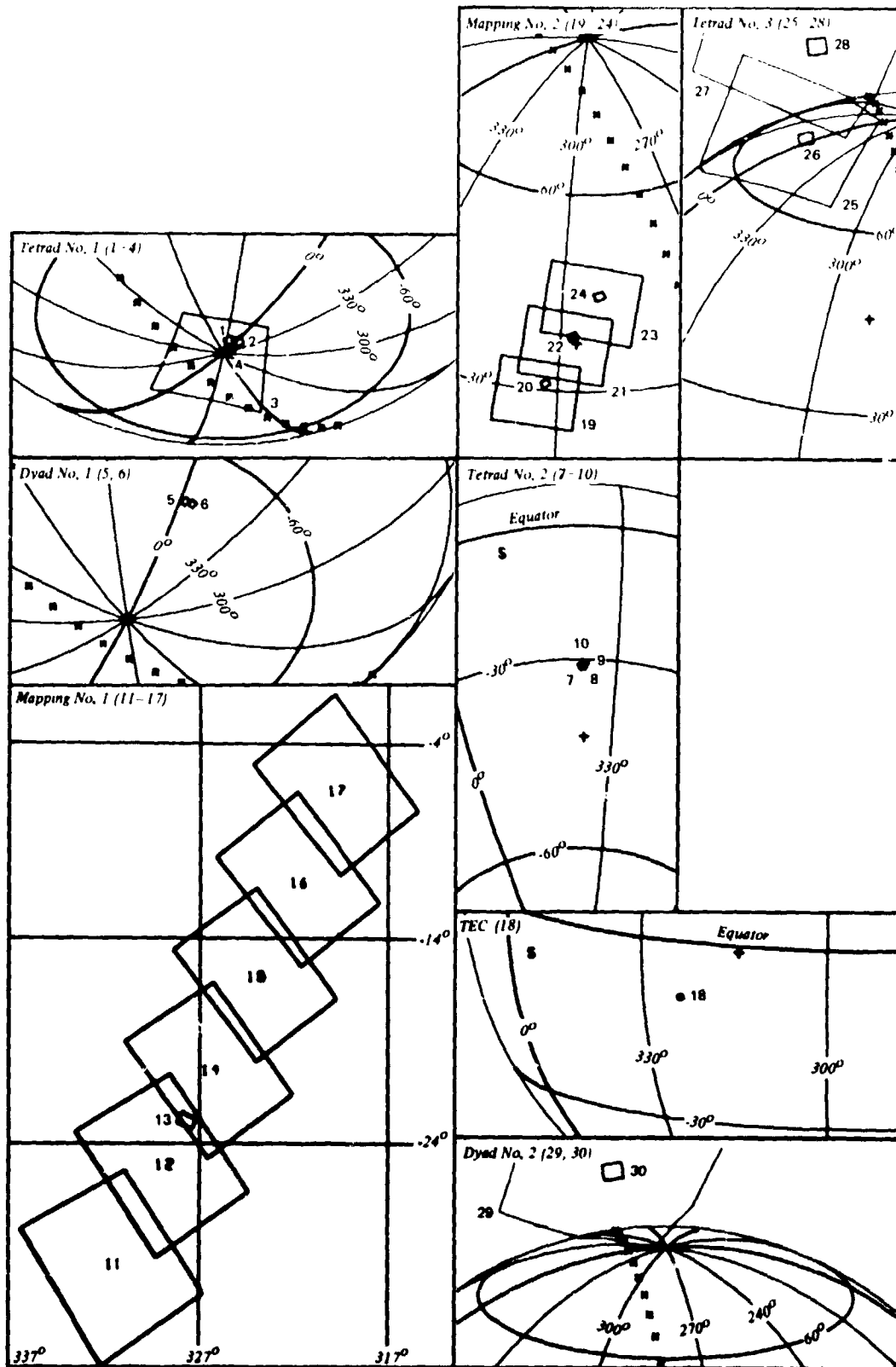


Fig. 32. Mapping cycle III, zenith revolution 188

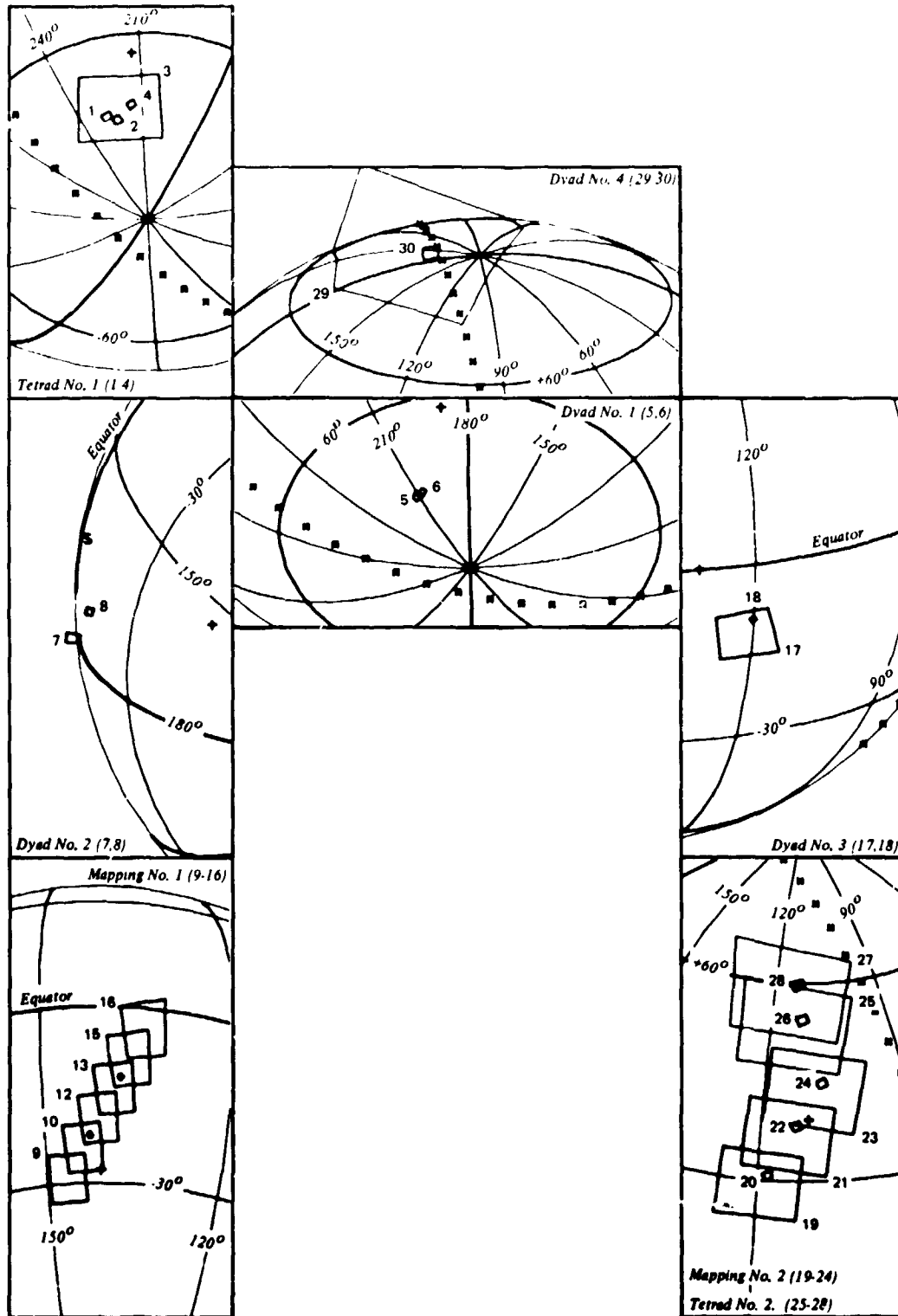


Fig. 33. Mapping cycle III, nadir revolution 189

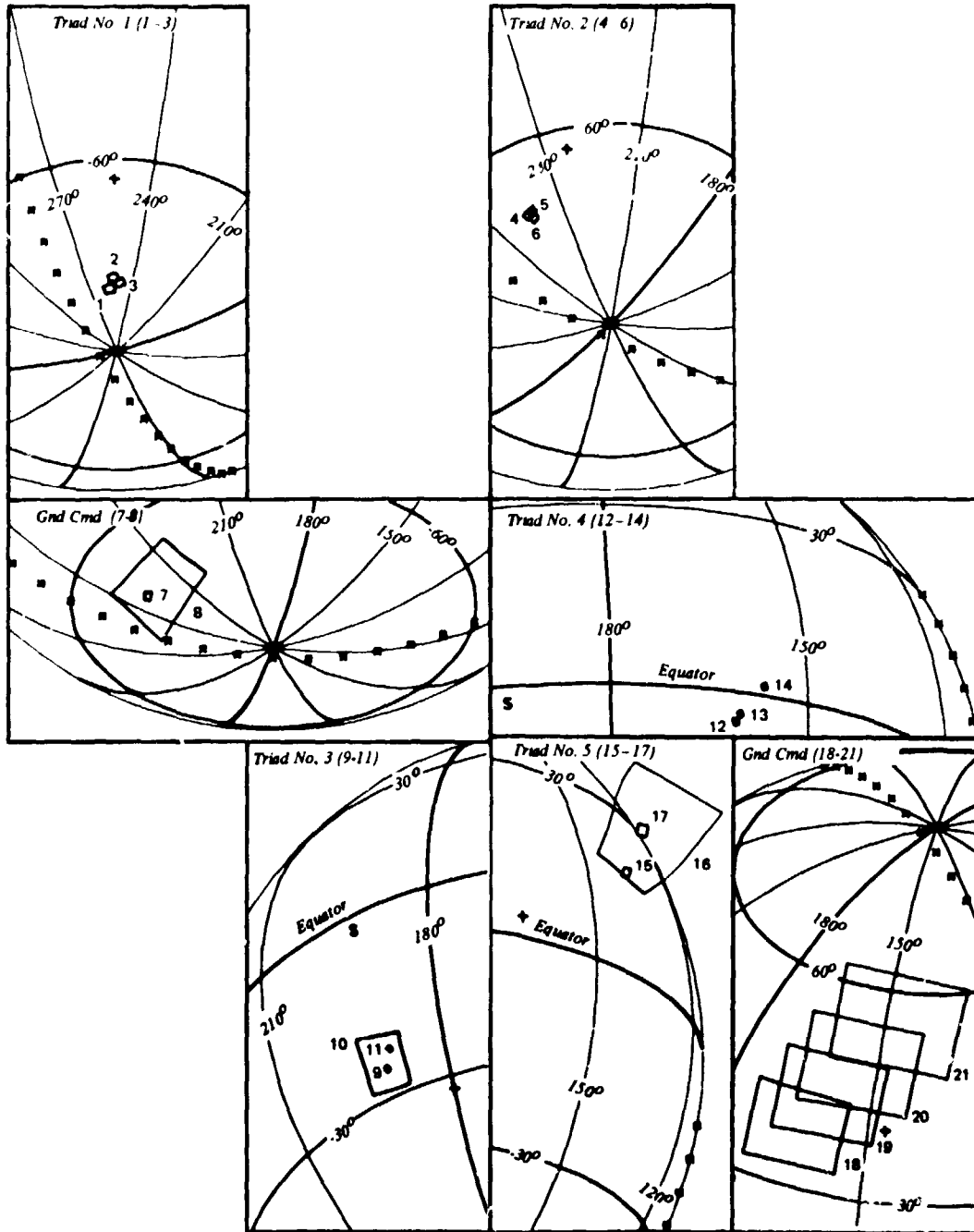


Fig. 34. Extended mission phase I, zenith revolution 220

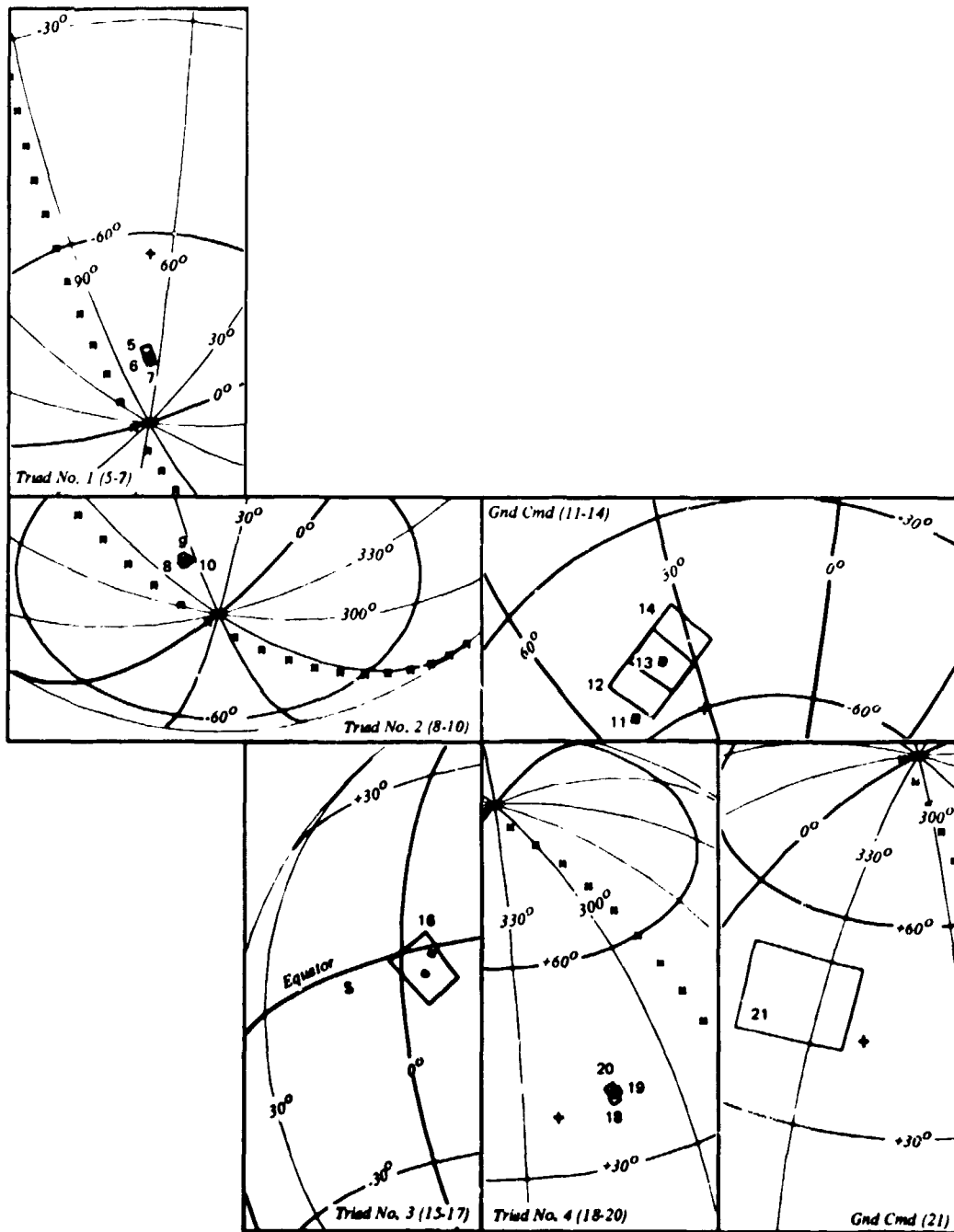
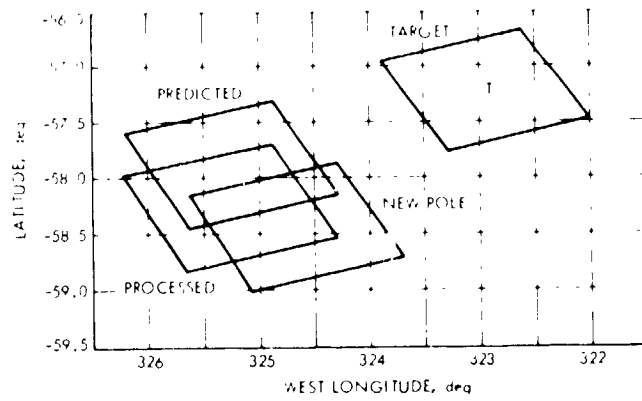
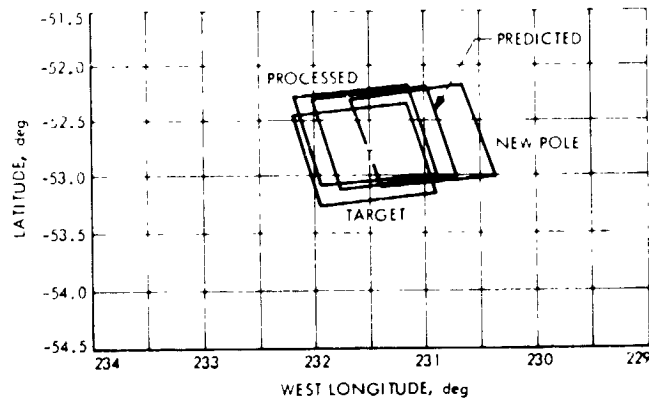


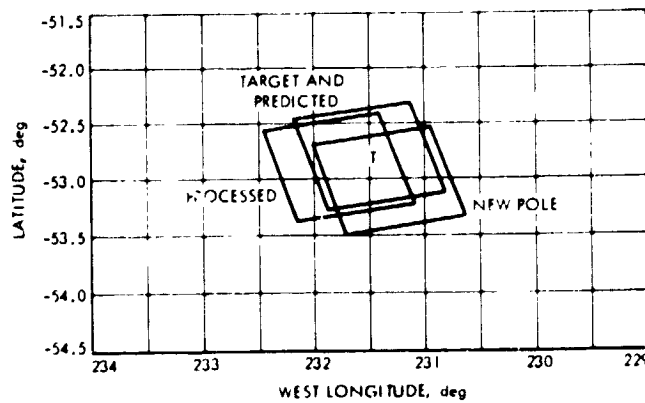
Fig. 35. Extended mission phase I, nadir revolution 221



REV. 157, PICTURE 6B



REV. 173, PICTURE 6B



REV. 173, PICTURE 6B

- NEW POLE - PROCESSED WITH LATITUDE AND LONGITUDE CORRESPONDING TO PROVISIONAL POLE
- PREDICTED - PREDICTED COVERAGE AT T-1 day
- PROCESSED - COVERAGE WITH BEST KNOWN POSITION OF SPACECRAFT AND POINTING
- TARGET - DESIGNED TARGET COVERAGE AT T-5 days

Fig. 36. TV narrow-angle frame targeting